Octavian Knoll

A Probabilistic Approach in Failure Modelling of Aluminium High Pressure Die-Castings

Thesis for the degree of Philosophiae Doctor

Trondheim, May 2015

Norwegian University of Science and Technology
Faculty of Engineering Science and Technology
Department of Structural Engineering

Karlsruhe Institute of Technology
Department of Civil Engineering, Geo and Environmental Sciences
Institute of Mechanics

NTNU – Trondheim
Norwegian University of
Science and Technology

NTNU
Norwegian University of Science and Technology

Thesis for the degree of Philosophiae Doctor

Faculty of Engineering Science and Technology
Department of Structural Engineering

ISBN 978-82-326-0930-7 (printed ver.)
ISBN 978-82-326-0931-4 (electronic ver.)
ISSN 1503-8181

Doctoral theses at NTNU, 2015:137

Printed by NTNU Grafisk senter

Preface

This thesis is submitted to the Norwegian University of Science and Technology (NTNU, Trondheim, Norway) as part of the academic degree “Philosophiae Doctor”, and to the Karlsruhe Institute of Technology (KIT, Karlsruhe, Germany) for obtainment of the academic title “Doktor-Ingenieur”. This was done in the framework of a cotutelle agreement between the two institutions. The work was carried out at the Department of Structural Engineering at NTNU under the supervision of Professor Magnus Langseth and Professor Odd Sture Hopperstad and at the Institute of Mechanics at KIT under the supervision of Professor Karl Schweizerhof. The research was performed within the Fracture and Crack Propagation programme at SFI-SIMLab, Centre for Research-based Innovation at NTNU, financially supported by the Research Council of Norway and national and international industrial partners. Furthermore, the research was financed by Audi AG in the framework of the cooperation Hochschulinstitute Neckarsulm (HIN, Neckarsulm, Germany) between the Institute of Mechanics at KIT and Audi AG. The Audi AG financing was their contribution in kind to SFI-SIMLab.

Abstract

Aluminium high pressure die-castings have become essential elements of a modern car body in recent years. The high pressure die-casting method enables to produce thin-walled components of complex geometries. This advantage is used to create structural nodes and connector elements as one-piece components. These components are subjected to extreme loads such as in crash situations and expected to maintain the structural integrity of the car body. Numerical models are required to analyse the structural behaviour of aluminium high pressure die-casting components and to guarantee their structural reliability.

The material ductility in aluminium high pressure die-casting components is strongly influenced by casting defects. Typical casting defects are shrinkage pores, gas pores and oxide films. These casting defects are caused by the casting system and fluctuations during the casting process. As a result, the casting defects are varying within a component. Moreover, the variation can be separated into a global systematic variation depending on the casting system and a local pseudo-random variation caused by the process fluctuations. A casting defect can be considered as initial material damage which leads to a decrease of the local material ductility. As a result, the material ductility exhibits a global systematic variation and a local pseudo-random variation. The main objective of the present work is the experimental and numerical analysis of these two types of variation.

The main objective of the experimental work was the investigation of the global systematic variation and the local pseudo-random variation in the material ductility of an aluminium HPDC alloy. Here, a generic high pressure die-casting component made of an AlSi9Mn alloy in casting condition was considered. An extensive material characterisation was performed using uniaxial tensile tests. The specimens were machined from different extraction positions as well as from duplicated extraction positions of the generic casting component. Through this sampling approach, it was possible to analyse the systematic variation as well as the local pseudo-random variation in the material ductility. The mechanical analysis of the tensile test results showed a reproducible strain hardening behaviour in duplicated extraction positions, but the failure strain varied between different extraction positions and within duplicated positions. A detailed statistical analysis was performed on the tensile test results and hypothesis tests were applied to identify extraction positions with comparable material ductility. Based on the results obtained from the hypothesis tests, it was concluded that the generic casting component can be separated into characteristic parts of comparable material ductility. Moreover, it was shown that the local pseudo-random variation of the material ductility can be described by a weakest-link Weibull distribution. In addition, the fracture surfaces of selected specimens were examined by a SEM analysis and, as expected, casting defects were found on each fracture surface and identified as the dominating factor for fracture. Besides material testing, bending tests and axial compression tests were carried out on the generic casting component. Especially, the experimental results obtained from the bending tests exhibited strong

scatter. According to the results obtained from material testing, it was concluded that the strong scatter is caused by the global systematic variation and the local pseudo-random variation in the material ductility.

As a result, a probabilistic approach in failure modelling was considered in the numerical work. Hence, it was possible to capture the local pseudo-random variation in the material ductility. The probabilistic failure model was based on the phenomenological Cockcroft-Latham failure criterion and the weakest-link model by Weibull. The required quantities stress state and equivalent plastic strain were given by an isotropic hypoelastic-plastic constitutive model. The focus was put on the numerical prediction of the failure probability of casting components. Usually, the failure probability is estimated from a Monte-Carlo simulation based on various finite element simulations using a pseudo-randomly distributed critical failure value. In the present work, an approach was presented to predict the failure probability from a single finite element simulation. Both approaches were compared in numerical analysis and it was shown that both approaches lead to the same prediction of the failure probability. The approach based on the direct computation of the failure probability was applied in finite element simulations of the bending test and the axial compression test of the generic casting component. According to the material characterisation, the FE model of the generic casting component was partitioned into three parts. For each part the parameters of the constitutive model and the probabilistic failure model were found from the corresponding experimental results. It was demonstrated that the numerically predicted failure probability and the experimentally estimated failure probability are very well correlated in both load cases. Consequently, the applied probabilistic failure model was considered as validated. Moreover, a novel approach for the pseudo-random distribution of a critical failure value was presented and the concept of the uncoupled modelling approach was introduced. Due the uncoupled modelling approach, it was possible to perform mesh convergence studies on finite element models using a pseudo-randomly distributed critical failure value. However, the probabilistic failure model captured only the local pseudo-random variation in the material ductility. Hence, a through-process modelling approach was presented based on a casting simulation result and the definition of casting qualities. This approach was only numerically investigated.

Acknowledgements

I would like to express my deep gratitude to my supervisors Professor Magnus Langseth and Professor Odd Sture Hopperstad at NTNU as well as my supervisor Professor Karl Schweizerhof at KIT for their motivation, support and guidance throughout the course of this work. They gave me the opportunity to do this work which challenged me and made me a better engineer. I also would like to thank my industrial supervisors Thomas Hambrecht and Arjan Strating at Audi AG who kept my focus on the industrial application of the research.

I wish to thank all my colleagues at the Department of Structural Engineering at NTNU and at the Institute of Mechanics at KIT for creating an inspiring and pleasant working environment at a high knowledge level. I am very grateful to Trond Auestad and Tore Wisth at the Department of Structural Engineering at NTNU for their great help to realise my extensive experimental test program. I am also very grateful to Torodd Berstad at the Department of Structural Engineering at NTNU for his assistance in numerical problems. Furthermore, I would like to thank my friend Basil el Jundi at the Department of Biology at Lund University (Lund, Sweden) for his support in the statistical analysis of experimental test data.

Especially, I wish to thank my mom and my dad for their support throughout my whole life. I wish to thank my sister and her family for always being there for me. Thanks to all my dear old friends Basil, Basti, Didi and Lars for distracting me whenever I needed it. Further, I would like to thank Ida and Gaute for giving me a home in Norway. Special thanks goes to Espen for great discussions and Christoph for unforgettable conferences.

Finally, I wish to thank my lovely wife Nina for believing in me. She was my muse whenever I missed inspiration. She was my strict supervisor whenever I was tired. She was my best friend whenever I needed one. She has given us our son Moritz. He is just a great boy and makes me always laugh. I love you two.

Contents

Chapter 1

Introduction

The lightweight design of a modern car body is characterised by weight reduction and an increase of structural stiffness and crashworthiness. These requirements are met using high strength steels, aluminium alloys and fibre reinforced plastics for the structural components. The structural behaviour is defined by the component geometry and the applied material. Further, the properties of the applied material are mostly influenced by the manufacturing process. Especially, aluminium high pressure-die castings have become essential elements in the car body design. The high pressure-die casting method enables to produce thin-walled aluminium components of complex geometries. This advantage is used to design performance optimised and multifunctional components. Therefore, aluminium high pressure-die casting components are mainly used as structural nodes and connector elements where high forces are introduced locally and various components need to be connected. However, the material ductility is dominated by casting defects which are caused by the high pressure-die casting process. As a consequence of the casting defects, the material ductility varies strongly within a component. This variation needs to be considered particularly in the crash design. Here, the most common tool for analysing the crash design is the finite element method. The deformation and failure behaviour of structures subjected to various loading scenarios can be predicted numerically using the finite element method. A reliable numerical design of an aluminium high pressure-die casting component requires that the variation in the material ductility caused by the casting defects is taken into account. This requirement is the overall objective of the present work. In the following, the motivation, the objectives and the scope of the present work are presented.

1.1 Motivation

The present work is motivated by the car body of the current Audi A8 (third generation (D4), production 2010 - present), see Figure 1.1.1. In particular, the two aluminium high pressure die-casting components in the rear-end are in the focus. For the first time, the high pressure die-casting method is used to produce such large structural components which are subjected to extreme loads in a rear-end crash. Furthermore, these two components are applied in casting condition due to the use of a special aluminium casting alloy. This means that these two components are processed directly after casting without any heat treatment which reduces significantly the particular production costs. Here, the applied aluminium casting alloy was introduced by Aluminium Rheinfelden GmbH in 2004 and is technically called Castasil-37. The objective of the entire automotive in-

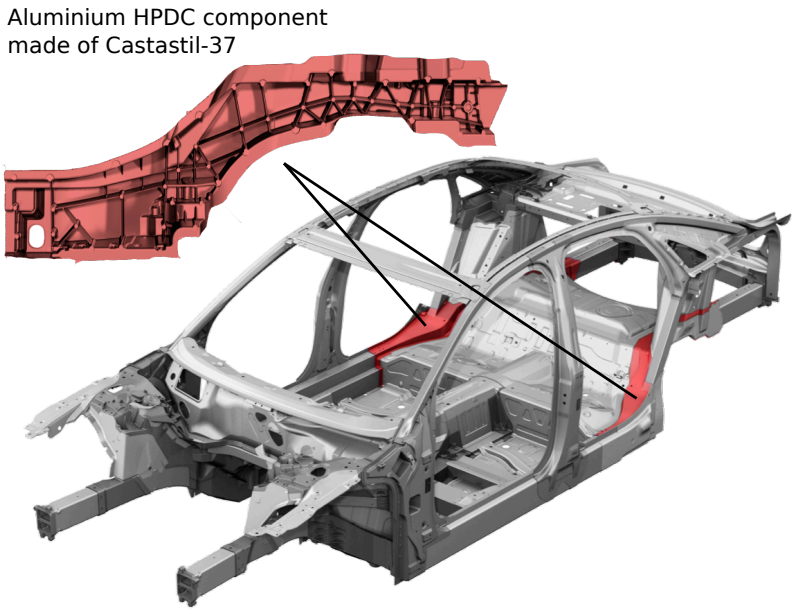

Figure 1.1.1: Application of two high pressure die-casting components made of the aluminium alloy Castasil-37 in the car body of the current Audi A8 (third generation (D4), production 2010 - present).

dustry is to increase the application of large structural components made of aluminium high pressure die-casting alloys like Castasil-37. Consequently, this increases the request of numerical material models which allow predicting the deformation and failure behaviour of aluminium casting alloys, especially when they are applied in casting condition.

1.2 Objectives

The main objective of the present work is the development of a numerical material model which allows to predict accurately the deformation and failure behaviour of aluminium casting alloys considering the influence of casting defects on the material ductility. Furthermore, the application of the numerical model in industrial applications should be taken into account. This means that computational costs are a relevant key factor. The present work is focused on the aluminium casting alloy Castasil-37. In summary, the main objective of the present work can be divided into three objectives which are defined as follows:

- Experimental analysis of the variation in the material ductility based on component and material testing.
- Development and numerical implementation of a material model for aluminium high pressure die-castings.
- Numerical analysis and validation of the material model based on finite element simulations of material and component tests.

1.3 Scope

The scope of the present work can be divided into three parts:

- Theoretical background: The high pressure die-casting process, the composition and the properties of aluminium casting alloys and the application of high pressure die-casting components in the car body need to be described to obtain a deeper understanding of the problem. This is given in Chapter 2. As already mentioned, the material ductility of aluminium casting alloys exhibits a strong variation. The analysis of experimental results which are expected to show a strong variation requires the use of statistical methods. Therefore, the basics of probability theory and statistics are introduced in Chapter 3. The main objective of the present work is the numerical prediction of the deformation and failure behaviour of aluminium high pressure die-castings. Hence, a material model consisting of a constitutive model and a failure criterion has to be defined. However, failure criteria are usually applied in a deterministic sense. This requires that all involved quantities need to be exactly known. This requirement cannot be met for aluminium casting alloys. Here, a probabilistic approach in failure modelling has to be applied. The probabilistic approach takes the variation in material quantities into account and assumes that the material quantities are given in form of probability distributions. The basics of failure modelling including the basics of continuum mechanics and finite element modelling are presented in Chapter 4. The field of probabilistic failure modelling with focus on the weakest-link approach is introduced in Chapter 5. A literature review on failure modelling of casting materials is provided in Chapter 6.

- Experimental work: The aim of the experimental work is to characterise the material behaviour of the aluminium casting alloy Castasil-37 and to analyse the variation in the material ductility. Material test specimens are usually machined from sheets. However, high pressure die-castings consist of ribs, ejector domes and varying wall thicknesses and, consequently, the flow conditions are different to the ones in a sheet. Since the flow conditions strongly influence the material behaviour, the use of sheets would provide artificial results. Here, material test specimens have to be machined from a generic high pressure die-casting component. Since it is expected that the material ductility of the aluminium casting alloy Castasil-37 exhibits a strong variation, a material characterisation has to be focused on analysing the variation. Here, the questions “How can the variation be described?” and “Does the variation show a spatial dependence?” need to be answered. This requires a detailed statistical analysis of the test results. In the current work, a generic U-shaped component including ribs and ejector domes is investigated. The two mentioned questions are answered using tensile test specimens which are machined from different extraction positions of the generic component and, further, from the same extraction position of various generic components. It is noted that the material characterisation is restricted to the analysis of the material tensile failure behaviour under quasi-static loading conditions. Besides this, the influence of the variation in the material ductility on the structural behaviour is analysed using component tests. The results obtained from the component tests are presented and discussed in Chapter 7 and the results obtained from the material characterisation are presented and discussed in Chapter 8.

- Numerical work: The numerical prediction of the deformation and failure behaviour of aluminium high pressure die-castings requires the definition of a material model.

As already mentioned, a probabilistic approach in failure modelling has to be applied to capture the variation in the material ductility of aluminium casting alloys. In the present work, the finite element method is used for the numerical analyses. The use of a probabilistic failure criterion leads to a pseudo-random distribution of the critical failure value within a finite element model. A single simulation of such a finite element model provides only one possible result and this result does not allow to draw any conclusion of the failure behaviour. Here, the prediction of the failure probability is the goal when a probabilistic failure criterion is applied. The most common approach to estimate numerically the failure probability is a Monte-Carlo simulation. This means that multiple simulations of a finite element model have to performed and a new pseudo-random distribution of the critical failure value is applied in each simulation. As a result, the failure probability can be estimated. The numerical work is focused on the prediction of the failure probability of aluminium high pressure die-castings. A novel approach to compute directly the failure probability using a single simulation is introduced. It is analysed if the failure probability obtained from this approach leads to the same failure probability estimated from an equivalent Monte-Carlo simulation. Moreover, different methods to distribute pseudo-randomly the critical failure within a finite element model are analysed. Numerical studies are performed on the uniaxial tensile tests and the component tests which are investigated in the experimental work. The comparison of the numerical and experimental results enables to validate the probabilistic approach in failure modelling. The applied material model consisting of a constitutive model and a probabilistic failure criterion based on the weakest-link approach and its implementation are presented in Chapter 9. The results of the numerical studies are presented and discussed in Chapter 10.

Chapter 2

About Aluminium Die-Casting

The casting process is probably one of the oldest manufacturing technologies. Liquid material is poured into a mould that includes the negative shape of the casting product. When the material is solidified the casting can be removed by opening or braking the mould. Most common casting materials solidify due to cooling or chemical reactions. In general, casting materials require, in liquid form, a high viscosity to flow into all parts of the mould and sufficient strength properties in solid form to meet the structural requirements. Hence, casting materials are evaluated regarding their casting and strength properties. The best known casting materials are concrete, metal alloys and plastics. In Figure 2.0.1, examples of castings made of these materials are presented. The casting technique enables to produce components of complex geometries in any size with high accuracy. Since the costs of the casting set-up and the moulds are relatively high, casting components are usually produced in large scale production. Moreover, casting components are manufactured individually when an alternative is not realisable or too cost intensive. In general, the applied technique is defined by casting material, shape, size and usage of the casting product. Common for all techniques is the fact that the work before and after casting takes most of the time and the casting itself is done within comparatively short time. The form filling is characterised by a complex flow and temperature field which reacts sensitively to slight fluctuations of the external environment and process parameters. This means that in reality a multiple repetition of an identical casting set-up produces varying flow and temperature fields. Especially, the solidification is influenced by this physical field and, further, the solidification influences the strength properties. Therefore, a variation of the flow and temperature field lead directly to a variation of the strength properties and a pseudo-random behaviour of the strength properties is natural. It is noted that even in large scale production with a high standard of quality this variation cannot be avoided.

The aim of this chapter is to introduce the high pressure die-casting method which enables to cast aluminium and magnesium alloys. Here, the basics of the process technology is described and the chemical composition of die-casting alloys is shown. The formation of casting defects and their influence on the material behaviour are discussed. Furthermore, the application of die-casting components in the car body is demonstrated by an example and the requirements on the structural behaviour of these components are shown. This chapter only covers briefly the topics since these are already well discussed in the technical literature. Especially, the standard book about metal casting by Campbell [17] is highly recommended to get a deeper understanding.

(a) V8 engine block made of aluminium, see Chevy Hi-Performance [19].

(b) Concrete bridge, see Schlaich Bergermann und Partner GmbH [102].

(c) Tool housing made of plastic, see Impetus Plastics Group [62].

Figure 2.0.1: Examples of casting products made of metal, concrete and plastic.

2.1 High Pressure Die-Casting Process

The High Pressure Die-Casting (HPDC) is a metal casting process which is characterised by injecting molten metal under high pressure into a mould cavity. This casting method enables to produce components with complex geometries in series. Here, only nonferrous metals such as aluminium, magnesium or zinc alloys can be used. An excellent example of an HPDC component is illustrated in Figure 2.1.1. It shows an aluminium gearbox of a KTM motorcycle and it demonstrates the geometrical complexity that becomes realisable. The basics of the HPDC production technique are introduced in the following. A detailed introduction can be found in the technical literature by Campbell [17] and Ostermann [92].

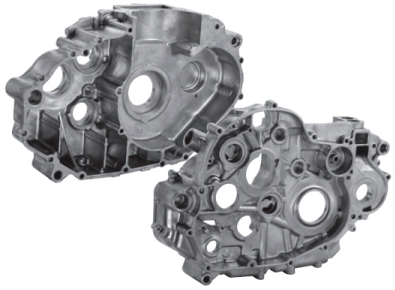

Figure 2.1.1: Aluminium HPDC gearbox of a KTM motorcycle, see Aluminium Rheinfelden GmbH [6].

In general, HPDC machines are classified into hot-chamber and cold-chamber machines. If casting machine and holding furnace are directly connected to each other, it is called a hot-chamber HPDC machine. Consequently, if casting machine and holding furnace are separated, it is called a cold-chamber HPDC machine. In Figure 2.1.2a, the casting process is illustrated based on a cold-chamber machine. It can be seen that the

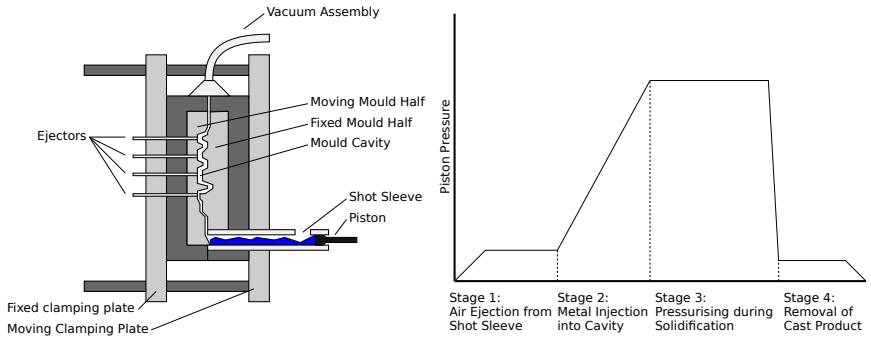

(a) HPDC machine. **(b)** Piston pressure.

Figure 2.1.2: Exemplary drawing of cold chamber HPDC machine with vacuum assembly and piston pressure during HPDC process.

machine consists of two parts. One machine part is fixed, while the other machine part is hydraulically movable to open and close the mould cavity. The two mould halves are mounted to these machine parts. Besides the negative shape of the casting component, the mould cavity includes incoming and outgoing casting channels. Usually, the mould is made of an hardened high strength steel which resists the high temperature of the melt. The two parts of the mould are technically called the casting tool. In the first step, the melt is poured into the shot sleeve. Then, the melt is injected by the piston into the cavity. The shot sleeve can be arranged in vertical or horizontal direction. After solidification, the machine opens and the casting component can be removed using ejectors. It is common to apply a release agent on each mould part prior to casting. The piston pressure is essential for the quality of the solidified microstructure of the casting material. Hence, the melt in the cavity is pressurised by the piston until the melt is solidified, see Figure 2.1.2b. Due to constant pressure during solidification, the formation of pores is reduced and the surface quality is improved. Furthermore, the solid material structure can additionally be improved by vacuuming the cavity. Gas within the melt and gas due to vaporised released agent is removed by the vacuum and the amount of gas pores is strongly reduced. It is common to combine the pressurising method with the vacuum method to produce casting components of high quality. Components made of an aluminium alloy are usually produced using a vertical cold-chamber HPDC machine with vacuum assembly.

The casting production cycle takes only a few seconds. The cavity is completely filled out between 20 msec and 200 msec depending on the component size. The melt reaches velocities of up to $140\,{}^{\mathrm{m}}/_{\mathrm{sec}}$. Here, the material flow is characterised by turbulent flow conditions. The time until the material is solidified depends on the applied wall thicknesses in the casting component. In modern production plants, the HPDC process is fully automated from the preparation of the mould until the removal of the solidified casting component. Since an HPDC machine, including the casting tool, is very cost intensive, HPDC components are only mass produced. Furthermore, it is common to heat treat the components to homogenise the material structure and, thus, to improve the mechanical properties. Here, component deformations due to thermal distortion are natural and have to be adjusted manually. Besides the required energy for the heat treatment, this manual work increases the production costs.

The HPDC technique enables engineers to create components with nearly unlimited

design possibilities. HPDC components with weight from 2 g until 2000 g and including wall thicknesses up to 1 mm are realisable. Hence, the integral construction principle can be applied with best results. Requirements on the technical function and the mechanical strength are best fulfilled by using HPDC components. Traditionally, the HPDC process is used to produce engine blocks and gearboxes. Several elements within the drive line and chassis of a car are die-casted. Moreover, HPDC components are applied as structural components in the car body. Here, high strength casting alloys are needed to resist the high mechanical loading in crash situations.

Furthermore, the HPDC process needs to be designed according to the component which is to be produced. Here, the most important process parameters are as follows:

- Melt temperature of the casting alloy
- Temperature of the casting tool
- Velocity and pressure of the piston
- Distribution of the release agent
- Clamping force of the casting machine

These parameters have to be carefully chosen since they are defining the quality of the casting product. Numerical simulations are commonly used for a precise parameter identification and to control the HPDC process. Cavity filling as well as material solidification can be predicted by a casting simulation software. The melt flow is described by the Navier-Stokes equations and the solidification is described by the heat equations. The numerical solution of these partial differential equations is the main topic in the field of Computational Fluid Dynamics (CFD). CFD software tools like MAGMAsoft [81], ProCAST [38] and FLOW-3D Cast [40] are specialised on the simulation of metal and polymer casting processes. However, it is noted that the viscosity parameters and the thermal coefficients of the applied casting material as well as the boundary conditions need to be known in advance. Based on a casting simulation result, thermal distortion and initial stresses of the solidified casting component can be computed. Furthermore, a casting simulation gives information about material flow length, air contact time, cooling rate and temperature gradient. These results are useful to draw conclusions about the material structure, as, for instance, the occurrence of pores and oxide films. In Figure 2.1.3, the result of a casting simulation is illustrated. The first figure, Figure 2.1.3a, shows the melt distribution at a certain filling state. The second figure, Figure 2.1.3b, shows the temperature distribution at a certain solidification state. It is noted that a casting simulation result only shows one possible outcome and any variation of the process parameters needs to be analysed through a stochastic approach.

2.2 Aluminium Die-Casting Alloys

Casting as well as strength properties are the most important items in the chemical composition of an aluminium HPDC alloy. Moreover, weldability, corrosion resistance and properties under heat treatment are important characteristics to consider. Aluminium HPDC alloys are separated into Aluminium-Silicon (Al-Si) and Aluminium-Magnesium (Al-Mg) based alloys. The characteristic phase diagrams of these alloys are presented in Figure 2.2.1. A phase diagram plots the temperature against relative concentration of two

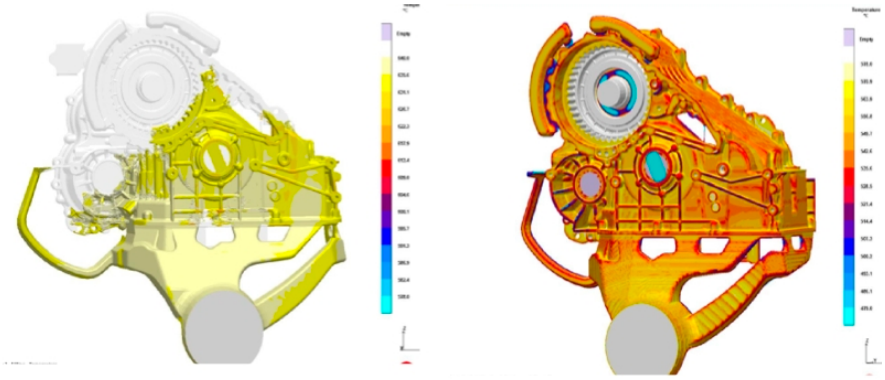

(a) Form filling. **(b)** Solidification.

Figure 2.1.3: Result of an HPDC simulation preformed with MAGMAsoft, see Kleeberg [66].

substances and shows the phases which are present in a binary material system, see Hornbogen and Warlimont [58]. The phase diagrams of Al-Si and Al-Mg alloys are well discussed by Bargel and Schulze [9]. A brief summary is given in the following.

Eutectic Al-Si alloys with a Si content of approximate 11.7 %, Figure 2.2.1a, are characterised by excellent casting and good strength properties. In contrast, eutectic Al-Mg alloys with a Mg content of approximately 34.5 %, Figure 2.2.1b, lead to a brittle material behaviour. The intermediary bond Al_3Mg_2 in Al-Mg alloys with a Mg content of approximately 37.5 % reduces ductility and corrosion resistance. In general, Al-Mg alloys with a Mg content between 3 % and 15 % are usually applied. However, eutectic Al-Si-Mg alloys are recommended for casting products with a Mg content of approximately 5 %, see Bargel and Schulze [9]. Other essential elements in the chemical composition are Iron (Fe), Manganese (Mn), Copper (Cu), Nickel (Ni), Zinc (Zn) and Titanium (Ti). Si enhances the casting properties, whereas Mg causes hardening. Fe reduces the melt adhesive tendency but also the ductility. Here, Mn can be used as an alternative or in addition. Cu and Ni increase the high-temperature strength. Zn and Ti improve the strength. The microstructure of an Al-Si-Mg HPDC alloy can be found in Figure 2.2.2. The light grey particles are α-Al crystals. The dark grey areas in between is the Al-Si eutectic including Fe and Mn. The image shows the microstructure directly after the HPDC process (heat-treatment is not applied). In European Standard DIN EN 515:1993-12 [26], the casting condition is marked with an F. Heat treated alloys are marked with a T and a number defining the degree of heat-treatment. Examples of chemical compositions of aluminium HPDC alloys can be found by the aluminium suppliers Aluminium Rheinfelden GmbH [5], Hydro Aluminium ASA [89, 90] or Aleris Switzerland GmbH [2].

2.3 Casting Defects and Material Behaviour

Casting metals show less ductile material behaviour compared to metals produced in another way such as sheet or extrusion production. The material behaviour is dominated by microstructural defects caused by the casting process. These casting defects have a strong influence on the fracture behaviour and lowers the material ductility. A high casting material quality is achieved by using the HPDC method. However, casting defects cannot

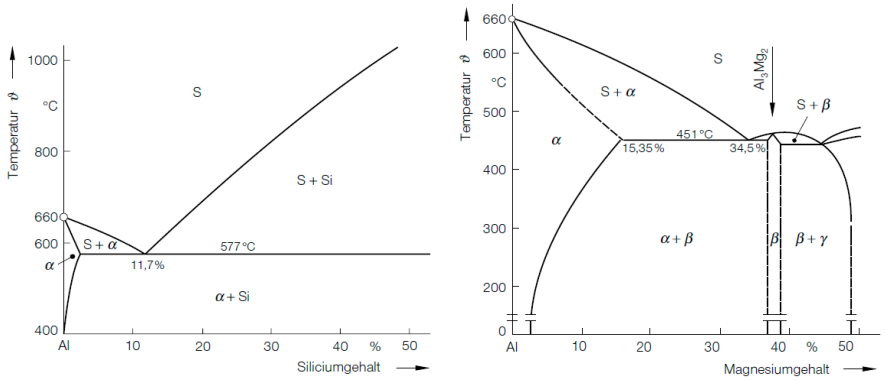

(a) Phase diagram Al-Si alloy. **(b)** Phase diagram Al-Mg alloy.

Figure 2.2.1: Characteristic phase diagrams of an Al-Si alloy and an Al-Mg alloy, see Bargel and Schulze [9].

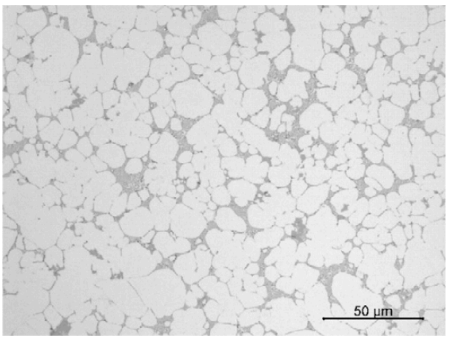

Figure 2.2.2: Microstructure of an HPDC Al-Si-Mg alloy, see Dørum et al. [33].

be avoided. The HPDC process is characterised by a turbulent form filling with long flow lengths, high cooling rates and high temperature gradients. These conditions lead to the formation of casting defects. The casting defects due to the HPDC process are very well described in the literature, see Bargel and Schulze [9], Campbell [17], Hornbogen and Warlimont [58] and Ostermann [92]. The formation of casting defects as well as the influence on the material behaviour is still discussed today. It is referred to Dispinar and Campbell [28, 29], Eisa Abadi et al. [34, 35, 36], Lee et al. [71, 72], Teng et al. [105, 106] and Mohr and Treitler [87]. Moreover, the PhD works by Dørum [30], Laukli [70] and Treitler [107] deal with this topic and provide an overview of the necessary basics. In the following, a brief introduction into this topic is given.

The casting defects can be classified into gas porosity, shrinkage porosity and oxide films, see Mohr and Treitler [87]. Images of a aluminium microstructure containing these casting defects are illustrated in Figure 2.3.1. The characteristics of the casting defects are presented in the following:

– Shrinkage porosity is a result of volume contraction which occurs during the phase transition from liquid to solid. Figure 2.3.1a shows a shrinkage pore and its characteristic bubble structure can be seen. Shrinkage pores arise due to the fast solidification of the material in the HPDC process. Furthermore, the high temperature

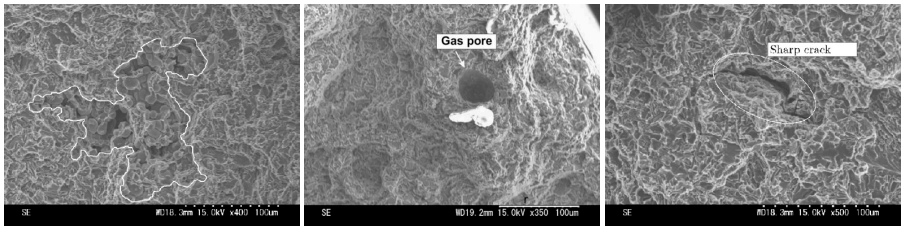

(a) Shrinkage pore. **(b)** Gas pore. **(c)** Oxide films.

Figure 2.3.1: Microstructure of an aluminium HPDC alloy (AlSi9Mg) containing casting defects, see Teng et al. [106].

gradients in thick parts are critical. Hence, shrinkage pores can especially be found in thick parts of an HPDC component. The pressurising method is used to avoid this kind of defect.

– Gas porosity occurs due to three main reasons. The first reason is gaseous hydrogen. The hydrogen solubility in liquid metals decreases during cooling. As a result, gaseous hydrogen exhausts from the solidifying HPDC melt and leads to gas porosity. The second reason is air which is enclosed in the melt due to the turbulent form filling in the HPDC process. The third reason is vaporised release agent. The characteristic spherical shape of a gas pore can be seen in Figure 2.3.1b. In general, gas porosity can be reduced when the vacuum technology and a controlled form filling are used.

– Besides shrinkage and gas porosity, oxide films are critical casting defects since these lead to internal microcracks. Molten metals have a strong tendency to form oxide films in contact with the atmosphere. These oxide films are likely to act like microcracks. In the HPDC process, oxide films can occur in the holding furnace, the shot sleeve and during form filling. An initial microcrack is illustrated in Figure 2.3.1c. Such material discontinuities arise also from so-called cold flow areas. Here, two melt fronts with solidifying material meet and continuous connection of the material is no longer possible. The amount of these casting defects are reduced using the vacuum technology and a heated casting tool. However, these defects can especially be found in HPDC component parts which are far off the gating system.

Unless the HPDC process is carried out under laboratory conditions, these casting defects cannot be avoided. Casting defects can be found in every HPDC component, see Dispinar and Campbell [28, 29]. However, the casting defect distribution within HPDC components is neither uniform nor reproducible. The distribution is primarily dominated by a stochastic character due to the sensitivity of the HPDC process, see Eisa Abadi et al. [36] and Lee et al. [71]. The distribution can be described as follows: The probability of the occurrence of a particular casting defect depends on the location within the HPDC component. For instance, the probability to find a shrinkage poor is higher in a thick part than in a thin part or the probability to find a discontinuity due to cold flow is higher in parts close to vacuum channels than in parts close to gating channels. In summary, the spatial distribution of casting defects consists of a systematic distribution depending on the HPDC set-up on the global level and of a pseudo-random distribution on the local level. Here, a casting simulation can be used to identify critical parts for casting defects as seen by Dørum et al. [32], Greve [45] and Leppin et al. [76]. The casting defect distribution

can be found from a scanning electron microscope analysis of the microstructure as seen in the works by Eisa Abadi et al. [35] and Teng et al. [106].

The casting defects have strong influence on the material behaviour. In general, a casting defect denotes a material discontinuity and can be considered as an initial material damage which lowers the material ductility. Therefore, the fracture initiation in HPDC components is dominated by the casting defects, see Campbell [17]. In case the casting material does not consist of any defect, the fracture initiation is a result of the nucleation, growth and coalescence of voids and consequently a crack starts to grow. This mechanism describes ductile failure in metals. However, usually the casting material contains defects. Consequently, fracture initiation is dominated by growth and formation of microcracks. A microcrack starts to grow from the casting defect when the material loading reaches a critical value. Consequently, the material ductility of the purely casting material decreases according to the magnitude and the amount of defects. It is noted that casting defects are almost invariant during loading compared to the voids which grow during loading. In contrast to the fracture behaviour, the elastic-plastic deformation behaviour of casting materials is assumed to be unaffected by the defects. Hence, the deformation behaviour can be described through standard metal plasticity such as v. Mises plasticity as seen by Dørum et al. [31], Greve [45], Leppin et al. [76] and Mohr and Treitler [87].

The fracture initiation is usually described by ductile failure criteria, see Dørum et al. [31], Greve [45], Leppin et al. [76] and Mohr and Treitler [87]. Here, the critical failure value defines the fracture initiation and stays in one-to-one correspondence to the casting defects. The critical failure value decreases when a casting defect is expected. Therefore, the influence of casting defects can be directly detected by measuring the critical failure value from mechanical material tests. Since the casting defects are of stochastic character, the measured critical failure value varies pseudo-randomly between material tests using the same test set-up and test specimens machined from the same position within an HPDC component, see Dørum et al. [31], Lee et al. [72] and Teng et al. [105]. Consequently, the critical failure value is given in form of a probability distribution. It is noted that the probability distribution describes only the variation of the critical failure value within the extraction position of the test specimen. This means that the probability distribution depends on the material location within an HPDC component, see Dørum et al. [32]. In summary, a failure analysis of HPDC components cannot be performed in a deterministic sense. Here, a probabilistic evaluation of the failure criterion depending on the material location within the component is required. Finally, it is noted that the influence of cast defects on the material ductility can be reduced when the casting material is homogenised through heat treatment, see Campbell [17].

2.4 Die-Castings in the Car Body

The HPDC process enables to produce aluminium components of complex geometries. This advantage is applied in the car body design to create structural nodes and connector elements. Here, HPDC components replace components of the car body which are assembled of several parts. Therefore, this design approach is called the integral construction principle. Using this principle, the production steps are reduced and no additional joining technique is required. Hence, the structural stiffness can be increased. Moreover, the usage of an aluminium alloy reduces the car weight and, thus, the fuel consumption can be reduced. An example is demonstrated in Figure 2.4.1. It shows the aluminium car body of the current Audi A8 and the application of the different aluminium materials. The green components mark aluminium sheets, the blue ones aluminium extrusions and the

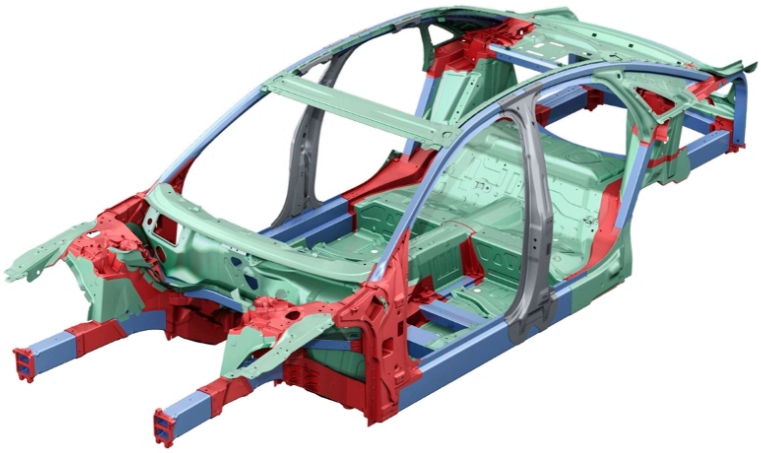

Figure 2.4.1: Car body of the current Audi A8 (third generation (D4), production 2010 - present): Application of aluminium sheets (green), aluminium extrusions (blue) and aluminium die-castings (red).

red ones aluminium HPDC components. Only the B pillar is made of a steel alloy. The connecting function of the aluminium HPDC components is clearly seen.

The design of a car body is mainly focused on the stiffness and the crash behaviour. The stiffness is a function of the entire car body, whereas, the crash performance is shared between the several components of the car body. In the Audi A8, the extrusions in the front and rear end are considered to absorb most of the kinetic energy in a crash situation. A side impact loading has to be carried by the B-pillar. The HPDC components are expected to preserve the connecting function in any crash situation. This means that the components have to obey only small deformations. Furthermore, it is expected that these components show no fracture initiation. In case an HPDC component fails and the connection function is lost, the passenger safety is no longer guaranteed. These requirements have to be considered in the design of aluminium HPDC components applied in the car body.

Before a car body prototype is produced and tested, the car body and its several parts are numerically analysed. Here, the most common approach is the finite element method. The deformation and failure behaviour of the car body under different load cases can be analysed by a finite element simulation. This makes it possible to optimise the structure before a real test is performed. Here, constitutive models and failure criteria are required to describe accurately the behaviour of the applied material. However, a reliable design is only guaranteed when the correct parameters of the material model are identified. The numerical prediction of fracture initiation in aluminium HPDC components is a challenging task. The influence of the casting defects on the fracture behaviour and the pseudo-random character of the casting defects are the main reasons. This means that the crashworthiness of aluminium HPDC components is defined by the casting defects within the most loaded area of the component.

Chapter 3

Probability and Statistics

The mathematical field of stochastics consists of the two parts probability theory and statistics. The probability theory deals with the mathematical modelling and analysis of non-deterministic and random phenomena. Probabilities, random variables and stochastic processes are central objects. Methods in probability theory enable to make conclusions about characteristics of a hypothetical sample taken from a known population. This is called a deductive reasoning. Statistics involves methods to gather, describe and interpret an experimental sample and compare it with other samples. The field of statistics can be subdivided into descriptive and interferential statistics. Descriptive statistics allows to summarise, quantify and illustrate the sample data. It allows to assume characteristics of the underlying population. The inferential statistics is applied to draw conclusions about a hypothetical underlying population based on the sample data and considerations from probability theory. This is called an inductive reasoning. The current chapter gives a brief introduction in the field of probability theory and statistics. The objective is to introduce the essential definitions and relations and to use them for further experimental and numerical investigations. This chapter is mainly based on the standard book on probability and statistics by Walpole [111]. Here, the underlying mathematical derivations are presented in detail and a great variety of examples can be found.

3.1 Statistical Experiment and Randomness

A statistical experiment is defined as a non-deterministic and random experiment. It is assumed that the experiment can be repeated indefinitely under the same conditions. The outcome is characterised by randomness which follows a certain pattern. It is called a stochastic or probabilistic process. However, it is not possible to determine a particular outcome of the experiment. It is only possible to state the probability of this particular outcome. A statistical experiment with true randomness can be generated only theoretically (neglecting the latest results in the research of quantum mechanics). In reality, the particular outcome is predictable when all conditions and relations of a particular experiment are known. It is called a deterministic causal process. If such a real experiment is repeated under exact same conditions, the outcome does not vary. However, such experimental conditions cannot be guaranteed and a variation of the conditions and the outcome is a natural consequence. In many real experiments, the observer often marks the variation of the outcome as scatter and assumes randomness which is called a pseudo-randomness. Pseudo-randomness is generated in deterministic systems where

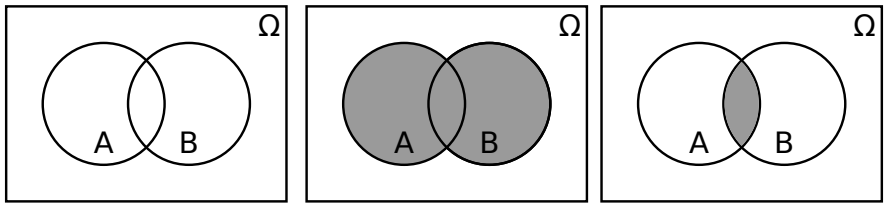

(a) $A \in \Omega$ and $B \in \Omega$. **(b)** $A \cup B$. **(c)** $A \cap B$.

Figure 3.2.1: Two events A and B taken from the sample space Ω.

differences between pseudo-randomness and true randomness cannot be observed.

3.2 Sample Space, Event and Probability

The set of all possible outcomes of a statistical experiment is defined as sample space Ω, also known as population. A sample space consists of sample points taken from either a discrete or continuous scale. Furthermore, a distinction is made between a finite and an infinite sample space. A sample space is finite if all possible outcomes are countable. Each continuous sample space is infinite even if the sample points are taken from a limited continuous scale. Only a discrete sample space can be finite. A subset of the sample space is defined as event A, also known as sample, see Figure 3.2.1a. The complement event A' consists of sample points which are not included in A. The union of two events A and B is denoted as $A \cup B$, see Figure 3.2.1b, and the intersection between two events A and B is denoted as $A \cap B$, see Figure 3.2.1c.

If n events A_i are considered, the total union is written as

$$A_1 \cup A_2 \cup \ldots \cup A_n = \bigcup_{i=1}^{n} A_i \tag{3.2.1}$$

and the total intersection as

$$A_1 \cap A_2 \cap \ldots \cap A_n = \bigcap_{i=1}^{n} A_i. \tag{3.2.2}$$

If the intersection $A \cap B$ is empty, event A and event B are defined as mutually exclusive. An empty intersection is written as $A \cap B = \phi$. Each sample space Ω can be subdivided in n mutually exclusive events A_i.

A probability ranging from 0 to 1 is assigned to every sample point in a way that the sum of all probabilities is 1. The probability of event A is the sum of all probabilities assigned to the sample points in A. Therefore, the probability $P(A)$ also ranges from 0 to 1 and becomes

$$0 \leq P(A) \leq 1. \tag{3.2.3}$$

In this context, the following statements are made

$$P(\Omega) = 1 \quad \text{and} \quad P(\phi) = 0 \tag{3.2.4}$$

and

$$P(A') = 1 - P(A). \tag{3.2.5}$$

If a sample space consists of n different equally likely outcomes and m of these outcomes correspond to an event A, the probability $P(A)$ becomes

$$P(A)=\frac{m}{n}. \tag{3.2.6}$$

The probability of the union $A\cup B$ becomes

$$P(A\cup B)=P(A)+P(B)-P(A\cap B). \tag{3.2.7}$$

In case, the union consists of n events A_i the corresponding probability becomes

$$P\left(\bigcup_{i=1}^{n}A_i\right)=P(A_1)+P\left(\bigcup_{i=2}^{n}A_i\right)-P\left(A_1\cap\bigcup_{i=2}^{n}A_i\right). \tag{3.2.8}$$

The probability simplifies to

$$P\left(\bigcup_{i=1}^{n}A_i\right)=P(A_1)+P(A_2)+\ldots+P(A_n)=\sum_{i=1}^{n}P(A_i), \tag{3.2.9}$$

if n events A_i are mutually exclusive. This leads to Boole's inequality

$$P\left(\bigcup_{i=1}^{n}A_i\right)\leq\sum_{i=1}^{n}P(A_i) \tag{3.2.10}$$

which is valid for any event A_i.

If the occurrence of an event B requires that an event A occurs previously, the probability of event B is called conditional probability and is denoted as $P(B\,|\,A)$. The conditional probability is defined by

$$P(B\,|\,A)=\frac{P(A\cap B)}{P(A)} \tag{3.2.11}$$

where $P(A)>0$ is provided. This equation allows to express the probability of the intersection $A\cap B$ as

$$P(A\cap B)=P(A)P(B\,|\,A)=P(B)P(A\,|\,B). \tag{3.2.12}$$

Event A and event B are said to be independent if the occurrence of A has no influence on the occurrence of B and it follows

$$P(B\,|\,A)=P(B) \tag{3.2.13}$$

otherwise A and B are dependent. Furthermore, the conditional probability $P(B\,|\,A)=P(B)$ implies the conditional probability $P(A\,|\,B)=P(A)$ and vice versa. If A and B are independent events, the probability that both events occur is the product of two individual probabilities,

$$P(A\cap B)=P(A)P(B). \tag{3.2.14}$$

If n events A_i can occur in a statical experiment, the probability of the total intersection is given by

$$\begin{aligned}P\left(\bigcap_{i=1}^{n}A_i\right) &= P(A_1)P(A_2\,|\,A_1)P(A_3\,|\,A_1\cap A_2)\ldots\\ &\quad\ldots P(A_n\,|\,A_1\cap A_2\ldots\cap A_{n-1}).\end{aligned} \tag{3.2.15}$$

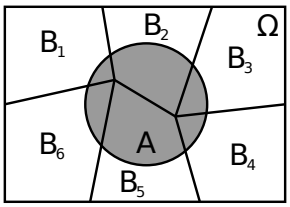

Figure 3.2.2: Bayes' theorem.

In case the n events A_i are independent, the probability of the total intersection becomes the product of each individual probability,

$$P\left(\bigcap_{i=1}^{n} A_i\right) = P(A_1)P(A_2)P(A_3)\dots P(A_n) = \prod_{i=1}^{n} P_i(A_i). \tag{3.2.16}$$

Furthermore, n events A_i are given in a collection $\mathscr{A} = \{A_1, A_2, \dots, A_n\}$. A subset of $\mathscr{A}$ is denoted as $\mathscr{A}^*$ and consists of k events of $\mathscr{A}$ with $k = 2, 3, \dots, n$. If any subset $\mathscr{A}^*$ follows Equation (3.2.16), the collection $\mathscr{A}$ is called mutually independent.

It is considered that the sample space Ω is divided into n mutually exclusive subsets B_i as illustrated in Figure 3.2.2. Using Equation (3.2.9) and Equation (3.2.12), the probability of any event A in Ω becomes

$$P(A) = P\left(\bigcup_{i=1}^{n} (B_i \cap A)\right) = \sum_{i=1}^{n} P(B_i \cap A) = \sum_{i=1}^{n} P(B_i)P(A \mid B_i) \tag{3.2.17}$$

which is known as theorem of total probability. Hence, the conditional probability for a subset B_k with $k = 1, 2, \dots, n$ given that A occurs can be expressed as

$$P(B_k \mid A) = \frac{P(B_k \cap A)}{P(A)} = \frac{P(B_k)P(A \mid B_k)}{\sum_{i=1}^{n} P(B_i)P(A \mid B_i)} \tag{3.2.18}$$

where $P(A) > 0$ and $P(B_i) > 0$ are provided. This relation is called Bayes' theorem, see Walpole [111].

3.3 Fundamentals of Probability Theory

Probability theory allows the modelling of a statistical experiment and the prediction of the probability that an event of the model occurs. The requirements, rules and constraints for statistical modelling are stated in probability theory. Here, the concept of random variables provides the essential basis. A random variable is a variable whose value varies randomly. Compared to other mathematical variables, a random variable has not a single (fixed) value. All possible values of the random variable correspond to all outcomes or sample points from a real-valued sample space. Therefore, a random variable is defined as a function that associates each sample point of a real-valued sample space. According to the difference between discrete and continuous sample spaces, random variables are classified in either discrete or continuous random variables.

3.3.1 Random Variables and Probability Distributions

The random variable is denoted as X and its varying value as x. If a discrete random variable is considered, the number of all possible values of x is countable and for each value x_i

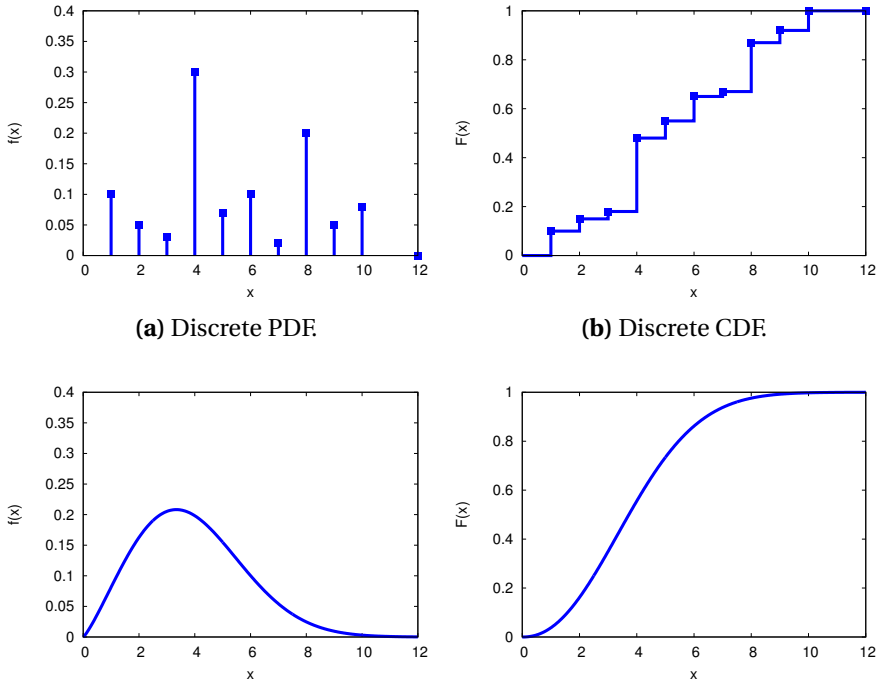

(a) Discrete PDF. **(b)** Discrete CDF.

(c) Continuous PDF. **(d)** Continuous CDF.

Figure 3.3.1: Probability Density Function (PDF) and Cumulative Distribution Function (CDF) of a discrete and a continuous random variable.

a certain probability $f(x_i)$ is assigned. This implies that the probability that x_i occurs becomes $P(X=x_i)=f(x_i)$. The set of n ordered pairs $\big(x_i, f(x_i)\big)$ is defined as the probability mass function of the discrete random variable X as long as the conditions

$$\begin{aligned} f(x_i) &\geq 0, \\ \sum_{i=1}^{n} f(x_i) &= 1, \\ P(X=x_i) &= f(x_i) \end{aligned} \tag{3.3.1}$$

are fulfilled for any $x \in \mathbb{R}$. The probability that a value of X is less than or equal a certain value x_k becomes

$$F(x_k)=P(X\leq x_k)=\sum_{i=1}^{k} f(x_i) \tag{3.3.2}$$

and $F(x_k)$ is defined as the cumulative distribution function of the discrete random variable X. An example of a probability mass function is given in Figure 3.3.1a with the corresponding cumulative distribution function in Figure 3.3.1b.

A continuous random variable X is characterised by an infinite number of its values x. Therefore, the substantial difference to a discrete random variable is that the probability that exactly the value x of a continuous random variable X occurs becomes $P(X=x)=0$.

This statement can be clearly seen using Equation (3.2.6) with $m = 1$,

$$P(X = x) = \lim_{n\to\infty} \frac{1}{n} = 0. \tag{3.3.3}$$

However, it is possible to determine the probability that X lies in the interval between a and b and the probability $P(a \leq X \leq b)$ is computed by

$$\begin{aligned} P(a \leq X \leq b) &= \underbrace{P(X = a)}_{=0} + P(a < X < b) + \underbrace{P(X = b)}_{=0} \\ &= P(a < X < b). \end{aligned} \tag{3.3.4}$$

It is seen that it does not matter if the endpoints a and b are included in the interval.

The probability distribution $f(x)$ of a continuous random variable X can be stated as a continuous formula of x. Then, the function $f(x)$ is defined as the Probability Density Function (PDF) of the continuous random variable X as long as the conditions

$$\begin{aligned} f(x) &\geq 0, \\ \int_{-\infty}^{+\infty} f(x)\,dx &= 1, \\ P(a \leq X \leq b) &= \int_a^b f(x)\,dx \end{aligned} \tag{3.3.5}$$

are fulfilled for any $x \in \mathbb{R}$. The corresponding Cumulative Distribution Function (CDF) $F(x)$ becomes

$$F(x) = P(X \leq x) = \int_{-\infty}^{x} f(x)\,dx \tag{3.3.6}$$

and it implies that $P(X < \infty) = 1$. Furthermore, the probability $P(a \leq X \leq b)$ is expressed as

$$P(a \leq X \leq b) = F(b) - F(a) \tag{3.3.7}$$

and thus the complement relation of the CDF $F(x)$ becomes

$$P(x \leq X < \infty) = P(X \geq x) = 1 - F(x). \tag{3.3.8}$$

The derivative of the CDF $F(x)$ reproduces the PDF $f(x)$,

$$\frac{dF(x)}{dx} = f(x). \tag{3.3.9}$$

An example of a continuous PDF with corresponding CDF is given in Figure 3.3.1c and Figure 3.3.1d, respectively.

From a strict mathematical point of view, the probability mass function of a discrete random variable can be expressed as a continuous function using the Dirac function $\delta(x)$. The Dirac delta function can be expressed as

$$\delta(x) = \begin{cases} \to \infty & x = 0 \\ 0 & x \neq 0 \end{cases} \tag{3.3.10}$$

with $x \in \mathbb{R}$. The function is characterised by the integral

$$\int_{-\infty}^{+\infty} \delta(x)\,dx = 1. \tag{3.3.11}$$

Then, the probability mass function can be expressed as a combination of Dirac functions as

$$f(x)=\sum_{i=1}^{n} f(x_i)\delta(x-x_i) \tag{3.3.12}$$

which follows the requirements of a PDF.

Discrete random variables are used in countable statistical experiments and continuous random variables in measurable statistical experiments. For instance, a countable experiment measures, if a specimen does or does not fail under a certain load level, whereas the measurement of the load level at failure of the specimen is a measurable experiment. The second case is of interest in the present work and thus only continuous random variables are considered in the following. However, the definitions and expressions for continuous random variables can be transformed into discrete random variables using Equation (3.3.12).

3.3.2 Statistical Independence

It is considered that a continuous sample space consists of two random variables X and Y. Then, the PDF function is defined above the $x-y$ plane, is called the joint density function and is denoted as $f(x,y)$. The three conditions

$$\begin{aligned} f(x,y) &\geq 0, \\ \int_{-\infty}^{+\infty}\int_{-\infty}^{+\infty} f(x,y)\,dx\,dy &= 1, \\ P[(a\leq X\leq b),(c\leq Y\leq d)] &= \int_c^d\int_a^b f(x,y)\,dx\,dy \end{aligned} \tag{3.3.13}$$

have to be satisfied for any $(x,y)\in\mathbb{R}$. The CDF of the joint density function $f(x,y)$ is given by

$$F(x,y)=P[(X\leq x),(Y\leq y)]=\int_{-\infty}^{y}\int_{-\infty}^{x} f(x,y)\,dx\,dy. \tag{3.3.14}$$

The PDF $g(x)$ of X alone as well as the PDF $h(y)$ of Y alone can be obtained from the joint density function $f(x,y)$,

$$\int_{-\infty}^{+\infty}\underbrace{\int_{-\infty}^{+\infty} f(x,y)\,dy}_{g(x)}\,dx=\int_{-\infty}^{+\infty}\underbrace{\int_{-\infty}^{+\infty} f(x,y)\,dx}_{h(y)}\,dy. \tag{3.3.15}$$

The PDFs $g(x)$ and $h(y)$ are called marginal distributions and are given by

$$g(x)=\int_{-\infty}^{+\infty} f(x,y)\,dy \quad\text{and}\quad h(y)=\int_{-\infty}^{+\infty} f(x,y)\,dx. \tag{3.3.16}$$

The CDFs of $g(x)$ and $h(y)$, respectively, are denoted as $G(x)$ and $H(y)$, respectively.

The conditional probability is defined in Equation (3.2.11). In case of continuous random variables, the conditional probability that X lies in the interval between a and b and Y is fixed by a value of y can be expressed as

$$P(a\leq X\leq b\mid Y=y)=\int_a^b f(x\mid y)\,dx \tag{3.3.17}$$

where $f(x \mid y)$ denotes the conditional probability function of X given that $Y = y$ and is defined by

$$f(x \mid y) = \frac{f(x,y)}{h(y)} \tag{3.3.18}$$

where $h(y) > 0$ is provided. The conditional probability function of Y given that $X = x$ is

$$f(y \mid x) = \frac{f(x,y)}{g(x)} \tag{3.3.19}$$

where $g(x) > 0$ is provided. This implies the relation

$$f(x,y) = h(y) f(x \mid y) = g(x) f(y \mid x). \tag{3.3.20}$$

Now, the statistical independence of two random variables X and Y can be defined as follows: The random variables X and Y are statistically independent if the joint density function $f(x,y)$ with marginal distributions $g(x)$ and $h(y)$ can be expressed as the product of the marginal distributions for any $(x,y) \in \mathbb{R}$,

$$f(x,y) = g(x) h(y). \tag{3.3.21}$$

Here, the conditional probability functions become

$$f(x \mid y) = g(x) \quad \text{and} \quad f(y \mid x) = h(y). \tag{3.3.22}$$

In this case, also the CDF of $f(x,y)$ becomes a product of $G(x)$ and $H(y)$ as shown in Equation (3.2.14),

$$F(x,y) = P[(X \leq x), (Y \leq y)] = G(x) H(y). \tag{3.3.23}$$

In this context, the n random variables X_i are mutually statistical independent if the joint density function $f(x_1, x_2, \ldots, x_n)$ is the product of the n marginal distributions $f_i(x_i)$ such as

$$f(x_1, x_2, \ldots, x_n) = f_1(x_1) f_2(x_2) \ldots f_n(x_n) = \prod_{i=1}^{n} f_i(x_i). \tag{3.3.24}$$

According to Equation (3.2.16), the corresponding CDF of n mutually statistically independent variables X_i is given by

$$\begin{aligned} F(x_1, x_2, \ldots, x_n) &= P[(X_1 \leq x_1), (X_2 \leq x_2), \ldots, (X_n \leq x_n)] \\ &= F(x_1) F_2(x_2) \ldots F_n(x_n) \\ &= \prod_{i=1}^{n} F_i(x_i). \end{aligned} \tag{3.3.25}$$

3.3.3 Functions of Random Variables

It is assumed that a function u depends on a continuous random variable X with PDF $f(x)$ such as $Y = u(X)$. If the inverse function of $Y = u(X)$ exists and can be solved uniquely so that $X = u^{-1}(Y)$, the probability distribution of Y becomes

$$g(y) = f\left(u^{-1}(y)\right) \mid J \mid \tag{3.3.26}$$

where J denotes the Jacobian of the transformation and is determined as

$$J(y) = \frac{d\left(u^{-1}(y)\right)}{dy}. \tag{3.3.27}$$

In case of two continuous random variables X_1 and X_2 with joint probability distribution $f(x_1,x_2)$ and two transformation functions $Y_1 = u_1(X_1,X_2)$ and $Y_2 = u_2(X_1,X_2)$ with existing and uniquely solvable inverse functions $X_1 = u_1^{-1}(Y_1,Y_2)$ and $X_2 = u_2(Y_1,Y_2)$, the joint probability function of Y_1 and Y_2 is given by

$$g(y_1,y_2) = f\left[u_1^{-1}(y_1,y_2), u_1^{-1}(y_1,y_2)\right] \det(\mathbf{J}) \tag{3.3.28}$$

where $\det(\mathbf{J})$ is the determinate of the Jacobi transformation matrix,

$$\mathbf{J} = \begin{pmatrix} \frac{\partial u_1^{-1}}{\partial y_1} & \frac{\partial u_1^{-1}}{\partial y_2} \\ \frac{\partial u_2^{-1}}{\partial y_1} & \frac{\partial u_2^{-1}}{\partial y_2} \end{pmatrix}. \tag{3.3.29}$$

3.3.4 Mathematical Expectations

In probability theory, random variables and their underlying PDF are characterised by mathematical expectations and statistical measurements. These measurements give information of central tendency and variability of a random variable. Furthermore, the correlation between random variables can be quantified by these measurements. In the following, definitions and expressions are given for continuous random variables.

The expected value or mean of a random variable X with PDF $f(x)$ is the weighted averaged of x and is denoted as μ. It gives information about the centre of the PDF $f(x)$ and is defined as

$$\mu = E[X] = \int_{-\infty}^{+\infty} x f(x)\, dx. \tag{3.3.30}$$

Here, the function $E[\cdot]$ is also known as expected value operator. If a random variable Y can be expressed as a function of X such as $Y = g(X)$, the expected value of Y becomes

$$\mu_{g(X)} = E\left[Y = g(X)\right] = \int_{-\infty}^{+\infty} g(x) f(x)\, dx. \tag{3.3.31}$$

The expected value of the random variable $g(X,Y)$ is given by

$$\mu_{g(X,Y)} = E\left[g(X,Y)\right] = \int_{-\infty}^{+\infty}\int_{-\infty}^{+\infty} g(x,y) f(x,y)\, dx dy \tag{3.3.32}$$

where X and Y are random variables with joint probability distribution $f(x,y)$. The expected values of X and Y alone becomes

$$\begin{aligned} \mu_X = E[X] &= \int_{-\infty}^{+\infty} x f(x,y)\, dx dy, \\ \mu_Y = E[Y] &= \int_{-\infty}^{+\infty} y f(x,y)\, dx dy. \end{aligned} \tag{3.3.33}$$

If n random variables X_i with joint probability distribution $f(x_1,x_2,\ldots,x_n)$ are considered, the expected value of the random variable $g(X_1,X_2,\ldots,X_n)$ can be expressed as

$$\begin{aligned} \mu_{g(X_1,X_2,\ldots,X_n)} &= E\left[g(X_1,X_2,\ldots,X_n)\right] \\ &= \int_{-\infty}^{+\infty}\ldots\int_{-\infty}^{+\infty}\int_{-\infty}^{+\infty} g(x_1,x_2,\ldots,x_n)\ldots \\ &\quad \ldots f(x_1,x_2,\ldots,x_n)\, dx_1 dx_2 \ldots dx_n. \end{aligned} \tag{3.3.34}$$

The dispersion or variability of a random variable X with PDF $f(x)$ and mean μ is measured by variance σ^2 and is given by

$$\begin{aligned}\sigma^2 &= E\left[(X-\mu)^2\right] \\ &= \int_{-\infty}^{+\infty}(x-\mu)^2 f(x)\,dx \\ &= E\left(X^2\right)-\mu^2. \end{aligned} \tag{3.3.35}$$

The positive square root of variance σ^2 is called standard deviation σ. The variation of the random variable $Y=g(X)$ becomes

$$\begin{aligned}\sigma^2 &= E\left[(Y-\mu_Y)^2\right] \\ &= E\left[\left(g(X)-\mu_{g(X)}\right)^2\right] \qquad (3.3.36) \\ &= \int_{-\infty}^{+\infty}\left(g(x)-\mu_{g(X)}\right)^2 f(x)\,dx. \qquad (3.3.37)\end{aligned}$$

The ratio of standard deviation σ and mean μ is known as coefficient of variation c_σ. It is a normalised measurement of the dispersion of a PDF and is given by

$$c_\sigma = \frac{\sigma}{\mu}. \tag{3.3.38}$$

The covariance of two random variables X and Y with joint probability distribution $f(x,y)$ is denoted as σ_{XY} and is defined as

$$\begin{aligned}\sigma_{XY} &= E\left[(X-\mu_X)(Y-\mu_Y)\right] \\ &= \int_{-\infty}^{+\infty}\int_{-\infty}^{+\infty}(x-\mu_X)(y-\mu_Y) f(x,y)\,dx\,dy \\ &= E[XY]-\mu_X\mu_Y. \end{aligned} \tag{3.3.39}$$

The covariance σ_{XY} gives information about the dependence of X and Y. It describes the linear relationship between X and Y. A positive value of σ_{XY} indicates that large values of X often result in large values of Y and small values of X often result in small values of Y. A negative value of σ_{XY} indicates the inverse behaviour, this means that large values of X often result in small values of Y and vice versa. If X and Y are statistically independent, the covariance is zero, $\sigma_{XY}=0$. However, if the covariance σ_{XY} is zero it does not necessarily indicate the independence of X and Y. If n random variables X_i with joint probability distribution $f(x_1,x_2,\ldots,x_n)$ are considered the covariance $\sigma_{X_iX_j}$ of the two random variables X_i and X_j becomes

$$\begin{aligned}\sigma_{X_iX_j} &= E\left[\left(X_i-\mu_{X_i}\right)\left(X_j-\mu_{X_j}\right)\right] \\ &= \int_{-\infty}^{+\infty}\ldots\int_{-\infty}^{+\infty}\int_{-\infty}^{+\infty}\left(x_i-\mu_{X_i}\right)\left(x_j-\mu_{X_j}\right)\ldots \\ &\quad f(x_1,x_2,\ldots,x_n)\,dx_1\,dx_2\ldots dx_n \\ &= E\left[X_iX_j\right]-\mu_{X_i}\mu_{X_j}. \end{aligned} \tag{3.3.40}$$

The covariance σ_{XY} gives also information about the linear relationship of X and Y. However, the magnitude of σ_{XY} does not indicate anything regarding the strength of the

relationship since it depends on the scale of X and Y. A scale-free coefficient is the correlation coefficient ρ_{XY}. The correlation coefficient can be expressed as

$$\rho_{XY} = \frac{E\left[\left(X-\mu_X\right)\left(Y-\mu_Y\right)\right]}{E\left[\left(X-\mu_X\right)^2\right]E\left[\left(X_Y-\mu_Y\right)^2\right]} = \frac{\sigma_{XY}}{\sigma_X\sigma_Y} \tag{3.3.41}$$

where $\sigma_X > 0$ and $\sigma_Y > 0$ are provided. This expression is known as Pearson's correlation coefficient. This coefficient always satisfies the inequality $-1 \leq \rho_{XY} \leq 1$. If X and Y have an exact linear relationship, ρ_{XY} becomes either 1 or -1. In case of statical independence of X and Y, ρ_{XY} is zero. Again, it does not necessarily indicate the converse conclusion. If n random variables X_i with joint probability distribution $f(x_1, x_2, \ldots, x_n)$ are considered, the correlation coefficient $\rho_{X_iX_j}$ of two random variables X_i and X_j becomes

$$\rho_{X_iX_j} = \frac{E\left[\left(X_i-\mu_{X_i}\right)\left(X_j-\mu_{X_j}\right)\right]}{E\left[\left(X_i-\mu_{X_i}\right)^2\right]E\left[\left(X_j-\mu_{X_j}\right)^2\right]} = \frac{\sigma_{X_iX_j}}{\sigma_{X_i}\sigma_{X_j}} \tag{3.3.42}$$

where $\sigma_{X_i} > 0$ and $\sigma_{X_j} > 0$ are provided.

If n random variables X_i are statistically independent and each belongs to a PDF $f_i(x_i)$ with mean μ_i and variance σ_i^2, then the random variable Y defined as

$$Y = \sum_{i=1}^{n} a_i X_i \tag{3.3.43}$$

has the mean

$$\mu_Y = \sum_{i=1}^{n} a_i \mu_i \tag{3.3.44}$$

and the variance

$$\sigma_Y^2 = \sum_{i=1}^{n} a_i^2 \sigma_i^2. \tag{3.3.45}$$

Finally, the skewness of the PDF $f(x)$ of a random variable X can be described through the mode and quantiles. The value that most often appears is defined as the mode, also known as the most likely. Therefore, the mode is the maximum value of $f(x)$,

$$\text{mode} = \max\left[f(x)\right]. \tag{3.3.46}$$

It is seen that this equation cannot always be uniquely solved and thus the PDF $f(x)$ can have more than one mode. Further, the range of the CDF $F(x)$ is divided into k regular intervals $\frac{1}{k}$ such as

$$\max\left[F(x)\right] - \min\left[F(x)\right] = 1 = \sum_{i=1}^{k} \frac{1}{k}. \tag{3.3.47}$$

Now, the value Q_i can be defined as the i^{th} quantile of k quantiles of the PDF $f(x)$ if Q_i satisfies the relation

$$F(Q_i) = P(X \leq Q_i) = \frac{i}{k}. \tag{3.3.48}$$

The quantile Q_i is defined so that $\frac{i}{k} \cdot 100\%$ of the sample space lies in the interval between $-\infty$ and Q_i. Therefore, the quantile is often denoted as $Q_{\frac{i}{k}\cdot 100\%}$. In general, the inverse function of the CDF F^{-1} is called the quantile function and can be expressed as

$$Q_{P(x \leq X)} = F^{-1}\left(P(x \leq X)\right). \tag{3.3.49}$$

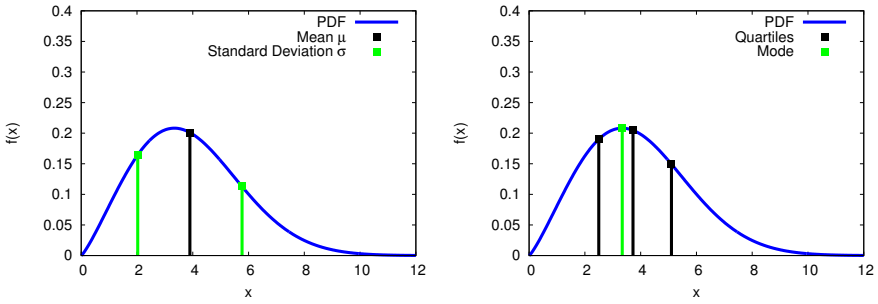

(a) Mean and standard deviation. **(b)** Quartiles and mode.

Figure 3.3.2: Mathematical expectations and statistical measurements.

If k is equal 2, the sample space is divided into two sub-sets and the $Q_{50\%}$ is known as the median. If k is equal 4, the sample space is divided into four sub-sets and the quantiles, $Q_{25\%}$, $Q_{50\%}$ and $Q_{75\%}$, are called the quartiles.

A comparison of the measurements mean, standard deviation, mode and quartiles of a continuous PDF is shown in Figure 3.3.2. Mean and standard deviation away from the mean $(\mu \pm \sigma)$ are marked in Figure 3.3.2a. Mode and quartiles are marked in Figure 3.3.2b.

3.3.5 Some Continuous Probability Distribution Functions

The PDF $f(x)$ of a continuous random variable X is often expressed in parametric form. Many formulations have been introduced in the history of stochastics. Here, the emphasis is putted on uniform, normal and Weibull distribution. The normal distribution is an essential PDF in probability theory. Numerical pseudo-random number generators are usually based on the uniform distribution. The Weibull function is found in many engineering applications. Other well-known and important parametric distribution functions are binomial, gamma, exponential, chi-squared and lognormal distributions as well as t-distribution and F-distribution, see Montgomery [88], Ross [101] and Walpole [111]. These and other functions can be found in the standard literature.

One of the simplest is the uniform distribution which is characterised by a constant PDF in an interval A and B and is given by

$$f_U(x;A,B) = \begin{cases} \frac{1}{B-A} & A \leq x \leq B \\ 0 & \text{elsewehere} \end{cases} \tag{3.3.50}$$

and the CDF becomes

$$F_U(x;A,B) = \begin{cases} \frac{1}{B-A}(x-A) & A \leq x \leq B \\ 0 & \text{elsewehere} \end{cases}. \tag{3.3.51}$$

Mean μ and variance σ^2 of the uniform distribution are

$$\mu = \frac{A+B}{2} \quad \text{and} \quad \sigma^2 = \frac{(B-A)^2}{12}. \tag{3.3.52}$$

The linear shape of the uniform PDF and corresponding CDF can be seen in Figure 3.3.3a and Figure 3.3.3b.

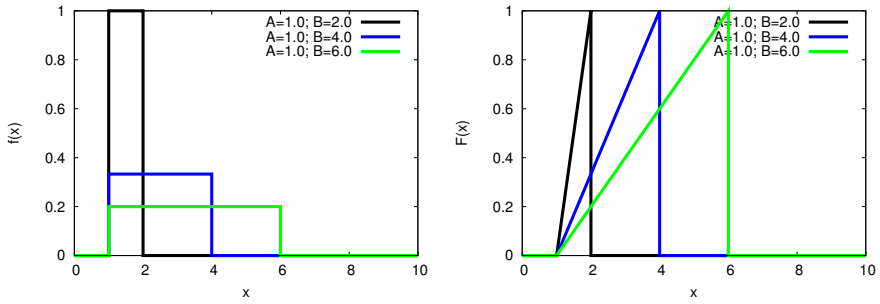

(a) $f_U(x;1,\{2,4,6\})$. **(b)** $F_U(x;1,\{2,4,6\})$.

Figure 3.3.3: Examples of uniform PDFs and CDFs ($A=1;B=2,4,6$).

The most important PDF in the field of stochastic is the normal distribution, also known as Gaussian distribution. The normal distribution is given in terms of its mean μ and variance σ^2,

$$f_N(x;\mu,\sigma) = \frac{1}{\sigma\sqrt{2\pi}} \exp\left(-\frac{(x-\mu)^2}{2\sigma^2}\right). \tag{3.3.53}$$

The graph of $f_N(x;\mu,\sigma)$ is symmetrical to μ and looks like a bell. In the case $\mu=0$ and $\sigma^2=1$, the normal distribution is called standard normal distribution. If $\mu=0$ and $\sigma^2\to 0$, the normal distribution leads to the Dirac function $f_N(z;\mu=0,\sigma=0)=\delta(x)$ given in Equation (3.3.10). The CDF of $f_N(x;\mu,\sigma)$ becomes

$$F_N(x;\mu,\sigma) = \frac{1}{\sigma\sqrt{2\pi}} \int_{-\infty}^{x} \exp\left(-\frac{(\hat{x}-\mu)^2}{2\sigma^2}\right) d\hat{x}. \tag{3.3.54}$$

Here, the integral cannot be expressed in terms of elementary functions. Therefore, the standard normal distribution $f_N(z;\mu=0,\sigma=1)$ has been considered and approximate solutions for discrete points $(z_i, F_N(z_i;\mu=0,\sigma=1))$ were found and listed in tables, see Walpole [111]. Today, numerical software tools are used to determine these points. It is not necessary to find values for other possible normal distributions due to the standardising of normal random variables. Here, it is considered that a random variable Z follows the standard normal distribution and another random variable X an arbitrary normal distribution, the relation between both reads

$$Z = \frac{X-\mu_X}{\sigma_X}. \tag{3.3.55}$$

This equation is called standardising of X and it allows to map any normal CDF of X into a standard normal CDF of Z, so that

$$F_N(x;\mu,\sigma) = F_N\left(z=\frac{x-\mu_X}{\sigma_X};\mu=0,\sigma=1\right). \tag{3.3.56}$$

It also includes the probability that X assumes a value between x_1 and x_2 becomes

$$P_N(x_1\le X\le x_2) = P_N\left(z_1=\frac{x_1-\mu_X}{\sigma_X}\le Z\le z_2=\frac{x_2-\mu_X}{\sigma_X}\right). \tag{3.3.57}$$

The influence of σ on the normal PDF and CDF, respectively, can be seen in Figure 3.3.4a and Figure 3.3.4b, respectively.

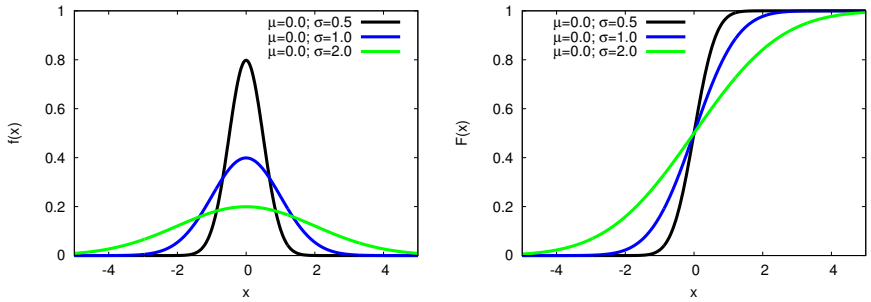

(a) $f_N(x;0,\{0.5,1,2\})$. **(b)** $F_N(x;0,\{0.5,1,2\})$.

Figure 3.3.4: Examples of normal PDFs and CDFs $(\mu=0;\sigma=0.5,1,2)$.

It is considered that n random variables X_i are normally distributed with $f_N(x_i;\mu_i,\sigma_i)$ and stored in a random vector $\mathbf{X}$. Consequently, the n means μ_i are given in a vector $\boldsymbol{\mu}$ and the covariances $\sigma_{X_iX_j}$ between the random variables X_i and X_j in a (positive definite) matrix $\boldsymbol{\Sigma}$. Then, the joint density function of $\mathbf{X}$ can be expressed as

$$f(\mathbf{x})=\frac{1}{(2\pi)^{\frac{n}{2}}\sqrt{\det(\boldsymbol{\Sigma})}}\exp\left(-\frac{1}{2}(\mathbf{x}-\boldsymbol{\mu})^T\boldsymbol{\Sigma}^{-1}(\mathbf{x}-\boldsymbol{\mu})\right) \tag{3.3.58}$$

where $\det(\boldsymbol{\Sigma})$ denotes the determinant of $\boldsymbol{\Sigma}$. It is called a multivariate normal distribution. For instance, if X_1 and X_2 are random variables following standard normal distributions $(\mu_{1,2}=0;\sigma_{1,2}=1)$, the bivariate normal distribution becomes

$$f(x_1,x_2)=\frac{1}{2\pi\sqrt{1-\sigma_{X_1X_2}}}\exp\left(-\frac{1}{2}\left(x_1^2+x_2^2+2\sigma_{X_1X_2}x_1x_2\right)\right). \tag{3.3.59}$$

Figure 3.3.5 shows this joint distribution for the case of $\sigma_{X_1X_2}=0$, $\sigma_{X_1X_2}=0.8$ and $\sigma_{X_1X_2}=-0.8$. The cases are given in 3D plots as well as in 2D colour maps.

The most flexible PDF is the Weibull function. It is especially used in engineering applications and analysis of reliability. The function is characterised by the shape parameters m and λ and is defined as

$$f_W(x;m,\lambda)=\begin{cases}\left(\frac{m}{\lambda}\right)\left(\frac{x}{\lambda}\right)^{m-1}\exp\left(-\left(\frac{x}{\lambda}\right)^m\right) & x\geq 0\\ 0 & x<0\end{cases} \tag{3.3.60}$$

where $m>0$ and $\lambda>0$ are provided. The Weibull CDF becomes

$$F_W(x;m,\lambda)=\begin{cases}1-\exp\left(-\left(\frac{x}{\lambda}\right)^m\right) & x\geq 0\\ 0 & x<0\end{cases}. \tag{3.3.61}$$

Mean μ and variance σ^2 of the Weibull distribution are

$$\mu=\lambda\Gamma\left(1+\frac{1}{m}\right)\quad\text{and}\quad\sigma^2=\lambda^2\left(\Gamma\left(1+\frac{2}{m}\right)-\Gamma\left(1+\frac{1}{m}\right)^2\right) \tag{3.3.62}$$

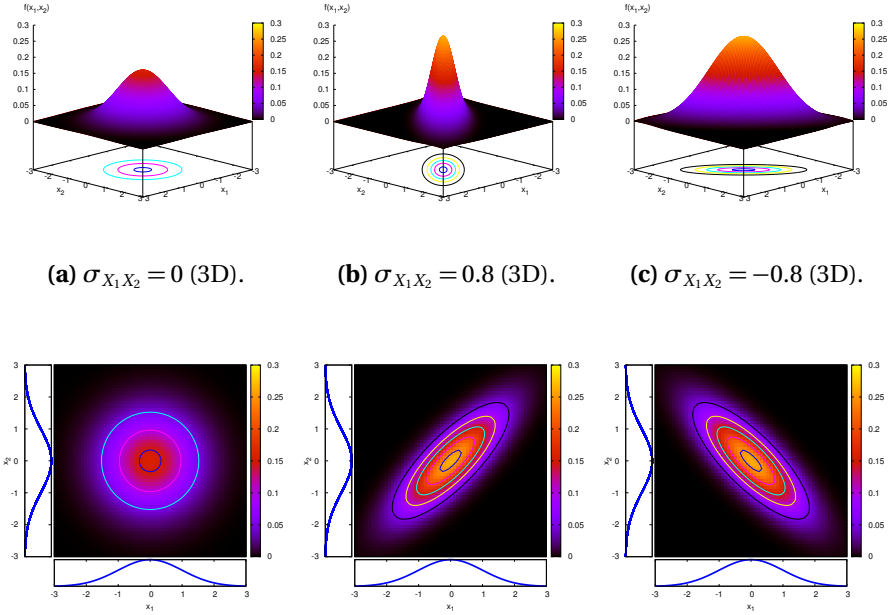

(a) $\sigma_{X_1X_2} = 0$ (3D). **(b)** $\sigma_{X_1X_2} = 0.8$ (3D). **(c)** $\sigma_{X_1X_2} = -0.8$ (3D).

(d) $\sigma_{X_1X_2} = 0$ (2D). **(e)** $\sigma_{X_1X_2} = 0.8$ (2D). **(f)** $\sigma_{X_1X_2} = -0.8$ (2D).

Figure 3.3.5: Bivariate normal distributions $\left(\sigma_{X_1X_2} = \{0, 0.8, -0.8\}\right)$.

where $\Gamma(\cdot)$ denotes the gamma function which is defined by

$$\Gamma(\alpha) = \int_0^\infty x^{\alpha-1} \exp(-x)\, dx \tag{3.3.63}$$

where $\alpha > 0$ is provided. Compared to the normal distribution, the Weibull distribution is not symmetric and is able to represent a skewness of a sample space. In Figure 3.3.6a and Figure 3.3.6b, the influence of shape parameters m and λ on the Weibull distribution are presented. In certain cases the Weibull distribution can be very similar to the normal distribution, see Figure 3.3.7. Here, the uniform, the normal and the Weibull distribution are plotted with identical mean $\mu = 3.6$ and standard deviation $\sigma = 1.0$.

Furthermore, the Weibull CDF can be linearised by transforming Equation (3.3.61) according to

$$\begin{aligned} 1 - F_W &= \exp\left(-\left(\frac{x}{\lambda}\right)^m\right) \\ \ln\left(\frac{1}{1-F_W}\right) &= \left(\frac{x}{\lambda}\right)^m \\ \underbrace{\ln\left(\ln\left(\frac{1}{1-F_W}\right)\right)}_{y(\tilde{x})} &= \underbrace{(m\ln(x))}_{m\tilde{x}} + \underbrace{(-m\ln(\lambda))}_{c}. \end{aligned} \tag{3.3.64}$$

The linear plot of $\ln\left(\ln\left(\frac{1}{1-F_W}\right)\right)$ versus $\ln(x)$ is called Weibull probability plot. This plot is often used to identify the Weibull distribution parameters.

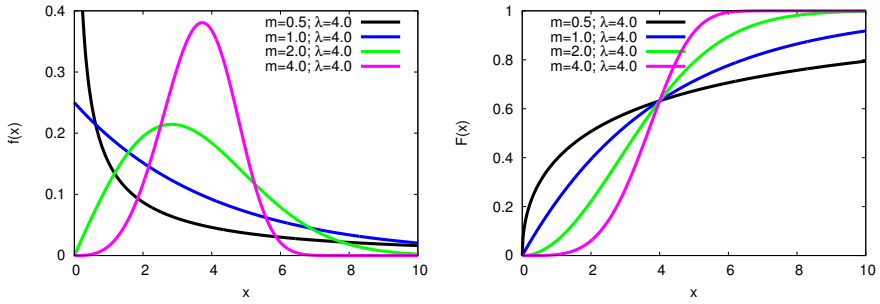

(a) $f_W(x;0,\{0.5,1,2,4\})$. **(b)** $F_W(x;0,\{0.5,1,2,4\})$.

Figure 3.3.6: Examples of Weibull PDFs and CDFs ($m=0.5,1,2,4;\lambda=4$).

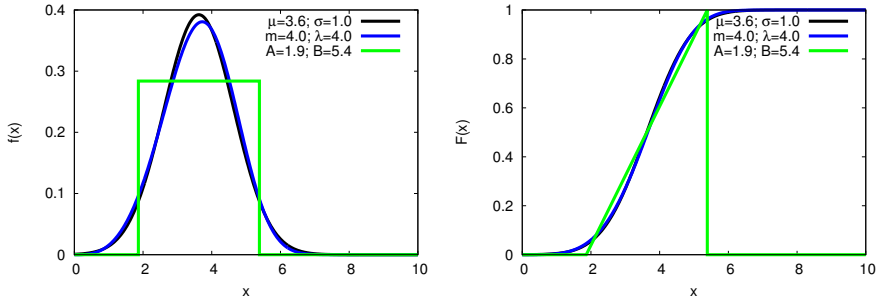

(a) Comparison of PDFs. **(b)** Comparison of CDFs.

Figure 3.3.7: Comparison of uniform, normal and Weibull distribution with equal mean and standard deviation $(\mu=3.6,\sigma=1.0)$.

3.3.6 Limit Theorems

The strong law of large numbers is one of the most well-known results in probability theory, see Walpole [111]. It states that a random variable $\overline{X}$ defined as the average of n independent random variables X_i each with identical distribution $f(x_i)$ converges to mean μ of $f(x_i)$ with a probability of 1. In mathematical expressions, if $\overline{X}$ is defined as

$$\overline{X}_n=\frac{1}{n}\sum_{i=1}^{n}X_i \quad \text{with} \quad f(x_1)=f(x_2)=\ldots=f(x_n), \tag{3.3.65}$$

then $\overline{X}$ converges to

$$\lim_{n\to\infty}\overline{X}_n=\lim_{n\to\infty}\frac{1}{n}\sum_{i=1}^{n}X_i=\mu \quad \text{with} \quad P\left(\lim_{n\to\infty}\overline{x}_n=\mu\right)=1. \tag{3.3.66}$$

This implies that, if a statistical experiment is repeated indefinitely under the same conditions, the average of the outcome $\bar{x}$ converges to the mean of the underlying PDF.

Probably the most important result in probability theory is the central limit theorem which is based on the law of large numbers, see Walpole [111]. Here, the averaged random

variable $\overline{X}$ defined in Equation (3.3.65) is considered. According to Equation (3.3.44) and Equation (3.3.45), the mean and standard deviation of $\overline{X}$ becomes

$$\mu_{\overline{X}} = \frac{1}{n}\sum_{i=1}^{n}\mu_X = \mu_X \quad \text{and} \quad \sigma^2_{\overline{X}} = \frac{1}{n^2}\sum_{i=1}^{n}\sigma^2_X = \frac{1}{n}\sigma^2_X. \tag{3.3.67}$$

Then, the random variable Z_n can be expressed by the means of Equation (3.3.55) as

$$Z_n = \frac{\overline{X} - \mu_{\overline{X}}}{\sigma_{\overline{X}}} = \frac{\left(\frac{1}{n}\sum_{i=1}^{n} X_i\right) - \mu_X}{\sigma_X/\sqrt{n}}. \tag{3.3.68}$$

The central limit theorem states that Z_n follows a standard normal distribution if n approaches infinity according to

$$\lim_{n\to\infty} F(z_n) = F_N(z_n; 0, 1) \tag{3.3.69}$$

Thus, it follows that $\overline{X}$ converges to a normal distribution given by

$$\lim_{n\to\infty} F(\bar{x}_n) = F_N\left(\bar{x}_n; \mu_X, \sigma_X/\sqrt{n}\right). \tag{3.3.70}$$

It is noted that this theorem holds for any distribution of X as long as μ_X and σ_X exist and both are finite. The central limit theorem can be interpreted as follows: The mean of a statistical experiment is normally distributed independent of the underlying distribution function. Thus, the central limit theorem demonstrates the importance of the normal distribution.

Another essential theorem is Chebyshev's inequality, see Walpole [111],

$$P\left(\mu - k\sigma \le X \le \mu - k\sigma\right) \ge 1 - \frac{1}{k^2} \tag{3.3.71}$$

where $k > 0$ is provided. It states that any random variable X with mean μ and standard deviation σ assumes a value within k standard deviations away from the mean with a probability of at least $1 - \frac{1}{k^2}$. This inequality enables to characterise samples of any arbitrary distribution provided μ and σ are known. For instance, more than 75% of an arbitrary sample lies within 2 standard deviations σ away from mean μ.

3.3.7 Simulation of Random Variables

The numerical simulation of statistical experiments requires the generation of random numbers. The complex task is to generate a sample of numbers drawn from a random variable X with known PDF $f(x)$. This is done by a random number generators. These can be classified in True Random Number Generators (TRNG) and Pseudo-Random Number Generators (PRNG), see Behnia et al. [11]. A TRNG is based on physical processes. It measures the variations of natural phenomena that are expected to be random such as the atmospheric noise, see RANDOM.ORG [96]. A PRNG computes a sequence of numbers based on a recursive algorithm, see Jennings and Sumeet [64] and Ross [101]. This sequence is used as a sample of X. Therefore, the random variable X becomes a pseudo-random variable in numerical simulations when a PRNG is applied. Most algorithms use an initial true random seed as a starting sequence. However, this approach produces always the same sequence while the same initial seed is used. It can be avoided when the initial seed is modified by physical conditions of the computer hardware (temperature, time, etc.). The advantage of a PRNG compared to a TRNG is the numerical efficiency.

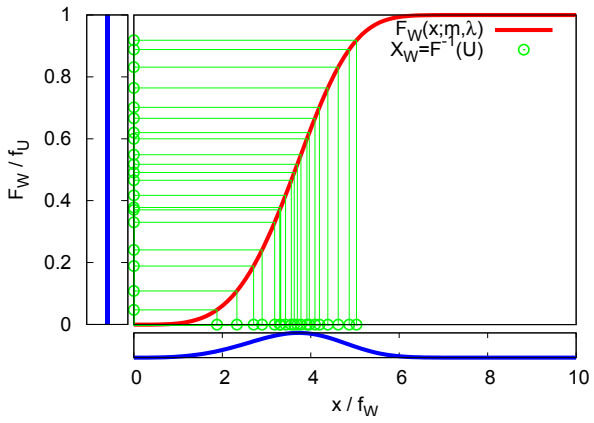

Figure 3.3.8: Inverse transformation technique.

Programming languages like Fortran, Java and C++ include PRNGs within subroutines. Conventional mathematical programs like MATLAB [83], Mathematica [116] and Excel [85] provide PRNGs as functions. In general, the implemented PRNG computes a sequence of uniform pseudo-random decimal fractions within the interval between 0 and 1. However, the design of random number generators is still today a challenge in computational and mathematical science.

In the following, it is provided that a sample of random numbers drawn from the uniform distribution $f_U(x;0,1)$ is correctly generated. The uniform distribution is often applied to simulate various continuous random variables with known PDF $f(x)$. A general and simple technique is the inverse transformation method and it is based on the uniform random variable U with PDF $f_U(x;0,1)$ and an arbitrary continuous random variable X with CDF $F(x)$. If X is a continuous random variable with CDF $F_X(x)$, the random variable

$$Y = F_X(X) \tag{3.3.72}$$

is uniformly distributed over the interval between 0 and 1, see Equation (3.3.26). The inverse relation becomes

$$X = F_X^{-1}(Y) = F_X^{-1}(U). \tag{3.3.73}$$

From a numerical point of view, it is convenient to define the unit interval without the boarders 0 and 1. For example, the Weibull distribution is defined in the domain $0 \leq x < \infty$ and a value of 1 in the uniform distribution leads to a value of ∞ in the Weibull distribution which is numerically not realisable. Therefore, most common uniform PRNGs produce numbers in the domain $0 < x < 1$. However, the inverse transformation method allows to draw a sequence of X by drawing a sequence of U. It requires that the inverse function $F_X^{-1}(u)$ can be expressed in terms of elementary functions. For example, a Weibull random variable X_W can be simulated using the expression

$$X_W = F_W^{-1}(U) = \lambda \sqrt[m]{-\ln(1-U)}. \tag{3.3.74}$$

Figure 3.3.8 demonstrates the inverse transformations technique. Here, a sequence of twenty uniform numbers is transformed into a sequence of Weibull numbers. Other approaches are the rejection method or the hazard rate method, see Ross [101].

The simulation of a normally distributed random variable X_N needs more specialised techniques. A simple method is called the Box-Muller transformation. This method generates a pair of independent and standard normal random variables Z_0 and Z_1 given a pair

of independent and uniform random variables U_1 and U_1 such as

$$\begin{aligned} Z_0 &= \sqrt{-2\ln(U_1)}\cos(2\pi U_2) \\ Z_1 &= \sqrt{-2\ln(U_1)}\sin(2\pi U_2). \end{aligned} \tag{3.3.75}$$

Using Equation (3.3.55), Z_0 and Z_1 can be transformed into any normal distribution. An extension of the Box-Muller method is known as the polar method, see Ross [101].

3.3.8 Stochastic Processes and Random Fields

A stochastic process is defined as a function of the vector $\mathbf{t} \in \mathbb{R}^r$ whose values are random variables such as $X(\mathbf{t})$. This means that a random variable $X(\mathbf{t})$ exists for any $\mathbf{t} \in \mathbb{R}^r$. $X(\mathbf{t})$ is often called a random field. For example, $X(\mathbf{t})$ can be defined in time ($\mathbf{t} \in \mathbb{R}$), in a spatial field $\left(\mathbf{t} \in \mathbb{R}^3\right)$ or in a time dependent spatial field $\left(\mathbf{t} \in \mathbb{R}^4\right)$. Also here a distinction is made between discrete, continuous and combined fields. According to Equation (3.3.30) and Equation (3.3.35), mean and variance of a random field $X(\mathbf{t})$ become

$$\mu(\mathbf{t}) = E[X(\mathbf{t})] \tag{3.3.76}$$

and

$$\sigma^2(\mathbf{t}) = E\left[\left(X(\mathbf{t}) - \mu(\mathbf{t})\right)^2\right]. \tag{3.3.77}$$

Furthermore, two random variables in $X(\mathbf{t})$ at location $\mathbf{t} = \mathbf{t}_i$ and location $\mathbf{t} = \mathbf{t}_j = \mathbf{t}_i + \mathbf{h}$ are denoted as $X_i = X(\mathbf{t}_i)$ and $X_j = X\left(\mathbf{t}_j = \mathbf{t}_i + \mathbf{h}\right)$. The vector $\mathbf{h} \in \mathbb{R}^r$ is called separation vector. Corresponding to Equation (3.3.40), the covariance of X_i and X_j becomes

$$\begin{aligned} \sigma_{X_i X_j} &= E\left[\left(X(\mathbf{t}_i) - \mu(\mathbf{t}_i)\right)\left(X\left(\mathbf{t}_j\right) - \mu\left(\mathbf{t}_j\right)\right)\right] \\ &= E\left[\left(X(\mathbf{t}_i) - \mu(\mathbf{t}_i)\right)\left(X(\mathbf{t}_i + \mathbf{h}) - \mu(\mathbf{t}_i + \mathbf{h})\right)\right]. \end{aligned} \tag{3.3.78}$$

A random field is said to be isotropic if the covariance $\sigma_{X_i X_j}$ only depends on the absolute value of $\mathbf{h}$, $|\mathbf{h}| = \sqrt{\mathbf{h}^T\mathbf{h}}$. However, the determination of $\sigma_{X_i X_j}$ requires the joint density function of $X(\mathbf{t})$.

In general, random fields are separated into three types of stationarity, see Corstanje et al. [21] and Fyllingen [41]. These are denoted as strictly, weakly and intrinsic stationarity. A random field $X(\mathbf{t})$ is said to be strictly stationary, if the joint distribution of $X(\mathbf{t})$ is the same as the one of $X(\mathbf{t}+\mathbf{h})$ for any $\mathbf{h} \in \mathbb{R}^r$. Consequently, mean and variance does not change between $\mathbf{t}$ and $\mathbf{t}+\mathbf{h}$, which which means $\mu(\mathbf{t}) = \mu(\mathbf{t}+\mathbf{h})$ and $\sigma^2(\mathbf{t}) = \sigma^2(\mathbf{t}+\mathbf{h})$. In case the mean of a strictly stationary field is constant, such as $\mu(\mathbf{t}) \equiv \mu$, and its covariance can be expressed as a pure function of $\mathbf{h}$ as

$$\sigma_{X_i X_j} = C(\mathbf{h}), \tag{3.3.79}$$

the random field is defined as weakly stationary. The function $C(\mathbf{h})$ is called covariance function. The corresponding correlation coefficient can simply be expressed as

$$\rho_{X_i X_j} = \frac{C(\mathbf{h})}{C(\mathbf{0})}. \tag{3.3.80}$$

The definition of a weakly stationary random field implies that the PDF of X_i alone is the same as the one of X_j alone and it leads to

$$E[X_i] = E\left[X_j\right] = \mu, \tag{3.3.81}$$

$$E\left[(X_i-\mu)^2\right]=E\left[\left(X_j-\mu\right)^2\right]=\sigma^2. \tag{3.3.82}$$

The random field is intrinsic stationary if the conditions

$$E\left[X(\mathbf{t}+\mathbf{h})-X(\mathbf{t})\right]=0 \tag{3.3.83}$$

and

$$E\left[(X(\mathbf{t}+\mathbf{h})-X(\mathbf{t}))^2\right]=2\gamma(\mathbf{h}) \tag{3.3.84}$$

are fulfilled for any $\mathbf{h}\in\mathbb{R}^r$. Here, $2\gamma(\mathbf{h})$ denotes the variogram and $\gamma(\mathbf{h})$ the semivariogram. The relation between semivariogram $\gamma(\mathbf{h})$ and covariance $C(\mathbf{h})$ becomes

$$\gamma(\mathbf{h})=C(\mathbf{0})-C(\mathbf{h}). \tag{3.3.85}$$

In case of isotropy, covariance function $C(\mathbf{h})$ and semivariogram function $\gamma(\mathbf{h})$ only depend on the scalar $d=|\,\mathbf{h}\,|$. Here, several parametric expressions for $C(d)$ are available. An isotropic and (weakly) stationary random field is called homogeneous. Popular homogenous covariance functions are exponential, Gaussian or the generalised Matérn function, see Abrahamsen [1]. The Gaussian covariance function is given by

$$C(d;d_0)=\sigma^2\exp\left(-\left(\frac{d}{d_0}\right)^2\right) \tag{3.3.86}$$

where $d_0>0$ can be seen as correlation length. In Figure 3.3.9a, plots of the Gaussian covariance function are shown for different values of correlation length d_0. If the random field $X(\mathbf{t})$ is mutually statistical independent, the Gaussian covariance function limits to

$$\lim_{d_0\to 0}C(d;d_0)=\begin{cases}\sigma^2 & d=0\\ 0 & d\neq 0\end{cases} \tag{3.3.87}$$

which is known as (Gaussian) white noise. It can also be expressed by the Dirac function as $C(d;d_0=0)=\sigma^2\delta(d)$ given in Equation (3.3.10). The white noise describes a complete chaotic phenomenon. The other extreme case is an everywhere constant Gaussian covariance function such as

$$\lim_{d_0\to\infty}C(d;d_0)=\sigma^2. \tag{3.3.88}$$

Here, the random field $X(\mathbf{t})$ with a everywhere covariance can be determined by a single random number x and a deterministic function $g(\mathbf{t})$,

$$X(\mathbf{t})=x\cdot g(\mathbf{t}). \tag{3.3.89}$$

A Gaussian random field is characterised by a multivariate normal distribution of $X(\mathbf{t})$ as given in Equation (3.3.58). Homogenous Gaussian fields combined with the Gaussian covariance function are often used due to their simplicity. The simulation of these is the base for many numerical studies. However, before a sample of a homogenous Gaussian random field can be simulated, the field has to be discretised into a grid of n nodes. Here, each node is found by $\mathbf{t}=\mathbf{t}_i$ with $i=1,2,\ldots,n$ and represents the random variable $X_i(\mathbf{t}=\mathbf{t}_i)$ with normal PDF $f_N\left(x_i;\mu,\sigma\right)$. Therefore, the Gaussian random field $X(\mathbf{t})$ is represented by a finite number of n random variables and is given in a vector as

$$\mathbf{X}=(X_1(\mathbf{t}_1),X_2(\mathbf{t}_2),\ldots,X_n(\mathbf{t}_n))^T. \tag{3.3.90}$$

Using the Gaussian covariance function, the $n\times n$ elements of the covariance matrix $\mathbf{\Sigma}$ become

$$\Sigma_{ij}=C\left(d=|\,\mathbf{t}_i-\mathbf{t}_j\,|;d_0\right)=\sigma^2\exp\left(-\left(\frac{|\,\mathbf{t}_i-\mathbf{t}_j\,|}{d_0}\right)^2\right) \tag{3.3.91}$$

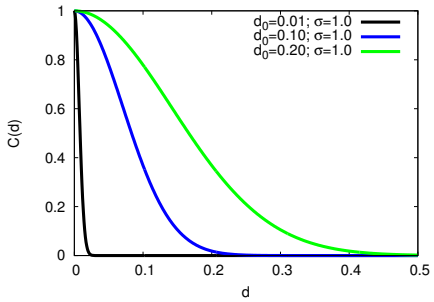

(a) Gaussian covariance function.

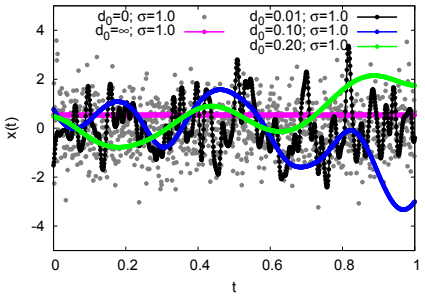

(b) Samples of 1D Gaussian random fields.

Figure 3.3.9: Influence of Gaussian correlation length d_0 on samples of 1D Gaussian random fields.

and the n identical means are given in a vector $\boldsymbol{\mu}$ of length n as

$$\boldsymbol{\mu} = (\mu, \mu, \ldots, \mu)^T. \tag{3.3.92}$$

Using $\boldsymbol{\Sigma}$ and $\boldsymbol{\mu}$ in Equation (3.3.58), a sample from the homogenous Gaussian Random field $\mathbf{X}$ can be drawn. Here, the statistical toolbox available in MATLAB [84] can be applied. It includes the function `mvnrnd` $(\boldsymbol{\mu}, \boldsymbol{\Sigma})$ which generates a sample (sequence) of $\mathbf{X}$ with mean vector $\boldsymbol{\mu}$ and covariance matrix $\boldsymbol{\Sigma}$.

In the following, two examples of homogeneous Gaussian random fields are given. Both fields use standard normal distributions $f_N(x_i; 0, 1)$ for the n random variables X_i. Furthermore, the Gaussian covariance function is applied to determine the elements of $\boldsymbol{\Sigma}$. The first example is given in Figure 3.3.9b. It shows samples of 1D Gaussian random fields along a line segment $\mathbf{t} = [0, 1]$ which is discretised with 1001 nodes. The samples are drawn form fields with different correlation lengths d_0, see Figure 3.3.9a. In addition, the extreme cases white noise (grey) and everywhere covariance (magenta) are plotted. It is clearly seen that the oscillations decrease with increasing correlation length d_0.

The second example is illustrated in Figure 3.3.10 and it shows samples of 2D Gaussian random fields on the plane segment $\mathbf{t} = ([0, 1], [0, 1])^T$ which is discretised with 51×51 nodes. The correlation length is set to $d_0 = 0.1$ and $d_0 = 0.2$, respectively. Also here, it can be seen that the oscillations decrease with increasing correlation length d_0. Furthermore, the samples are drawn as 3D plots as well as 2D colour maps with interpolated values between nodes. It is important to mention that a random field with a large number of nodes is a numerical challenge due to the generation of a big amount of random numbers and the matrix inversion of $\boldsymbol{\Sigma}$.

3.3.9 Monte-Carlo Simulation

A vector $\mathbf{X} = (X_1, X_2, \ldots, X_n)^T$ containing n random variables X_i with joint density function $f(x_1, x_2, \ldots, x_n)$ is considered and Y is defined as a function of $\mathbf{X}$ such as $Y = g(\mathbf{X})$.

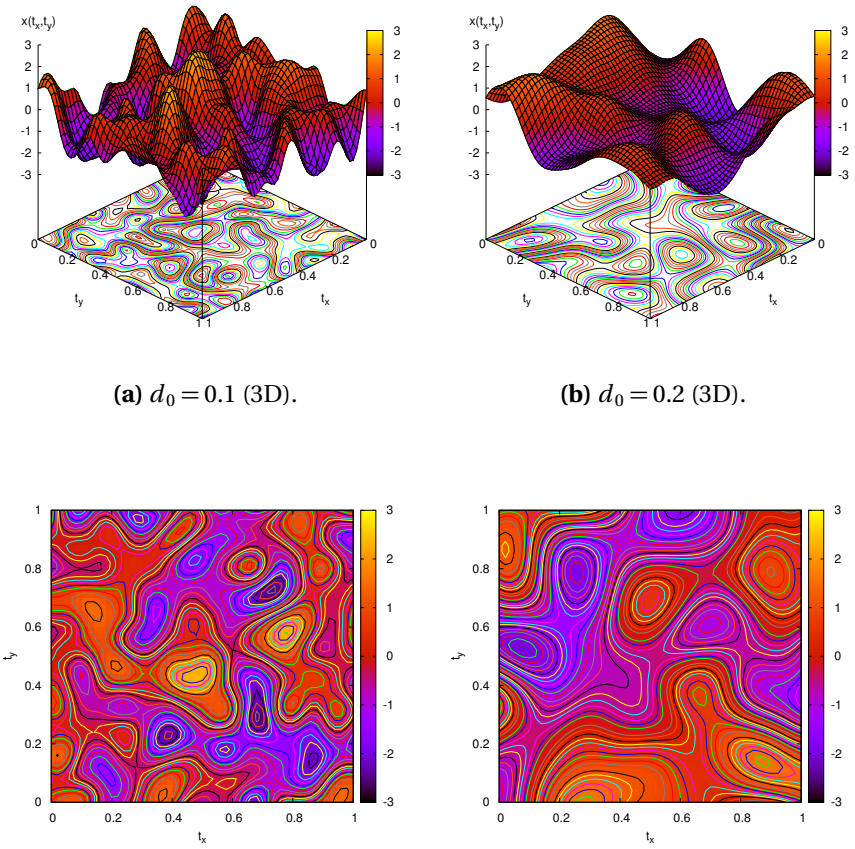

(a) $d_0 = 0.1$ (3D). **(b)** $d_0 = 0.2$ (3D).

(c) $d_0 = 0.1$ (2D). **(d)** $d_0 = 0.2$ (2D).

Figure 3.3.10: Influence of Gaussian correlation length d_0 on samples of 2D Gaussian random fields.

According to Equation (3.3.34), the mean of the function $g(\mathbf{X})$ becomes

$$\begin{aligned} E[Y] &= E[g(\mathbf{X})] \\ &= \int_{-\infty}^{+\infty} \dots \int_{-\infty}^{+\infty} \int_{-\infty}^{+\infty} g(\mathbf{X}) \dots \\ &\quad \dots f(x_1, x_2, \dots, x_n)\, dx_1 dx_2 \dots dx_n. \end{aligned} \tag{3.3.93}$$

In many applications, the multiple integral in $E[g(\mathbf{X})]$ cannot be determined analytically. Here, $E[g(\mathbf{X})]$ can be estimated by a stochastic simulation. Therefore, a random number vector $\mathbf{x}_k$ of $\mathbf{X}$ has to be generated. It is noted that $\mathbf{x}_k$ has to satisfy the joint density function $f(x_1, x_2, \dots, x_n)$. Then a random number y_k of Y can be determined using the function $y_k = g(\mathbf{x}_k)$. This procedure is repeated m times and a sample of Y (with size m)

is generated and the average of the sample becomes

$$\bar{y}_m = \frac{1}{m}\sum_{k=1}^{m} y_k. \tag{3.3.94}$$

By the strong law of large numbers, see Equation (3.3.66), $\bar{y}_m$ converges to the expected value $E[Y]$ and therefore to $E\left[g(\mathbf{X})\right]$, so that

$$\lim_{m\to\infty} \bar{y}_m = E[Y] = E\left[g(\mathbf{X})\right]. \tag{3.3.95}$$

This approach allows to use the average of $\bar{y}_m$ to estimate $E\left(g(\mathbf{X})\right)$ and is called a Monte-Carlo simulation, see Ross [101]. The precision of the Monte-Carlo simulation can be expressed by

$$e = \frac{1}{\sqrt{m}}\sigma_Y \tag{3.3.96}$$

where σ_Y denotes standard deviation of Y and $g(\mathbf{X})$, respectively. The necessary number of runs m has to be chosen large enough so that e is exactable small. It is seen that the convergency rate is $1/\sqrt{m}$, see Siebertz et al. [103]. This means that the number of runs has to increase four times to halve the error e. However, the difficulty is that σ_Y is unknown in advance. It can be estimated by a prior Monte-Carlo simulation and be determined by

$$s_Y = \sqrt{\frac{1}{m-1}\sum_{k=1}^{m}\left(y_k - \bar{y}_m\right)^2}. \tag{3.3.97}$$

Besides the number of runs, the computing of the function values $y_k = g(\mathbf{x}_k)$ might be very time consuming. The performance of a Monte-Carlo simulation is a straight forward procedure: Definition of a joint density function, generation of random numbers, assigning of function values to the random numbers, statistical analysis of the output. Therefore, the Monte-Carlo simulation is applied in many numerical studies of statistical experiments.

3.4 Experimental Sample and Sample Size

It is considered that n experiments are performed in an experimental study. Here, each experiment represents a random variable X_i and each experimental result x_i is a possible outcome of X_i. If n experiments are performed under nearly equal conditions, it can be assumed that n random variables X_i are statistical independent and identically distributed and it follows

$$f(x_1) = f(x_2) = \ldots = f(x_n) = f(x) \tag{3.4.1}$$

and

$$f(x_1, x_2, \ldots, x_n) = f(x_1) f(x_2) \ldots f(x_n) = \left[f(x)\right]^n \tag{3.4.2}$$

and thus the n experimental results x_i can be grouped together as a sample of X with PDF $f(x)$. The experimental study represents the random variable X with $n-1$ degrees of freedom.

The sample size n plays a crucial role in descriptive and interferential statistics. It is clearly seen that a large sample size increases the quality of the statistical analysis and allows a more precise characterisation of the underlying distribution (or PDF). Here, the determination of n depends on many factors as seen in the Composite Materials Handbook Volume I [25]:

- Statistical model which the sample is thought to represent
- Degree of reproducibility which is desired
- Statistical measurement which is estimated
- Variability of the experimental results
- Expenses of the experimental study

The challenge in most studies is that the underlying distribution (or PDF) is unknown a priori and assumptions have to be made to determine n. Here, a sample size $n \geq 30$ is often recommended as a guideline for statistical studies, see Walpole [111] and Campbell [17].

3.5 Descriptive Statistics

The descriptive statistic provides an overview of a given set of data which is taken from a frequently repeated experiment. If the conditions during testing are constant or nearly constant, the set of data can be detected as sample and a descriptive analysis can be performed. Statistical measurements are used to quantify sample data. These give information about central tendency and variability of the data. Both allow to describe the general nature of the sampling distribution. Large sample sizes can be displayed clearly in graphs using these measurements. Here, several techniques are provided to display data. In general, the descriptive analysis allows to summarise a sample and to draw conclusions about characteristics of the underlying distribution.

3.5.1 Statistical Measurements

A sample X of a quantity consists of n data values, each value denoted by x_i. It is provided that the sample is taken randomly from the underlying sample space. The sample mean $\bar{x}$ is given by

$$\bar{x} = \frac{1}{n}\sum_{i=1}^{n} x_i \tag{3.5.1}$$

and the sample variance s^2 by

$$s^2 = \frac{1}{n-1}\sum_{i=1}^{n}(x_i - \bar{x})^2. \tag{3.5.2}$$

The sample standard deviation becomes $s = \sqrt{s^2}$ and thus the sample coefficient of variation c_s becomes

$$c_s = \frac{s}{\bar{x}}. \tag{3.5.3}$$

If two quantities x_i and y_i are measured, the covariance s_{XY} between sample X and sample Y is defined as

$$s_{XY} = \frac{1}{n-1}\sum_{i=1}^{n}(x_i - \bar{x})\left(y_i - \bar{y}\right) \tag{3.5.4}$$

where $\bar{x}$ is the mean of X and $\bar{y}$ the mean of the Y. Using the corresponding sample standard deviations s_X and s_Y, the correlation between X and Y becomes

$$r_{XY} = \frac{s_{XY}}{s_X s_Y}. \tag{3.5.5}$$

The sample range d is simply given by

$$d = x_{max} - x_{min} \tag{3.5.6}$$

where x_{max} is the largest value and x_{min} the smallest in the sample. If the n sample values x_i are sorted by size and renumbered as well as divided in k subsets of size n/k, the subset boundaries are known as the k sample quantiles $Q_{\frac{j}{k}\cdot 100\%}$. The j^{th} quantile of k quantiles is given by

$$Q_{\frac{j}{k}\cdot 100\%} = \begin{cases} x_i & \text{with } i = \text{ceiling}\left[n \cdot \frac{j}{k}\right] \text{ if } i \notin \mathbb{Z} \\ \frac{1}{2}(x_i + x_{i+1}) & \text{with } i = n \cdot \frac{j}{k} \text{ if } i \in \mathbb{Z} \end{cases} \tag{3.5.7}$$

where $\mathbb{Z}$ denotes the set of integers and the operator ceiling $[\cdot]$ is the ceiling function which maps a real number to the smallest following integer. The sample quartiles, $Q_{25\%}$, $Q_{50\%}$ and $Q_{75\%}$, are usually used in statical analyses. Here, the sample quartile $Q_{50\%}$ is known as sample median. The range between two sample quantiles becomes

$$RQ_{\frac{p}{k}\cdot 100\%} = Q_{\frac{j+p}{k}\cdot 100\%} - Q_{\frac{j}{k}\cdot 100\%}. \tag{3.5.8}$$

This implies that $\frac{p}{k} \cdot 100\%$ of the data lies in the range $RQ_{\frac{p}{k}\cdot 100\%}$. For example, 50% of the sample data lies in the interquartile range $IRQ = RQ_{50\%} = Q_{75\%} - Q_{25\%}$. Another measurement is the mode defined in Equation (3.3.46) which is not measurable if the data values are drawn from a continuous sample space.

The measurements described here are categorised in measurements of central tendency ("Where is the data located?") and of variability ("How does the data scatter?"). Therefore, mean $\bar{x}$ and median $Q_{50\%}$ are measurements of central tendency of a sample. Variation s^2, standard deviation s and coefficient of variation c_s as well as range r, quartiles $Q_{25\%}$ and $Q_{75\%}$ and inter quartile range IQR are measurements of variability of the sample.

3.5.2 Graphical Representation of Statistical Data

Graphs and histograms are common tools to analyse visually experimental studies and their set of data. The objective is to display the data in a way that enables to extract information about the sample properties. Furthermore, differences and connections between samples can easily be demonstrated using graphical methods. The choice of presentation depends on the type and amount of data as well as the requested information. A broad overview of graphical representation methods are provided in the book by Matange and Heath [82]. In the following just a few techniques are presented.

In order to explain some of the presentation methods, two samples X and Y of size $n = 30$ are considered. The corresponding statistical measurements are listed in Table 3.5.1. The sample data is presented in Figure 3.5.1a and Figure 3.5.1b. Here, the sample values are plotted in the order they are measured. In addition, sample mean $\bar{x}$ as well as sample standard deviation $\bar{x} \pm s$ are drawn as straight lines. It can be seen how many data points lie within one standard deviation away from the mean. However, the whole sample can be expressed clearly in a box-plot. The box-plot provides an overview of sample range d and sample quartiles $Q_{25\%}$, $Q_{50\%}$ and $Q_{75\%}$, see Figure 3.5.2. A box is drawn from $Q_{25\%}$ to $Q_{75\%}$ and the median $Q_{50\%}$ is marked in the box. The box includes 50% of the sample data. Furthermore, so-called whiskers are plotted out of the box and their lengths range to the most extreme data point within the maximum whisker lengths. The whisker ends are usually defined as

$$W_u = \min\left[Q_{75\%} + 1.5 \cdot IQR, x_{max}\right] \tag{3.5.9}$$

	Sample X	Sample Y
n	30	30
x_{min}	1.88	0.33
x_{max}	5.12	4.24
d	3.24	3.91
$Q_{25\%}$	3.31	1.01
$Q_{50\%}$	3.80	1.49
$Q_{75\%}$	4.18	2.09
IQR	0.87	1.08
$\bar{x}$	3.74	1.69
s	0.71	0.99
c_s	19%	59%
s_{XY}	0.02	0.02
r_{XY}	0.03	0.03

Table 3.5.1: Statistical measurements of sample X and sample Y.

for the upper whisker and

$$W_l = \max\left[Q_{25\%} - 1.5 \cdot IQR, x_{min}\right] \tag{3.5.10}$$

for the lower whisker. The data values are marked as outliers when these are lager than W_u or smaller than W_l. Variability and skewness of the data can be seen in a box-plot. Furthermore, box-plots are used to compare data of different samples without making any assumption of the underlying distribution. For instance, if sample mean $\bar{x}$ and standard deviation s are used for comparison, a normal distribution and thus a symmetric distribution is assumed. The samples X and Y are compared via box-plots in Figure 3.5.1c. Sample X shows a homogeneous data distribution, whereas the large upper whisker W_U of sample Y suggests a slight skewness of the data. By comparing both, it is seen that the quartiles of X are much larger than the quartiles of Y, but the interquartile range appears to be equal.

In general, two samples can easily be evaluated regarding any correlation in a scatter plot. It requires that the samples are taken from the same experimental study where sample points of X and Y are measured simultaneously. The scatter plot of the samples X and Y is given in Figure 3.5.1d and no distinct correlation is found ($r_{XY} = 0.03$).

The histogram plot of a sample is probably the most widely used method to illustrate the density of a sample. Here, sample range d is divided in N bins of length d/N, then the density can be estimated using the definition

$$\tilde{f}(x) = \frac{1}{n} \frac{(\text{Number of } x_i \text{ in same bin as } x)}{(d/N)}. \tag{3.5.11}$$

It is seen that the histogram shape strongly depends on the sample size and consequently on the number of bins. Therefore, histograms are only useful for large sample sizes. In Figure 3.5.1e and Figure 3.5.1f, the histograms of the sample X and sample Y are demonstrated. The red dots are the underlying data values. Also here, the slight skewness of sample Y can be seen. Based on the graphs in Figure 3.5.1, it can be assumed that sample X is taken from a symmetric population and sample Y from a left-side skewed population (box-plots), both populations are differently located with different dispersions (histograms) and further the populations are independent (scatter plot).

Now, it is considered that the n data values x_i of a sample are sorted in an ascending order. Then, each data value x_i can be interpreted as a quantile with a specified fraction

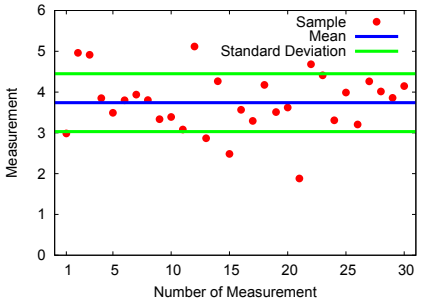

(a) Sample X including $\bar{x}$ and s_X.

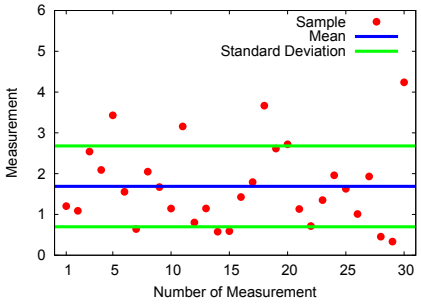

(b) Sample Y including $\bar{y}$ and s_Y.

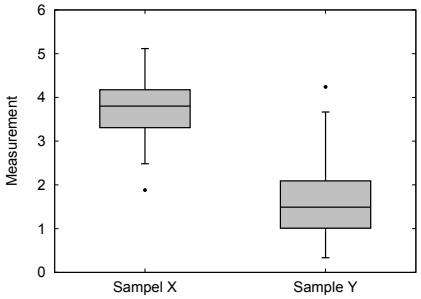

(c) Box-plot of sample X and sample Y.

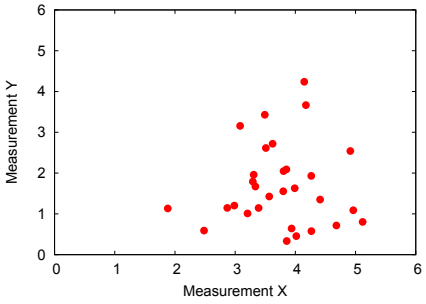

(d) Scatter plot of sample X and sample Y.

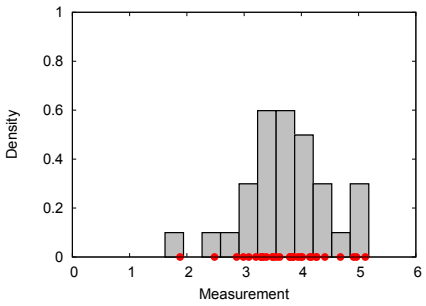

(e) Histogram of sample X.

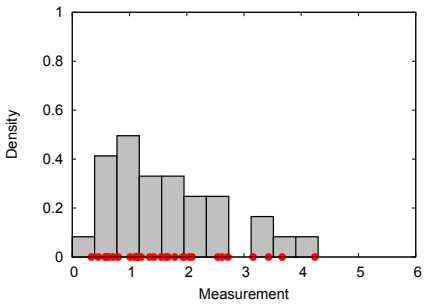

(f) Histogram of sample Y.

Figure 3.5.1: Graphical representation of sample X and sample Y.

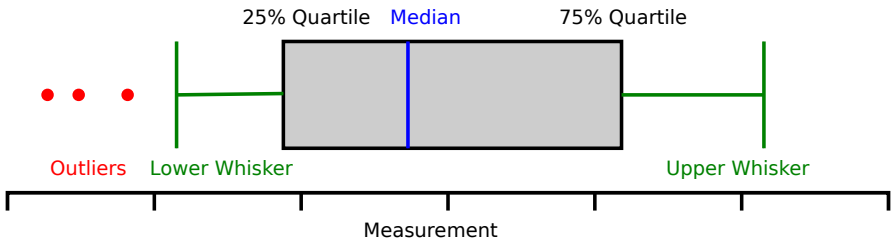

Figure 3.5.2: Details of a box-plot.

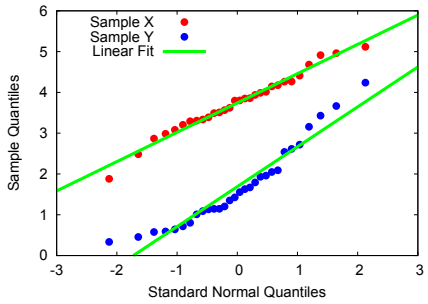

(a) Normal Q-Q plot of sample X and sample Y.

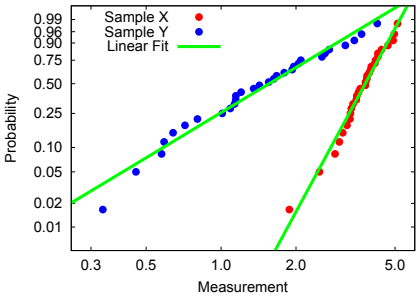

(b) Weibull plot of sample X and sample Y.

Figure 3.5.3: Distribution estimation of sample X and sample Y.

$\overline{F}_i$. This implies that $\overline{F}_i \cdot 100\%$ of the data values is less than or equal x_i. The n pairs $\left(x_i, \overline{F}_i\right)$ are an estimate of the CDF $F(x)$ of the underlying distribution and can be computed by

$$\overline{F}_i = \frac{i-a}{n+b} \tag{3.5.12}$$

where a and b are constants, see Campbell [17]. Here, a common approach is to set parameter $a = 0.5$ and parameter $b = 0$. $\overline{F}_i$ is also called the experimental probability.

A graph is called a probability-probability plot (P-P plot) when the n empirical fractions $\overline{F}_i$ are plotted versus the n theoretical $F(x_i)$. A graph is called quantile-quantile plot (Q-Q plot) when the n empirical quantiles x_i are plotted versus the n theoretical quantiles $F^{-1}\left(\overline{F}_i\right)$. In both plots, a nearly straight relationship suggests that the n data values x_i are drawn from $f(x)$. However, in most cases the CDF $F(x)$ is unknown and an estimated function $\widetilde{F}(x)$ has to be used. Therefore, P-P plots and Q-Q plots are helpful methods to check the distribution estimates. Two special types of these plots are normal Q-Q plot and Weibull plot.

The normal Q-Q plot shows the n values x_i versus the n corresponding quantiles of the standard normal distribution $F_N^{-1}\left(\overline{F}_i; 0, 1\right)$. A nearly linear relationship between these data suggests a normal distribution of the considered sample. This plot is based on the standardising of a normal distribution, see Equation (3.3.55). Consequently, an arbitrary normal distribution with mean μ and standard deviation σ can be expressed in this plot by the linear function

$$z(x) = \sigma \cdot x + \mu. \tag{3.5.13}$$

This means that a linear curve fit on sample data given in a normal Q-Q plot produces estimates of mean μ and standard deviation σ. Figure 3.5.3a shows the normal Q-Q plots of the samples X and Y and the corresponding linear curve fits. Especially sample X shows a strong linear relationship and suggests a normal distribution of the data.

The Weibull plot is based on the linear transformation of the Weibull CDF given in Equation (3.3.64). Here, each data value x_i is transformed according to

$$\tilde{x}_i = \ln(x_i), \tag{3.5.14}$$

and each empirical fraction $\overline{F}_i$ is transformed according to

$$\tilde{F}_i = \ln\left(\ln\left(\frac{1}{1-\overline{F}_i}\right)\right). \tag{3.5.15}$$

	Normal Fit			Weibull Fit		
	μ	σ	R^2	m	λ	R^2
Sample X	3.74	0.72	98%	5.91	4.04	98%
Sample Y	1.69	0.98	93%	1.92	1.88	97%

Table 3.5.2: Estimated distribution parameters of sample X and sample Y.

Based on these transformations, the n pairs $\left(x_i, \overline{F}_i\right)$ can be expressed in Weibull plot and a nearly linear relationship between these data suggests a Weibull distribution of the considered sample. In a Weibull plot, an arbitrary Weibull distribution with shape parameters m and λ can be expressed by the linear function

$$y(\tilde{x}) = m\tilde{x} + c \tag{3.5.16}$$

with

$$c = -m\ln(\lambda). \tag{3.5.17}$$

This means that a linear curve fit on sample data given in a Weibull plot produces estimates of the shape parameters m and λ. Figure 3.5.3b shows the Weibull plots of the samples X and Y and the corresponding linear curve fits. Both samples show a distinct linear relationship and a Weibull distribution can be assumed.

A common approach to fit a model function into a set of data is the method of least-squares, see Walpole [111]. The set of data consists of n data pairs (x_i, y_i) and it is assumed that the relation between the independent variable x and the dependent variable y can be expressed by a model function $f(x;\boldsymbol{\alpha})$. The $n_{\boldsymbol{\alpha}}$ function parameters are given in a vector $\boldsymbol{\alpha}$ and the objective is to find the parameter values which fit best the data points. In the least-square method, the best fit is reached when the sum of residuals

$$r(\boldsymbol{\alpha}) = \sum_{i=1}^{n} \left(y_i - f(x_i;\boldsymbol{\alpha})\right)^2 \tag{3.5.18}$$

reaches a minimum and the fitted values for $\boldsymbol{\alpha}$ are found. The problem $\min[r(\boldsymbol{\alpha})]$ is usually solved numerically. It is obvious that $n_{\boldsymbol{\alpha}}$ has to be much smaller than n for a reliable fit. The number $n - n_{\boldsymbol{\alpha}}$ is the number of degrees of freedom of the fit. A possible measure of the quality of the fit is the coefficient of determination

$$R^2 = 1 - \frac{\sum_{i=1}^{n} \left(y_i - f(x_i;\boldsymbol{\alpha})\right)^2}{\sum_{i=1}^{n} \left(y_i - \bar{y}\right)^2} \tag{3.5.19}$$

where fitted values of $\boldsymbol{\alpha}$ are applied. $R^2 = 1$ denotes a perfect fit. However, R^2 is not suitable to compare the fit results of different models, see Walpole [111]. The least-squares method is applied for both fits above and the results are listed in Table 3.5.2. The high values of R^2 confirm good fit results for all cases. Here, the fits were performed using the plotting program gnuplot [115]. The implemented fitting function solves the minimisation problem $\min[r(\boldsymbol{\alpha})]$ by using the well-known Marquardt-Levenberg algorithm.

3.6 Inferential Statistics

The goal of a statistical study is to characterise and to approximate the underlying population of a random sample based on estimates. For instance, sample mean $\bar{x}$ is used as

an estimate of population mean μ. Here, inferential statistics can be used for checking if a sample belongs to a known population at a distinct level of uncertainty. Furthermore, inferential statistics is applied to check if different random samples belong to the same population. Here, it is distinguished between the classical method of estimating population parameters and the Bayesian method. In the classical method, inferences are made based on properties obtained from of a sample taken from the population. In the Bayesian method, the prior subjective knowledge about the probability distribution of the unknown parameters is utilised together with the properties obtained from the sample, see Walpole [111]. Furthermore, the field of statistical inference can be divided into estimation of population parameters and hypothesis testing. In the present work, the focus is set on the classical method for univariate problems.

3.6.1 Unbiased Estimators

A point estimate of a population parameter θ is a value $\hat{\theta}$ of the random variable or statistic $\widehat{\Theta}$. The PDF of $\widehat{\Theta}$ is called the sampling distribution. If the expected value of a statistic $\mu_{\widehat{\Theta}}$ is equal to θ, the statistic $\widehat{\Theta}$ is said to be an unbiased estimator, so that

$$\mu_{\widehat{\Theta}} = E\left[\widehat{\Theta}\right] = \theta. \tag{3.6.1}$$

The variance of $\widehat{\Theta}$ is called the mean squared error of $\widehat{\Theta}$ and becomes

$$\sigma^2_{\widehat{\Theta}} = E\left[\left(\widehat{\Theta} - \mu_{\widehat{\Theta}}\right)^2\right]. \tag{3.6.2}$$

Consequently, the standard deviation $\sigma_{\widehat{\Theta}}$ is the standard error of $\widehat{\Theta}$. If more than one unbiased estimator exists, the estimator with the smallest variance $\sigma^2_{\widehat{\Theta}}$ should be chosen which is called the most efficient estimator of θ.

For example, statistic $\widehat{\Theta}$ is defined as

$$\widehat{\Theta} = \overline{X} = \frac{1}{n}\sum_{i=1}^{n} X_i \tag{3.6.3}$$

where X_i are n independent and identically distributed continuous random variables with mean μ_X and standard deviation σ_X. A possible outcome of $\widehat{\Theta}$ is computed as

$$\hat{\theta} = \bar{x} = \frac{1}{n}\sum_{i=1}^{n} x_i \tag{3.6.4}$$

where x_i is a random outcome of X_i. The expected value of $\widehat{\Theta}$ becomes

$$\begin{aligned} \mu_{\widehat{\Theta}} &= E\left[\widehat{\Theta}\right] \\ &= \int_{-\infty}^{+\infty} \dots \int_{-\infty}^{+\infty} \int_{-\infty}^{+\infty} \widehat{\Theta} \prod_{i=1}^{n} f_i(x)\, dx_1 dx_2 \dots dx_n \\ &= \frac{1}{n}\sum_{i=1}^{n} \mu_X = \mu_X. \end{aligned} \tag{3.6.5}$$

Therefore, statistic $\widehat{\Theta} = \overline{X}$ with outcome $\hat{\theta} = \bar{x}$ is called unbiased estimator of population mean $\theta = \mu$. The mean squared error of it becomes

$$\sigma^2_{\overline{X}} = E\left[\left(\overline{X} - \mu_X\right)^2\right] = \frac{\sigma^2_X}{n}. \tag{3.6.6}$$

It can be shown that the statistic of the sample variance,

$$\widehat{\Theta} = S^2 = \frac{1}{n-1}\sum_{i=1}^{n}\left(X_i - \underbrace{\frac{1}{n}\sum_{i=1}^{n}X_i}_{\overline{X}}\right)^2, \tag{3.6.7}$$

is an unbiased estimator of the population variance σ^2 using same conditions. A brief derivation is given by

$$\begin{aligned} E\left[S^2\right] &= E\left[\frac{1}{n-1}\sum_{i=1}^{n}\left(X_i-\overline{X}\right)^2\right] \\ &= \frac{1}{n-1}E\left[\sum_{i=1}^{n}\left(\left(X_i-\mu_X\right)-\left(\overline{X}-\mu_X\right)\right)^2\right] \\ &= \frac{1}{n-1}E\left[\sum_{i=1}^{n}\left(\left(X_i-\mu_X\right)^2\right)-n\left(\overline{X}-\mu_X\right)^2\right] \\ &= \frac{1}{n-1}\left(n\sigma_X^2 - n\sigma_{\overline{X}}^2\right) \\ &= \frac{1}{n-1}\left(n\sigma_X^2 - n\frac{\sigma_X^2}{n}\right) = \sigma_X^2. \end{aligned} \tag{3.6.8}$$

The mean squared error of the sample variance estimator is given by

$$\sigma_{S^2}^2 = E\left[\left(S^2-\sigma_X^2\right)^2\right] = \frac{2}{n-1}\sigma_X^4. \tag{3.6.9}$$

It is noted that a point estimator is still an estimate of a population parameter and the exact value cannot be estimated even for large sample sizes. However, it is possible to determine an interval within the value of the population parameter is expected with a known degree of uncertainty. The interval is expressed by

$$\hat{\theta}_L \le \theta \le \hat{\theta}_U \tag{3.6.10}$$

where the boundaries $\hat{\theta}_L$ and $\hat{\theta}_U$ depend on the estimated value $\hat{\theta}$. Since different samples yield to various values of $\hat{\theta}$, the boundaries $\hat{\theta}_L$ and $\hat{\theta}_U$ are not constant which means $\hat{\theta}_L$ is the outcome of the random variable $\widehat{\Theta}_L$ and the outcome $\hat{\theta}_U$ of the random variable $\widehat{\Theta}_U$. Further, $\widehat{\Theta}_L$ and $\widehat{\Theta}_U$ are functions of $\widehat{\Theta}$. This means that the interval becomes random and is given by

$$\widehat{\Theta}_L \le \theta \le \widehat{\Theta}_U. \tag{3.6.11}$$

The random endpoints $\widehat{\Theta}_L$ and $\widehat{\Theta}_U$ can be determined so that

$$P\left(\widehat{\Theta}_L \le \theta \le \widehat{\Theta}_U\right) = 1-\alpha \tag{3.6.12}$$

for $0 < \alpha < 1$. Then, the probability of taking a random sample which produces an interval containing θ becomes $1-\alpha$. This interval is called $(1-\alpha)\cdot 100\%$ confidence interval. An example of a two-sided confidence interval is illustrated in Figure 3.6.1a.

The confidence interval of the example above is determined as follows. According to the central limit theorem, the sampling distribution of the mean estimator $\widehat{\Theta} = \overline{X}$, see

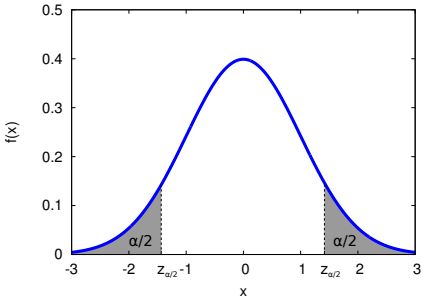

(a) Two-sided confidence-interval of a symmetric PDF.

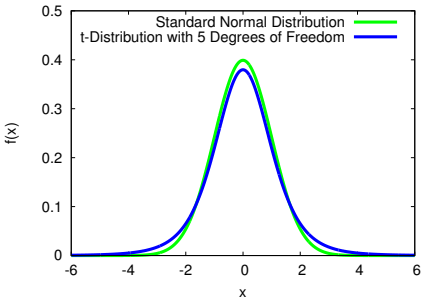

(b) Standard normal distribution and t-distribution.

Figure 3.6.1: Illustration of the $(1-\alpha)\cdot 100\%$ confidence interval and the t-distribution.

Equation (3.6.3), can be expected to be normally distributed with mean μ and standard deviation $\sigma/\sqrt{n}$. Using the standard normal transformation in Equation (3.3.55), the confidence interval of $\theta=\mu$ is found by solving

$$\begin{aligned} P\left(-z_{\alpha/2} \leq \frac{\overline{X}-\mu}{\sigma/\sqrt{n}} \leq z_{\alpha/2}\right) &= 1-\alpha \\ P\left(\underbrace{\overline{X}-z_{\alpha/2}\sigma/\sqrt{n}}_{\widehat{\Theta}_L} \leq \mu \leq \underbrace{\overline{X}+z_{\alpha/2}\sigma/\sqrt{n}}_{\widehat{\Theta}_R}\right) &= 1-\alpha \end{aligned} \tag{3.6.13}$$

where $\pm z_{\alpha/2}$ are symmetric ordinates of the standard normal distribution where an array of $2\cdot\alpha/2$ is found, see Figure 3.6.1a. Now the confidence interval of a given sample mean $\bar{x}$ can be determined as

$$\bar{x}-z_{\alpha/2}\sigma/\sqrt{n} \leq \mu \leq \bar{x}+z_{\alpha/2}\sigma/\sqrt{n} \tag{3.6.14}$$

and the probability that the error does not exceed $z_{\alpha/2}\cdot\sigma/\sqrt{n}$ is $1-\alpha$. Furthermore, a sample size of

$$n=\left(\frac{z_{\alpha/2}\sigma}{e}\right)^2 \tag{3.6.15}$$

guarantees with $(1-\alpha)\cdot 100\%$ confidence that the error does not exceed a specified error e. In this example, it is provided that standard deviation σ of the underlying population is known. The realistic case is that mean as well as standard deviation are unknown and both have to be estimated from the sample. Therefore, a random variable is defined as

$$T=\frac{\overline{X}-\mu}{S/\sqrt{n}} \quad \text{with} \quad S^2=\frac{1}{n-1}\sum_{i=1}^{n}\left(X_i-\overline{X}\right)^2 \tag{3.6.16}$$

where X_i are n independent and identically random variables with normal distribution. Then, the random variable T follows the t-distribution with $n-1$ degrees of freedom, see Walpole [111]. The t-distribution is a symmetric PDF and converges with increasing number of degrees of freedom to the standard normal distribution. In Figure 3.6.1b, both distributions are compared. Provided that the sample is drawn from a population with

normal distribution, the confidence interval is found by solving

$$\begin{aligned} P\left(-t_{\alpha/2} \leq \frac{\overline{X}-\mu}{S/\sqrt{n}} \leq t_{\alpha/2}\right) &= 1-\alpha \\ P\left(\overline{X}-t_{\alpha/2}S/\sqrt{n} \leq \mu \leq \overline{X}+t_{\alpha/2}S/\sqrt{n}\right) &= 1-\alpha \end{aligned} \tag{3.6.17}$$

where $\pm t_{\alpha/2}$ are symmetric ordinates of the t-distribution with $n-1$ degrees of freedom. This enables to predict the confidence interval of population mean μ based on sample mean $\bar{x}$ and variance s,

$$\bar{x}-t_{\alpha/2}s/\sqrt{n} \leq \mu \leq \bar{x}+t_{\alpha/2}s/\sqrt{n}. \tag{3.6.18}$$

The example shows that assumptions are necessary for making statistical inference when the underlying distribution is unknown.

3.6.2 Tolerance Intervals

The tolerance interval covers a fixed proportion of the population with a stated confidence. For example, Chebyshev's inequality given in Equation (3.3.71) produces a tolerance interval. In general, the tolerance limits are defined by

$$P\left(\mu-k\sigma \leq X \leq \mu+k\sigma\right) = 1-\alpha. \tag{3.6.19}$$

Here, the tolerance interval covers the middle $(1-\alpha)\cdot 100\%$ of the population in case of a symmetric PDF. For instance, the tolerance limits $\mu \pm k\sigma$ can be used to detect outliers in a sample. However, the population parameters as well as the PDF are usually unknown and have to be estimated by the empirical data. Therefore, the tolerance limits $\mu \pm k\sigma$ become random variables such as $\overline{X} \pm k\sqrt{S^2}$ and thus the tolerance interval is a random variable. As a result, a $(1-\gamma)\cdot 100\%$ confidence interval is used. If a sample X is drawn from a normal distribution, the tolerance limits are found by $\bar{x} \pm k\sqrt{s^2}$ and k is computed so that it can be guaranteed with $(1-\gamma)\cdot 100\%$ confidence that the limits contain at least the proportion $(1-\alpha)\cdot 100\%$ of the population. Provided that the sample is taken from a normal distribution, values of k for selected combinations of γ and α can be found in statistical tables, see Walpole [111].

3.6.3 Hypothesis Testing

A statistical hypothesis is a conjecture concerning one or more populations based on a formal statement. An absolute acceptance or rejection of the statistical hypothesis is not achievable unless the population is known. But the population and its properties are unknown in most applications and therefore samples are taken from that population. Then, the sample data is used to provide evidence that either supports or does not support the statistical hypothesis. The statistical hypothesis is rejected when the sample evidence is inconsistent with the statistical hypothesis. However, a probability exists that a rejection of the statistical hypothesis is wrong.

A statistical hypothesis test consists of a null hypothesis and an alternative hypothesis. The null hypothesis is denoted by H_0 and refers to the conjuncture. The alternative or opposite hypothesis is denoted by H_1 and is applied when H_0 is rejected. A hypothesis test leads to either rejecting H_0 or not rejecting H_0, see Montgomery [88]. For example, if two means μ and μ_0 are tested for equality, H_0 and H_1 become

$$\begin{aligned} H_0: &\quad \mu = \mu_0 \\ H_1: &\quad \mu \neq \mu_0 \end{aligned} \tag{3.6.20}$$

	H_0 **is true.**	H_0 **is not true.**
H_0 **is not rejected.**	Correct Decision	Type II Error
H_0 **is rejected.**	Type I Error	Correct Decision

Table 3.6.1: Possible situations in hypothesis testing.

where H_1 is called a two-sided alternative hypothesis because it would be true if $\mu_1 < \mu_2$ or $\mu_1 > \mu_2$. A hypothesis test is characterised by two kind of errors. If H_0 is rejected when it is actually true, the error is called a type I error and its probability to occur is α,

$$\alpha = P\left(H_0 \text{ is rejected} \,|\, H_0 \text{ is true}\right). \tag{3.6.21}$$

If H_0 is not rejected when it is actually not true, the error is called a type II error and its probability to occur is β,

$$\beta = P\left(H_0 \text{ is not rejected} \,|\, H_0 \text{ is not true}\right). \tag{3.6.22}$$

In conclusion, any test of a statistical hypothesis leads to four possible situations as presented in Table 3.6.1. The probability α of committing a type I error is called level of significance and is assigned prior to testing by the user. The probability β of committing a type II error is not predictable since the alternative hypothesis H_1 is not clearly specified. Both probabilities are related in a way that a decrease of one generally results in the increase of the other. Further, both probabilities are reduced with increasing sample size n. The probability $1-\beta$ is defined as power of the statistical hypothesis test and can be interpreted as probability of rejecting H_0 given that H_1 is true.

In the following example, it is considered that a sample of size n is drawn from a normal distribution with mean μ and standard deviation σ. Both are unknown and estimated by sample mean $\bar{x}$ and sample variance s. Now it is tested if the population mean μ equals a certain mean μ_0 at a significance level of α and the hypothesis and alternative hypothesis are formulated as

$$\begin{aligned} H_0: &\quad \mu &=& \quad \mu_0 \\ H_1: &\quad \mu &\neq& \quad \mu_0. \end{aligned} \tag{3.6.23}$$

Provided that H_0 is true, the probability that the random variable T with t-distribution (with $n-1$ degrees of freedom) lies in the interval $-t_{\alpha/2} \leq T \leq t_{\alpha/2}$ is given by

$$P\left(-t_{\alpha/2} \leq \underbrace{\frac{\overline{X}-\mu_0}{S/\sqrt{n}}}_{T} \leq t_{\alpha/2}\right) = 1-\alpha. \tag{3.6.24}$$

Due to the symmetry of the t-distribution this equation can be simply rewritten as

$$P\left(|\,T\,| > t_{\alpha/2}\right) = P\left(T > t_{\alpha/2}\right) + P\left(T < -t_{\alpha/2}\right) = \alpha. \tag{3.6.25}$$

Here, the inequality $|\,T\,| > t_{\alpha/2}$ is used to test the hypothesis. The value of T for the given sample with the properties n, $\bar{x}$ and s becomes

$$t = \frac{\bar{x}-\mu_0}{s/\sqrt{n}}. \tag{3.6.26}$$

If $\mid t \mid < t_{\alpha/2}$ is true, H_0 is not rejected and it can be assumed that $\mu = \mu_0$. If $\mid t \mid < t_{\alpha/2}$ is not true, H_0 is rejected at significance level α and H_1 is adopted. This hypothesis test is known as one-sample t-test and it is applied to check if the mean μ estimated by $\bar{x}$ is significantly different from a known mean μ_0 provided that the sample is drawn from a normal distribution. A common method is to use the inequality

$$P(\mid T \mid > t) > \alpha. \tag{3.6.27}$$

If $P(\mid T \mid > t) > \alpha$ is not true, H_0 is rejected at significance level α. Furthermore, the example has shown that testing $H_0 : \mu = \mu_0$ against $H_1 : \mu \neq \mu_0$ at significant level α is equivalent to compute the $(1-\alpha)\cdot 100\%$ confidence interval of μ based on $\bar{x}$ and rejecting H_0 if μ_0 lies not within the confidence interval. However, in many studies it is of interest to verify if two independent samples are drawn from the same normal distribution. This can be done by testing the hypothesis $H_0 : \mu_1 = \mu_2$ against the alternative hypothesis $H_1 : \mu_1 \neq \mu_2$. Here, a modified one-sample t-test can be applied provided that $\sigma_1 = \sigma_2 = \sigma$. The first step is to define a random variable D as the difference of two independent and identically normally distributed random variables such as

$$D = X_1 - X_2. \tag{3.6.28}$$

The random variable D is normally distributed with mean $\mu_D = 0$ and standard deviation $\sigma_D = \sqrt{2}\sigma$, see Walpole [111]. Therefore, the random variable

$$T_D = \frac{\overline{D} - \mu_D}{S_D \sqrt{1/n_1 + 1/n_2}} \tag{3.6.29}$$

where

$$\overline{D} = \overline{X}_1 - \overline{X}_2 \quad \text{and} \quad S_D^2 = \frac{(n_1-1)S_1^2 + (n_2-1)S_2^2}{n_1 + n_2 - 2} \tag{3.6.30}$$

follows a t-distribution with $n_1 + n_2 - 2$ degrees of freedom, see Walpole [111]. Now, the hypothesis and alternative hypothesis can be reformulated as

$$\begin{aligned} H_0 &: \quad \mu_1 \quad = \quad \mu_2 \quad \text{or} \quad \mu_D = \mu_1 - \mu_2 = 0 \\ H_1 &: \quad \mu_1 \quad \neq \quad \mu_2 \quad \text{or} \quad \mu_D = \mu_1 - \mu_2 \neq 0. \end{aligned} \tag{3.6.31}$$

Using the results from two samples of size n_1 and n_2, respectively, the corresponding value of T_D becomes

$$t_d = \frac{\bar{x}_1 - \bar{x}_2}{s_d \sqrt{1/n_1 + 1/n_2}} \tag{3.6.32}$$

where

$$s_d^2 = \frac{(n_1-1)s_1^2 + (n_2-1)s_2^2}{n_1 + n_2 - 2}. \tag{3.6.33}$$

If $P(\mid T_D \mid > t_d) > \alpha$ is true, H_0 is not rejected and it can be assumed that both independent samples are drawn from normal distributions with equal means but unknown variances. If $P(\mid T_D \mid > t_d) > \alpha$ is not true, H_0 is rejected at significance level α and it can be assumed that the sample data are drawn from different normal distributions. This test is called two-sample t-test. It is common to combine the two-sample t-test with the two-sample F-test, see Walpole [111]. The two-sample F-test returns a test decision for the null hypothesis that two samples are drawn from normal distributions with equal variances. The alternative hypothesis is that the samples are drawn from normal distributions with different variances.

The example above has shown the general procedure of statistical hypothesis testing. Besides the definition of null hypothesis H_0 and alternative hypothesis H_1, it is of major importance to clarify the assumptions prior testing. The result of a hypothesis test becomes useless when any of the assumptions is not met. A statistical hypothesis test can be structured as follows

1. Clarification of assumptions regarding populations characteristics
2. Definition of null hypothesis H_0 and alternative hypothesis H_1
3. Purpose of significance level α
4. Selection of an appropriate test statistic $\widehat{\Theta}$
5. Computing of the critical region based on α
6. Test of H_0 hypothesis using the critical region

Furthermore, classical hypothesis tests are separated into parametric and non-parametric tests. Most of the traditional tests are based on the assumption that the random samples are drawn from normal distributions. Due to the parametric form of the normal distribution these test methods are called parametric. In modern statistics, alternative test methods were introduced where no assumption about the distribution of the underlying population is made. These tests are referred as non-parametric or distribution-free methods. In general, with an increasing number of assumptions the result of hypothesis test becomes stronger. Detailed explanations and hypothesis tests of both methods can be found in the standard literature of statistics by Walpole [111], Lehmann and Romano [73], Montgomery [88] and Wilcox [114].

3.6.4 Simple Linear Regression

The distribution properties are estimated by a linear fit using the method of least-squares, see Chapter 3.5.2. This procedure is called a simple linear regression approach, see Walpole [111]. The statistical model of the simple linear regression is given by

$$Y(x) = \beta_0 + \beta_1 x + \epsilon \tag{3.6.34}$$

where β_0 is the intercept and β_1 is the slope and ϵ is a random variable which is also called the random error and is characterised by zero mean $\mu_\epsilon = 0$ and error variance σ_ϵ^2. Therefore the expected value of Y becomes

$$E[Y(x)] = \beta_0 + \beta_1 x. \tag{3.6.35}$$

The fitted regression line is given by

$$\hat{y}(x) = b_0 + b_1 x \tag{3.6.36}$$

where b_0 and b_1 are estimates of β_0 and β_1. Therefore, the fitted regression line $\hat{y}(x)$ is an estimate of the true regression line $Y(x)$.

For a given set of n data points (x_i, y_i) with corresponding estimates $\hat{y}(x_i)$ the n residuals are

$$e_i = y_i - \hat{y}(x_i). \tag{3.6.37}$$

As already mentioned, the least-squares method solves the function $\min\left[\sum_{i=1}^{n} e_i^2\right]$ in terms of b_0 and b_1. In case of linear regression combined with the least-squares method, the coefficients b_1 and b_0 can directly be computed by the unbiased estimators

$$B_1 = \frac{\sum_{i=1}^{n}(x_i - \bar{x})\left(Y_i - \overline{Y}\right)}{\sum_{i=1}^{n}(x_i - \bar{x})^2} \tag{3.6.38}$$

and

$$B_0 = \overline{Y} - B_1\bar{x}. \tag{3.6.39}$$

It can be shown that B_1 and B_0 follow normal distributions, see Walpole [111]. The expected values and the mean squared errors of these estimators are

$$E[B_1] = \beta_1 \quad \text{and} \quad \sigma_{B_1}^2 = \frac{\sigma_\epsilon^2}{\sum_{i=1}^{n}(x_i - \bar{x})} \tag{3.6.40}$$

and

$$E[B_0] = \beta_0 \quad \text{and} \quad \sigma_{B_0}^2 = \frac{\sum_{i=1}^{n} x_i^2}{\sum_{i=1}^{n}(x_i - \bar{x})^2}\sigma_\epsilon^2. \tag{3.6.41}$$

It is seen that both estimators depend on the n data points x_i of the independent variable x. The parameter σ_ϵ^2 used in both estimators is the model error variance and reflects random variation around the regression line. An unbiased estimator of σ_ϵ^2 is

$$S_\epsilon^2 = \frac{1}{n-2}\sum_{i=1}^{n}(Y_i - E[Y])^2 \tag{3.6.42}$$

which is also called mean squared error.

The t-test can be used to perform statistical hypothesis tests on the fitted regression coefficients b_0 and b_1. For instance, a hypothesis test on the slope β_1 can be expressed as

$$\begin{aligned} H_0: &\quad \beta_1 = \beta_1^* \\ H_1: &\quad \beta_1 \neq \beta_1^*. \end{aligned} \tag{3.6.43}$$

Considering that H_0 is true, the test statistic becomes

$$T_{B_1} = \frac{B_1 - \beta_1^*}{\sqrt{S_\epsilon^2/\sum_{i=1}^{n}(x_i - \bar{x})^2}} \tag{3.6.44}$$

for n values of x. Here, the random variable T_{B_1} follows a t-distribution with $n-2$ degrees of freedom. For a data set consisting of n observations (x_i, y_i), the value of T_{B_1} becomes

$$t_{b_1} = \frac{b_1 - \beta_1^*}{\sqrt{s_{b_1}}} \tag{3.6.45}$$

with

$$s_{b_1} = \frac{1}{n-2}\frac{\sum_{i=1}^{n}\left(y_i - \hat{y}(x_i)\right)^2}{\sum_{i=1}^{n}(x_i - \bar{x})^2} \tag{3.6.46}$$

If $P\left(|\, T_{B_1} \,| > t_{b_1}\right) > \alpha$ is not true, H_0 is rejected at significance level α. If $\beta_1^* = 0$, the hypothesis test is called a significance of regression test and proves the linear correlation of the n observations (x_i, y_i). However, this test needs to be handled carefully. The non-rejection of the null hypothesis does not indicate that the observations are totally uncorrelated. Here, a scatter plot is helpful to check for any non-linear correlation.

3.6.5 Goodness of Fit Test

An important class of hypothesis tests are so-called distribution tests or Goodness of Fit (GoF) tests, see D'Agostino and Stephens [22]. The method of least-squares can be used to identify parameters of an arbitrary function, see Chapter 3.5.2. This method can be also used to estimate distribution parameters. From a statistical point of view, it is important to prove the assumption that the underlying population of a sample follows the selected and fitted distribution function. Here, a formal procedure is to perform a hypothesis test which is called GoF test. GoF tests play a significant role for the correct performance of further hypothesis tests. For instance, the two-sample t-test requires two samples drawn from normal distributions. GoF tests are essentially based on either the CDF or the PDF. This means that null and alternative hypothesis are stated either as

$$\begin{aligned} H_0: \quad F(x) &= F_0(x) \\ H_1: \quad F(x) &\neq F_0(x) \end{aligned} \tag{3.6.47}$$

or as

$$\begin{aligned} H_0: \quad f(x) &= f_0(x) \\ H_1: \quad f(x) &\neq f_0(x). \end{aligned} \tag{3.6.48}$$

A well known test for normality is the chi-square test and it is based on the assumed normal PDF, see Romeu [100]. An alternative is the Kolmogorov-Smirnov test, see Romeu [99]. It is a typical nonparametric test which proves the equality of two continuous CDF. Therefore, it can also be applied as a GoF test. A modification of the Kolmogorov-Smirnov GoF test is the Anderson-Darling GoF test, see Romeu [98]. Both tests belong to the class of distance tests which means that the distances between the empirical $\overline{F}_i(x_i)$, see Equation (3.5.12), and the estimated $F_i(x_i)$ are the mandatory measurements. Especially, the Anderson-Darling GoF test is perfectly suitable for small sample sizes and allows to prove a normal fit as well as a Weibull fit and is presented in the following according to the Composite Materials Handbook Volume I [25].

It is considered that n sample points x_i are given in an ordered set and the specified distribution parameters are estimated from this set. The n corresponding values of the estimated CDF are denoted by $F_i(x_i)$. The Anderson-Darling test statistic is given by

$$AD = -n + \sum_{i=1}^{n} \frac{1-2i}{n} \left(\ln\left[F_i(x_i)\right] + \ln\left[1 - F_{n+1-i}(x_i)\right] \right) \tag{3.6.49}$$

and is adjusted to sample size n in form of

$$AD^* = \left(1 + \frac{0.2}{\sqrt{n}}\right) AD. \tag{3.6.50}$$

The observed significance level is denoted by OSL and depends on the specified distribution. OSL measures the probability of observing an Anderson-Darling test statistic at least as extreme as the measured value of AD if the sample is actually drawn from the specified distribution. Then, the null hypothesis is rejected at a significance level of $\alpha = 0.05$ when $OSL < 0.05$. Otherwise, the hypothesis that the sample data follows the specified distribution is not rejected. The value of OSL can be written as

$$OSL = \left(1 + \exp\left(-0.10 + 1.24 \ln\left(AD^*\right) + 4.48 AD^*\right)\right)^{-1} \tag{3.6.51}$$

	Normal Fit			Weibull Fit		
	μ	σ	OSL	m	λ	OSL
Sample X	3.74	0.72	$0.72 > 0.05$	5.91	4.04	$0.64 > 0.05$
Sample Y	1.69	0.98	$0.08 > 0.05$	1.92	1.88	$0.74 > 0.05$

Table 3.6.2: Estimated distribution parameters of sample X and sample Y.

for normal distributions and

$$OSL = \left(1 + \exp\left(-0.48 + 0.78 \ln\left(AD^*\right) + 4.58 AD^*\right)\right)^{-1} \tag{3.6.52}$$

for Weibull distributions. The results of the Anderson-Darling test for the example in Chapter 3.5.2 are presented in Table 3.6.2. It can be assumed that sample X follows either a normal distribution or a Weibull distribution. Due to the similarity of both estimated distribution functions the test results are reasonable as demonstrated in Figure 3.6.2a. Further, it can be assumed that sample X is drawn from a Weibull distribution. Here, the estimated Weibull function is able to capture the skewness of the sample data as seen in Figure 3.6.2b. Figure 3.6.2c and Figure 3.6.2d, respectively, show sample data, fitted normal CDF and fitted Weibull CDF of sample X and of sample Y, respectively. Especially, the CDF of sample Y is better approximated by a Weibull than by a normal fit.

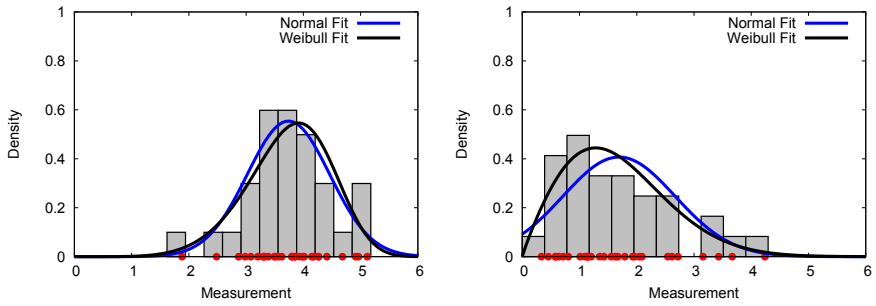

(a) Fitted PDFs of sample X.

(b) Fitted PDFs of sample Y.

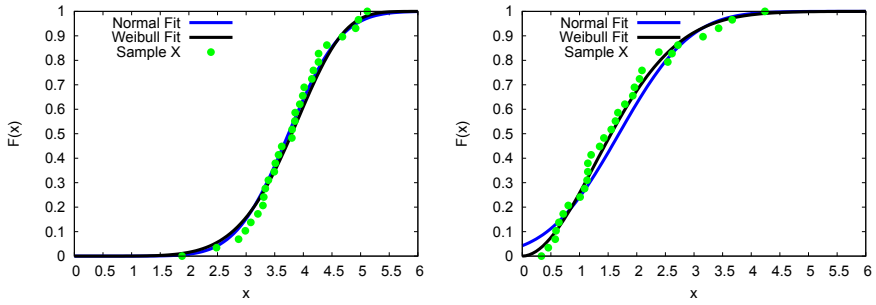

(c) Fitted CDFs of sample X.

(d) Fitted CDFs of sample Y.

Figure 3.6.2: Estimated normal distribution and Weibull distribution of sample X and sample Y.

3.6.6 Applied Hypothesis Tests and Testing Procedure

The main objective of a common statistical analysis of experimental data is to prove the questions, first, "Does the data follow a hypothetical distribution function?" and, second, "Which samples belong to the same population?". For instance, two series of a component are produced. Samples of both are taken and compared by means of load capacity. Here, hypothesis tests can be used to prove if the difference between the series regarding load capacity is significant. In the following, two general approaches are presented to compare $k = 2$ and $k > 2$ samples.

The most commonly used hypothesis tests are already implemented in conventional mathematical programs such as MATLAB [83], Mathematica [116] and Excel [85]. Furthermore, SPSS [61] and OriginLab [91] are specialised programs for statistical analysing and visualising of experimental data. In the present work, the statistical toolbox available in MATLAB [84] was applied. Most of the implemented statistical test functions return two values. The first value is the result of the hypothesis test given by `H = 0` or `H = 1` which means the null hypothesis H_0 is not rejected or rejected at significance level α. The default value α is set to 0.05, but can be changed by the user. The second value is the p-value of the applied statistic model given by $0 < \mathrm{p} < 1$. The p-value is the lowest level of significance at which the observed or empirical value of the test statistic is significant, see Walpole [111]. In other words, the p-value is the probability of obtaining a test statistic $\widehat{\Theta}$ at least extreme as the measured $\hat{\theta}$ assuming in fact H_0 is true,

$$p = P\left(|\,\widehat{\Theta}\,| > \hat{\theta}\right). \tag{3.6.53}$$

If $p < \alpha$ is true, the null hypothesis H_0 is rejected at significance level α. For instance, the OSL value of the Anderson-Darling GoF test is the corresponding p-value.

Two samples X and Y can be compared through the F-test and t-test when it can be assumed that both samples are drawn from normal distributions. If the null hypothesis of the F-test as well as the null hypothesis of the t-test cannot be rejected, it can be assumed that both samples X and Y are drawn from the same population with normal distribution. If at least one is not normally distributed, the Kolmogorov-Smirnov test denoted as KS-test can be performed to prove if these samples are dawn from the same unknown population. An overview of $k = 2$ sample tests are given in Table 3.6.3.

If more than two samples X_i are analysed through a hypothesis test, a common procedure is the one-way Analysis of Variance (ANOVA), see Walpole [111]. The one-way ANOVA is a special form of a linear regression hypothesis test of the slope β_1 against a slope of 0, see Equation (3.6.43). Here, it is assumed that k populations are mutually independent and normally distributed with means $\mu_1, \mu_2, \ldots, \mu_k$ and a common variance σ^2. Furthermore, the k corresponding samples have the same size n and given in a sample matrix $\mathbf{X}$ of size $n \times k$. Then, the one-way ANOVA tests the hypothesis

$$\begin{aligned} H_0: &\quad \mu_1 = \mu_2 = \ldots = \mu_k \\ H_1: &\quad \text{At least one } \mu_i \text{ is differnet.} \end{aligned} \tag{3.6.54}$$

The Bartlett's test can be used to prove the assumption of the equality of the k variances by testing the hypothesis

$$\begin{aligned} H_0: &\quad \sigma_1^2 = \sigma_2^2 = \ldots = \sigma_k^2 \\ H_1: &\quad \text{At least one } \sigma_i \text{ is differnet.} \end{aligned} \tag{3.6.55}$$

In case, the k samples are not drawn from a normal distribution or the variances cannot be assumed to be equal, the nonparametric Kruskal-Wallis test can be applied, see Walpole

[111]. The Kruskal-Wallis test proves if the k samples are drawn form the same population. Thus, the null hypothesis and the alternative hypothesis are stated as

$$\begin{aligned} H_0: &\quad \text{The } k \text{ samples are drawn from the same population.} \\ H_1: &\quad \text{The } k \text{ samples are not drawn from the same population.} \end{aligned} \tag{3.6.56}$$

In general, the testing procedure is based on the k sample medians. However, the objective of these three tests is to find out if the k samples belong to the same population. Table 3.6.4 provides an overview of these tests.

Hypothesis Test	H_0	H_1
F-Test $([\texttt{H},\texttt{p}] = \texttt{vartest2}(\texttt{X},\texttt{Y}))$	$\sigma_X^2 = \sigma_Y^2$	$\sigma_X^2 \neq \sigma_Y^2$
t-Test $([\texttt{H},\texttt{p}] = \texttt{ttest2}(\texttt{X},\texttt{Y}))$	$\mu_X = \mu_Y$	$\mu_X \neq \mu_Y$
KS-Test $([\texttt{H},\texttt{p}] = \texttt{kstest2}(\texttt{X},\texttt{Y}))$	$F_X = F_Y$	$F_X \neq F_Y$

(a) Null hypothesis H_0 and alternative hypothesis H_1.

Hypothesis Test	Requirements
F-Test	Normality and Independence of X and Y
t-Test	Normality and Independence of X and Y, $\sigma_X^2 = \sigma_Y^2$
KS-Test	Independence of X and Y

(b) Requirements.

Table 3.6.3: Two-sample hypothesis tests using MATLAB [84].

Hypothesis Test	H_0	H_1
Bartlett's Test $([\texttt{H},\texttt{p}] = \texttt{vartestn}(\mathbf{X}))$	$\sigma_1^2 = \sigma_2^2 = \ldots = \sigma_k^2$	At least one σ_i is different.
One-Way ANOVA $([\texttt{H},\texttt{p}] = \texttt{anova1}(\mathbf{X}))$	$\mu_1 = \mu_2 = \ldots = \mu_k$	At least one μ_i is different.
Kruskal-Wallis Test $([\texttt{H},\texttt{p}] = \texttt{kruskalwallis}(\mathbf{X}))$	$F_1 = F_2 = \ldots = F_k$	At least one F_i is different.

(a) Null hypothesis H_0 and alternative hypothesis H_1.

Hypothesis Test	Requirements
Bartlett's Test	Normality and Independence of $\mathbf{X}$
One-Way ANOVA	Normality and Independence of $\mathbf{X}$, common σ^2
Kruskal-Wallis Test	Independence of $\mathbf{X}$

(b) Requirements.

Table 3.6.4: k-sample hypothesis tests using MATLAB [84].

3.7 Concluding Remarks

The fundamental equations of probability theory were introduced in the current chapter. These are necessary for the definition of probabilistic failure criteria. A failure criterion is usually formulated in a deterministic sense. This implies that each involved quantity needs to be exactly known. In a probabilistic failure criterion, each involved quantity is considered as a random variable. These random variables might be statistical dependent and their correlation is given by a joint density function. As a result, the handling of such a full randomised failure criterion becomes almost possible. Hence, it is necessary to state assumptions regarding the probabilistic failure criterion in the same way assumptions are made in the definition of a failure criterion. Assumptions can be made about distribution functions, statistical dependence and probability models. These assumptions can be analysed through experimental studies under statistical conditions. A data analysis using descriptive and inferential statistics as described in the current chapter provide a statistical characterisation of the experimental results. It is noted that the number of experiments increases rapidly in a statistical study and useless data are easily produced. Experience and knowledge are most important for keeping time, effort and cost of an experimental study at a minimum.

Chapter 4

Failure Modelling

The concept of failure modelling in structural materials is the subject of the following chapter. Only the topics out of the wide field of failure modelling are considered and discussed which are relevant for the present work. The chapter contains the topics continuum mechanics, fracture characteristics and failure modelling. Furthermore, the finite element method is briefly described and aspects of numerical failure modelling are discussed. A numerical-experimental example of a simple tensile test is presented that shows the complexity of the calibration of failure models.

4.1 Basic Concepts in Continuum Mechanics

The aim of continuum mechanics is the mathematical formulation of the mechanical behaviour of solid materials. In the continuum mechanical framework, it is assumed that the real material structure is idealised by a continuum structure where the material is distributed homogeneously and continuously. Here, a material point within a continuum body is characterised by its stress and strain state. In the following, the concept of stresses and strains is briefly introduced. Both quantities are necessary to describe material failure. Moreover, the mechanical balance laws as well as the first and second law of thermodynamics are presented. The relation between stresses and strains is described by constitutive equations. Here, two constitutive models are presented for demonstration of material modelling. Finally, a brief description of the finite element method is given. For further interest, detailed descriptions of the underlying definitions and relations as well as the mathematical derivations are provided in the classical literature on continuum mechanics and finite elements. It is referred to the books by Belytschko et al. [13], Irgens [63], Holzapfel [56], Lemaitre and Chaboche [74] and Lubliner [79]. It is noted that the equations in continuum mechanics are usually given in tensor or index notation. An easy to read introduction into tensor algebra can be found by Parisch [93]. Further, all equations in this chapter are formulated in tensor notation using a rectangular Cartesian coordinate system x_1, x_2, x_3 with unit base vectors $\mathbf{e}_1, \mathbf{e}_2, \mathbf{e}_3$.

4.1.1 Deformation and Strain

The configuration of a solid body at time $t = 0$ is defined as the undeformed or reference configuration and the body is given by its occupied region Ω_0. An arbitrary material point P in Ω_0 is defined by its (material) position vector $\mathbf{X}$, see Figure 4.1.1. The solid body occupies the region Ω in the current (deformed) configuration at time t and P is displaced to

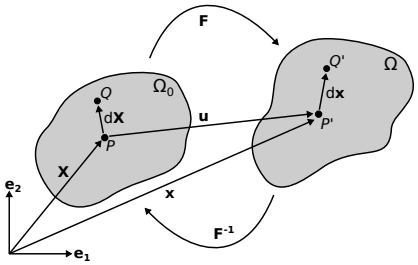

Figure 4.1.1: Deformation measurements of a solid body.

P'. The position of P' in Ω is given by the spatial position vector $\mathbf{x}$. The displacement from P to P' is expressed by the displacement vector

$$\mathbf{u} = \mathbf{x} - \mathbf{X}. \tag{4.1.1}$$

Displacement vector $\mathbf{u}$ as well as current position vector $\mathbf{x}$ can be defined as functions of the Lagrangian coordinates $\mathbf{X}$ as

$$\mathbf{u} = \mathbf{u}(\mathbf{X}, t) \quad \text{and} \quad \mathbf{x}(t) = \mathbf{x}(\mathbf{X}, t) \tag{4.1.2}$$

where $\mathbf{X}$ and t are the free variables. Alternatively, displacement vector $\mathbf{u}$ can be defined as function of the Eulerian coordinates $\mathbf{x}$ as

$$\mathbf{u} = \mathbf{u}(\mathbf{x}(\mathbf{X}, t), t) \tag{4.1.3}$$

where $\mathbf{x}$ and t are the free variables. Lagrangian coordinates $\mathbf{X}$ refer to a material point in its reference configuration and, thus, the Lagrangian coordinates are called material coordinates. In continuum mechanics, the material deformation is described by Lagrangian coordinates. Eulerian coordinates $\mathbf{x}$ refer to a spatial position where the material passes through and, thus, Eulerian coordinates are called spatial coordinates. Eulerian coordinates are usually used in fluid dynamics. In the following, only Lagrangian coordinates are considered.

The velocity vector $\mathbf{v}$ is defined by the time derivative of $\mathbf{u}$ and is expressed by

$$\mathbf{v}(\mathbf{X}, t) = \dot{\mathbf{u}}(\mathbf{X}, t) = \frac{\partial \mathbf{u}(\mathbf{X}, t)}{\partial t} \tag{4.1.4}$$

and the corresponding acceleration vector $\mathbf{a}$ becomes

$$\mathbf{a}(\mathbf{X}, t) = \ddot{\mathbf{u}}(\mathbf{X}, t) = \frac{\partial^2 \mathbf{u}(\mathbf{X}, t)}{\partial t^2} = \dot{\mathbf{v}}(\mathbf{X}, t). \tag{4.1.5}$$

It is noted that dots above a function denote derivatives with respect to time.

The partial derivative of $\mathbf{x}$ in terms of $\mathbf{X}$ leads to the tensor

$$\mathbf{F}(\mathbf{X}, t) = \frac{\partial \mathbf{x}}{\partial \mathbf{X}} = \frac{\partial (\mathbf{X} + \mathbf{u})}{\partial \mathbf{X}} \tag{4.1.6}$$

where $\mathbf{F}$ is called the deformation gradient and represents the Jacobian matrix of the deformation. The determinant of $\mathbf{F}$ is called the Jacobian determinant J and is defined by

$$J = \det(\mathbf{F}) > 0 \tag{4.1.7}$$

which is required to transform integrals from the current to the reference configuration such as

$$\int_{\Omega} f(\mathbf{X},t)\,d\Omega = \int_{\Omega_0} f(\mathbf{X},t)\,J\,d\Omega_0 \tag{4.1.8}$$

where $f(\mathbf{X},t)$ can be any function.

Now, an adjunct point Q of P is considered and its reference position is given by $\mathbf{X}+d\mathbf{X}$ as illustrated in Figure 4.1.1. Q is displaced to Q' and the displaced position of Q' is given by $\mathbf{x}+d\mathbf{x}$. The relation between $d\mathbf{X}$ and $d\mathbf{x}$ can be expressed by deformation gradient $\mathbf{F}$ as

$$d\mathbf{x} = \mathbf{F}d\mathbf{X}. \tag{4.1.9}$$

The square of the line segments $d\mathbf{X}$ and $d\mathbf{x}$ is determined by the scalar products

$$\begin{aligned} dS^2 &= d\mathbf{X}\cdot d\mathbf{X}, \\ ds^2 &= d\mathbf{x}\cdot d\mathbf{x}. \end{aligned} \tag{4.1.10}$$

Using Equation (4.1.6), the change in the squares can be written as

$$\begin{aligned} ds^2 - dS^2 &= d\mathbf{x}\cdot d\mathbf{x} - d\mathbf{X}\cdot d\mathbf{X} \\ &= d\mathbf{X}\cdot\left(\mathbf{F}^T\cdot\mathbf{F}-\mathbf{I}\right)\cdot d\mathbf{X} \\ &= d\mathbf{X}\cdot 2\mathbf{E}\cdot d\mathbf{X} \end{aligned} \tag{4.1.11}$$

where $\mathbf{I}$ denotes the identity tensor and $\mathbf{E}$ denotes the Green-Lagrange strain tensor. The definition of $\mathbf{F}$ in Equation (4.1.6) allows to express $\mathbf{E}$ in terms of material derivatives of $\mathbf{u}$, so that

$$\begin{aligned} \mathbf{E}(\mathbf{X},t) &= \frac{1}{2}\left(\mathbf{F}^T\cdot\mathbf{F}-\mathbf{I}\right) \\ &= \frac{1}{2}\left(\left(\frac{\partial\mathbf{u}}{\partial\mathbf{X}}\right)+\left(\frac{\partial\mathbf{u}}{\partial\mathbf{X}}\right)^T+\left(\frac{\partial\mathbf{u}}{\partial\mathbf{X}}\right)^T\left(\frac{\partial\mathbf{u}}{\partial\mathbf{X}}\right)\right). \end{aligned} \tag{4.1.12}$$

The velocity gradient $\mathbf{L}$ is defined by the spatial derivative of $\mathbf{v}$ as

$$\mathbf{L}(\mathbf{X},t) = \frac{\partial\mathbf{v}}{\partial\mathbf{x}} = \frac{\partial\mathbf{v}}{\partial\mathbf{x}}\frac{\partial\mathbf{X}}{\partial\mathbf{x}} = \dot{\mathbf{F}}\mathbf{F}^{-1} \tag{4.1.13}$$

and can be decomposed in an additive manner as

$$\begin{aligned} \mathbf{L}(\mathbf{X},t) &= \frac{1}{2}\left(\left(\frac{\partial\mathbf{v}}{\partial\mathbf{x}}\right)+\left(\frac{\partial\mathbf{v}}{\partial\mathbf{x}}\right)^T\right)+\frac{1}{2}\left(\left(\frac{\partial\mathbf{v}}{\partial\mathbf{x}}\right)-\left(\frac{\partial\mathbf{v}}{\partial\mathbf{x}}\right)^T\right) \\ &= \mathbf{D}(\mathbf{X},t)+\mathbf{W}(\mathbf{X},t) \end{aligned} \tag{4.1.14}$$

where $\mathbf{D}$ is the symmetric part of $\mathbf{L}$ and $\mathbf{W}$ is the skew symmetric part of $\mathbf{L}$. The symmetric tensor $\mathbf{D}$ is called the rate-of-deformation tensor and is characterised by

$$\mathbf{D} = \mathbf{D}^T. \tag{4.1.15}$$

The skew symmetric tensor $\mathbf{W}$ is called the spin tensor. The time derivative of $\mathbf{E}$ can be expressed in terms of $\mathbf{D}$ and $\mathbf{F}$ as

$$\dot{\mathbf{E}}(\mathbf{X},t) = \frac{\partial\mathbf{E}}{\partial t} = \mathbf{F}^T\cdot\mathbf{D}\cdot\mathbf{F}. \tag{4.1.16}$$

A multiplication of $\mathbf{D}$ with a time increment dt yields the so-called natural strain increment

$$d\boldsymbol{\epsilon}(\mathbf{X},t)=\mathbf{D}\cdot dt. \tag{4.1.17}$$

If a displacement of a solid body does not result in any straining or deformation, the displacement is called a rigid body motion which consists of a translation and a rotation about the origin. Consequently, the current position vector can be expressed as

$$\mathbf{x}(\mathbf{X},t)=\mathbf{x}_T(t)+\mathbf{R}(t)\cdot\mathbf{X} \tag{4.1.18}$$

where $\mathbf{x}_T$ is the translation vector and $\mathbf{R}$ is the orthogonal rotation tensor which is defined by

$$\mathbf{R}\cdot\mathbf{R}^T=\mathbf{I}. \tag{4.1.19}$$

4.1.2 Mechanical Balance Laws

The mechanical balance laws allow to specify the state of equilibrium of a solid body. These laws are established in the current configuration and have to be satisfied at any material point in Ω and at any time t. Therefore, the balance laws can be formulated either in an integral form based on Ω or in a local form based on a differential volume element of Ω. In the following, the balance laws are presented in both formulations. It is noted that the local formulation is stated directly. Details on the derivation from global formulations to local formulations can be found by Lemaitre and Chaboche [74].

An essential law in physics postulates the conservation of mass in a closed system. This means that the mass of a solid body is constant and independent of its configuration and it follows

$$\begin{aligned}\int_{\Omega_0}\rho_0 d\Omega_0 &= \int_{\Omega}\rho\, d\Omega\\ \rho_0 &= J\rho\end{aligned} \tag{4.1.20}$$

where $\rho_0=\rho_0(\mathbf{X},t_0)$ is the local mass density in the reference configuration and $\rho=\rho(\mathbf{X},t)$ is the local mass density in the current configuration.

According to Newton's second law, the sum of all external forces subjected to a solid body is equal to the rate of the linear momentum known as the inertia force. Here, a solid body with boundary Γ is subjected to body forces $\mathbf{b}$ and surface tractions $\mathbf{t}$. Vector $\mathbf{b}$ corresponds to a force per unit mass and vector $\mathbf{t}$ corresponds to a force per unit area as illustrated in Figure 4.1.2a. The balance of linear momentum is given by

$$\begin{aligned}\int_{\Omega}\rho\mathbf{b}d\Omega+\int_{\Gamma}\mathbf{t}d\Gamma &= \frac{D}{Dt}\int_{\Omega}\rho\mathbf{v}d\Omega\\ \frac{\partial\boldsymbol{\sigma}}{\partial\mathbf{x}}+\rho\mathbf{b} &= \rho\frac{\partial\mathbf{v}}{\partial t}=\rho\mathbf{a}\end{aligned} \tag{4.1.21}$$

where $\boldsymbol{\sigma}=\boldsymbol{\sigma}(\mathbf{X},t)$ is the Cauchy stress tensor. The term $\rho\mathbf{v}$ on the right hand side is the linear momentum per unit volume and its time derivative is the inertia force per unit volume and becomes $\rho\mathbf{a}$. The local form produces a system of partial differential equations and their solution is the motivation to apply the finite element method in continuum mechanics. Further, the balance of angular momentum is obtained by the cross product of each term in the linear momentum equation and position vector $\mathbf{x}$, so that

$$\begin{aligned}\int_{\Omega}\mathbf{x}\times\rho\mathbf{b}d\Omega+\int_{\Gamma}\mathbf{x}\times\mathbf{t}d\Gamma &= \frac{D}{Dt}\int_{\Omega}\mathbf{x}\times\rho\mathbf{v}d\Omega\\ \boldsymbol{\sigma} &= \boldsymbol{\sigma}^T.\end{aligned} \tag{4.1.22}$$

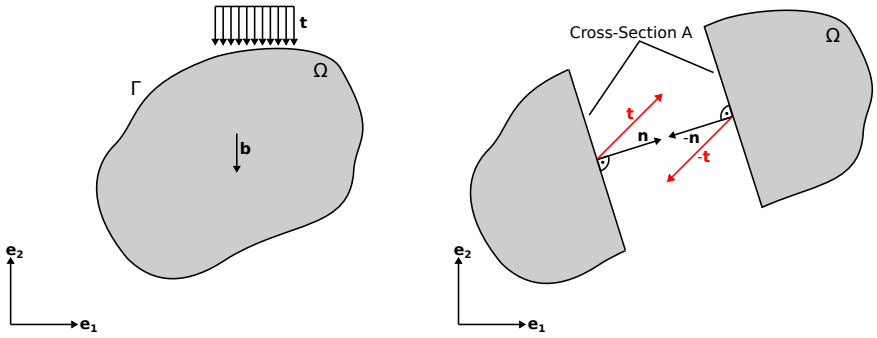

(a) Solid body with boundary Γ subjected to external loads $\mathbf{b}$ and $\mathbf{t}$.

(b) Stress vector $\mathbf{t}$ acting on cross-section A with normal $\mathbf{n}$.

Figure 4.1.2: Illustration of a solid body subjected to of external loads and the Cauchy theorem.

Here, the local form that Cauchy stress tensor $\boldsymbol{\sigma}$ has to be a symmetric tensor. The balance laws of linear and angular momentum are also known as the Euler's equation of motion.

4.1.3 Stresses

Stresses can be interpreted as internally distributed forces in a solid body as a result of external loads. The Cauchy stress tensor $\boldsymbol{\sigma}$ introduced in Equation (4.1.21) is obtained from the Cauchy theorem which is illustrated in Figure 4.1.2b. Here, a solid body is virtually cut into two bodies and the cross-section A is defined by its unit normal vector $\mathbf{n}$. According to the third Newton's law, the internal forces $\mathbf{F}$ acting on both surfaces are equal in magnitude and opposite in direction. Hence, the stress vector $\mathbf{t}$ in a material point on a surface with normal vector $\mathbf{n}$ is given by the limit

$$\mathbf{t} = \lim_{\triangle A \to 0} \frac{\triangle \mathbf{F}}{\triangle A} = \frac{d\mathbf{F}}{dA}. \tag{4.1.23}$$

The Cauchy theorem states that the relation between stress vector $\mathbf{t}$ and normal vector $\mathbf{n}$ is given by the Cauchy stress tensor $\boldsymbol{\sigma}$ and reads

$$\mathbf{t} = \boldsymbol{\sigma} \cdot \mathbf{n}. \tag{4.1.24}$$

The components of $\boldsymbol{\sigma}$ can be given in matrix form as

$$\boldsymbol{\sigma} \equiv \begin{pmatrix} \sigma_{11} & \sigma_{12} & \sigma_{13} \\ \sigma_{21} & \sigma_{22} & \sigma_{23} \\ \sigma_{31} & \sigma_{32} & \sigma_{33} \end{pmatrix} \tag{4.1.25}$$

where the components $\sigma_{11}, \sigma_{22}, \sigma_{33}$ are called normal stresses and the remaining components are called shear stresses.

It is noted that stress tensor $\boldsymbol{\sigma}$ is unique in a material point, but the values of the components depend on the orientation of the applied coordinate system. Here, a particular coordinate system is the principal system where only normal stresses are present. The

principal system requires that **t** and **n** have the same direction in cross-sections perpendicular to the principal coordinate axes. Then, the three principal stresses are found by solving the eigenvalue problem

$$(\boldsymbol{\sigma} - \sigma \mathbf{I}) \cdot \mathbf{n} = \mathbf{0} \tag{4.1.26}$$

where σ is an eigenvalue of $\boldsymbol{\sigma}$. This equation system has a non-trivial solution for the unknown **n** only if its determinant becomes zero,

$$\det(\boldsymbol{\sigma} - \sigma \mathbf{I}) = 0. \tag{4.1.27}$$

This leads to the equation

$$\sigma^3 - I_\sigma \sigma^2 - II_\sigma \sigma - III_\sigma = 0 \tag{4.1.28}$$

where the three (coordinate) independent scalars $I_\sigma, II_\sigma, III_\sigma$ are called the stress invariants given by

$$I_\sigma = \operatorname{tr}[\boldsymbol{\sigma}] = \boldsymbol{\sigma} : \mathbf{I}, \tag{4.1.29}$$

$$II_\sigma = \frac{1}{2}\left(\operatorname{tr}[\boldsymbol{\sigma} \cdot \boldsymbol{\sigma}] - \operatorname{tr}[\boldsymbol{\sigma}]^2\right) = \frac{1}{2}\left(\boldsymbol{\sigma} : \boldsymbol{\sigma} - \operatorname{tr}[\boldsymbol{\sigma}]^2\right), \tag{4.1.30}$$

$$III_\sigma = \det(\boldsymbol{\sigma}). \tag{4.1.31}$$

The three solutions of Equation (4.1.28) are called the principal stresses $\sigma_I, \sigma_{II}, \sigma_{III}$ and the corresponding directions are the principal axes $\mathbf{n}_I, \mathbf{n}_{II}, \mathbf{n}_{III}$. Due to the symmetry of $\boldsymbol{\sigma}$, the solutions $\sigma_I, \sigma_{II}, \sigma_{III}$ are real. In mathematics, this is called an eigenvalue problem and $\sigma_I, \sigma_{II}, \sigma_{III}$ are the eigenvalues of $\boldsymbol{\sigma}$ and $\mathbf{n}_I, \mathbf{n}_{II}, \mathbf{n}_{III}$ are the corresponding eigenvectors. In continuum mechanics, the principal stresses are ordered by $\sigma_I \geq \sigma_{II} \geq \sigma_{III}$. Accordingly, the maximum shear stress τ_{max} becomes

$$\tau_{max} = \frac{\sigma_I - \sigma_{III}}{2}. \tag{4.1.32}$$

Further, stress tensor $\boldsymbol{\sigma}$ can be decomposed into the hydrostatic stress tensor $\boldsymbol{\sigma}_h$ and the deviatoric stress tensor **s** such as

$$\boldsymbol{\sigma} = \boldsymbol{\sigma}_h + \mathbf{s} = \frac{\operatorname{tr}[\boldsymbol{\sigma}]}{3}\mathbf{I} + \mathbf{s} \tag{4.1.33}$$

where the hydrostatic stresses cause a volume change of Ω and the deviatoric stresses cause a distortion of Ω. Consequently, **s** is determined by

$$\mathbf{s} = \boldsymbol{\sigma} - \frac{\operatorname{tr}[\boldsymbol{\sigma}]}{3}\mathbf{I}. \tag{4.1.34}$$

Since $\boldsymbol{\sigma}$ and $\boldsymbol{\sigma}_h$ are symmetric tensors, **s** is also a symmetric tensor and it follows $\mathbf{s} = \mathbf{s}^T$. The invariants of **s** are given by

$$I_s = 0, \tag{4.1.35}$$

$$II_s = \frac{1}{2}(\mathbf{s} : \mathbf{s}), \tag{4.1.36}$$

$$III_s = \det(\mathbf{s}). \tag{4.1.37}$$

The invariants of **s** can be also expressed in terms $\sigma_I, \sigma_{II}, \sigma_{III}$, so that

$$I_s = 0, \tag{4.1.38}$$

$$II_s = \frac{1}{6}\left[(\sigma_I - \sigma_{II})^2 + (\sigma_{II} - \sigma_{III})^2 + (\sigma_{III} - \sigma_I)^2\right], \tag{4.1.39}$$

$$III_s = s_{11} s_{22} s_{33}. \tag{4.1.40}$$

The deformation or mechanical power of a solid body can be defined in terms of Cauchy stress $\boldsymbol{\sigma}$ and rate-of-deformation $\mathbf{D}$ as

$$P^{def} = \int_{\Omega} \boldsymbol{\sigma} : \mathbf{D} d\Omega. \tag{4.1.41}$$

Using Equation (4.1.8) and Equation (4.1.16), the mechanical power can also be computed referred to the reference configuration as

$$\begin{aligned} P^{def} &= \int_{\Omega} \boldsymbol{\sigma} : \mathbf{D} d\Omega \\ &= \int_{\Omega_0} J\boldsymbol{\sigma} : \left(\mathbf{F}^{-T} \cdot \dot{\mathbf{E}} \cdot \mathbf{F}^{-1}\right) d\Omega_0 \\ &= \int_{\Omega_0} \left(J\mathbf{F}^{-1} \cdot \boldsymbol{\sigma} \cdot \mathbf{F}^{-T}\right) : \dot{\mathbf{E}} d\Omega_0 \\ &= \int_{\Omega_0} \mathbf{S} : \dot{\mathbf{E}} d\Omega_0 \end{aligned} \tag{4.1.42}$$

where $\mathbf{S}$ denotes the second Piola-Kirchhoff stress tensor which is defined as

$$\mathbf{S} = J\mathbf{F}^{-1} \cdot \boldsymbol{\sigma} \cdot \mathbf{F}^{-T}. \tag{4.1.43}$$

$\mathbf{S}$ is a symmetric tensor and it follows $\mathbf{S} = \mathbf{S}^T$. It is said that Cauchy stress $\boldsymbol{\sigma}$ and rate-of-deformation $\mathbf{D}$ are an energy conjugate pair referred to the current configuration. In the same manner, second Piola-Kirchhoff stress $\mathbf{S}$ and Green-Lagrange strain rate $\dot{\mathbf{E}}$ are an energy conjugate pair referred to the reference configuration.

The material response is described by the relation between stresses and strains. The principle of material objectivity states that the material response is independent of a superimposed rigid body rotation on the current configuration. A tensor is called objective when the tensor remains invariant during rotation of the coordinate system. Only objective tensors satisfy the principal of material objectivity, see Belytschko et al. [13]. Stress and strain tensors defined with respect to the reference configuration are expected to be objective such as second Piola-Kirchhoff stress $\mathbf{S}$ and Green-Lagrange strain $\mathbf{E}$. Also, the stress- and strain-rate tensors which are defined with respect to the reference configuration are expected to be objective such as second Piola-Kirchhoff stress rate $\mathbf{S}$ and Green-Lagrange strain rate $\dot{\mathbf{E}}$. In contrast, rates of tensors which are defined in the current configuration are not objective. For instance, Cauchy stress $\boldsymbol{\sigma}$ and rate-of-deformation tensor $\mathbf{D}$ are objective, but the rate of Cauchy stress $\boldsymbol{\sigma}$ is not objective. An objective rate of Cauchy stress $\boldsymbol{\sigma}$ is given by the Jaumann stress rate $\boldsymbol{\sigma}^{\nabla J}$ which is expressed as

$$\boldsymbol{\sigma}^{\nabla J} = \frac{\partial \boldsymbol{\sigma}}{\partial t} + \mathbf{W} \cdot \boldsymbol{\sigma} - \boldsymbol{\sigma} \cdot \mathbf{W} \tag{4.1.44}$$

where spin tensor $\mathbf{W}$ is used. Alternative objective formulations are the Truesdell stress rate and Green-Naghdi stress rate, see Belytschko et al. [13].

4.1.4 First and Second Law of Thermodynamics

The mechanical balance laws state the conservation of mass as well as the balance of linear and angular momentum. The conservation of energy in a thermo-mechanical system is stated by the first law of thermodynamics. It is considered that a solid body exists in a

closed system and the only source of energy is mechanical work and heat. The rate of change of the total energy of a solid body is given by

$$P^{tot} = P^{kin} + P^{int} \tag{4.1.45}$$

where P^{kin} denotes the rate of change of the kinetic energy and P^{int} the rate of change of the internal energy. The kinetic power P^{kin} is defined by

$$P^{kin} = \frac{D}{Dt}\int_{\Omega}\frac{1}{2}\rho\mathbf{v}\cdot\mathbf{v}d\Omega. \tag{4.1.46}$$

The internal energy per unit mass is denoted as $w^{int} = w^{int}(\mathbf{X},t)$ and, thus, the internal power P^{int} of a solid body can be expressed as

$$P^{int} = \frac{D}{Dt}\int_{\Omega}\rho w^{int}d\Omega. \tag{4.1.47}$$

The rate of work done by external forces becomes

$$P^{ext} = \int_{\Omega}\mathbf{v}\cdot\rho\mathbf{b}d\Omega + \int_{\Gamma}\mathbf{v}\cdot\mathbf{t}d\Gamma \tag{4.1.48}$$

and the power supplied by heat sources $s = s(\mathbf{X},t)$ and the heat flux vector $\mathbf{q} = \mathbf{q}(\mathbf{X},t)$ becomes

$$P^{heat} = \int_{\Omega}\rho s d\Omega - \int_{\Gamma}\mathbf{n}\cdot\mathbf{q}d\Gamma. \tag{4.1.49}$$

The conservation of energy requires that the rate of change of the total energy P^{tot} equals the power of the external forces P^{ext} and the heat power P^{heat}. Hence, the first law of thermodynamics reads

$$\begin{aligned} P^{tot} &= P^{ext} + P^{heat} \\ P^{kin} + P^{int} &= P^{ext} + P^{heat}. \end{aligned} \tag{4.1.50}$$

The local form of the first law is directly postulated by

$$\rho\dot{w}^{int} = \rho\frac{\partial w^{int}}{\partial t} = \boldsymbol{\sigma} : \mathbf{D} + \rho s - \frac{\partial \mathbf{q}}{\partial \mathbf{x}} \tag{4.1.51}$$

and an integration over the domain Ω leads to the form

$$\begin{aligned} \int_{\Omega}\rho w^{int}d\Omega &= \int_{\Omega}\boldsymbol{\sigma} : \mathbf{D}d\Omega + \int_{\Omega}\rho s d\Omega - \int_{\Omega}\frac{\partial \mathbf{q}}{\partial \mathbf{x}}d\Omega \\ P^{int} &= P^{def} + P^{heat}. \end{aligned} \tag{4.1.52}$$

It shows that the inter-convertibility of heat and mechanical work in a thermo-mechanical system. Here, the rate of the mechanical work P^{def} can be derived from the balance of linear momentum in Equation (4.1.21), so that

$$P^{def} = P^{kin} - P^{ext}. \tag{4.1.53}$$

A thermo-mechanical process is characterised by its irreversibility and the restriction that heat only flows from a warm to a cold body. The first law of thermodynamics does

not include this restriction. Here, the second law of thermodynamics postulates this imbalance in the direction of energy transformations. A mathematical expression is given by the Clausius-Duhem inequality, see Belytschko et al. [13]. It reads

$$\frac{D}{Dt}\int_{\Omega}\rho\eta d\Omega \geq \int_{\Omega}\frac{1}{\theta}\rho s d\Omega - \int_{\Gamma}\mathbf{h}\cdot\mathbf{n}d\Gamma \tag{4.1.54}$$

where $\eta = \eta(\mathbf{X},t)$ denotes the entropy per unit mass of a solid body and $\theta = \theta(\mathbf{X},t)$ the thermodynamical temperature. The vector $\mathbf{h} = \mathbf{h}(\mathbf{X},t)$ is called the entropy flow vector and is defined by

$$\mathbf{h} = \frac{\mathbf{q}}{\theta}. \tag{4.1.55}$$

The second law states that the internal production of entropy is never less than the entropy provided by external sources. In case of a reversible process, the internal entropy production equals the external entropy supply, whereas in case of an irreversible process, the internal entropy production is always larger than the external entropy supply as described in the work by Hassler [52]. The local form of the Clausius-Duhem inequality reads

$$\rho\theta\dot{\eta} \geq \rho s - \frac{\partial \mathbf{q}}{\partial \mathbf{x}} + \mathbf{h}\cdot\frac{\partial\theta}{\partial\mathbf{x}}. \tag{4.1.56}$$

Substituting Equation (4.1.51) in the local form of the Clausius-Duhem inequality leads to the expression

$$\begin{aligned} \rho\theta\dot{\eta} &\geq \rho\dot{w}^{int} - \boldsymbol{\sigma}:\mathbf{D} + \mathbf{h}\cdot\frac{\partial\theta}{\partial\mathbf{x}} \\ 0 &\leq \underbrace{\left[\boldsymbol{\sigma}:\mathbf{D} - \rho\left(\dot{w}^{int} - \theta\dot{\eta}\right)\right]}_{\geq 0} + \underbrace{\left[-\mathbf{h}\cdot\frac{\partial\theta}{\partial\mathbf{x}}\right]}_{\geq 0} \end{aligned} \tag{4.1.57}$$

where the first square bracket represents the mechanical energy dissipation due to deformation and the second square bracket the thermal energy dissipation due to heat conduction. The energy available to do mechanical work at constant temperature is given by the free energy function ψ which is defined by

$$\psi = w^{int} - \theta\eta. \tag{4.1.58}$$

Using the time derivative of ψ given by

$$\dot{\psi} = \dot{w}^{int} - \dot{\theta}\eta - \theta\dot{\eta}, \tag{4.1.59}$$

the local mechanical energy dissipation leads to the inequality

$$0 \leq \boldsymbol{\sigma}:\mathbf{D} - \rho\dot{\psi} - \rho\dot{\theta}\eta \tag{4.1.60}$$

in the current configuration and

$$0 \leq \mathbf{S}:\dot{\mathbf{E}} - \rho_0\dot{\psi} - \rho_0\dot{\theta}\eta \tag{4.1.61}$$

in the reference configuration.

4.1.5 Constitutive Equations

A constitutive equation defines the relation between two physical quantities connected to a material. It approximates the response of the material when it is subjected to external loads. These equations are necessary to solve primary equations governing physical laws. Usually, reasonable assumptions are stated to express the constitutive equations by elementary functions which follow the laws of thermodynamics. In continuum mechanics, the constitutive equations provide the relation between the stress state and the strain state in a solid and deformable material point. The set of constitutive equations and the underlying assumptions defining the material behaviour are summarised in the material model. Here, a distinction is made between reversible and irreversible material behaviour. In a reversible material, the deformation energy is stored in the material and is fully recoverable after unloading, consequently deformations and strains are reversible and the deformed body returns to its original shape after unloading. Here, the only source of energy dissipation is heat conduction. The modelling of reversible material behaviour is subject of the theory of elasticity. In contrast, the internal energy of an irreversible material is totally or partially dissipated as heat and mechanical work. Here, the internal structure of the material changes irreversibly under loading. These materials are defined as plastic materials. The modelling of irreversible material behaviour is subject of the theory of plasticity.

In case of thermo-elasticity, the dissipation of mechanical energy is zero and it follows

$$\rho\dot{\psi} = \boldsymbol{\sigma} : \mathbf{D} - \rho\dot{\theta}\eta \tag{4.1.62}$$

$$\rho_0\dot{\psi} = \boldsymbol{S} : \dot{\mathbf{E}} - \rho_0\dot{\theta}\eta. \tag{4.1.63}$$

The free energy function ψ only depends on the state (observable) variables Green-Lagrange strain $\mathbf{E}$ and temperature θ, so that

$$\rho_0\psi = \rho_0\psi(\mathbf{E},\theta). \tag{4.1.64}$$

The corresponding time derivative becomes

$$\rho_0\dot{\psi}(\mathbf{E},\theta) = \rho_0\frac{\partial\psi(\mathbf{E},\theta)}{\partial\mathbf{E}} : \dot{\mathbf{E}} + \rho_0\frac{\partial\psi(\mathbf{E},\theta)}{\partial\theta}\dot{\theta}. \tag{4.1.65}$$

Substituting Equation (4.1.65) in Equation (4.1.63) leads to

$$0 = \underbrace{\left[\mathbf{S} - \rho_0\frac{\partial\psi(\mathbf{E},\theta)}{\partial\mathbf{E}}\right]}_{=0} : \dot{\mathbf{E}} + \rho_0\underbrace{\left[-\eta - \frac{\partial\psi(\mathbf{E},\theta)}{\partial\theta}\right]}_{=0}\dot{\theta}. \tag{4.1.66}$$

In the absence of any internal constraints, this equation holds for any possible Green-Lagrange strain rate $\dot{\mathbf{E}}$ and, further, the temperature change $\dot{\theta}$ can be arbitrary. The vanishing of the coefficients leads to expressions for the associated variables second Piola-Kirchhoff stress $\mathbf{S}$ and entropy density η,

$$\mathbf{S} = \rho_0\frac{\partial\psi(\mathbf{E},\theta)}{\partial\mathbf{E}} \quad \text{and} \quad \eta = -\frac{\partial\psi(\mathbf{E},\theta)}{\partial\theta}. \tag{4.1.67}$$

These relations are called the constitutive equations of thermo-elasticity. It is noted that energy can still be dissipated through heat conduction. Here, the challenge is to identify an analytical expression of free energy function ψ. A commonly used simplification in structural engineering is to neglect the influence of temperature and to assume isothermal conditions ($\dot{\theta} = 0$). It follows that the temperature in the closed thermo-mechanical system is

kept constant which requires a permanent heat energy exchange with the outer world. In this case, the relation between second Piola-Kirchhoff stress **S** and Green-Lagrange strain **E** becomes

$$\mathbf{S} = \rho_0 \frac{\partial \psi(\mathbf{E})}{\partial \mathbf{E}}. \tag{4.1.68}$$

Assuming isotropic and elastic material properties, a widely used approach to express free energy function $\psi(\mathbf{E})$ is given by the linear St. Venant-Kirchhoff model. The model reads

$$\rho_0 \psi(\mathbf{E}) = \frac{1}{2}\lambda(\mathrm{tr}(\mathbf{E}))^2 + \mu \mathbf{E} : \mathbf{E} \tag{4.1.69}$$

where λ and μ are the Lamé coefficients which are defined as

$$\lambda = \frac{\nu E}{(1+\nu)(1-2\nu)} \quad \text{and} \quad \mu = \frac{E}{2(1+\nu)} \tag{4.1.70}$$

where E denotes the Young's modulus and ν the Poisson's ratio. The derivative of this approach enables to express second Piola-Kirchhoff stress **S** (dependent variable) in terms of Green-Lagrange strain **E** (independent variable) as

$$\mathbf{S} = \lambda \mathrm{tr}[\mathbf{E}]\,\mathbf{I} + 2\mu \mathbf{E}. \tag{4.1.71}$$

This relation is called a material model and it describes the behaviour of a material point. It assumes isotropic and linear-elastic properties and isothermal conditions are considered. Due to the definition of λ, the model is not suitable for incompressible materials with $\nu = 0.5$ or nearly incompressible materials with $\nu \approx 0.5$. Further, the model is restricted to small strains but large rigid body motions of a material point. This model is commonly applied to describe the elastic behaviour of metals.

The above described procedure has shown the derivation of the constitutive equations of thermo-elasticity. Assuming isothermal conditions and isotropic linear material behaviour, the relationship between the associated variable **S** and the observable variable **E** is expressed by the St. Venant-Kirchhoff material model. The derivation of the constitutive equations becomes much more complex if a mechanical energy dissipation exists. This topic is left out here since this would go beyond the scope of the present work. It is referred to the books by Lemaitre and Chaboche [74] and Lubliner [79]. Here, the fundamentals of plasticity theory are well discussed and the mathematical derivations of the constitutive equations starting from the free energy function ψ can be found. A material model is generally formulated depending on its requirements regarding elasticity, plasticity, anisotropy, viscosity and temperature dependence.

These requirements are defined by the characteristics of the material as well as the field of application (type of external loading). Furthermore, they go along with assumptions which are necessary for an analytical expression of the material model. It is obvious that the assumptions limit the applicability of the model. However, a wide range of different plasticity models is presented in the referred literature. An example of a standard material model to describe metal plasticity is presented in the following.

Before the model formulation is presented, its assumptions and limitations are stated. The presented model is considered to describe isotropic hypoelastic-plastic material behaviour without any strain-rate dependence. In addition, isothermal conditions are adopted and, thus, a temperature dependent behaviour is neglected. It is assumed that the elastic deformations are infinitesimally small, whereas the plastic deformations may be finite. The hypoelastic behaviour is given by a linear relation. Further, plasticity is given by an isotropic yield criterion with nonlinear isotropic hardening and the associated flow

rule. It is assumed that a hydrostatic stress state results in a purely elastic response of the volumetric strains. This assumption includes plastic incompressibility. Since the model is considered for large deformations including large rotations, the formulation adopts the Jaumann stress rate $\boldsymbol{\sigma}^{\nabla J}$, Equation (4.1.44), to ensure material objectivity.

The rate-of-deformation tensor $\mathbf{D}$ is decomposed into an elastic part and a plastic part,

$$\mathbf{D} = \mathbf{D}^e + \mathbf{D}^p \tag{4.1.72}$$

where $\mathbf{D}^e$ is the elastic rate-of-deformation tensor and $\mathbf{D}^p$ is the plastic rate-of-deformation tensor. From plastic incompressibility, it follows that $\mathrm{tr}\,[\mathbf{D}^p] = 0$. Jaumann stress rate $\boldsymbol{\sigma}^{\nabla J}$ is related to the elastic rate-of-deformation tensor $\mathbf{D}^e$ by the linear hypoelastic relation

$$\boldsymbol{\sigma}^{\nabla J} = \lambda_{el}\,\mathrm{tr}\,[\mathbf{D}^e]\,\mathbf{I} + 2\mu_{el}\mathbf{D}^e \tag{4.1.73}$$

where λ_{el} and μ_{el} are the Lamé coefficients given in Equation (4.1.70). An important point in the formulation of a material model is the definition of a yield surface. When the stress state $\boldsymbol{\sigma}$ in a material point reaches a point on the yield surface, the material is said to yield and the deformations become plastic. This point is defined by the continuous and convex yield function. The yield function may be interpreted as a surface in the nine-dimensional space of the stresses σ_{ij} where a stress state inside the surface is elastic. During plastic loading, the stress state $\boldsymbol{\sigma}$ is restricted to stay on the yield surface. In case of isotropic hardening, the yield surface generating function is given by the equation

$$f(\boldsymbol{\sigma}, R) = \bar{\sigma}(\boldsymbol{\sigma}) - (\sigma_0 + R) = 0 \tag{4.1.74}$$

where $\bar{\sigma}(\boldsymbol{\sigma}) \geq 0$ is the equivalent stress, σ_0 the yield stress and R the isotropic hardening variable which induces to a self similar growth of the yield surface during plastic loading. This equation is also called the yield criterion. The inequality

$$f(\boldsymbol{\sigma}, R) \leq 0 \tag{4.1.75}$$

defines the set of all possible stress states $\boldsymbol{\sigma}$. Using the assumptions of isotropic material behaviour and plastic incompressibility, yield criterion $f(\boldsymbol{\sigma}, R) = 0$ and equivalent stress $\bar{\sigma}(\boldsymbol{\sigma})$ only depend on the deviatoric invariants II_s, Equation (4.1.39), and III_s, Equation (4.1.40), so that

$$f(\boldsymbol{\sigma}, R) = f(II_s, III_s, R) \quad \text{and} \quad \bar{\sigma}(\boldsymbol{\sigma}) = \bar{\sigma}(II_s, III_s) \tag{4.1.76}$$

The probably best know equivalent stress is the v. Mises stress given by

$$\bar{\sigma}(\boldsymbol{\sigma}) = \sqrt{3II_s}. \tag{4.1.77}$$

A generalised isotropic yield criterion is proposed by Hershey [54] and Hosford [59]. Here, the equivalent stress is given in the high-exponent form

$$\bar{\sigma}(\boldsymbol{\sigma}) = \left[\frac{1}{2}\left(|\,\sigma_I - \sigma_{II}\,|^m + |\,\sigma_{II} - \sigma_{III}\,|^m + |\,\sigma_{III} - \sigma_I\,|^m\right)\right]^{\frac{1}{m}} \tag{4.1.78}$$

where exponent m is a positive integer. This definition includes the special cases of v. Mises stress ($m = 2$ and $m = 4$) and Tresca stress ($m = 1$ and $m \to \infty$). If aluminium alloys are considered, an exponent of $m = 8$ is recommended. The high-exponent yield criterion is compared for exponents of $m = 1$, $m = 2$, $m = 8$ in Figure 4.1.3a (plane stress state). It is seen that v. Misses stress and Tresca stress define the limits.

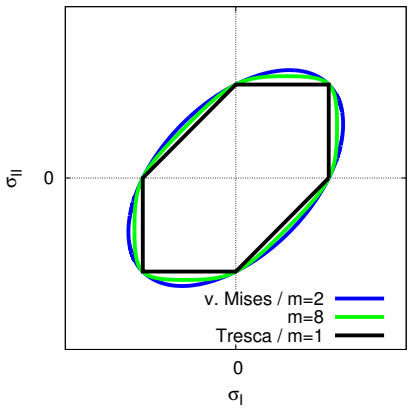

(a) Influence of exponent m on the high-exponent yield surface.

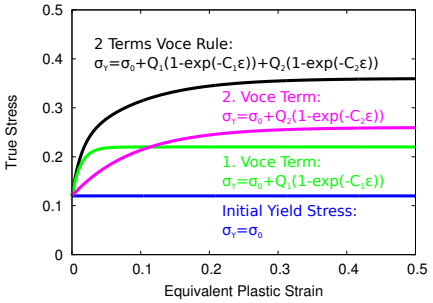

(b) Decomposition of the two-terms Voce rule.

Figure 4.1.3: High-exponent yield surface in plane stress and two-terms Voce rule.

In contrast to elastic deformations, plastic deformations are path dependent. This issue is captured by the internal variable $\bar{\varepsilon}$ known as the equivalent plastic strain. $\bar{\varepsilon}$ is determined by

$$\bar{\varepsilon} = \int_0^t \dot{\bar{\varepsilon}}\, dt \geq 0 \tag{4.1.79}$$

where $\dot{\bar{\varepsilon}}$ denotes the equivalent plastic strain rate. Due to the dependency of hardening variable R on internal variable $\bar{\varepsilon}$, the isotropic hardening rule is defined as

$$\sigma_Y(\bar{\varepsilon}) = \sigma_0 + R(\bar{\varepsilon}). \tag{4.1.80}$$

where $\sigma_Y(\bar{\varepsilon})$ is a positive continuous and monotonic increasing function of $\bar{\varepsilon}$. Several formulations of $\sigma_Y(\bar{\varepsilon})$ can be found in the technical literature. The physical based hardening rule by Voce is often applied. A expression of the Voce rule using two terms is given by

$$\sigma_Y = \sigma_0 + \sum_{i=1}^{2} Q_i \left(1 - \exp(-C_i \bar{\varepsilon})\right). \tag{4.1.81}$$

The influence of each part in the two terms Voce rule is demonstrated in Figure 4.1.3b. It shows that the first term has a strong influence on the beginning of the hardening and the second term dominates the long range hardening. The two internal variables $\mathbf{D}^p$ and $\dot{\bar{\varepsilon}}$ are defined as the dissipative fluxes in plasticity theory. These are determined by the flow rule which is derived from the so-called flow potential. If the yield criterion is used as the flow potential, it is called associated flow rule and the dissipative fluxes $\mathbf{D}^p$ and $\dot{\bar{\varepsilon}}$ become

$$\mathbf{D}^p = \dot{\lambda} \frac{\partial f(\boldsymbol{\sigma}, R)}{\partial \boldsymbol{\sigma}} \quad \text{and} \quad \dot{\bar{\varepsilon}} = -\dot{\lambda} \frac{\partial f(\boldsymbol{\sigma}, R)}{\partial R} \tag{4.1.82}$$

where $\dot{\lambda} \geq 0$ is the the plastic rate parameter which is zero for pure elastic deformations and positive for plastic deformations. It is seen that plastic flow $\mathbf{D}^p$ is directly related to the yield surface. From a geometrical point of view, associated flow means that plastic flow $\mathbf{D}^p$ stays normal on the yield surface. Furthermore, associated flow adopts the principle of

maximum plastic dissipation. Using the yield criterion in Equation (4.1.74), it follows that the equivalent plastic strain rate $\dot{\bar{\varepsilon}}$ equals the the plastic rate parameter $\dot{\lambda}$,

$$\dot{\bar{\varepsilon}} = -\dot{\lambda}\frac{\partial f(\boldsymbol{\sigma}, R)}{\partial R} = \dot{\lambda}\frac{\partial (\sigma_0 + R)}{\partial R} = \dot{\lambda}. \tag{4.1.83}$$

The plastic deformation energy is defined as $\boldsymbol{\sigma} : \mathbf{D}^p$, so that

$$\boldsymbol{\sigma} : \mathbf{D}^p = \dot{\bar{\varepsilon}}\left(\boldsymbol{\sigma} : \frac{\partial f(\boldsymbol{\sigma}, R)}{\partial \boldsymbol{\sigma}}\right) = \dot{\bar{\varepsilon}}\left(\boldsymbol{\sigma} : \frac{\partial \bar{\sigma}(\boldsymbol{\sigma})}{\partial \boldsymbol{\sigma}}\right) = \bar{\sigma}(\boldsymbol{\sigma})\dot{\bar{\varepsilon}}. \tag{4.1.84}$$

It is obvious that $(\boldsymbol{\sigma}, \mathbf{D}^p)$ and $\left(\bar{\sigma}, \dot{\bar{\varepsilon}}\right)$ are energy conjugate pairs and $\dot{\bar{\varepsilon}}$ can be written as

$$\dot{\bar{\varepsilon}} = \frac{\boldsymbol{\sigma} : \mathbf{D}^p}{\bar{\sigma}(\boldsymbol{\sigma})}. \tag{4.1.85}$$

The model is completed by the loading/unloading condition in Kuhn-Tucker form,

$$f \leq 0, \quad \dot{\lambda} \geq 0, \quad \dot{\lambda} f = 0. \tag{4.1.86}$$

The material constants E, ν and m are usually taken from the technical literature or standard material tests. The hardening coefficients σ_0, Q_1, C_1, Q_2 and C_2 can be estimated by simple tensile tests. This isotropic hypoelastic-plastic material model is summarised in Figure 4.1.4.

4.1.6 Finite Element Method and Explicit Time Integration

The Finite Element Method (FEM) is a numerical approach to solve partial differential equations by discretising the domain of interest into a collection of subdomains. Simple equations are defined on the subdomain which solves approximately the partial differential equations within the subdomain. These subdomains are called Finite Elements (FE). The solution of the partial differential equations for the whole domain is approximated by the connection of all results obtained from the FE equations. Here, the solution requires the definition of boundary conditions. In general, mathematical problems which can be solved by FEM are called boundary value problems. FEM is usually associated with the numerical stress analysis of solid structures where the partial differential equations obtained from the balance of linear momentum are solved approximately. Over the last twenty years FEM became the most important tool in continuum mechanics and structural engineering.

In the following, the general procedure to generate a FE solution is briefly presented. Further, an explicit time integration algorithm which solves the structural problem in time is shown. The aim is to demonstrate the basic idea of FEM in continuum mechanics. A large number of books about FEM can be found in the technical literature. In particular, it is referred to the books by Bathe [10], Belytschko et al. [13], Braess [16], Hughes [60], Knothe and Wessels [67] and Wriggers [117].

The local form of the balance of linear momentum leads to a system of partial differential equations, see Equation (4.1.21). This local form is also called the strong form and is here repeated

$$\frac{\partial \boldsymbol{\sigma}}{\partial \mathbf{x}} + \rho \mathbf{b} = \rho \mathbf{a}. \tag{4.1.87}$$

The strong form has to be fulfilled in any material point of a solid body. Further, the solution of the strong form has to satisfy the boundary conditions which can be separated into

1. Additive decomposition:

$$\mathbf{D} = \mathbf{D}^e + \mathbf{D}^p$$

2. Linear hypoelasticity:

$$\boldsymbol{\sigma}^{\nabla J} = \lambda_{el}\,\mathrm{tr}\,[\mathbf{D}^e]\,\mathbf{I} + 2\mu_{el}\mathbf{D}^e$$

3. Isotropic high-exponent yield criterion:

$$f(\boldsymbol{\sigma},\bar{\varepsilon}) = \bar{\sigma}(\boldsymbol{\sigma}) - \sigma_Y(\bar{\varepsilon}) = 0$$

with

$$\bar{\sigma}(\boldsymbol{\sigma}) = \left[\frac{1}{2}(|\,\sigma_I - \sigma_{II}\,|^m + |\,\sigma_{II} - \sigma_{III}\,|^m + |\,\sigma_{III} - \sigma_I\,|^m)\right]^{\frac{1}{m}}$$

4. Isotropic hardening rule (two-terms Voce rule):

$$\sigma_Y(\bar{\varepsilon}) = \sigma_0 + \sum_{i=1}^{2} Q_i\left(1 - \exp(-C_i\bar{\varepsilon})\right) \quad \text{with} \quad \bar{\varepsilon} = \int_0^t \dot{\bar{\varepsilon}}\,dt$$

5. Associated flow rule:

$$\mathbf{D}^p = \dot{\lambda}\frac{\partial f(\boldsymbol{\sigma},\bar{\varepsilon})}{\partial \boldsymbol{\sigma}} \quad \text{and} \quad \dot{\bar{\varepsilon}} = \dot{\lambda} = \frac{\boldsymbol{\sigma} : \mathbf{D}^p}{\bar{\sigma}(\boldsymbol{\sigma})}$$

6. Loading/unloading conditions:

$$f \le 0, \quad \dot{\lambda} \ge 0, \quad \dot{\lambda} f = 0$$

7. Material constants:

$$\left[\begin{array}{cccccccc} E & \nu & m & \sigma_0 & Q_1 & Q_2 & C_1 & C_2 \end{array}\right]$$

Figure 4.1.4: Isotropic hypoelastic-plastic material model for metals assuming isothermal conditions.

displacement or Dirichlet conditions on Γ_D and traction or Neumann conditions on Γ_N as seen in Figure 4.1.5a. Both boundary conditions are expressed as

$$\mathbf{v} = \bar{\mathbf{v}} \quad \text{on} \quad \Gamma_D, \tag{4.1.88}$$

$$\boldsymbol{\sigma} \cdot \mathbf{n} = \bar{\mathbf{t}} \quad \text{on} \quad \Gamma_N \tag{4.1.89}$$

where $\bar{\mathbf{v}}$ is a predefined velocity on Γ_D and $\bar{\mathbf{t}}$ is a predefined traction force on Γ_N. An analytical solution of the strong form can only be found for simple geometries and boundary conditions. However, before the FE approach can be applied the strong form needs to be transformed into the so-called weak form of the balance of linear momentum. For this, the strong form given in Equation (4.1.87) is multiplied by a virtual velocity $\delta\mathbf{v}$ and integrated over domain Ω such as

$$\int_\Omega \delta\mathbf{v} \cdot \left(\frac{\partial \boldsymbol{\sigma}}{\partial \mathbf{x}} + \rho\mathbf{b} \right) d\Omega = \int_\Omega \delta\mathbf{v} \cdot (\rho\mathbf{a})\, d\Omega. \tag{4.1.90}$$

It is noted that virtual velocity $\delta\mathbf{v}$ has to vanish wherever velocity $\mathbf{v}$ is prescribed by Dirichlet conditions defined in Equation (4.1.88). After some transformations, see Belytschko et al. [13], the weak form can be expressed as

$$\underbrace{\left(\int_\Omega \delta\mathbf{v} \cdot \rho\mathbf{b} d\Omega + \int_{\Gamma_N} \delta\mathbf{v} \cdot \bar{\mathbf{t}} d\Gamma_N \right)}_{\delta P^{ext}} - \underbrace{\int_\Omega \frac{\partial \delta\mathbf{v}}{\partial \mathbf{x}} : \boldsymbol{\sigma}\, d\Omega}_{\delta P^{int}} = \underbrace{\int_\Omega \delta\mathbf{v} \cdot \rho\mathbf{a} d\Omega}_{\delta P^{kin}} \tag{4.1.91}$$

which is called the principal of virtual power consisting of virtual external power δP^{ext}, virtual internal power δP^{int} and virtual kinetic power δP^{kin}. It is called a weak form since the equilibrium needs to be satisfied only in integral form. However, the weak form allows to develop the FE solution of the structural problem defined in Equation (4.1.87). Here, domain Ω subdivided into n non-overlapping subdomains Ω_e called finite elements as demonstrated in Figure 4.1.5b. This process is called discretisation. Usually, Ω cannot exactly be discretised and, thus, Ω is approximated by Ω_h, so that

$$\Omega \approx \Omega_h = \bigcup_{e=1}^{n} \Omega_e. \tag{4.1.92}$$

Now, an integral over Ω can be approximated by

$$\int_\Omega (\ldots)\, d\Omega \approx \int_{\Omega_h} (\ldots)\, d\Omega_h = \bigcup_{e=1}^{n} \int_{\Omega_e} d\Omega_e \tag{4.1.93}$$

where the operator $\bigcup$ denotes the assembling process of the elements defined in Ω_h. This operator describes the transition conditions between elements and serves the boundary conditions, see Knothe and Wessels [67] and Wriggers [117]. The elements are connected through their nodes and element edges in common indicate continuity between neighbouring elements. In summary, a solid body is approximated by Ω_h and is discretised by a FE mesh consisting of nodes and elements. The FE mesh moves and deforms with the approximated solid body. This implies that the constitutive equations are always evaluated at the same material point in Ω_h. Therefore, this kind of mesh is called a Lagrangian mesh and is the common approach in structural mechanics.

The discretised weak form becomes

$$\begin{aligned} &\textstyle\bigcup_{e=1}^{n} \left(\int_{\Omega_e} \delta\mathbf{v}_e \cdot \rho_e \mathbf{b} d\Omega_e + \int_{\Gamma_{Ne}} \delta\mathbf{v}_e \cdot \bar{\mathbf{t}} d\Gamma_{N_e} \right) - \\ &\textstyle\bigcup_{e=1}^{n} \int_{\Omega_e} \frac{\partial \delta\mathbf{v}_e}{\partial \mathbf{x}} : \boldsymbol{\sigma}_e d\Omega_e = \bigcup_{e=1}^{n} \int_{\Omega_e} \delta\mathbf{v}_e \cdot \rho_e \mathbf{a}_e d\Omega_e. \end{aligned} \tag{4.1.94}$$

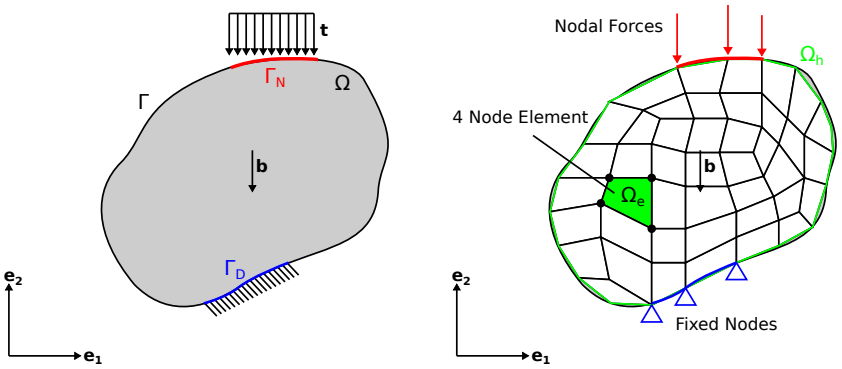

(a) Structural problem.

(b) Discretisation of the structural problem.

Figure 4.1.5: FEM applied on a structural problem.

Accordingly, the weak form defined on the element level becomes

$$\left(\int_{\Omega_e} \delta\mathbf{v}_e \cdot \rho_e \mathbf{b} d\Omega_e + \int_{\Gamma_{N_e}} \delta\mathbf{v}_e \cdot \bar{\mathbf{t}} d\Gamma_{N_e}\right) - \int_{\Omega_e} \frac{\partial \delta\mathbf{v}_e}{\partial \mathbf{x}} : \boldsymbol{\sigma}_e d\Omega_e = \int_{\Omega_e} \delta\mathbf{v}_e \cdot \rho_e \mathbf{a}_e d\Omega_e. \tag{4.1.95}$$

An element is defined by its k nodes and each node is given by its current position $\mathbf{x}_i$. The current position of an arbitrary material point in Ω_e is found by the interpolation

$$\mathbf{x}_e(\mathbf{X},t) = \sum_{i=1}^{k} N_i(\mathbf{X})\mathbf{x}_i(t) \tag{4.1.96}$$

where the k functions $N_i(\mathbf{X})$ are called shape functions which only depend on the material position $\mathbf{X}$. In the same way, the displacement field of an element is interpolated by

$$\mathbf{u}_e(\mathbf{X},t) = \sum_{i=1}^{k} N_i(\mathbf{X})\mathbf{u}_i(t) \tag{4.1.97}$$

where $\mathbf{u}_i$ is the displacement of node i and the k functions $N_i(\mathbf{X})$ are the same shape functions as for the geometry interpolation. The motion of a four node element is illustrated in Figure 4.1.6. The use of identical shape functions for geometry and displacement interpolation is called isoparametric concept. Further, the interpolated velocity field can be derived from $\mathbf{u}_e$ and becomes

$$\mathbf{v}_e(\mathbf{X},t) = \frac{\partial \mathbf{u}_e(\mathbf{X},t)}{\partial t} = \sum_{i=1}^{k} N_i(\mathbf{X}) \frac{\partial \mathbf{u}_i(t)}{\partial t} = \sum_{i=1}^{k} N_i(\mathbf{X})\mathbf{v}_i(t) \tag{4.1.98}$$

and, accordingly, the interpolated acceleration field becomes

$$\mathbf{a}_e(\mathbf{X},t) = \frac{\partial^2 \mathbf{u}_e(\mathbf{X},t)}{\partial t^2} = \sum_{i=1}^{k} N_i(\mathbf{X}) \frac{\partial^2 \mathbf{u}_i(\mathbf{X})}{\partial t^2} = \sum_{i=1}^{k} N_i(\mathbf{X})\mathbf{a}_i(t). \tag{4.1.99}$$

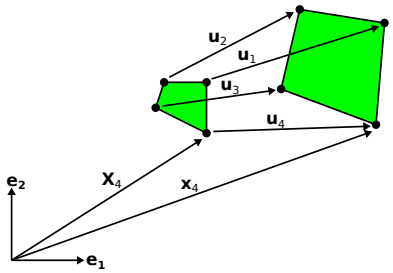

Figure 4.1.6: Deformation of a four node element.

In the same manner, the virtual velocities are interpolated by shape functions $N_i(\mathbf{X})$ as

$$\delta\mathbf{v}_e(\mathbf{X}) = \sum_{i=1}^{k} N_i(\mathbf{X})\,\delta\mathbf{v}_i. \tag{4.1.100}$$

The interpolated vectors $\mathbf{u}_e, \mathbf{v}_e, \mathbf{a}_e$ are inserted into Equation (4.1.95) and it follows the weak form evaluated on node j by

$$\delta\mathbf{v}_j \cdot \underbrace{\left(\int_{\Omega_e} N_j(\mathbf{X})\rho_e \mathbf{b}_e\, d\Omega_e + \int_{\Gamma_{N_e}} N_j(\mathbf{X})\bar{\mathbf{t}}_e\, d\Gamma_{N_e} \right)}_{\mathbf{f}_j^{ext}} -$$

$$\delta\mathbf{v}_j \cdot \underbrace{\int_{\Omega_e} \frac{\partial N_j(\mathbf{X})}{\partial \mathbf{x}} \cdot \boldsymbol{\sigma}_e\, d\Omega_e}_{\mathbf{f}_j^{int}} = \delta\mathbf{v}_j \cdot \underbrace{\int_{\Omega_e} \sum_{i=1}^{k} N_j(\mathbf{X}) \cdot N_i(\mathbf{X})\rho\, d\Omega_e \mathbf{a}_i}_{\mathbf{f}_j^{kin}}. \tag{4.1.101}$$

Using external nodal force vector $\mathbf{f}_j^{ext}$, internal nodal force vector $\mathbf{f}_j^{int}$ and nodal inertia force vector $\mathbf{f}_j^{kin}$, the weak form evaluated on node j is rewritten as

$$\delta\mathbf{v}_j \cdot \left(\mathbf{f}_j^{ext} - \mathbf{f}_j^{int} \right) = \delta\mathbf{v}_j \cdot \mathbf{f}_j^{kin}. \tag{4.1.102}$$

As a result, the discretised weak form of an element with k nodes can be expressed in matrix form as

$$\delta\mathbf{v}_e^T \left(\mathbf{f}_e^{ext} - \mathbf{f}_e^{int} \right) = \delta\mathbf{v}_e^T \mathbf{M}_e \mathbf{a}_e \tag{4.1.103}$$

where $\delta\mathbf{v}_e$, $\mathbf{f}_e^{int}$, $\mathbf{f}_e^{ext}$ and $\mathbf{a}_e$ are vectors of length k and defined as

$$\delta\mathbf{v}_e = \begin{pmatrix} \delta\mathbf{v}_1 \\ \delta\mathbf{v}_2 \\ \vdots \\ \delta\mathbf{v}_k \end{pmatrix} \quad \mathbf{f}_e^{ext} = \begin{pmatrix} \mathbf{f}_1^{ext} \\ \mathbf{f}_2^{ext} \\ \vdots \\ \mathbf{f}_k^{ext} \end{pmatrix} \quad \mathbf{f}_e^{int} = \begin{pmatrix} \mathbf{f}_1^{int} \\ \mathbf{f}_2^{int} \\ \vdots \\ \mathbf{f}_k^{int} \end{pmatrix} \quad \mathbf{a}_e = \begin{pmatrix} \mathbf{a}_1 \\ \mathbf{a}_2 \\ \vdots \\ \mathbf{a}_k \end{pmatrix} \tag{4.1.104}$$

and the $k \times k$ matrix $\mathbf{M}_e$ is called the consistent element mass matrix

$$\mathbf{M}_e = \int_{\Omega_e} \begin{pmatrix} N_1N_1 & N_1N_2 & \cdots & N_1N_k \\ N_2N_1 & N_2N_2 & \cdots & N_2N_k \\ \vdots & \vdots & \ddots & \vdots \\ N_kN_1 & N_kN_2 & \cdots & N_kN_k \end{pmatrix} \rho_e \, d\Omega_e. \tag{4.1.105}$$

The element formulation and, thus, the arithmetic operations on the element level depend on the mechanical model, the number of nodes and the shape functions. The general case of a mechanical model is given by the model of a volume element. This model can be reduced by assuming shell theory or beam theory. Here, assumptions are made on the geometrical dimensions. For instance, shell theory assumes that the element thickness is much smaller than the element edges. Furthermore, the integrals are computed numerically by introducing integration points and corresponding weight factors, for instance by Gauss integration. Consequently, stresses are computed in these integration points using the underlying constitutive equations. An overview of some widely used element formulations can be found in the books by Bathe [10], Belytschko et al. [13] and Wriggers [117].

Equation (4.1.95) is inserted into Equation (4.1.94) and the discretised weak form of a solid body becomes

$$\bigcup_{e=1}^{n} \delta \mathbf{v}_e^T \left(\mathbf{f}_e^{ext} - \mathbf{f}_e^{int} - \mathbf{M}_e \mathbf{a}_e \right) = 0. \tag{4.1.106}$$

Assembling all elements leads to the matrix formulation

$$\delta \mathbf{v}^T \left(\mathbf{f}^{ext} - \mathbf{f}^{int} - \mathbf{M}\mathbf{a} \right) = 0 \tag{4.1.107}$$

where $\delta\mathbf{v}$, $\mathbf{a}$, $\mathbf{f}^{ext}$ and $\mathbf{f}^{int}$ are vectors of the unconstrained virtual nodal velocities, the nodal accelerations and the external and internal nodal forces and $\mathbf{M}$ is the consistent mass matrix. Due to the arbitrariness of the unconstrained virtual velocities, see Bathe [10], the fundamental system of algebraic equations reads

$$\mathbf{f}^{ext} - \mathbf{f}^{int} = \mathbf{M}\mathbf{a}. \tag{4.1.108}$$

These equations are also known as the semidiscrete momentum equations. It is called semidiscrete since FEM solves the structural problem by spatial discretisation and the time t is still kept continuous. Equation (4.1.108) is rewritten as

$$\mathbf{f}^{ext}(\mathbf{u}(t)) - \mathbf{f}^{int}(\mathbf{u}(t)) = \mathbf{M} \frac{\partial \mathbf{v}(t)}{\partial t} \tag{4.1.109}$$

where $\mathbf{u}$ and $\mathbf{v}$ are vectors of the unconstrained nodal displacements and the unconstrained nodal velocities. It shows an ordinary differential equation with respect to time t. This is mathematically called an initial value problem. The initial conditions of a solid body are given in form of

$$\mathbf{u}(t_0) = \mathbf{u}_0 \quad \text{and} \quad \mathbf{v}(t_0) = \mathbf{v}_0 \tag{4.1.110}$$

where $\mathbf{u}_0$ and $\mathbf{v}_0$ are vectors of predefined nodal displacements and predefined nodal velocities. Often, the differential equation given in Equation (4.1.109) is solved by time integration algorithms where the time period $0 \leq t \leq t^*$ is discretised in time intervals $\triangle t$ such as

$$t_{n+1} = t_n + \triangle t_{n+1}. \tag{4.1.111}$$

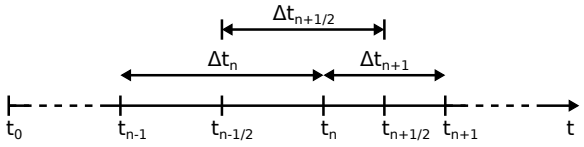

Figure 4.1.7: Discretisation of time t.

As a result, the differential equation is solved at discrete points in time t and the solution is interpolated between t_n and t_{n+1} in so-called one-step algorithms. Time integration algorithms can be categorised into explicit and implicit time integration algorithms, see Belytschko et al. [13] and Hughes [60]. In the following, the focus is put on an explicit time integration algorithm. Thus, Equation (4.1.108) is evaluated at time t_n.

The most popular explicit time integration algorithm is the central difference approach which is an one-step algorithm. This method is developed from the central difference formulas for velocities and accelerations and is characterised by a varying time step $\triangle t$. The notation is defined as follows: The discrete accelerations, velocities and displacements at time t_n are denoted as $\mathbf{a}_n$, $\mathbf{v}_n$ and $\mathbf{u}_n$ and, accordingly, the quantities at time t_{n+1} are denoted as $\mathbf{a}_{n+1}$, $\mathbf{v}_{n+1}$ and $\mathbf{u}_{n+1}$. Further, an intermediate time between t_n and t_{n+1} is denoted as $t_{n+\frac{1}{2}}$ and is determined by the average

$$t_{n+\frac{1}{2}} = \frac{1}{2}(t_{n+1} + t_n) \tag{4.1.112}$$

and the intermediate time step $\triangle t_{n+\frac{1}{2}}$ reads

$$\triangle t_{n+\frac{1}{2}} = t_{n+\frac{1}{2}} - t_{n-\frac{1}{2}} = \frac{1}{2}\left(\triangle t_{n+1} + \triangle t_n\right). \tag{4.1.113}$$

This form of time discretisation is illustrated in Figure 4.1.7.

Now, velocities $\mathbf{v}_{n+\frac{1}{2}}$ are computed by the central difference formula

$$\mathbf{v}_{n+\frac{1}{2}} = \frac{\mathbf{u}_{n+1} - \mathbf{u}_n}{t^{n+1} - t^n} = \frac{\mathbf{u}_{n+1} - \mathbf{u}_n}{\triangle t_{n+1}} \tag{4.1.114}$$

and, consequently, displacements $\mathbf{u}_{n+1}$ are given by

$$\mathbf{u}_{n+1} = \mathbf{u}_n + \triangle t_{n+1}\mathbf{v}_{n+\frac{1}{2}}. \tag{4.1.115}$$

In the same manner, accelerations $\mathbf{a}_n$ are computed by the central difference formula

$$\mathbf{a}_n = \frac{\mathbf{v}_{n+\frac{1}{2}} - \mathbf{v}_{n-\frac{1}{2}}}{t^{n+\frac{1}{2}} - t^{n-\frac{1}{2}}} = \frac{\mathbf{v}_{n+\frac{1}{2}} - \mathbf{v}_{n-\frac{1}{2}}}{\triangle t_{n+\frac{1}{2}}} \tag{4.1.116}$$

and velocities $\mathbf{v}_{n+\frac{1}{2}}$ can be rewritten as

$$\mathbf{v}_{n+\frac{1}{2}} = \mathbf{v}_{n-\frac{1}{2}} + \triangle t_{n+\frac{1}{2}}\mathbf{a}_n. \tag{4.1.117}$$

By substituting Equation (4.1.114) at time $t_{n-\frac{1}{2}}$ and time $t_{n+\frac{1}{2}}$ into Equation (4.1.116), accelerations $\mathbf{a}_n$ can be expressed in terms of displacements by

$$\mathbf{a}_n = \frac{\triangle t_n(\mathbf{u}_{n+1} - \mathbf{u}_n) - \triangle t_{n+1}(\mathbf{u}_n - \mathbf{u}_{n-1})}{\triangle t_n \triangle t_{n+\frac{1}{2}} \triangle t_{n+1}}. \tag{4.1.118}$$

Considering equidistant time steps $\triangle t_n = \triangle t_{n+\frac{1}{2}} = \triangle t_{n+1}$, accelerations $\mathbf{a}_n$ become

$$\mathbf{a}_n = \frac{\mathbf{u}_{n+1} - 2\mathbf{u}_n + \mathbf{u}_{n-1}}{(\triangle t_n)^2}. \tag{4.1.119}$$

The central difference method can be applied to solve the FE equations given in Equation (4.1.108) at time t_n. Here, accelerations $\mathbf{a}_n$ are computed by

$$\mathbf{a}_n = \mathbf{M}^{-1}\left(\mathbf{f}^{ext}(\mathbf{u}_n, t_n) - \mathbf{f}^{int}(\mathbf{u}_n, t_n) - \mathbf{C}\mathbf{v}_{n-\frac{1}{2}}\right) \tag{4.1.120}$$

where the additional nodal force $\mathbf{C}\mathbf{v}_{n-\frac{1}{2}}$ is introduced. This force represents a rate dependent damping force also known as Rayleigh damping and is determined by velocities $\mathbf{v}_{n-\frac{1}{2}}$ and damping matrix $\mathbf{C}$ which is given by a combination of stiffness and mass matrix. Velocities $\mathbf{v}_{n-\frac{1}{2}}$ are used for numerical efficiency since the velocities $\mathbf{v}_n$ given by

$$\mathbf{v}_n = \mathbf{v}_{n-1} + \triangle t_n \mathbf{a}_{n-\frac{1}{2}} \tag{4.1.121}$$

would require the computation of the accelerations $\mathbf{a}_{n-\frac{1}{2}}$. This modification is known as Verlet algorithm, see Verlet [110]. The simplification by using $\mathbf{v}_{n-\frac{1}{2}}$ instead of $\mathbf{v}_n$ reduces the order of accuracy of the time integration scheme. However, in case of undamped and non-viscous problems, this simplification has no influence on accuracy. In the usual case of slightly damped and viscous problems, this simplification has just a minor influence on accuracy since the used time steps are usually very small. The conditional stability of this method is defined by a critical time step $\triangle t_{crit}$, see Belytschko et al. [13]. If $\triangle t$ exceeds $\triangle t_{crit}$, the solution of the time integration scheme becomes unstable. A stable time step $\triangle t$ is usually determined by the Courant criterium which reads

$$\triangle t = \alpha \triangle t_{crit} \quad \text{with} \quad \triangle t_{crit} = \frac{2}{\omega_{max}} \leq \frac{2}{\max\left[\omega_{e,i}\right]} = \min\left[\frac{l_e}{c_e}\right] \tag{4.1.122}$$

where ω_{max} is the largest eigenfrequency of the underlying solid body which is approximated by the largest element eigenfrequency $\omega_{e,i}$ found in the discretised solid body. $\triangle t_{crit}$ can be directly computed from the critical element by the relation of its characteristic length l_e and its wave speed c_e. Essentially, l_e is the shortest distance between element nodes respectively the shortest distance between element nodes to appropriate element edges. It is noted that $\triangle t_{crit}$ is calculated in the current configuration and, thus, the critical element may change with the deformation of the discretised solid body. The scale factor α accounts for approximations concerning the estimation of ω_{max} in principle for destabilising effects and nonlinearities. To be on the safe side, α is usually set in the range of $0.8 \leq \alpha \leq 0.98$. In some cases, it might be advantageous to use even lower values. The general explicit time integration procedure is demonstrated in Figure 4.1.8. By the law of mass conservation in Equation (4.1.20), the inverse mass matrix $\mathbf{M}^{-1}$ needs to be computed only once. Further, it can be seen that the solution of $\mathbf{u}_{n+1}$ does only depend on known quantities from the previous time step. Therefore, it is called an explicit time integration. In implicit time integration algorithms, the solution of $\mathbf{u}_{n+1}$ depends on known quantities from the previous time step as well as on unknown quantities from the next time step. Then, a nonlinear equation system has to be solved in each time step.

Commercial FE programs like LS-DYNA (explicit and implicit) [77], Abaqus (explicit and implicit) [24], ANSYS (implicit) [7] or PAM-CRASH (explicit) [37] make it possible to simulate and analyse the behaviour of complex structures with advanced material properties under various loading conditions. These programs combine FEM with a time integration

1. Time update:
$$t_n = t_{n-1} + \triangle t_n$$
2. Nodal forces using $\mathbf{f}^{int}$ computed on element level:
$$\mathbf{f}_n = \mathbf{f}^{ext}(\mathbf{u}_n, t_n) - \mathbf{f}^{int}(\mathbf{u}_n, t_n)$$
3. Time step update using $\triangle t_{crit}$ computed on element level:
$$\triangle t_{n+1} = \alpha \triangle t_{crit}$$
4. Compute accelerations:
$$\mathbf{a}_n = \mathbf{M}^{-1}\left(\mathbf{f}_n - \mathbf{C}\mathbf{v}_{n-\frac{1}{2}}\right)$$
5. Update velocities:
$$\mathbf{v}_{n+\frac{1}{2}} = \mathbf{v}_{n-\frac{1}{2}} + \frac{1}{2}\left(\triangle t_n + \triangle t_{n-1}\right)\mathbf{a}_n$$
6. Update displacements:
$$\mathbf{u}_{n+1} = \mathbf{u}_n + \triangle t_{n+1}\mathbf{v}_{n+\frac{1}{2}}$$

Figure 4.1.8: Flow chart of the explicit time integration algorithm using the central differences method in the form proposed by Verlet [110].

algorithm. Furthermore, a wide range of material models are offered for different materials and fields of application. However, the FE program itself is only a numerical solver and, thus, the generation of FE models (pre-processing) and the analysis and visualisation of simulation results (post-processing) are performed with software tools with a graphical user interface such as LS-PrePost [78]. Advanced pre-processors like ANSA [14] or HyperMesh [3] enable to discretise structures using available CAD data. A detailed visualisation and animation of a simulation result can be performed using advanced post-processors like META [15] or Animator4 [42]. In the present work, the FE simulations were performed in LS-DYNA 971 (explicit) [51] and ANSA [14] and LS-PrePost [78] were applied for the pre- and post-processing.

Finally, it is noted that the numerical results presented in the present work are based on FE simulations using so-called underintegrated elements. As already mentioned, the element integrals given in Equation (4.1.103) are computed numerically by introducing integration points and corresponding weight factors, for instance by Gauss integration. Here, a full integration order of an element solves the exact values of the integrals provided that the considered element is not distorted, see Bathe [10]. In case of a distorted element, a full integration order cannot deliver the exact values of the integrals. However, this error is negligible when the element distortion is limited. For instance, a plane stress 4-node element can be fully integrated by 2×2 Gauss integration, see Bathe [10]. This means that four integration points are required to achieve sufficient accuracy. A fully integrated element shows a too stiff behaviour known as locking, for instance in case of incompressible (or nearly incompressible) materials or under pure shear loading. Locking can be avoided

by increasing the integration order which implies that the number of element nodes needs to be increased. Alternatively, a lower integration order than necessary can be applied. This approach is called underintegration. In case of the plane stress 4-node element, only one integration point is applied by underintegration. As a result of underintegration, an element provides unphysical zero energy modes. An unphysical zero energy mode can be defined as: Any motion which is not a rigid body motion and results in no straining of the element is an unphysical zero energy mode, see Belytschko et al. [13]. An unphysical zero energy mode is often called hourglass mode or hourglassing. Therefore, underintegrated elements are not recommend for structural analyses without any further action such as additional element stabilisation which prevent hourglass modes. Here, different hourglass stabilisation schemes can be applied. Most common hourglass stabilisation schemes are based on additional forces which are applied on the element nodes when the element shows hourglassing. These nodal forces stop the formation of hourglass modes and, thus, stabilise the element. Since these additional nodal forces are artificial, it is important to check the so-called hourglass energy produced by these nodal forces in a FE simulation. In case the hourglass energy takes on a substantial part of the total energy in a FE simulation, the numerical results become questionable and a modification of the underlying FE model should be considered. Often, a good way to reduce the hourglass energy is to refine the FE mesh and, thus, to avoid single mode locking or similar. More details on hourglass stabilisation schemes can be found in the book by Belytschko et al. [13] and in the LS-DYNA - Theory Manual by Hallquist [50]. A widely used hourglass stabilisation scheme is based on the elastic material properties and the geometry of the element. Such a hourglass stabilisation scheme is said to be stiffness based. In the present work, Belytschko-Tsay shell elements (which are underintegrated 4-node shell elements) and 8-node underintegrated solid elements were applied in combination with a stiffness based hourglass control available in LS-DYNA 971 [51]. A FE simulation is usually considered as not critical regarding hourglassing if the hourglass energy is less than 1% of the total energy.

4.2 Brittle and Ductile Fracture

In material science, fracture is defined as the separation of a material into two or more pieces. Two major forms of fracture can occur: Brittle and ductile fracture. Therefore, structural materials are categorised according to their fracture form into brittle and ductile materials. In the following, both fracture types are briefly presented and an engineering interpretation of them is given. The internal mechanisms which lead to brittle or ductile fracture initiation are described in detail by Lemaitre and Chaboche [75].

4.2.1 Brittle Fracture

A material is defined brittle when it ruptures without any irreversible strains and no mechanical energy is dissipated prior to fracture. It is defined quasi-brittle when an energy dissipation exists prior to fracture with no or small irreversible strains. Materials like ceramics, glasses or concrete exhibit a typical brittle to quasi-brittle fracture behaviour, but also in metals and polymers a quasi-brittle behaviour can be observed. In general, brittle and quasi-brittle materials are characterised by a strong material matrix which acts sensitively to internal imperfections. Therefore, an increase of the material strength results in quasi-brittle fracture behaviour. For instance, high-strength steels tend to a quasi-brittle fracture behaviour. Furthermore, brittle or quasi-brittle fracture can occur in every material under cyclic loading, high strain rates or low temperatures. The graphs plotted in Figure 4.2.1

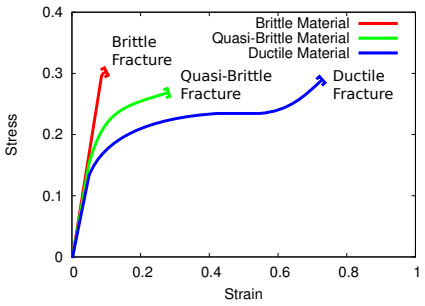

Figure 4.2.1: Characteristic stress-strain curves for brittle, quasi-brittle and ductile materials.

show characteristic stress-strain curves for brittle (red) and quasi-brittle (green) materials subjected to tension loading.

Brittle fracture is characterised by a fast crack propagation induced mainly by atomic decohesion. The fracture initiation is caused by microscopic defects of the material such as cleavage planes, inclusions, porosities or any other kind of discontinuities. The defects are defined as initial defects and they are assumed to be constant. This means that the defects do not evolve during loading. A macroscopic fracture in brittle and quasi-brittle materials occurs as the result of formation and growth of microcracks in the vicinity of initial defects, see Figure 4.2.2a. These defects are size, shape and orientation dependent as well as inhomogenous and pseudo-randomly distributed. Especially, the last two characteristics lead to a material behaviour which is characterised by pseudo-random occurrence of fracture initiation. This means that time and location of fracture initiation vary pseudo-randomly and cannot be predicted in a deterministic sense.

4.2.2 Ductile Fracture

A material is defined ductile when large irreversible strains take place prior to fracture. A typical stress-strain curve for ductile materials subjected to tension loading is presented by the blue graph in Figure 4.2.1. It shows that fracture takes place after the strains in the material has been localised and a neck has developed. Most common metal alloys and a large number of polymers exhibit a ductile material behaviour. In general, high purity as well as high temperatures and low strain rates increase the material ductility.

In ductile metals, a crack develops as result of nucleation, growth and coalescence of microscopic voids. The metallic microstructure consists of crystalline defects such as second-phase particles or inclusions. When the bond between these defects and the metal matrix is broken voids start to form. Due to further loading, voids nucleate, grow and merge together until a macroscopic fracture develops as illustrated in Figure 4.2.2b. High stresses and plastic deformations are necessary for void nucleation and growth. In particular, a positive hydrostatic stress state is required. Naturally, voids arise in the (diffuse) necked region of a specimen where the strains localise and increase rapidly. From a microscopic point of view, the strains localise between voids and, consequently, a localised neck develops. This means that ductile fracture occurs where strains localise. However, it is clearly seen that fracture toughness is dominated by the strength of the interfacial bond. The evolution of voids is also known as the damage evolution. A damaged material, but not yet fractured, can show a change in the elastic-plastic behaviour. This phenomenon is called material softening.

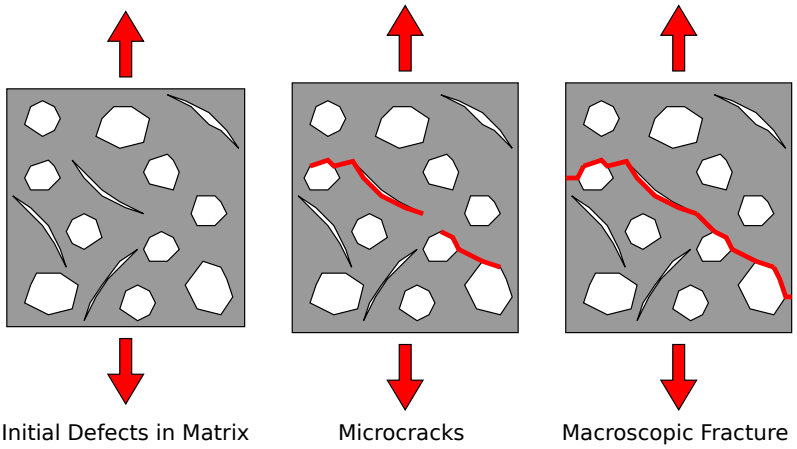

(a) Brittle fracture.

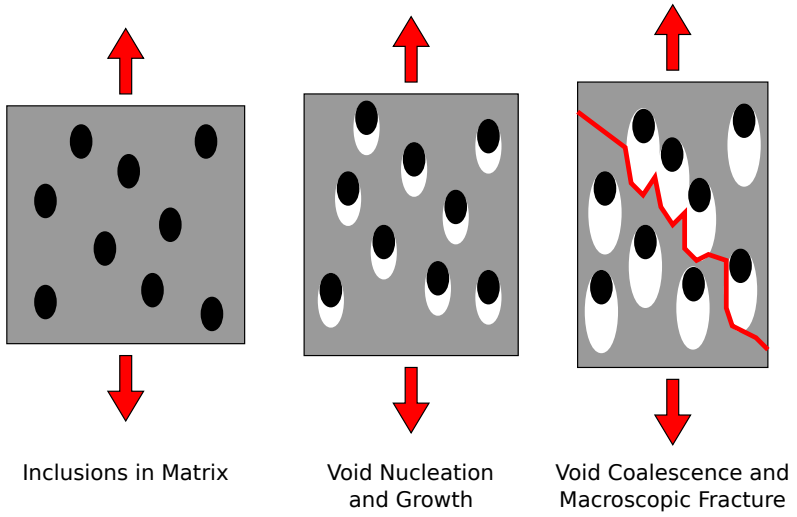

(b) Ductile fracture.

Figure 4.2.2: Schematic representation of the fracture mechanisms in brittle and ductile materials.

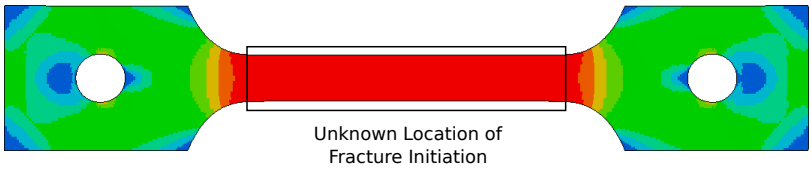

(a) Stress distribution prior to brittle fracture.

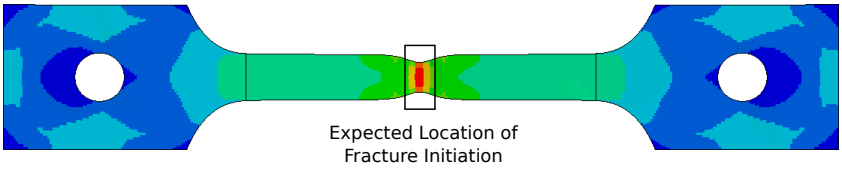

(b) Stress distribution prior to ductile fracture.

Figure 4.2.3: Stress distribution prior to fracture in a tensile test specimen.

4.2.3 Engineering Interpretation

A uniaxial tensile test is considered. Figure 4.2.3 shows the longitudinal stress distribution (obtained from a FE simulation) in a tensile test specimen right before fracture initiation. The quasi-brittle case is illustrated in Figure 4.2.3a. Here, the stress distribution is nearly uniform before fracture occurs. It is noted that the stress distribution only changes in magnitude during loading and is uniform until a neck develops. Since it is usually unknown where the fracture relevant internal defect is located and which size (including shape and orientation) the defect adopts, it is not possible to estimate where and when fracture occurs. As already mentioned, the distribution of fracture relevant defects is commonly expected to be pseudo-random and, thus, the fracture initiation becomes pseudo-random in space and time. The ductile case is given in Figure 4.2.3b. The stress distribution is localised in the neck and fracture will occur in the vicinity of this plastic instability. Therefore, the location of fracture initiation is known. The exact time depends on the material ductility (or fracture toughness) which could be pseudo-random.

However, if fracture initiation is considered from a weakest-link approach, the specimen is said to fail at the weakest-link. In the brittle case, the weakest-link is the largest fracture related defect found in the material structure. In the ductile-case, the weakest-link is given by the strain localisation due to plastic deformations. The difference is that the weakest-link is given by an initial defect in brittle materials and that the weakest-link evolves during loading in a ductile material. However, strains usually localise in the vicinity of a material imperfection. In a strict sense, the mandatory material imperfection can be seen as the weakest-link.

4.3 Failure Modelling

The field of fracture mechanics can be separated into three specific groups: Linear-elastic, elastic-plastic and phenomenological fracture mechanics. The first theory to explain fracture from a continuum mechanical point of view was introduced by Griffith during World War I, see Griffith [46]. He described the behaviour of a crack in a linear-elastic material.

His criterion is based on the approach that crack growth requires the creation of two new surfaces and, thus, an increase in the surface energy. During World War II, Irwin modified Griffith's criterion to model fracture in ductile materials. Therefore, the plastic zone around a crack tip is considered in his approach. Furthermore, Irwin introduced the well known K-concept based on stress intensity factors, see Gross and Seelig [47]. In the 1960's, Cherepanov and Rice developed independently the theoretical concept of the J-integral, see Cherepanov [18] and Rice [97]. The J-integral allows to determine the energy per unit fracture surface area. It was a first approach in the field of elastic-plastic fracture mechanics. The elastic-plastic and nonlinear fracture mechanics are more and more important in modern material science. In summary, the objective of fracture mechanics is the prediction of fracture initiation and crack propagation. For a detailed introduction into the field of fracture modelling, also from an engineering point of view, it is referred to the books by Lemaitre and Desmorat [75] and Gross and Seelig [47]. Several theories are presented and compared. In addition, the calibration and application of failure criteria are well discussed.

In the analysis of fracture, it is necessary to define a criterion which states if fracture initiates in the material under a certain load level. Such criteria are derived from first principles, but most of them are of phenomenological nature. Phenomenological criteria are derived from experimental observations. A variety of phenomenological criteria (depending on the underlying material and the field of application) has been established in the history of mechanics. Due to their simplicity, phenomenological criteria are applied in many engineering applications. Moreover, crack propagation is often predicted numerically by combining phenomenological criteria and FEM. However, the prediction of fracture initiation is of major importance in order to guarantee structural reliability. Therefore, fracture initiation is often defined as failure. It is noted that also the point of yielding could be defined as failure which is the common case in civil engineering. In the present work, failure means fracture initiation and the aim is to predict the fracture initiation based on a phenomenological failure criterion. In the following, the concept of failure modelling is introduced, some widely used failure criteria are presented and the calibration of failure criteria is briefly discussed. In addition, a short introduction into numerical failure modelling is given.

4.3.1 Phenomenological Failure Criteria

Material properties and fields of application are essential topics in the definition of phenomenological failure criteria. Here, a scalar function f representing the material loading is used. When material loading f reaches a critical value f_{crit}, fracture initiates and the material fails. Consequently, the failure criterion can be defined in form of

$$f = f_{crit}. \tag{4.3.1}$$

Furthermore, all admissible loading states must satisfy the inequality

$$f < f_{crit}. \tag{4.3.2}$$

f may depend on stress state $\boldsymbol{\sigma}$, equivalent plastic strain $\bar{\varepsilon}$, equivalent plastic strain rate $\dot{\bar{\varepsilon}}$ and temperature θ. f_{crit} is mostly assumed to be constant. However, f_{crit} may also depend on $\boldsymbol{\sigma}$, $\bar{\varepsilon}$, $\dot{\bar{\varepsilon}}$ and θ. As a result, the failure criterion can be written as

$$f\left(\boldsymbol{\sigma}, \bar{\varepsilon}, \dot{\bar{\varepsilon}}, \theta\right) = f_{crit}\left(\boldsymbol{\sigma}, \bar{\varepsilon}, \dot{\bar{\varepsilon}}, \theta\right). \tag{4.3.3}$$

The evolution of material damage D such as void growth is often expressed by evolution of f, for instance

$$D = \frac{1}{f_{crit}} \int_{t_0}^{t_1} \frac{\partial f}{\partial t} dt \quad \text{with} \quad D \in [0,1] \tag{4.3.4}$$

where t_0 and t_1 covers the loading period. D grows within the loading period and when D reaches unity the material fails. In a coupled approach, damage evolution affects the elastic-plastic relationship and the stress-strain response, respectively. Hence, yield condition, plastic flow as well as hardening can be affected by damage evolution. The Gurson model for porous plasticity is probably the best-known model to describe material softening, see Gurson [49]. In general, a coupled approach allows to model material softening in the fracture process zone, but the experimental identification of material parameters becomes more involved and increasingly complex compared to uncoupled models. However, in many engineering applications the damage coupling can be neglected. For instance, it is assumed that plastic deformations in metals are controlled by the deviatoric part of the stress tensor, whereas fracture initiating voids mainly grow in metals under hydrostatic tension, see Dey [27]. Some representative failure criteria are presented in the following. They are intended to show different approaches in phenomenological failure modelling. Numerous other failure criteria can be found in the technical literature.

Brittle failure criteria usually depend on $\boldsymbol{\sigma}$. In particular, these are given in terms of principal stresses $\sigma_I, \sigma_{II}, \sigma_{III}$, see Equation (4.1.28). For instance, the maximum principle stress criterion is one of the oldest and it states that the material fails when the maximum stress in tension σ_t or compression σ_c is reached,

$$\begin{aligned} \sigma_I &= \sigma_t \\ \sigma_{III} &= \sigma_c. \end{aligned} \tag{4.3.5}$$

It is also common to express a stress depended failure criterion in terms of an equivalent stress σ_{eq} in the same way as for a yield criterion. Here, it is assumed that the material fractures when σ_{eq} reaches a critical value σ_{fr},

$$\sigma_{eq} = \sigma_{fr}. \tag{4.3.6}$$

For instance, σ_{eq} can be expressed according to the v. Mises stress

$$\sigma_{eq} = \sqrt{\frac{1}{2}\left[(\sigma_I - \sigma_{II})^2 + (\sigma_{II} - \sigma_{III})^2 + (\sigma_{III} - \sigma_I)^2\right]} \tag{4.3.7}$$

or the Tresca stress

$$\sigma_{eq} = \max\left[\left|\frac{\sigma_I - \sigma_{II}}{2}\right|, \left|\frac{\sigma_{II} - \sigma_{III}}{2}\right|, \left|\frac{\sigma_{III} - \sigma_I}{2}\right|\right]. \tag{4.3.8}$$

If initial defects are considered, the equivalent stress criterion in Equation (4.3.6) could be rewritten as

$$\sigma_{eq} = (1 - D_0)\sigma_{fr} \quad \text{with} \quad D_0 \in [0,1] \tag{4.3.9}$$

where D_0 represents initial defects, see Lemaitre and Desmorat [75]. D_0 takes values between 0 and 1, with 0 as the pure material and 1 as the pure defect or zero material. σ_{fr} is the failure stress of the pure material. For instance, D_0 can represent the material porosity defined by a pore volume V_p in a representative material volume V_0,

$$D_0 = \frac{V_p}{V_0}. \tag{4.3.10}$$

Another well known stress dependent criterion is the Mohr-Coulomb criterion given by

$$\frac{1}{2}\left[\left(\sqrt{1+c_1^2}+c_1\right)\sigma_I-\left(\sqrt{1+c_1^2}-c_1\right)\sigma_{III}\right]=c_2. \tag{4.3.11}$$

where c_1 denotes the internal friction coefficient and c_2 is the material cohesion. If $c_1=0$, the Mohr-Coulomb criterion reduces to the Tresca criterion.

In ductile materials such as metals, the strains to fracture are usually considered since the strains increase much faster than the stresses within the plastic region. Here, the most common approach is the usage of $\bar{\varepsilon}$. In the simplest case, it is assumed that the material fails when a critical value $\bar{\varepsilon}_{fr}$ is reached, so that

$$\bar{\varepsilon}=\bar{\varepsilon}_{fr}. \tag{4.3.12}$$

Since plastic deformations and hydrostatic tension are necessary for void growth, $\bar{\varepsilon}_{fr}$ is often related to stress triaxiality σ^*, so that

$$\bar{\varepsilon}=\bar{\varepsilon}_{fr}\left(\sigma^*\right). \tag{4.3.13}$$

σ^* is a measure of the influence of the hydrostatic stress in an arbitrary stress state and it is defined through the relation

$$\sigma^*=\frac{1}{3}\frac{\mathrm{tr}(\boldsymbol{\sigma})}{\sigma_{eq}} \tag{4.3.14}$$

where σ_{eq} is determined as the v. Mises stress. Some characteristic values of σ^* are $2/3$ for biaxial tension, $1/3$ for axial tension, 0 for pure shear and $-1/3$ for axial compression. The function $\bar{\varepsilon}_{fr}(\sigma^*)$ is technically called the fracture locus. This approach is the most common way to model failure in metals. Here, a well known criterion is introduced by Johnson and Cook [65]. It postulates that $\bar{\varepsilon}_{fr}$ can be expressed as a monotonic function of σ^* as

$$\varepsilon_{fr}=d_1+d_2\exp\left(d_3\sigma^*\right) \tag{4.3.15}$$

where d_1, d_2 and d_3 are material constants. The original Johnson-Cook criterion combines this equation in a multiplicative manner with a strain-rate dependent and temperature dependent term and it reads

$$\bar{\varepsilon}_{fr}=\left[d_1+d_2\exp\left(d_3\sigma^*\right)\right]\left(1+d_4\ln\left(\frac{\dot{\bar{\varepsilon}}}{\dot{\bar{\varepsilon}}_0}\right)\right)(1-d_5(\theta_H)) \tag{4.3.16}$$

where d_4 and d_5 are further material constants. In the strain-rate term, $\dot{\bar{\varepsilon}}$ is related to a reference strain-rate $\dot{\bar{\varepsilon}}_0$. In the thermal dependent term, the homologous temperature θ_H is applied and it is defined as

$$\theta_{H=}\frac{\theta-\theta_R}{\theta_M-\theta_R} \tag{4.3.17}$$

where θ is the current temperature, θ_R the reference temperature and θ_M the material melt temperature. In summary, the original Johnson-Cook failure model requires eight material constants which need to be calibrated. In case damage evolution D is considered, D is expressed in terms of $\dot{\bar{\varepsilon}}$ and $\bar{\varepsilon}_{fr}$ as

$$D=\int_{t_0}^{t_1}\frac{\dot{\bar{\varepsilon}}}{\bar{\varepsilon}_{fr}}dt. \tag{4.3.18}$$

In the work by Bao and Wierzbicki [8], the range of σ^* is separated into different ranges and the fracture locus function is defined within each of them. It is distinguished between

compression and tension branch. In the compression range with $\sigma^* < 0$, $\bar{\varepsilon}_{fr}$ is given by a hyperbolic failure strain function $f_1(\sigma^*)$. In the tension range with $\sigma^* \geq \frac{1}{3}$, the failure strain function $f_3(\sigma^*)$ is given by the Johnson-Cook model, see Equation (4.3.15). In the intermediate range with $0 < \sigma^* < \frac{1}{3}$, the failure strain function $f_2(\sigma^*)$ is given by a linear interpolation. In summary, the Bao-Wierzbicki fracture locus reads

$$\bar{\varepsilon}_{fr} = \begin{cases} f_1(\sigma^*) = \frac{d_4}{3\sigma^*+1} & -\frac{1}{3} < \sigma^* \leq 0 \\ f_2(\sigma^*) = f_1(0) + 3\left(f_3\left(\frac{1}{3}\right) - f_1(0)\right)\sigma^* & 0 < \sigma^* < \frac{1}{3} \\ f_3(\sigma^*) = d_1 + d_2 \exp(d_3\sigma^*) & \frac{1}{3} \leq \sigma^* \end{cases} \tag{4.3.19}$$

where d_1, d_2 and d_3 are the Johnson-Cook material coefficients and d_4 is an additional material coefficient.

In the book by Lemaitre and Desmorat [75], a more advanced brittle fracture criterion is presented. Here, the v. Mises equivalent stress is multiplied by the triaxiality function R_v given by

$$R_v = \left[\frac{2}{3}(1+\nu) + 3(1-2\nu)\left(\sigma^*\right)^2\right] \tag{4.3.20}$$

and, thus, the brittle criterion becomes

$$\sigma_{eq}\sqrt{R_v} = \sigma_{fr}. \tag{4.3.21}$$

Another approach to describe ductile failure is introduced by Cockcroft and Latham [20]. Here, the material loading is defined by the integral

$$W = \int_0^{\bar{\varepsilon}} \max[0, \sigma_I]\, d\bar{\varepsilon}. \tag{4.3.22}$$

It is seen that the integral W vanishes when the first principal stress is compressive. The Cockcroft-Latham criterion states that fracture occurs when W reaches a critical value W_c, so that

$$\int_0^{\bar{\varepsilon}} \max[0, \sigma_I]\, d\bar{\varepsilon} = W_c. \tag{4.3.23}$$

In contrast to the Johnson-Cook criterion and the other presented criteria, this criterion depends on the combination of stress and strain and not on only one of those.

4.3.2 Calibration of Failure Criteria

The fracture behaviour of a material is characterised by mechanical material tests where the test specimen is loaded until it fractures. The specimens are usually machined from larger objects such as sheets, profiles or structural components. Different specimen geometries are used to analyse the fracture behaviour under different load states (or stress triaxialities). Figure 4.3.1 shows typical specimen geometries to enforce fracture under uniaxial tension, plane strain tension, shear and notched tension. If anisotropy is expected, identical tests have to be performed using specimens with different extraction directions. If the loading velocity is varied, strain-rate dependency can be analysed. Accordingly, the influence of temperature can be analysed. It is seen that a full material characterisation regarding failure leads to an enormous test program and the influence of any material scatter is not yet included. Therefore, assumptions need to be made to reduce the experimental effort. Usually, the failure behaviour of a material is characterised first, then a suitable failure model is selected (or a new one is formulated based on the experimental observations).

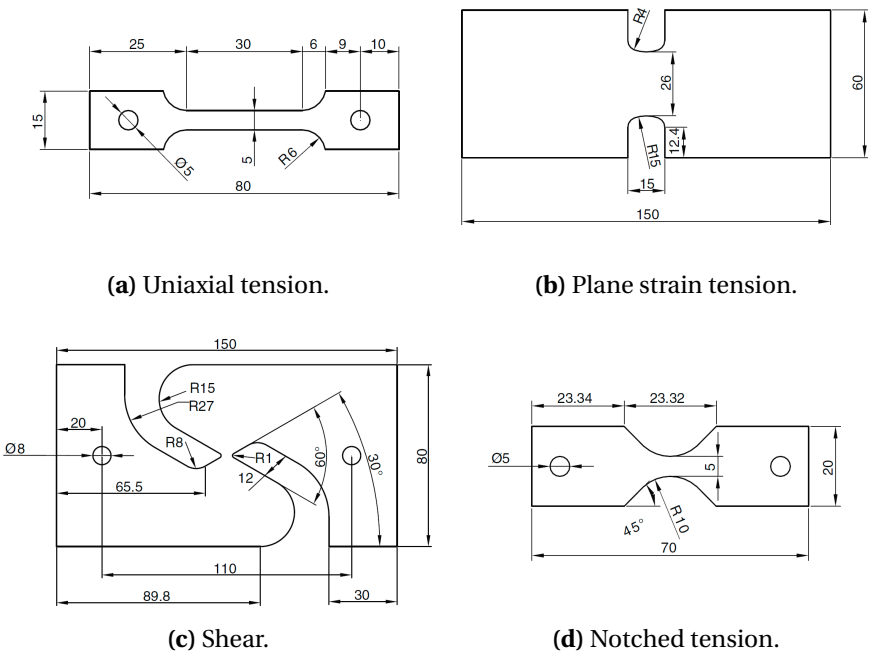

(a) Uniaxial tension.

(b) Plane strain tension.

(c) Shear.

(d) Notched tension.

Figure 4.3.1: Typical specimen geometries for mechanical material tests.

The calibration of a failure model requires a certain number of different material tests. This number is defined by the number of parameters used in the failure criterion. For instance, the simple Johnson-Cook model, see Equation (4.3.15), requires at least three different types of material tests for calibration. In contrast, the Cockcroft-Latham criterion expressed in Equation (4.3.23) only needs an uniaxial tensile test for calibration. However, it is recommended to do more different material tests than necessary. This allows a meaningful validation of the applied failure model. A technical overview of the calibration of ductile failure criteria is presented in the work by Wierzbicki et al. [113]. Based on an experimental fracture characterisation of an aluminium alloy, the calibration procedure of some commonly used failure criteria is demonstrated and discussed.

In modern material science, failure parameters are often identified in an experimental-numerical approach, also known as reverse engineering approach. Here, the experimental results are compared with FE simulations of the realised material tests. Considering the deformation behaviour to be accurately reproduced, the failure parameter is taken from the simulation just before fracture initiates in the material test. The best result is achieved when the displacement field of the specimen surface is measured by the Digital Image Correlation (DIC) during testing. Details on the DIC technique can be found in the book by Sutton et al. [104]. This allows to find the best match between simulation and experiment. For instance, equivalent plastic strain and stress triaxiality at fracture initiation can be precisely identified using this method. A good example of a reverse engineering approach for failure model calibration is shown in the work by Gruben et al. [48].

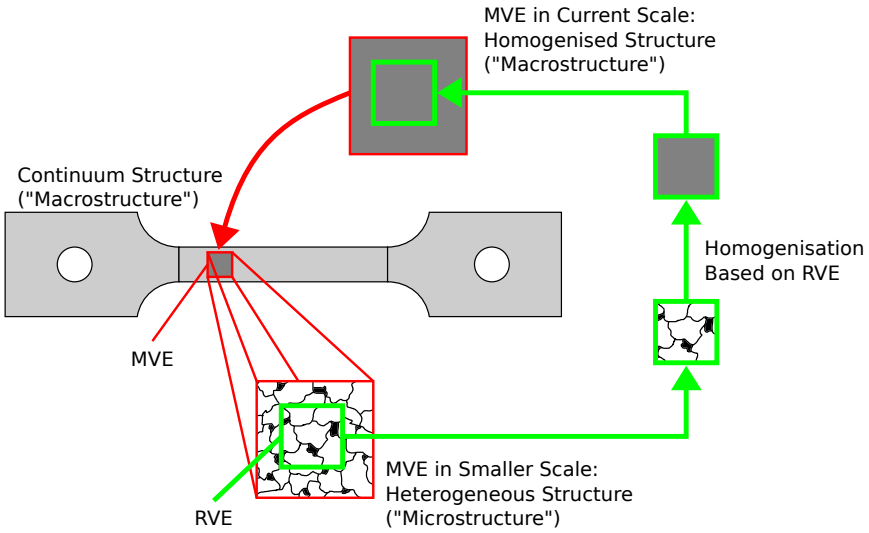

Figure 4.3.2: Schematic representation of the homogenisation procedure.

4.3.3 Remark on Homogenisation

The objective of the continuum mechanical framework is to determine stresses and strains in a material point. It is assumed that the solid material exists as a continuum. This implies that the matter is continuously distributed throughout the space occupied by the matter, see Irgens [63]. The space can be subdivided into Material Volume Elements (MVE) of any smaller size with the same continuously distributed matter. Constitutive relations and failure criteria are defined on a material point within a MVE. Here, material properties and model constants are represented as homogenised variables, see Lemaitre and Desmorat [75]. This means that these are homogeneously and continuously distributed within this material volume element. This also implies that any kind of discontinuities of a smaller scale are assumed to be homogeneous and continuously distributed by means of variables. The MVE which represents best the material behaviour of the current scale is defined as the Representative Volume Element (RVE). The concept of a RVE is essential for homogenisation, material modelling and parameter identification. The general idea of homogenisation in continuum mechanics is illustrated in Figure 4.3.2.

In most applications, the scale of interest is the macroscopic structure. Therefore the microscopic structure including porosity, initial defects and inclusions has to be homogenised. The quantification of the two scales is not clearly defined and depends on the material and the field of application. In the following, the macrostructure is defined as the current scale and the microstructure as the next smaller scale. There are two main approaches to detect the size of the RVE as stated in the work by Kouznetsova [68]. The first approach states that the RVE corresponds to a statistical representative sample of the microstructure. Especially in brittle and quasi-brittle materials, the material behaviour is characterised by a strong scatter. This indicates a strong heterogeneous and non-repeatable microstructure. Here, a statistical representative RVE has to be used. Consequently, material parameters are given in form of random variables which are related to the statistical representative RVE. The second approach becomes more specific and complex. The RVE is the smallest microstructural volume which adequately represents the overall macroscopic properties of interest. Consequently, the RVE depends on the ma-

terial behaviour under investigation. For instance, the RVE which is responsible for the plastic behaviour might be different from the RVE being responsible for the failure behaviour. Further, periodicity of the microstructure is assumed in the second approach. If the whole space consists of identical and repeated RVEs, it is called global periodicity and fully homogeneously distributed material properties are expected. However, it is more realistic to assume that the material properties are distributed heterogeneously on the macroscopic scale and periodicity of identical RVEs is only found locally. This is called local periodicity. Beyond the rather global view on homogenisation techniques and RVE modelling are particularly important in the field of multi-scale modelling.

In the experimental identification of material properties, it is often assumed that the measurements and the derived properties, respectively, are representative for a material point. First of all, the results represent only the structural behaviour of the test specimen and belong to the considered gauge volume of the test specimen. Due to precise measurement tools and extended evaluation techniques, the previous assumption is acceptable in many cases. An extension could be the identification of fracture properties in a necked specimen where plastic instabilities are expected as seen in the numerical example presented in Chapter 4.3.5.

4.3.4 Numerical Failure Modelling

The numerical analysis of failure in materials and engineering structures is usually done by FEM. Based on the stress and strain computation, failure criteria can be used to predict time and place of fracture initiation in a FE model. Usually, a failure criterion is evaluated within in the material routine where the constitutive equations are solved and, consequently, the criterion is evaluated at the element integration points. The most common failure criteria are already implemented in commercial FE programs.

It is obvious that a reliable and precise prediction of failure directly depends on the accuracy of the prediction of stresses and strains. Provided that geometry and boundary conditions as well as material behaviour are sufficiently achieved, the accuracy goes along with the FE mesh and its degree of discretisation. In particular, element size and initial element distortion are key factors in the numerical computation of stresses and strains. Therefore, a mesh convergence study is often performed by decreasing the element size within a FE model. Mesh convergence is reached when a finer mesh nearly leads to the same result as the previous one. Here, the definition of a convergence criterion is mandatory. A convergence criterion can be the global structural response like the force-displacement behaviour of a component, but could also be the equivalent plastic strain in a defined point. If the strain field localises in this defined point, a mesh convergence study becomes a challenging task. In numerical elasticity, the stresses grow indefinitely with decreasing mesh size in a localisation and mesh convergence cannot be reached. In contrast, in numerical plasticity, mesh convergence can be reached in a localisation using small element sizes. However, the calibration of the used failure criterion may depend on the applied mesh size. This issue is discussed in the following numerical example.

The FE simulation of crack propagation is a highly complex topic when linear-elastic or elastic-plastic fracture mechanics are applied. Hence, crack propagation is often predicted in FE simulations using phenomenological failure criteria. A very common approach is called element deletion. Here, the element stresses are set to zero when the failure criterion is met in an integration point. If the element contains of more than one integration point, a defined number of failed integration points need to be reached before the element is eroded. Due to simplicity and computational efficiency, this technique is often used successfully. Another approach is called node splitting technique. Multiple nodes

are generated for adjacent elements and the nodes are tied together. When the failure criterion is met in a multiple node or in an element, the bond is released. This approach becomes numerical inefficient in large models respectively a crack zone needs to be defined in advance.

However, the results of both approaches are strongly mesh dependent. In both cases, mesh orientation influences strongly the course of the crack path. A scheme avoiding mesh dependence in the numerical analysis of crack propagation is the extended FEM known as XFEM, see Moës et al. [86] and Belytschko et al. [12]. The XFEM combines classical FEM with mesh-free methods to solve problems involving localisation of the stress field and the strain field, respectively. This approach is so far only applied in science. Unfortunately, there is a number of problems for 3D continua and dynamics.

4.3.5 Numerical Example

The following example demonstrates an experimental-numerical calibration of a failure criterion and the influence of element size on the calibration. The objective is the identification the critical value of the Cockcroft-Latham criterion, Equation (4.3.23). Here, a ductile and a quasi-brittle aluminium HPDC alloy are investigated. The underlying experimental results in form of force-elongation curves were obtained from standard uniaxial tensile tests.

The force was measured by the testing machine and the elongation of the gauge section was measured by an extensometer. All details about the applied test set-up can be found in Chapter 8.1.1. A technical drawing of the specimen geometry can be found in Figure 4.3.1a. The thickness of the ductile specimen was 2.51 mm and the thickness of the quasi-brittle specimen was 2.29 mm. The force-elongation curves obtained from the ductile specimen and the quasi-brittle specimen are given in Figure 4.3.3b. The ductile specimen ruptured at an extensometer elongation of 4.25 mm and the quasi-brittle specimen ruptured at an extensometer elongation of 0.58 mm. Moreover, the critical value of the Cockcroft-Latham criterion was computed directly from the force-elongation curve as described in Chapter 8.1.2. From that, the experimentally measured value W_c^{exp} adopts a value of $0.035\,^{\mathrm{kN}}/_{\mathrm{mm}^2}$ for the ductile specimen and a value of $0.003\,^{\mathrm{kN}}/_{\mathrm{mm}^2}$ for the quasi-brittle specimen. It is noted that the force-elongation curve as well as all derived measurements such as the critical value W_c are results of the gauge section and, thus, belong to the gauge volume of the specimen.

The FE simulations were performed in LS-DYNA 971 [51]. The specimens were discretised with 8-node underintegrated solid elements. A stiffness based hourglass control was applied to avoid unphysical zero energy modes. Three uniform meshes were investigated with element edge lengths (mesh sizes) of $l_e = 1.00\,\mathrm{mm}$, $l_e = 0.50\,\mathrm{mm}$ and $l_e = 0.25\,\mathrm{mm}$. The pins were modelled as cylindrical rigid walls, while one was fixed and the other one moved constantly in longitudinal direction. The hypoelastic-plastic model given in Figure 4.1.4 was used to describe the material deformation behaviour. Young's modulus E was set to $72.00\,^{\mathrm{kN}}/_{\mathrm{mm}^2}$ and Poisson's ratio ν to 0.33. Exponent m in the yield criterion was set to 8. The Voce hardening parameters were found from curve fitting and a reverse engineering approach. The results are presented in Table 4.3.1. Furthermore, the value of the Cockcroft-Latham integral W was computed according to Equation (4.3.22).

The cross-section force in longitudinal direction as well as the elongation of the gauge section were taken from the FE simulations. Hence, it was guaranteed that numerical and experimental measurements were performed in the same fashion. Figure 4.3.4a shows the ductile results and Figure 4.3.4b shows the quasi-brittle results. It can be seen that a satisfying result regarding force-elongation behaviour is already achieved with a mesh

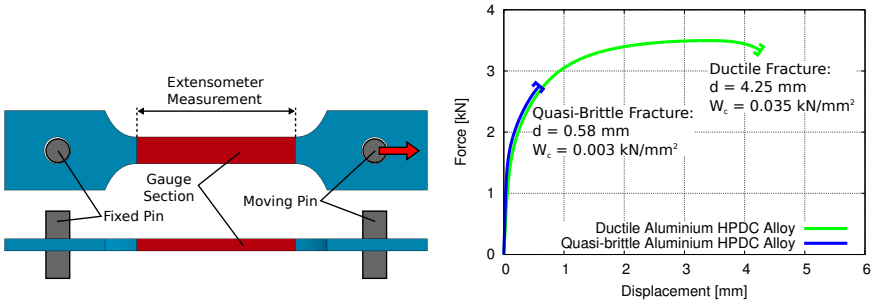

(a) Tensile test set-up. **(b)** Force-elongation curves.

Figure 4.3.3: Uniaxial tensile test: Tensile test set-up and experimental force-elongation curves obtained from the ductile and the quasi-brittle specimen.

Specimen	σ_0 [kN/mm²]	Q_1 [kN/mm²]	C_1 [−]	Q_2 [kN/mm²]	C_2 [−]
Ductile	0.12	0.10	91.03	0.11	0.03
Quasi-Brittle	0.14	0.09	125.76	2.05	1.05

Table 4.3.1: Voce hardening parameters found from curve fitting and a reverse engineering approach.

size of $l_e = 1.00\,\text{mm}$ for both specimens. No increase in accuracy can be observed using smaller mesh sizes.

Figure 4.3.5a shows the numerically predicted W distribution for all three meshes of the ductile specimen. Each W distribution is given at the moment when the elongation of the gauge section reaches the experimental rupture elongation. As expected, the W distribution localises in the middle of the specimen. Here, a slight neck develops and the gradient of the W distribution becomes steeper with decreasing mesh size. In the same manner, Figure 4.3.5b shows the numerically predicted W distribution for all three meshes of the quasi-brittle specimen. Here, the W distributions is uniform within the gauge section and no distinct changes can be observed between the three meshes.

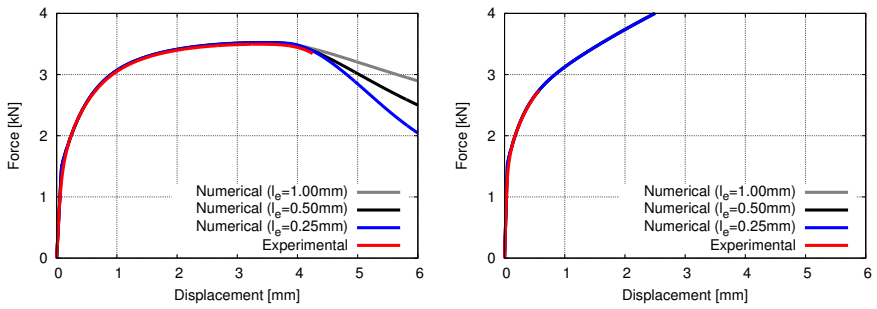

(a) Ductile specimen. **(b)** Quasi-brittle specimen.

Figure 4.3.4: Numerical and experimental force-elongation curves: Comparison of the three mesh sizes $l_e = 1.00\,\text{mm}$, $l_e = 0.50\,\text{mm}$ and $l_e = 0.25\,\text{mm}$.

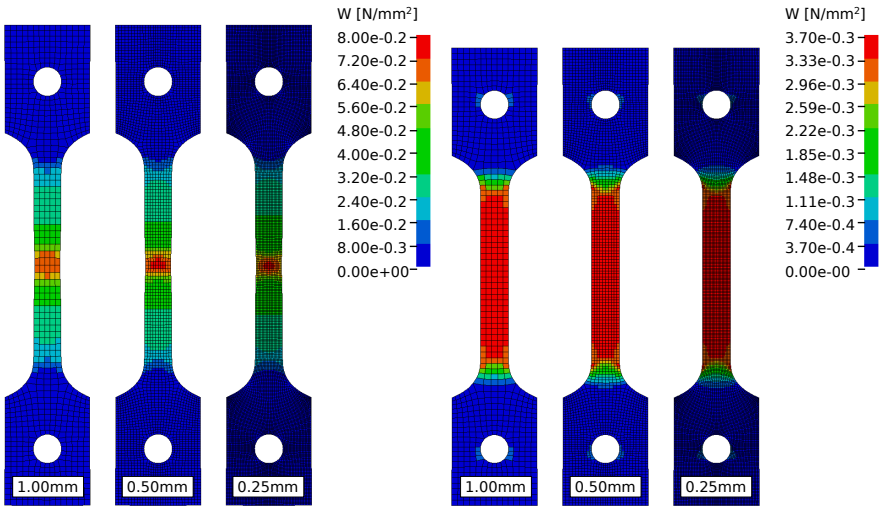

(a) Ductile specimen. **(b)** Quasi-brittle specimen.

Figure 4.3.5: W distributions at the moment when the elongation of the gauge section reaches the experimental rupture elongation: Comparison of the three mesh sizes $l_e = 1.00\,\text{mm}$, $l_e = 0.50\,\text{mm}$ and $l_e = 0.25\,\text{mm}$.

The maximum value found in the W distribution at fracture initiation was taken as critical value W_c. In addition, an averaged critical value $\overline{W}_c$ was computed from all values of the W distribution within the gauge section at fracture initiation. The results obtained from both specimens are presented in Figure 4.3.6. Each graph shows the computed values of W_c (red) and $\overline{W}_c$ (blue) related to mesh size l_e. The grey curve indicates a critical value W_c^{exp} computed directly from the experimental force-elongation curve according to Equation (8.1.13). The ductile results are plotted in Figure 4.3.6a. Due to the localisation in the neck, the computed values of W_c increases with decreasing mesh size l_e. However, it is seen that the difference in the computed values of W_c is also decreasing. Therefore, it is expected that mesh convergence in terms of computation of W_c can be reached by further mesh refinements. In contrast, the computed values of average $\overline{W}_c$ shows a mesh independent behaviour and corresponds to the experimentally computed value W_c^{exp}. However, a large gap is found between the computed values of W_c and the computed values of average $\overline{W}_c$. The quasi-brittle results are plotted in Figure 4.3.6b. Since fracture occurred within a uniform W distribution, mesh size l_e has only a minor influence on the computation of W_c. Consequently, the computation of average $\overline{W}_c$ is unaffected by mesh size l_e and is identical to the experimentally computed value W_c^{exp}. Hence, the computed values of W_c and the computed values of average $\overline{W}_c$ are almost identical.

The results can be summarised as follows:

– Ductile specimen: The computation of W_c showed a strong mesh dependence and, thus, a unique identification W_c became difficult. This means that the computed value of W_c was directly related to the element size l_e which was used for calibration. This size effect needs to be considered in numerical modelling of ductile failure. For instance, this mesh sensitivity can be reduced when the value of W_c is given as function of element size l_e. A more advanced approach, is known as nonlocal regularisation. Here, a field describing a mechanical quantity is modified by

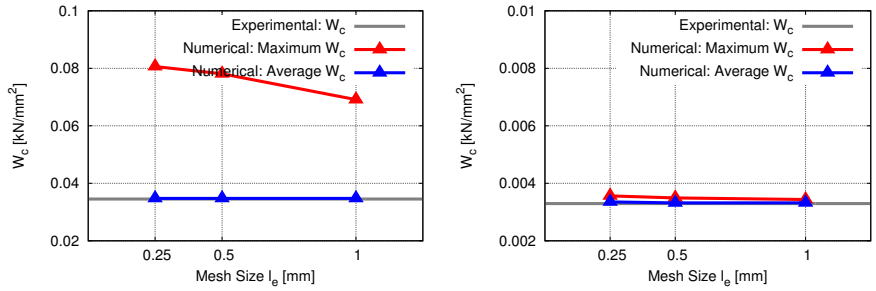

(a) Ductile specimen. **(b)** Quasi-brittle specimen.

Figure 4.3.6: Influence of mesh size l_e on critical value W_c and averaged critical value $\overline{W}_c$ in an experimental-numerical approach.

a chosen weight function when the field starts to localise. This function influences the field magnitude within a radius which surrounds the current element integration point. A detailed description can be found in the work by Pijaudier-Cabot and Bažant [95].

– Quasi-brittle specimen: The Cockcroft-Latham criterion could easily be calibrated for the quasi-brittle specimen. Since fracture occurred within a uniform W distribution, the computed values of W_c were nearly independent of mesh size l_e. It can be concluded that the value of W_c could be identified uniquely. Moreover, it was shown that the value of W_c can be directly computed according to Equation (8.1.13). This means that the experimentally computed value W_c^{exp} can be used as the value of W_c.

– In general: The numerical study showed that the computation of average $\overline{W}_c$ was almost independent of mesh size l_e. Even the localisation in the ductile specimen did not influenced the computation of average $\overline{W}_c$. It is noted that the value of average $\overline{W}_c$ was computed from all values of the W distribution within the gauge section. This implies that the value of average $\overline{W}_c$ is directly related to the gauge volume and may vary if the gauge volume varies. From a mechanical point of view, the computation of average $\overline{W}_c$ is equivalent to a homogenisation of the W distribution at fracture initiation. In other words, this corresponds to a uniform (homogenised) W distribution at fracture initiation with magnitude $\overline{W}_c$. As a result, it can be said "Failure occurs in the gauge section when a uniform distribution representing the average of the W distribution reaches the critical value $\overline{W}_c$". Furthermore, the numerical study showed that the computed values of average $\overline{W}_c$ are nearly identical to the experimentally computed value W_c^{exp}. This is reasonable since the computation of $W_c^{exp}$is based on measurements of the entire gauge section (cross-section force and gauge section elongation). These measurements can be seen as averaged measurements of the entire gauge section.

From a homogenisation point of view, the gauge volume as well as each element volume are MVEs of different sizes, see Chapter 4.3.3. Based on this, a failure criterion could be formulated as "Failure occurs in a MVE when the material loading reaches in average a critical value". According to Equation (3.3.30), the average of material loading given by the

Cockcroft-Latham integral, Equation (4.3.22), is determined by

$$E\left[W_{MVE}(\mathbf{x})\right] = \int_{V_{MVE}} \mathbf{x} \cdot W_{MVE}(\mathbf{x})\, d\, V_{MVE} \tag{4.3.24}$$

where $W_{MVE}(\mathbf{x})$ denotes the W distribution within a MVE of volume V_{MVE} and $\mathbf{x}$ is the spatial position vector. Consequently, the failure criterion can expressed in terms of the average of $W_{MVE}(\mathbf{x})$, so that

$$E\left[W_{MVE}(\mathbf{x})\right] = W_c\left(V_{MVE}\right) \tag{4.3.25}$$

where $W_c(V_{MVE})$ is the critical value related to volume V_{MVE}. If the average of $W_{MVE}(\mathbf{x})$ becomes nearly independent of volume V_{MVE} below a certain volume limit, the RVE and its volume is found and, thus, the critical value related to the RVE volume is found. This reflection should demonstrate that a material parameter such as critical failure value W_c depends on the volume under consideration and can be only applied for this volume.

4.4 Concluding Remarks

Failure models in form of failure criteria are formulated in a deterministic sense. Therefore, the application of a failure model requires that all model quantities are exactly known. For instance, the Cockcroft-Latham criterion given in Equation (4.3.23) requires that equivalent plastic strain $\bar{\varepsilon}$ as well as maximum principal stress σ_I are computed precisely and critical value W_c is exactly known. Quantities $\bar{\varepsilon}$ and σ_I are determined by an appropriate constitutive model which also demands exactly known material parameters. However, a material parameter such as critical value W_c is calibrated using results from an experimental study. Considering that the experimental study is performed under nearly identical conditions and the applied specimens are taken from the same material, the experimental study produces varying values of the measurements. By the nature of materials, it is very unlikely that each specimen consists of the same identical material structure. Consequently, each measurement obeys a pseudo-randomness, see Chapter 3.1, and is characterised by its scatter. The scatter is negligible when only the failure behaviour of a particular specimen is analysed. In engineering applications, however, a failure criterion needs to be suitable in a general manner. Then, the reliability of a deterministic failure criterion is directly related to the degree of scatter of the involved material parameters. When the scatter cannot be neglected, a probabilistic approach in failure modelling as described in the following chapter is necessary to guarantee a reliable design.

Chapter 5

Probabilistic Failure Modelling

In structural engineering, failure analyses are performed on structures and their elements to guarantee a reliable design. The prediction of failure (fracture initiation) is based on failure criteria as presented in Chapter 4.3.1. These criteria are mathematically formulated in a deterministic sense. It requires that all involved quantities are exactly known. This condition can only be met in theoretical examples. Since material constants are identified by experimental studies, a certain scatter in the measurements is a natural fact. As already discussed in Chapter 3.1, this fact is called pseudo-randomness. In the standard engineering approach, it is common to use averaged values for material quantities. In case of small variations, this approach is acceptable and a deterministic analysis provides useful results. However, if the variations cannot be neglected, the use of averaged values leads to vague and uncertain results. An obvious alternative is the usage of lower limit values. This approach might produce safe, but also too conservative results. Furthermore, these lower limit values are also not known exactly. In such a case, it is not the applied value itself that guarantees a reliable design, but the knowledge of the risk that failure occurs using this applied value. Therefore, a probabilistic approach is required in failure modelling. In contrast to a deterministic approach, the probabilistic approach takes the pseudo-random character of material quantities into account. Here, it is assumed that the quantities are given in form of probability distributions. The probabilistic approach enables a stochastic analysis of a failure criterion and a determination of the failure risk, also known as the probability of failure.

The present chapter deals with the probabilistic approach in failure modelling. Here, the focus is on the well known weakest-link approach. In the first part of the chapter, the theoretical basis of this approach is shown by the concept of a mechanical chain. Then, the results are transformed into the framework of continuum mechanics. Here, two analytical expressions are introduced to compute the probability of failure. The classical expression by Weibull [112] as well as a novel expression by Unosson et al. [108] are presented. Further, the calibration of probabilistic failure criteria as well as the influence of the test specimen and its gauge volume are briefly discussed. In the second part of the chapter, possibilities are shown for the application of the weakest-link approach in numerical FE analyses. Here, it is distinguished between two modelling strategies. The first strategy enables to compute directly the probability of failure of a FE simulation. The second strategy is based on randomly distributed failure parameters within a FE model. Finally, conclusions and recommendations for probabilistic failure modelling are given.

5.1 The Weakest-Link Approach

The weakest-link approach forms the theoretical basis for the most common probabilistic failure models in continuum mechanics. The fundamental assumptions and equations are obtained from the concept of a mechanical chain subjected to a tensile force. It is well-known that the chain fails at its weakest-link. Further, this approach includes that total failure of the chain occurs when the weakest-link fails. If more than one weakest-link is expected, total failure occurs when at least one of the weakest-links fails. The probability of the event "At least one weakest-link fails" is called the probability of failure and is determined by a geometric approach in probability theory. In the following, the weakest-link approach and the underlying probability model are introduced using this chain model. Afterwards, the obtained results are transformed into the framework of continuum mechanics. More details on probabilistic failure modelling can be found in the books by Gross and Seelig [47] and Lemaitre and Desmorat [75].

5.1.1 The Chain Concept

A chain of length l_Ω is considered and each link of the chain is considered as a continuous point x along chain length l_Ω. This model includes that size and shape of a link as well as connection properties between links are taken into account in form of homogenised parameters. Thus, the mechanical behaviour of the chain can be described by a simple tension bar model. It is assumed that the chain contains n weakest-links Q_i. Furthermore, it is assumed that the probability to find a weakest link Q_i is the same in every point x along chain length l_Ω. According to probability theory, this implies that a weakest-link Q_i is considered as a random variable which is uniformly distributed along chain length l_Ω and the distribution is given by the uniform PDF

$$g_{Q_i}(x_i) = \frac{1}{l_\Omega}. \tag{5.1.1}$$

It is assumed that the n weakest-links Q_i are considered as independent and identically distributed uniform random variables. This means that statistical independence of the n weakest-links Q_i is adopted. Hence, the joint density function of the n weakest-links Q_i becomes

$$g(x_1, x_2, \ldots, x_n) = g_{Q_1}(x_1) g_{Q_2}(x_2) \ldots g_{Q_n}(x_n) = \frac{1}{l_\Omega^n}, \tag{5.1.2}$$

see Equation (3.3.24). Now, the chain is subjected to a tensile force F and, consequently, the loading N of the chain is uniform along chain length l_Ω and equals the tensile force F.

A segment Λ of length l is taken from the chain provided that $l \leq l_\Omega$. The probability that segment Λ contains a weakest-link Q_i is denoted as $P(Q_i \in \Lambda)$ and is computed by

$$P(Q_i \in \Lambda) = \frac{l}{l_\Omega}. \tag{5.1.3}$$

The inverse probability that segment Λ does not contain a weakest-link Q_i is denoted as $P(Q_i \ni \Lambda)$ and is computed by

$$P(Q_i \ni \Lambda) = 1 - P(Q_i \in \Lambda) = 1 - \frac{l}{l_\Omega} = \frac{l_\Omega - l}{l_\Omega}. \tag{5.1.4}$$

Here, the probability calculations are based on simple geometrical considerations. Since a weakest-link Q_i is considered as a discrete point and is assumed to be uniformly distributed, the probability $P(Q_i \in \Lambda)$ does not depend on the extraction position of segment Λ and increases linearly with segment length l.

According to Equation (3.2.12), the conditional probability that two weakest-links Q_i and Q_j are found in segment Λ reads

$$P\left[(Q_i \in \Lambda) \cap \left(Q_j \in \Lambda\right)\right] = P(Q_i \in \Lambda) \cdot P\left(Q_j \in \Lambda \,|\, Q_i \in \Lambda\right). \tag{5.1.5}$$

Since the two weakest-links Q_i and Q_j are defined as statistically independent, the conditional probability becomes

$$P\left[(Q_i \in \Lambda) \cap \left(Q_j \in \Lambda\right)\right] = P(Q_i \in \Lambda) \cdot P\left(Q_j \in \Lambda\right) = \left(\frac{l}{l_\Omega}\right)^2. \tag{5.1.6}$$

From that, the probability that n weakest-links Q_i are found in segment Λ is determined by the product

$$P\left(\bigcap_{i=1}^{n} Q_i \in \Lambda\right) = \prod_{i=1}^{n} P(Q_i \in \Lambda) = \left(\frac{l}{l_\Omega}\right)^n. \tag{5.1.7}$$

Hence, the probability that none of the n weakest-links Q_i are found in segment Λ is given by

$$P_S^\Lambda = P\left(\bigcap_{i=1}^{n} Q_i \ni \Lambda\right) = \prod_{i=1}^{n} P(Q_i \ni \Lambda) = \left(1 - \frac{l}{l_\Omega}\right)^n. \tag{5.1.8}$$

It follows that the probability to find at least one weakest-link Q_i in segment Λ is computed by the inverse of probability P_S^Λ as

$$P_F^\Lambda = 1 - P_S^\Lambda = 1 - \left(1 - \frac{l}{l_\Omega}\right)^n. \tag{5.1.9}$$

Since a single weakest-link Q_i causes total failure of segment Λ, the probability P_F^Λ is called the failure probability of segment Λ and, accordingly, the probability P_S^Λ is called the survival probability of segment Λ. This means that the failure probability P_F^Λ is equivalent to the probability that at least one weakest-link Q_i becomes critical in segment Λ subjected to uniform loading N.

The amount of weakest-links per unit length is given by the relation

$$c = \frac{n}{l_\Omega} \tag{5.1.10}$$

which can be interpreted as weakest-link density. Using weakest-link density c, the survival probability in Equation (5.1.8) can be rewritten as

$$P_S^\Lambda = \left(1 - \frac{l}{l_\Omega}\right)^{c l_\Omega}. \tag{5.1.11}$$

Since chain length l_Ω is not finite, the survival probability is determined by the limit

$$P_S^\Lambda = \lim_{l_\Omega \to \infty} \left(1 - \frac{l}{l_\Omega}\right)^{c l_\Omega} = e^{-cl} \tag{5.1.12}$$

using the limit theorem that

$$\lim_{x \to \infty} \left(1 - \frac{1}{x}\right)^x = e^{-1}. \tag{5.1.13}$$

Consequently, the failure probability in Equation (5.1.9) can be rewritten as

$$P_F^\Lambda = 1 - e^{-cl}. \tag{5.1.14}$$

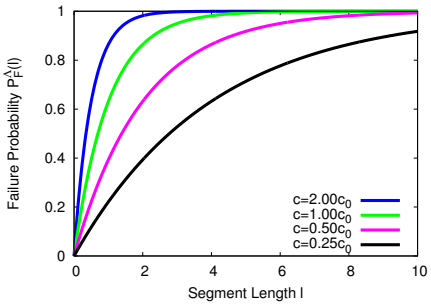

Figure 5.1.1: Failure probability $P_F^\Lambda = 1 - e^{-cl}$ plotted as function of segment length l for varying weakest-link densities c.

In Figure 5.1.1, the failure probability P_F^Λ given in Equation (5.1.14) is plotted as function of segment length l for varying weakest-link densities c. It is seen that the failure probability P_F^Λ increases with increasing segment length l. It can be concluded that the probability to find at least one weakest-link increases with the segment length under consideration. This is the fundamental statement of the weakest-link approach. Furthermore, it is seen that a higher weakest-link density c leads to a higher failure probability P_F^Λ at same segment length l.

The weakest-link density c is a function which also depends on the uniform loading N. It gives information about the amount of weakest-links Q_i which become critical at a certain uniform loading N. It is obvious that an increasing uniform loading N leads to an increasing number n of critical weakest-links Q_i and, consequently, to an increasing weakest-link density c. Hence, the failure probability P_F at a constant segment length l increases with increasing weakest-link density c.

5.1.2 Continuum Mechanical Approach

The weakest-link approach based on the presented chain model can be applied within the continuum mechanical framework. Here, a solid material subjected to uniform loading f is considered. The volume occupied by the material is denoted as V_Ω. It is assumed that the material contains internal defects or material imperfections which influence the material failure behaviour. These defects are expected to be invariant. This means that the defects do not grow or change during loading. Furthermore, it is supposed that the defects do not interact, so that these can be considered independently of each other. A defect is denoted as D_i and the total number of defects is n. The material failure behaviour is described by the chain concept: Total failure of the material takes place when a single defect D_i becomes critical at uniform loading f. According to the continuum mechanical approach, each internal defect D_i is introduced as a homogenised and isotropic material constant. This implies that size, shape and orientation as well as physical properties of a defect D_i are summarised in a scalar value which is applied in each material point in material volume V_Ω, see Chapter 4.3.3. It follows that each defect D_i is characterised by its critical value $f_{c,i}$. Therefore, failure occurs in material volume V_Ω when uniform loading f reaches the smallest critical value $f_{c,i}$ found in material volume V_Ω. Accordingly, the failure criterion can be written as

$$f = \min\left[f_{c,i}\right]. \tag{5.1.15}$$

It implies that the defect D_i with the smallest critical value $f_{c,i}$ becomes the critical defect in material volume V_Ω which leads to failure. In case the uniform loading f reaches the

highest critical value $f_{c,i}$, so that $f = \max[f_{c,i}]$, all n defects D_i in material volume V_Ω become critical. From that follows, the number of defects D_i which become critical in material volume V_Ω subjected to uniform loading f is given by the condition

$$\{n_c(f) \mid f_{c,i} \leq f\}. \tag{5.1.16}$$

Here, the number $n_c(f)$ consists of the number of defects D_i which already became critical at lower uniform loading f $(f_{c,i} < f)$ and the number of defects D_i which become critical at uniform loading f $(f_{c,i} = f)$.

Now, it is assumed that all n defects D_i are randomly distributed within material volume V_Ω. For simplicity, each defect D_i is idealised as a random discrete point within material volume V_Ω. Moreover, it is assumed that each defect D_i can be described by a uniformly distributed random variable. As a result, the PDF of a defect D_i is defined by material volume V_Ω and reads

$$g_{D_i}(\mathbf{X}) = \frac{1}{V_\Omega} \tag{5.1.17}$$

where $\mathbf{X}$ denotes the material position vector. Since the n defects D_i are supposed to be independent of each other, the n defects D_i can be considered as independent and identically distributed uniform random variables. It is concluded that each defect D_i is mechanically characterised by its homogenised critical value $f_{c,i}$ and statistically as a random discrete point which is uniformly distributed within material volume V_Ω.

A volume V is taken from material volume V_Ω provided that $V \leq V_\Omega$. The probability that failure occurs in volume V subjected to uniform loading f is equivalent to the probability of finding at least one defect D_i which becomes critical at uniform loading f in volume V. According to Equation (5.1.9), the failure probability of volume V is determined by

$$P_F^V = 1 - \left(1 - \frac{V}{V_\Omega}\right)^{n_c(f)}. \tag{5.1.18}$$

The (specific) density function $c(f)$ is defined as

$$c(f) = \frac{n_c(f)}{V_\Omega}. \tag{5.1.19}$$

This function is defined as a positive and non-decreasing function which vanishes when the material is unloaded, see Weibull [112]. Using this general expression of density function $c(f)$ and the limit theorem in Equation (5.1.13), the failure probability of volume V is found by the limit operation

$$P_F^V = \lim_{V_\Omega \to \infty} \left[1 - \left(1 - \frac{V}{V_\Omega}\right)^{c(f)V_\Omega}\right] = 1 - e^{-c(f)V}. \tag{5.1.20}$$

Accordingly, the survival probability of volume V becomes

$$P_S^V = 1 - P_F = e^{-c(f)V}. \tag{5.1.21}$$

In summary, Equation (5.1.20) and Equation (5.1.21), respectively, provide the possibility to determine the failure probability P_F^V and the survival probability P_S^V, respectively, of an arbitrary volume V subjected to an arbitrary uniform loading f.

In Figure 5.1.2, the failure probability P_F^V given in Equation (5.1.20) is plotted as function of volume V with a constant value of density function $c(f)$. It is seen that the failure probability P_F^V increases with increasing volume V. This effect is called the size effect and

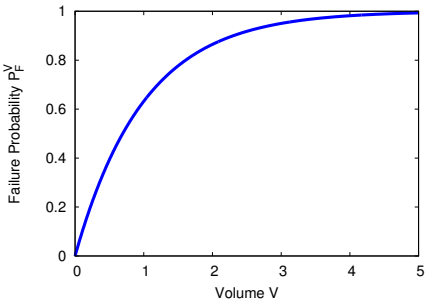

Figure 5.1.2: Failure probability $P_F^V = 1 - e^{-c(f)V}$ plotted as function of material volume V with a constant value of density function $c(f)$.

it means that the probability to find at least one critical defect increases with the volume under consideration. The above presented equations form the basis for probabilistic failure models which follow the requirements of the weakest-link approach.

In general, a probabilistic failure model based on the weakest-link approach requires a constant failure criterion and a definition of density function $c(f)$. Here, a constant criterion means that the critical value is constant and does not depend on the loading conditions. The equivalent stress criterion, Equation (4.3.6), the equivalent plastic strain criterion, Equation (4.3.12), or the Cockcroft-Latham criterion, Equation (4.3.23), are typical examples of such criteria. However, it is necessary to ensure that loading f is uniformly distributed within volume V. Besides the failure criterion, the density function $c(f)$ needs to be defined. It gives information about the number of defects D_i which become critical at uniform loading f. The form of the density function $c(f)$ depends on the applied material and can be interpreted as a material property. It is almost impossible to estimate the density function $c(f)$ from experimental observations and, thus, it is often expressed as a empirical function. If failure is described by a failure locus criterion where the critical value is not constant and depends on the loading conditions, the density function $c(f)$ has to be identified separately for each loading condition. For instance, when failure is described by the Johnson and Cook criterion given in Equation (4.3.15), the density function $c(f)$ changes with stress triaxiality σ^*. Since the weakest-link approach assumes invariant material defects D_i, only those failure criteria are suitable which describe brittle or quasi-brittle fracture initiation, see Chapter 4.2.1. Furthermore, it is remarked that the failure probability P_F^V in Equation (5.1.20) predicts the probability that a first fracture initiates in volume V subjected to uniform loading f. Probabilistic statements on the material behaviour beyond fracture initiation, such as the crack propagation, are not considered within the weakest-link approach.

A constant failure criterion in form of

$$f = f_c \tag{5.1.22}$$

is randomised by introducing the critical value f_c as a continuous random variable F_c with CDF $G(f_c)$. Assuming the weakest-link approach, the CDF $G(f_c)$ is found by Equation (5.1.20), so that

$$P_F^V = P(F_c \leq f_c) = G(f_c) = 1 - e^{-c(f_c)V}. \tag{5.1.23}$$

This means that the failure probability P_F^V of volume V subjected to uniform loading $f = f_c$ is equivalent to the probability that the random variable F_c is smaller than or equal to a critical value f_c found in volume V. Further, the risk of failure can be assigned to

the criterion when a certain critical value f_c is applied. Based on Equation (3.3.9), the corresponding PDF $g(f_c)$ is determined by the derivative

$$g(f_c) = \frac{\partial G(f_c)}{\partial f_c} = \frac{\partial c(f_c)}{\partial f_c} V e^{-c(f_c)V} \quad \text{with} \quad f_c \geq 0. \tag{5.1.24}$$

It should be noted that the CDF is usually denoted by F and the PDF by f, respectively. Here, G and g, respectively, are used for a clear presentation. However, the PDF $g(f_c)$ is important when stochastic simulations are performed on the failure criterion $f = f_c$. For instance, a Monte-Carlo simulation, see Chapter 3.3.9, performed on the criterion requires an expression for $g(f_c)$.

5.1.3 Probability Calculations

Equation (5.1.20) as well as Equation (5.1.21) enable to determine the failure probability P_F^V as well as the survival probability P_S^V of volume V subjected to uniform loading f. These equations are based on the assumption that the defects are considered as independent and identically distributed uniform random variables. In the following it is shown in which way the failure probability P_F^V and the survival probability P_S^V are determined when loading f is not uniformly distributed.

Volume V is theoretically subdivided into k non-overlapping volume elements $\triangle V_i$, so that

$$V = \sum_{i=1}^{k} \triangle V_i. \tag{5.1.25}$$

The assumption of statistical independence of the defects within volume V implies that the defects are also independent and identically distributed in each volume element $\triangle V_i$ as well as between the k volume elements $\triangle V_i$. In other words, the k volume elements $\triangle V_i$ are statistically independent. When the loading in each volume element $\triangle V_i$ equals uniform loading f, the probability that no failure occurs in each volume element $\triangle V_i$ can be expressed by the product of the k survival probabilities $P_S^{\triangle V_i}$ as

$$\begin{aligned} P_S^{\sum_{i=1}^{k} \triangle V_i} &= \prod_{i=1}^{k} P_S^{\triangle V_i} \\ &= \prod_{i=1}^{k} \exp\left(-c(f) \triangle V_i\right) \\ &= \exp\left(-\sum_{i=1}^{k} c(f) \triangle V_i\right). \end{aligned} \tag{5.1.26}$$

Consequently, the probability that at least one defect becomes critical in at least one volume element $\triangle V_i$ can be written as

$$\begin{aligned} P_F^{\sum_{i=1}^{k} \triangle V_i} &= 1 - P_S^{\sum_{i=1}^{k} \triangle V_i} \\ &= 1 - \exp\left(-\sum_{i=1}^{k} c(f) \triangle V_i\right). \end{aligned} \tag{5.1.27}$$

Using Equation (5.1.25), it becomes clear that the survival probability and the failure probability, respectively, of the discretised volume V are identical to the survival probability

and the failure probability, respectively, of the continuous volume V,

$$\begin{aligned} P_S^{\sum_{i=1}^{k} \triangle V_i} &= \exp\left(-\sum_{i=1}^{k} c\left(f\right) \triangle V_i\right) \\ &= \exp\left(-c\left(f\right) V\right) = P_S^V \end{aligned} \tag{5.1.28}$$

$$\begin{aligned} P_F^{\sum_{i=1}^{k} \triangle V_i} &= 1 - \exp\left(-\sum_{i=1}^{k} c\left(f\right) \triangle V_i\right) \\ &= 1 - \exp\left(-c\left(f\right) V\right) = P_F^V . \end{aligned} \tag{5.1.29}$$

In summary, the survival probability P_S^V of volume V subjected to uniform loading f can be reproduced by the product of all survival probabilities obtained from any smaller volume element $\triangle V_i$ of volume V within the weakest-link approach. This property of the weakest-link approach is important when structural problems are numerically analysed in terms of failure probabilities.

The objective is the prediction of the failure probability of an engineering structure subjected to a non-uniform loading. For this purpose, volume V is subdivided into k volume elements $\triangle V_i$ according to Equation (5.1.25) and it is assumed that loading f in volume V can be expressed by k uniform loadings f_i in each volume element $\triangle V_i$. Hence, loading f can be expressed as

$$f = \begin{cases} f_1 & \text{in } \triangle V_1 \\ f_2 & \text{in } \triangle V_2 \\ \vdots & \vdots \\ f_k & \text{in } \triangle V_k \end{cases} . \tag{5.1.30}$$

According to Equation (5.1.27), the failure probability of volume V becomes

$$P_F^V = 1 - \exp\left(-\sum_{i=1}^{k} c\left(f_i\right) \triangle V_i\right) . \tag{5.1.31}$$

In case the k volume elements $\triangle V_i$ are of same size $\triangle V$, the failure probability of volume V becomes

$$P_F^V = 1 - \exp\left(-\sum_{i=1}^{k} c\left(f_i\right) \triangle V\right) . \tag{5.1.32}$$

Performing a limit process on this equation yields to the expression

$$P_F^V = 1 - \exp\left(-\int_V c\left(f(\mathbf{x})\right) dV\right) \tag{5.1.33}$$

where the function $f(\mathbf{x})$ denotes the loading distribution in volume V. This expression enables to determine the failure probability P_F^V of an arbitrary volume V subjected to an arbitrary loading distribution $f(\mathbf{x})$.

Furthermore, Equation (5.1.31) and Equation (5.1.33), respectively, can be applied to determine the failure probability P_F^V of a volume V which consists of m various materials. Here, volume V is separated into m partial volumes V^j, so that

$$V = \sum_{j=1}^{m} V^j . \tag{5.1.34}$$

Each partial volume V^j is characterised by its density function $c^j(f)$. Now, the failure probability P_F^V can be computed either in discrete form according to Equation (5.1.31) or in integral form according to Equation (5.1.33). The failure probability reads in discrete form

$$P_F^V = 1 - \exp\left(- \left[\sum_{i=1}^{k} c^1(f_i) \triangle V_i^1 + \ldots + \sum_{i=1}^{k} c^m(f_i) \triangle V_i^m \right] \right) \tag{5.1.35}$$

or in integral form

$$P_F^V = 1 - \exp\left(- \left[\int_{V^1} c^1(f(\mathbf{x}))\, dV^1 + \ldots + \int_{V^m} c^m(f(\mathbf{x}))\, dV^m \right] \right). \tag{5.1.36}$$

Both equations can be used to predict the failure probability of any engineering structure. It is important to notice that the equations are based on the weakest-link approach. This means that total structural failure only requires one material defect that becomes critical. Furthermore, the assumption of statistical independence of the material defects within the entire structure is very critical. It might be more reasonable to assume statistical independence within a defined volume element, but the volume elements could be statistically correlated.

5.1.4 The Weibull Approach

The best-known empirical expression for the density function $c(f)$ given in Equation (5.1.19) was introduced by W. Weibull in 1951 [112]. The Weibull density function is defined as

$$c(f) = \frac{1}{V_0} \left(\frac{f}{f_0} \right)^m \quad \text{with} \quad f \geq 0 \tag{5.1.37}$$

where V_0 is the scaling volume, f_0 is a parameter that normalises the uniform loading f with respect to scaling volume V_0 and exponent m is called the Weibull modulus. In the literature, the density function is often expressed as

$$c(f) = \frac{1}{V_0} \left(\frac{f - f_u}{f_0} \right)^m \quad \text{with} \quad f - f_u \geq 0 \tag{5.1.38}$$

where f_u is a threshold value of uniform loading f related to scaling volume V_0. However, the first definition is used in the following. Insertion of Equation (5.1.37) into Equation (5.1.20) yields to the failure probability by Weibull,

$$P_F^V = 1 - \exp\left(- \frac{V}{V_0} \left(\frac{f}{f_0} \right)^m \right) \quad \text{with} \quad f \geq 0 \ . \tag{5.1.39}$$

The failure probability by Weibull is plotted as a function of uniform loading f in Figure 5.1.3. The first graph shows failure probability functions for a constant volume relation $\frac{V}{V_0}$ and varying values of Weibull modulus m, see Figure 5.1.3a. It is seen that the variability decreases with increasing Weibull modulus m. Hence, Weibull modulus m is a measurement of the scattering behaviour of the considered material. The second graph shows failure probability functions for a constant value of Weibull modulus m and varying volume relations $\frac{V}{V_0}$, see Figure 5.1.3b. It is seen that the failure probability increases with increasing volume relation $\frac{V}{V_0}$. The parameters V_0, f_0 and m can be found from experimental studies.

A modification of the failure probability by Weibull, Equation (5.1.39), is introduced by Zhang et al. [119]. Here, the failure probability is given by

$$P_F^V = 1 - \exp\left(- \left(\frac{V}{V_0} \right)^{\lambda} \left(\frac{f}{f_0} \right)^m \right) \quad \text{with} \quad f \geq 0 \tag{5.1.40}$$

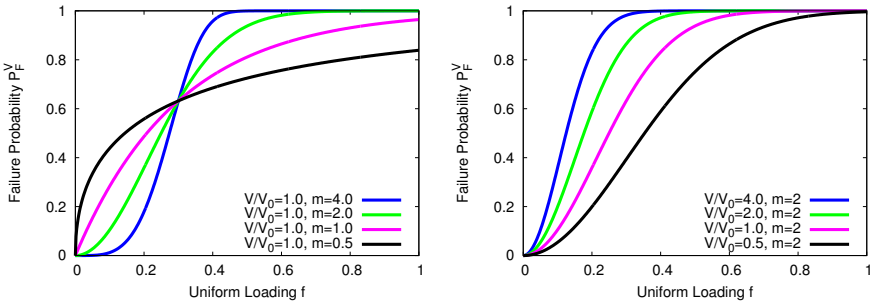

(a) Varying Weibull modulus m. **(b)** Varying volume relation $\frac{V}{V_0}$.

Figure 5.1.3: Failure probability by Weibull plotted as function of uniform loading f for either varying Weibull modulus m or varying volume relation $\frac{V}{V_0}$.

where exponent λ is defined between 0 and 1. This exponent controls the volume dependency. A value of $\lambda = 1$ restores the original Weibull failure probability. A value of $\lambda = 0$ neglects any volume dependency. If exponent λ takes a value between 0 and 1, the volume dependency is lowered. In the work by Zhang et al. [119], exponent λ is described as a parameter which takes geometrical variations into account. However, this parameter is purely empirical and a physical meaning in terms of a probabilistic failure model is not pointed out. Furthermore, the physical problem of this approach can easily be shown by computing the failure probability of a discretised volume.

Equation (5.1.40) returns the failure probability P_F^V of the continuous volume V subjected to uniform loading f. Now, the volume V is discretised in the manner $V = \sum_{i=1}^{k} \triangle V_i$ and, consequently, each volume element $\triangle V_i$ is subjected to uniform loading f. According to Equation (5.1.29), the failure probability of the discretised volume V is computed by

$$P_F^{\sum_{i=1}^{k} \triangle V_i} = 1 - \exp\left(-\sum_{i=1}^{k} \left(\frac{\triangle V_i}{V_0} \right)^{\lambda} \left(\frac{f}{f_0} \right)^{m} \right). \tag{5.1.41}$$

The use of exponent λ which is defined between 0 and 1 leads to the inequality

$$\left(\sum_{i=1}^{k} \triangle V_i \right)^{\lambda} \leq \sum_{i=1}^{k} \left(\triangle V_i \right)^{\lambda}. \tag{5.1.42}$$

Based on this inequality, the comparison of the failure probability of the continuous volume V with the failure probability of the discretised volume V yields to the inequality

$$P_F^V \leq P_F^{\sum_{i=1}^{k} \triangle V_i}. \tag{5.1.43}$$

This means that the failure probability of the discretised volume V is higher or equal to the failure probability of the continuous volume V at same uniform loading f. Therefore, the approach presented by Zhang et al. [119] is not valid in terms of the weakest-link approach.

5.1.5 An Alternative Approach

The weakest-link approach says: The material defect which lowers the material strength most within a considered volume becomes the critical defect that leads to failure. Usually,

this material defect is the largest defect found within the considered volume. Based on this assumption, a novel approach to express the density function $c\left(f\right)$ given in Equation (5.1.19) is presented in the work by Unosson et al. [108]. Here, a material defect density per unit volume is introduced and is defined as

$$g\left(s\right)=\frac{dn}{ds} \quad \text{with} \quad a\leq s\leq b \tag{5.1.44}$$

where s is the defect magnitude and n is the average number of defects per unit volume. The defect magnitude s ranges between the limits a and b. It follows that the total number of defects per unit volume is given by

$$n_{tot}=\int_a^b g\left(s\right)ds. \tag{5.1.45}$$

From that, the integral

$$n=\int_s^b g\left(s\right)ds \quad \text{with} \quad a\leq s\leq b \tag{5.1.46}$$

provides the number of defects with a magnitude larger than an arbitrary magnitude s. This enables to express the mandatory number of defects by

$$n\left(s\right)=\begin{cases}\infty & s\leq 0\\ \int_a^b g\left(s\right)ds & 0<s\leq a\\ \int_s^b g\left(s\right)ds & a<s\leq b\\ 0 & b<s\end{cases}. \tag{5.1.47}$$

Here, it is seen that the number of defects with a magnitude s equal or smaller than a theoretical zero magnitude goes to infinity. This general expression is substituted into Equation (5.1.20) and the probability to find at least one defect with a magnitude larger than an arbitrary magnitude s in volume V subjected to uniform loading f becomes

$$P_F^V=\begin{cases}1 & s\leq 0\\ 1-\exp\left(-\int_a^b g\left(s\right)ds\,V\right) & 0<s\leq a\\ 1-\exp\left(-\int_s^b g\left(s\right)ds\,V\right) & a<s\leq b\\ 0 & b<s\end{cases}. \tag{5.1.48}$$

This expression forms the basis to determine the failure probability according to the approach by Unosson et al. [108].

Material failure is described in terms of damage evolution by Unosson et al. [108], so that

$$D^m=D_0^m+\frac{f}{f_{c0}} \quad \text{with} \quad 0\leq D_0^m\leq 1 \tag{5.1.49}$$

where D^m is the current material damage, D_0^m is the constant initial damage and f_{c0} is a failure parameter which belongs to an undamaged material. The material fails when damage D^m reaches unity. Consequently, failure occurs when

$$1-\frac{f}{f_{c0}}=D_0^m. \tag{5.1.50}$$

In the work by Unosson et al. [108], it is assumed that the maximum defect size s is in a one-to-one correspondence with the initial material damage D_0^m, so that

$$s\equiv D_0^m=1-\frac{f}{f_{c0}}. \tag{5.1.51}$$

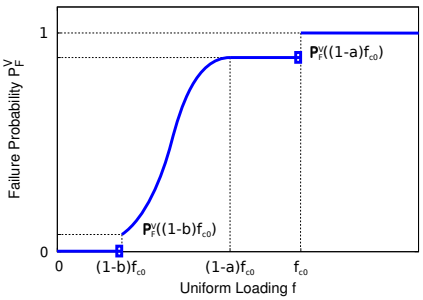

Figure 5.1.4: Failure probability according to the approach by Unosson et al. [108] plotted as function of loading f.

Using the integral transformation

$$\int_a^b g(s)\,ds = \frac{1}{f_{c0}} \int_{(1-b)f_{c0}}^{(1-a)f_{c0}} g\left(1-\frac{f}{f_{c0}}\right) df, \tag{5.1.52}$$

the density function $c(f)$ given in Equation (5.1.19) can be expressed as

$$c(f) = \begin{cases} 0 & f < (1-b)f_{c0} \\ \frac{1}{f_{c0}} \int_{(1-b)f_{c0}}^{f} g\left(1-\frac{f}{f_{c0}}\right) df & (1-b)f_{c0} \le f < (1-a)f_{c0} \\ \frac{1}{f_{c0}} \int_{(1-b)f_{c0}}^{(1-a)f_{c0}} g\left(1-\frac{f}{f_{c0}}\right) df & (1-a)f_{c0} \le f < f_{c0} \\ \infty & f_{c0} \le f \end{cases}. \tag{5.1.53}$$

Insertion of this density function $c(f)$ into Equation (5.1.20) yields to the failure probability according to the approach by Unosson et al. [108],

$$P_F^V = \begin{cases} 0 & f < (1-b)f_{c0} \\ 1-\exp\left(-\frac{V}{f_{c0}} \int_{(1-b)f_{c0}}^{f} g\left(1-\frac{f}{f_{c0}}\right) df\right) & (1-b)f_{c0} \le f < (1-a)f_{c0} \\ 1-\exp\left(-\frac{V}{f_{c0}} \int_{(1-b)f_{c0}}^{(1-a)f_{c0}} g\left(1-\frac{f}{f_{c0}}\right) df\right) & (1-a)f_{c0} \le f < f_{c0} \\ 1 & f_{c0} \le f \end{cases}. \tag{5.1.54}$$

The model parameters a, b and f_{c0} can be found from experimental studies. However, an expression for the defect density function $g(s)$ needs to be defined first. A graphical representation of the probability model by Unosson et al. [108] is presented in Figure 5.1.4. It clearly shows the functional distinction within the loading range.

The material defect density $g(s)$ can be formulated in many ways as long as it is guaranteed that the function is positive within the limits a and b. Usually, a material structure contains many small defects and a only few large defects and, thus, a decreasing function is reasonable. In the work by Unosson et al. [109], a constant, linear and exponential formulation are analysed. The best result is found by the exponential formulation

$$g(s) = c_0 e^{-c_1 s} \quad \text{with} \quad a \le s \le b \tag{5.1.55}$$

where c_0 and c_1 are shape parameters. The exponential coefficient c_1 characterises the distribution of small and large defects. Coefficient c_0 marks the number of defects of zero size. Usually, coefficient c_0 adopts very high values which are much larger than the values found for coefficient c_1, see Unosson et al. [108, 109]. This strong difference in the

value dimensions may lead to numerical problems in the parameter identification. In both works by Unosson et al. [108, 109], the model parameters are calibrated using results from mechanical tests. An obvious alternative could be a calibration using mechanical test results combined with results obtained from a microscopic analysis. A microscopic analysis of the material structure and its defects provides the possibility to estimate directly the material defect density $g(s)$ and the limits a and b. The failure parameter f_{c0} can be found from the mechanical test results. In summary, Unosson et al. [108, 109] presented an approach which combines the weakest-link approach with considerations of the microscopic structure.

5.1.6 Calibration and the Influence of the Gauge Volume

The statistical model given by the weakest-link approach is calibrated in the same way as a statistical distribution function is estimated from a sample. In the weakest-link approach, a sample is drawn from a considered material in form of multiple repeated material tests which provide measurements of the critical failure value f_c. Here, it is required that each material test is repeated under same or nearly same conditions. This implies that each material test is performed using the same test set-up, the same measurement technique and the same specimen geometry and the specimens are taken from material of the same charge. It is assumed that only the material structure varies within a specimen and between each specimen. Finally, a sample consists of the multiple measurements of the critical failure value f_c. According to the weakest-link approach, it is noted that this sample is related not only to the test set-up, but also to the specimen and its gauge volume.

It is considered that a sample consists of the n data values f_c^i which are sorted in an ascending order. The n corresponding experimental probabilities $\overline{F}_i$ are determined according to Equation (3.5.12). From that, the n pairs $\left(f_c^i, \overline{F}_i\right)$ are an estimate of the CDF of the weakest-link approach given in Equation (5.1.23). The weakest-link CDF reads

$$G\left(f_c\right) = 1 - e^{-c\left(f_c\right)V}. \tag{5.1.56}$$

The weakest-link CDF and its density function $c\left(f_c\right)$ are found using the n pairs $\left(f_c^i, \overline{F}_i\right)$. Here, the volume V equals the gauge volume of the applied specimen geometry. In case density function $c\left(f_c\right)$ is formulated according to the Weibull approach, see Equation (5.1.37), the weakest-link CDF becomes

$$G_W\left(f_c\right) = 1 - \exp\left(-\frac{V}{V_0}\left(\frac{f_c}{f_{c0}}\right)^m\right). \tag{5.1.57}$$

Usually, scale volume V_0 is set to the gauge volume of the applied specimen geometry. Hence, only Weibull modulus m and scale failure value f_{c0} needs to be identified. The n pairs $\left(f_c^i, \overline{F}_i\right)$ can be expressed in a Weibull plot as described in Chapter 3.5.2. Then, a linear curve fit provides estimates of shape parameters m and λ using the linear transformation of the Weibull distribution, see Equation (3.3.64). The relation between shape parameter λ and scale failure value f_{c0} is given comparing Equation (3.3.61) and Equation (5.1.57) and reads

$$\lambda = \sqrt[m]{\frac{V_0}{V}} f_{c0}. \tag{5.1.58}$$

The shape parameters m and λ are found from a linear curve fit based on the least-squares method, see Chapter 3.5.2. The quality of the linear fit can be measured by the coefficient of determination given in Equation (3.5.19). From a statistical point of view, it is important to check statistically if the sample data are drawn from the calibrated weakest-link

distribution. Here, statistical hypothesis tests in form of a GoF tests can be used, see 3.6.5. In case a calibrated Weibull distribution is analysed through a GoF test, the Anderson-Darling for Weibull distributions can be applied.

In the calibration procedure described above, it is considered that the sample is generated from a single specimen geometry. However, it is of interest to verify the size effect mentioned in the weakest-link approach: The probability to find at least one critical defect increases with the volume under consideration, see Chapter 5.1.2. Hence, it is recommended to generate further samples generated from specimens of different size and different gauge volumes, respectively. It is noted that the specimens have to be equal in shape, but different in size. This guarantees that the material in each specimen fails under the same loading conditions provided that the same test set-up is applied. The comparison of the different samples enables to verify the size effect. Here, a possibility is to analyse separately the samples according to the procedure described above and to compare the results of the calibrated weakest-link distributions. In general, if the considered material complies with the weakest-link approach, the CDF estimated from a sample generated from a large gauge volume is larger than the CDF estimated from a sample generated from a small gauge volume. In case Weibull distributions are calibrated using samples generated from specimens of different gauge volumes, a comparison of the results can be as follows:

- If the samples are generated from the same material, the calibrated Weibull moduli m are equal or nearly equal, but the estimated failure scale values f_{c0} might be different depending on the gauge volumes.
- If the samples are generated from the same material and the material complies with the weakest-link approach, the failure scale value f_{c0} of the small gauge volume is larger than the failure scale value f_{c0} of the large gauge volume.

These statements can easily be verified using a Weibull plot as seen in Figure 5.1.5. Here, Weibull plots for three different cases are shown. Each case shows a red curve representing a Weibull curve obtained from a small gauge volume and a blue curve representing a Weibull curve obtained from a large gauge volume. In the first case given in Figure 5.1.5a both curves are equal in slope and the blue curve is to the left of the red one. Consequently, it can be assumed that both curves are calibrated from samples of the same material which complies the weakest-link approach. In the second case given in Figure 5.1.5b both curves are equal in slope, but the blue curve is to right of the red one. This means that both curves might be calibrated from samples of the same material, but the underlying material does not comply the weakest-link approach. Alternatively, it can be assumed that the curves are calibrated from samples of two different materials. In the third case given in Figure 5.1.5c the curves are clearly calibrated from samples of two different materials. It is noted that the fitted parameters of different Weibull distribution can be also compared through statistical tolerance intervals, see Chapter 3.6.2. For instance, this can be used to prove if the Weibull modulus obtained from a large gauge volume lies within the tolerance interval of the Weibull modulus obtained from a small gauge volume. Furthermore, samples of different gauge volumes can be analysed for interferential statistics, see Chapter 3.6. Here, statistical hypothesis tests are used to prove if these samples belong to the same population. If the material complies with the weakest-link approach, the hypothesis tests should lead to the assumption that these samples are drawn from different populations. Alternatively, if the hypothesis leads to the result that the samples are drawn from the same population, it can be assumed that the considered material does not comply with the weakest-link approach.

In case the graphical comparison of samples generated from specimens of different sizes shows that the underlying material complies with the weakest-link approach, the

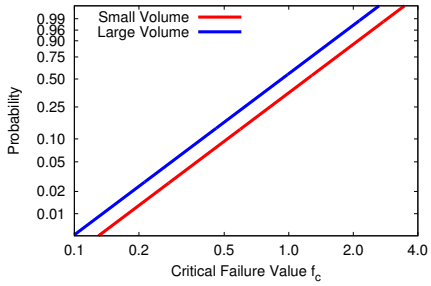

(a) Both curves are obtained from samples of the same material which complies with the weakest-link approach.

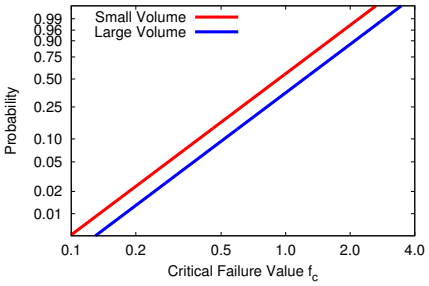

(b) The curves might be obtained from samples of the same material, but the underlying material does not comply with the weakest-link approach.

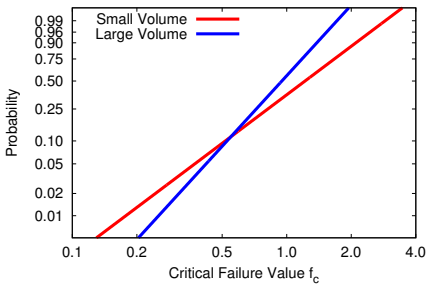

(c) The curves are obtained from samples of two different materials.

Figure 5.1.5: Weibull plots including a Weibull curve obtained from a small gauge volume (red) and a Weibull curve obtained from a large gauge volume (blue).

weakest-link CDF and its density function $c\left(f_c\right)$ can be calibrated using all samples. For simplicity, it is assumed that the CDF can be described by the Weibull CDF given in Equation (5.1.57). It is considered that k samples are generated from a material which complies the weakest-link approach are generated. Each sample is defined by the n_j pairs $\left(f_c^{i,j}, \overline{F}_{i,j}\right)$ and the gauge volume V_j. According to the least-square method, the sum of residuals, see Equation (3.5.18), becomes

$$r\left(m, f_{c0}, V_0\right) = \sum_{j=1}^{k} \sum_{i=1}^{n_j} \left(\overline{F}_{i,j} - \left(1 - \exp\left(-\frac{V_j}{V_0} \left(\frac{f_c^{i,j}}{f_{c0}} \right)^m \right) \right) \right)^2 . \tag{5.1.59}$$

The best fit of the parameters m, f_{c0} and V_0 is found when this function reaches a minimum. In the present work, the Nelder-Mead method implemented in MATLAB [83] was used to find the minimum. It is noted that the function can be also expressed as

$$r(m,\kappa) = \sum_{j=1}^{k} \sum_{i=1}^{n_j} \left(\overline{F}_{i,j} - \left(1 - \exp\left(-\frac{V_j}{\kappa} \left(f_c^{i,j} \right)^m \right) \right) \right)^2 \tag{5.1.60}$$

with

$$\kappa = V_0 \left(f_{c0}\right)^m . \tag{5.1.61}$$

Consequently only parameters m and κ need to be fitted. Failure scale value f_{c0} is found by the relation

$$f_{c0} = \sqrt[m]{\frac{V_0}{\kappa}} \tag{5.1.62}$$

where scale volume V_0 can be arbitrarily chosen. In case the weakest-link CDF given by Equation (5.1.56) is successfully calibrated for a material (for one or various gauge volumes), the CDF can be applied for any arbitrary volume V. In contrast, if the same material is described by a volume independent CDF such as the normal CDF, the CDF needs to be calibrated separately for each volume. This means that the volume independent CDF is calibrated separately for each sample and the gauge volume of the applied specimen geometry. Furthermore, this means that the volume independent CDF is restricted to the gauge volume used for calibration. This fact shows the advantage of the weakest-link CDF.

A final comment is given on the statistical analysis of the material failure behaviour under different loading conditions. The presented approach for the calibration of the weakest-link approach is related to material tests which allow to analyse the material failure behaviour under a single loading condition. Usually, the material failure behaviour is analysed under different loading conditions such as tension, compression, shear and plane strain tension. Each loading condition is investigated through different test set-ups. Consequently, samples need to be drawn for each test set-up. Now, the objective is the identification of the relation between the different samples and the different material failure modes, respectively. In case the samples are drawn from a material which complies with the weakest-link approach, it has to be guaranteed that each test set-up uses specimen geometries with equal or nearly equal gauge volume sizes, see Figure 5.1.6. If this requirement is met, the probability to find a critical defect within the gauge volume is equal for each test set-up. Then, a comparison of the different samples, for instance through interferential statistics, see Chapter 3.6, provides reliable results and enables to draw conclusions of the material failure behaviour under different loading conditions. Moreover, the requirement of equal gauge volumes is already stated by the homogenisation in continuum mechanics, see Chapter 4.3.3: The result obtained from a material test is related to the volume which is occupied by the gauge volume of the applied specimen. This means that a comparison of the results obtained from different material tests requires that all material tests use the same gauge volumes. These considerations are important if a failure criterion just as the fracture locus, see Equation 4.3.13, is calibrated in a deterministic sense as well as in probabilistic sense. However, standard specimens for different loading conditions are of different shape and size, see Figure 4.3.1, and the requirement of equal gauge volumes is not satisfied.

5.2 Numerical Application

In general, structural problems can be solved using the FEM which is a numerical method based on a purely deterministic approach, see Chapter 4.1.6. It implies that failure within a FE model is predicted by deterministic failure criteria and a possible scatter of the failure parameter is not taken into account. However, it is possible to vary randomly the failure parameter within a FE model and between several simulations of the FE model. Such FE models are called stochastic models or randomised models. Here, it is required that the underlying distribution function of the failure parameter is known. As already discussed,

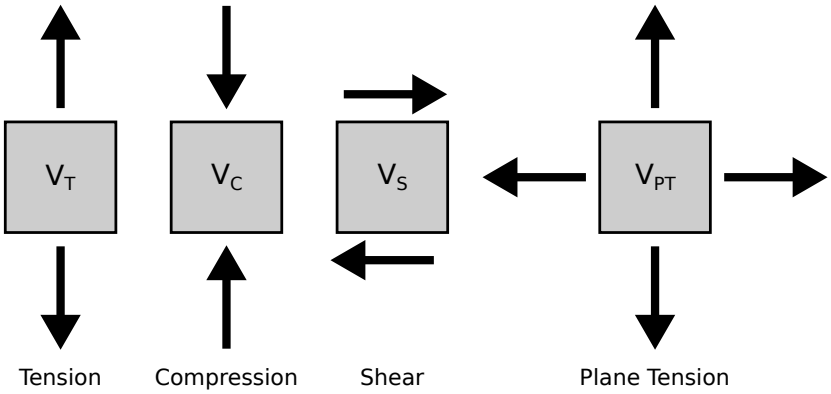

Figure 5.1.6: Gauge parts under different loading conditions with equal gauge volumes ($V_T = V_C = V_S = V_{PT}$).

the weakest-link approach provides the distribution as a function of loading and volume and, thus, the weakest-link approach is perfectly suitable for the FEM.

Moreover, the weakest-link approach can be applied to compute the risk of failure of an entire FE model or particular parts of it directly. In the following, two general techniques in probabilistic failure modelling are presented based on the weakest-link approach. The first one shows the generation of stochastic FE models and the second one shows the direct computation of failure probabilities within a FE model. Here, it is assumed that failure can be described through the weakest-link approach. However, it is first repeated that the FEM is based on the discretisation of the structure of volume V into non-overlapping volume elements V_e. The constitutive equations are evaluated at integration points defined in volume element V_e. According to the numerical approach, the results from an integration point represent the loading within a fraction of volume element V_e. Within this fraction volume, the loading is assumed to be uniformly distributed. For simplicity, elements with only one integration point are supposed in the following.

5.2.1 Requirements

The failure probability of a continuum body can be determined by probabilistic failure models. In the following, the requirements on these models are discussed based on the example of a continuum body and its discretisation.

The volume occupied by the body is denoted as V and the loading which leads to failure is denoted as $f(\mathbf{x})$. It is assumed that volume V can be discretised into k non-overlapping volume elements $\triangle V_i$, so that

$$V = \sum_{i=1}^{k} \triangle V_i. \tag{5.2.1}$$

Consequently, the uniform loading within each volume element $\triangle V_i$ is given $f_i(\mathbf{x})$ according to

$$f(\mathbf{x}) = \begin{cases} f_1(\mathbf{x}) & \text{in } \triangle V_1 \\ f_2(\mathbf{x}) & \text{in } \triangle V_2 \\ \vdots & \vdots \\ f_k(\mathbf{x}) & \text{in } \triangle V_k \end{cases}. \tag{5.2.2}$$

It is assumed that the failure probability of the continuous volume V is known and is denoted as P_F^V. The failure probability of the discretised volume is denoted as $P_F^{\sum_{i=1}^{k} \triangle V_i}$. Since loading $f(\mathbf{x})$ as well as volume V does not change by the discretisation, the failure probability of the volume V is not affected by the discretisation and it follows

$$P_F^V = P_F^{\sum_{i=1}^{k} \triangle V_i}. \tag{5.2.3}$$

This requirement must be satisfied if the failure probability of volume V is determined by its discretisation. Moreover, this requirement is especially important if the failure probability is determined by a FE analysis.

In case, the k volume elements $\triangle V_i$ are statistical independent, the failure probability of the discretised volume is determined by the product

$$P_F^{\sum_{i=1}^{k} \triangle V_i} = 1 - \prod_{i=1}^{k} \left(1 - P_F^{\triangle V_i}\right) \tag{5.2.4}$$

where $P_F^{\triangle V_i}$ denotes the failure probability of volume element $\triangle V_i$. Substituting this expression in Equation (5.2.3) leads to

$$1 - P_F^V = \prod_{i=1}^{k} \left(1 - P_F^{\triangle V_i}\right). \tag{5.2.5}$$

Consequently, the failure probability $P_F^{\triangle V_i}$ depends on loading $f_i(\mathbf{x})$ within volume element $\triangle V_i$ as well as the size of volume element $\triangle V_i$. It follows that $P_F^{\triangle V_i}$ can be determined a function φ which is defined as

$$P_F^{\triangle V_i} = \varphi\left(f_i(\mathbf{x}), \triangle V_i\right) \tag{5.2.6}$$

where function φ adopts values between 0 and 1. If the volume dependence is not considered, so that $P_F^{\triangle V_i} = \varphi\left(f_i(\mathbf{x})\right)$, the previous substitution leads to the inequality

$$1 - P_F^V \leq \prod_{i=1}^{k} \left(1 - P_F^{\triangle V_i}\right). \tag{5.2.7}$$

This relation implies that the failure probability of the discretised volume is larger or equal than the failure probability of the continuous volume under same loading conditions. This violates the first requirement given in Equation (5.2.3). Therefore, Equation (5.2.4) defines the second requirement which must be satisfied by determination of failure probability $P_F^{\triangle V_i}$ provided that the k volume elements $\triangle V_i$ are statistical independent. The definition of function φ is the key part in probabilistic failure modelling. Here, the weakest-link approach given in Equation (5.1.20) offers the possibility to express loading and volume dependence analytically. As shown in Equation (5.1.31), the weakest-link approach satisfies the first requirement in Equation (5.2.3). If the volume dependence cannot be expressed analytically, the function φ needs to be identified for any possible volume element $\triangle V_i$ so that the second requirement in Equation (5.2.4) is satisfied. This, for instance, is the case when the failure probability is determined based on normal distributions, see Equation (3.3.54).

In case, the k volume elements $\triangle V_i$ are statistically dependent, the failure probability of the discretised volume has to be determined according to Equation (3.2.15). This requires the knowledge of the particular conditional probabilities. For instance, volume V is

discretised into two volume elements $\triangle V_1$ and $\triangle V_2$. Event A_1 describes "No failure occurs in volume element $\triangle V_1$" and, accordingly, event A_2 describes "No failure occurs in volume element $\triangle V_2$". Then, the failure probability of the discretised volume reads

$$P_F^{\triangle V_1+\triangle V_2} = 1 - P(A_1)\,P(A_2 \mid A_1) \tag{5.2.8}$$

where $P(A_1)$ denotes the probability of event A_1 and $P(A_2 \mid A_1)$ denotes the conditional probability of event A_2 given that event A_1 occurs. The identification of the conditional probabilities becomes nearly impossible when volume V is discretised into many volume elements $\triangle V_i$. Here, a common approach is to perform a Monte-Carlo simulation, see Chapter 3.3.9, on a random field, see Chapter 3.3.8. However, the first requirement, Equation (5.2.3), must be still satisfied if the failure probability of the discretised volume is determined either by conditional probabilities or by a Monte-Carlo simulation.

5.2.2 Assumptions

The FEM in structural engineering is based on the discretisation of the structural geometry into a mesh of elements, see Chapter 4.1.6. The material properties of an element are assigned according to the properties found at the element position within the structure. The constitutive equations are solved in the integration points of each element. Furthermore, the failure criterion is evaluated in the integration points. In the following, assumptions and definitions are made to keep the mathematical effort within this chapter low.

The difference between the real structural volume and the approximated volume by the FE discretisation is neglected. Further, it is assumed that the spatial distribution of the material properties are captured by discrete parts of the structure. It follows that the structural volume V can be expressed as

$$V = \sum_{j=1}^{n_p} \sum_{i=1}^{n_j} V_{j,i} \tag{5.2.9}$$

where n_p denotes the number of parts, n_j denotes the number of elements within part j and $V_{j,i}$ denotes the volume of element i in part j. Further, it is assumed that the same material is used within part j. It is underlined that volume V corresponds to the initial structural volume and, consequently, element volume $V_{j,i}$ corresponds to the initial element volume of element i in part j.

The element equations are numerically solved using integration points and corresponding weight factors. From that, an element volume fraction can be assigned to each integration point and the loading within this volume fraction can be assumed to be uniform. For simplicity, elements with only one integration point are considered in the following.

It is assumed that the constitutive equations and loading f which leads to failure are correctly solved in the integration point. Finally, it is assumed that failure is evaluated in terms of a probabilistic failure model according to the weakest-link approach given in Equation (5.1.20). It is noted that this approach is based on a constant failure criterion in form of Equation (5.1.22).

5.2.3 Calculation of Failure Probabilities

The failure probability of an element is determined according to Equation (5.1.20) and reads

$$P_F^{V_{j,i}} = 1 - \exp\left(-V_{j,i}\, c_j\left(f_{j,i}\right)\right) \tag{5.2.10}$$

where function $c_j\left(f_{j,i}\right)$ denotes the density function related to the material applied in part j and $f_{j,i}$ denotes the current loading in element i in part j. From that, the survival probability of an element is simply given by

$$P_S^{V_{j,i}} = 1 - P_F^{V_{j,i}} = \exp\left(-V_{j,i}\, c_j\left(f_{j,i}\right)\right). \tag{5.2.11}$$

Both probabilities are evaluated on the element integration point.

Since the weakest-link approach is assumed, all elements of the FE model are considered as statistically independent. Hence, the failure probability of the FE model as well as the failure probabilities of the n_p parts of the FE model are determined according to Equation (5.2.4). The survival probability of part j is given by the product

$$P_S^{V_j} = \prod_{i=1}^{n_j} P_S^{V_{j,i}} = \prod_{i=1}^{n_j} \exp\left(-V_{j,i}\, c_j\left(f_{j,i}\right)\right) \tag{5.2.12}$$

and the failure probability is given by

$$P_F^{V_j} = 1 - P_S^{V_j} = 1 - \prod_{i=1}^{n_j} P_S^{V_{j,i}} = 1 - \prod_{i=1}^{n_j} \exp\left(-V_{j,i}\, c_j\left(f_{j,i}\right)\right). \tag{5.2.13}$$

Consequently, the survival probability of the FE model becomes

$$P_S^{V} = 1 - \prod_{i=1}^{n_p} P_S^{V_j} = \prod_{j=1}^{n_p}\prod_{i=1}^{n_j} \exp\left(-V_{j,i}\, c_j\left(f_{j,i}\right)\right) \tag{5.2.14}$$

and the failure probability of the FE model becomes

$$P_F^{V} = 1 - P_S^{V} = 1 - \prod_{j=1}^{n_p}\prod_{i=1}^{n_j} \exp\left(-V_{j,i}\, c_j\left(f_{j,i}\right)\right). \tag{5.2.15}$$

It is noted that these probability calculations are in accordance with the requirements in Equation (5.2.3) and Equation (5.2.4).

The failure probability of the FE model computes the probability of the event "At least one element fails in the FE model at the current loading state". The same holds for the failure probability of model part j. This implies that the behaviour beyond fracture initiation is not considered in the presented procedure. Therefore, no element deletion algorithm is required when the failure probabilities are determined according to this procedure. Here, it is only required that loading $f_{j,i}$ is precisely computed within each element. It is pointed out that the probability calculations can be done within the post-processing of a FE analysis and the probabilities can be computed for each time step. That enables to express the probabilities as a function of model results, for instance the failure probability as a function of the movement of an impactor.

5.2.4 Randomly Distributed Failure Parameters

As already stated, an element is assumed to fail when loading $f_{j,i}$ reaches a critical value f_c in the element integration point. Hence, element deletion is defined by the failure criterion

$$f_{j,i} = f_c. \tag{5.2.16}$$

This criterion is randomised by introducing the critical value f_c as a continuous random variable F_c as shown in Chapter 5.1.2. The required PDF $g\left(f_c\right)$ of the random variable F_c

is derived from the underlying probabilistic model. In case of the weakest-link approach, the PDF $g\left(f_c\right)$ is given by Equation (5.1.24). Thus, the PDF of element i in part j is given by

$$g_{j,i}\left(f_c\right) = \frac{\partial c_j\left(f_c\right)}{\partial f_c} V_{j,i} e^{-c_j(f_c)V_{j,i}} \quad \text{with} \quad f_c \geq 0. \tag{5.2.17}$$

The critical value f_c of element i in part j is found by drawing it from the PDF $g_{j,i}\left(f_c\right)$. This can be done by a simulation of the random variable F_c using the inverse transformation method, see Chapter 3.3.7. Here, the substituting of Equation (5.1.23) in Equation (3.3.73) leads to the expression

$$F_c = G_{j,i}^{-1}(U) = c_j^{-1}\left(-\frac{\ln(1-U)}{V_{j,i}}\right) \tag{5.2.18}$$

where c_j^{-1} denotes the inverse of the density function, Equation (5.1.19), and U denotes a uniform random variable. Here, the inverse transformation is applied to draw a sample of F_c by drawing a sample of U. Since most common programming languages offer a uniform PRNG, the above mentioned expression enables to generate numerically a pseudo-random number of the weakest-link distribution $g_{j,i}\left(f_c\right)$. In summary, the critical failure value f_c of the element i in part j depends on its initial volume $V_{j,i}$, its density function $c_j\left(f_c\right)$ and the random number drawn from a uniform distribution.

The procedure described above is performed in each element and in each integration point, respectively. As a results, the critical failure value f_c is randomly distributed within a FE model according to the weakest-link approach. The numerical simulation of such a randomised model can be used to analyse the behaviour beyond fracture initiation and to predict possible crack paths. Here, an element is deleted when the failure criterion in Equation (5.2.16) is met. From a statistical point of view, the simulation result represents the result of a sample of the structural model defined by Equation (5.2.9). Therefore, a single simulation does not lead to a reliable result and no conclusions can be made regarding the failure probability. Here, a multiple repetition of the randomised model each drawn as a new sample allows to estimate the mean behaviour and the failure probability (the probability of first fracture initiation). The mean behaviour can be estimated by a Monte-Carlo simulation described in Chapter 3.3.9. The failure probability can be estimated using the empirical expression in Equation (3.5.12). Here, the data base is created using simulation results at the time when the first element fails.

In Figure 5.2.1, the FE modelling of a structure with a randomly distributed critical failure value f_c is graphically presented. For simplicity, a plane and square structure with only one material part is applied in the following. First, the structure is discretised into a square mesh. Then, f_c is randomly distributed within the mesh according to the weakest-link approach. The figure shows three samples of the randomised model. Since a weakest-link distribution can be generated by a uniform distribution, f_c is scattered within the meshes according to a uniform distribution.

This modelling approach depends directly on the mesh and the number of elements defines the sample size. The initial volume of the elements specifies the applied weakest-link distribution. In case all initial element volumes are equal, $V_{j,i} = V_e$, and a Weibull distribution is adopted, the Weibull quantile is determined according to Equation (3.3.49) and becomes

$$\frac{f_c^{P_F^{V_e}(x \leq X)}}{f_{c0}} = \sqrt[m]{\frac{-\ln\left(1 - P_F^{V_e}(x \leq X)\right)}{\left(\frac{V_e}{V_0}\right)}}. \tag{5.2.19}$$

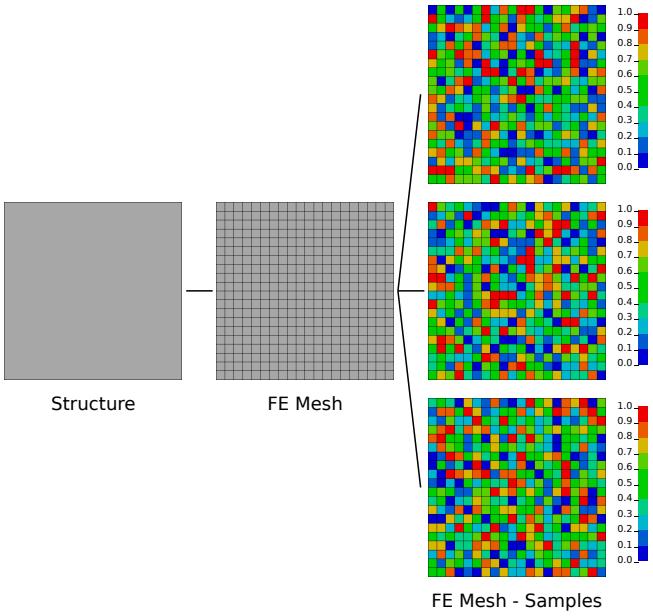

Figure 5.2.1: Randomly distributed failure parameters: The failure parameters are uniformly distributed within the FE mesh.

This quantile function can be used to determine the range of the middle 95% of a Weibull distributed population,

$$R_{f_c}^{95\%} = f_c^{97.5\%} - f_c^{2.5\%} \tag{5.2.20}$$

In Figure 5.2.2, the 97.5% quantile, $f_c^{97.5\%}$ (blue), and the 2.5% quantile, $f_c^{2.5\%}$ (magenta), are plotted as function of volume fraction $\frac{V_e}{V_0}$. The ordinate shows the critical value fraction $\frac{f_c}{f_{c0}}$. The range between the quantiles $f_c^{97.5\%}$ and $f_c^{2.5\%}$shows the range $R_{f_c}^{95\%}$ (grey area). It is seen that the range $R_{f_c}^{95\%}$ goes to infinity when fraction $\frac{V_e}{V_0}$ approaches 0. This means that a small initial element volume V_e leads to a high $R_{f_c}^{95\%}$. In other words, the probability of drawing a critical failure value f_c which exceeds a certain value increases when the initial element volume V_e decreases. Especially, the sample range is influenced by this fact. For instance, a sample of a finely discretised model is drawn from a wider range than a sample of a coarsely discretised model. Hence, a mesh sensitivity analysis is not possible using this modelling approach. From a continuum mechanical point of view, this stochastic characteristic might be interpreted as follows: The material structure is defined by the mesh and changes with each mesh refinement. This means that the FE mesh and the mesh defining the Material Structure (MS mesh) are congruent. This leads to an alternative modelling approach where FE mesh and MS mesh are decoupled.

The uncoupled modelling approach is presented in Figure 5.2.3. Here, the structure is firstly discretised into a square mesh of MS elements. This mesh forms the basis to scatter critical value f_c according to the weakest-link approach. Hence, the initial volume of a MS element enters in the weakest-link equations. Then, critical value f_c is randomly distributed within the MS mesh according to a weakest-link distribution. Figure 5.2.3 contains three samples of the randomised MS mesh. It is noted that critical value f_c is scattered according to a uniform distribution for the same reasons as described before. Finally, the MS

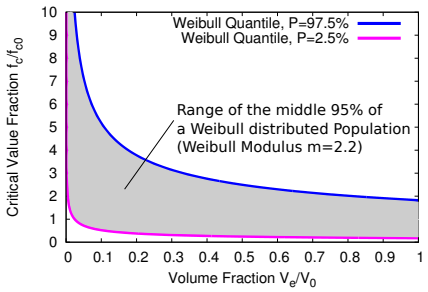

Figure 5.2.2: Range of the middle 95% of a Weibull distributed population.

meshes are discretised into FE meshes as shown in Figure 5.2.3. Alternatively, it is possible to map the distribution of critical value f_c within the MS mesh on an arbitrary FE mesh of the considered structure. The uncoupled modelling approach enables to perform a FE mesh sensitivity analysis without changing the sample of the random material structure. In general, it is recommended to use a FE mesh size which is equal or smaller than the MS mesh size. In case the FE mesh size is larger than the MS mesh size, the initial volume of an element of the FE mesh needs to be used to serve the weakest-link approach.

Both modelling approaches assume statistical independence between the elements of the FE mesh as well as the elements of the MS mesh, respectively. Therefore, these are consistent with the probability calculations described in the previous section. Consequently, both approaches are in accordance with the requirements given in Equation (5.2.3) and Equation (5.2.4).

From a statistical point of view, the FE mesh of the coupled modelling approach as well as the MS mesh of the uncoupled modelling approach are discrete spatial random fields. Since the elements of both approaches are considered as statistically independent, the discrete random fields are mutually statistically independent and no correlation exists between the elements. However, it is also possible to model the discrete random fields with correlated elements. In the work by Yang et al. [118], a Gaussian random field is transformed into a Weibull random field. Based on this work, an extended form of the uncoupled modelling approach is presented in the following.

The basis of the random field forms a discrete and homogeneous Gaussian random field, see Chapter 3.3.8. Here, each element of the MS mesh is first considered as a Gaussian random variable with zero mean and a unit variance and the spatial position of an element is given by its midpoint. Then, the Gaussian random field reads

$$\mathbf{X} = (X_1(\mathbf{t}_1), X_2(\mathbf{t}_2), \ldots, X_n(\mathbf{t}_n))^T \tag{5.2.21}$$

where $X_i(\mathbf{t}_i)$ denotes a Gaussian random variable with PDF $g_N(x_i; \mu = 0, \sigma = 1)$ representing the MS element i and vector $\mathbf{t}_i$ denoted the midpoint position of the MS element i. The n identical means μ are given in a vector $\boldsymbol{\mu}$ of length n,

$$\boldsymbol{\mu} = (\mu, \mu, \ldots, \mu)^T. \tag{5.2.22}$$

The $n \times n$ elements of the Gaussian covariance matrix $\boldsymbol{\Sigma}$ become

$$\Sigma_{ij} = C\left(d = |\,\mathbf{t}_i - \mathbf{t}_j\,|; d_0\right) = \sigma^2 \exp\left(-\left(\frac{|\,\mathbf{t}_i - \mathbf{t}_j\,|}{d_0}\right)^2\right) \tag{5.2.23}$$

where d_0 denotes the correlation length between the MS elements, see Equation (3.3.91). According to Equation (3.3.72), the discrete and homogenous Gaussian random field $\mathbf{X}$ is

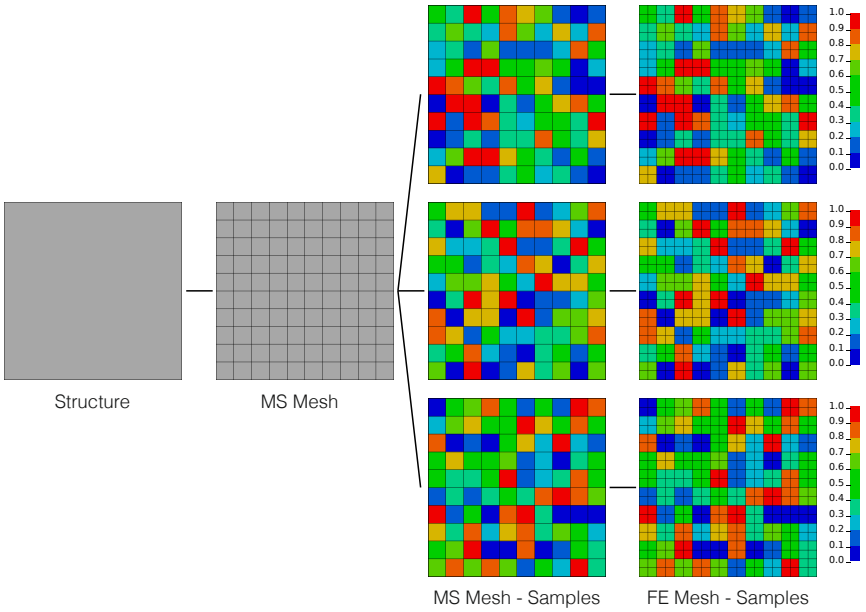

Figure 5.2.3: Randomly distributed failure parameters: The failure parameters are uniformly distributed within the MS mesh, then the MS mesh is discretised into a FE mesh.

transformed into a discrete and homogenous uniform random field $\mathbf{U}$, so that

$$\mathbf{U} = G_N\left(\mathbf{X}; \mu = 0, \sigma = 1\right) \tag{5.2.24}$$

where G_N denotes the CDF of the standard normal distribution, see Equation (3.3.54). According to Equation (3.3.73), the discrete and homogenous uniform random field $\mathbf{U}$ is transformed into a random field $\mathbf{F}_c$ which follows the weakest-link approach, so that

$$\mathbf{F}_c = c_i^{-1}\left(-\frac{\ln(1-\mathbf{U})}{V_i}\right) \tag{5.2.25}$$

where the subscript i refers to the MS element i. This procedure implies that a sample of $\mathbf{F}_c$ is generated by drawing a sample of $\mathbf{X}$. For instance, the sample can be generated using the MATLAB function `mvnrnd` $(\boldsymbol{\mu}, \boldsymbol{\Sigma})$ [84]. In Figure 5.2.4, the uncoupled approach is illustrated using a Gaussian random field which is transformed into a uniform random field. Here, correlation length d_0 is set to four times of the edge length of a MS element. Here, three samples of a uniform random field which is generated using the MS mesh are shown. Afterwards, the three samples are discretised into a FE mesh. However, the most complex task is to calibrate the random field and to take care that the first requirement given in Equation (5.2.3) is satisfied. This topic is not further discussed in the present work.

5.3 Concluding Remarks

The principles of probabilistic failure modelling were introduced in this chapter. Here, the emphasis was on the weakest-link approach. Based on this approach, a method to

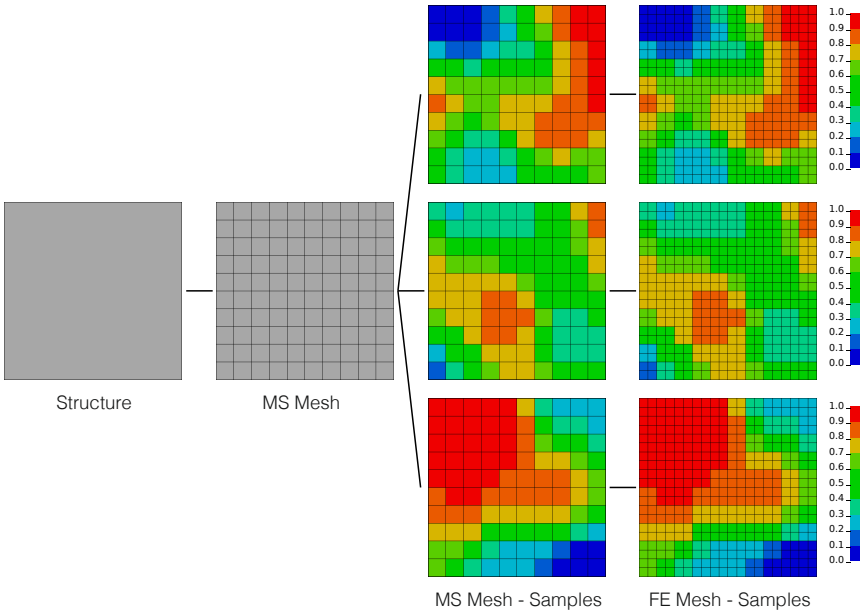

Figure 5.2.4: Randomly distributed failure parameters: The failure parameters are distributed within the MS mesh according to a uniform random field, then the MS mesh is discretised into a FE mesh.

compute the failure probability of a FE model was presented. Here, the probability gives information about the risk that a first fracture initiates. Moreover, a second method was presented based on randomly distributed failure properties. Here, the critical value of a failure criterion was introduced as a random variable which follows a weakest-link distribution. This method enables to scatter the critical value in a FE model. Hence, the behaviour beyond fracture initiation can be analysed from a stochastic point of view.

The weakest-link approach is based on strong statistical assumptions of the material defects which lead to failure. These are summarised as follows:

1. The material defect is considered as a point defect.
2. The spatial probability distribution of the material defect is uniform.
3. All material defects are statistically independent.

These assumptions are made to simplify the stochastic operations. From a physical point of view, these assumptions are critical as neither shape nor size of a defect are considered. A uniform distribution of the defects in space are not reasonable. It is more appropriate that the spatial probability distribution is influenced by parameters from the manufacturing process and, thus, it is not uniform. Finally, the assumption of statistical independence implies that all material defects can be found at the same position in the material. In case the character of a material defect and its spatial probability distribution are considered, the stochastic operations become increasingly complex. A statistical dependence of the critical defects can be taken into account using a random field definition as already shown. It is also important to mention that the weakest-link approach assumes invariant defects. Hence, the approach is especially suitable for brittle and quasi-brittle materials. It is important to realise these assumptions when the weakest-link approach is applied.

In this chapter, only the failure criterion was randomised. In general, every parameter of a structural model can be introduced as a random variable. Geometrical parameters such as thicknesses or imperfections, boundary conditions such as loading and mounting, material parameters such as Young's modulus or yield stress can vary randomly. If several parameters are introduced as random variables and all distribution functions are known, only a Monte-Carlo simulation enables to evaluate the structural reliability.

Chapter 6

Literature Review

The mechanical behaviour of aluminium and magnesium HPDC alloys has been studied in detail within the past years. Several material models are introduced and analysed in the technical literature. The main subject is especially the prediction of fracture initiation in HPDC components using ductile failure criteria. As already described in Chapter 2.3, the HPDC process causes a large variation in ductility due to casting defects in the material microstructure. This variation can be separated into a global systematic variation depending on the casting system and a local pseudo-random variation depending on casting process fluctuations. The consideration of both variations in failure modelling of HPDC alloys became a major issue in recent material science. In the following, some of the most representative material models for HPDC alloys are presented. Here, the topics constitutive modelling, failure modelling, material parameter identification, numerical application, consideration of the casting process and validation are discussed. The literature review closes with concluding remarks.

6.1 Constitutive Modelling

The stress-strain relation of HPDC alloys is in general described through standard metal plasticity for isotropic hypoelastic-plastic materials. The casting process causes a very fine microstructure with pseudo-randomly distributed casting defects. Consequently, no distinct direction dependence can be clearly identified through experiments and the assumption of material isotropy is reasonable as seen in the PhD thesis by Dørum [30]. The elastic material behaviour is commonly described by the isotropic linear-hypoelastic relation given in Equation (4.1.73). The plastic material behaviour is described by the isotropic v. Mises plasticity model in combination with isotropic hardening as seen in the works by Greve [45], Leppin et al. [76], Mae et al. [80] and Mohr and Treitler [87]. A similar plasticity model is applied in the work by Dørum et al. [31]. Here, the high exponent yield criterion proposed by Hershey [54] and Hosford [59] is used instead of the v. Mises yield criterion. Moreover, the material behaviour of HPDC alloys is found to be strain-rate independent in these works. Therefore, the applied plasticity models are strain-rate independent except for the work by Greve [45]. The influence of damage evolution on the constitutive model is neglected in these works. This means that the constitutive model and the failure model are considered to be uncoupled.

6.2 Failure Modelling

The material ductility of HPDC alloys is influenced by casting defects. These defects are material discontinuities which lower the material ductility. As a consequence, the material ductility of HPDC alloys is very low compared to alloys processed in another way. However, the failure behaviour and the prediction of fracture initiation, respectively, are commonly described by ductile failure criteria. Failure criteria in terms of fracture loci, see Equation (4.3.13), are often suggested.

In the work by Greve [45], a novel damage-based failure criterion is presented. Here, the material damage is given as function of stress triaxiality and failure occurs when the material damage reaches a critical value. The criterion distinguishes between failure in the tension branch and failure in the shear and compression branch. In the work by Leppin et al. [76], the failure model presented by Hooputra et al. [57] is applied. This model accounts for three different failure mechanisms in metals: Ductile failure, shear failure and sheet instability, also know as localised necking. Each mechanism is evaluated separately. Ductile and shear failure are evaluated by two different fracture loci and sheet instability is evaluated by a forming limited diagram. The material fails when one of these criteria is met. The Bao-Wierzbicki fracture locus given in Equation (4.3.19) is applied in the work by Mae et al. [80]. The Bao-Wierzbicki fracture locus distinguishes between the tension branch, the compression branch and an intermediate branch. In the work by Mohr and Treitler [87], failure is described in terms of a fracture locus presented in the PhD thesis by Henn [53]. Here, the maximum principal strain at failure is defined as function of stress triaxiality. The same approach is used in the PhD thesis by Treitler [107]. It is noted that these failure criteria include that the ductility decreases with increasing stress triaxiality within the tension branch.

In contrast to the above presented works, a probabilistic approach in failure modelling is applied in the work by Dørum et al. [31]. Here, the Cockcroft-Latham failure criterion, see Equation (4.3.23), is used to describe failure. This criterion implies that failure cannot occur when the maximum principal stress is compressive and neither stresses nor strains alone are sufficient to cause failure. Furthermore, it includes that the ductility decreases with increasing stress triaxiality as seen by Wierzbicki et al. [113] and Gruben et al. [48]. However, the critical failure value is assumed to follow a weakest-link Weibull distribution, see Equation (5.1.39). This means that the critical failure value is introduced as a random Weibull distributed variable and the failure criterion is randomised as described in Chapter 5.1.2.

In Table 6.2.1, the presented failure criteria for HPDC alloys are summarised. The table contains the number of failure parameters and the number of different material tests which are required to identify the failure parameters. It is noted that the seven parameters of the failure model by Hooputra et al. [57] belong to the ductile and shear criterion, the sheet instability criterion is not considered. Furthermore, it is noted that the Cockcroft-Latham criterion can be calibrated by a single test but the identification of the Weibull distribution of the critical failure parameter requires a multiple repetition of the calibration test, see Chapter 3.5.2.

6.3 Material Parameter Identification

Material parameters need to be identified for the constitutive model as well as for the failure criterion. As explained above, the elastic-plastic deformation behaviour of HPDC alloys is commonly described by the isotropic v. Mises plasticity model (or modifications of

Publication	Failure Criterion	Parameters	Calibration Tests
Greve [45]	Greve [45]	3	6
Leppin et al. [76]	Hooputra et al. [57]	7	8
Mae et al. [80]	Bao-Wierzbicki [8]	4	8
Mohr and Treitler [87]	Henn [53]	2	4
Dørum et al. [31]	Cockcroft-Latham [20]	1	1

Table 6.2.1: Failure criteria for HPDC alloys: Number of failure parameters and applied number of different material tests for calibration.

it) in combination with isotropic hardening. Hence, all material parameters of the constitutive model can be found from a uniaxial tension test. In contrast, the parameter identification of a failure model is more complex. When failure is described in terms of a fracture locus, material tests for different stress triaxialities are required. Furthermore, fracture initiation is dominated by casting defects which are non-uniformly distributed within an HPDC component, see Chapter 2.3. The influence of the global systematic distribution can be captured using specimens extracted from different positions within an HPDC component. The local pseudo-random distribution can be captured using specimens extracted from an identical position from several HPDC components. Based on these two aspects, the parameter identification of the failure criteria given in Table 6.2.1 is discussed in the following.

In the work by Greve [45], a magnesium HPDC alloy is analysed. The failure criterion is calibrated using specimens for uniaxial tension, multiaxial tension, shear and compression loading. The specimens are extracted from thin and thick walled parts of a magnesium clutch housing. The results show that the specimens extracted from thin walled parts behave more ductile than specimens extracted from thick walled parts. It is mentioned that the ductility in thick walled parts is mainly dominated by shrinkage porosity. Thus, the failure criterion is calibrated for thin and thick walled parts. Further, the experimental results show that the ductility decreases with increasing stress triaxiality. The work does not contain a study of the local variation in ductility. Greve [45] mentions that the pseudo-random distribution of the casting defects and the specimen size have a strong influence on the test result. Here, it is referred to the weakest-link approach: The probability to find a critical defect increases with the volume under consideration, see Chapter 5.1.6. Therefore, the equivalent plastic strains at failure obtained from specimen geometries with different gauge volumes are not directly comparable.

In the work by Leppin et al. [76], an aluminium HPDC alloy is analysed. The parameters of the failure model by Hooputra et al. [57] are identified using specimens extracted from a generic aluminium HPDC component. The ductile fracture locus is calibrated using five different specimen geometries and the shear fracture locus is calibrated using three different specimen geometries. All specimens are extracted from two positions with different porosity levels (high and low porosity). Both extraction positions are found from a computer tomography scan of the HPDC component. It is obvious that the test results from the low porosity position are more ductile than the results from the high porosity position. The test results from both porosity levels show clearly the local scatter in ductility. Nevertheless, the failure parameters are identified using averaged values for each porosity level (including both failure criteria). It is noted that the averaged graph of the ductile fracture locus show a decreasing ductility with increasing stress triaxiality for both porosity levels.

In the work by Mae et al. [80], an aluminium HPDC alloy is analysed. The failure parameters of the fracture locus by Bao-Wierzbicki [8] are identified from smooth and notched

round bar specimens as well as from flat butterfly specimens. The specimens are extracted from an HPDC component which is part of an automotive engine mounting system. Furthermore, the specimens are extracted from identical positions of six components. Here, the extraction position corresponds to the position of fracture initiation in the component subjected to compression loading. Tensile tests are performed on the round bar specimens and biaxial loading tests are performed on the flat butterfly specimens. The tensile tests are repeated twice. The fractured tensile specimens show a flat fracture pattern without a distinct necking deformation. Consequently, the force-displacement curves obtained from the tensile tests show that fracture occurs prior to the point of diffuse necking. Furthermore, it is seen that the force-displacement curves are comparable but the displacements at fracture initiation differs strongly from each other. Here, it is mentioned that the spread is caused by pseudo-randomly distributed casting defects. Further, it is clearly seen that the measured equivalent plastic strain at failure decreases with increasing stress triaxiality. Hence, only the failure parameters of the tensile branch are identified. In the work by Mae et al. [80], it is pointed out that it is necessary to describe the failure parameters in a stochastic way for HPDC alloys.

In the work by Mohr and Treitler [87], an aluminium HPDC alloy in heat treated condition (T7) is analysed. The failure criterion presented by Henn [53] is calibrated using specimens extracted from an aluminium HPDC component. It is mentioned that the component is heat treated to increase the ductility. Furthermore, the specimens are extracted from positions close to the gating channels to ensure low porosity in the specimens. Sixteen specimens are extracted from four HPDC components. A biaxial testing technique is applied which allows material testing over a wide range of stress triaxialities using the same flat specimen geometry. In total, four different loading combinations are tested and each test is repeated four times. The experimental results of the four combinations show that the force-displacement curves are comparable but the displacements at fracture initiation differ strongly from each other. It is noted that a strong scatter in ductility exists, even though the specimens are extracted from the gating part of a heat treated HPDC component. Mohr and Treitler [87] mention that the strong scatter is caused by pseudo-randomly distributed casting defects and it is pointed out that the local ductility of HPDC alloys exhibits a considerable scatter which needs to be analysed in further research. Nevertheless, the failure parameters are identified using averaged values. In the PhD work by Treitler [107], the same failure criterion is calibrated using the same test procedure as in the work by Mohr and Treitler [87]. Here, an aluminium HPDC alloy in casting condition (F) is analysed using flat specimens extracted from several identical HPDC components. The flat specimens are extracted from two characteristic positions which are expected to be of a low and a high porosity level. In total, 64 specimens are tested in the biaxial testing device. The force-displacement curves differ strongly from each other in all loading combinations for both porosity levels. Especially, the strains at fracture initiation exhibit strong scatter. Nevertheless, the failure parameters are identified for both porosity levels using averaged values. However, the graphical comparison of both calibrations shows that the ductility decreases with increasing stress triaxiality and, obviously, the ductility is higher in specimens extracted form low porosity positions than in specimens extracted from high porosity positions.

In the work by Dørum et al. [31], a magnesium HPDC alloy is analysed. The critical value of the Cockcroft-Latham criterion is identified using uniaxial tension tests. The tensile specimens are extracted from the three sides of an U-shaped HPDC component. Each side is considered to belong to parts with different casting conditions: The first part is defined by the flange close to the gating channels, the second part is defined by the flange close to the vacuum channels and the third part is defined by the intermediate web.

In summary, six specimens per part are extracted from three components. This testing procedure enables to analyse the global systematic variation as well as the local pseudo-random variation in ductility. The experimental results of the three characteristic parts show the same behaviour: The engineering stress-strain curves show a comparable stress-strain relation, but the strain at fracture initiation exhibits significant scatter. Moreover, the results show that failure occurs prior to the point of diffuse necking. The comparison between the three characteristic parts shows a general tendency: The ductility obtained from specimens of the gating part is larger than the ductility obtained from specimens of the vacuum part. The largest ductility is obtained from specimens of the web part. The critical value is computed for each result. From that, the Weibull distribution of the critical value is identified for each characteristic part and, thus, the probabilistic failure criterion is calibrated. In the work by Dørum et al. [31], it is pointed out that an accurate prediction of fracture initiation in HPDC alloys requires that the global systematic distribution as well as the local pseudo-random distribution of the casting defects are considered. In a previous work by Dørum et al. [32], the same testing procedure is applied to characterise an aluminium HPDC alloy in heat treated condition (T1). Here, tensile specimens are also extracted from the three sides of an U-shaped HPDC component. The experimental results show also a significant scatter in ductility and the influence of the specimen extraction position. Hence, the same probabilistic failure model is calibrated for the three characteristic parts.

Finally, it is referred to the work by Teng et al. [105]. Here, a total of 32 round bar specimens are extracted from the same aluminium HPDC components which are used in the work by Mae et al. [80]. The tensile test results show a strong scatter in tensile strength and tensile failure strain. The fracture surfaces are also analysed. Teng et al. [105] mention that shrinkage pores and oxide films are dominating the tensile failure behaviour. However, the work by Teng et al. [105] focuses on the statistical analysis of the tensile test results in terms of tensile strength and tensile failure strain. The probability distributions of both quantities are analysed. The normal and the Weibull distribution are applied to describe the probability distributions. The distribution parameters are identified from a linear regression on the test data which are presented in normal plots and Weibull plots, respectively. The Anderson-Darling GoF test is applied to prove both distribution parameter identifications, see Chapter 3.6. The GoF results on the tensile strength data confirm that the Weibull distribution cannot be rejected. The GoF results on the tensile failure strain data show that the Weibull distribution as well as the normal distribution cannot be rejected. Teng et al. [105] recommend to use the Weibull distribution for both quantities since the Weibull distribution is only defined for positive values. However, Teng et al. [105] conclude that the test data should be classified according to the type of casting defect which causes failure. This means that each type of casting defect represents a separated population of defects which causes different forms of fracture initiation.

6.4 Numerical Application

In the works by Greve [45], Leppin et al. [76], Mae et al. [80], Mohr and Treitler [87], the failure criteria are applied in a deterministic sense. Thus, unique values of the failure parameters are required and, consequently, the failure criteria are uniquely evaluated. As described before, averaged values are used in these works, even though the experimental results show a significant scatter. This (deterministic) approach leads to vague and uncertain results as discussed in Chapter 5. Further, this (deterministic) approach entails that the same values of the failure parameters are used in a FE model (neglecting

the differentiation between the porosity levels). Consequently, the simulation of such a FE model provides only one possible result. Moreover, the usage of averaged values of the failure parameters does not necessarily lead to a simulation result representing the averaged structural behaviour. The simulation result corresponds essentially to only one possible case. Finally, the occurrence of this scenario and the probability of failure, respectively, are unknown.

In contrast to the above mentioned works, a probabilistic approach in failure modelling is applied in the work by Dørum et al. [31]. Here, the critical value of the Cockcroft-Latham criterion is considered as a random variable which follows a weakest-link Weibull distribution. Thus, the stochastic character of HPDC alloys and the influence of the size effect are taken into account by this approach, see Chapter 5.1.4. Here, the critical value is randomly distributed within a FE model (neglecting the differentiation between the three characteristic parts) according to a Weibull distribution. Hence, a sample of the Weibull distribution needs to be drawn when a simulation is preformed. Consequently, the simulation result represents the result of this sample. Multiple repetitions of the simulation, each using a new sample, provides an estimation of the failure probability. A detailed description of FE models using randomly distributed failure parameters can be found in Chapter 5.2.4. However, it is noted that the probabilistic failure model by Dørum et al. [31] is not strictly applied in a stochastic sense. The critical value is limited by a maximum value which cannot be exceeded. This means that a sample cannot exist of values larger than the maximum value, which violates the requirements on a distribution function of a continuous random variable, see Equation (3.3.5). Further, a sample drawn from a Weibull distribution can include critical values which become very small. In case of small element sizes, these small values lead to element failure at low element loading. In the work by Dørum et al. [31], this fact is described as simulation of micro-cracks and, thus, the critical value is defined as a non-local variable. This implies that the critical value of an element is taken as the minimum of all critical values of the elements within a predefined radius emanating from the centre of the actual element. This non-local regularisation is described in detail in the work by Fagerholt et al. [39]. As a consequence, each sample of the Weibull distribution is spatially transformed according to the non-local regularisation. In summary, Dørum et al. [31] modify the Weibull sample, first, by introducing a maximum value and, second, by using a non-local regularisation. As a result, the sample cannot be considered as a sample drawn from a Weibull distribution.

6.5 Consideration of the Casting Process

The local pseudo-random variation of casting defects can be considered by a probabilistic approach in failure modelling as presented in the work by Dørum et al. [31]. The global systematic variation depends on the casting system. The casting system is defined through the casting component geometry, die-halves, arrangements of gating and vacuum channels and process parameters. The influence of the casting system can be taken into account in a FE model using the result of a corresponding casting simulation. Hereby, the casting simulation result is mapped onto the FE model and the material model parameters are linked to the casting simulation result. A casting simulation result can be described by different quantities, such as flow length, air contact time and cooling rate at the end of form filling.

A common approach is the identification of correlation functions. Here, a mechanical quantity such as yield stress, tensile strength, tensile failure strain or any material model parameter is given as a function of casting simulation quantities. Such a correlation func-

tion needs to be identified for each parameter which is considered to be process dependent. It is noted that these correlation functions are actually of empiric character. In the work by Treitler [107], correlation functions are identified for yield stress and tensile failure strain based on the cooling rate. Here, the cooling rate is expected to provide a good measurement of the solidification which causes shrinkage porosity and leads to poor material properties. Tensile specimens are extracted from various position within a generic HPDC component. From the experimental results, the spatial distribution of yield stress and tensile failure strain is found. From the casting simulation, the spatial distribution of the cooling rate is found. Then, the correlation functions are identified combining both results. However, it is noted that also the tensile test results exhibit a strong scatter and averaged values are used to identify the correlation functions. In the work by Hildebrand [55], correlation functions for yield stress, tensile strength and tensile failure strain are identified in the same way as presented by Treitler [107]. However, the correlation functions are based on several casting simulation quantities. In the work by Greve [45], yield stress and failure model parameters are given by correlation functions. Here, the cooling rate is also considered as indicator for shrinkage porosity. The parameters are found by comparison of mechanical test results and the results of a casting simulation. In general, the identification of correlation functions is critical due to the strong scatter in the material behaviour and the material parameters, respectively. Further, the correlation functions are usually used to predict material parameters in a deterministic sense. The local variation of the material parameters might be predicted by a variation of the boundary conditions of a casting simulation. However, this procedure is numerically very expensive and the variation of the boundary conditions still needs to be known.

The usage of correlation functions leads to a continuous distribution of material model parameters within a FE model. An alternative approach is applied in the works by Leppin et al. [76], Treitler [107] and Dørum et al. [32]. Here, the set of material model parameters is distributed discretely within a FE model. Hence, the material is classified into discrete quality levels. Each quality level is given by a unique set of material model parameters. The distribution of the quality levels within the FE model is found from a corresponding casting simulation. Here, a casting simulation quantity needs to be identified as a quality measurement. In the work by Leppin et al. [76], the material is classified into low and high porosity material. Both porosity levels are given by different sets of failure model parameters as described above. The distribution of the two porosity levels is predicted from a casting simulation and the bivalent distribution is mapped onto the FE model. It is noted that the prediction of porosity from a casting simulation is also based on a correlation function of casting simulation quantities. In the work by Treitler [107], the material is also classified into low and high porosity material and each is defined by a set of material model parameters. The spatial distribution of the failure strain is found from correlation functions as described above and the distribution is mapped on a FE model. A critical value of the failure strain is defined. The low porosity material parameters are used in an element when the mapped failure strain is larger than the critical value. Consequently, the high porosity material parameters are used in an element when the mapped failure strain is smaller than the critical value. In the work by Dørum et al. [32], the material is classified into three different casting qualities according to the component parts: Gating part (intermediate quality), web part (high quality) and vacuum part (low quality). Each part is characterised by a unique hardening curve and a unique Weibull distribution of the critical failure value. Here, the air contact time of the melt is used as quality measurement. It is assumed that material with long air contact time tends to build oxide films. Hence, the material quality decreases with increasing air contact time. The total range of the air contact time is divided into three branches and each branch corresponds to one of the

defined casting qualities. The trivalent distribution is mapped onto the FE model. From that, a casting quality is assigned to each element. Further, the critical failure value of each element is drawn from the mapped Weibull distribution. In summary, this mapping approach enables to consider the global systematic variation and the local pseudo-random variation of the casting defects in a FE model of an HPDC component. In FE modelling, each set of material parameters is defined in a so-called material card. Thus, this approach leads practically to a mapping of material cards.

6.6 Validation

In some of the above presented works, the material model and the identification of its parameters are validated through component testing. Here, numerical simulations of the component tests are performed and compared with experimental results. As already described, the pseudo-random character of the casting defects leads to a pseudo-random failure behaviour of HPDC alloys. Consequently, the structural failure behaviour of HPDC components is characterised by pseudo-randomness. The validation of the material models by Greve [45], Treitler [107] and Dørum et al. [32] are discussed in the following. The validation of the material model by Leppin et al. [76] cannot be discussed since a detailed description of the validation is not presented.

In the work by Greve [45], a segment is extracted from a HPDC clutch housing and is subjected to three point bending loading. Here, quasi-static and dynamic loading conditions are applied. It is noted that only one test result is presented for each loading condition and, thus, no information about experimental scatter is given. Two different types of solid meshes are investigated. A fine cubical mesh is analysed through three variants of spatially distributed material parameters. The first variant uses a mapped material parameter distribution based on a cast simulation result and correlation functions. The second variant uses material parameters obtained from thin walled parts and the third variant uses material parameters obtained from thick walled parts. In addition, a coarse tetrahedron mesh is analysed. Here, only a mapped material parameter distribution is considered. In the quasi-static load case, the comparison of experimental result and numerical results obtained from the two meshes with a mapped material parameter distribution shows a good agreement in terms of force-displacement behaviour. The numerical result obtained from the mesh with thick walled material parameters underestimates the experimental result. The one obtained from the mesh with thin walled material parameters overestimates the experimental result. In the dynamic load case, the comparison of experimental result and numerical results leads to the same conclusions as in the quasi-static load case. Since the validation is performed using only one experimental result for each loading condition, the validation result is critical in terms of the pseudo-random character of HPDC alloys.

In the work by Treitler [107], a generic HPDC component is subjected to quasi-static tension and compression loading. Each component test is repeated five times. The experimental results obtained from both loading conditions show a similar force-displacement behaviour: The comparison of the measured force-displacement curves shows a comparable deformation behaviour but a strong scatter in the displacements at fracture initiation. In the work by Treitler [107], a shell mesh and a solid tetrahedron mesh are investigated. The parameters of the applied failure model are spatially distributed according to a cast simulation result. In addition, a shell mesh with failure parameters representing low porosity is investigated for comparison. Here, all material model parameters are distributed uniformly. In the tension load case, the force-displacement behaviour is accurately

predicted from all numerical variants. However, the displacement at fracture initiation is differently predicted. The shell model using low porosity failure parameters overestimates the experimental results, whereas the shell model using mapped failure parameters predicts a displacement at fracture initiation which lies within the experimental scatter. The solid model using mapped failure parameters underestimates the experimental results. In the compression load case, the force-displacement behaviour is accurately predicted from the solid mesh. In contrast, the force-displacement curves predicted form the two shell meshes show a consistently lower force level than the experimental results beyond the linear range. However, the ultimate force magnitude is correctly predicted form all numerical variants. The shell mesh as well the solid mesh which use mapped failure parameters predict a comparable displacement at fracture initiation which lies within the experimental scatter. The shell model using low porosity failure parameters overestimates the experimental results. The location of fracture initiation in the tension load case is well predicted by the meshes using mapped failure parameters. In contrast, the location of fracture initiation in the compression load case is not correctly predicted by the meshes using mapped failure parameters. Here, it is reasonable that the location of fraction initiation is dominated by structural instability. In summary, the work by Treitler [107] shows clearly that the global systematic variation of the casting defects needs to be considered in the numerical design of HPDC components.

In the work by Dørum et al. [32], the probabilistic failure criterion is validated through a three-point bending test of a U-shaped aluminium HPDC component. The test is repeated three times under quasi-static conditions. The three experimental force-displacement curves show a comparable behaviour until first fracture initiation. The displacements at first fracture initiation differ strongly from each other. When the displacement at first fracture initiation is reached, the three force-displacement curves drop to a comparable force level. The second drop in the force-displacement curves indicate a further fracture initiation. Also, the displacement at second fracture initiation differs strongly from each other. From the experiments, it is seen that first fracture occurs in the vacuum part and second fracture in the gating part. The bending test is simulated by a shell mesh model. As already described, the material parameters are calibrated separately for the three sides of the U-shaped component. These three sets of material parameters are spatial distributed according to a cast simulation result. Here, the above mentioned material card mapping procedure is applied. Further, three samples of FE models are generated based on the probabilistic failure criterion. The comparison of the experimental results with the numerically predicted results shows a good correlation until first fracture initiation. Due to the probabilistic failure model, the three samples predict different displacements at first fracture initiation. However, the three numerically predicted force-displacement curves do not show clearly the second force level as seen by the experiments. In a previous work by Dørum et al. [33], a numerical simulation is performed on the same bending tests. Here, the three sets of material parameters are distributed according to the three sides of the U-shaped component. However, the critical failure value of each part is given as an averaged value. The numerical force-displacement curve predicted by this model shows qualitatively a very good correlation to the experimental force-displacement curves. This means that the two drops at fracture initiation are clearly seen and the force level beyond first fracture initiation is correctly predicted. In summary, the probabilistic failure model enables to describe the experimentally observed scatter. However, the numerical model using a material distribution according to the three component parts provides a qualitatively better prediction of the force-displacement behaviour than the numerical model using a material distribution based on a casting simulation result. A reason for this could be as follows: The material distribution based on the casting simulation result leads to a dis-

tribution which is different from the one considered in the material parameter identification. Finally, it is noted that the probabilistic failure model is not validated in a stochastic sense in the work by Dørum et al. [32]. A multiple repetition of the component test is required to generate a sample of the probability distribution of the component test. The same needs to be done numerically as the probabilistic failure model can be considered as validated when the numerically predicted failure probability correlates to the experimentally estimated failure probability.

6.7 Concluding Remarks

The presented literature review on failure modelling in HPDC components leads to following conclusions:

- The material behaviour of HPDC alloys is dominated by casting defects. The experimental results show the influence of the global systematic variation as well as the local pseudo-random variation of the casting defects on the material behaviour. Hence, it is necessary to consider both variations in the mechanical characterisation of an HPDC alloy. Thus, specimens have to be extracted from various positions in an HPDC component and, further, several specimens from the same extraction position are required. In general, it is seen from the literature review that the material behaviour needs to be analysed using specimens extracted from real casting components and not from simple casting sheets. Besides the mechanical analysis of the experimental results, a statistical analysis of the experimental results is of major importance to characterise the influence of the local pseudo-random variation. Finally, it is important to take the size effect into account when results obtained from different specimen geometries are compared.

- The elastic-plastic deformation behaviour is less influenced by casting defects. The scatter in the stress-strain relation is negligible compared to the scatter in the failure strain. Further, no distinct strain-rate dependence of HPDC alloys can be identified. In engineering applications, the isotropic v. Mises plasticity model (or modifications of it) in combination with isotropic hardening is sufficient to describe the elastic-plastic deformation behaviour. The presented validations show that the structural behaviour until first fracture initiation is well predicted by this constitutive model.

- As a result of the local pseudo-random variation of the casting defects, the failure behaviour is expected to be pseudo-random. Consequently, the parameter identification of a failure model exhibits a significant scatter. Therefore, a probabilistic approach in failure modelling is seen as the only reasonable approach to predict fracture initiation in HPDC components. As already mentioned, failure parameters are defined as random variables in a probabilistic failure model. This approach requires to identify the probability distribution of each failure parameter and the statistical correlation between the different failure parameters. Therefore, it is more practicable to use failure criteria with a minimum of parameters. A probabilistic failure model enables to analyse the influence of randomly distributed failure parameters on the structural behaviour. However, a probabilistic failure model needs to be validated in a stochastic sense which requires multiple repeated experimental tests. Finally, it is noted that the usage of a non-local regularisation can be avoided by decoupling the FE mesh and the MS mesh as described in Chapter 5.2.4.

- The influence of the global systematic variation can be captured by a casting simulation and a mapping procedure. The approach which is based on material card mapping is more robust compared to the approach which is based on correlation functions. From the presented validations, it is seen that the results obtained from heterogenous FE models are more precise than the results obtained from homogeneous FE models. However, it is not clearly seen that this is related to the applied mapping procedure or to the fact that the material parameters are not homogeneously distributed. This means that it is not possible to identify the most reasonable mapping procedure out of the presented ones. In summary, the combination of a probabilistic failure model and a heterogeneous and reasonable distribution of material cards enables to take both forms of variation of casting defects into account in FE modelling of HPDC components.

- A material model for HPDC alloys is validated using tests performed on corresponding HPDC components. Since the casting defects influence the structural behaviour, a multiple repetition of the component test is required and the experimental results are expected to scatter. In case a deterministic failure model is applied, the numerical result should at least predict a result which lies within the experimentally observed scatter. However, this approach cannot be treated as a correct validation since the information of the failure probability is missing. In case a probabilistic failure model is applied, the result of a stochastic study should predict the experimental observed scatter. If the numerically predicted failure probability correlates to the experimentally estimated failure probability, the probabilistic failure model can be considered as validated.

- Finally, it is noted that the complex geometries of HPDC components are usually discretised by volume elements which leads to long computation times. In case the geometry allows the use of shell elements and, thus, thickness stress are of little influence, the results are comparable to the results obtained from solid elements.

Chapter 7

Structural Behaviour

The structural behaviour of a generic aluminium HPDC component was analysed through experimental component testing. Bending tests as well as axial compression tests were carried out under quasi-static loading conditions. The experimental results are presented and discussed in this chapter. The applied aluminium HPDC alloy as well as the generic component are introduced and the test set-ups used for bending and compression tests are shown. Based on the experimental results, conclusions are drawn on the structural behaviour and consequences for material testing are pointed out.

7.1 Aluminium Die-Casting Alloy and Test Component

Generic HPDC components made of an AlSi9Mn alloy in casting condition (F) were investigated in the experimental work. The applied aluminium HPDC alloy was introduced by Aluminium Rheinfelden GmbH in 2004 and is technically called Castasil-37. The major chemical components and their weight percentages are given in Table 7.1.1 according to a material data sheet by the producer [4]. In this material data sheet, it is noted that the element strontium (Sr) is applied to refine the Al-Si eutectic and, consequently, to avoid material porosity. Furthermore, it is noted that the alloy is characterised by excellent castability, very good weldabiltiy and high strength material properties in casting condition (F). Castasil-37 is commonly used in engineering applications to cast thin-walled and large structural components which do not need any heat treatment. For instance, the two longitudinal HPDC components in the rear end structure of the current Audi A8, see Figure 1.1.1, are made of Castasil-37. This example shows that Castasil-37 can be used for crash relevant components which are subjected to extreme loadings. It is noted that the production costs of HPDC components can be reduced if heat treatment can be omitted. Hence, the automotive industry has a particular interest to use aluminium HPDC alloys such as Castasil-37.

[%]	Si	Fe	Cu	Mn	Mg	Zn	Ti	Sr
min.	8.5			0.35				0.006
max.	10.5	0.15	0.05	0.60	0.06	0.07	0.15	0.025

Table 7.1.1: Chemical composition of the aluminium HPDC alloy Castasil-37 (AlSi9Mn) in weight-% according to a material data sheet by Aluminium Rheinfelden GmbH [4].

Images of the generic HPDC component investigated in the present work are presented in Figure 7.1.1. The component is U-shaped with a typical casting structure inside, see Figure 7.1.1a. The casting structure is defined by a single longitudinal rib and several transverse ribs as well as the characteristic ejector domes (thick cylinders) which are required to remove the component from the casting tool. The relevant component dimensions can be taken from Figure 7.1.1b and Figure 7.1.1c. The total width is approximately 200 mm, the total height approximately 150 mm and the total length approximately 900 mm. The rib height is approximately 50 mm. The wall thickness in thin parts is approximately 2.5 mm. This component geometry was designed by Audi AG for research and development purposes and is technically denoted as U900-1. The components which were analysed in the present work were produced in a horizontal cold chamber HPDC machine including a vacuum system. A Müller Weingarten Vakural DGM machine with a locking force of 2000 t was applied. As already mentioned, the components were not heat treated after casting. This means that the material structure was given in casting condition (F). The applied casting system is presented in Figure 7.1.1d. Due to the symmetry in longitudinal direction, only one half of the casting system is shown. According to the casting system, the U900-1 component is classified into three characteristic parts as illustrated in Figure 7.1.1e. The characteristic parts are gating side (blue), vacuum side (red) and intermediate part (green). The gating side is defined by the component side close to the gating channels, the vacuum side is defined by the component side close to the vacuum channels and the intermediate part is defined in between. The material ductility was expected to be higher on the gating side than on the vacuum side, see Chapter 2.3.

7.2 Bending Tests

The structural behaviour of the HPDC component U900-1 was analysed in a bending deformation mode. Seven parallel component tests were carried out in a three-point bending test set-up. In the following, the applied test set-up and the experimental results are presented and discussed.

7.2.1 Test Set-Up

The requirement on the design of the test set-up was to guarantee structural failure of the U900-1 component under three-point bending. A technical drawing of the applied three-point bending test set-up is given in Figure 7.2.1a. The load was applied in the middle of a component and the supports were arranged symmetrically to the middle with equal distance of 305 mm. Each component was placed on two cylindrical steel bars with equal diameter of 40 mm and the load was introduced by a cylindrical steel punch with outer diameter of 200 mm. The aim of the support construction was to avoid local cracking in the vicinity of the bars. Hence, holes with equal diameter of 40 mm were drilled through each component. Each hole was reinforced by an aluminium sheet of 2 mm thickness and the sheets were fixed by welding. It was expected that the bars move almost without friction in horizontal direction. Further, it was expected that a component rotates almost without friction around the bars. A technical drawing of the left support construction is given in Figure A.1.2 of Appendix A.1. The bars were placed on two steel walls of 10 mm thickness and the walls were welded onto a steel plate. Each bar end was milled to the middle of the cross-section. Consequently, the bars could slide along the walls during testing. Friction was reduced using Teflon strips of 1 mm thickness. Friction between bars and component was reduced using Polyacetal (POM) rings of 2 mm thickness. Suitable notches were

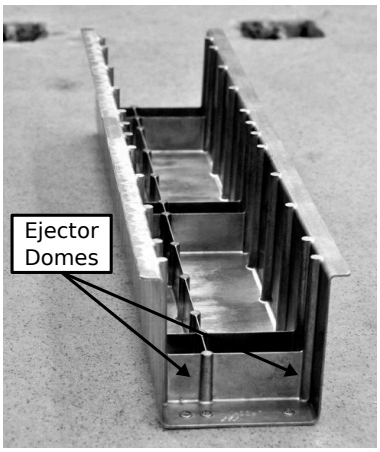

(a) Overall image.

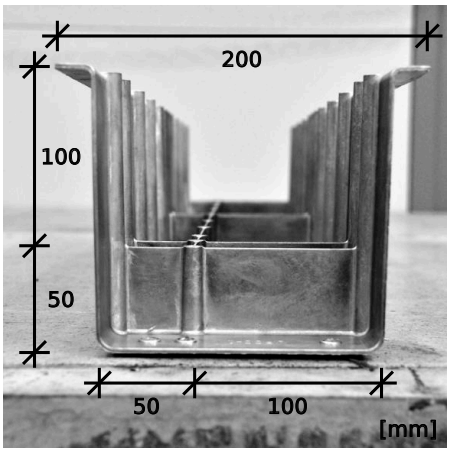

(b) Image of the cross section.

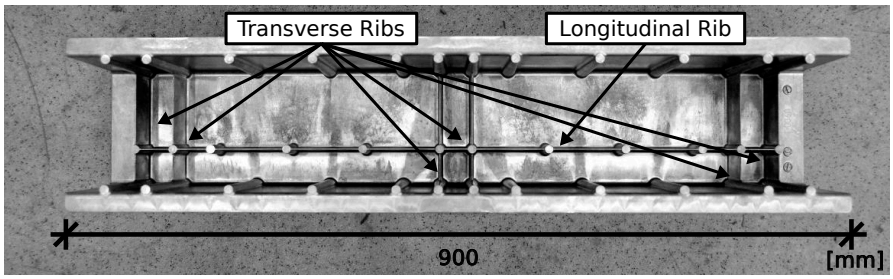

(c) Image of the casting structure including ribs and ejector domes.

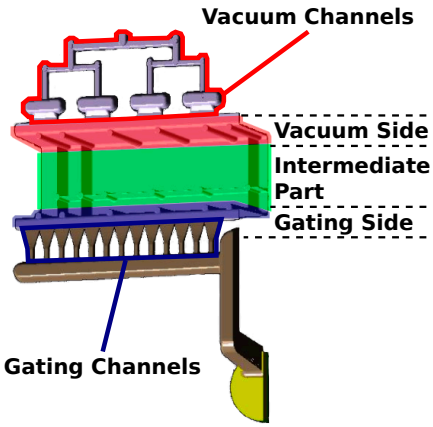

(d) Casting system.

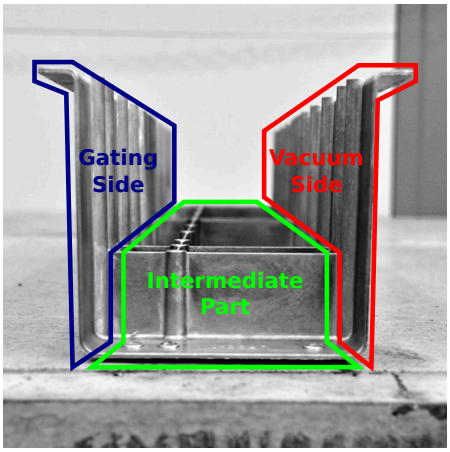

(e) Characteristic parts.

Figure 7.1.1: Images of the aluminium HPDC component U900-1.

milled around each bar to position the POM rings. A technical drawing of the punch construction is given in Figure A.1.3 of Appendix A.1. The steel punch was attached with a bolt to a steel plate which was mounted to the testing machine via a threaded joint. All parts of the support construction and the punch construction were made of high strength steel and assumed to behave rigidly. The supports were bolted onto two parallel high strength steel H-beams which were joined through welding. The H-beams were not expected to deform during testing. The complete three-point bending support was placed into the testing machine as illustrated in Figure 7.2.1b.

Seven parallel bending tests were performed in an Instron servo-hydraulic 250 kN testing machine. The load was applied by means of a predefined and constant punch velocity of 3 $\frac{\text{mm}}{\text{min}}$. It is assumed that each test was performed under quasi-static loading conditions. Force and displacement were measured by the testing machine. In addition, the relative displacements between H-beams and punch were measured using extensometers at gating side and at vacuum side as seen in Figure 7.2.1c. Two cameras were positioned with focus on gating side and on vacuum side to detect which one failed first, see Figure 7.2.1d.

7.2.2 Experimental Results

The observations during testing showed a qualitatively comparable behaviour of all three-point bending tests: The U900-1 component deformed only slightly during loading. When the critical load was reached, a crack formed on the vacuum side. The component deformed further until a crack formed on the gating side. Afterwards, the intermediate part carried the load by plate bending. Each test was stopped at this point. The analysis of the camera images obtained from each bending test confirms this result as seen in Figure A.2.1 and Figure A.2.2 of Appendix A.2. Only test #6 showed another behaviour. Here, the first crack formed on the gating side. Furthermore, the image analysis shows that the cracks started to grow from the bottom. Here, the material expired nearly pure tension and the material with the poorest ductility caused fracture initiation. This belongs to the assumption that the poorest material ductility was expected on the vacuum side. In Figure 7.2.2, images from both sides of a deformed and fractured U900-1 component are shown. It can be seen that the component exhibited only small permanent deformations. Further, the location of fracture initiation on the gating side and on the vacuum side, respectively, can be clearly identified. Equivalent images of the other components are given in Figure A.2.3 of Appendix A.2 and lead to the same result. However, it is seen that the location of fracture initiation was not reproducible within a component side.

The force-displacement curves obtained from the seven parallel bending tests are displayed in Figure 7.2.3a. The force-displacement curves were measured by the testing machine. The curves also show a qualitatively comparable behaviour: The force increases non-linearly until an ultimate load is reached. Subsequently, the force decreases rapidly and starts to increase slightly until a second maximum load is reached. Once more, the force decreases rapidly and reaches an almost constant minimum. A quantitative comparison of the curves shows that the initial non-linear behaviour is reproducible, but the force magnitude at ultimate load and the corresponding displacement vary significantly. Further, the comparison shows that the force magnitude at second maximum load is comparable, but the corresponding displacement varies significantly. The mechanical interpretation is as follows: The bending load was carried by the entire component until a crack formed on the vacuum side (or on the gating side at test #6). Then, the bending load was carried by the intermediate part and the undamaged side. When a crack formed on this side, the bending load was carried by the intermediate part. The failure behaviour under bending load indicates a significant difference in the material ductility between both

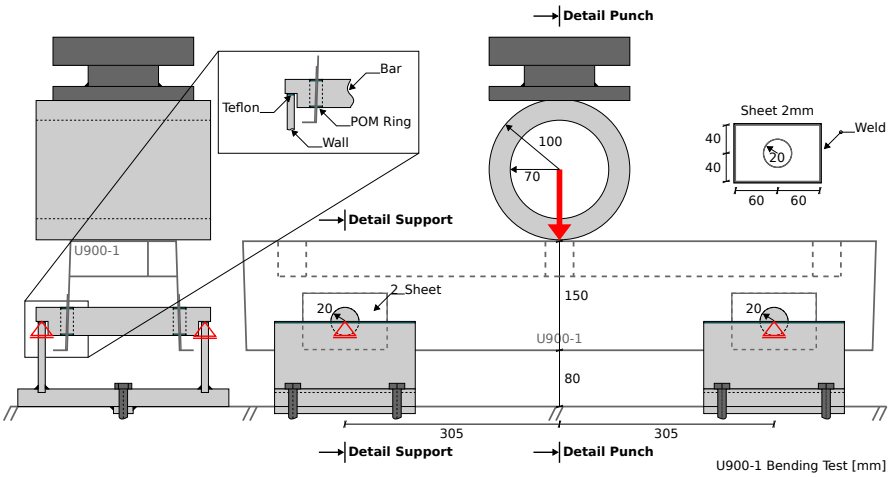

(a) Technical drawing of the three-point bending test set-up.

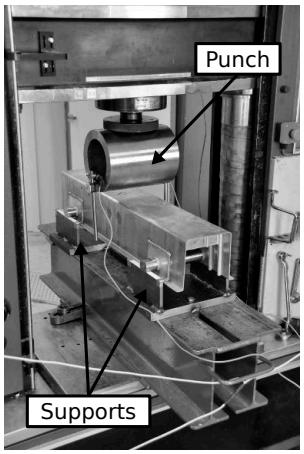

(b) Image of test set-up.

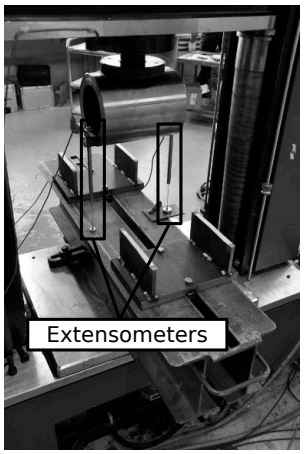

(c) Image of extensometer positions.

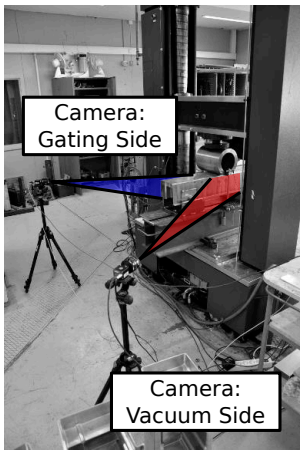

(d) Image of camera positions.

Figure 7.2.1: Three-point bending test set-up: Technical drawing and images of the test set-up.

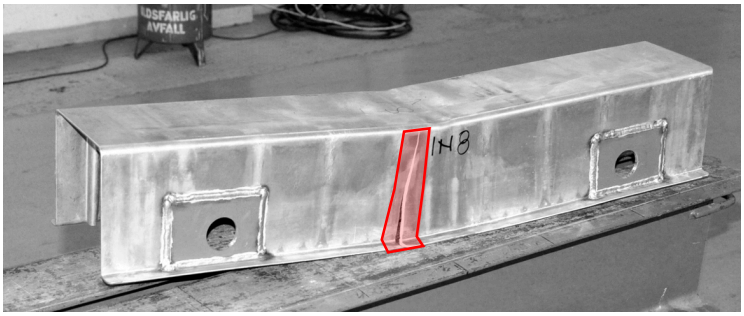

(a) Fracture initiation on gating side.

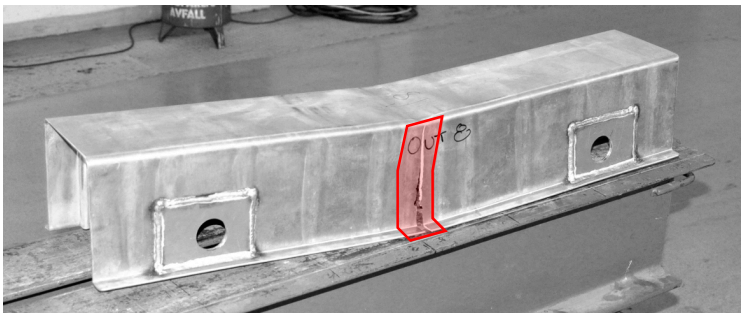

(b) Fracture initiation on vacuum side.

Figure 7.2.2: Deformed and fractured U900-1 component subjected to three-point bending.

component sides. Furthermore, the strong scatter in the displacement at first and second fracture initiation suggests a strong scatter in the material ductility within each component side. The repeatable force-displacement behaviour prior to first fracture initiation as well as the comparable force magnitude prior to second fracture initiation suggest a reproducible material deformation behaviour within both component sides.

Based on this observation, the measured force-displacement curves can be separated into two load stages as demonstrated in Figure 7.2.3b. Each load stage is defined by maximum force F_i and corresponding displacement d_i. Dissipated energy E_i within a load stage can be computed by numerical integration. Table 7.2.1a contains these measurements for all three-point bending tests. The relationship between both energies is given in the last column. It is obvious that the relationship is not constant. A scatter plot of energy E_1 and energy E_2 is given in Figure 7.2.3c. According to Equation (3.5.5), the correlation coefficient of both energies becomes $r_{E_1E_2} = -0.15$ which indicates no distinct linear correlation as seen in the scatter plot. Therefore, it is considered that the results obtained from first load stage and the results obtained from second load stage are not correlated. This implies that a high ductility in the first load stage does not necessarily indicate a high ductility in the second load stage. Furthermore, this means that failure on the gating side and failure on the vacuum side can be considered as independent events.

The graph presented in Figure 7.2.4a shows the results obtained from the different displacement measurements of a three-point bending test (test #7). The graph shows displacement of the testing machine on the abscissa, force of the testing machine on the right ordinate and displacement measurement on the left ordinate. The displacement measured by the extensometer at vacuum side is plotted in red ($d_3(d_1)$) and the displacement

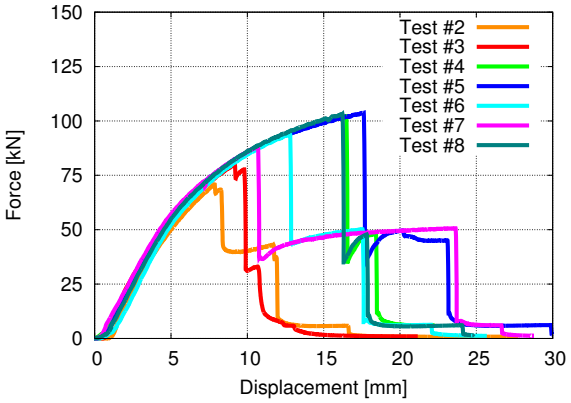

(a) Experimental force-displacement curves obtained from seven parallel tests.

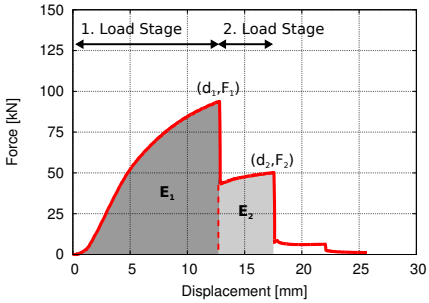

(b) Definition of first load stage and second load stage (including energy E_1 and energy E_2).

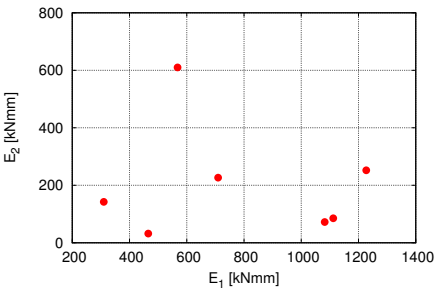

(c) Scatter plot of energy E_1 and energy E_2 obtained from seven parallel tests.

Figure 7.2.3: Experimental results obtained from seven parallel three-point bending tests (measured by the testing machine).

measured by the extensometer at gating side in blue ($d_2(d_1)$). The displacement measured by the testing machine is plotted in black ($d_1(d_1)$). In addition, the force-displacement curve measured by the testing machine is given in grey ($F_1(d_1)$). It is seen that the extensometer measurements do not correspond to each other. The displacement measured at the vacuum side is larger than the displacement measured at the gating side as well as the displacement measured by the testing machine. The mean of both extensometer measurements is given by the green curve $\left(d_{\mu 23}(d_1)\right)$. It is seen that the mean corresponds exactly to the displacement measured by the testing machine. The gap between both extensometer measurements is given by the magenta curve ($d_{\delta 23}(d_1)$). It is seen that the gap increases during loading. An offset in the gap curve is found when the vacuum side fails. A reverse offset in the gap curve is found when the gating side fails. Afterwards, the gap curve reaches an almost constant level. In the same way, results obtained from six of seven parallel three-point bending tests are analysed, see Figure A.2.4 of Appendix A.4. The gap curves obtained from these tests are compared in the graph of Figure 7.2.4b. The measured gaps show comparable behaviour with test #6 as an exception. Here, the gating side failed first and, consequently, the graph shows the inverse behaviour.

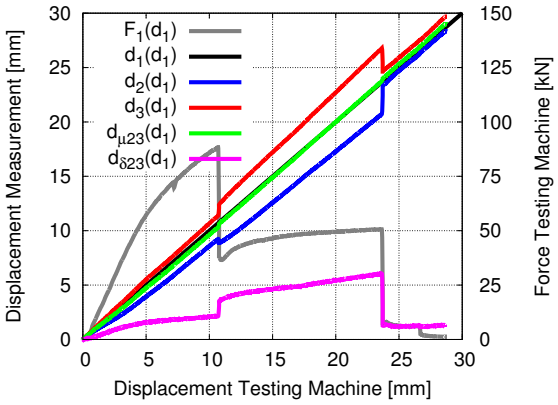

(a) Experimental measurements obtained from a three-point bending test (test #7): Force $F_1(d_1)$ measured by testing machine (grey), displacement $d_1(d_1)$ measured by testing machine (black), displacement $d_2(d_1)$ measured by extensometer at gating side (blue), displacement $d_3(d_1)$ measured by extensometer at vacuum side (red), mean $d_{\mu 23}(d_1)$ of both extensometer measurements (green) and gap $d_{\delta 23}(d_1)$ between both extensometer measurements (magenta).

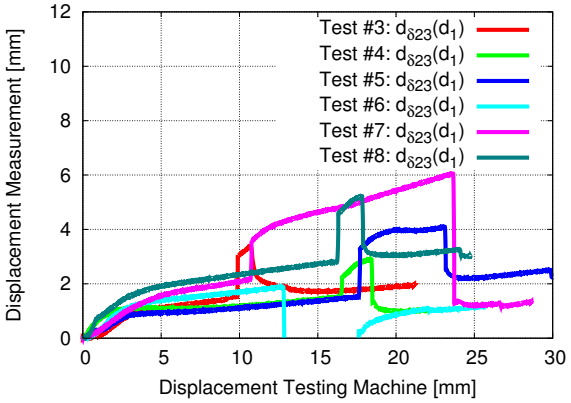

(b) Gap $d_{\delta 23}(d_1)$ between both extensometer measurements obtained from six parallel three-point bending tests.

Figure 7.2.4: Experimental results obtained from six parallel three-point bending tests: Force and displacement measured by testing machine and relative displacements measured by extensometers on gating side and vacuum side.

#	First Load Stage			Second Load Stage			
	F_1 [kN]	d_1 [mm]	E_1 [kNmm]	F_2 [kN]	d_2 [mm]	E_2 [kNmm]	E_2/E_1 [%]
2	68.48	7.52	310.19	43.00	10.92	142.44	45.92
3	77.75	9.78	465.59	33.05	10.66	32.04	6.88
4	102.23	16.47	1111.81	48.06	18.34	85.24	7.67
5	103.70	17.62	1226.91	45.12	23.09	252.29	20.56
6	93.85	12.54	709.51	50.24	17.25	226.50	31.92
7	88.44	10.65	567.78	50.66	23.56	609.99	107.43
8	103.15	16.22	1081.92	47.81	17.81	72.27	6.68

(a) Maximum force F_i, displacement at maximum force d_i and energy E_i for each load stage (measured by the testing machine).

#	First Load Stage		Second Load Stage	
	g_1 [mm]	α_1 [°]	g_2 [mm]	α_2 [°]
3	1.42	0.33	3.37	0.78
4	1.52	0.35	2.91	0.67
5	1.54	0.36	4.10	0.95
7	2.18	0.50	6.05	1.40
8	2.81	0.65	5.23	1.21
$\bar{x}$	1.89	0.44	4.33	1.00

(b) Gap magnitudes g_i and rotation angles α_i for each load stage (measured by the extensometers).

Table 7.2.1: Quantities measured from the experimental results obtained from seven parallel three-point bending tests.

Based on these measurements, it is suggested that the punch rotated slightly towards the vacuum side during loading. The rotation mode is illustrated enlarged in Figure 7.2.5. It seems reasonable that the rotation was due to the additional bending stiffness of the long rib close to the gating side, see Figure 7.1.1c, and a non-rigid connection between punch and testing machine. Further, each gap curve starts to increase from zero without any initial gap. Hence, it is supposed that the punch rotations during testing were only of elastic nature. Each gap curve can be separated according to the load stages and the offsets, respectively. The gap magnitudes g_i were measured at the beginning of each offset. Based on gap magnitudes g_i, the equivalent angle α_i of the punch rotation was estimated according to

$$\alpha_i = \arctan\left(\frac{g_i}{l_p}\right) \tag{7.2.1}$$

where l_p denotes the length of the punch which is approximately 248 mm. In Table 7.2.1b, gap magnitudes g_i and rotation angles α_i measured from each three-point bending test result are summarised. The gap between both extensometer measurements reached in average a magnitude of approximately 1.89 mm within the first load stage and a magnitude of approximately 4.33 mm within the second load stage. These averaged gaps correspond to rotation angles of 0.44° and 1.00°.

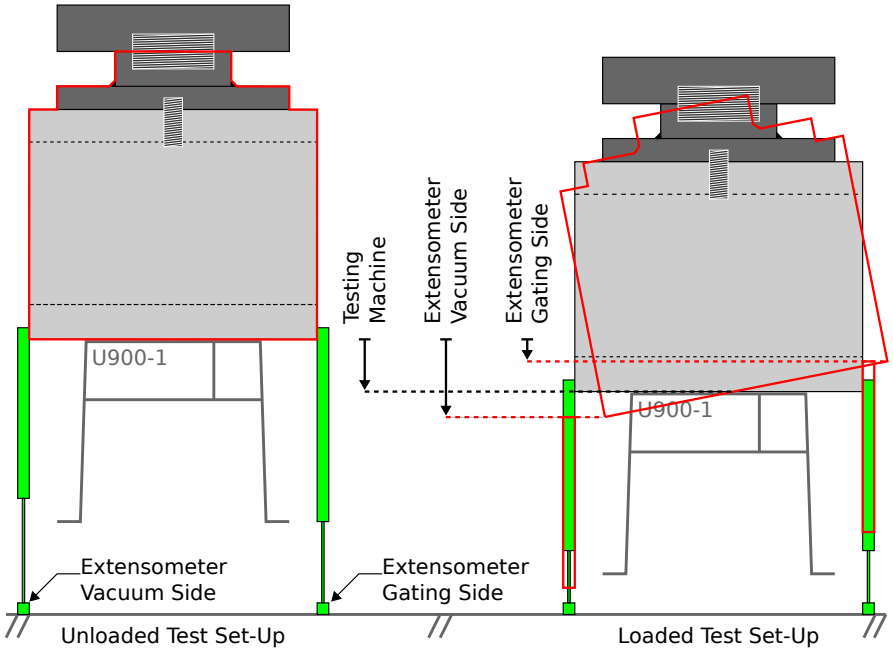

Figure 7.2.5: Drawing of the punch rotation during three-point testing.

7.3 Axial Compression Tests

In addition to the bending test analysis, the structural behaviour of the HPDC component U900-1 was analysed in an axial compression deformation mode. Four axial compression tests were performed on the halves of U900-1 components. In the following, the applied test set-up and the experimental results are presented and discussed.

7.3.1 Test Set-Up

Axial compression tests were performed on half U900-1 components to avoid column buckling. Hence, two U900-1 components were cut into equal parts of 440 mm length prior to testing. The applied cutting pattern is shown in Figure 7.3.1a. All cut surfaces were machined parallel to ensure pure axial loading. A technical drawing of the axial compression test set-up is illustrated in Figure 7.3.1. The modified U900-1 component was placed between the test foundation and a circular loading plate with radius of 120 mm. The loading plate was made of high strength steel and mounted to the testing machine via a threaded joint. The axial compression loading was applied between test foundation and loading plate which were assumed to be rigid. An image of the axial compression test set-up is given in Figure 7.3.1c.

The four compression specimens were tested in an Instron servo-hydraulic 250 kN testing machine. The loading plate was displaced at a predefined and constant velocity of $3\,\frac{\text{mm}}{\text{min}}$. It is assumed that each test was performed under quasi-static loading conditions. Force and displacement were measured by the testing machine. In addition, the relative displacement between test foundation and loading plate was measured using an extensometer. The extensometer position is shown in Figure 7.3.1b and Figure 7.3.1c.

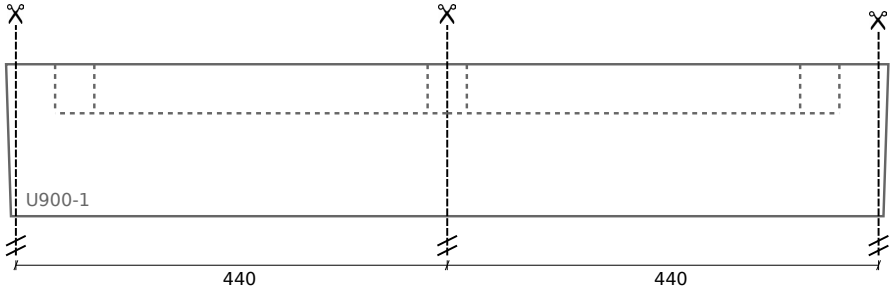

(a) Cutting pattern of the U900-1 component for axial compression tests.

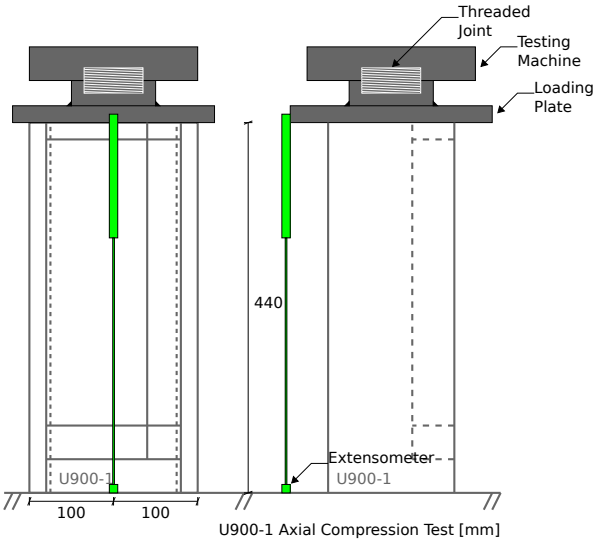

(b) Technical drawing of the axial compression test set-up.

(c) Image of the test set-up.

Figure 7.3.1: Axial compression test set-up: Cutting pattern, technical drawing and image of the test set-up.

7.3.2 Experimental Results

The structural behaviour of the modified U900-1 components subjected to axial compression was dominated by local buckling. Local buckling started first in the upper third of the gating side as well as the vacuum side. Subsequently, local buckling continued in the intermediate part. In Figure 7.3.2, images of the deformed and fractured compression specimens are presented. Cracks formed first on the outer parts of gating side and vacuum side, see Figure 7.3.2a. Afterwards, cracks formed in the most deformed area close to the edges between both component sides and intermediate part, see Figure 7.3.2b. The axial compression loading of each specimen was limited by buckling of gating side and vacuum side as well as subsequent buckling of the intermediate part. It is well known that local buckling is defined by geometry and material properties as well as their imperfection. Hence, the buckling pattern differed somewhat between the four specimens.

The force-displacement curves obtained from the four parallel axial compression tests are presented in Figure 7.3.3. The curves were measured by the testing machine. The test results show a repeatable force-displacement behaviour with a negligible scatter com-

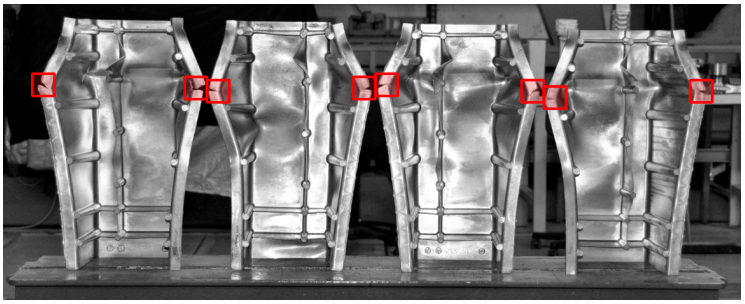

(a) Fracture initiation on the outer parts of gating side and vacuum side.

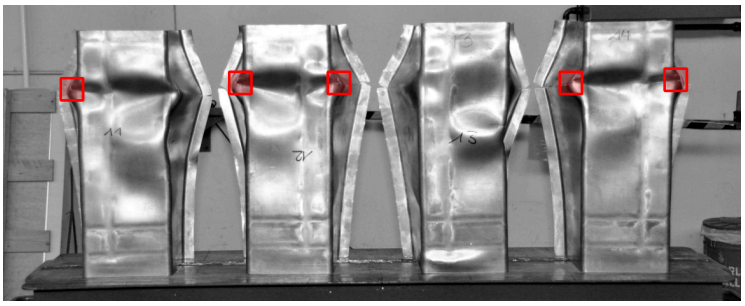

(b) Fracture initiation in the edges between both component sides (gating side and vacuum side) and intermediate part.

Figure 7.3.2: Deformed and fractured modified U900-1 component subjected to axial compression.

pared to the bending test results. Test #11 exhibits a higher ultimate load. The distinct steep drops in force level indicate fracture initiation and the corresponding measurements can be found in Table 7.3.1a. However, these drops have only a minor influence on the overall force-displacement behaviour.

The graph presented in Figure 7.3.4a shows the results obtained from the different displacement measurements of an axial compression test (test #13). The graph shows displacement of the testing machine on the abscissa, force of the testing machine on the right ordinate and displacement measurement on the left ordinate. The displacement measured by the extensometer is plotted in blue ($d_2(d_1)$). The displacement measured by the testing machine is plotted in black ($d_1(d_1)$). In addition, the force-displacement curve measured by the testing machine is given in grey ($F_1(d_1)$). The gap between the displacement measurements is given by the magenta curve ($d_{\delta 12}(d_1)$). It is seen that the displacement measured by the extensometer and the displacement measured by the testing machine do not correspond to each other. When a certain load level is reached, the extensometer measurement intersects the testing machine measurement and the gap between them starts to grow. It is seen that the intersection separates the force-displacement curve into its linear and non-linear part. However, it is seen that the gap curve is not influenced by the fracture initiation. In the same way, the results obtained from four parallel axial compression tests are analysed, see Figure A.4.2 of Appendix A.4. The gap curves obtained from these tests are compared in the graph of Figure 7.3.4b. The measured gaps show comparable behaviour except from test #11. Here, it is assumed that the extensometer

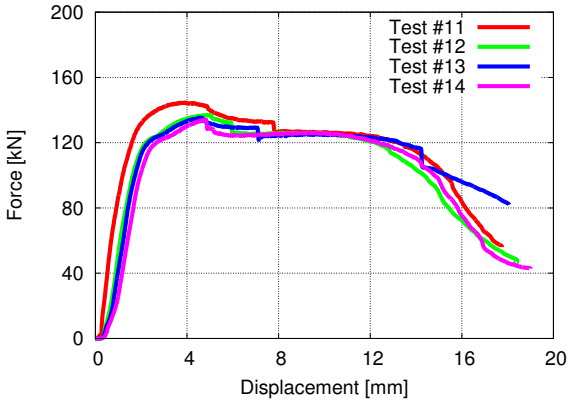

Figure 7.3.3: Experimental force-displacement curves obtained from four parallel axial compression tests (measured by the testing machine).

#	F_1 [kN]	d_1 [mm]
11	132.25	8.77
12	132.06	6.93
13	128.91	7.08
14	133.01	4.84

(a) Force at fracture initiation F_1 and displacement at fracture initiation d_1 (measured by the testing machine).

#	g_1 [mm]	α_1 [°]
(11	0.91	0.22)
12	2.55	0.61
13	2.78	0.66
14	2.33	0.56
$\bar{x}$	2.55	0.61

(b) Gap magnitude g_1 and rotation angle α_1 (measured by the extensometer and the testing machine).

Table 7.3.1: Quantities measured from the experimental results obtained from four parallel axial compression tests.

was not accurately fixed and has slid during testing.

Based on these measurements, it is suggested that the loading plate rotated slightly during loading towards the open side of the U900-1 component as illustrated enlarged in Figure 7.3.5. It is obvious that the rotation was caused by the non-symmetric cross-section, see Figure 7.1.1b, and a non-rigid connection between loading plate and testing machine as already seen in the bending tests. Moreover, each gap curve starts to increase from zero without any initial gap. Hence, it is also supposed that the loading plate rotations during testing were only of elastic nature as already observed in the bending tests. The ultimate magnitude g_1 was measured from each gap curve. Based on magnitude g_1, the equivalent angle α_1 of the loading plate rotation was estimated according to

$$\alpha_1 = \arctan\left(\frac{g_1}{r_p}\right) \tag{7.3.1}$$

where r_p denotes the radius of the loading plate which is approximately 120 mm. In Table 7.3.1b, gap magnitude g_1 and rotation angle α_1 measured from each axial compression

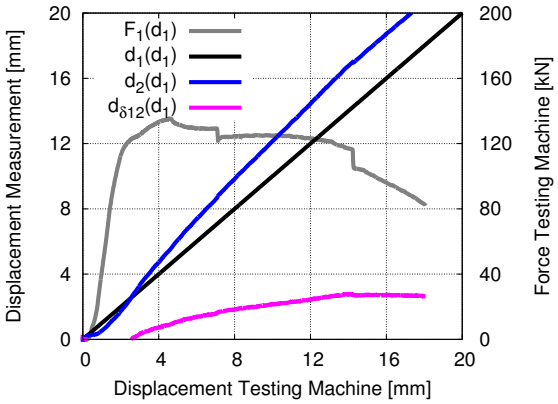

(a) Experimental measurements obtained from an axial compression tests (test #13): Force $F_1(d_1)$ measured by the testing machine (grey), displacement $d_1(d_1)$ measured by the testing machine (black), displacement $d_2(d_1)$ measured by the extensometer (blue) and gap $d_{\delta 12}(d_1)$ between both displacement measurements (magenta).

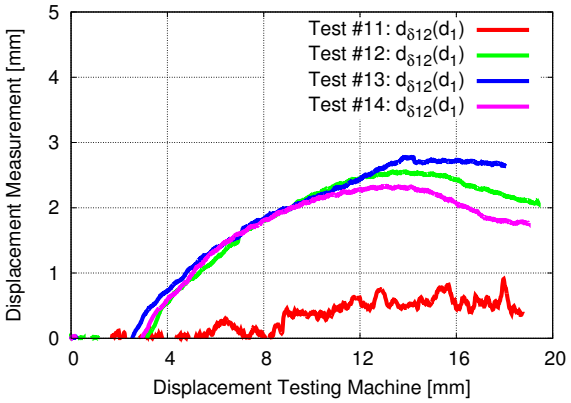

(b) Gap $d_{\delta 12}(d_1)$ between both displacement measurements obtained from four parallel axial compression tests.

Figure 7.3.4: Experimental results obtained from four parallel axial compression tests: Force and displacement measured by the testing machine and relative displacement measured by the extensometer.

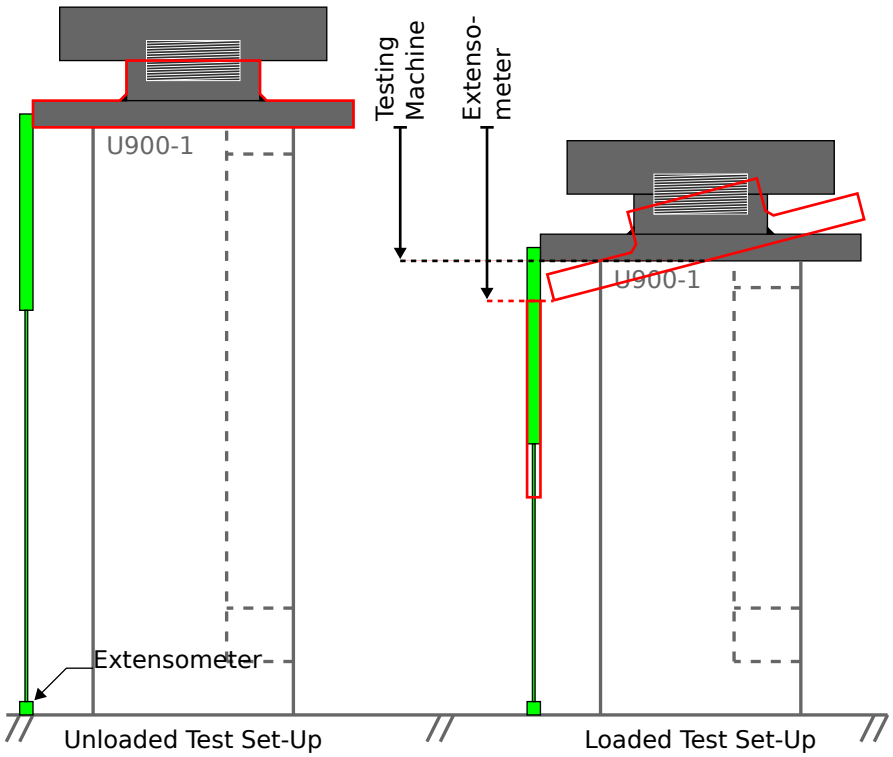

Figure 7.3.5: Drawing of the loading plate rotation during axial compression testing.

test result are summarised. The gap between the two displacement measurements reaches in average a magnitude of approximately 2.55 mm. This averaged gap corresponds to a rotation angle of 0.61 °.

7.4 Concluding Remarks

The experimental results of the three-point bending tests showed that the structural behaviour of the U900-1 component made of the HPDC alloy Castasil-37 in casting condition (F) was dominated by the material ductility in gating side and vacuum side. A crack formed usually first on the vacuum side. This observation confirmed the assumption that the material ductility was not homogeneously distributed. It can be assumed that the material ductility was essentially influenced by the casting system. Moreover, the scattering failure behaviour on both component sides caused a strong scatter in the structural response. In particular, the material tensile ductility dominated fracture initiation. As a result, it is assumed that the material ductility exhibited strong scatter caused by casting defects. In contrast, the experimental results of the axial compression tests showed a repeatable structural behaviour of the U900-1 component in terms of force-displacement measurements. Here, local buckling and geometrical imperfections had a major influence on the structural response. The local displacement measurements by the extensometers in the three-point bending tests as well as in the axial compression tests showed that the connection between impactor and testing machine was not rigid.

In summary, it is concluded that the global systematic variation as well as the local

pseudo-random variation of casting defects influenced strongly the material ductility in the U900-1 components. Especially, the experimental results obtained from the three-point bending tests confirmed this statement:

- Most components failed first on the vacuum side. This was caused by the global systematic variation depending on the casting system.
- Fracture initiation on both component sides occurred at different force and displacement levels: This was caused by the local pseudo-random variation depending on casting process fluctuations.

Therefore, a detailed experimental characterisation of the material ductility of the HPDC alloy Castasil-37 in casting condition (F) is required to achieve a deeper understanding of the influence of casting defects. Tensile test specimens need to be machined from the gating side, the vacuum side and the intermediate part of U900-1 components. Furthermore, Tensile test specimens need to be machined from duplicated positions within these parts. This sampling approach enables an experimental analysis of the global systematic variation and the local pseudo-random variation of casting defects and their influence on the material tensile ductility.

Chapter 8

Material Characterisation

In the previous chapter, the structural behaviour of the U900-1 component made of the HPDC alloy Castasil-37 in casting condition (F) was analysed under bending loading as well as under axial compression loading. Especially, the bending test results showed a strong variation in the structural response. It was concluded that the variation was caused by the two characteristic variations of casting defects and their influence on the material ductility. Therefore, it can be stated that the casting system causes a global systematic variation in the material ductility and the fluctuations during the casting process causes a local pseudo-random variation in the material ductility.

The objective of the material characterisation presented in the current chapter is the experimental analysis of this statement. This means that the material characterisation was focused on measuring the global systematic variation as well as the local pseudo-random variation in the material ductility of the HPDC alloy Castasil-37 in casting condition (F). Hence, uniaxial tensile test specimens were machined from different extraction positions of the U900-1 component. Further, tensile test specimens were machined from duplicated extraction positions of multiple U900-1 components. Standard tensile tests were carried out using these specimens and the material ductility was measured from the test results. This sampling approach enabled an analysis of the global systematic variation as well as the local pseudo-random variation in the material ductility. Two material characterisations were performed. The first one was used to get a basic understanding of the material behaviour. The second one was focused on an extensive statistical analysis of the material ductility and on the two types of variation. Moreover, the influence of the gauge volume on the material ductility was investigated using tensile test result obtained from specimens which were equal in shape but different in size. The results obtained from the first and second material characterisation are presented, discussed and concluded in the current chapter. But first, the applied test set-up, the analysis of a test result and an approach to analyse statistically the samples generated in each material characterisation are presented.

8.1 Uniaxial Tensile Test

The uniaxial tensile test is probably the best known and most common mechanical material test. A sample of a material in form of a tensile specimen is subjected to a controlled tensile loading until it fractures. Here, the specimen shape ensures a uniaxial tensile stress state in the gauge section until a neck develops. The applied force and the elongation of the specimen are measured during testing. Based on these measurements, the force-

displacement relation of the uniaxial tensile test is obtained. The analysis and interpretation of the force-displacement relation provide basic information on the strength and the ductility of the considered material. Furthermore, the material behaviour in terms of direction, strain-rate and thermal dependence can be analysed by a combination of various separate tensile tests. The uniaxial tensile test is a fundamental test in material science and a standard test in engineering applications. The uniaxial tensile test set-up applied in the present work is presented in the following. Further, the analysis of the measurements obtained from this test set-up is shown. Moreover, an approach to analyse statistically a database generated from multiple tensile tests is described.

8.1.1 Test-Set Up

In the present work, uniaxial tensile tests were performed on standard flat tensile specimens. The flat tensile specimen geometry is characterised by two shoulders, a long gauge section in between and a constant thickness as seen in Figure 8.1.1a. The uniaxial tensile loading in the gauge section was applied through the shoulders. Since the gauge section width is constant and smaller than the shoulder width, deformation and fracture initiation were expected to occur within the gauge section. Each tensile specimen was mounted to the testing machine by metal pins which were placed through the holes in the shoulders as demonstrated in Figure 8.1.1a. The pins were assumed to be rigid compared to the tensile specimens. The uniaxial tensile tests were performed in a universal Dartec M1000/RK hydraulic testing machine at ambient temperature. The lower pin was fixed while the upper pin was displaced at a predefined and constant velocity of $1.8\,\frac{\text{mm}}{\text{min}}$. It is assumed that each tensile test was performed under quasi-static loading conditions. The applied force was obtained from the testing machine, whereas the elongation of the gauge section was measured by a MTS clip-on extensometer with a gauge length of 30 mm. This measuring approach implies that any strain localisation due to necking within the gauge section was measured in an averaged manner, see Chapter 4.3.5. However, the uniaxial tensile tests were expected to show only small deformations and no distinct strain localisation prior to fracture initiation. Hence, the applied measuring approach was considered to provide sufficient results. The Instron 8800 controller including the software Console was used for controlling the test procedure and recording data from the testing machine and the extensometer. The initial width and thickness of the gauge section were measured by a Limit micrometer prior to testing. An image of a mounted tensile specimen in the testing machine including the attached extensometer is illustrated in Figure 8.1.1b.

The tensile specimens were machined from various positions within the U900-1 component according to a predefined extraction plan. All details on the U900-1 component and the applied HPDC alloy Castasil-37 can be found in Chapter 7.1. The extraction plan was chosen according to the underlying casting system, see Figure 7.1.1d. A technical drawing of the unfolded U900-1 component is presented in Figure 8.1.2. The component is theoretically divided into the five parts Inlet Flange (IF), Inlet Web (IW), Big Flange (BF), Outlet Web (OW) and Outlet Flange (OF). Part IF is the part where the gates are located and part OF is the part where the vacuum channels are located. Here, the specimens were only machined from thin-walled parts with an approximate thickness of 2.5 mm. Further, the same extraction plan was applied to several U900-1 components. Through this sampling approach, it was possible to analyse the influence of the extraction position as well as the local scatter (within an extraction position) on the material tensile behaviour. Moreover, specimen geometries with different gauge volumes were investigated in order to analyse any size effects.

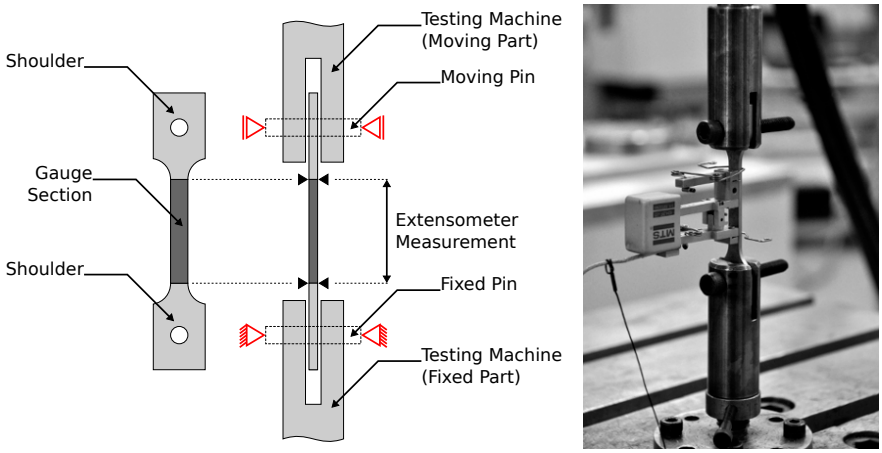

(a) Technical drawing of a flat tensile specimen and the applied uniaxial tensile test set-up.

(b) Image of a mounted specimen with clip-on extensometer.

Figure 8.1.1: Technical drawing and image of the applied uniaxial tensile test set-up.

8.1.2 Mechanical Analysis

The above described test set-up provides the force-elongation curve of a uniaxial tensile test. The applied force F on the specimen is measured by the testing machine and the elongation$\triangle l$ of the gauge section is measured by the extensometer. In Figure 8.1.3a, a typical force-elongation curve of a metal is presented. Stress-strain curves can be constructed from the force-elongation curve and, as a result, basic information of strength and ductility of the underlying material is provided. In the present work, the mechanical analysis of a uniaxial tensile test is based on the one presented in the ASM Handbook Volume 8 [69]. A brief description is presented in the following.

The engineering stress s is given by the relation of force F and initial cross-sectional area A_0 (of the gauge section),

$$s = \frac{F}{A_0}. \tag{8.1.1}$$

The engineering strain e is given by the relation of elongation $\triangle l$ and initial gauge length l_0,

$$e = \frac{\triangle l}{l_0} = \frac{l - l_0}{l_0} \tag{8.1.2}$$

where l denotes the displaced gauge length. Figure 8.1.3b shows the engineering stress-strain curve derived from the current force-elongation curve. Since engineering stress s and engineering strain e are derived by dividing force F and elongation $\triangle l$ by constant factors, the engineering stress-strain curve has the same shape as the force-elongation curve.

The engineering stress-strain curve given in Figure 8.1.3b is representative for most common metal alloys. The curve can be separated into an elastic region and a plastic region. In the elastic region, stress s is linearly proportional to strain e. When stress s exceeds the yield stress, the deformations become plastic and the material hardens. Consequently, stress s increases with increasing strain e until the tensile strength at peak force is reached. During material hardening, the cross-sectional area decreases uniformly due

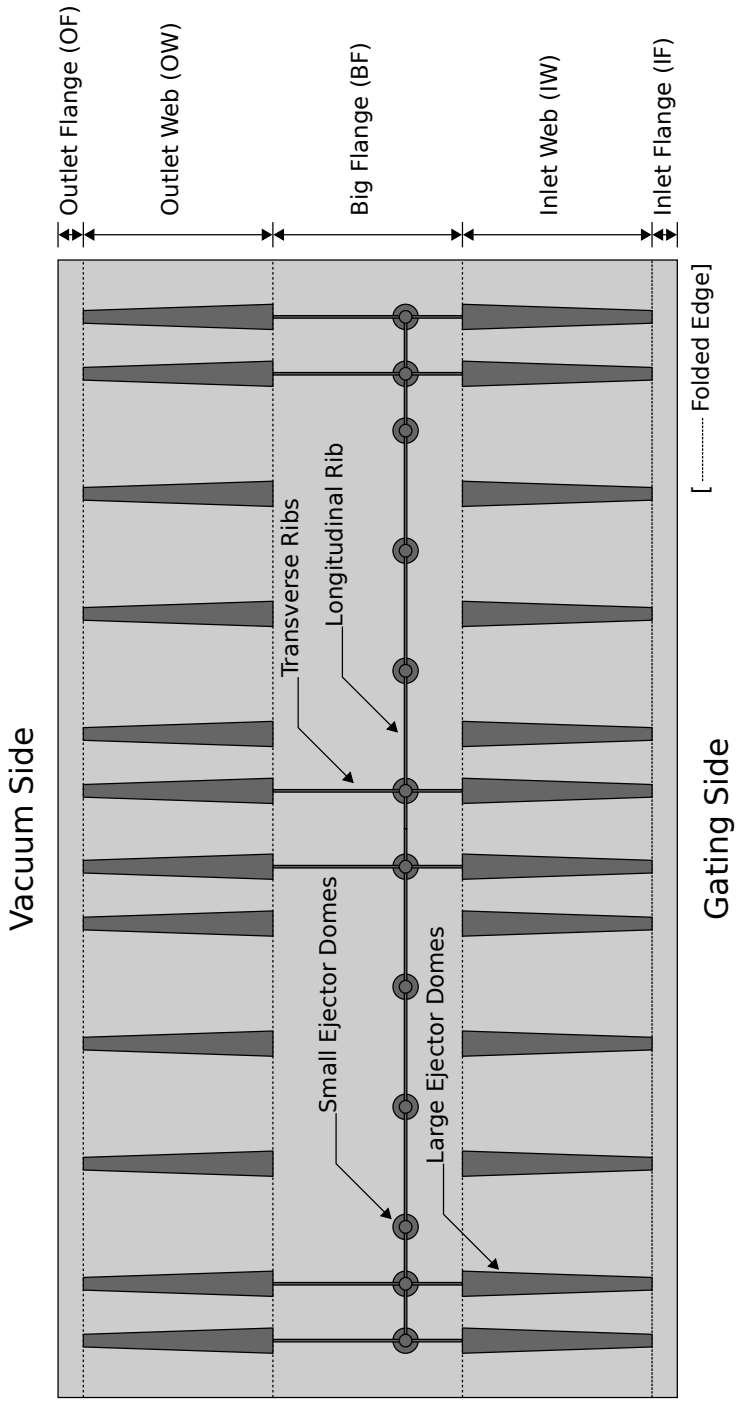

Figure 8.1.2: Definition of U900-1 component parts (unfolded geometry).

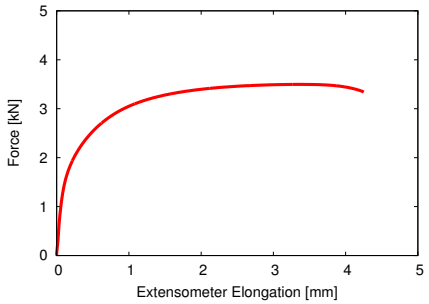

(a) Force-displacement curve.

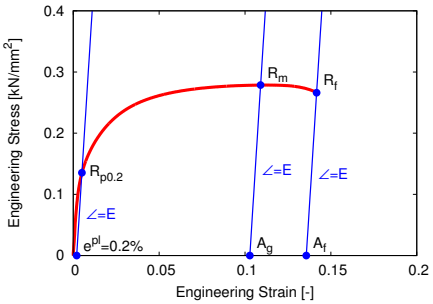

(b) Engineering stress-strain curve.

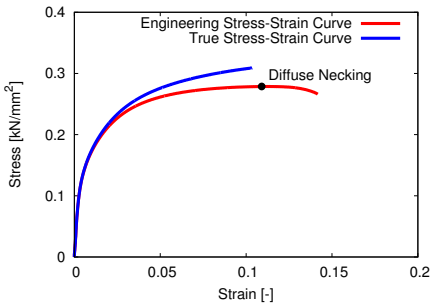

(c) Engineering stress-strain curve and true stress-strain curve.

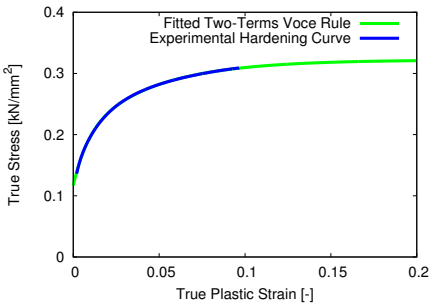

(d) Experimental hardening curve and fitted two-terms Voce rule.

Figure 8.1.3: Mechanical analysis of the result obtained from a uniaxial tensile test.

to the conservation of volume during plastic flow, also known as Poisson effect, and the stress distribution is nearly uniform within the gauge section. In case of metals, small elastic strains are assumed. When the tensile strength is reached, the material behaviour becomes unstable due to diffuse necking. The stress distribution localises in the weakest point of the gauge section and a neck develops. As a result, the cross-sectional area in the neck decreases more quickly than in other parts of the gauge section. Consequently, stress s decreases with increasing strain e until the specimen fractures.

According to metal plasticity, engineering strain e can be additively decomposed into an elastic part e^{el} and a plastic part e^{pl},

$$e = e^{el} + e^{pl} \tag{8.1.3}$$

where $e^{el} \ll e^{pl}$ is expected. The elastic strain e^{el} is given by Hooke's law

$$e^{el} = \frac{s}{E} \tag{8.1.4}$$

where E denotes Young's modulus. Based on this, the engineering stress-strain curve is characterised through the following quantities:

- Offset yield stress $R_{p0.2}$: The stress which corresponds to a plastic strain e^{pl} of 0.2 % is defined as offset yield stress $R_{p0.2}$.
- Tensile strength R_m and uniform strain A_g: The stress at peak load is defined as tensile strength R_m and the corresponding plastic strain is uniform strain A_g.

– Fracture strength R_f and fracture strain A_f: The stress at fracture initiation is defined as fracture strength R_f and the corresponding plastic strain is fracture strain A_f.

In Figure 8.1.3b, these quantities are highlighted.

The engineering stress-strain curve is based on initial cross-sectional area A_0 and initial gauge length l_0. However, gauge length l and cross-sectional area A change continuously during tensile loading. When the point of diffuse necking is reached, cross-sectional area A decreases rapidly and the load required to continue deformation falls off. Consequently, engineering stress s decreases beyond the point of diffuse necking. Actually, the flow stress increases until fracture initiation due to strain hardening. This means that the true stress σ required to continue deformation should also increase. Hence, the measurement of true stress σ is based on the actual cross-sectional area A and increases continuously until fracture initiation. The corresponding strain measurement is based on the actual gauge length l and is called true strain or logarithmic strain ε.

True strain ε can be determined directly from engineering strain e according to

$$\varepsilon = \ln\left(\frac{l}{l_0}\right) = \ln(1+e). \tag{8.1.5}$$

True stress σ is given by the relation

$$\sigma = \frac{F}{A}. \tag{8.1.6}$$

Due to nearly plastic incompressibility of metals, the volume is considered to remain constant during loading, so that

$$A_0 l_0 = A l. \tag{8.1.7}$$

Here, the elastic volume change is neglected due to the small elastic strains in metals. As a result, true stress σ can be expressed in terms of engineering stress s and engineering strain e,

$$\sigma = \frac{F}{A_0}\frac{l}{l_0} = s(1+e). \tag{8.1.8}$$

It is noted that a uniform strain distribution along the gauge section is assumed in Equation (8.1.5) and Equation (8.1.8). As already mentioned, the strain distribution localises within the gauge section when the point of diffuse necking is reached. The extensometer measures the elongation of the entire gauge section. Hence, the elongation is measured in an averaged manner. This is correct as long as the strain distribution is uniform within the gauge section. Hence, Equation (8.1.5) and Equation (8.1.8), respectively, are only applicable until the point of diffuse necking. In Figure 8.1.3c, the engineering stress-strain curve (red) and the corresponding true stress-strain curve (blue) are compared. It is seen that the true stress-strain curve is always to the left. It is noted that the force is measured in terms of a cross-section force. This means that the force equals the resultant force of the stress distribution on the cross-section and the particular stress state in a material point is unknown.

The hardening curve can be derived from the true stress-strain curve. According to Equation (8.1.3) and Equation (8.1.4), the true plastic strain ε^{pl} can be expressed as

$$\varepsilon^{pl} = \varepsilon - \frac{\sigma}{E}. \tag{8.1.9}$$

The graph of true stress σ versus true plastic strain ε^{pl} is called hardening curve. The hardening curve derived from the current true stress-strain curve is given in Figure 8.1.3d. The hardening curve is usually described by a mathematical expression, see Chapter 4.1.5,

and the respective hardening coefficients are identified from curve fitting. In the present work, the physically based two-terms Voce rule is applied,

$$\sigma_Y\left(\varepsilon^{pl}\right) = \sigma_0 + \sum_{i=1}^{2} Q_i\left(1 - \exp\left(-C_i\,\varepsilon^{pl}\right)\right) \tag{8.1.10}$$

where the hardening coefficients σ_0, Q_1, C_1, Q_2 and C_2 can be found from a least-squares curve fit. In Figure 8.1.3d, an experimental hardening curve (blue) and a fitted two-terms Voce rule (green) are compared. For further information on the mechanical analysis of uniaxial tensile tests, it is referred to the book by Lemaitre and Chaboche [74] and the ASM Handbook Volume 8 [69].

Based on a uniaxial tensile test, the material ductility can be measured by the true strain at fracture initiation ε_{fr} which can be estimated by

$$\varepsilon_{fr} = \ln\left(\frac{l_{fr}}{l_0}\right) \tag{8.1.11}$$

where l_{fr} denotes the gauge length at fracture initiation. Consequently, the true plastic strain at fracture initiation ε_{fr}^{pl} can be estimated using Equation (8.1.9) and Equation (8.1.10),

$$\varepsilon_{fr}^{pl} = \varepsilon_{fr} - \frac{\sigma_Y\left(\varepsilon_{fr}^{pl}\right)}{E}. \tag{8.1.12}$$

In the present work, the material ductility is measured according to the Cockcroft-Latham criterion given in Equation (4.3.23). The critical value W_c can be found by integration of Equation (8.1.10) and the evaluation of the integral between $\varepsilon^{pl} = 0$ and $\varepsilon^{pl} = \varepsilon_{fr}^{pl}$, so that

$$W_c = \int_0^{\varepsilon_{fr}^{pl}} \sigma_Y\left(\varepsilon^{pl}\right) d\,\varepsilon^{pl}. \tag{8.1.13}$$

The mechanical analysis of a uniaxial tensile test is summarised in Figure 8.1.4. It is noted that the hardening coefficients σ_0, Q_1, C_1, Q_2 and C_2 were found from a least-squares curve fit using gnuplot [115] and the values for ε_{fr}^{pl} and W_c were numerically computed using MATLAB [83].

As already mentioned, the above presented measurements including the measurements of the material ductility by Equation (8.1.11), Equation (8.1.12) and Equation (8.1.13) are based on the force measured by the testing machine and the elongation measured by the extensometer. Hence, these measurements are correct as long as the strain distribution is uniform within the gauge section. When the point of diffuse necking is reached and the strain distribution localises, these quantities are computed in an averaged manner (especially the measurements of the material ductility) and are no longer representative for a material point. The numerical study discussed in Chapter 4.3.5 showed that critical value W_c computed according to Equation (8.1.13) is equivalent to the average of all values of the W distribution within the gauge section at fracture initiation. This means that critical value W_c represents an averaged critical value which is directly related to the volume of the gauge section. This implies that the material within the gauge section fails when the averaged loading reaches a critical value. Consequently, the above presented measurements are primary measurements related to the volume of the gauge section. Moreover, the tensile specimens made of the HPDC alloy Castasil-37 in casting condition (F) were expected to fail without distinct necking and, consequently, the above presented measurements can be used without any concern.

1. Force-displacement curve $F(\triangle l)$:
   (a) Force obtained from testing machine: F
   (b) Elongation measured by extensometer: $\triangle l = l - l_0$
2. Engineering stress-strain curve $s(e)$:
   (a) Engineering strain: $e = \frac{l-l_o}{l_0}$
   (b) Engineering stress: $s = \frac{F}{A_0}$
3. Mechanical quantities $\left[R_{p0.2}, R_m, R_f, A_g, A_f\right]$:
   (a) Engineering plastic strain: $e^{pl} = e - \frac{s}{E}$
   (b) Offset yield stress: $R_{p0.2} = s\left(e^{pl} = 0.002\right)$
   (c) Tensile strength and uniform strain: $R_m(A_m) = \max\left[s\left(e^{pl}\right)\right]$
   (d) Fracture strength and fracture strain: $R_f\left(A_f\right) = s\left(\max\left[e^{pl}\right]\right)$
4. True stress-strain curve $\sigma(\varepsilon)$:
   (a) True strain: $\varepsilon = \ln(1+e)$
   (b) True stress: $\sigma = s(1+e)$
5. Hardening curve $\sigma\left(\varepsilon^{pl}\right)$ and Voce rule $\sigma_Y\left(\varepsilon^{pl}\right)$:
   (a) True plastic strain: $\varepsilon^{pl} = \varepsilon - \frac{\sigma}{E}$
   (b) Voce rule (two-terms): $\sigma_Y\left(\varepsilon^{pl}\right) = \sigma_0 + \sum_{i=1}^{2} Q_i\left(1 - \exp\left(-C_i\varepsilon^{pl}\right)\right)$
   (c) Hardening parameters: $\sigma_Y\left(\varepsilon^{pl}\right) \equiv \sigma\left(\varepsilon^{pl}\right) \rightarrow [\sigma_0, Q_i, C_i]$
6. Cockcroft-Latham failure parameter W_c:
   (a) True failure strain: $\varepsilon_{fr} = \ln\left(\frac{l_{fr}}{l_0}\right)$
   (b) True plastic failure strain: $\varepsilon_{fr}^{pl} = \varepsilon_{fr} - \frac{\sigma_Y\left(\varepsilon_{fr}^{pl}\right)}{E}$
   (c) Cockcroft-Latham parameter: $W_c = \int_0^{\varepsilon_{fr}^{pl}} \sigma_Y\left(\varepsilon^{pl}\right) d\varepsilon^{pl}$

Figure 8.1.4: Mechanical analysis of the result obtained from a uniaxial tensile test.

8.1.3 Statistical Analysis

The sampling approach applied in the present work provided samples generated from various extraction positions within the U900-1 component. A sample consists of all uniaxial tensile specimens which were machined from the same position. This implies that the number of samples equals the number of extraction positions and the size of a sample equals the number of components which were used for testing. The tensile test results obtained from specimens of the same sample as well as the measurements derived from these enables to quantify the sample. As a result, a database is generated for an extensive statistical analysis. The main objective of the statistical analysis is to study the influence of casting process and casting defects on the material failure behaviour. It is expected that the material failure behaviour is most affected by casting defects. Hence, the statistical analysis is restricted to measurements of critical value W_c. This means that a sample is given by the n critical values W_c^i obtained from the n specimens which belong to this sample. The statistical analysis applied in the present work is presented in the following.

The first objective of the statistical analysis is the identification of areas in the U900-1 component with comparable material failure behaviour. Here, samples generated from different extraction positions are analysed through statistical hypothesis testing. In the following, the applied approach of statistical hypothesis testing is presented. The basics of statistical hypothesis testing were already introduced in Chapter 3.6.

Two samples are compared through F-test and t-test. The t-test is used to check if two sample means are equal and requires that both samples follow normal distributions with equal variances. The F-test is used to check if two sample variances are equal and requires that both samples follow normal distributions. If the null hypothesis of F-test as well as the null hypothesis of t-test are not rejected, it can be assumed that both samples are drawn from the same population with normal distribution. If at least one sample does not follow a normal distribution or the null hypothesis of F-test or the null hypothesis of t-test are rejected, the nonparametric two sample KS-test is used. If the null hypothesis of KS-test is not rejected, it can be assumed that both samples are drawn from the same population, but the distribution of the population is different from a normal distribution. If more than two samples are statistically analysed, Bartlett's test and one-way ANOVA are used. The one-way ANOVA is used to check if all sample means are equal and requires that all samples follow normal distributions with equal variances. The Bartlett's test is used to check if all sample variances are equal and requires that all samples follow normal distributions. If the null hypothesis of Bartlett's test as well as the null hypothesis of one-way ANOVA are not rejected, it can be assumed that all samples are drawn from the same population with normal distribution. If at least one sample does not follow a normal distribution or the null hypothesis of Bartlett's test or the null hypothesis of one-way ANOVA are rejected, the nonparametric Kruskal-Wallis test is used. If the null hypothesis of Kruskal-Wallis test is not rejected, it can be assumed that all samples are drawn from the same population, but the distribution of the population is different from a normal distribution. The Anderson-Darling test for normality is used to check if it can be assumed that a sample follows a normal distribution. In the present work, the statistical toolbox implemented in MATLAB [84] was applied, see Chapter 3.6.6, and all hypothesis tests were performed with a significance level of 5%. However, Anderson-Darling test for normal distributions (AD_N-test) and Anderson-Darling test for Weibull distributions (AD_W-test) are not implemented yet. Hence, these hypothesis tests were implemented as user-defined functions according to the procedure presented in Chapter 3.6.5:

– Anderson-Darling tests for normal distributions (AD_N-test) of sample X:
  $[\mathtt{H},\mathtt{p}] = \mathtt{adtestn(X)}$

Statistical Hypothesis Testing of Two Samples X_1 and X_2												
Case	Samples		AD_N-Test A		AD_N-Test B		F-Test		t-Test		KS-Test	
#	A	B	H_0	p	H_0	p	H_0	p	H_0	p	H_0	p
1	X_1	X_2	0	0.71	0	0.53	0	0.62	0	0.80	0	0.88
2	X_1	X_2	0	0.71	0	0.62	**0**	**0.04**	~~0~~	~~0.71~~	**1**	**0.02**
3	X_1	X_2	0	0.71	**1**	**0.02**	~~0~~	~~0.17~~	~~0~~	~~0.53~~	0	0.44

Table 8.1.1: Statistical hypothesis testing of two samples X_1 and X_2: Results of AD_N-test, F-test, t-test and KS-test (significance level $\alpha = 0.05$).

– Anderson-Darling tests for Weibull distributions (AD_W-test) of sample X: $[\mathtt{H},\mathtt{p}] = \mathtt{adtestw(X)}$

The syntax of these functions follows the usual syntax of hypothesis tests in MATLAB [84].

The presented approach of statistical hypothesis testing is summarised in the flow chart given in Figure 8.1.5. According to this flow chart, the outcome of a statistical analysis of two samples X_1 and X_2 is shown in Table 8.1.1 for three different cases. If a hypothesis test is rejected at a significance level of $\alpha = 0.05$, the result is highlighted in bold and the results of the hypothesis tests which depend on this result are crossed out. The outcome of each case can be concluded as follows:

– Case #1: The null hypothesis is not rejected for any test. It can be assumed that the two samples X_1 and X_2 are drawn from the same population with normal distribution.

– Case #2: The null hypothesis of the F-test is rejected at a significance level of $\alpha = 0.05$. Consequently, the t-test cannot be used. Further, the null hypothesis of the KS-test is rejected at a significance level of $\alpha = 0.05$. It can be assumed that the two samples X_1 and X_2 are drawn from different populations, but these are normally distributed.

– Case #3: The null hypothesis of the AD_N-test of sample X_2 is rejected at a significance level of $\alpha = 0.05$. Consequently, the F-test and the t-test cannot be used. However, the null hypothesis of the KS-test is not rejected. It can be assumed that the two samples X_1 and X_2 are drawn from the same population, but the distribution of the population is different from a normal distribution.

In the current chapter, the outcome of a statistical analysis is presented according to this kind of table. However, samples are firstly analysed through box-plots. The box-plot shows if a statistical analysis between different samples is reasonable, see Chapter 3.5.2. In case two or more samples (generated from the same specimen geometry) can be assumed to be drawn from the same population, these are merged together into a new sample for further analysis.

The second objective of the statistical analysis is the estimation of the underlying distribution of a sample consisting of measurements of critical value W_c. Therefore, the considered sample is modified so that the n data values W_c^i are sorted in ascending order. Further, the n corresponding experimental probabilities $\overline{F}_i$ are computed according to Equation (3.5.12) with parameters $a = 0.5$ and $b = 0.5$, so that

$$\overline{F}_i = \frac{i - 0.5}{n}. \tag{8.1.14}$$

1. AD_N-test for normality:
   (a) Sample X_1: $[\mathtt{H},\mathtt{p}] = \mathtt{adtestn}(\mathtt{X_1})$
   If $\mathtt{H} = 0$ $(\mathtt{p} \geq 0.05)$ go to 2(a). If $\mathtt{H} = 1$ $(\mathtt{p} < 0.05)$ go to 4(a).
   (b) Sample X_2: $[\mathtt{H},\mathtt{p}] = \mathtt{adtestn}(\mathtt{X_2})$
   If $\mathtt{H} = 0$ $(\mathtt{p} \geq 0.05)$ go to 2(a). If $\mathtt{H} = 1$ $(\mathtt{p} < 0.05)$ go to 4(a).
   (c) ...
   (d) Sample X_k: $[\mathtt{H},\mathtt{p}] = \mathtt{adtestn}(\mathtt{X_k})$
   If $\mathtt{H} = 0$ $(\mathtt{p} \geq 0.05)$ go to 2(a). If $\mathtt{H} = 1$ $(\mathtt{p} < 0.05)$ go to 4(a).
2. F-test in case $k = 2$ or Bartlett's test in case $k > 2$ for equal variances:
   (a) $k = 2$: $[\mathtt{H},\mathtt{p}] = \mathtt{vartest2}(\mathtt{X_1},\mathtt{X_2})$
   If $\mathtt{H} = 0$ $(\mathtt{p} \geq 0.05)$ go to 3(a). If $\mathtt{H} = 1$ $(\mathtt{p} < 0.05)$ go to 4(a).
   (b) $k > 2$: $[\mathtt{H},\mathtt{p}] = \mathtt{vartestn}([\mathtt{X_1},\mathtt{X_2},\ldots,\mathtt{X_k}])$
   If $\mathtt{H} = 0$ $(\mathtt{p} \geq 0.05)$ go to 3(b). If $\mathtt{H} = 1$ $(\mathtt{p} < 0.05)$ go to 4(b).
3. t-test in case $k = 2$ or one-way ANOVA in case $k > 2$ for equal means:
   (a) $k = 2$: $[\mathtt{H},\mathtt{p}] = \mathtt{ttest2}(\mathtt{X_1},\mathtt{X_2})$
   If $\mathtt{H} = 0$ $(\mathtt{p} \geq 0.05)$ it can be assumed that the samples are drawn from the same population with normal distribution. If $\mathtt{H} = 1$ $(\mathtt{p} < 0.05)$ go to 4(a).
   (b) $k > 2$: $[\mathtt{H},\mathtt{p}] = \mathtt{anova1}([\mathtt{X_1},\mathtt{X_2},\ldots,\mathtt{X_k}])$
   If $\mathtt{H} = 0$ $(\mathtt{p} \geq 0.05)$ it can be assumed that the samples are drawn from the same population with normal distribution. If $\mathtt{H} = 1$ $(\mathtt{p} < 0.05)$ go to 4(b).
4. Non-parametric KS-test in case $k = 2$ or non-parametric Kruskal-Wallis test in case $k > 2$:
   (a) $k = 2$: $[\mathtt{H},\mathtt{p}] = \mathtt{kstest2}(\mathtt{X_1},\mathtt{X_2})$
   If $\mathtt{H} = 0$ $(\mathtt{p} > 0.05)$ it can be assumed that the samples are drawn from the same population. If $\mathtt{H} = 1$ $(\mathtt{p} < 0.05)$ it can be assumed that the samples are drawn from different populations.
   (b) $k > 2$: $[\mathtt{H},\mathtt{p}] = \mathtt{kruskalwallis}([\mathtt{X_1},\mathtt{X_2},\ldots,\mathtt{X_k}])$
   If $\mathtt{H} = 0$ $(\mathtt{p} > 0.05)$ it can be assumed that the samples are drawn from the same population. If $\mathtt{H} = 1$ $(\mathtt{p} < 0.05)$ it can be assumed that the samples are drawn from different populations.

Figure 8.1.5: Approach of statistical hypothesis testing of k samples X_i at a significance level of $\alpha = 0.05$ using MATLAB [84].

The n pairs $\left(W_c^i, \overline{F}_i\right)$ provide an estimate of the CDF of the underlying distribution. It is assumed that a sample follows a weakest-link Weibull distribution in form of the CDF given in Equation (5.1.57), so that

$$F_W(W_c) = 1 - \exp\left(-\frac{V}{V_0}\left(\frac{W_c}{W_{c0}}\right)^m\right) \tag{8.1.15}$$

where the Weibull parameters are scale volume V_0, scale failure parameter W_{c0} and Weibull modulus m. Scale volume V_0 as well as considered volume V are set to the gauge volume of the applied specimen geometry. As described in Chapter 5.1.6, scale failure parameter W_{c0} and Weibull modulus m can be identified from a linear curve fit on the n pairs $\left(W_c^i, \overline{F}_i\right)$ given in a Weibull plot. In the present work, the least-squares method implemented in gnuplot [115] was applied to identify the Weibull parameters. The quality of the fit is measured by the coefficient of determination, see Equation (3.5.19). Moreover, the assumption that a sample follows a Weibull distribution is checked through AD_W-test. It is noted that AD_N-test and AD_W-test can lead to the result that a sample follows a normal distribution as well as a Weibull distribution. This is due to the fact that the shape of both distributions can be similar as seen in Figure 3.3.7.

The third objective of the statistical analysis is to proof if the gauge volume influences the material ductility according to the weakest-link approach, see Chapter 5.1.2. Here, two samples generated from equivalent extraction positions but from specimens of different gauge volumes are compared as described in Chapter 5.1.6. A graphical comparison of the samples in a Weibull plot shows if the samples are generated from a material which shows a volume dependence according to the weakest-link approach. Furthermore, the two samples are compared through two sample hypothesis tests. If this analysis leads to the assumption that the two samples are drawn from different populations, it is a further indication that the considered material shows a volume dependence. Then, the parameters m, f_{c0} and V_0 can be found from a least-square fit on both samples according to the approach presented in Chapter 5.1.6. The best fit of these parameters is found when the sum of residuals, Equation (5.1.59), reaches a minimum. In the present work, the Nelder-Mead method implemented in MATLAB [83] was applied to find the minimum.

8.2 Material Characterisation I

The investigation of the mechanical behaviour and the analysis of the influence of the casting process on the material ductility are the objectives of the first material characterisation. Uniaxial tensile specimens of the same geometry were machined from different extraction positions within the U900-1 component. The applied specimen geometry is denoted as UT80 and is illustrated in Figure 8.2.1. The extraction plan of the specimens and the corresponding labelling system can be found in Figure B.1.2 and Figure B.1.3 of Appendix B.1. It is seen that the specimens were machined from the five characteristic parts IF, IW, BF, OW and OF on the locations Left (L), Middle (M) and Right (R). Further, specimens were machined from a total of five components according to this extraction plan. Each specimen can be clearly identified by its label consisting of

Component Number	–	Characteristic Part	–	Location
[1,2,3,4,5]	–	[IF, IW, BF, OW, OF]	–	[L, M, R]

.

In summary, samples of five specimens were generated from 15 extraction positions. Parallel tensile tests were carried out on these 75 specimens using the test set-up given in Figure 8.1.1. Each test result was analysed according to the procedure presented in Figure

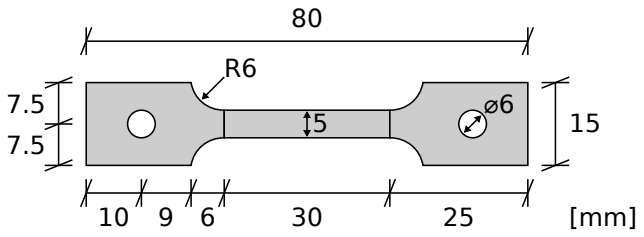

Figure 8.2.1: Uniaxial tensile test specimen UT80 ($t = 2.5\,\text{mm}$).

8.1.4. Furthermore, the measurements of critical value W_c were statistically analysed as described in Chapter 8.1.3. The results of the two analyses are presented and discussed in the following. In addition, the result of a microstructural study on the identification of casting defects is shown. Finally, the conclusions obtained from the first material characterisation are summarised.

8.2.1 Mechanical Analysis

The engineering stress-strain curves obtained from UT80 specimens machined from each extraction position of a U900-1 component (component #1) are compared in Figure 8.2.2. The curves are coloured according to the five parts: Curves obtained from specimens machined from part IF are plotted in red, curves obtained from specimens machined from part IW in green, curves obtained from the specimens machined from part BF in blue, curves obtained from specimens machined from part OW in magenta and curves obtained from specimens machined from part OF in cyan. Since three specimens were machined from each part (location L, location M and location R), three curves are shown for each part. It is seen that the stress-strain behaviour is not reproducible within the same component. Especially, the fracture strain shows a strong variation between the different extraction positions. The fracture strain obtained from specimens machined from part OW and part OF is generally smaller than the fracture strain obtained from specimens machined from part IF and part IW. Moreover, the fracture strain obtained from specimens machined from the same part shows a strong variation, too. In contrast, the variation in the strain hardening behaviour is much smaller than the variation in the fracture strain. The results obtained from the remaining four components lead to the same conclusions, see Figure B.2.1 of Appendix B.2.

In Figure 8.2.3, the engineering stress-strain curves obtained from the 75 specimens machined from a total of five components are presented. The figure consists of five graphs, each showing the curves obtained from specimens machined from the same part. Each graph is structured identically: The curves obtained from specimens machined from location L are plotted in green, the curves obtained from specimens machined from location M in blue and the curves obtained from specimens machined from location R in magenta. It becomes obvious that the fracture strain cannot be reproduced from specimens machined from the same extraction position. Moreover, the fracture strain scatters independently of the extraction position. However, the strain hardening behaviour obtained from specimens machined from the same part is comparable within each part. The specimens showing the most ductile behaviour can be found in part IF, Figure 8.2.3a, part IW, Figure 8.2.3b, and part BF, Figure 8.2.3c, but these parts also contain specimens showing a poor material ductility. The results obtained from part OW, Figure 8.2.3d and part OF, Figure 8.2.3e, are obtained only from specimens showing a poor material ductility. It can be ob-

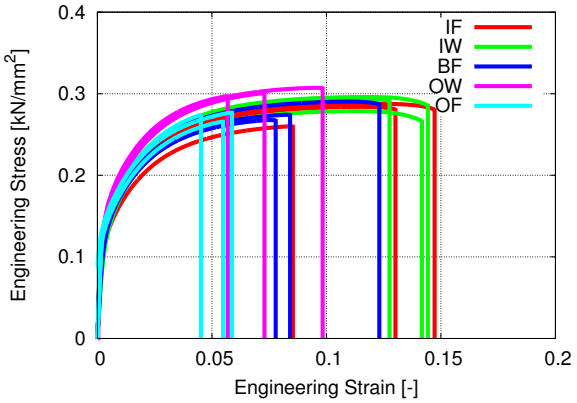

Figure 8.2.2: Engineering stress-strain curves obtained from UT80 specimens machined from an U900-1 component (component #1).

served that specimens showing a poor material ductility failed before the point of diffuse necking was reached.

The mechanical quantities $R_{p0.2}$, R_m, R_f, A_g and A_f as well as critical value W_c were measured from each tensile test result. The measurements of these quantities are summarised in tables given in Appendix B.2. The experimental average and the experimental Coefficient Of Variation (COV), see Equation (3.5.3), of the measured quantities were computed separately for each part. In Figure 8.2.4a, the averages and the COVs of $R_{p0.2}$ (grey), R_m (blue) and R_f (green) are compared using a double bar plot. The averages are given in the upper bar plot and the corresponding COVs are given in the lower bar plot. Here, the most interesting fact to notice is that the average of R_m is slightly larger than the average of R_f in part IF, part IW and part OW, whereas these averages are almost identical in part OW and part OF. The comparison of the corresponding COVs shows a maximum value of approximately 8% which is acceptable in terms of experimental testing. In contrast, the comparison of the averages and the COVs of A_g (blue) and A_f (green) are more interesting, see Figure 8.2.4b. It is seen that the averages of A_g are comparable in part IF, part IW, and part BF as well as in part OW and part OF. However, the averages of A_f are much smaller in part OW and part OF than in part IF, part IW and part BF. The average of A_f is larger than the average of A_g in part IF, part IW and part BF. This indicates a ductile material behaviour in the specimens machined from these parts. The averages of A_g and A_f are nearly identical in part OW and part OF. This indicates that most specimens machined from these parts failed before the point of diffuse necking was reached. The comparison of the COVs of A_f shows a minimum value of approximately 20% in part BF and a maximum value of more than 40% in part OW. Accordingly, the COVs of A_g show same critical values. It is reasonable that the measurements of A_f were dominated by casting defects, see Chapter 2.3. The difference in the averages of A_f in the inlet parts, part IF and part IW, and the outlet parts, part OW and part OF, confirms the assumption that the casting systems has a major influence on the distribution of casting defects (global systematic variation of casting defects). Further, the high values of the COVs of A_f in each part confirms the assumption that casting defects are also pseudo-randomly distributed (pseudo-random variation of casting defects). Moreover, these results explains the fact that the U900-1 components subjected to bending loading failed first in the vacuum part, part OW and part OF, and the strong scatter in bending test results becomes reasonable, see Chapter 7.2.2. More de-

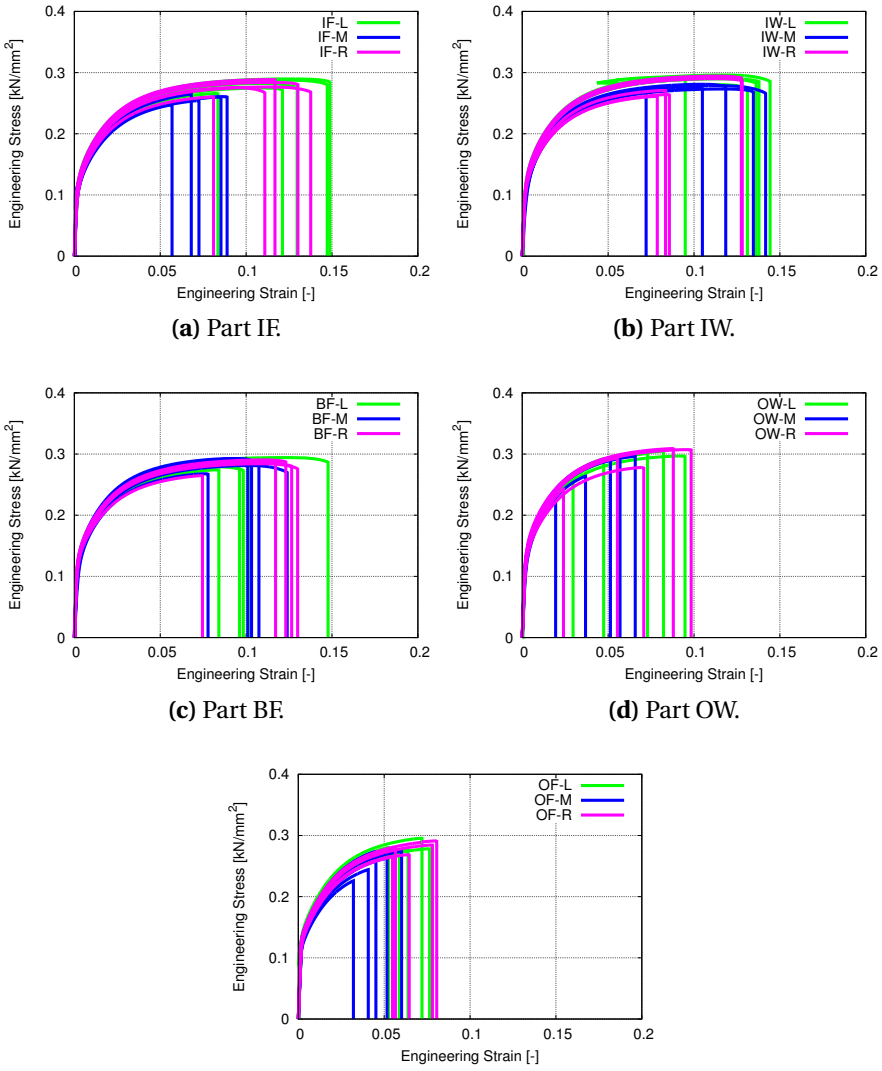

(a) Part IF.

(b) Part IW.

(c) Part BF.

(d) Part OW.

(e) Part OF.

Figure 8.2.3: Engineering stress-strain curves obtained from UT80 specimens machined from five U900-1 components presented according to the extraction position.

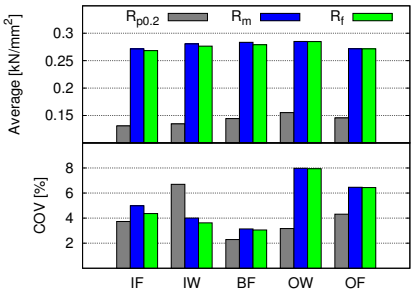

(a) Comparison of averages and COVs of $R_{p0.2}$, R_m and R_f.

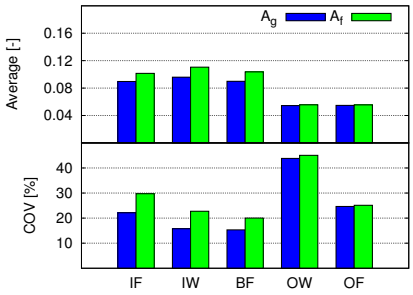

(b) Comparison of averages and COVs of A_g and A_f.

Figure 8.2.4: Averages and COVs of the measured mechanical quantities obtained from UT80 specimens machined from five U900-1 components.

tailed bar plots with comparison of the locations L, M and R are given in Figure B.2.4 and Figure B.4.2 of Appendix B.2.

In the following, the measurements of R_m and R_f as well as A_g and A_f are used to identify specimens which failed before the point of diffuse necking was reached. The engineering stress-strain curve obtained from the most ductile specimen is given in Figure 8.2.5a. It is seen that the measurement of R_f is smaller than the one of R_m and the measurement of A_g is smaller than the one of A_f. The engineering stress-strain curve obtained from the least ductile specimen is given in Figure 8.2.5b. Since the specimen failed before the point of diffuse necking was reached, the measurements of R_m and R_f as well as the measurements of A_g and A_f are identical. Based on these observations, a simple and effective method to identify specimens showing diffuse necking is the comparison of the measurements R_m and R_f as follows: If the measured R_m is larger than 101% of the measured R_f, it can be concluded that the considered specimen failed beyond the point of diffuse necking. In Figure 8.2.5c, the measurements of R_m and R_f are presented as red and blue data points in a scatter plot. If the measured R_m is larger than 101% of the measured R_f the considered data point is coloured in blue and, alternatively, the considered data point is coloured in red. In addition, a straight line through the origin with unit slope is given in the scatter plot. It is seen that the red data points lie along this line which implies that the measurements of R_m and R_f are almost identical. Accordingly, the measurements of A_g and A_f are presented as red and blue data points in a scatter plot given in Figure 8.2.5d. A data point is coloured in blue when the corresponding measurements of R_m and R_f are different $\left(R_m > 1.01 \cdot R_f\right)$. A data point is coloured in red when the corresponding measurements of R_m and R_f are almost identical $\left(R_m \leq 1.01 \cdot R_f\right)$. It is seen that the red data points lie along a straight line through the origin with unit slope. This indicates that the red data points are obtained from specimens which failed before the point of diffuse necking was reached. Consequently, the blue data points are obtained from specimens which failed beyond the point of diffuse necking was reached. Based on this approach, it is concluded that 49 out of 75 specimens (65.33%) failed before the point of diffuse necking was reached.

Representative images of fractured UT80 specimens machined from each extraction position are presented in Figure 8.2.6. The corresponding measured fracture strain is given in the subfigure title. It is seen that the fracture surfaces are characterised by a rough tex-

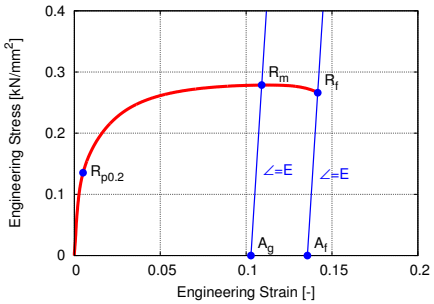

(a) Engineering stress-strain curve obtained from the most ductile specimen (1-IW-M).

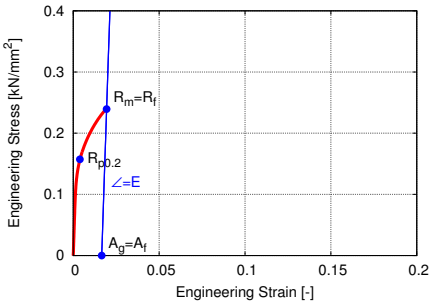

(b) Engineering stress-strain curve obtained from the least ductile specimen (3-OW-M).

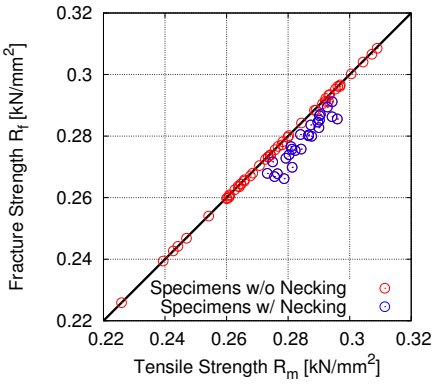

(c) Scatter plot: R_f versus R_m.

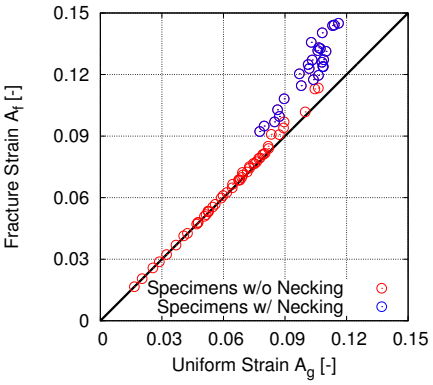

(d) Scatter plot: A_f versus A_g.

Figure 8.2.5: Engineering stress-strain curves obtained from the most ductile specimen and the least ductile specimen and scatter plots of the measured mechanical quantities obtained from UT80 specimens machined from five U900-1 components.

ture with visible sharp irregularities. Furthermore, it is seen that the fractured specimens do not show large plastic deformations or necking before fracture has initiated. Actually, the fractured specimens with a measured fracture strain larger than 0.10 do not show any distinct necking. Besides, the fractured specimens with a measured fracture strain smaller than 0.10 are characterised by a fracture surface which is almost normal to the applied tensile loading. This is characteristic for quasi-brittle materials.

8.2.2 Statistical Analysis

The objective of the statistical analysis is the identification of extraction positions with comparable material behaviour. The tensile test results demonstrated that, especially, the material ductility exhibits a strong variation. Therefore, the statistical analysis is based on measurements of critical value W_c. Here, a sample consists of the measurements of W_c obtained from specimens machined from the same extraction position. These fifteen samples were analysed through hypothesis testing according to the flow chart given in

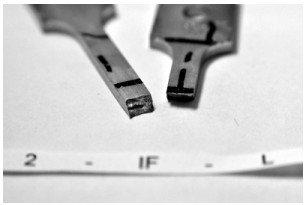

(a) Specimen 2-IF-L $\left(A_f = 0.14\right)$.

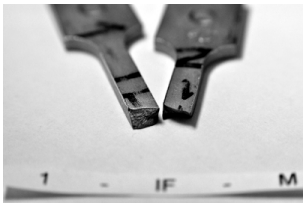

(b) Specimen 1-IF-M $\left(A_f = 0.08\right)$.

(c) Specimen 3-IF-R $\left(A_f = 0.08\right)$.

(d) Specimen 5-IW-L $\left(A_f = 0.13\right)$.

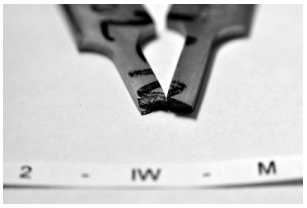

(e) Specimen 2-IW-M $\left(A_f = 0.13\right)$.

(f) Specimen 1-IW-R $\left(A_f = 0.12\right)$.

(g) Specimen 4-BF-L $\left(A_f = 0.10\right)$.

(h) Specimen 1-BF-M $\left(A_f = 0.07\right)$.

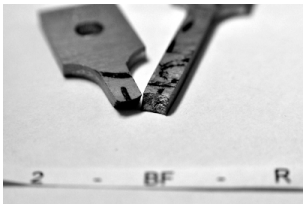

(i) Specimen 2-BF-R $\left(A_f = 0.12\right)$.

(j) Specimen 1-OW-L $\left(A_f = 0.07\right)$.

(k) Specimen 3-OW-M $\left(A_f = 0.02\right)$.

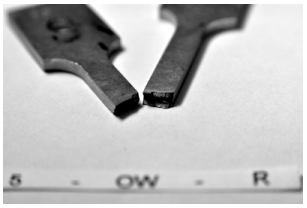

(l) Specimen 5-OW-R $\left(A_f = 0.02\right)$.

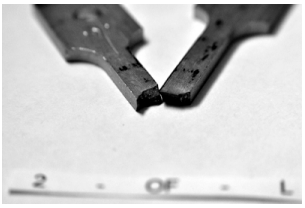

(m) Specimen 2-OF-L $\left(A_f = 0.06\right)$.

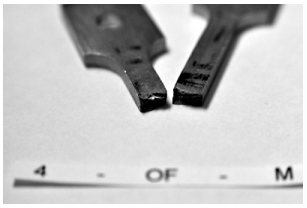

(n) Specimen 4-OF-M $\left(A_f = 0.04\right)$.

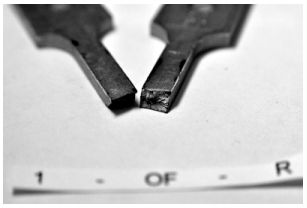

(o) Specimen 1-OF-R $\left(A_f = 0.05\right)$.

Figure 8.2.6: Images of fractured UT80 specimens machined from the fifteen extraction positions of the U900-1 component.

Uniaxial Tensile Test Specimen UT80 / W_c

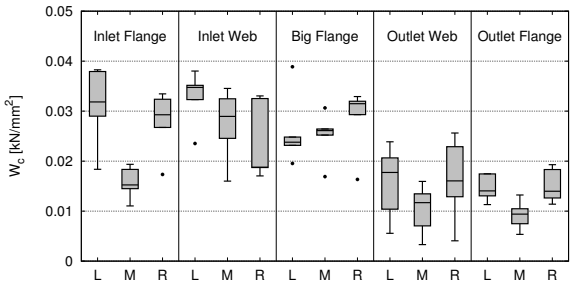

Samples		AD_N-Test A		AD_N-Test B		F-Test		t-Test		KS-Test	
A	B	H_0	p	H_0	p	H_0	p	H_0	p	H_0	p
IF-L	IF-R	0	0.43	0	0.36	0	0.66	0	0.50	0	0.70
IW-L	IW-R	0	0.27	0	0.08	0	0.49	0	0.08	0	0.21
BF-L	BF-R	0	0.10	**1**	0.05	~~0~~	~~0.88~~	~~0~~	~~0.62~~	0	0.21
OW-L	OW-R	0	0.62	0	0.67	0	0.81	0	0.90	0	1.00
OF-L	OF-R	0	0.42	0	0.42	0	0.64	0	0.82	0	0.70

Table 8.2.1: Statistical hypothesis testing of samples based on measurements of W_c obtained from UT80 specimens machined from five U900-1 components: Results of AD_N-tests, F-test, t-test and KS-test (significance level $\alpha = 0.05$).

Figure 8.1.5. In particular, it was analysed which samples can be assumed to be drawn from the same population. The result of the statistical analysis is presented in Table 8.2.1. Additionally, the table contains a box-plot of the fifteen samples. Here, the comparison of the samples obtained from specimens machined from part IF shows that the samples obtained from specimens machined from location L and location R are comparable, whereas the sample obtained from specimens machined from location M is different. The same can be observed for the samples obtained from specimens machined from part OW and part OF, respectively. Hence, only the samples obtained from specimens machined from location L and location R of the same part were analysed through hypothesis testing. The null hypothesis cannot be rejected for any test in part IF, part IW, part OW and part OF. The null hypothesis of AD_N-test of sample BF-R is rejected. Consequently, the results obtained from F-test and t-test of sample BF-L and sample BF-R are invalid. However, the null hypothesis of KS-test of sample BF-L and sample BF-R cannot be rejected. In summary, it can be assumed that samples obtained from location L and location R of the same part are drawn from the same population. This means that it can be assumed that the material failure behaviour is comparable in location L and location R in each part. This result is reasonable since the underlying U900-1 components were produced in a symmetric casting system (symmetry in longitudinal direction) as seen in Figure 7.1.1d. However, it is noted that the result of the statistical analysis is critical since each sample consists of only five measurements of W_c.

Based on the result of the statistical analysis, the samples obtained from location L and location R were merged together for each part and these five samples each consisting of ten measurements of W_c are considered in the following. It is assumed that each sample follows a Weibull distribution. The corresponding Weibull parameters were estimated according to the procedure described in Chapter 8.1.3. Furthermore, the assumption that a sample follows a Weibull distribution was checked through the AD_W-test. In Table 8.2.2,

Uniaxial Tensile Test Specimen UT80 / W_c

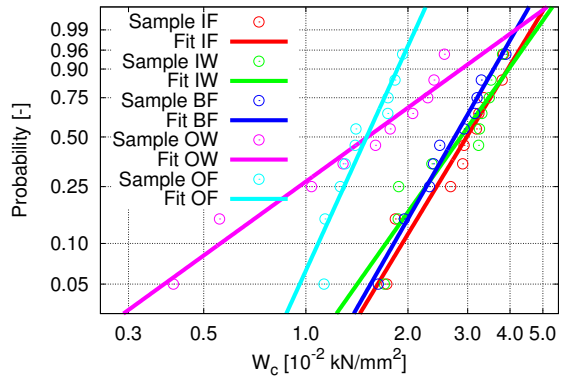

	AD_W-Test		Weibull Fit			
Position	H_0	p	m [−]	W_{c0} [kN/mm²]	V_0 [mm³]	R^2 [%]
IF-[L, R]	0	0.39	5.39	0.0321	375.00	92.60
IW-[L, R]	**1**	0.03	4.61	0.0313	375.00	87.19
BF-[L, R]	0	0.72	4.70	0.0298	375.00	97.60
OW-[L, R]	0	0.37	2.41	0.0180	375.00	95.26
OF-[L, R]	0	0.15	5.90	0.0161	375.00	87.53

Table 8.2.2: Weibull analysis of samples based on measurements of W_c obtained from UT80 specimens machined from five U900-1 components: AD_W-test result ($\alpha = 0.05$), estimated Weibull modulus m, estimated scaling parameter W_{c0}, scaling volume V_0 and coefficient of determination R^2.

the estimated Weibull parameters and the AD_W-test results are presented. In addition, the table contains a Weibull plot including the sample data and the estimated Weibull distribution function (Weibull fit) of each sample. The sample data obtained from part IF and the corresponding Weibull fit are plotted in red, the sample data obtained from part IW and the corresponding Weibull fit in green, the sample data obtained from part BF and the corresponding Weibull in blue, the sample data obtained from part OW and the corresponding Weibull in magenta and the sample data obtained from part OF and the corresponding Weibull in cyan. The graphical comparison of the Weibull fits shows that the results obtained from part IF, part IW and part BF are comparable, whereas the results obtained from part OW and part OF are significantly different. As seen from the AD_W-tests, it can be assumed that the samples obtained from part IF, part BF, part OW and part OF follow Weibull distributions. However, the null hypothesis of the AD_W-test is rejected for the sample obtained from part IW. This implies that the sample cannot be assumed to follow a Weibull distribution. It is noted that the coefficient of determination R^2 is above 80% for all Weibull fits which indicates a high fit quality, but the AD_W-test is still meaningful. The scale volume V_0 for each sample was set to the gauge volume of the UT80 specimen, see Figure 8.2.1. As already mentioned, these results are critical due to the small sample sizes.

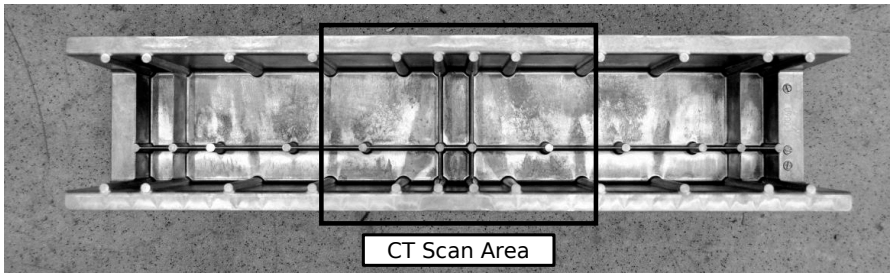

(a) Definition of the CT scan area within a U900-1 component.

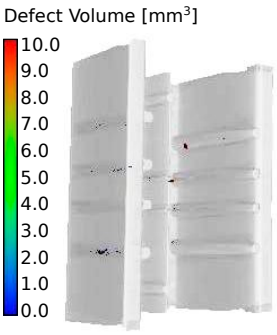

(b) CT scan of U900-1 component #1 showing porosity.

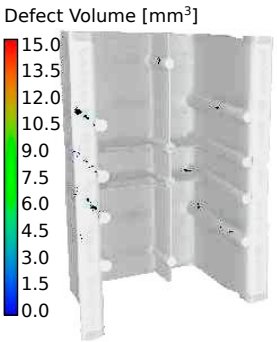

(c) CT scan of U900-1 component #2 showing porosity.

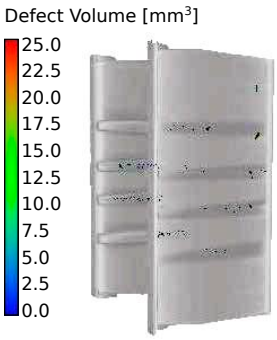

(d) CT scan of U900-1 component #3 showing porosity.

Figure 8.2.7: Identification of casting defects in form of porosity using CT scanning of the middle section of three U900-1 components.

8.2.3 Identification of Casting Defects

The material ductility in aluminium HPDC components is dominated by casting defects, see Chapter 2.3. Hence, a microstructural study on the identification of casting defects was carried out using Computed Tomography (CT) scanning and Scanning Electron Microscopy (SEM). In the following, the results of the microstructural study are presented.

Three U900-1 components were investigated through CT scanning. The middle section of each component was scanned. The scan area is highlighted in Figure 8.2.7a. It is noted that CT scanning shows differences in density of the considered object. For instance, porosity in a metallic structure can be detected by CT scanning. The results of the three CT scans are presented in Figure 8.2.7b, Figure 8.2.7c and Figure 8.2.7d. Here, pores with a volume larger than 1.0 mm^3 are coloured. It is seen that most of these pores were found in the ejector domes. Since these are very thick walled, it is suggested that these pores are shrinkage and gas pores. However, the resolution of the CT scans do not show any pore in thin walled parts.

Therefore, a selection of fractured UT80 specimens machined from thin walled parts were analysed through SEM. Casting defects of different sizes were identified from the fracture surfaces and captured in images of high resolution. The results are illustrated in Figure 8.2.8 and the identified casting defects are highlighted in red. According to the work by Teng et al. [105], casting defects were found in form of shrinkage pores and initial cracks. Typical shrinkage pores are shown in Figure 8.2.8a and Figure 8.2.8b. Sharp initial

cracks are shown in Figure 8.2.8c and Figure 8.2.8d. As seen in the work by Dai et al. [23], it is suggested that these cracks were caused by oxide films. Besides shrinkage pores and initial cracks, other microstructural irregularities were found on the fracture surfaces. Theses are shown in Figure 8.2.8e and Figure 8.2.8f. It is seen that castings defects were found in fractured specimens obtained from different extraction positions. Here, a detailed microscopic examination of all fractured specimens is required to identify a correlation between casting defect and extraction position. However, it can be summarised that these casting defects are the leading factor causing the global systematic variation and the local pseudo-random variation in the material ductility.

8.2.4 Concluding Remarks

The results of the first material characterisation can be concluded as follows:

- The material ductility of the HPDC alloy Castasil-37 in casting condition (F) was analysed using uniaxial tensile specimens machined from various extraction positions of the U900-1 component. The material ductility was measured from the test results and showed a strong variation. The material ductility varied within the same component as well as within duplicated extraction positions.

- The material ductility obtained from specimens machined from the vacuum part of the U900-1 component (part OW and part OF) was much lower than the material ductility obtained from specimens machined from the gating part of the U900-1 component (part IW and part IF). However, the material ductility varied pseudo-randomly within all parts.

- The experimental results showed that the spatial variation in the material ductility is systematic. It can be assumed that this systematic variation was caused by the applied casting system. In contrast, the observed local variation in the material ductility can be described as pseudo-random. It is suggested that this local pseudo-random variation was caused by fluctuations during the casting process. In summary, the results of the first material characterisation showed that the variation in the material ductility can be separated into a global systematic variation depending on the casting system and a local pseudo-random variation depending on fluctuations during the casting process.

- The result of the statistical analysis confirmed that the symmetric casting system of the U900-1 component caused symmetrically distributed material properties within the U900-1 component. It was shown that the local distributions of the material ductility measured by critical value W_c can be described by Weibull distributions. However, it is important to notice that the database generated from the applied sampling approach was too small for a reliable statistical analysis.

- The detailed analysis of the measured mechanical quantities led to the conclusion that most specimens failed before the point of diffuse necking was reached. The images of fractured specimens showed that most of the specimens failed without any large plastic deformation and diffuse necking. Moreover, the microstructural study confirmed that casting defects are the leading factor causing failure.

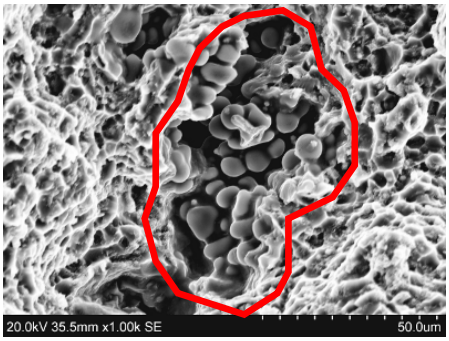

(a) SEM image of a shrinkage pore on the fracture surface of tensile specimen 1-IF-M.

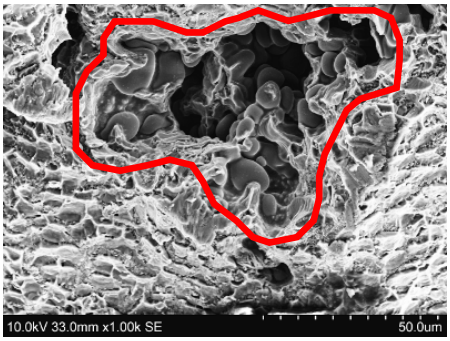

(b) SEM image of a shrinkage pore on the fracture surface of tensile specimen 2-BF-R.

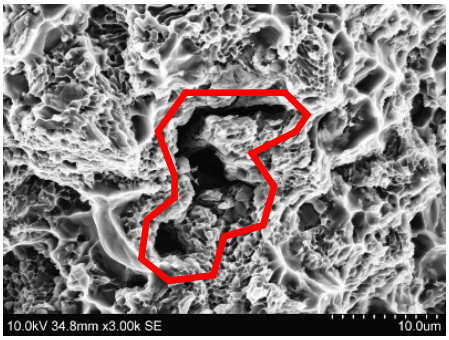

(c) SEM image of an initial crack on the fracture surface of tensile specimen 2-IW-M.

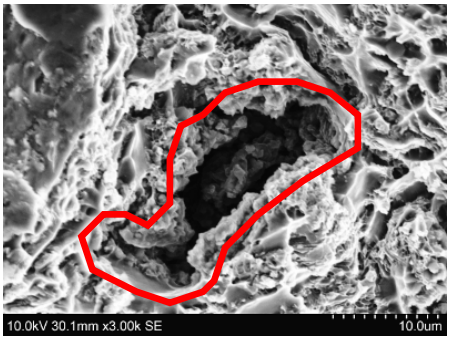

(d) SEM image of an initial crack on the fracture surface of tensile specimen 1-OW-L.

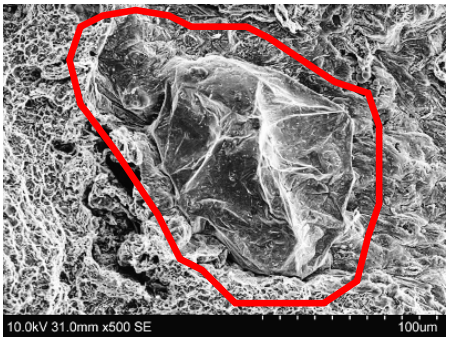

(e) SEM image of a microstructural irregularity on the fracture surface of tensile specimen 5-OW-R.

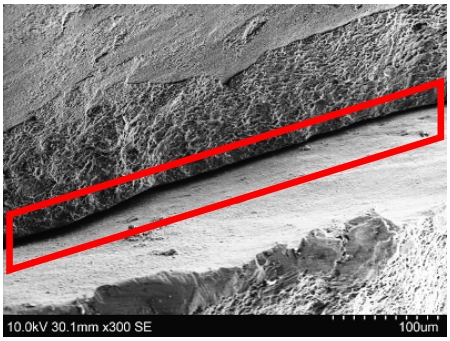

(f) SEM image of a microstructural irregularity on the fracture surface of tensile specimen 4-OF-M.

Figure 8.2.8: Identification of casting defects in form of shrinkage pores, initial cracks and other microstructural irregularities using SEM of fractured UT80 specimens machined from U900-1 components.

8.3 Material Characterisation II

In the first material characterisation, the general material behaviour of the aluminium HPDC alloy Castasil-37 was analysed. Here, uniaxial tensile specimens were machined from different extraction positions of five U900-1 components. The results obtained from these specimens showed that the material ductility depends on the extraction position and, further, varies pseudo-randomly within duplicated extraction position. These conclusions were checked by statistical hypothesis testing. However, it was mentioned that the underlying database was too small for a reliable statistical study. Hence, the second material characterisation is focused on a detailed analysis of the local pseudo-random variation of the material ductility. Furthermore, the influence of the gauge volume was analysed. Two uniaxial tensile specimen geometries which are equal in shape but different in size were investigated, see Figure 8.3.1. The geometry of the small specimen is denoted as UT75 and the geometry of the large specimen is denoted as UT117. The gauge volume of the UT117 specimen is approximately 2.38 times larger than the gauge volume of the UT75 specimen. Both types of specimens were machined from part IW, part BF and part OW of the U900-1 component. Based on the results of the first material characterisation, symmetric conditions were expected in longitudinal direction of the U900-1. Therefore, UT117 specimens were machined from six locations on the left side of the U900-1 component and UT75 specimens from six locations on the right side of the U900-1 component. The extraction plan and the corresponding labelling system can be found in Figure B.3.2 and Figure B.3.3 of Appendix B.3. It is seen that UT75 and UT117 specimens were machined symmetrically from each part and were machined from a total of six components according to this extraction plan. Each specimen can be clearly identified by its technical name, UT75 or UT117, and its label consisting of

$$\begin{array}{ccccc} \text{Component Number} & - & \text{Characteristic Part} & - & \text{Location} \\ [1,2,3,4,5,6] & - & [\text{IW},\text{BF},\text{OW}] & - & [1,2,3,4,5,6] \end{array} .$$

In summary, samples of six specimens were generated from 36 extraction positions within the U900-1 component. Parallel tensile tests were carried out on these 216 specimens using the test set-up given in Figure 8.1.1. Each test result was analysed according to the procedure presented in Figure 8.1.4. Then, an extensive statistical study was performed on the measurements of critical value W_c as described in Chapter 8.1.3. The results of both analyses are presented and discussed in the following. Special attention is put on the comparison of the result obtained from the two specimen geometries. Finally, the conclusions obtained from the second material characterisation are summarised.

8.3.1 Mechanical Analysis

The engineering stress-strain curves obtained from the 216 specimens machined from a total of six components are presented in Figure 8.3.2. The figure consists of three graphs each showing the engineering stress-strain curves obtained from specimens machined from the same part. Each graph compares the curves obtained from UT75 specimens (red) and the curves obtained from UT117 specimens (blue). As already seen from the first material characterisation, the fracture strain cannot be reproduced from specimens machined from the same part and underlies a local pseudo-randomness. Further, the measured material ductility is larger in part IW, Figure 8.3.2a, than in part OW, Figure 8.3.2c. A distinct influence of the gauge volume can be found in the curves obtained from specimens machined from part BF, Figure 8.3.2b. Here, the curves obtained from UT75 specimens reach a larger fracture strain than the curves obtained from UT117 specimens.

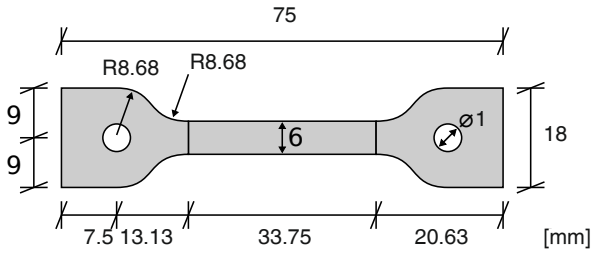

(a) Uniaxial tensile test specimen UT75 ($t = 2.5\,\text{mm}$).

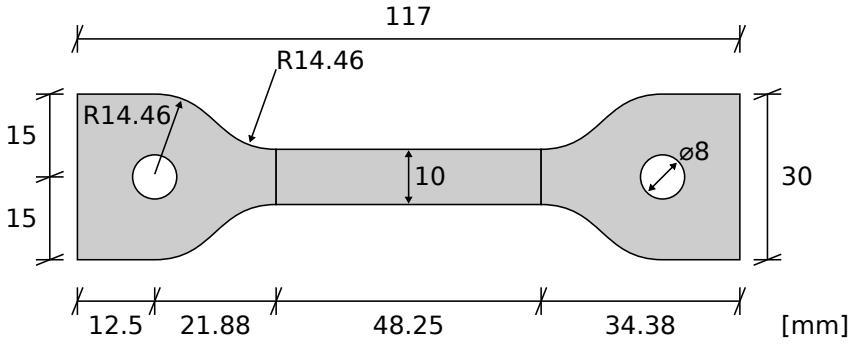

(b) Uniaxial tensile test specimen UT177 ($t = 2.5\,\text{mm}$).

Figure 8.3.1: Uniaxial tensile test specimen UT75 and uniaxial tensile test specimen UT117.

The curves obtained from specimens machined from part IW and part OW do not show such a clear difference. However, the strain hardening behaviour can be reproduced from specimens machined from the same part and do not show any dependence on the applied specimen geometry. In general, these results confirm the results obtained from the first material characterisation. More comparisons of these curves are given in Figure B.4.1, Figure B.4.2 and Figure B.4.3 of Appendix B.4.

The mechanical quantities $R_{p0.2}$, R_m, R_f, A_g and A_f as well as the critical value W_c were measured from each tensile test result. The measurements of these quantities are summarised in tables given in Appendix B.4. The experimental average and the experimental COV of the measured quantities were computed separately for the two specimen geometries and for each part. In Figure 8.3.3a, the averages and the COVs of $R_{p0.2}$ (grey), R_m (blue) and R_f (green) are compared in a double bar plot. The averages of $R_{p0.2}$, R_m and R_f obtained from UT75 specimens do not differ significantly from the ones obtained from UT117 specimens machined from the same part. As already seen, the average of R_m is slightly larger than the average of R_f in part IW and part BF (independent of the specimen geometry), whereas the average of R_m and the average of R_f are nearly identical in part OW (independent of the specimen geometry). The comparison of the corresponding COVs shows a maximum value of approximately 4% which is acceptable in terms of experimental testing. Furthermore, this slight variations in the measured quantitates $R_{p0.2}$, R_m and R_f indicate a reproducible strain hardening behaviour. In Figure 8.3.3b, the averages and the COVs of A_g (blue) and A_f (green) are compared. The results obtained from specimens machined from part IW are comparable. Here, the average of A_f is larger than

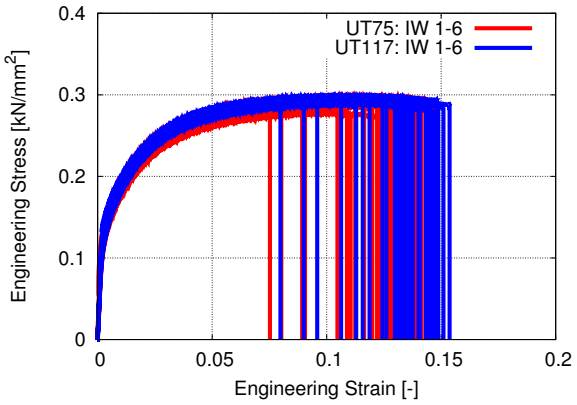

(a) Part IW.

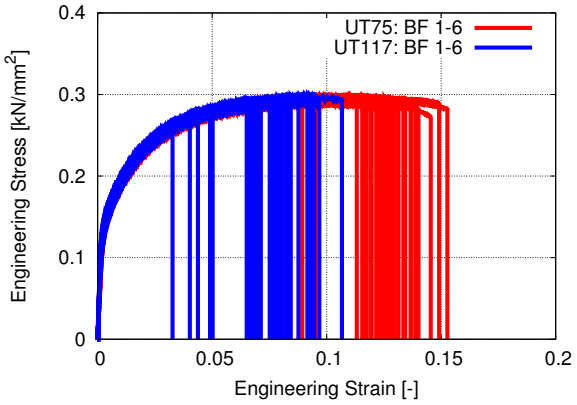

(b) Part BF.

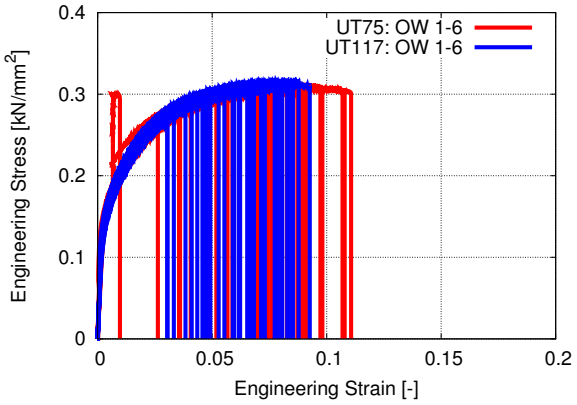

(c) Part OW.

Figure 8.3.2: Engineering stress-strain curves obtained from UT75 and UT117 specimens machined from six U900-1 components presented according to extraction positions.

the average of A_g and both averages are almost independent of the specimen geometry. The comparison of the corresponding COVs reach values of about 10%. The results obtained from specimens machined from part BF show a clear difference. The average of A_f obtained from UT117 specimens is much smaller than the one obtained from UT75 specimens. Further, the difference between the averages of A_g and A_f is smaller in the results obtained from UT117 specimens than in the results obtained from UT75 specimens. The comparison of the corresponding COVs show clearly that the measurements of A_f obtained from UT117 specimens scatter more than the ones obtained from UT75 specimens. The results obtained from specimens machined from part OW show also that the average of A_f obtained from UT117 is smaller than the one obtained from UT75 specimens. Further, the averages of A_g and A_f reach almost same values within each specimens geometry. The corresponding COVs reach values of more than 20%. An overall comparison shows that the results obtained from UT75 and UT117 specimens machined from part IW and from UT75 specimens machined from part BF are comparable in average and in variation. Accordingly, the results obtained from UT117 specimens machined from part BF and UT75 and UT117 specimens machined from part OW are comparable. Further, it is seen that the first group shows more material ductility in average and less variation in the material ductility than the second group. Finally, the results obtained from specimens machined from part BF and part OW suggest a dependence on the applied specimen geometry and the gauge volume, respectively. More detailed bar plots with comparison of averages and COVs obtained from specimens machined from locations 1 to 6 are given in Figure B.4.6 and Figure B.4.7 of Appendix B.4.

Specimens which failed before the point of diffuse necking are identified using the same method as in the first material characterisation. The measurements of R_m and R_f obtained from UT75 specimens are presented in the scatter plot given in Figure 8.3.4a and the ones obtained from UT117 specimens in the scatter plot given in Figure 8.3.4c. If the measured R_m is larger than 101% of the measured R_f the considered data point is coloured in blue and, alternatively, the considered data point is coloured in red. The measurements of A_g and A_f obtained from UT75 specimens are presented in the scatter plot given in Figure 8.3.4b and the ones obtained from UT117 specimens in the scatter plot given in Figure 8.3.4d. Here, a data point is coloured in blue when the corresponding measurements of R_m and R_f are different $\left(R_m > 1.01 \cdot R_f\right)$. A data point is coloured in red when the corresponding measurements of R_m and R_f are almost identical $\left(R_m \leq 1.01 \cdot R_f\right)$. As already described, it is suggested that red data points are obtained from specimens which failed before the point of diffuse necking and the blue data points are obtained from specimens which failed beyond the point of diffuse necking. Consequently, 38 out of 108 UT75 specimens (35.19%) and 64 out of 108 UT117 specimens (59.26%) failed before the point of diffuse necking was reached. This indicates that the UT117 specimens with a gauge volume larger than the gauge volume of the UT75 specimens tended rather to fail before the point diffuse necking was reached.

The influence of the extraction positions in longitudinal direction on the measurements of A_f is analysed in the following. In Figure 8.3.5, three graphs, each showing the measurements of A_f obtained from specimens machined from the same part, are presented. Each graph shows the extraction position of the UT117 specimens and the UT75 specimens on the abscissa and the measured A_f on the ordinate. It is noted that the abscissa shows the location 6 to 1 of the UT117 specimens on the left side and the locations 1 to 6 of the UT75 specimens on the right side. Thus, the measurements of A_f are plotted according to the extraction positions in longitudinal direction of the U900-1 component, see Figure B.3.2 and Figure B.3.3 of Appendix B.3. The measurements of A_f obtained from the specimens machined from the same U900-1 component are uniformly coloured. The results obtained

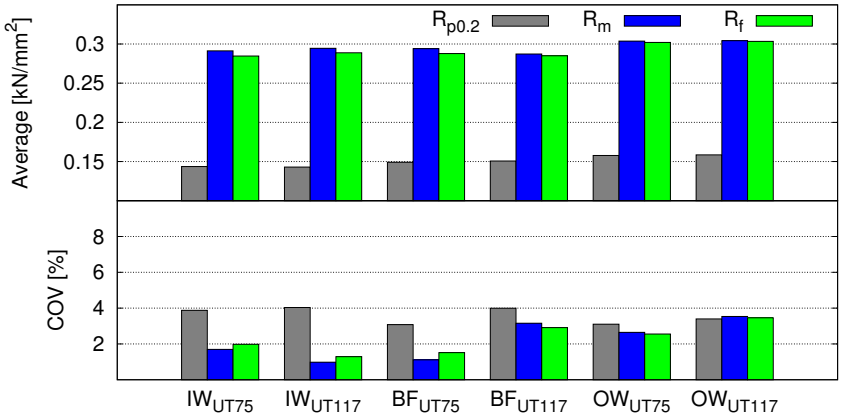

(a) Comparison of averages and COVs of $R_{p0.2}$, R_m and R_f.

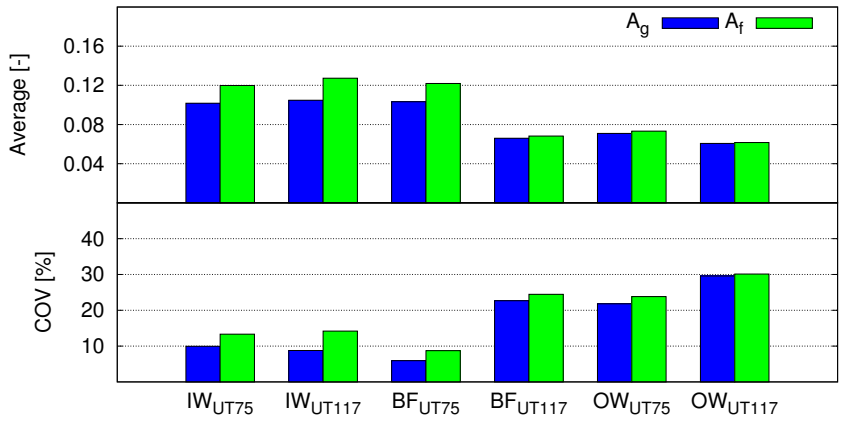

(b) Comparison of averages and COVs of A_g and A_f.

Figure 8.3.3: Average and COVs of the measured mechanical quantities obtained from UT75 and UT117 specimens machined from six U900-1 components.

from specimens machined from part IW are given in Figure 8.3.5a. Here, any dependence of the extraction position in longitudinal direction and the specimen geometry cannot be found. The results obtained from specimens machined from part BF are given in Figure 8.3.5b. The influence of the specimen geometry is clearly seen, but any influence of the extraction position cannot be found, too. The results obtained from specimens machined from part OW are given in Figure 8.3.5c. Here, a slight increase of the measurements of A_f from location 6 to location 1 of both specimens geometries can be detected. However, an influence of the specimen geometry cannot be detected. In summary, it can be concluded that the part has a stronger influence on the measurements of A_f than the position of the extraction position in longitudinal direction.

The influence of the specimen geometry and the gauge volume, respectively, is analysed using scatter plots of the measurements of A_f as seen in Figure 8.3.6. Here, three scatter plots are illustrated each showing the measurements of A_f obtained from specimens machined from the same part. Each scatter plot shows the measured A_f obtained from a

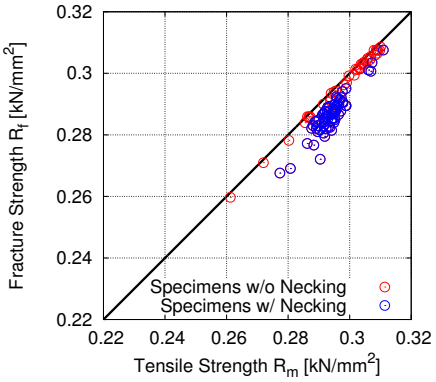

(a) UT75: R_f versus R_m.

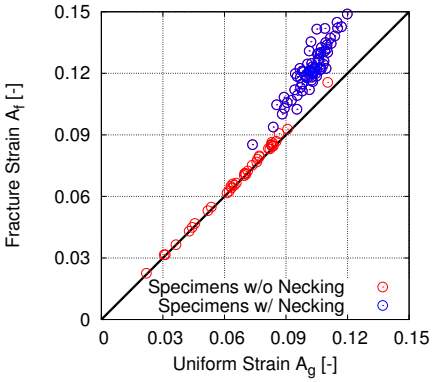

(b) UT75: A_f versus A_g.

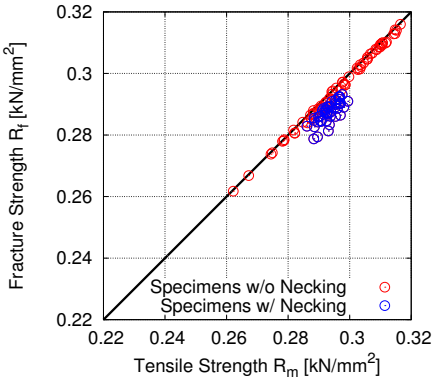

(c) UT117: R_f versus R_m.

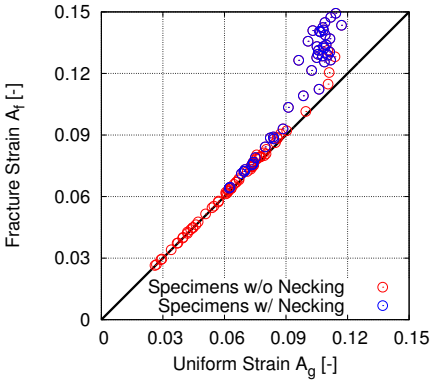

(d) UT117: A_f versus A_g.

Figure 8.3.4: Scatter plots of the measured mechanical quantities obtained from UT75 and UT117 specimens machined from six U900-1 components.

UT75 specimen on the abscissa and the measured A_f obtained from a UT117 specimen on the ordinate. A data point within a scatter plot is given by the measured A_f obtained from a UT75 specimen and the measured A_f obtained from a UT117 specimen machined from the same extraction position at the same U900-1 component. For instance, a data point is given by the two measurements A_f (UT75: 2-OW-4) and A_f (UT117: 2-OW-4). This analysis is based on the conclusions obtained from the experimental results presented in Figure 8.3.5. In addition, each scatter plot includes a straight line through the origin with unit slope. Data points which are on the left side to this line are coloured in red and data points lying on the right side to this line are coloured in blue. This implies that a data point is coloured in red when the measured A_f obtained from a UT75 specimen is smaller than the measured A_f obtained from a corresponding UT117 specimen and a data point is coloured in blue when the measured A_f obtained from a UT75 specimen is larger than the measured A_f obtained from a corresponding UT117 specimen. This means that a

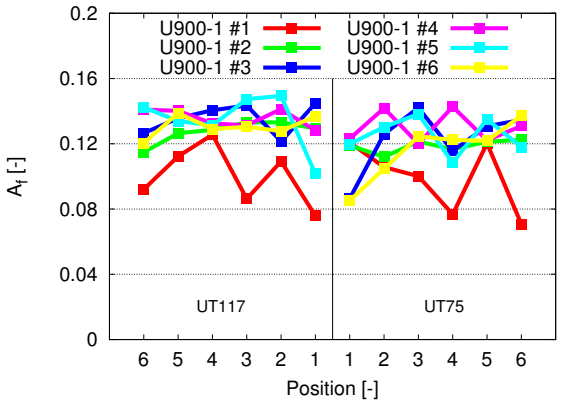

(a) Part IW: A_f versus extraction position.

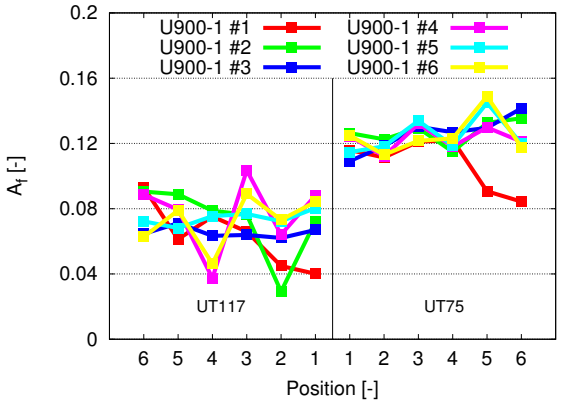

(b) Part BF: A_f versus extraction position.

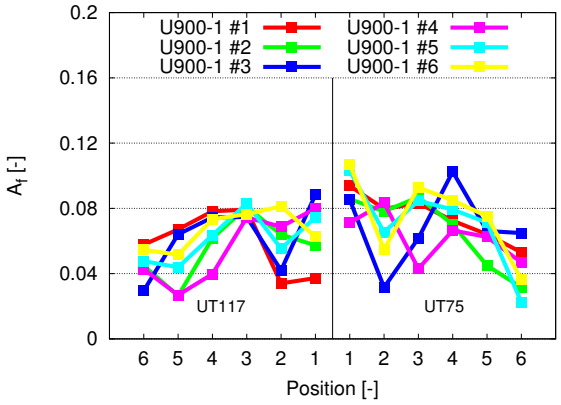

(c) Part OW: A_f versus extraction position.

Figure 8.3.5: Measured fracture strain A_f obtained from UT75 and UT117 specimens machined from six U900-1 components plotted according to extraction positions in longitudinal direction.

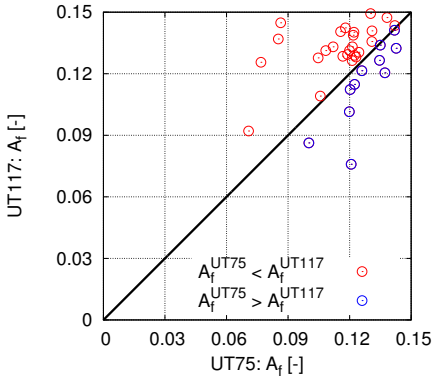

(a) Part IW: A_f^{UT117} versus A_f^{UT75}.

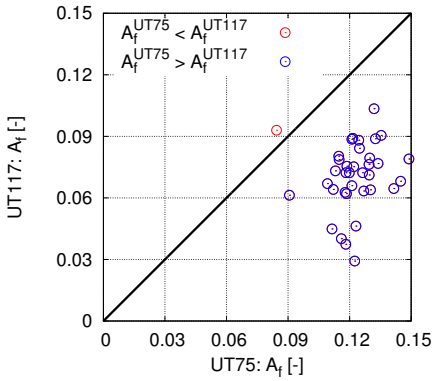

(b) Part BF: A_f^{UT117} versus A_f^{UT75}.

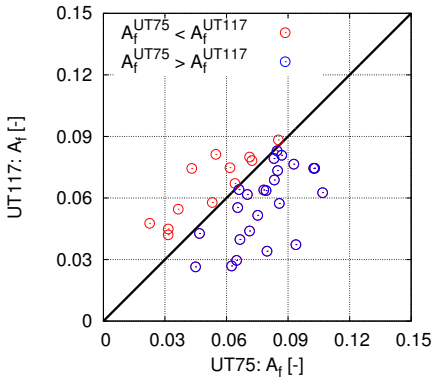

(c) Part OW: A_f^{UT117} versus A_f^{UT75}.

Figure 8.3.6: Scatter plots of the measured fracture strain A_f obtained from UT75 and UT117 specimens machined from six U900-1 components.

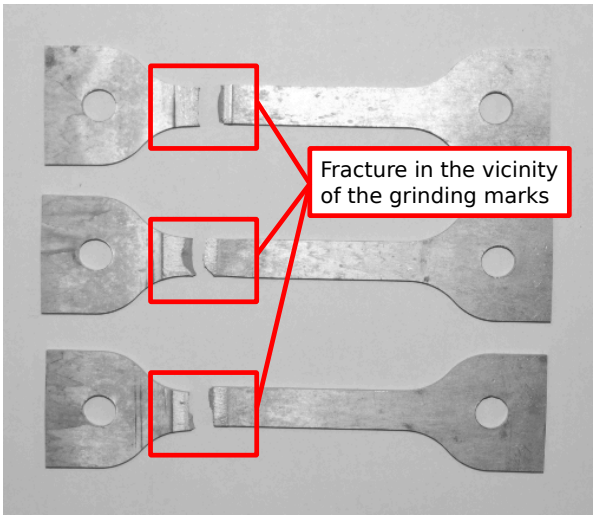

Figure 8.3.7: Three fractured UT117 specimens machined from part BF of U900-1 components.

blue data point represents a material which shows a dependence on the considered gauge volume according to the weakest-link approach. The scatter plot of the measured A_f obtained from specimens machined from part IW is presented in Figure 8.3.6a. It is seen that only 11 out of 36 data points (30.56%) are coloured in blue. In contrast, the scatter plot of the measured A_f obtained from specimens machined from part BF shows that 35 out of 36 data points (97.22%) are coloured in blue, see Figure 8.3.6b. Further, the scatter plot of the measured A_f obtained from specimens machined from part OW shows that 24 out of 36 data points (66.76%) are coloured in blue, see Figure 8.3.6c.

Based on the above presented analyses, the results obtained from specimens machined from part BF are considered as critical. The measured A_f obtained from UT117 specimens is much more smaller than the measured A_f obtained from UT75 specimens. In comparison to the results obtained from specimens machined from part IW and part OW this difference in the measured A_f is extreme. This might be caused by the extraction position and the machining of the UT117 specimens. As seen in the extraction plan, Figure B.3.2 of Appendix B.3, the extraction positions of the UT117 specimens are crossed by the long rib within the U900-1 component. The rib was cut and the cut surface was ground before a UT117 specimens was machined. Most of the UT117 specimens failed in the vicinity of the rib as seen in Figure 8.3.7. It can be assumed that the irregularities due to the grinding marks influenced the failure behaviour more than any casting defect within the gauge section of the specimen. Therefore, it is concluded that the test results obtained from these UT117 specimens are not relevant in the current study. In summary, a distinct volume dependence cannot be observed in the experimental results. The results obtained from specimens machined from part IW do not indicate a volume dependence and the results obtained from specimens machined from part OW only suggest a volume dependence.

8.3.2 Statistical Analysis

The objective of the statistical analysis is the identification of extraction positions with comparable material behaviour. As already described in the first material characterisation, the statistical analysis is based on measurements of critical value W_c. In summary,

36 samples each consisting of six measurements of W_c were analysed through hypothesis testing according to the flow chart given in Figure 8.1.5. First of all, it was analysed if

- the samples obtained from specimens machined from location 1 and location 2
- the samples obtained from specimens machined from location 3 and location 4
- the samples obtained from specimens machined from location 5 and location 6

can be assumed to be drawn from the same population. This analysis was performed separately for samples obtained from UT75 specimens and for samples obtained from UT117 specimens. The results of these 18 statistical comparisons can be found in Table B.4.7, Table B.4.8 and Table B.4.9 of Appendix B.4. In summary, it is seen that the assumption is confirmed in each part and for both specimen geometries. As a result, corresponding samples were merged together into new samples for further analysis. These 18 samples each consisting of 12 measurements of W_c are considered in the following.

The results of the statistical analysis of the samples obtained from UT75 specimens are presented in Table 8.3.1. Bartlett's test and one-way ANOVA cannot be applied for the samples obtained from specimens machined from part IW since AD_N-test of the sample obtained from specimens machined from extraction position IW-[5-6] fails. However, the result of Kruskal-Wallis test shows that it can be assumed that these three samples are drawn from the same population. One-way ANOVA cannot be applied for the samples obtained from specimens machined from part BF since the corresponding Bartlett's test fails. However, the result of Kruskal-Wallis test shows that it can be assumed that these three samples are drawn from the same population. One-way ANOVA as well as Kruskal-Wallis test of the samples obtained from specimens machined from part OW fail. This means that it can be assumed that these three samples are drawn from different populations. In addition, the two samples obtained from specimens machined from extraction positions OW-[1-2] and OW-[3-4] were analysed using two-sample tests. The results of F-test and the t-test show that it can be assumed that these two samples are drawn from the same population.

The result of the statistical analysis of the samples obtained from UT117 specimens are presented in Table 8.3.2. Bartlett's test and one-way ANOVA cannot be applied for the samples obtained from specimens machined from part IW since AD_N-test of the sample obtained from specimens machined from extraction position IW-[3-4] fails. However, the result of Kruskal-Wallis test shows that it can be assumed that these three samples are drawn from the same population. The results of the hypothesis tests of the samples obtained from specimens machined from part BF show that it can be assumed that these three samples are drawn from the same population. One-way ANOVA cannot be applied for the samples obtained from specimens machined from part OW since AD_N-test of the sample obtained from specimens machined from extraction position OW-[3-4] fails. Since Kruskal-Wallis test fails also, it can be assumed that the these three samples are drawn from different populations. In addition, the two samples obtained from specimens machined from extraction positions OW-[1-2] and OW-[3-4] were analysed using two-sample tests. Here, the result of the KS-test shows that it can be assumed that these two samples are drawn from the same population.

Based on the results obtained from these statistical analysis, the following samples were merged together for further analysis:

- The samples obtained from UT75 specimens machined from extraction positions IW-[1-2], IW-[3-4] and IW-[5-6] were merged together.

Uniaxial Tensile Test Specimen UT75 / W_c

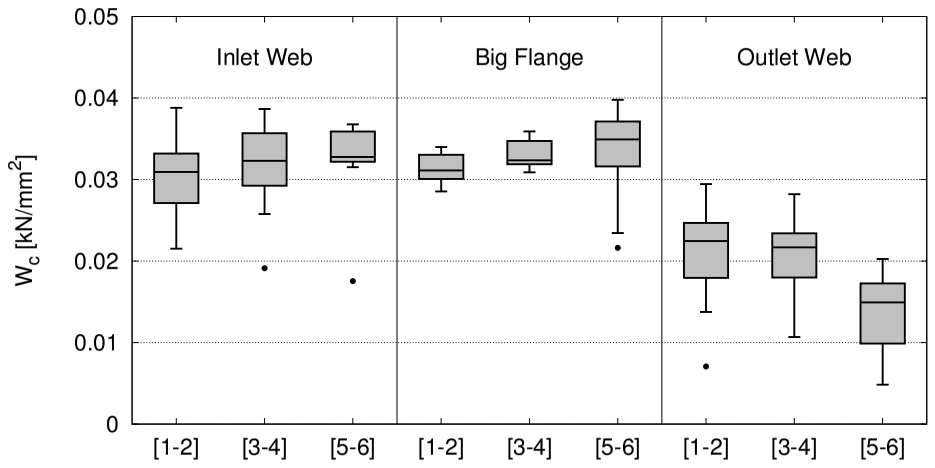

Samples			AD_N-Test A		AD_N-Test B		AD_N-Test C		Bartlett's Test		ANOVA		Kruskal-Wallis Test	
A	B	C	H_0	p	H_0	p	H_0	p	H_0	p	H_0	p	H_0	p
IW-[1-2]	IW-[3-4]	IW-[5-6]	0	0.55	0	0.38	**1**	0.00	~~0~~	~~0.95~~	~~0~~	~~0.49~~	0	0.29
BF-[1-2]	BF-[3-4]	BF-[5-6]	0	0.38	0	0.09	0	0.12	**1**	0.00	~~0~~	~~0.36~~	0	0.05
OW-[1-2]	OW-[3-4]	OW-[5-6]	0	0.41	0	0.66	0	0.38	0	0.59	**1**	0.00	**1**	0.00

									F-Test		t-Test		KS Test	
OW-[1-2]	OW-[3-4]		0	0.41	0	0.66			0	0.85	0	0.35	0	0.99

Table 8.3.1: Statistical hypothesis testing of samples based on measurements of W_c obtained from UT75 specimens machined from six U900-1 components: Results of AD_N-tests, Bartlett's test / F-test, one-way ANOVA / t-test and Kruskal-Wallis test / KS-test (significance level $\alpha = 0.05$).

Uniaxial Tensile Test Specimen UT117 / W_c

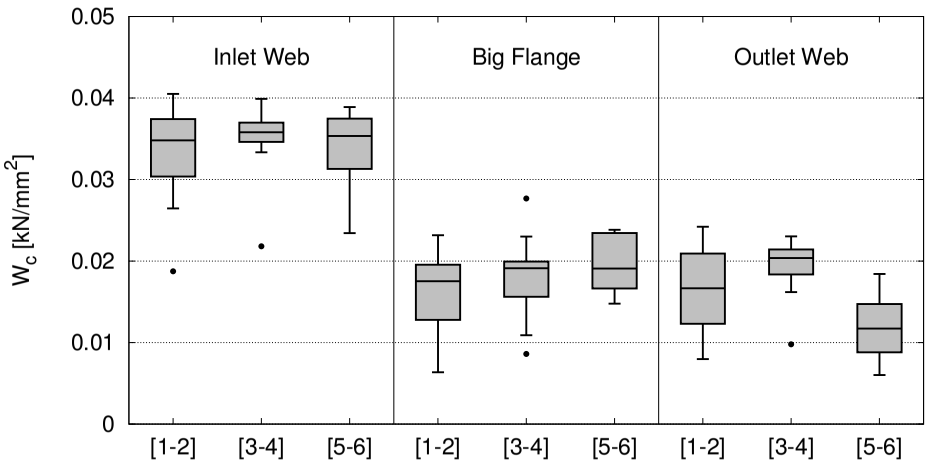

Samples			AD_N-Test A		AD_N-Test B		AD_N-Test C		Bartlett's Test		ANOVA		Kruskal-Wallis Test	
A	B	C	H_0	p	H_0	p	H_0	p	H_0	p	H_0	p	H_0	p
IW-[1-2]	IW-[3-4]	IW-[5-6]	0	0.20	**1**	0.00	0	0.22	~~0~~	~~0.50~~	~~0~~	~~0.72~~	0	0.86
BF-[1-2]	BF-[3-4]	BF-[5-6]	0	0.27	0	0.41	0	0.20	0	0.36	0	0.23	0	0.36
OW-[1-2]	OW-[3-4]	OW-[5-6]	0	0.64	**1**	0.01	0	0.58	~~0~~	~~0.45~~	~~**1**~~	~~0.00~~	**1**	0.00

									F-Test		t-Test		KS-Test	
OW-[1-2]	OW-[3-4]		0	0.64	**1**	0.01			~~0~~	~~0.12~~	~~0~~	~~0.23~~	0	0.19

Table 8.3.2: Statistical hypothesis testing of samples based on measurements of W_c obtained from UT117 specimens machined from six U900-1 components: Results of AD_N-tests, Bartlett's test / F-test, one-way ANOVA / t-test and Kruskal-Wallis test / KS-test (significance level $\alpha = 0.05$).

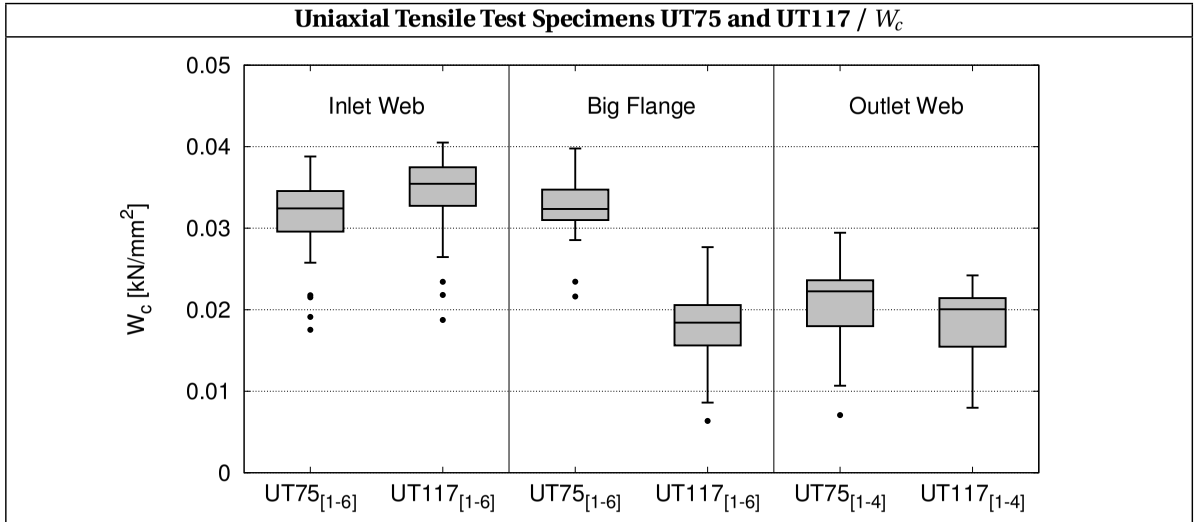

Samples		AD_N-Test A		AD_N-Test B		F-Test		t-Test		KS-Test	
A	B	H_0	p	H_0	p	H_0	p	H_0	p	H_0	p
UT75: IW-[1-6]	UT117: IW-[1-6]	**1**	0.01	**1**	0.00	~~0~~	~~0.86~~	~~**1**~~	~~0.03~~	**1**	0.00
UT75: BF-[1-6]	UT117: BF-[1-6]	0	0.05	0	0.15	0	0.12	**1**	0.00	**1**	0.00
UT75: OW-[1-4]	UT117: OW-[1-4]	0	0.28	**1**	0.01	~~0~~	~~0.50~~	~~**1**~~	~~0.05~~	**1**	0.02

Table 8.3.3: Statistical hypothesis testing of samples based on measurements of W_c obtained from UT75 and UT117 specimens machined from six U900-1 components: Results of AD_N-tests, F-test, t-test and KS-test (significance level $\alpha = 0.05$).

- The samples obtained from UT117 specimens machined from extraction positions IW-[1-2], IW-[3-4] and IW-[5-6] were merged together.
- The samples obtained from UT75 specimens machined from extraction positions BF-[1-2], BF-[3-4] and BF-[5-6] were merged together.
- The samples obtained from UT117 specimens machined from extraction positions BF-[1-2], BF-[3-4] and BF-[5-6] were merged together.
- The samples obtained from UT75 specimens machined from extraction positions OW-[1-2] and OW-[3-4] were merged together.
- The samples obtained from UT117 specimens machined from extraction positions OW-[1-2] and OW-[3-4] were merged together.

It was investigated if the samples obtained from UT75 and UT117 specimens machined from the same part can be assumed to be drawn from the same population. The three sample pairs were analysed using two-sample tests and the result is presented in Table 8.3.3. It is seen that at least KS-test fails for each sample pair. This implies that it can be assumed that the samples obtained from UT75 and UT117 specimens machined from the same part are drawn from different populations. Furthermore, the box-plot of the samples obtained from UT75 and UT117 specimens machined from part BF shows the extreme difference in the material ductility between both specimens geometries. Consequently, the failed t-test and the failed KS-test, respectively, confirms this difference. As already mentioned, it is assumed that the poor ductility of the UT117 specimens machined from part BF were mostly influenced by the machining of these specimens. However, KS-test fails also for the sample pairs obtained from UT75 and UT117 specimens machined from part IW and part OW, respectively. Based on this result, it can be assumed that the gauge volume influenced the material ductility measured by the critical value W_c at least in part IW and part OW.

Now, these six samples are considered. It is assumed that each sample follows a Weibull distribution. The corresponding Weibull parameters were estimated according to the procedure described in Chapter 8.1.3. Furthermore, the assumption that a sample follows a Weibull distribution is checked through AD_W-test. The results of these six Weibull analyses are presented in the same way as described in the first material characterisation, see Table 8.2.2. Here, scale volume V_0 was set either to the gauge volume of the UT75 specimen, see Figure 8.3.1a, or to the gauge volume of the UT117 specimen, see Figure 8.3.1b. The results of the Weibull analysis of the samples obtained from UT75 and UT117 specimens machined from part IW are presented in Table 8.3.4. As seen from the AD_W-test results, it can be assumed that the sample obtained from UT75 specimens follows a Weibull distribution, whereas the sample obtained from UT117 specimens does not follow a Weibull distribution. However, the Weibull plot of the two corresponding Weibull fits shows that the estimated Weibull modulus m is comparable for both distributions. However, it is important to notice that the Weibull fit of the sample obtained from UT117 specimens (blue) is to the right of the Weibull fit of the sample obtained from U75 specimens (red). This implies that the material in part IW does not show a volume dependence according to the weakest-link approach. As a conclusion, it can be assumed that both samples are drawn from Weibull distributions with a comparable Weibull modulus m. The results of the Weibull analyses of the samples obtained from UT75 and UT117 specimens machined from part BF are presented in Table 8.3.5. Based on the AD_W-test results results, it can be assumed that the two samples follow Weibull distributions. As expected, the Weibull plot shows a clear difference in the two Weibull fits. Again, the influence of

Uniaxial Tensile Test Specimens UT75 and UT117 / W_c (Part IW)

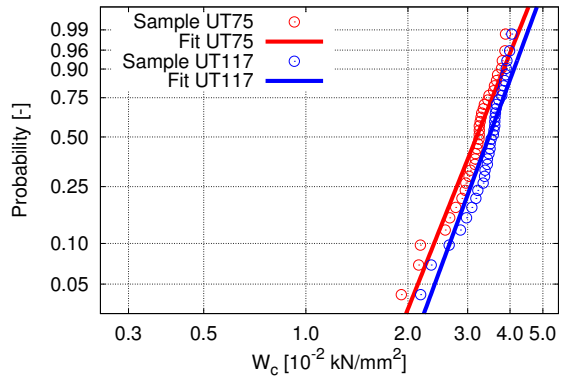

	AD_W-Test		Weibull Fit			
Position	H_0	p	m [−]	W_{c0} [kN/mm²]	V_0 [mm³]	R^2 [%]
UT75: IW-[1-6]	0	0.11	8.0072	0.0334	506.25	94.87
UT117: IW-[1-6]	**1**	0.03	9.9252	0.0360	1206.25	92.41

Table 8.3.4: Weibull analysis of samples based on measurements of W_c obtained from UT75 and UT117 specimens machined from part IW of six U900-1 components: AD_W-test result ($\alpha = 0.05$), estimated Weibull modulus m, estimated scaling parameter W_{c0}, scaling volume V_0 and coefficient of determination R^2.

the machining of the UT117 specimens on the ductility is assumed to be the main reason. As a result, the Weibull parameters estimated from the sample obtained from UT75 specimens are assumed to be the reliable ones for the underlying material. The results of the Weibull analyses of the samples obtained from UT75 and UT117 specimens machined from part OW are presented in Table 8.3.5. As seen from the AD_W-test results, it can be assumed that the sample obtained from UT75 specimens follows a Weibull distribution, whereas the sample obtained from UT117 specimens does not follow a Weibull distribution. Apart from that, the comparison of the two Weibull fits shows that the estimated Weibull modulus m is comparable for both distributions. Further, the comparison shows that the Weibull fit of the sample obtained from UT117 specimens (blue) is to the left of the Weibull fit of the sample obtained from UT75 specimens (red). This implies that the material in part OW shows a volume dependence according to the weakest-link approach. Hence, it can be assumed that the two samples are drawn from Weibull distributions with a comparable Weibull modulus m and a volume dependence according to the weakest-link approach.

Based on the result of the Weibull analysis of the samples obtained from UT75 and UT117 specimens machined from part OW, an extend Weibull fit was performed. Here, the Weibull parameters were estimated using both samples and the approach presented in Chapter 5.1.6. The best fit of the Weibull parameters m and W_{c0} was found when the function given in Equation (5.1.59) reached a minimum. Here, scale volume V_0 was set to 1000 mm³. The result of the extended Weibull fit is presented in Figure 8.3.8. It is noted that the result of the extended fit provides a unique Weibull distribution which should fit both samples. The sample data obtained from UT75 specimens are plotted as red points and the sample data obtained from UT117 specimens are plotted as blue data points. The fitted Weibull CDF using a considered volume of $V = V_{\mathrm{UT75}}$ is plotted as red line and the

Uniaxial Tensile Test Specimens UT75 and UT117 / W_c (Part BF)

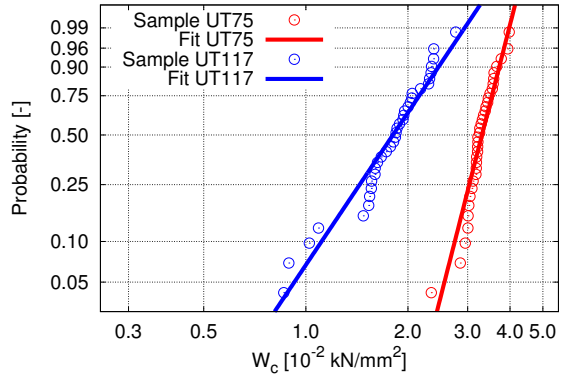

	AD_W-Test		Weibull Fit			
Position	H_0	p	m [−]	W_{c0} [kN/mm²]	V_0 [mm³]	R^2 [%]
UT75: BF-[1-6]	0	0.05	10.5923	0.0341	506.25	93.21
UT117: BF-[1-6]	0	0.25	4.5075	0.0196	1206.25	95.87

Table 8.3.5: Weibull analysis of samples based on measurements of W_c obtained from UT75 and UT117 specimens machined from part BF of six U900-1 components: AD_W-test result ($\alpha = 0.05$), estimated Weibull modulus m, estimated scaling parameter W_{c0}, scaling volume V_0 and coefficient of determination R^2.

Uniaxial Tensile Test Specimens UT75 and UT117 / W_c (Part OW)

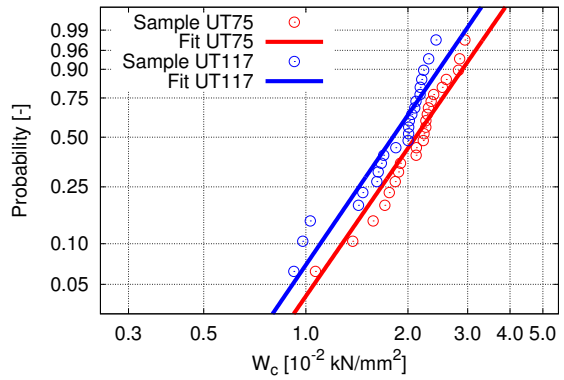

	AD_W-Test		Weibull Fit			
Position	H_0	p	m [−]	W_{c0} [kN/mm²]	V_0 [mm³]	R^2 [%]
UT75: OW-[1-4]	0	0.43	4.7526	0.0228	506.25	94.91
UT117: OW-[1-4]	**1**	0.01	4.9797	0.0196	1206.25	92.95

Table 8.3.6: Weibull analysis of samples based on measurements of W_c obtained from UT75 and UT117 specimens machined from part OW of six U900-1 components: AD_W-test result ($\alpha = 0.05$), estimated Weibull modulus m, estimated scaling parameter W_{c0}, scaling volume V_0 and coefficient of determination R^2.

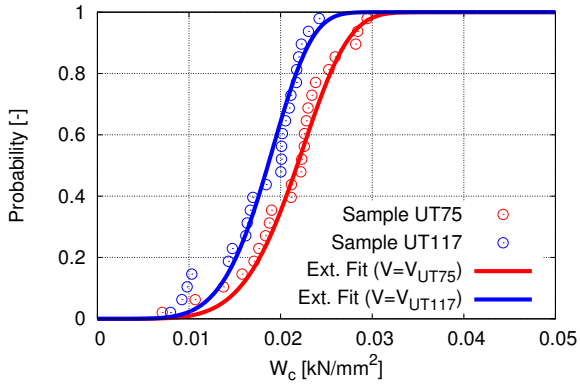

Figure 8.3.8: Probability plot of the samples based on measurements of W_c obtained from UT75 and UT117 specimens machined from part OW of six U900-1 components and extendedly fitted Weibull probability function using a considered volume of $V = V_{\mathrm{UT75}}$ and $V = V_{\mathrm{UT117}}$ $\left(m = 5.4829, W_{c0} = 0.0206^{\mathrm{kN}/\mathrm{mm}^2}, V_0 = 1000.0\mathrm{mm}^3\right)$.

same fitted Weibull CDF using a considered volume of $V = V_{\mathrm{UT117}}$ is plotted as blue line. It is seen that the Weibull distribution based on the extended fit correlates very well to both samples. Hence, it can be assumed that each sample is drawn from a common Weibull distribution which is modified by the considered gauge volume.

8.3.3 Concluding Remarks

The results of the second material characterisation can be concluded as follows:

- The results obtained from the first material characterisation were confirmed: The material ductility exhibits a global systematic variation and a local pseudo-random variation. In contrast to the first material characterisation, the strain hardening behaviour was better reproduced from specimens machined from the same part.

- The results of the mechanical analysis showed that the material ductility in part IW was less influenced by the applied gauge volumes, whereas the material ductility in part BF and part OW were strongly influenced by the applied gauge volumes. However, the analysis of the fractured UT117 specimens machined from part BF showed that the machining of specimens had a stronger influence on the material ductility than any casting defect. Hence, it was considered that the results obtained from UT117 specimens machined from part BF are not representative. Furthermore, it was observed that the symmetric casting system caused almost homogeneously distributed material properties in longitudinal direction. Finally, it was seen that the strain hardening behaviour was not influenced by the applied gauge volume in each part.

- The results of the statistical analyses showed that samples obtained from UT75 specimens machined from the same part belonged to the same population as well as samples obtained from UT117 specimens machined from the same part belonged to the same population. Based on this, all samples obtained from the same specimen geometry machined from the same part were merged together for further analysis. The statistical analyses of the merged samples showed that the samples obtained

from UT75 and UT117 specimens machined from the same part were drawn from different populations.

- A Weibull analysis was performed separately on each merged sample. The result of the Weibull analysis of the samples obtained from UT75 and UT117 specimens machined from part IW showed that Weibull modulus m estimated from samples obtained from UT75 and UT117 specimens was comparable, but a volume dependence according to the weakest-link approach could not be observed. As already mentioned, only the Weibull analysis of samples obtained from UT75 specimens machined from part BF provided a reliable result. The result of the Weibull analysis of samples obtained from UT75 and UT117 specimens machined from part OW was the only result which confirmed the weakest-link approach. Here, the estimated Weibull modulus m was comparable and the comparison of the two estimated Weibull distributions indicated a volume dependence. This result led to the conclusion that these samples were drawn from Weibull distributions with a comparable Weibull modulus m and a volume dependence according to the weakest-link approach. Based on this, an extended Weibull analysis was performed using the samples obtained from UT75 and UT117 specimens machined from part OW. The result of the extended Weibull analysis confirmed the assumption that each sample is drawn from a common Weibull distribution which is modified by the considered gauge volume. This result implies that a volume dependence according to the weakest-link approach could be only found in the material in part OW.

- Weibull modulus m is a material specific parameter, see Chapter 5.1.4. Theoretically, the same Weibull modulus m can be identified from samples obtained from specimens with different gauge volumes provided that all samples are drawn from the same material. Weibull modulus m estimated from the samples obtained from UT75 and UT117 specimens machined from part IW and from part OW, respectively, was comparable. This means that the Weibull modulus m could be reproduced using samples obtained from UT75 and UT117 specimens machined from part IW and from part OW, respectively. Hence, it can be concluded that Weibull modulus m of the material in part IW and part OW, respectively, could be correctly estimated. However, a volume dependence according to the weakest-link approach could be only identified by the samples obtained from UT75 and UT117 specimens machined from part OW. This means that only the less ductile material in part OW exhibited a typical weakest-link characteristic.

- In summary, the result of the Weibull analysis showed that at least the three samples obtained from UT75 specimens can be assumed to be drawn from different weakest-link Weibull distributions. This means that the local pseudo-random variation of the material ductility in part IW, part BF and part OW can be described by these estimated weakest-link Weibull distributions.

8.4 Concluding Remarks

The material behaviour of the HPDC alloy Castasil-37 in casting condition (F) was investigated using two material characterisations. Uniaxial tensile tests were carried out on specimens which were machined from U900-1 components and the results were analysed in detail. From that, the material behaviour of an HPDC alloy can be described as follows.

The casting system and the fluctuations during the casting process have a strong influence on the distribution of the casting defects within an HPDC component. The distribu-

tion of the casting defects is characterised by a global systematic variation caused by the casting system and by a local pseudo-random variation caused by casting process fluctuations. Since the casting defects lower mostly the material ductility, the material ductility is heterogeneously distributed within an HPDC component. The material ductility exhibits a global systematic variation and a local pseudo-random variation. Both variations can be estimated by measuring the material ductility as demonstrated in the two material characterisations. The two material characterisations showed that the U900-1 component can be separated in characteristic parts with comparable material ductility and, further, the local pseudo-random variation of the material ductility can be described by a weakest-link Weibull distribution. Based on these conclusions, it is recommend for the design of an HPDC component to use a probabilistic failure criterion to capture the local pseudo-randomness. Further, the global systematic variation might be captured by partitioning the HPDC component in characteristic parts and each part uses unique material parameters and unique Weibull distribution parameters.

Chapter 9

Numerical Material Modelling

In the material characterisation presented in the previous chapter, it was demonstrated that the casting defects causes a variation of the material ductility of HPDC alloy Castasil-37 in casting condition (F). An extensive statistical analysis was performed and it was shown that the variation of the material ductility can be separated into a global systematic variation and local pseudo-random variation. Consequently, a probabilistic approach in failure modelling is required to capture the local pseudo-random variation in the material ductility. In the present work, the weakest-link approach, see Chapter 5, is considered for the formulation of a probabilistic failure criterion. Inspired by the work by Dørum et al. [31], a material model consisting of an isotropic hypoelastic-plastic constitutive model and a probabilistic failure criterion based on the Cockcroft-Latham criterion and the Weibull distribution is introduced. As discussed in Chapter 5.2, a probabilistic failure criterion can be applied in different ways. Accordingly, the probabilistic failure criterion is applied in the following variants:

- Material routine MR#1: The first variant enables to compute directly failure probabilities in a FE model. The failure probabilities give information about the risk of first fracture initiation in the FE model, its different parts and in each element, see Chapter 5.2.3. Here, the probability calculations are based on the assumption that the elements are statistically independent. Since the risk of first fracture initiation is computed, this variant does not consider element deletion.

- Material routine MR#2: The second variant provides the possibility to analyse fracture initiation and the behaviour beyond fracture initiation using element deletion. Here, the critical failure value is distributed pseudo-randomly within the FE mesh, see Chapter 5.2.4. This variant considers statistical independence of the elements of the FE mesh. It is noted that this variant is applied in the work by Dørum et al. [31].

- Material routine MR#3: The third variant is based on the second variant, but the critical failure value is distributed pseudo-randomly in the FE model according to the uncoupled modelling approach, see Chapter 5.2.4. This means that FE mesh and MS mesh are uncoupled and the failure parameter is distributed pseudo-randomly within the MS mesh. This variant considers only statistical independence of the elements of the MS mesh.

- Material routine MR#4: The forth variant is almost equivalent to the third variant. However, the random distribution of the critical failure value is given as an initial

condition by the user. This approach enables to consider statistical dependence of the elements of the MS mesh.

Each variant was implemented as user-defined material routine in the explicit FE solver LS-DYNA 971 [51] can be applied for shell elements and for solid elements. However, the material routines are restricted to underintegrated elements with a single integration point for solid elements and with a single in-plane integration point for shell elements. Further, it is noted that the material routines were coded in the programming language Fortran 95. The formulation and the numerical implementation of these four material routines variants are presented in the following.

9.1 Basis of Material Routines MR#x

A material model is implemented in an explicit FE solver in form of a subroutine known as material routine. Here, it is referred to Chapter 4.1.6 which describes the FEM and the explicit time integration algorithm. In each time step, the material routine is called by the element routine in each integration point. According to the applied element formulation, the strains in each integration point are computed by the element routine based on the nodal displacements at the current time. According to the applied constitutive model, the stress tensor and the internal variables are computed by the material routine based on the strains at the current time. Then, the element routine computes the nodal forces at the current time based on the stress tensors obtained from the integration points. Based on the nodal forces at the current time, the explicit time integration algorithm computes the nodal displacements of the next time. In addition, a failure criterion can be evaluated within the material routine and the result can be used for element deletion which is important for the prediction of crack propagation. As already mentioned, the material model introduced in the current work is applied in four variants and these four variants are given by material routines MR#1, MR#2, MR#3 and MR#4. These material routines are based on the same constitutive model and the same failure criterion. In the following, formulation and implementation of constitutive model and failure criterion are described.

9.1.1 Constitutive Model and and Stress Update Algorithm

The literature review given in Chapter 6.1 showed that HPDC alloys can be well described by isotropic hypoelastic-plastic constitutive models. According to the work by Dørum et al. [31], an isotropic hypoelastic-plastic constitutive model including a linear hypoelastic relation, a high-exponent isotropic yield criterion, a nonlinear isotropic hardening rule and associated flow rule is applied in material routines MR#1, MR#2, MR#3 and MR#4. It is assumed that the elastic strains are infinitesimal, whereas the plastic strains and rotations may be finite. Further, the Jaumann stress rate is adopted to ensure material objectivity. It is noted that this constitutive model does not include strain-rate dependence and the influence of damage evolution on the deformation behaviour is neglected. More details on the formulation of this constitutive model can be found in Chapter 4.1.5.

The numerical algorithm for integrating the constitutive equations is called stress update algorithm. The objective of the stress update algorithm is the computation of stress tensor and internal variables at the current time based on the result of the previous time. In case of plasticity, the stress update algorithm ensures that the update of stress tensor and internal variables are consistent with yield condition, flow rule and hardening rule. The most common stress update algorithms for plasticity are based on the backward Euler return mapping scheme. The backward Euler return mapping scheme consists of two

steps. The first step is called elastic-predictor step. The stress tensor is updated assuming that the response is purely elastic. The second step is called plastic-corrector step. If the updated stress tensor is outside the yield surface, the updated stress tensor is projected on the closest point of the yield surface. In case the yield surface expands during plastic flow, the updated stress tensor is projected on the updated yield surface. Finally, stress tensor and internal variables are updated. A detailed description of various stress update algorithms can be found in the book by Belytschko et al. [13]. In the present work, the backward Euler return mapping scheme is applied to update stress tensor $\boldsymbol{\sigma}$ and equivalent plastic strain $\bar{\varepsilon}$ according to the constitutive equations summarised in Figure 4.1.4. Its implementation in a material routine is described in the following. It is noted that the implementation is restricted for explicit time integration. In case of implicit time integration, the material tangent stiffness needs to be determined.

Stress tensor $\boldsymbol{\sigma}_n$ and equivalent plastic strain $\bar{\varepsilon}_n$ are known at time t_n in the material routine. Further, rate-of-deformation tensor $\mathbf{D}_{n+\frac{1}{2}}$ at time $t_{n+\frac{1}{2}}$ is known from the element solution. The change of strain tensor $\boldsymbol{\varepsilon}$ between time t_{n+1} and time t_n is computed by the strain increment

$$\triangle\boldsymbol{\varepsilon}_{n+1} = \mathbf{D}_{n+\frac{1}{2}}(t_{n+1} - t_n). \tag{9.1.1}$$

Based on stress tensor $\boldsymbol{\sigma}_n$, equivalent plastic strain $\bar{\varepsilon}_n$ and strain increment $\triangle\boldsymbol{\varepsilon}_{n+1}$, stress tensor $\boldsymbol{\sigma}_{n+1}$ and equivalent plastic strain $\bar{\varepsilon}_{n+1}$ at time t_{n+1} are computed by the backward Euler return mapping scheme in the material routine.

The elastic-predictor is determined according to Equation (4.1.73) and reads

$$\boldsymbol{\sigma}^{tr}_{n+1} = \boldsymbol{\sigma}_n + \lambda_{el}\,\mathrm{tr}\left[\triangle\boldsymbol{\varepsilon}_{n+1}\right]\mathbf{I} + 2\mu_{el}\triangle\boldsymbol{\varepsilon}_{n+1} \tag{9.1.2}$$

where $\boldsymbol{\sigma}^{tr}_{n+1}$ denotes the trial stress tensor at time t_{n+1}. Trial stress tensor $\boldsymbol{\sigma}^{tr}_{n+1}$ is inserted in the high-exponent isotropic yield criterion given by

$$\begin{aligned} f\left(\boldsymbol{\sigma}^{tr}_{n+1}, \bar{\varepsilon}_n\right) \;=\; & \left((\sigma_I)^{tr}_{n+1} - (\sigma_{II})^{tr}_{n+1}\right)^{2p} + \left((\sigma_{II})^{tr}_{n+1} - (\sigma_{III})^{tr}_{n+1}\right)^{2p} + \\ & + \left((\sigma_{III})^{tr}_{n+1} - (\sigma_I)^{tr}_{n+1}\right)^{2p} - 2(\sigma_Y(\bar{\varepsilon}_n))^{2p} = 0 \end{aligned} \tag{9.1.3}$$

where $\left(\sigma_{I,II,III}\right)^{tr}_{n+1}$ denotes the trial principal stresses which are computed according to Equation (4.1.28). Here, the high-exponent yield surface is restricted to a continuously differentiable yield surface and, thus, the exponent is set to $2p$ where p is a positive integer. The current yield stress $\sigma_Y(\bar{\varepsilon}_n)$ is given by the two-terms Voce rule, see Equation (4.1.3b), and reads

$$\sigma_Y(\bar{\varepsilon}_n) = \sigma_0 + \sum_{i=1}^{2} Q_i\left(1 - \exp(-C_i\bar{\varepsilon}_n)\right). \tag{9.1.4}$$

From that, the yield criterion is evaluated and the result leads to the conclusions

$$\begin{aligned} f\left(\boldsymbol{\sigma}^{tr}_{n+1}, \bar{\varepsilon}_n\right) \leq 0: &\quad \text{Elastic Response.} \\ f\left(\boldsymbol{\sigma}^{tr}_{n+1}, \bar{\varepsilon}_n\right) > 0: &\quad \text{Plastic Response.} \end{aligned} \tag{9.1.5}$$

If the response is elastic, updated stress tensor $\boldsymbol{\sigma}_{n+1}$ equals trial stress tensor $\boldsymbol{\sigma}^{tr}_{n+1}$ and updated equivalent plastic strain $\bar{\varepsilon}_{n+1}$ remains unchanged and equals the previous one $\bar{\varepsilon}_n$. However, if the response is plastic, updated stress tensor $\boldsymbol{\sigma}_{n+1}$ and updated equivalent plastic strain $\bar{\varepsilon}_{n+1}$ needs to be calculated so that the yield condition is satisfied. The plastic-corrector is written in form of

$$\boldsymbol{\sigma}_{n+1} = \boldsymbol{\sigma}^{tr}_{n+1} - \left[\lambda_{el}\,\mathrm{tr}\left[\triangle\bar{\varepsilon}_{n+1}\mathbf{n}_{n+1}\right]\mathbf{I} + 2\mu_{el}\triangle\bar{\varepsilon}_{n+1}\mathbf{n}_{n+1}\right] \tag{9.1.6}$$

where $\triangle\bar{\varepsilon}_{n+1}$ denotes the increment of equivalent plastic strain and $\mathbf{n}_{n+1}$ is the plastic flow direction. Updated equivalent plastic strain $\bar{\varepsilon}_{n+1}$ becomes

$$\bar{\varepsilon}_{n+1} = \bar{\varepsilon}_n + \triangle\bar{\varepsilon}_{n+1} \tag{9.1.7}$$

Plastic direction $\mathbf{n}_{n+1}$ is determined according to associated flow rule, see Equation (4.1.83), so that

$$\mathbf{n}_{n+1} = \frac{\partial f\left(\boldsymbol{\sigma}^{tr}_{n+1}, \bar{\varepsilon}_{n+1}\right)}{\partial \boldsymbol{\sigma}^{tr}_{n+1}}. \tag{9.1.8}$$

Consequently, the plastic corrector is rewritten as

$$\boldsymbol{\sigma}_{n+1} = \boldsymbol{\sigma}^{tr}_{n+1} - \left[\lambda_{el}\,\mathrm{tr}\left[\triangle\bar{\varepsilon}_{n+1}\frac{\partial f\left(\boldsymbol{\sigma}^{tr}_{n+1}, \bar{\varepsilon}_{n+1}\right)}{\partial \boldsymbol{\sigma}^{tr}_{n+1}}\right]\mathbf{I} + 2\mu_{el}\triangle\bar{\varepsilon}_{n+1}\frac{\partial f\left(\boldsymbol{\sigma}^{tr}_{n+1}, \bar{\varepsilon}_{n+1}\right)}{\partial \boldsymbol{\sigma}^{tr}_{n+1}}\right]. \tag{9.1.9}$$

The yield condition still has to be satisfied at time t_{n+1} and reads

$$f(\boldsymbol{\sigma}_{n+1}, \bar{\varepsilon}_{n+1}) = f_{n+1} = \bar{\sigma}(\boldsymbol{\sigma}_{n+1}) - \sigma_Y(\bar{\varepsilon}_{n+1}) = 0 \tag{9.1.10}$$

where equivalent plastic strain increment $\triangle\bar{\varepsilon}_{n+1}$ is the remaining unknown quantity. The corresponding derivative f'_{n+1} with respect to the equivalent plastic strain increment $\triangle\bar{\varepsilon}_{n+1}$ is given by

$$f'(\boldsymbol{\sigma}_{n+1}, \bar{\varepsilon}_{n+1}) = f'_{n+1} = \frac{\partial f(\boldsymbol{\sigma}_{n+1}, \bar{\varepsilon}_{n+1})}{\partial \triangle\bar{\varepsilon}_{n+1}}. \tag{9.1.11}$$

The unknown quantity $\triangle\bar{\varepsilon}_{n+1}$ is found numerically using Newton's iteration method in form of

$$\triangle\bar{\varepsilon}^{(k+1)}_{n+1} = \triangle\bar{\varepsilon}^{(k)}_{n+1} - \frac{f^{(k)}_{n+1}}{f'^{(k)}_{n+1}} \tag{9.1.12}$$

where integer k denotes the iteration step. A solution of $\triangle\bar{\varepsilon}_{n+1}$ is found when the Newton's method converges, so that

$$f^{(k+1)}_{n+1} = 0. \tag{9.1.13}$$

Using the solution of strain increment $\triangle\bar{\varepsilon}_{n+1}$, stress tensor $\boldsymbol{\sigma}_{n+1}$ is updated according to Equation (9.1.6) and equivalent plastic strain $\bar{\varepsilon}_{n+1}$ is updated according to Equation (9.1.7). It is noted that Newton's iteration method might not be exactly solved. Therefore, it is common to stop the iteration when an abort criterion is met. For instance, the abort criterion can be defined as

$$\left|\frac{f^{(k+1)}_{n+1}}{\sigma_Y\left(\bar{\varepsilon}^{(k+1)}_{n+1}\right)}\right| < tol \tag{9.1.14}$$

where tol denotes a tolerance level which has to be defined in advance. This abort criterion is applied in the current work and the tolerance level is set to $tol = 1.0 \cdot 10^{-8}$. The implementation of the applied stress update algorithm is summarised in Figure C.1.1 of Appendix C.1.

9.1.2 Failure Criterion and Element Deletion

As seen in the work by Dørum et al. [31], the failure behaviour of a HPDC alloy can be well described by the Cockcroft-Latham criterion. The criterion states that fracture occurs when Cockcroft-Latham integral W, Equation (4.3.22), reaches critical value W_c as expressed in Equation (4.3.22). This failure criterion forms the basis for element deletion

in material routines MR#2, MR#3 and MR#4 and its implementation is described in the following.

When the stress update algorithm is converged, Cockcroft-Latham integral W_{n+1} at time t_{n+1} is computed numerically according to

$$W_{n+1} = W_n + \max\left[0, \max\left[\left(\sigma_{I,II,III}\right)_{n+1}\right] \triangle\bar{\varepsilon}_{n+1}\right] \tag{9.1.15}$$

where W_n denotes the Cockcroft-Latham integral at time t_n and $\left(\sigma_{I,II,III}\right)_{n+1}$ denote the principal stresses of updated stress tensor $\boldsymbol{\sigma}_{n+1}$. The principal stresses are computed according to Equation (4.1.28). When the updated integral W_{n+1} is equal or larger than critical value W_c, the element deletion flag is set true. When updated Cockcroft-Latham integral W_{n+1} is smaller than critical value W_c, the element deletion flag is set false. This means that the element deletion flag is set true when a single integration point fails.

The element deletion flag is a logical variable used in the element routine. In each time step, the material routine is called by the element routine in each integration point. When the element deletion flag was set false in the previous time step, the stress update algorithm is performed and the failure criterion is evaluated in each integration point. When the element deletion was set true in the previous time step, the components of the stress tensor are set to zero in each integration point. Furthermore, the element deletion flag remains unchanged for all remaining time steps. This approach implies that an element with an element deletion flag set true deforms without any resistance. Moreover, the element deletion flag is important for the post-processing. An element with an element deletion flag set true is deleted from the animation of a FE simulation. The implementation of the applied element deletion algorithm is summarised in Figure C.1.2 of Appendix C.1.

9.2 Material Routine MR#1

The Cockcroft-Latham criterion given in Equation (4.3.22) and the Weibull failure probability given in Equation (5.1.39) are used to determine the failure probability P_F of material volume V according to

$$P_F = 1 - \exp\left(-\frac{V}{V_0}\left(\frac{W}{W_{c0}}\right)^m\right) \quad \text{with} \quad W \geq 0 \tag{9.2.1}$$

where W denotes the value of the Cockcroft-Latham integral and V_0, W_{c0} and m denote the Weibull distribution parameters. This expression forms the basis of material routine MR#1. The approach described in Chapter 5.2.3 is used to compute the failure probability of an integration point, an element, the FE model as well as of the different model parts. The same requirements as defined in Chapter 5.2.1 are provided and the same assumptions as defined in Chapter 5.2.2 are made. This implies that all elements and their integration points are considered as statistically independent. The objective of material routine MR#1 is to compute failure probabilities. As already mentioned, a failure probability gives information about the risk of first fracture initiation and, consequently, element deletion is not considered in material routine MR#1.

The following element properties are required in material routines MR#1, MR#2, MR#3 and MR#4:

- The number of integration points is denoted as n.
- The current integration point is denoted as i.

- The initial element volume is denoted as V_{ini}.
- The proportional initial volume of an integration point is given by $\frac{V_{ini}}{n}$.
- The part which belongs to the current element is denoted as j.
- The number of element nodes is denoted as n_{nod}.
- The nodal coordinates are denoted as x_k, y_k and z_k.

Cockcroft-Latham integral W^i_{n+1} at time t_{n+1} is computed in integration point i according to Equation (9.1.15). Based on integral W^i_{n+1}, the survival probability $\left(P_S^{i,j}\right)_{n+1}$ of integration point i at time t_{n+1} is computed by

$$\left(P_S^{i,j}\right)_{n+1} = \exp\left(-\frac{\frac{V_{ini}}{n}}{V_0}\left(\frac{W_{n+1}}{W_{c0}}\right)^m\right) \tag{9.2.2}$$

Consequently, the failure probability $\left(P_F^{i,j}\right)_{n+1}$ of integration point i at time t_{n+1} is computed by

$$\left(P_F^{i,j}\right)_{n+1} = 1 - \left(P_S^{i,j}\right)_{n+1}. \tag{9.2.3}$$

It is known that the element routine calls the material routine in each integration and the integration points are processed in an ascending order. This fact allows to compute the survival probability $\left(P_S^{elem,j}\right)_{n+1}$ and the failure probability $\left(P_F^{elem,j}\right)_{n+1}$ of the actual element at time t_{n+1} within material routine MR#1 as follows

$$\text{if } i = 1: \quad \rightarrow \quad X^{elem} = \left(P_S^{1,j}\right)_{n+1} \tag{9.2.4}$$

$$\text{if } i > 1: \quad \rightarrow \quad X^{elem} = X^{elem} \cdot \left(P_S^{i,j}\right)_{n+1} \tag{9.2.5}$$

$$\text{if } i = n: \quad \rightarrow \quad \left(P_S^{elem,j}\right)_{n+1} = X^{elem} \tag{9.2.6}$$

$$\left(P_F^{elem,j}\right)_{n+1} = 1 - X^{elem} \tag{9.2.7}$$

where X^{elem} is a variable which is stored in a common block used in the element routine. When material routine MR#1 is called at the first integration point, variable X^{elem} is initialised by probability $\left(P_S^{1,j}\right)_{n+1}$. Then, variable X^{elem} is updated by probability $\left(P_S^{i,j}\right)_{n+1}$ each time material routine MR#1 is called until the last integration point is reached. This implementation approach implies that the element probabilities $\left(P_S^{elem,j}\right)_{n+1}$ and $\left(P_F^{elem,j}\right)_{n+1}$ are available only on the last integration point.

The survival probability $\left(P_S^{model}\right)_{n+1}$ and the failure probability $\left(P_F^{model}\right)_{n+1}$ of the FE model at time t_{n+1} are also computed within material routine MR#1 as follows

$$\left(P_S^{model}\right)_{n+1} = \left(X^{model}\right)_n \tag{9.2.8}$$

$$\left(P_F^{model}\right)_{n+1} = 1 - \left(P_S^{model}\right)_{n+1} \tag{9.2.9}$$

$$\left(X^{model}\right)_{n+1} = \left(X^{model}\right)_{n+1} \cdot \left(P_S^{i,j}\right)_{n+1} \tag{9.2.10}$$

where X^{model} is a variable which is stored in a common block used in the FE solver. Variable$\left(X^{model}\right)_{n+1}$ is updated by probability $\left(P_S^{i,j}\right)_{n+1}$ each time material routine MR#1

is called in the FE model at time t_{n+1}. If variable $\left(X^{model}\right)_{n+1}$ is used to compute the model probabilities $\left(P_S^{model}\right)_{n+1}$ and $\left(P_F^{model}\right)_{n+1}$, then the model probabilities are only correctly computed in the integration point which is called last at time t_{n+1}. Hence, the model probabilities are computed using the result of variable $\left(X^{model}\right)_n$ at time t_n. Consequently, the model probabilities are available in each integration point of the FE model at time t_{n+1}. This simplification has only a minor influence on the accuracy due the very small time steps used in the explicit time integration.

The survival probability $\left(P_S^j\right)_{n+1}$ and the failure probability $\left(P_F^j\right)_{n+1}$ of part j at time t_{n+1} are computed in the same manner, so that

$$\left(P_S^j\right)_{n+1} = \left(\mathbf{X}(j)\right)_n \tag{9.2.11}$$

$$\left(P_F^j\right)_{n+1} = 1-\left(P_S^j\right)_{n+1} \tag{9.2.12}$$

$$\left(\mathbf{X}(j)\right)_{n+1} = \left(\mathbf{X}(j)\right)_{n+1}\cdot\left(P_S^{i,j}\right)_{n+1} \tag{9.2.13}$$

where $\mathbf{X}$ is a vector which is stored in a common block used in the FE solver. The size of vector $\mathbf{X}$ equals the number of the different model parts. This implementation approach guarantees that the probabilities $\left(P_S^j\right)_{n+1}$ and $\left(P_F^j\right)_{n+1}$ of part j at time t_{n+1} are computed only by the elements which belong to part j. It is important to consider that the different parts need to be defined in a continuous ascending order. The procedure in material routine MR#1 is summarised in Figure C.2.1 of Appendix C.2.

9.3 Material Routine MR#2

Material routine MR#2 is based on the element deletion algorithm presented in Figure C.1.2. However, critical value W_c is introduced as a pseudo-random variable which follows a Weibull distribution in form of the CDF

$$F(W_c) = 1-\exp\left(-\frac{V}{V_0}\left(\frac{W_c}{W_{c0}}\right)^m\right) \quad \text{with} \quad W_c \geq 0 \ . \tag{9.3.1}$$

A detailed description of this approach can be found in Chapter 5.2.4. Therefore, the same requirements as defined in Chapter 5.2.1 are provided and the same assumptions as defined in Chapter 5.2.2 are made. It is noted that a uniform critical value W_c is applied in an element when material routine MR#2 is applied. Consequently, critical value W_c is randomly distributed according to a Weibull distribution between the elements of a FE model, but each element uses a uniform critical value W_c. The usage of material routine MR#2 implies that all elements are considered as statistically independent.

In material routine MR#2, critical value W_c is computed by the inverse transformation of the Weibull distribution and a uniform PRNG, see Chapter 3.3.7. The programming language Fortran 95 includes a PRNG available by the function rand_number [·] [43] which returns a single pseudo-random number or an array of pseudo-random numbers from the uniform distribution. The PRNG used by function rand_number [·] is reset to a default state each time a Fortran 95 program is executed. This means that function rand_number [·] returns uniform pseudo-random numbers from the same sequence each time a Fortran 95 program is executed. This can be avoided using the function rand_seed [·] [44] which enables to initialise the PRNG used by function rand_number [·] to a default state or to a varying state. Function rand_seed [·] is necessary to ensure that function rand_number [·] does not return uniform pseudo-random numbers from the same sequence each time a Fortran 95 program is executed. In the present work, the PRNG used by

```
subroutine init_random_seed(t)
implicit none
integer ::  i, n, t
integer, dimension(:), allocatable ::  seed
call random_seed(size = n)
allocate(seed(n))
seed = clock + 37 * (/ (i - 1, i = 1, n) /)
call random_seed(PUT = seed)
deallocate(seed)
end subroutine init_random_seed
```

Figure 9.3.1: Fortran 95 code of subroutine init_random_seed(t) taken from the course "FORTRAN Programming for Engineers" by D. Hogan [94].

function rand_number[·] is initialised using subroutine init_random_seed($clock$) which includes function rand_seed[·]. The code is taken from the course "FORTRAN Programming for Engineers" by D. Hogan [94] and is shown in Figure 9.3.1. Here, the PRNG used by function rand_number[·] is initialised to a varying state based on the integer $clock$. This subroutine enables to control the initialisation of the PRNG used by function rand_number[·].

Material routine MR#2 calls subroutine init_random_seed($clock$) during a FE simulation only once at time $t = 0$. This implies that this subroutine is only called when material routine MR#2 is called the first time in a FE simulation. Afterwards, a flag is set so that this subroutine is skipped each time material routine MR#2 is called. In case function rand_number[·] should return uniform pseudo-random numbers from the same sequence each time a FE simulation is performed, integer $clock$ needs to be set constant ($clock = 8888$). In case function rand_number[·] should return uniform pseudo-random numbers from varying sequences each time a FE simulation is performed, integer $clock$ needs to be set to the actual computer time t_{cpu}^{ini} at initialisation of the FE model $\left(clock = t_{cpu}^{ini}\right)$.

As already mentioned, the same critical value W_c is used in an element and, thus, the same uniform pseudo-random number needs to be used in an element. Hence, function rand_number(·) is only called in the first integration point and returns a uniform pseudo-random number u. Then, the variable x^{elem} which is stored in a common block used in the element routine is set to number u, so that

$$\text{if } i = 1: \quad \rightarrow \quad \text{rand\_number}[u] \tag{9.3.2}$$

$$x^{elem} = u \tag{9.3.3}$$

Based on variable x^{elem}, the Weibull CDF given in Equation (9.3.1) and the inverse transformation given in Equation (3.3.73), critical value W_c is computed in each integration point by

$$W_c = W_{c0} \sqrt[m]{\left(-\frac{V_0}{V_{ini}}\right) \ln\left(1 - x^{elem}\right)} \tag{9.3.4}$$

It is noted that critical value W_c needs to be computed in each element only at time $t = 0$. The procedure in material routine MR#2 is summarised in Figure C.3.1 of Appendix C.3.

9.4 Material Routine MR#3

The usage of material routine MR#2 leads to a pseudo-random distribution of critical value W_c in a FE model. The underlying modelling approach was defined as a coupled

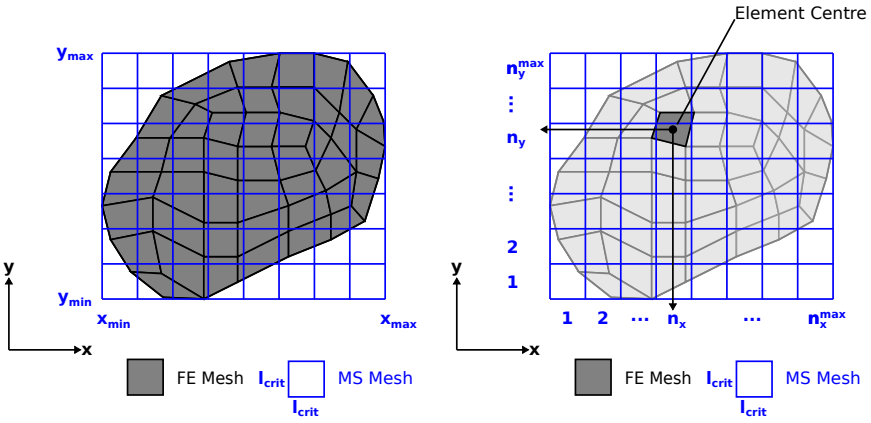

(a) Creation of the MS mesh.

(b) Mapping of the MS mesh onto the FE mesh.

Figure 9.4.1: Creation of the MS mesh based on the dimensions of the FE mesh and mapping of the MS mesh onto the FE mesh.

modelling approach in Chapter 5.2.4. This means that FE mesh and MS mesh are coupled (congruent). However, an uncoupled modelling approach in probabilistic failure modelling was introduced in Chapter 5.2.4. Here, FE mesh and MS mesh are uncoupled and the critical failure parameter is pseudo-randomly distributed in the MS mesh and the pseudo-random distribution is mapped onto the FE mesh. The uncoupled modelling approach is adopted in the material routine MR#3. Critical value W_c is pseudo-randomly distributed in the MS mesh based on the Weibull CDF given in Equation (9.3.1). Apart from this, material routine MR#3 corresponds to material routine MR#2. In contrast to material routine MR#2, material routine MR#3 allows to perform mesh convergence studis, see Figure 5.2.3. It is noted that the implementation of material routine MR#3 is based on the same requirements as defined in Chapter 5.2.1 and the same assumptions as defined in Chapter 5.2.2. Further, the usage of material routine MR#3 implies that all elements of the MS mesh are considered as statistically independent.

The MS mesh using elements of equal edge lengths is created based on the minimum and maximum dimensions of the considered FE mesh. The MS mesh uses the same coordinate system as the FE mesh. The edge length of an element of the MS mesh is denoted as l_{crit}. The approach of creating the MS mesh based on the dimensions of a FE mesh and the mapping of the MS mesh onto the FE mesh is illustrated in Figure 9.4.1. For simplicity, a plane problem is considered. Figure 9.4.1b shows the underlying FE mesh in grey and the MS mesh in blue. It is seen that the MS mesh is created based on the minimum and maximum dimensions of the FE mesh and a MS mesh size of l_{crit}. The MS mesh is mapped onto the FE mesh as shown in Figure 9.4.1b. Here, the centre of an element of the FE mesh is used to identify the corresponding element of the MS mesh.

The creation of the MS mesh and the mapping of the MS mesh onto the FE mesh is performed within material routine MR#3 according to the following approach. The number of elements of the MS mesh in x, y and z direction is computed in the first integration as

follows

$$\text{if } i=1: \quad \rightarrow \quad n_x^{max} = \text{ceiling}\left[\frac{x_{max}-x_{min}}{l_{crit}}\right] \tag{9.4.1}$$

$$n_y^{max} = \text{ceiling}\left[\frac{y_{max}-y_{min}}{l_{crit}}\right] \tag{9.4.2}$$

$$n_z^{max} = \text{ceiling}\left[\frac{z_{max}-z_{min}}{l_{crit}}\right] \tag{9.4.3}$$

where n_x^{max}, n_y^{max} and n_z^{max} denote the number of elements of the MS mesh in x, y and z direction and x_{max} and x_{min} denote the minimum and maximum dimensions in x direction, y_{max} and y_{min} the minimum and maximum dimensions in y direction and z_{max} and z_{min} the minimum and maximum dimensions in z direction. Since n_x^{max}, n_y^{max} and n_z^{max} are integers, the function ceiling$[\cdot]$ is applied. This function maps a real number to the smallest following integer. It is noted that the minimum and maximum dimensions of the FE mesh as well as the edge length l_{crit} need to be specified by the user in advance.

The centre of the current element of the FE mesh is computed in the first integration point using its nodal coordinates and the number of nodes, so that

$$\text{if } i=1: \quad \rightarrow \quad x_m = \frac{1}{n_{nod}}\sum_{k=1}^{n_{nod}} x_k \tag{9.4.4}$$

$$y_m = \frac{1}{n_{nod}}\sum_{k=1}^{n_{nod}} y_k \tag{9.4.5}$$

$$z_m = \frac{1}{n_{nod}}\sum_{k=1}^{n_{nod}} x_k \tag{9.4.6}$$

where x_m, y_m and z_m are the coordinates of the centre. Based on these coordinates and the minimum and maximum dimensions of the FE mesh, the corresponding element of the MS mesh is found by

$$\text{if } i=1: \quad \rightarrow \quad n_x = \text{ceiling}\left[\frac{x_m-x_{min}}{l_{crit}}\right] \tag{9.4.7}$$

$$n_y = \text{ceiling}\left[\frac{y_m-y_{min}}{l_{crit}}\right] \tag{9.4.8}$$

$$n_z = \text{ceiling}\left[\frac{z_m-z_{min}}{l_{crit}}\right] \tag{9.4.9}$$

where n_x, n_y and n_z denote the required number of elements of the MS mesh in x, y and z direction to identify the corresponding element of the MS mesh. Then, the number of the corresponding element of the MS mesh is computed according to

$$\text{if } i=1: \quad \rightarrow \quad n = (n_z-1)\, n_y^{max} n_z^{max} + \left(n_y-1\right) n_x^{max} + n_x \tag{9.4.10}$$

where n denoted the number of the corresponding element of the MS mesh.

The uniform pseudo-random number of the element n of the MS mesh is computed in the first integration according to

$$\text{if } i=1: \quad \rightarrow \quad \text{init\_random\_seed}\,[clock] \tag{9.4.11}$$

$$\text{rand\_number}\left[\mathbf{u}\begin{pmatrix}1\\ \vdots \\ n\end{pmatrix}\right] \tag{9.4.12}$$

$$x^{elem} = \mathbf{u}(n) \tag{9.4.13}$$

where x^{elem} is a variable which is stored in a common block used in the element routine. The PRNG used by function rand_number [·] is initialised using function rand_number [$clock$]. Then, the function rand_number [·] is called n times which is expressed by the vector $\mathbf{u}$ and the variable x^{elem} is set to the last outcome. This procedure guarantees that the same uniform pseudo-random number is used in each element which belongs to element n of the MS mesh. However, this procedure requires that the same value of integer $clock$ is used each time material routine MR#3 is called. Hence, the value of integer $clock$ is defined when material routine MR#3 is called the first time in a FE simulation and is stored in an common block used by the FE solver.

Based on variable x^{elem}, the Weibull CDF given in Equation (9.3.1) and the inverse transformation given in Equation (3.3.73), critical value W_c is computed in each integration point by

$$W_c = W_{c0} \sqrt[m]{-\frac{V_0}{\min[V_{ini}, V_{crit}]} \ln\left(1 - x^{elem}\right)} \tag{9.4.14}$$

where V_{crit} denotes the element volume of in the MS mesh and is computed by

$$V_{crit} = \begin{cases} l_{crit} \cdot l_{crit} \cdot t_{ini} & \text{for shell elements with inital thickness } t_{ini} \\ l_{crit} \cdot l_{crit} \cdot l_{crit} & \text{for solid elements} \end{cases}. \tag{9.4.15}$$

As discussed in Chapter 5.2.4, it is recommended to use a FE mesh size which is equal or smaller than the MS mesh size. In case the initial volume V_{ini} of an element of the FE mesh is larger than the volume V_{crit} of an element of the MS mesh, the initial volume V_{ini} needs to be used to serve the weakest-link approach. It is noted that critical value W_c needs to be computed in each element only at time $t = 0$. The procedure in material routine MR#3 is summarised in Figure C.4.1 and Figure C.4.2 of Appendix C.4.

9.5 Material Routine MR#4

Material routine MR#4 is almost equivalent to material routine MR#3. However, in contrast to material routine MR#3, the creation of the MS mesh, the mapping of the MS mesh onto the FE mesh and the distribution of the uniform pseudo-random numbers are not performed in material routine MR#4. Here, the distribution of the uniform pseudo-random numbers is given as user-input of the FE model such as an initial condition. This means that a uniform pseudo-random number is defined for each integration point of an element in the FE model. For instance, the MS mesh can be created in MATLAB [83] in the same way as in material routine MR#3. Based on the MS mesh, the distribution of the uniform pseudo random numbers can be also computed in the same way as in material routine MR#3. However, the MS mesh can be also modelled as a uniform pseudo-random field as described in Chapter 5.2.4. This implies that the elements of the MS mesh are considered as statistically dependent. A sample drawn from this uniform pseudo-random field defines the distribution of the uniform pseudo-random numbers. This distribution is mapped onto the underlying FE mesh in the same way as in material routine MR#3 and the result provides the input of the underlying FE model. Here, the statistical toolbox implemented in MATLAB [84] can be used to draw a sample of the uniform pseudo-random field. An example of this approach is illustrated in Figure 5.2.3.

The uniform pseudo-random number which is defined for the current integration point is denoted as u_{ini} and is read by material routine MR#4. Based on this, material routine

MR#4 computes critical value W_c according to material routine MR#3, so that

$$W_c = W_{c0} \sqrt[m]{-\frac{V_0}{\min[V_{ini}, V_{crit}]} \ln(1-u_{ini})}. \tag{9.5.1}$$

The procedure in material routine MR#4 is summarised in Figure C.5.1 of Appendix C.5.

9.6 Concluding Remarks

The material routines presented in the current chapter allow to consider the local pseudo-random variation in the material ductility of HPDC alloys in FE simulations. Each material routine needs a set of material parameters to solve the constitutive model and the probabilistic failure criterion:

- Constitutive model: Young's modulus E, Poisson's ratio ν, exponent p of the yield criterion and hardening coefficients σ_0, Q_1, Q_2, C_1 and C_2.
- Probabilistic failure criterion: Weibull modulus m, scale volume V_0 and scale failure parameter W_{c0}

However, the global systematic variation in the material ductility is not considered in the material routines. In the present work, the global systematic variation is captured in a FE model of an HPDC component using different sets of material parameters as discussed in Chapter 6.5. A set of material parameters can be representative for a characteristic part of the underlying HPDC component or for a specified casting quality. As a result, the FE model of an HPDC component is partitioned into different parts each using a unique set of material parameters. The partition can be found by the underlying casting system or by a casting simulation which is the most advanced approach. Since, each set of material parameters is defined in a so-called material card, this approach leads practically to a spatial distribution of material cards. In summary, the material routines presented in the current chapter and a reasonable distribution of material cards enable to analyse numerically the deformation and failure behaviour of HPDC components.

Chapter 10

Numerical Studies

The four material routines MR#1, MR#2, MR#3 and MR#4 presented in the previous chapter are investigated and analysed in three experimental-numerical studies:

- Numerical study #1: Uniaxial tensile test
- Numerical study #2: Bending test
- Numerical study #3: Validation

The objective of the first and second numerical study is to demonstrate the difference between the four material routines. These studies show the difference in the computation of the failure probability based on material routine MR#1 and material routine MR#2. Further, the advantage of the uncoupled modelling approach implemented in material routine MR#3 and MR#4 is demonstrated by mesh convergence studies. Here, the first study is based on a uniaxial tensile test and the second study is based on a U-shaped component subjected to three-point bending. The objective of the third numerical study is the validation of the probabilistic failure model implemented in material routine MR#1 and material routine MR#2, respectively. The validation is based on the numerical prediction of the failure probability of the U900-1 component subjected to three-point bending as well as subjected to axial compression. The results of the three numerical studies are presented and discussed in the current chapter. It is noted that all simulations were performed in the explicit FE solver LS-DYNA 971 [51].

10.1 Uniaxial Tensile Test

The first numerical study is based on FE simulations of the uniaxial tensile tests investigated in the first material characterisation, see Chapter 8.2. Parallel uniaxial tensile tests were carried out on UT80 specimens machined from different extraction positions of five U900-1 components made of the alloy Castasil-37 in casting condition (F). The analysis of the experimental data showed that the variation in the material ductility can be separated into a global systematic variation and a local pseudo-random variation. Therefore, the objective of the first numerical study is to analyse if the local pseudo-random variation in the material ductility can be numerically reproduced using material routines MR#1 and MR#2. Here, the experimental results obtained from UT80 specimens machined from location L and location R of part OW are considered. It is noted that the experimental results obtained from UT80 specimens machined from the other parts could have been

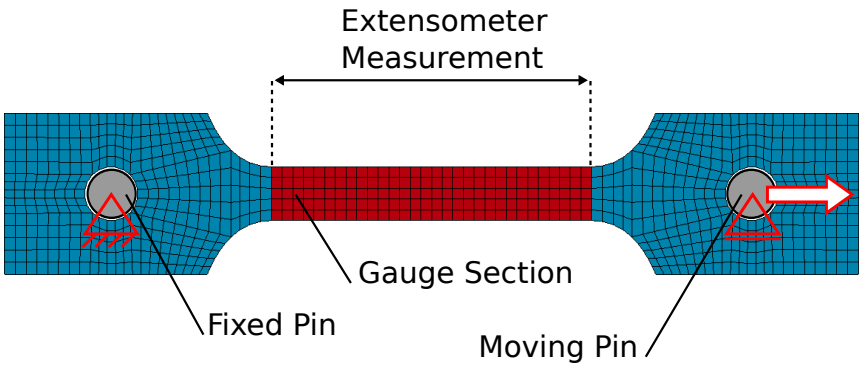

Figure 10.1.1: FE model of the uniaxial tensile test using a UT80 specimen.

considered also, but the conclusions would not change. In addition, the prediction of fracture initiation is investigated in a mesh convergence study using material routines MR#2, MR#3 and MR#4. It is shown how these material routines influence the numerical result.

10.1.1 Numerical Model

The FE model of the uniaxial tensile test set-up is illustrated in Figure 10.1.1. The UT80 specimen was discretised with Belytschko-Tsay shell elements with one integration point through thickness since a plane stress problem could be assumed. Due to the reduced in-plane integration, a stiffness based hourglass control was applied. Average element edge lengths (mesh sizes) of $l_e = 1.00\,\text{mm}$, $l_e = 0.50\,\text{mm}$, $l_e = 0.25\,\text{mm}$ and $l_e = 0.125\,\text{mm}$ were used. The element thickness was set to the average thickness of 2.362 mm measured by the UT80 specimens machined from part OW, see Figure B.5.1 of Appendix B.5. According to the experimental test set-up, see Chapter 8.1.1, the two pins were modelled as cylindrical rigid walls, while one was fixed and the other one moved constantly in longitudinal direction. A constant loading velocity of $4.0\,\frac{\text{mm}}{\text{msec}}$ was adopted. This loading velocity is much faster than the experimental loading velocity of $1.8\,\frac{\text{mm}}{\text{min}}$ which was assumed to be quasi-static. It was checked that kinetic energy and hourglass energy are less than 1% of total energy in each simulation. Hence, quasi-static loading conditions and minimal hourglassing were ensured. A friction coefficient of 0.2 was assumed for between rigid walls and FE mesh. According to the the experimental measurements, the cross-section force in longitudinal direction as well as the elongation of the gauge section were taken from the FE simulations.

As already mentioned, material routines MR#1, MR#2, MR#3 and MR#4 were applied to describe the material behaviour. Young's modulus E was set to $72.00\,^{\text{kN}}/_{\text{mm}^2}$, Poisson's ratio ν to 0.33 and the exponent p applied in the yield criterion to 4. Based on the hardening curves obtained from UT80 specimens machined from location L and location R of part OW, the five parameters of the two-terms Voce rule were found from a least-squares curve fit using gnuplot [115]. In Figure 10.1.2, the experimental hardening curves (blue) and the fitted two-terms Voce rule (green) are shown. The Weibull parameters were taken from the corresponding results of the Weibull analysis provided in Table 8.2.2. The material model parameters are summarised in Table 10.1.1.

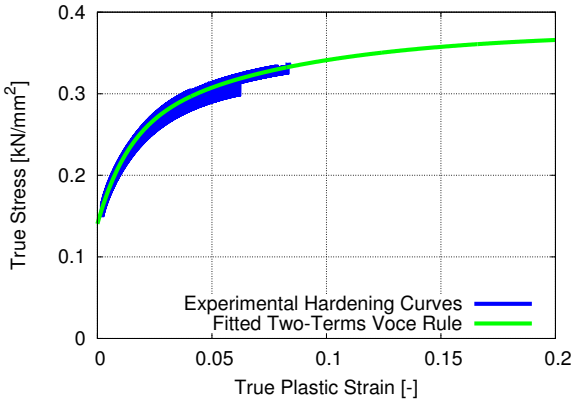

Figure 10.1.2: Fitted two-terms Voce rule based on experimental hardening curves obtained from UT80 specimens machined from part OW.

Material Model Parameters (UT80)					
Part	ρ [kg/mm³]	E [kN/mm²]	ν [−]	p [−]	
OW	$2.75 \cdot 10^{-6}$	72.00	0.33	4	
Part	σ_0 [kN/mm²]	Q_1 [kN/mm²]	C_1 [−]	Q_2 [kN/mm²]	C_2 [−]
OW	0.14	0.11	76.47	0.13	13.07
Part	m [−]	W_{c0} [kN/mm²]	V_0 [mm³]		
OW	2.41	0.0180	375.00		

Table 10.1.1: Material model parameters obtained from UT80 specimens machined from part OW.

10.1.2 Prediction of Failure Probability

The result obtained from a single simulation using material routine MR#1 and a mesh size of $l_e = 1.00\,\text{mm}$ are compared with the experimental results in Figure 10.1.3a. The graph shows engineering strain on the abscissa, engineering stress on the left ordinate and failure probability on the right ordinate. The experimental engineering stress-strain curves are plotted in grey and the predicted engineering stress-strain curve is plotted in red. Since material routine MR#1 does not include element deletion, the predicted engineering stress-strain curve does not show failure and the drop beyond peak load indicates necking. However, it is seen that the predicted engineering stress-strain curve is in good agreement with the experimental engineering stress-strain curves neglecting failure. Based on Equation (8.1.14), the experimental failure probability was estimated from the measurements of engineering fracture strain and is plotted as a row of blue triangles. The failure probability predicted by the simulation using material routine MR#1 is plotted in blue. It is seen that the predicted failure probability and the experimental failure probability are well correlated. Accordingly, the result obtained from a simulation using a mesh size of $l_e = 0.50\,\text{mm}$ and a mesh size of $l_e = 0.25\,\text{mm}$, respectively, are compared with the experimental results in Figure, 10.1.3b, and Figure 10.1.3c, respectively. It is seen that the well correlation between experimental results and numerical results is not influenced by the mesh size.

Furthermore, it is seen that the usage of material routine MR#1 enables to compute dir-

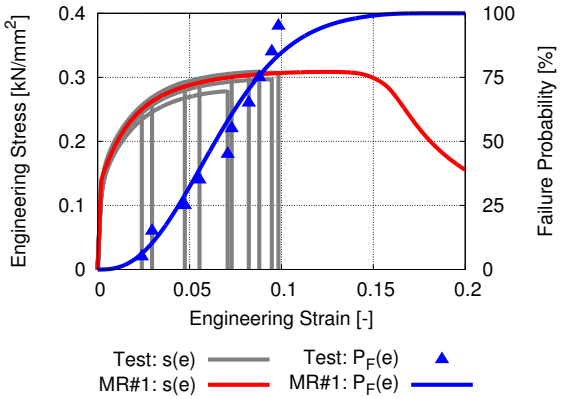

(a) $l_e = 1.00\,\text{mm}$.

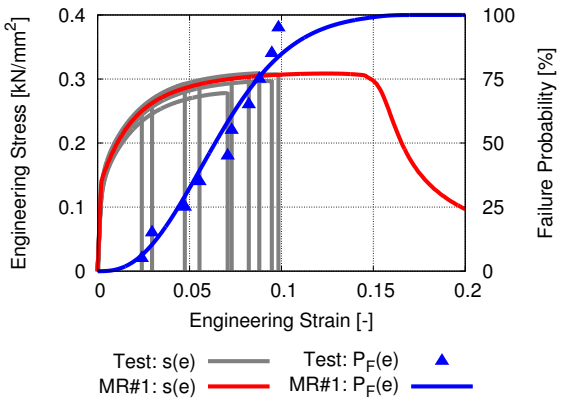

(b) $l_e = 0.50\,\text{mm}$.

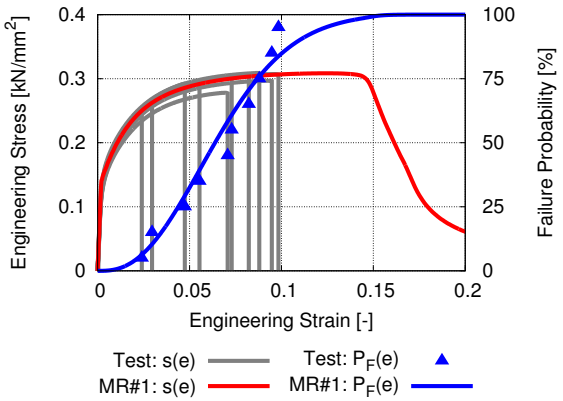

(c) $l_e = 0.25\,\text{mm}$.

Figure 10.1.3: Comparison of predicted engineering stress-strain curve using material routine MR#1 (red) and experimental engineering stress-strain curves (grey) as well as comparison of predicted failure probability using material routine MR#1 (blue) and experimental failure probability (blue triangles).

ectly the failure probability of the uniaxial tensile test. Alternatively, the failure probability can be numerically estimated using material routine MR#2 (which includes element deletion) and a Monte-Carlo simulation. Here, parallel FE simulations need to be performed on a FE model using material routine MR#2 and each simulation has to use a new pseudo-random distribution of critical value W_c. According to this approach, 36 parallel simulations were performed on each mesh size of the FE model of the uniaxial tensile test. It is noted that each time a simulation was performed, the PRNG applied in material routine MR#2 was initialised to a varying state based on the actual computer time at the beginning of the simulation, see Chapter 9.3. Hence, it was guaranteed that each simulation uses a new pseudo-random distribution of critical value W_c. The results obtained from 36 parallel simulations using material routine MR#2 and a mesh size of $l_e = 1.00\,\text{mm}$ are compared with the result obtained from a single simulation using material routine MR#1 in Figure 10.1.4a. The graph is structured identically to the one above. The 36 predicted engineering stress-strain curves are plotted in red. From each simulation, the engineering fracture strain is found when the first element was deleted. This implies that fracture initiation is defined by the first deletion of an element. Accordingly, each predicted engineering stress-strain curve is cut when the first element was deleted. It is seen that the predicted engineering fracture strain varies pseudo-randomly as observed in the tensile test results. Figure 10.1.5 shows five representative deformed and fractured UT80 specimens obtained from the 36 simulations. The corresponding pseudo-random distribution of critical value W_c is given as contour plot for each sample. As expected, the pseudo-random distribution varies and, consequently, the predicted location of fracture initiation varies. Based on the 36 measurements of the predicted engineering fracture strain, the failure probability is estimated accordingly to the experimental failure probability, see Equation (8.1.14), and is plotted as a row of blue triangles. The failure probability predicted by the numerical simulation using material routine MR#1 is plotted in blue. It is seen that the predicted failure probability using material routine MR#1 and the predicted failure probability using material routine MR#2 are well correlated. In the same way, the results obtained from a mesh size of $l_e = 0.50\,\text{mm}$ and a mesh size of $l_e = 0.25\,\text{mm}$, respectively, are compared in Figure 10.1.4b and Figure 10.1.4c, respectively. It is seen that both predictions of the failure probability are well correlated independently of the applied mesh size.

The first analysis demonstrated that the predicted failure probability using material routine MR#1 and the experimental failure probability are well correlated. The same probabilistic failure criterion is applied in material routines MR#1 and MR#2, but the probabilistic failure criterion is applied differently. The second analysis demonstrated the consistency of these two material routines: The predicted failure probability using material routine MR#1 can be reproduced by a Monte-Carlo simulation using material routine MR#2. This implies that the varying results obtained from parallel simulations using material routine MR#2 reproduce the varying experimental results. Moreover, it was shown that the predicted failure probability does not show any mesh size dependence as long as the deformation behaviour until fracture initiation is well captured by the constitutive model such as the one implemented in material routines MR#1, MR#2, MR#3 and MR#4.

10.1.3 Prediction of Fracture Initiation

Material routine MR#2 was applied in the previous analysis to predict fracture initiation. Here, each time a simulation was performed, the PRNG applied in material routine MR#2 was initialised to a varying state. Consequently, each simulation used a new pseudo-random distribution of critical value W_c. The same FE model of the uniaxial tensile test was investigated in a mesh convergence study using mesh sizes of $l_e = 1.00\,\text{mm}$, $l_e =$

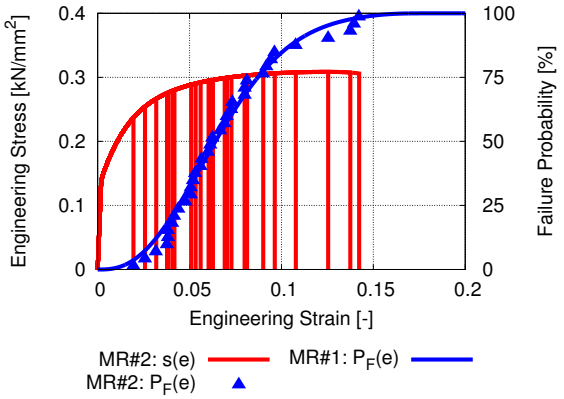

(a) $l_e = 1.00\,\text{mm}$.

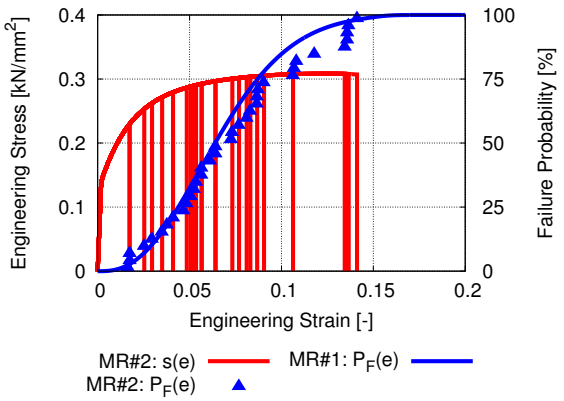

(b) $l_e = 0.50\,\text{mm}$.

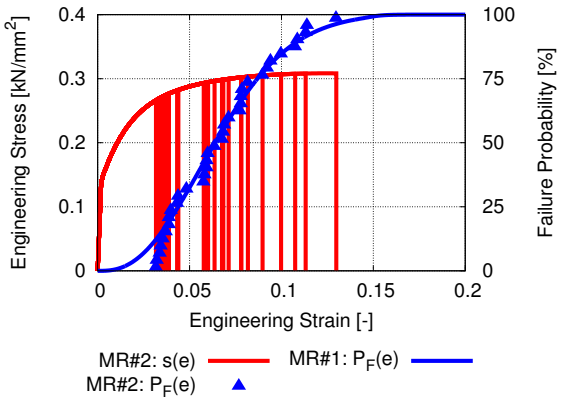

(c) $l_e = 0.25\,\text{mm}$.

Figure 10.1.4: Predicted engineering stress-strain curves using material routine MR#2 (red) and comparison of predicted failure probability using material routine MR#1 (blue) and predicted failure probability using material routine MR#2 (blue triangles).

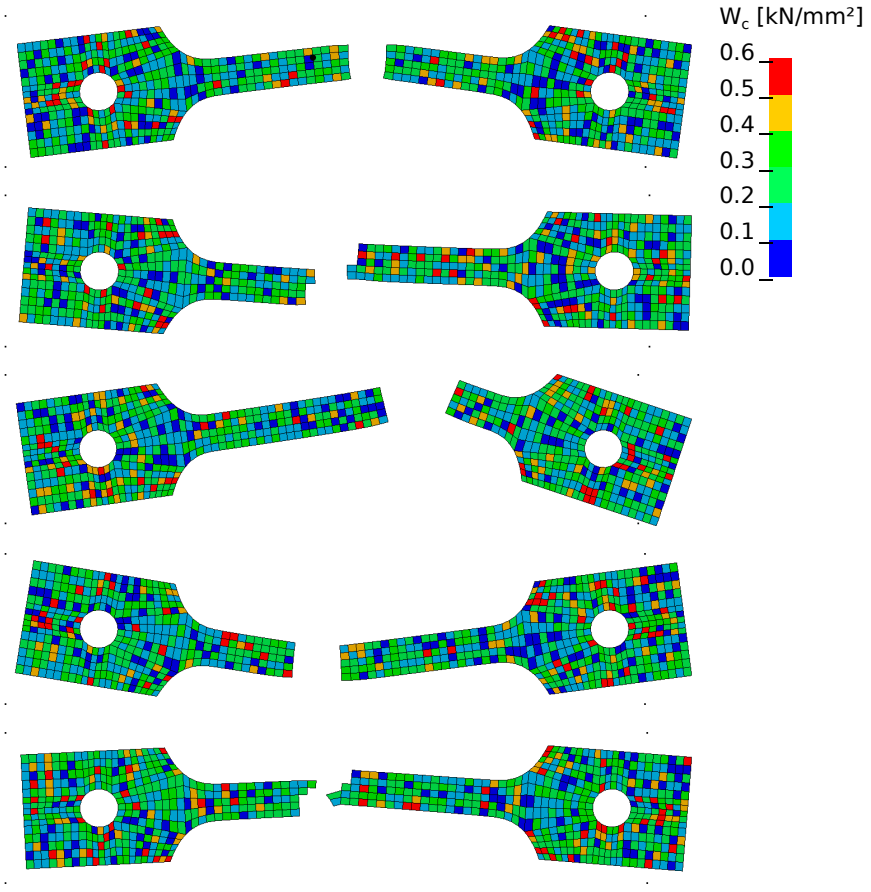

Figure 10.1.5: Five deformed and fractured UT80 specimens obtained from FE simulations using material routine MR#2 including the pseudo-random distributions of critical value W_c ($l_e = 1.00\,\text{mm}$).

0.50 mm, $l_e = 0.25\,\text{mm}$ and $l_e = 0.125\,\text{mm}$. In contrast to the previous analysis, the PRNG was initialised to the same state in each simulation. The result obtained from the mesh convergence study is shown in Figure 10.1.6a. The graph shows the engineering stress-stain curves predicted by the four mesh sizes: The result obtained from a mesh size of $l_e = 1.00\,\text{mm}$ is plotted in grey, the result obtained from a mesh size of $l_e = 0.50\,\text{mm}$ in green, the result obtained from a mesh size of $l_e = 0.25\,\text{mm}$ in blue and the result obtained from a mesh size of $l_e = 0.125\,\text{mm}$ in magenta. The steep drop in each curve indicates fracture initiation (first element deletion). It is seen that the results are identical until fracture initiation. However, mesh convergence cannot be reached in terms of fracture initiation. Moreover, the engineering fracture strain varies independently of the mesh size. Figure 10.1.6b shows the deformed and fractured UT80 specimens obtained from the mesh convergence study. The corresponding pseudo-random distribution of critical value W_c is given as contour plot for each mesh size. It is seen that the predicted location of fracture initiation varies between the different mesh sizes, even though the PRNG was initialised to the same state in each simulation. Since the number of elements increases with decreasing mesh size, the sample drawn from the underlying Weibull distribution increases with

decreasing mesh size. Hence, the pseudo-random distribution of critical value W_c varies between the different mesh sizes. Consequently, mesh convergence cannot be reached using material routine MR#2 even though the PRNG is initialised to the same state each time a simulation is performed. Obviously, the element with the lowest critical value W_c within the gauge section failed first and caused fracture initiation. However, the fractured specimens using mesh sizes of $l_e < 1.00\,\text{mm}$ shows non-failed elements along the predicted crack paths. These elements show a very high critical value W_c. This is caused by the weakest-link approach: The probability of drawing a critical value W_c which exceeds a certain value increases with decreasing initial element volume as mentioned in Chapter 5.2.4. In the work by Dørum et al. [31], this phenomenon is avoided using a non-local regularisation of critical value W_c. As already discussed in Chapter 6.4, the pseudo-random distribution of critical value W_c is modified by the non-local regularisation and this is not correct in terms of probabilistic failure modelling.

In Chapter 5.2.4, it was mentioned that mesh convergence cannot be reached when FE mesh and MS mesh are coupled. The usage of material routine MR#2 implies the coupled approach, see Chapter 9.3. The uncoupled approach is implemented in material routine MR#3, see Chapter 9.4. The application of material routine MR#3 on the FE model of the UT80 specimen is demonstrated in Figure 10.1.7a and can described as follows:

- Step 1: Generation of the FE mesh of the UT80 specimen with mesh size l_e
- Step 2: Definition of critical edge length of l_{crit} and generation of the uniform MS mesh
- Step 3: Distribution of uniform pseudo-random numbers within the MS mesh
- Step 4: Mapping of the uniform pseudo-random distribution onto the FE mesh and transformation into a pseudo-random Weibull distribution of critical value W_c

In the demonstration example, a FE mesh size of $l_e = 0.50\,\text{mm}$ and a critical edge length of $l_{crit} = 1.00\,\text{mm}$ was used. As a result, all elements of the FE mesh which belong to the same element of the MS mesh have the same critical value W_c. It is noted that the uncoupled modelling approach implemented in material routine MR#3 implies statistical independence between the elements of the MS mesh. Further, material routine MR#4 is also based on the uncoupled modelling approach, see Chapter 9.5. However, in contrast to material routine MR#3 the uniform pseudo-random number distribution is given as input of the FE model. This enables to consider statistical dependence of the elements of the MS mesh. The application of material routine MR#3 combined with a Gaussian pseudo-random field on the FE model of the UT80 specimen is demonstrated in Figure 10.1.7b and can described as follows:

- Step 1: Generation of the FE mesh of the UT80 specimen with mesh size l_e
- Step 2: Definition of critical edge length of l_{crit} and generation of the uniform MS mesh
- Step 3: Distribution of pseudo-random numbers within the MS mesh according to a sample of a discrete and homogeneous Gaussian pseudo-random field
- Step 4: Mapping of the pseudo-random distribution onto the FE mesh and transformation into a pseudo-random Weibull distribution of critical value W_c

In the demonstration example, the FE mesh of the UT80 specimen with a mesh size of $l_e = 0.50\,\text{mm}$ was read in MATLAB [83] and the uniform MS mesh with a critical edge

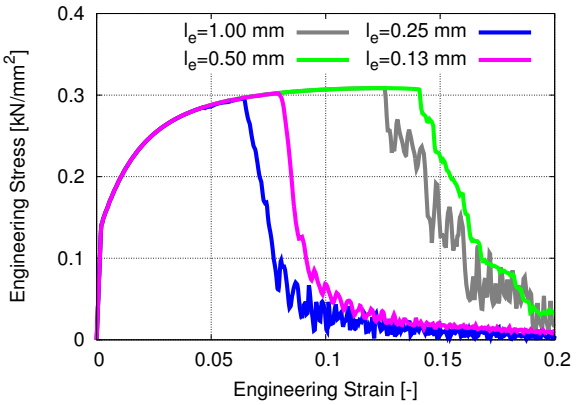

(a) Comparison of predicted engineering stress-strain curves using material routine MR#2.

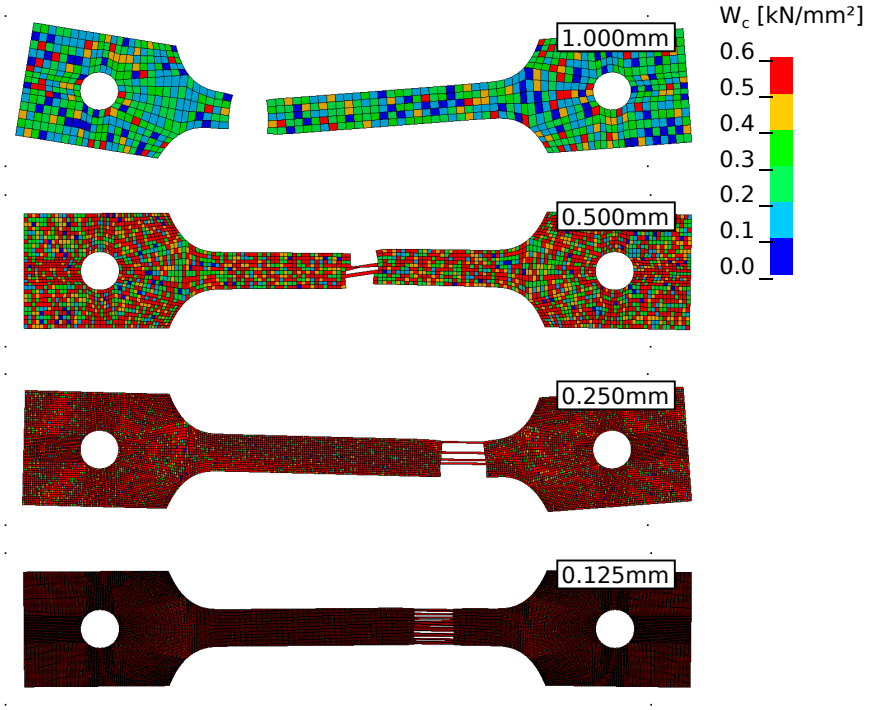

(b) Comparison of deformed and fractured UT80 specimens obtained from FE simulations using material routine MR#2 including the distributions of critical value W_c.

Figure 10.1.6: Mesh convergence study of the FE model of the uniaxial tensile test using material routine MR#2 ($l_e = \{1.00\,\text{mm}, 0.50\,\text{mm}, 0.25\,\text{mm}, 0.125\,\text{mm}\}$).

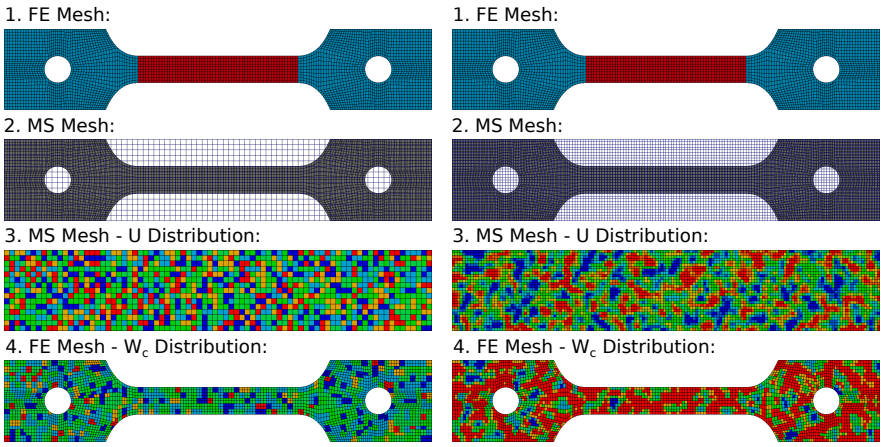

(a) Uncoupled modelling approach using material routine MR#3.

(b) Uncoupled modelling approach using material routine MR#4.

Figure 10.1.7: Uncoupled modelling approach applied on the FE model of the UT80 specimen using material routine MR#3 and material routine MR#4.

length of $l_{crit} = 0.50\,\text{mm}$ was generated. Here, a sample of a discrete and homogeneous Gaussian pseudo-random field with a correlation length of $d_0 = 1.00\,\text{mm}$ was generated using the MS mesh and the statistical toolbox implemented in MATLAB [84]. This sample of the Gaussian pseudo-random field was transformed into a sample of a uniform pseudo-random field and mapped onto the FE mesh. Finally, the distribution of the pseudo-random numbers was used as input for material routine MR#4 and, consequently, a sample of a Weibull pseudo-random field of critical value W_c was generated. Since the elements of the MS mesh were considered as statistical independent, the distribution of critical value W_c is characterised by smooth transitions.

The mesh convergence study of the FE model of the uniaxial tensile test was repeated using material routine MR#3 and a critical edge length of $l_e = 1.00\,\text{mm}$ was chosen. It is noted that the PRNG was initialised to the same state each time a simulation was performed. The predicted engineering stress-strain curves are presented in Figure 10.1.8a and it is clearly seen that mesh convergence is reached. In Figure 10.1.8b, the deformed and fractured UT80 specimens obtained from the mesh convergence study using material routine MR#3 are illustrated. It is seen that the predicted location of fracture initiation does not vary and the predicted crack paths are free of non-failed elements. The pseudo-random distribution of critical value W_c is given as contour plot for each mesh size. Since the same size of the MS mesh was applied in each simulation and the PRNG was initialised to the same state in each simulation, the same distribution of critical value W_c was applied in each simulation and causes mesh convergence.

Again, the mesh convergence study of the FE model of the uniaxial tensile test was repeated using material routine MR#4 and a critical edge length of $l_{crit} = 0.50\,\text{mm}$ was chosen. As described above, the uniform pseudo-random number distribution was created in MATLAB [83] and was given as input for each mesh size. The correlation length of the underlying Gaussian pseudo-random field was set to $d_0 = 1.00\,\text{mm}$. It is noted that the PRNG implemented in MATLAB [83] was set to the default state each time a sample of the Gaussian pseudo-random field was generated. The predicted engineering stress-

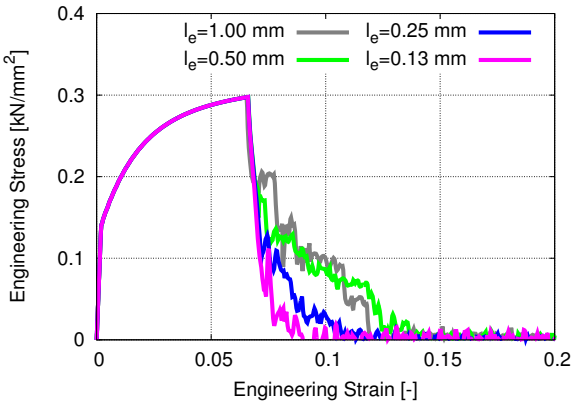

(a) Comparison of predicted engineering stress-strain curves using material routine MR#3.

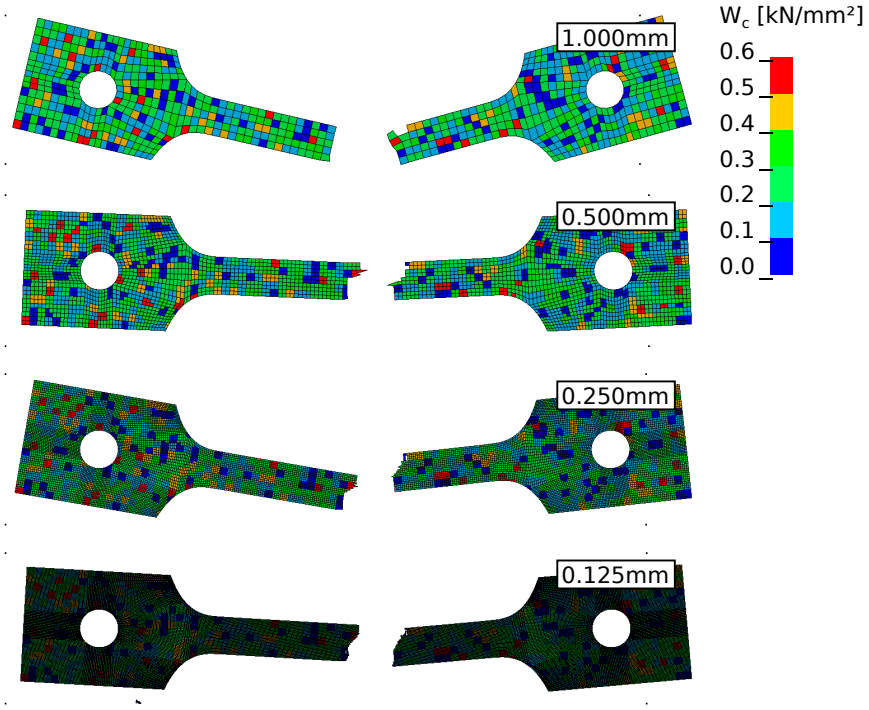

(b) Comparison of deformed and fractured UT80 specimens obtained from FE simulations using material routine MR#3 including the distributions of critical value W_c.

Figure 10.1.8: Mesh convergence study of the FE model of the uniaxial tensile test using material routine MR#3 ($l_e = \{1.00\,\text{mm}, 0.50\,\text{mm}, 0.25\,\text{mm}, 0.125\,\text{mm}\}$).

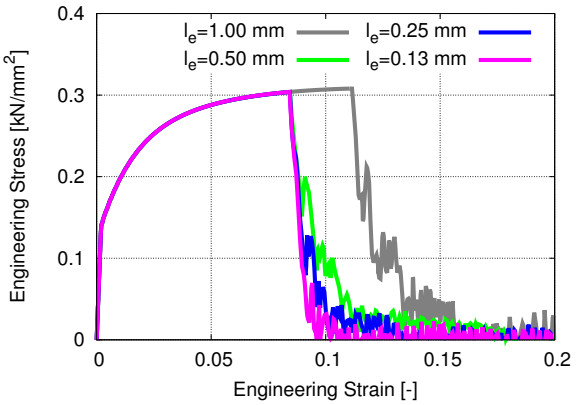

(a) Comparison of predicted engineering stress-strain curves using material routine MR#4.

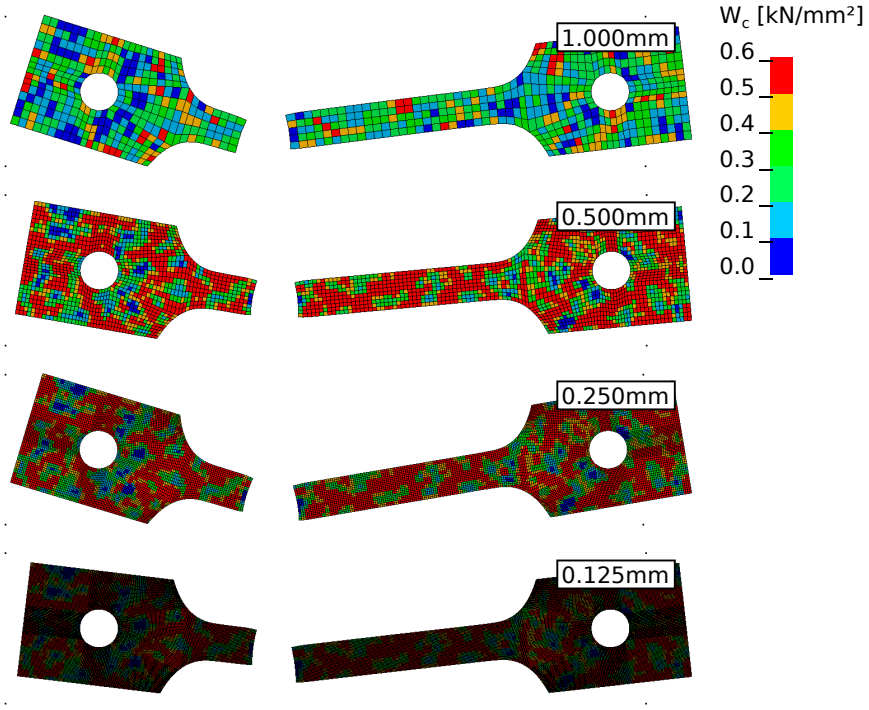

(b) Comparison of deformed and fractured UT80 specimens obtained from FE simulations using material routine MR#4 including the distributions of critical value W_c.

Figure 10.1.9: Mesh convergence study of the FE model of the uniaxial tensile test using material routine MR#4 ($l_e = \{1.00\,\text{mm}, 0.50\,\text{mm}, 0.25\,\text{mm}, 0.125\,\text{mm}\}$).

strain curves are presented in Figure 10.1.9a and it is clearly seen that mesh convergence is reached. However, the predicted engineering stress-strain obtained from the simulation using a FE mesh size of $l_e = 1.00\,\text{mm}$ differs strongly from the other ones. This is caused by the fact that the FE mesh size of $l_e = 1.00\,\text{mm}$ is larger than the MS mesh size of $l_{crit} = 0.50\,\text{mm}$. In Figure 10.1.8b, the deformed and fractured UT80 specimens obtained from the mesh convergence study using material routine MR#4 are illustrated. The pseudo-random distribution of critical value W_c is given as contour plot for each mesh size. It is clearly seen that the distribution of the mesh size of $l_e = 1.00\,\text{mm}$ is different to the distributions of the smaller mesh sizes. As already mentioned, this is caused by the fact the FE mesh size of $l_e = 1.00\,\text{mm}$ is larger than the MS mesh size of $l_{crit} = 0.50\,\text{mm}$. However, the distribution of the smaller mesh sizes are identical and, consequently, the predicted location of fracture initiation does not vary. All simulation results are free of non-failed elements along the predicted crack-paths. Mesh convergence is reached for the same reason as described in the previous one.

The three mesh convergence studies demonstrated that the results converge only when the uncoupled modelling approach is used (provided that the applied PRNG is set to the same state each time a simulation is performed). In each study, the critical edge length of the MS mesh was chosen freely without stating any scientific justification. The correct critical edge length is equivalent to a material property and needs to be analysed more in detail. Moreover, the Gaussian pseudo-random field used in the mesh convergence study was also generated without stating any scientific justification. Here, a detailed material characterisation would be necessary to identify the correct parameters. As already discussed in Chapter 5.2.4, material routine MR#3 is consistent to material routines MR#1 and MR#2, whereas material routine MR#4 combined with a Gaussian pseudo-random field is not consistent to these material routines. However, it is seen that the uncoupled approach combined with a Gaussian pseudo-random field is a statistical alternative to the non-local regularisation.

10.2 Bending Test

In the previous chapter, a uniaxial tensile test was numerically analysed using material routines MR#1, MR#2, MR#3 and MR#4. It was demonstrated that the experimentally observed scatter can be numerically reproduced either in terms of the prediction of the failure probability using material routine MR#1 or in terms of pseudo-randomly varying results using material routine MR#2. However, these results could be expected since the material model parameters were identified from the underlying tensile test results. This implies that the parameters applied in material routines MR#1 and MR#2 were calibrated correctly. Moreover, it was shown that mesh convergence can be reached using material routines MR#3 and MR#4.

The second numerical study is based on FE simulations of a U-shaped HPDC component (U-profile) subjected to three-point bending. The U-profile was made of an aluminium HPDC alloy in heat treated condition (T1). Test set-up, experimental results and FE model were obtained from the work by Dørum et al. [33]. In Figure 10.2.1a, an image of the experimental bending test set-up is presented. It is seen that the U-profile is placed on two cylindrical steel supports and the load is applied through a cylindrical steel punch. In addition, U-shaped supports are fixed at the edges of the U-profile. The force-displacement curves obtained from three parallel bending tests are presented in Figure 10.2.1b. The results show the typical scatter as expected from an HPDC component. Further, the first drop in a force-displacement curve indicates failure in the U-profile part

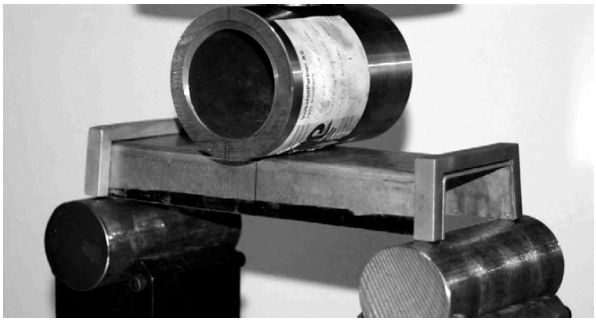

(a) Image of the three-point bending test set-up.

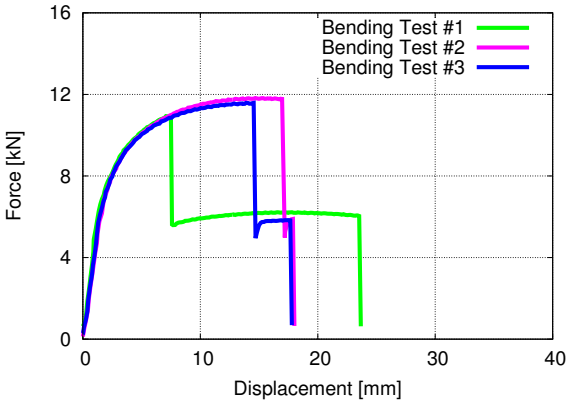

(b) Experimental force-displacement curve obtained from three parallel three-point bending test.

Figure 10.2.1: Image of the three-point bending test set-up and experimental results.

which is close to the vacuum channels and the second drop indicates failure in the U-profile part which is close to the gating channels. More information on the test set-up and a detailed discussion of the experimental results can be found in the work by Dørum et al. [33].

The objective of the current study is to demonstrate that the failure probability predicted by a single simulation using material routine MR#1 can be reproduced by parallel simulations using material routine MR#2 based on a component test. In addition, the result of a mesh convergence study using material routine MR#3 is presented and discussed. Finally, a potential through-process mapping approach is presented. It is shown how the result of casting process simulation can be used to redefine the parts of a FE model.

10.2.1 Numerical Model

The FE model of the U-profile subjected to three point bending is illustrated in Figure 10.2.2a. It is noted that this FE model was generated according to the one presented in the work by Dørum et al. [33]. The considered U-profile was 300 mm long, 92 mm wide and 40 mm high and the wall thickness was approximately 2.5 mm. The U-profile was discretised with Belytschko-Tsay shell elements with five integration points through thick-

ness and a stiffness based hourglass control was applied. Average element edge lengths of $l_e = 3.00\,\text{mm}$, $l_e = 1.50\,\text{mm}$, $l_e = 0.75\,\text{mm}$ and $l_e = 0.38\,\text{mm}$ were investigated. The supports were modelled as cylindrical rigid bodies with diameter equal to 50 mm and were fixed in space. The punch was also modelled as a cylindrical rigid body with diameter equal to 100 mm and was only allowed to move normal to the U-profile. A constant loading velocity of $1.3 \cdot 10^4 \frac{\text{mm}}{\text{min}}$ was adopted. This loading velocity is much faster than the experimental loading velocity of $20 \frac{\text{mm}}{\text{min}}$ which was assumed to be quasi-static. It was checked that kinetic energy and hourglass energy are less than 1% of total energy in each simulation. Hence, quasi-static loading conditions and minimal hourglassing were ensured. A friction coefficient of 0.2 was assumed for the global contact modelling. According to the experimental measurements, reaction force and displacement were taken from the rigid body output of the punch.

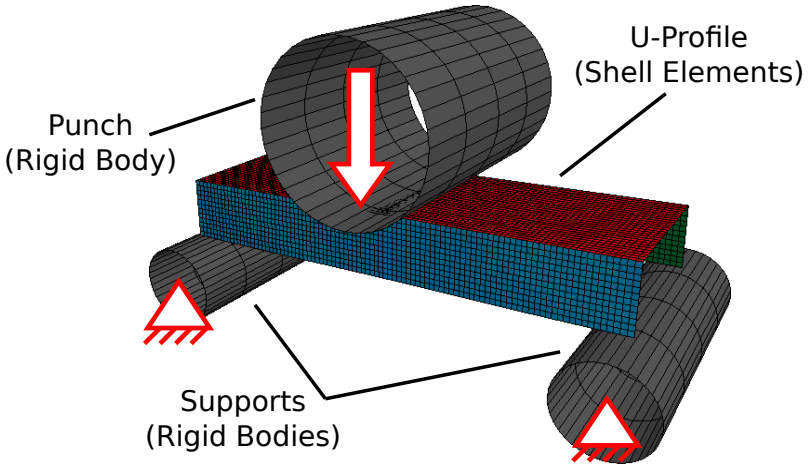

(a) Modelling of the three-point bending test set-up.

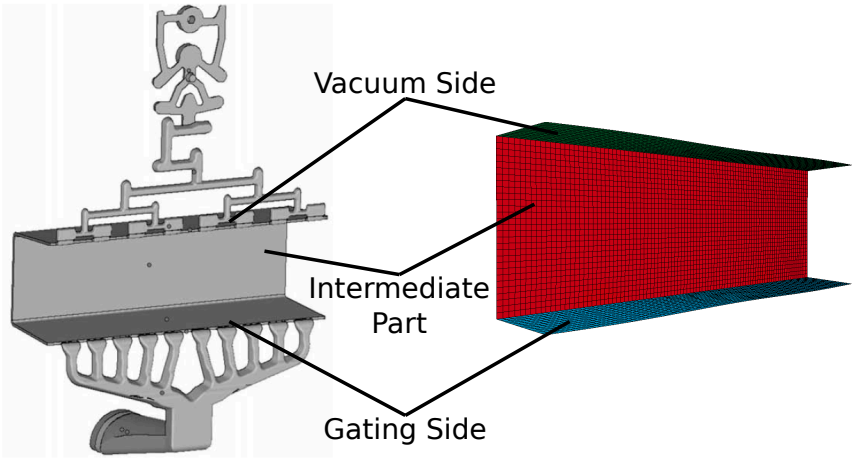

(b) Part definition of the U-profile according to the applied casting system: Gating side (blue), intermediate part (red) and vacuum side (green).

Figure 10.2.2: FE model of the U-profile subjected to three-point bending.

Material Model Parameters (U-Profile)					
Part	ρ [kg/mm³]	E [kN/mm²]	ν [−]	p [−]	
Gating Side	$2.75 \cdot 10^{-6}$	72.00	0.33	4	
Intermediate Part	$2.75 \cdot 10^{-6}$	72.00	0.33	4	
Vacuum Side	$2.75 \cdot 10^{-6}$	72.00	0.33	4	
Part	σ_0 [kN/mm²]	Q_1 [kN/mm²]	C_1 [−]	Q_2 [kN/mm²]	C_2 [−]
Gating Side	0.108	0.052	172.5	0.158	27.8
Intermediate Part	0.105	0.040	373.2	0.181	33.2
Vacuum Side	0.105	0.026	481.4	0.186	44.3
Part	m [−]	W_{c0} [kN/mm²]	V_0 [mm³]		
Gating Side	7.13	0.0289	825.6		
Intermediate Part	3.06	0.0160	800.0		
Vacuum Side	3.41	0.0123	755.2		

Table 10.2.1: Material model parameters obtained from the work by Dørum et al. [33] and the work by Dørum et al. [32] .

As seen in the work by Dørum et al. [33], three parts within the U-profile were defined according the applied casting system, see Figure 10.2.2b. The flange close to the gating channels was defined as the gating side (blue), the flange close to the vacuum channels as the vacuum side (green) and the web between the flanges as the intermediate part (red). Material routines MR#1, MR#2 and MR#3 were used to describe the material behaviour. Different material model parameters were applied in each part. Table 10.2.1 contains the three sets of material model parameters which were found in the work by Dørum et al. [33] and the work by Dørum et al. [32].

10.2.2 Prediction of Failure Probabilities

The result obtained from a single simulation using material routine MR#1 and a mesh size of $l_e = 3.00\,\text{mm}$ is compared to the experimental results in Figure 10.2.3a. The graph shows the displacement of the punch on the abscissa, the reaction force of the punch on the left ordinate and the failure probability on the right ordinate. The three experimental force-displacement curves are plotted in grey and the predicted force-displacement curve is plotted in red. As already mentioned, material routine MR#1 does not include element deletion and, thus, the predicted force-displacement curve does not show failure. However, it is seen that the predicted force-displacement curve is in fairly good agreement with the experimental force-displacement curves until first fracture initiation. In addition, the predicted failure probability obtained from the entire FE model is plotted in blue. Since only three experimental results were available, the experimental failure probability cannot be estimated and, thus, the predicted failure probability cannot be verified. The predicted failure probabilities of the three parts of the FE model are given in Figure 10.2.3b. The graph shows the displacement of the punch on the abscissa and the failure probability on the left ordinate. The predicted failure probability obtained from the gating side is plotted in blue, the one obtained from the intermediate part in red and the one obtained from the vacuum side in green. Here, it is clearly seen that the predicted failure probability obtained from the vacuum side dominates the predicted failure probability of the entire FE model. The comparison of the three predicted failure probabilities shows that the one obtained from the gating side starts to rise when the one obtained from the vacuum side reaches

nearly 100%. Further, the comparison shows that the predicted failure probability of the intermediated part has only a minor contribution to the predicted failure of the entire FE model. Based on the numerical results, it can be concluded that failure on the gating side occurs beyond failure on the vacuum side in most cases and the intermediate part is not critical regarding failure. Even though it is known in advance that the vacuum side is usually the most critical one, this numerical example demonstrates how the failure behaviour of a structure can be evaluated in terms of failure probabilities.

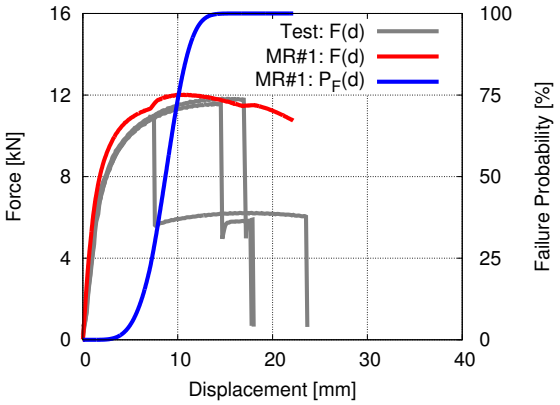

(a) Comparison of predicted force-displacement curve (red) and experimental force-displacement curves (grey) as well as predicted failure probability of the entire U-profile (blue).

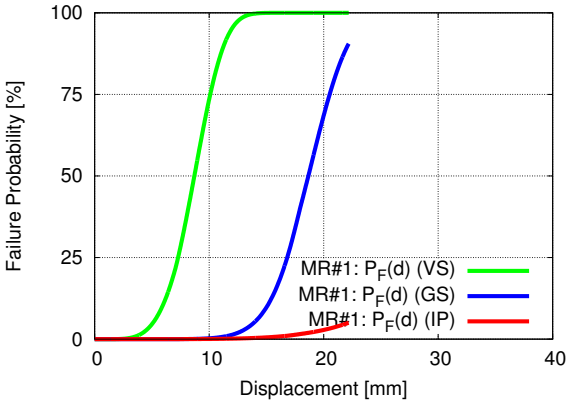

(b) Comparison of predicted failure probabilities of the U-profile parts gating side (blue), intermediate part (red) and vacuum side (green).

Figure 10.2.3: Numerical results obtained from a single simulation of the U-profile subjected to three-point bending using material routine MR#1 ($l_e = 3.00\,\text{mm}$).

In Figure 10.2.4, the result obtained from a simulation using material routine MR#2 and a mesh size of $l_e = 3.00\,\text{mm}$ is shown. The graph given in Figure 10.2.4a shows the predicted force-displacement curve (red) and the experimental force displacement curves (grey). The simulation is based on a pseudo-randomly distributed critical value W_c. There-

fore, the predicted force-displacement curve and the experimental force-displacement curves can only be compared qualitatively in terms of fracture initiation on vacuum side (first drop) and gating side (second drop). However, the predicted force-displacement curve reaches nearly the same force level as the experimental force-displacement curves beyond fracture initiation on the vacuum side, see Figure 10.2.4b. When fracture initiates on the gating side, see Figure 10.2.4c, the numerical force level falls off to nearly zero as seen by the experimental force-displacement curves. As a result, it can be concluded that the deformation behaviour can be well described by the constitutive model implemented in the four material routines MR#1, MR#2, MR#3 and MR#4.

Additionally, a Monte-Carlo simulation was carried out on the FE model of the U-profile subjected to three-point bending. Here, 36 parallel FE simulations were performed using material routine MR#2 and a mesh size of $l_e = 3.00\,\text{mm}$. Each time a simulation was performed the PRNG applied in material routine MR#2 was initialised to a varying state based on the actual computer time at the beginning of the simulation. Hence, it was guaranteed that each simulation uses a new pseudo-random distribution of critical value W_c. The results are given in the graph of Figure 10.2.5a. The graph shows the displacement of the punch on the abscissa, the force of the punch on the left ordinate and the failure probability on the right ordinate. The 36 predicted force-displacement curves are plotted in red. Each curve is cut when the first element was deleted. As expected, the punch displacement at fracture initiation varies pseudo-randomly due to the usage of material routine MR#2. Based on the 36 measurements of the punch displacement at first element deletion, the failure probability of the FE model can be estimated according to Equation (8.1.14) and is plotted as a row of blue triangles. This failure probability is compared with the failure probability obtained from the simulation using material routine MR#1 plotted in blue. It is clearly seen that these are well correlated and the usage of both material routines lead to the same failure probability. Moreover, this comparison shows that the failure probability of a structural component can be predicted by a single simulation using material routine MR#1 instead of parallel simulations using material routine MR#2.

The same comparison as described above is done for the gating side and the vacuum side of the U-profile and is presented in Figure 10.2.5b. The graph shows the displacement of the punch on the abscissa and the failure probability on the left ordinate. The failure probability obtained from the gating side using material routine MR#1 is plotted in blue. The corresponding failure probability estimated from the 36 parallel simulations using material routine MR#2 is plotted as a row of blue triangles. Here, the estimation is based on the measurements of the punch displacement when the first element was deleted on the gating side. The failure probability obtained from the vacuum side using material routine MR#1 is plotted in green. The corresponding failure probability estimated from the 36 parallel simulations using material routine MR#2 is plotted as a row of green triangles. Here, the estimation is based on the measurements of the punch displacement when the first element was deleted on the vacuum side. It is seen that the results obtained from the usage of material routines MR#1 and MR#2 are also well correlated for the two parts. This means that the failure probability of a structural part can be predicted by a single simulation using material routine MR#1 instead of parallel simulations using material routine MR#2.

Finally, it is noted that these results are related to the prediction of the probability of first fracture initiation in an entire FE model or in its parts. The prediction of the probability of further fracture initiations in the entire FE model or in same parts remains unknown using material routine MR#1. This implies that any information on subsequent fracture initiation and crack propagation is still unknown. Here, the application of material routine MR#2 (respectively material routines MR#3 and MR#4) is required to analyse

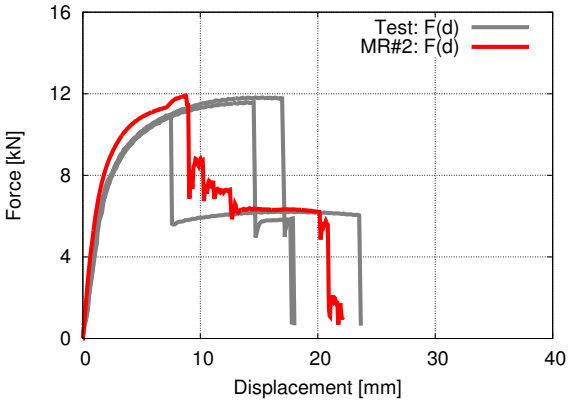

(a) Comparison of predicted force-displacement curve (red) and experimental force displacement curves (grey).

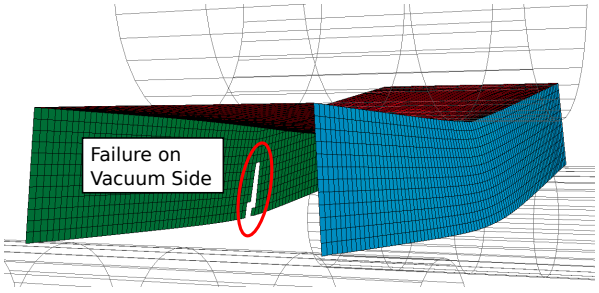

(b) Prediction of fracture initiation on vacuum side.

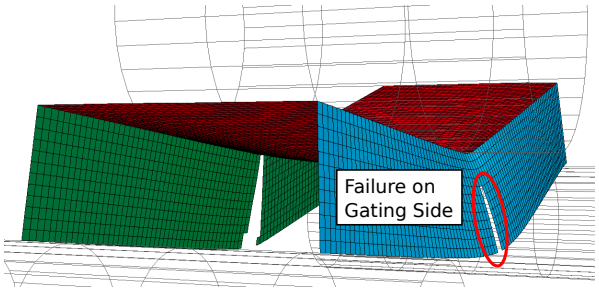

(c) Prediction of fracture initiation on gating side.

Figure 10.2.4: Numerical results obtained from a single simulation of the U-profile subjected to three-point bending using material routine MR#2 ($l_e = 3.00\,\text{mm}$).

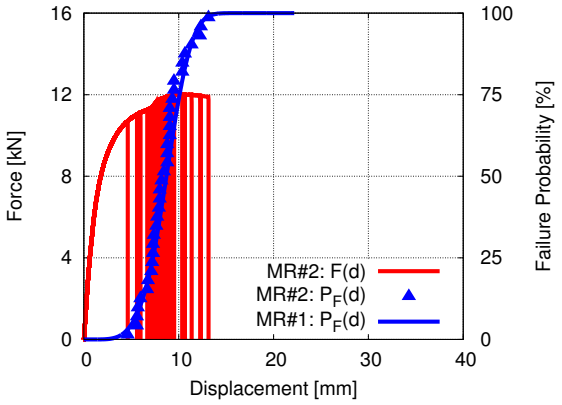

(a) Predicted force-displacement curves using material routine MR#2 (red) and comparison of predicted failure probabilities using material routine MR#1 (blue) and material routine MR#2 (blue triangles).

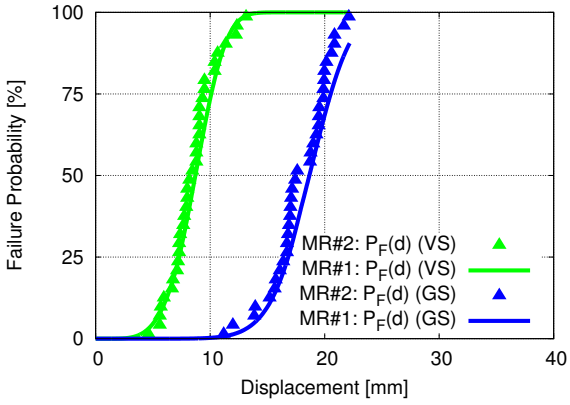

(b) Comparison of predicted failure probabilities obtained from the gating side using material routine MR#1 (blue) and material routine MR#2 (blue triangles) as well as comparison of predicted failure probabilities obtained from the vacuum side using material routine MR#1 (green) and material routine MR#2 (green triangles).

Figure 10.2.5: Comparison of the numerical results obtained from simulations of the U-profile subjected to three-point bending using material routines MR#1 and MR#2 ($l_e = 3.00\,\text{mm}$).

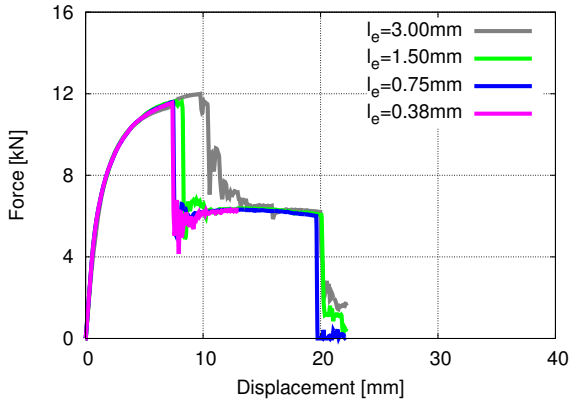

Figure 10.2.6: Mesh sensitivity analysis of the FE model of the U-profile subjected to three-point bending using material routine MR#3: Predicted force-displacement curves ($l_e = \{3.00\,\text{mm}, 1.50\,\text{mm}, 0.75\,\text{mm}, 0.38\,\text{mm}\}$).

the influence of fracture initiation and crack propagation with a pseudo-randomly distributed critical value. As already shown in the first numerical study, see Chapter 10.1.2, the same failure probability can be predicted by a single FE simulation using material routine MR#1 and a Monte-Carlo simulation based on multiple repeated FE simulations using material routine MR#2. Hence, the consistency of material routines MR#1 and MR#2 was confirmed by a component test and, further, the numerical efficiency of material routine MR#1 was clearly demonstrated.

10.2.3 Prediction of Fracture Initiation

In addition to the failure probability analysis, a mesh convergence study was performed on the FE model of the U-profile subjected to three-point bending. Here, the focus was put on a pure numerical analysis of fracture initiation. The mesh convergence studies of the uniaxial tensile test showed that material routine MR#3 and material routine MR#4 need to be used to reach mesh convergence, see Chapter 10.1.3. Therefore, material routine MR#3 was applied and a critical edge length of $l_{crit} = 3.00\,\text{mm}$ was chosen for the uniform MS mesh. Further, the PRNG applied in material routine MR#3 was initialised to the same state each time a simulation was performed. Four mesh sizes were investigated and the result of mesh convergence study is presented in Figure 10.2.6. The graph shows the force-displacement curves obtained from the four mesh sizes: Mesh size of $l_e = 3.00\,\text{mm}$ in grey, mesh size of $l_e = 1.50\,\text{mm}$ in green, mesh size of $l_e = 0.75\,\text{mm}$ in blue and mesh size of $l_e = 0.38\,\text{mm}$ in magenta. Mesh convergence is reached in terms of the force-displacement behaviour. Moreover, the prediction of fracture initiation on the vacuum side (first drop) as well as the prediction of fracture initiation on the gating side (second drop) converge. However, it is seen that the force-displacement curve obtained from a mesh size of $l_e = 0.38\,\text{mm}$ ends earlier than the other ones. This is caused by the fact that the required simulation time was larger than the maximum available computational time on the applied computer cluster.

The pseudo-random distribution of critical value W_c on the vacuum side is given as contour plot for each mesh size in Figure 10.2.7a. It is seen that the same distribution was used for each mesh size due to the uncoupled modelling approach implemented in material routine MR#3 and the initialising of the PRNG. As a result, the predicted location of frac-

ture initiation does not vary as seen in Figure 10.2.7b. This figure shows location of fracture initiation and propagation of a crack on the vacuum side for each mesh size at a punch displacement of approximately 11.1 mm. Additionally, the distribution of failure integral W is given as a contour plot. The location of fracture initiation does not vary between the four mesh sizes and the crack path converges with decreasing mesh size. It can be concluded that material routine MR#3 including the uncoupled modelling approach can be applied for numerical analyses of stochastic crack propagation on component level.

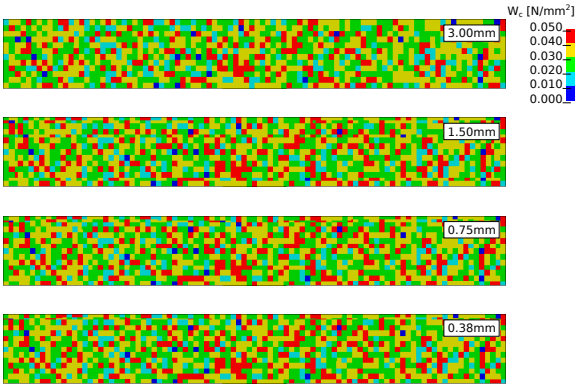

(a) Comparison of the undeformed vacuum side including the distributions of critical value W_c.

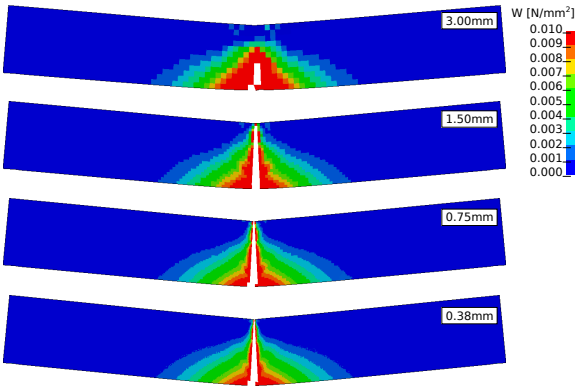

(b) Comparison of fracture initiation on vacuum side including the distributions of failure integral W at a punch displacement of approximately 11.1 mm.

Figure 10.2.7: Mesh convergence study of the FE model of the U-profile subjected to three-point bending using material routine MR#3: Prediction of fracture initiation in the vacuum side ($l_e = \{3.00\,\text{mm}, 1.50\,\text{mm}, 0.75\,\text{mm}, 0.38\,\text{mm}\}$).

10.2.4 Through-Process Modelling Approach

The two previous numerical analyses of the U-profile subjected to three-point bending were based on a part definition according to the underlying casting system as illustrated

in Figure 10.2.8a. The flange close to the gating channels was defined as gating side (blue), the flange close to the vacuum channels as vacuum side (green) and the web between both flanges as intermediate part (red). In the work by Dørum et al. [32], the result of a casting simulation of the U-profile is presented and a through-process modelling approach is introduced. The through-process modelling approach can be described as follows:

- The casting simulation result provides a quantitative measurement for the spatial distribution of discrete casting qualities.
- Each casting quality is defined as a unique set of material model parameters and corresponds to a unique casting quality.
- The casting simulation result is mapped onto a corresponding FE mesh.
- The parts of the FE mesh are defined according to the spatial distribution of the discrete casting qualities.

In the work by Dørum et al. [32], the Air Contact Time (ACT) distribution predicted by the casting simulation is used as casting quality measurement and the three casting qualities are defined by the material model parameters found on gating side, intermediate part and vacuum side. In the present work, the same approach was considered. The predicted ACT distribution given in Figure 10.2.8b was mapped onto the FE mesh of the U-profile (mesh size of $l_e = 3.00\,\text{mm}$) and the part definition of the FE mesh was defined based on the predicted ACT distribution according to the mapping rule:

- $0.0\,\text{msec} \leq \text{ACT} < 0.1\,\text{msec}$: High casting quality - Usage of material model parameters found in gating side (blue)
- $0.1\,\text{msec} \leq \text{ACT} < 0.6\,\text{msec}$: Intermediate casting quality - Usage of material model parameters found in intermediate part (red)
- $0.6\,\text{msec} \leq \text{ACT}$: Low casting quality - Usage of material model parameters found in vacuum side (green)

The redefined part definition of the FE model of the U-profile is presented in Figure 10.2.8c. It is seen that the new part definition becomes more heterogeneous compared to the initial part definition. Since each part was linked to a set of unique material model parameters, this through-process modelling approach can be also defined as material card mapping as already described in Chapter 6.5.

Based on the through-process modelling approach, a simulation of the U-profile subjected to three-point bending was performed using material routine MR#1. The numerical results obtained from the simulation are compared with the results obtained from the simulation without a through-process modelling approach in Figure 10.2.9. The graph given in Figure 10.2.9a shows the displacement of the punch on the abscissa, the applied force of the punch on the left ordinate and the failure probability on the right ordinate. The force-displacement obtained from the simulation without mapping is plotted as blue line and the one obtained from the simulation with mapping is plotted as red line. The predicted force-displacement behaviour is almost unaffected by the through-process mapping approach. The failure probability of the entire FE model obtained from the simulation without mapping is plotted as blue dashed line and the one obtained from the simulation with mapping is plotted as red dashed line. Here, a minor difference between both predicted failure probabilities can be identified. The failure probability obtained from the simulation with mapping is slightly smaller than the one obtained from the simulation

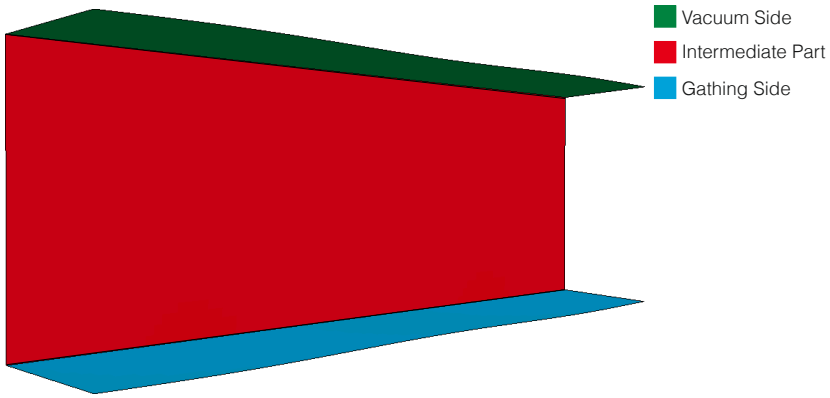

(a) Part definition according to the casting system.

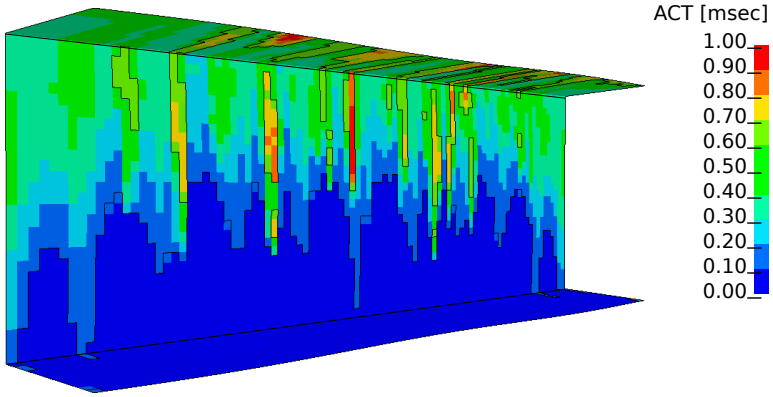

(b) Predicted ACT distribution obtained from the work by Dørum et al. [32].

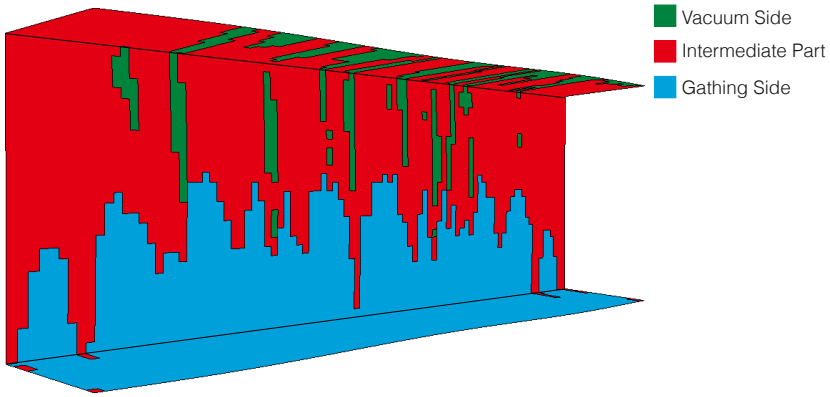

(c) Part definition according to the predicted ACT distribution.

Figure 10.2.8: Through-process modelling approach applied on the FE model of the U-profile ($l_e = 3.00\,\text{mm}$).

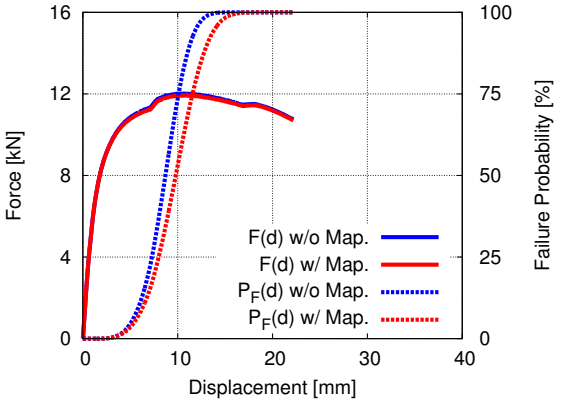

(a) Comparison of predicted force-displacement curves obtained from a simulation without mapping (blue line) and a simulation with mapping (red line) as well as comparison of predicted failure probabilities (entire U-profile) obtained from a simulation without mapping (blue dashed line) and a simulation with mapping (red dashed line).

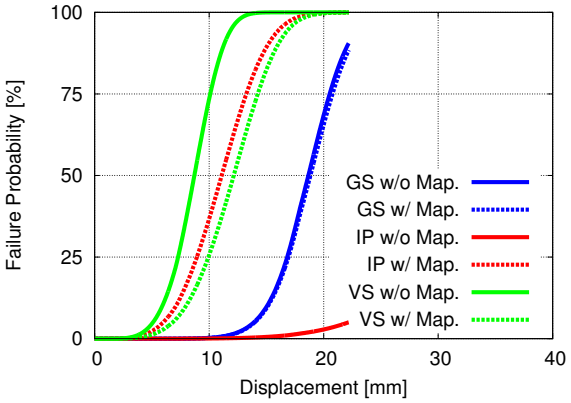

(b) Comparison of predicted failure probabilities obtained from a simulation without mapping (gating side (blue line), intermediate part (red line), vacuum side (green line)) and a simulation with mapping (gating side or high casting quality (blue dashed line), intermediate part or intermediate casting quality (red dashed line), vacuum side or low casting quality (green dashed line)).

Figure 10.2.9: Comparison of numerical results obtained from simulations (material routine MR#1) of the U-profile subjected to three-point bending without mapping and with mapping ($l_e = 3.00\,\text{mm}$).

without mapping at same punch displacement. The graph given in Figure 10.2.9b shows the displacement of the punch on the abscissa and the failure probability on the left ordinate. Here, the failure probabilities obtained from the three parts of the FE model are compared. The failure probabilities of gating side, intermediate part and vacuum side obtained from a simulation without mapping are plotted as blue line, red line and green line. The failure probabilities of gating side (high casting quality), intermediate part (intermediate casting quality) and vacuum side (low casting quality) obtained from a simulation with mapping are plotted as blue dashed line, red dashed line and green dashed line. Since the part definition of gating side is comparable in both FE models, the corresponding failure probabilities are comparable. However, the part definitions of intermediate part as well as vacuum side are strongly different in the two FE models and, obviously, the corresponding failure probabilities are strongly different from each other.

The numerical results could not be compared with a sufficient large experimental database and, thus, could not be validated. Moreover, it is noted that the applied mapping rule was chosen without any experimental correlation. However, the objective of this analysis was to demonstrate how the result obtained from a casting simulation can be used in FE modelling of HPDC components. The presented through-process modelling approach shows a possibility to consider the global systematic variation in the ductility of casting materials in a FE model depending on discrete casting qualities.

10.3 Validation

The objective of the last numerical study is the validation of the probabilistic approach in failure modelling using the U900-1 component made of the aluminium HPDC alloy Castasil-37 in casting condition (F). Parallel three-point bending tests and parallel axial compression tests were carried out on U900-1 components and the results were presented in Chapter 7. These test results form the basis for the validation. Both types of component tests were numerically analysed using material routine MR#1. It is checked if the numerically predicted failure probability correlates to the failure probability estimated from the experimental results. It is noted that a successful validation of material routine MR#1 implies a successful validation of material routines MR#2 as demonstrated in the previous numerical studies. Moreover, the influence of the discretisation on the numerical behaviour of the U900-1 component is analysed. Here, three different types of FE meshes were investigated. In the following, the discretisation and the creation of these three FE meshes are described. The results of the validation study are presented and discussed separately for the three-point bending test and the axial compression test.

10.3.1 Numerical Model

The U900-1 component is U-shaped with a typical casting structure inside as seen in Figure 7.1.1a. The discretisation of such a structure is very difficult due to the strong variation in the thicknesses as seen in Figure 10.3.1a. The image shows a cross-section machined from the U900-1 component and it can be seen that the thickness of an ejector dome is much larger than the wall thickness of the ribs and the U-shaped part. Such a geometry can be best discretised by solid elements as shown in Figure 10.3.1b (8-node underintegrated solid elements, mesh size of $l_e \leq 1.0\,\text{mm}$). However, the usage of solid elements leads to high computational cost and, thus, is not applicable for industrial applications such as for full scale car crash simulations. Figure 10.3.1c shows a typical shell mesh which is applied in industrial applications (Belytschko-Tsay shell elements with five integration

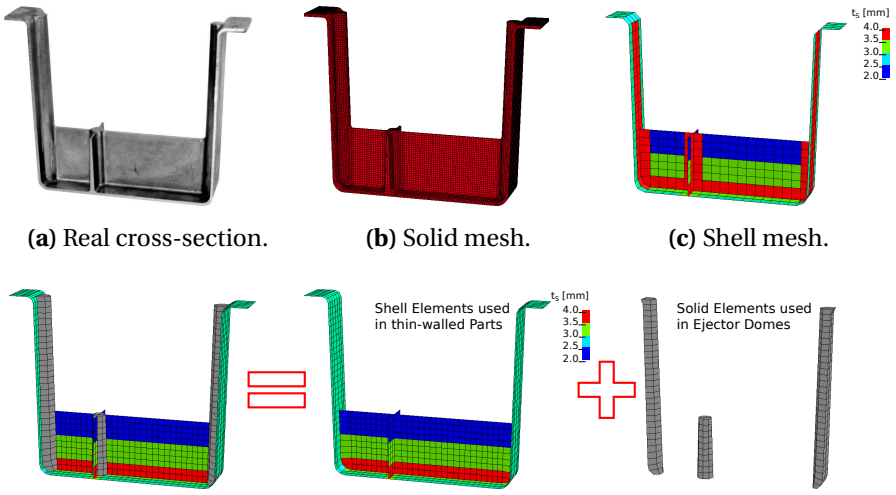

(a) Real cross-section. **(b)** Solid mesh. **(c)** Shell mesh.

(d) Hybrid mesh.

Figure 10.3.1: Discretisation of the cross-section of the U900-1 component using a solid mesh ($l_e \leq 1.0\,\text{mm}$), a shell mesh ($l_e \leq 8.0\,\text{mm}$) and a hybrid mesh ($l_e \leq 5.0\,\text{mm}$).

points through thickness, mesh size of $l_e \leq 8.0\,\text{mm}$). Here, the shell thickness distribution is given as contour plot and it is seen that the wall thicknesses by the local shell element thickness. The thickness of the ejector domes are also captured by the local shell element thickness and, thus, it can be expected that the stiffness of the ejector domes is not well captured. An alternative discretisation approach is the usage of hybrid meshes which consist of shell elements and solid elements. Here, the thin walled parts are modelled with shell elements and the thick parts such as the ejector domes are modelled with solid elements as demonstrated in Figure 10.3.1d (Belytschko-Tsay shell elements with five integration points through thickness and 8-node underintegrated solid elements, mesh size of $l_e \leq 5.0\,\text{mm}$). The solid elements are modelled on top of the shell elements. This implies that congruent nodes of shell and solid elements are merged. Consequently, a bending resistant connection of shell and solid elements can be guaranteed.

These three modelling approaches are compared in an eigenfrequency analysis of the small ejector dome which is placed in the intersections of ribs. The computation of eigenfrequencies enables to draw conclusions of the structural stiffness of the considered FE model. The eigenfrequency analysis was performed in the implicit FE solver LS-DYNA 971 [51]. Here, a linear-elastic material behaviour was adopted and Young's modulus E was set to $72.00\,\text{kN}/\text{mm}^2$, Poisson's ratio ν to 0.33 and density ρ to $2.75 \cdot 10^{-6}\,\text{kg}/\text{mm}^3$. Figure 10.3.2a shows the FE model of the small ejector dome using the solid element mesh. It is seen that all nodes at the bottom were fixed. The FE model using the shell mesh and the FE model using the hybrid mesh were created accordingly.

The first bending eigenfrequency ω_{B1}, see Figure 10.3.2b, and the first torsional eigenfrequency ω_{T1}, see Figure 10.3.2c, of each FE model were computed. These eigenfrequencies are used to characterise numerically the bending and the torsional stiffness of the small ejector dome depending on the modelling approach. The computed eigenfrequencies are compared in Table 10.3.1. The eigenfrequencies obtained from the solid mesh form the basis for the comparison. The bending eigenfrequencies obtained from the shell mesh and the hybrid mesh are comparable, but these are more than 10% smaller than the

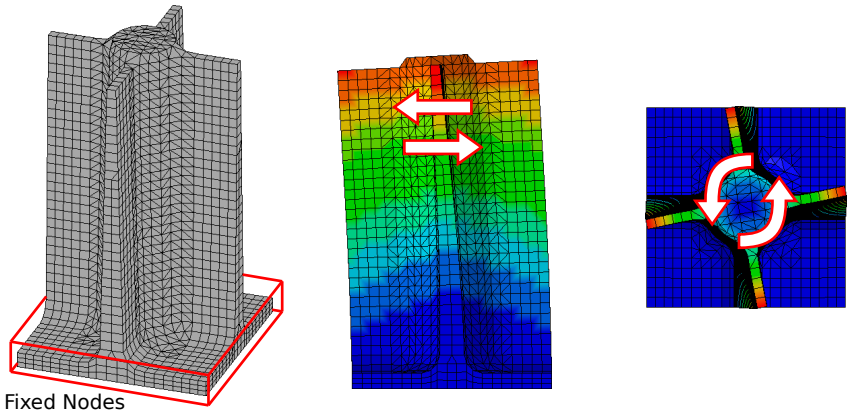

(a) FE model. **(b)** ω_{B1}. **(c)** ω_{T1}.

Figure 10.3.2: FE model of the small ejector dome applied for eigenfrequency analysis and numerical results of the first bending eigenfrequency ω_{B1} and the first torsional eigenfrequency ω_{T1} (solid mesh).

Eigenfrequency Analysis of the Small Ejector Dome		
Modelling Approach	ω_{B1} [1/msec]	ω_{T1} [1/msec]
Solid Mesh	45.74 (100%)	58.80 (100%)
Shell Mesh	37.95 (−17%)	27.47 (−53%)
Hybrid Mesh	39.20 (−14%)	41.08 (−30%)

Table 10.3.1: Comparison of the first bending eigenfrequency ω_{B1} and the first torsional eigenfrequency $\omega_{T1}$of the small ejector dome obtained from a solid mesh, a shell mesh and a hybrid mesh.

bending eigenfrequency obtained from the solid mesh. However, the comparison of torsional eigenfrequencies shows a clear difference between the shell mesh and hybrid mesh. The torsional eigenfrequency obtained from the shell mesh is more than 50% smaller than the torsional eigenfrequency obtained from the solid mesh. In contrast, the torsional eigenfrequency obtained from the hybrid mesh is only 30% smaller than the torsional eigenfrequency obtained from the solid mesh. These results show clearly that the shell mesh cannot reproduce the stiffness of the solid mesh, whereas the hybrid mesh provides an appropriate alternative to the solid mesh.

The solid mesh, the shell mesh and the hybrid mesh shown in Figure 10.3.1 were investigated in the validation study. In the material characterisation presented in Chapter 8, it was shown by hypothesis testing that the U900-1 component can be classified into three characteristic parts with comparable material ductility. These were defined as part IW (gating side), part BF (intermediate part) and part OW (vacuum side), see Figure 8.1.2. Accordingly, the FE meshes of the U900-1 component were partitioned into the three characteristic parts gating side (blue), intermediate part (red) and vacuum side (green), see Figure 7.1.1d.

As already mentioned, material routine MR#1 was used to describe the material behaviour and to compute failure probabilities. The material characterisation presented in Chapter 8 was based on uniaxial tensile test specimens machined from the characteristic

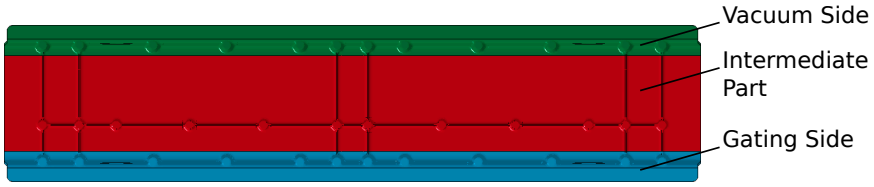

Figure 10.3.3: Part definition of the U900-1 component: Gating side (blue), intermediate part (red) and vacuum side (green).

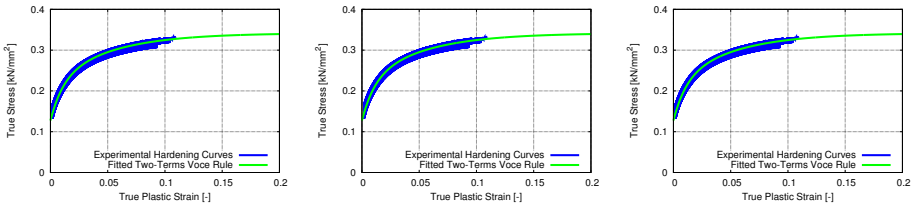

(a) Gating side (IW). **(b)** Intermediate part (BF). **(c)** Vacuum side (OW).

Figure 10.3.4: Fitted two-terms Voce rules based on experimental hardening curves obtained from UT75 specimens machined from gating side (IW), intermediate part (BF) and vacuum side (OW).

parts gating side (IW), intermediate part (BF) and vacuum side (OW). Three different specimen geometries (UT80, UT75 and UT117) were investigated. Here, the results obtained from the UT75 specimens showed the best reproducible strain hardening behaviour in each of these parts, see Chapter 8.3.1. Furthermore, it was shown that the pseudo-random distribution of critical value W_c in each part can be described by a unique Weibull distribution, see Chapter 8.3.2. Hence, the experimental results obtained from UT75 specimens were considered as the most reliable ones for the identification of the material model parameters. In each part, Young's modulus E was set to $72.00^{\mathrm{kN}/\mathrm{mm}^2}$, Poisson's ratio ν to 0.33 and the exponent p applied in the yield criterion to 4. The five parameters of the two-terms Voce rule were found separately for each part from a least-squares curve fit using gnuplot [115]. The results are presented in Figure 10.3.4a for gating side (IW), in Figure 10.3.4b for intermediate part (BF) and in Figure 10.3.4c for vacuum part (OW). Each figure shows the experimental hardening curves obtained from UT75 specimens machined from the same part (blue) and the fitted two-terms Voce rule (green). The Weibull parameters were taken from the corresponding results of the Weibull analysis provided in Table 8.3.4, Table 8.3.5 and Table 8.3.6. The material model parameters are summarised in Table 10.3.2.

10.3.2 Bending Test

The numerical model of the three-point bending test set-up was created according to the experimental test set-up described in Chapter 7.2.1 and is illustrated in Figure 10.3.5. The supports in form of steel bars were modelled as cylindrical rigid bodies, see Figure 10.3.5a. According to the applied support construction given in Figure A.1.2, the supports were fixed in space except of the horizontal direction and, consequently, the supports were allowed to move in the horizontal direction. The three FE meshes of the U900-1 com-

Material Model Parameters (U900-1 Component)					
Part	ρ [kg/mm³]	E [kN/mm²]	ν [−]	p [−]	
Gating Side (IW)	$2.75 \cdot 10^{-6}$	72.00	0.33	4	
Intermediate Part (BF)	$2.75 \cdot 10^{-6}$	72.00	0.33	4	
Vacuum Side (OW)	$2.75 \cdot 10^{-6}$	72.00	0.33	4	
Part	σ_0 [kN/mm²]	Q_1 [kN/mm²]	C_1 [−]	Q_2 [kN/mm²]	C_2 [−]
Gating Side (IW)	0.128	0.091	93.0	0.123	19.7
Intermediate Part (BF)	0.132	0.086	91.3	0.122	20.7
Vacuum Side (OW)	0.141	0.069	102.6	0.136	28.8
Part	m [−]	W_{c0} [kN/mm²]	V_0 [mm³]		
Gating Side (IW)	8.00	0.033	506.25		
Intermediate Part (BF)	10.59	0.034	506.25		
Vacuum Side (OW)	4.75	0.023	506.25		

Table 10.3.2: Material model parameters obtained from UT75 specimens machined from gating side (IW), intermediate part (BF) and vacuum side (OW).

ponent were modified so that supports could be placed through holes in it, see Figure 10.3.5a. The aluminium sheets which were used to reinforce the holes were discretised with Belytschko-Tsay shell elements with five integration points through thickness and a mesh size of $l_e = 8.0\,\text{mm}$, see Figure 10.3.5b. The sheet material behaviour was described by a linear-elastic material model with Young's modulus E of 72.00 kN/mm², Poisson's ratio ν of 0.33 and density ρ of $2.75 \cdot 10^{-6}$ kg/mm³. The aluminium sheets were attached to the three FE meshes of the U900-1 component using a tied contact definition. The steel punch was modelled as a cylindrical rigid body and was only allowed to move perpendicular to the U900-1 component. It was observed that the punch rotates slightly about 1.00° during testing, see Figure 7.2.5. Consequently, the punch was initially rotated about 1.00° in each FE model as seen in Figure 10.3.5a. A constant loading velocity of $4.5 \cdot 10^4 \frac{\text{mm}}{\text{min}}$ was adopted. This loading velocity is much faster than the experimental loading velocity of $3 \frac{\text{mm}}{\text{min}}$ which was assumed to be quasi-static. Due to the usage of underintegrated elements, a stiffness based hourglass control was applied. It is noted that mass scaling was applied for the solid mesh to reduce the computational time. The applied mass scaling algorithm adds mass to only those elements whose time step is less than a minimum time step. Here, the minimum time step was set to $2.8 \cdot 10^{-4}$ msec. It was checked that kinetic energy and hourglass energy are less than 1% of total energy in each simulation. Hence, quasi-static loading conditions and minimal hourglassing were ensured. A friction coefficient of 0.2 was assumed for the global contact modelling. According to the experimental measurements, reaction force and displacement were taken from the rigid body output of the punch.

The numerical force-displacement curves obtained from the solid mesh (blue), the shell mesh (green) and the hybrid mesh (magenta) are compared with the experimental force-displacement curves (grey) in Figure 10.3.6a. The experimental force-displacement behaviour until fracture initiation is perfectly captured by the solid mesh as well as the hybrid mesh. Further, the results obtained from the solid mesh and the hybrid mesh show that the force increases constantly during deformation. In contrast, the result obtained from the shell mesh shows that the force increases during deformation until a maximum force level is reached and, then, the force decreases further during deformation. The deformation of the cross-section directly under the punch was monitored in each simulation and the results at four deformation states are provided in Figure 10.3.7. It can be observed that

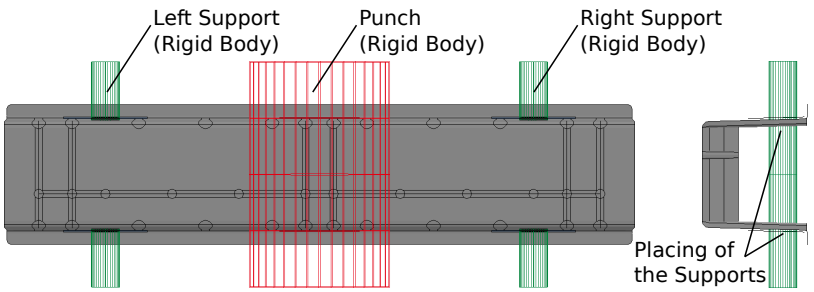

(a) Modelling of supports and punch as rigid bodies (top view).

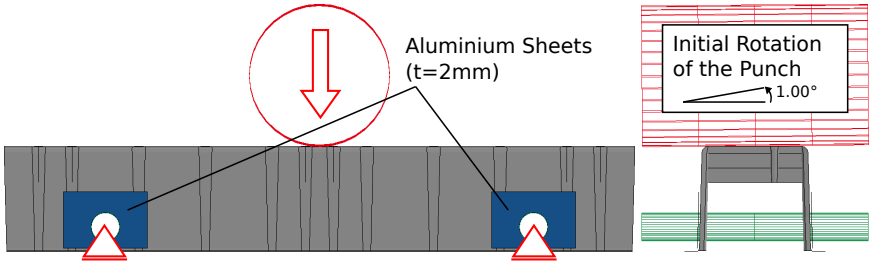

(b) Modelling of reinforcement sheets and initial rotation of the punch (side view).

Figure 10.3.5: Numerical model of the three-point bending test set-up.

the cross-section of the solid mesh shows only minor bending of gating side and vacuum side during deformation. The cross-section of the hybrid mesh shows a similar behaviour. In contrast, the cross-section of the shell mesh shows a kind of buckling of gating side and of vacuum side. As expected, the discretisation of the ejector domes using shell elements cannot capture the stiffness of the cross-section. The buckling phenomenon of the cross-section causes the maximum force level and the subsequent decrease of the force level. It can be concluded that the structural behaviour of the U900-1 component subjected to three-point bending is captured best by the solid mesh and the hybrid mesh. Moreover, these results imply that the structural behaviour can be well described by the applied constitutive model and the calibrated model parameters.

Figure 10.3.6b shows the force-displacement curves (grey) obtained from the seven parallel tests and the point of fracture initiation in each curve is marked by red squares. The underlying data are provided in Table 7.2.1a. Based on these measurements, the failure probability of the U900-1 component subjected to three-point bending was estimated according to Equation (8.1.14). The experimental failure probability and the numerical failure probabilities obtained from the three FE meshes are compared in the graph given in Figure 10.3.6c. The graph shows the failure probability on the ordinate and the punch displacement on the abscissa. The experimental failure probability is plotted as a row of red triangles. The numerical failure probability obtained from the solid mesh is plotted in blue, the numerical failure probability obtained from the shell mesh in green and the numerical failure probability obtained from the hybrid mesh in magenta. A very good correlation is achieved between the experimental failure probability and the numerical failure probability obtained from the solid mesh. The numerical failure probability obtained

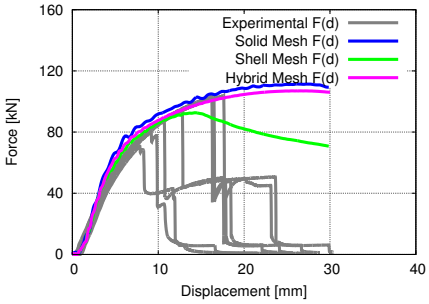

(a) Comparison of experimental force-displacement curves (grey) and numerical force-displacement curves obtained from solid mesh (blue), shell mesh (green) and hybrid mesh (magenta).

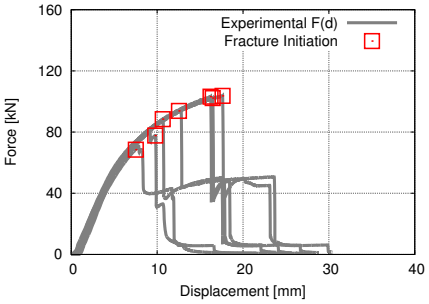

(b) Identification of fraction initiation (red squares) in the experimental force-displacement curves (grey) .

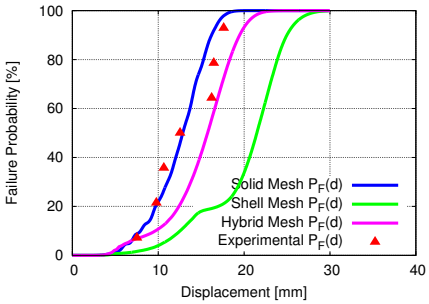

(c) Comparison of experimental failure probability (red triangles) and numerical failure probability obtained from solid mesh (blue), shell mesh (green) and hybrid mesh (magenta).

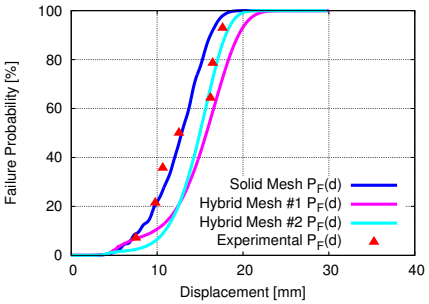

(d) Comparison of experimental failure probability (red triangles) and numerical failure probability obtained from solid mesh (blue), hybrid mesh (magenta) and refined hybrid mesh (cyan).

Figure 10.3.6: Comparison of experimental results and numerical results obtained from solid mesh, shell mesh and hybrid mesh (U900-1 component subjected to three-point bending).

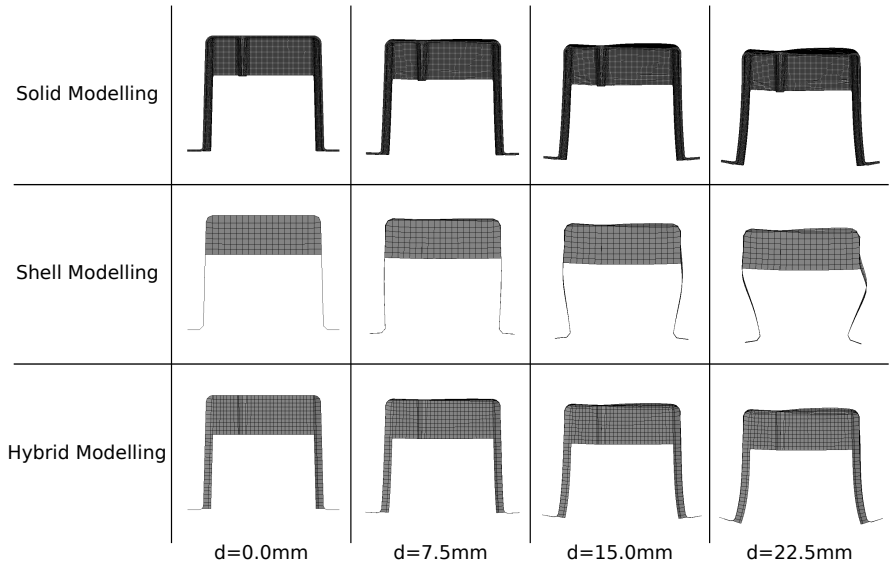

Figure 10.3.7: Numerical prediction of the cross-section deformation of the U900-1 component subjected to three-point bending using solid modelling, shell modelling and hybrid modelling.

from the shell mesh underestimates strongly the experimental failure probability. Here, the buckling of the cross-section is the main reason for this poor result. The numerical failure probability obtained from the hybrid mesh underestimates also the experimental failure probability, but the underestimation is less than the one obtained from the shell mesh. Nevertheless the solid mesh as well as the hybrid mesh capture the experimental force-displacement behaviour, the solid mesh captures the local stress distribution (and W distribution) better than the hybrid mesh. This might be caused by the smaller mesh size of the solid mesh. Hence, a mesh refinement was performed on the hybrid mesh (mesh size of $l_e \leq 2.5\,\text{mm}$). A comparison of the experimental failure probability (red triangles) and the numerical failure probabilities obtained from the solid mesh (blue), the hybrid mesh (magenta) and the refined hybrid mesh (cyan) is provided in Figure 10.3.6d. Here, the numerical failure probability obtained from the refined hybrid mesh is in a very good agreement with the experimental failure probability above 60%, whereas the numerical failure probability obtained from the solid mesh is in a very good agreement with the experimental failure probability below 60%. It is noted that the experimental failure probability is estimated based on only seven parallel test results and more test results provide a more reliable estimation. Consequently, the comparison between experimental failure probability and numerical failure probability becomes more reliable. However, these results demonstrate that the solid mesh and the hybrid mesh as well as the applied probabilistic failure criterion based on the Cockcroft-Latham criterion and the weakest-link approach by Weibull provide a very good predication of the failure probability of the U900-1 component subjected to three point bending. It is important to note that the computation of the failure probability using material routine MR#1 only requires a single simulation of the considered FE model.

Finally, the computational costs of the applied FE meshes are compared in Table 10.3.3. As expected, the shell mesh is the cheapest one and the solid mesh is the most expensive one. In the hybrid mesh, the discretisation of the ejector domes by solid elements

Computational Cost - U900-1 Subjected to Three-Point Bending			
Modelling	Computational Time	Number of CPU's	Mass Scaling
Solid Mesh	26504 sec (+1765%)	64	Yes
Shell Mesh	1421 sec (100%)	8	No
Hybrid Mesh	4271 sec (+201%)	8	No
Refined Hybrid Mesh	23419 sec (+1548%)	16	No

Table 10.3.3: Comparison of computational cost of the different modelling approaches of the U900-1 component subjected to three-point bending.

increases the computational cost. Here, the computational costs of the hybrid mesh can easily be reduced using mass scaling and, thus, the computational cost of the shell mesh can be reached. The same holds for the refined hybrid mesh.

10.3.3 Axial Compression Test

The numerical model of the axial compression test set-up was created according to the experimental test set-up described in Chapter 7.3.1 and is illustrated in Figure 10.3.8. Accordingly, the three FE meshes of the U900-1 component were cut in half and the cut surfaces were modelled parallel and each mesh was placed between two plates which were modelled as rigid bodies, see Figure 10.3.8a and Figure 10.3.8b. The bottom plate was fixed in space and the loading plate was allowed to move in the longitudinal direction of the U900-1 component. It was observed that the loading plate rotates slightly about 0.61° during testing, see Figure 7.3.5. Consequently, the punch was initially rotated about 0.61° in each FE model as seen in Figure 10.3.5a. A constant loading velocity of $4.5 \cdot 10^4 \frac{\text{mm}}{\text{min}}$ was adopted. This loading velocity is much faster than the experimental loading velocity of $3 \frac{\text{mm}}{\text{min}}$ which was assumed to be quasi-static. Due to the usage of underintegrated elements, a stiffness based hourglass control was applied. It is noted that mass scaling was applied for the solid mesh to reduce the computational time. The applied mass scaling algorithm adds mass to only those elements whose time step is less than a minimum time step. Here, the minimum time step was set to $2.8 \cdot 10^{-4}$ msec. It was checked that kinetic energy and hourglass energy are less than 1% of total energy in each simulation. Hence, quasi-static loading conditions and minimal hourglassing were ensured. A friction coefficient of 0.2 was assumed for the global contact modelling. According to the experimental measurements, reaction force and displacement were taken from the rigid body output of the loading plate.

The numerical force-displacement curves obtained from the solid mesh (blue), the shell mesh (green) and the hybrid mesh (magenta) are compared with the experimental force-displacement curves (grey) in Figure 10.3.9a. It is seen that the initial stiffness of the U900-1 component until peak load is well captured by the solid mesh, the shell mesh as well as the hybrid mesh. The peak load is overestimated by the solid mesh as well as by the hybrid mesh, whereas the peak load obtained from the shell mesh is closer to the experimental results. The force level beyond peak load shown by the experimental results cannot be captured by the three different meshes. Here, the solid mesh provides a closer result. However, it is important to take into account that the simulations were performed using material routine MR#1. This implies that element deletion was not considered. Consequently, the numerical and experimental results can only be compared until first fracture initiation. Figure 10.3.9b shows the force-displacement curves (grey) obtained from the four parallel tests and the point of fracture initiation in each curve is marked by red

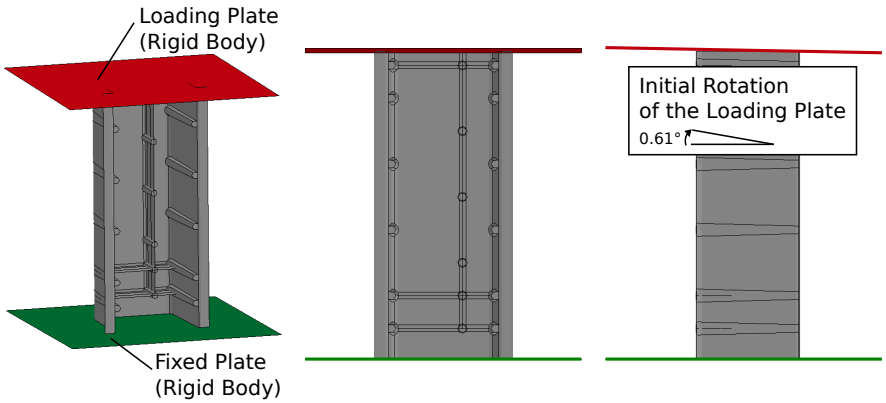

(a) Perspective view. **(b)** Front view. **(c)** Side view.

Figure 10.3.8: Numerical modelling of the axial compression test set-up.

squares. The underlying data are provided in Table 7.3.1a. Now, experimental results and numerical results are compared in terms of dissipated energy at fracture initiation. Here, the dissipated energy is defined as the integral of the force-displacement curve until the displacement at fracture initiation is reached. Table 10.3.4 compares the dissipated energy obtained from the experimental results with the dissipated energy obtained from the numerical results for each test separately and in average. It is seen that the dissipated energy until first fracture initiation is numerically well captured in average by all mesh variants. Figure 10.3.10 shows the deformation of the solid mesh, the shell mesh and the hybrid mesh at a loading plate displacement of 7.5 mm. Here, the resultant displacement is given as a contour plot for each mesh type. The deformation of the solid mesh as well as the deformation of the shell mesh show a buckling mode which leads to an opening of the U900-1 component. However, the deformation of the shell mesh shows a more extreme opening which is caused by the discretisation of the ejector domes using shell elements. As already seen, the correct stiffness of the cross-section cannot be captured by the shell mesh. The deformation of the hybrid mesh shows a buckling mode which leads to a closing of the U900-1 component. The experimental results show only an opening of the tested U900-1 components, see Figure 7.3.2. It is noted that slight modifications in the mesh size of the hybrid mesh can also lead to an opening of the U900-1 component due to the sensitivity of the buckling instability. In summary, it can be concluded that the structural behaviour of the U900-1 component subjected to axial compression is better captured by the solid mesh as well as the hybrid mesh. The nearly perfect correlation between experimental and numerical results for the bending load case cannot be achieved for the compression load case which is common for cases showing some kind of buckling behaviour.

Figure 10.3.9b shows the force-displacement curves (grey) obtained from the four parallel tests and the point of fracture initiation in each curve is marked by red squares. The underlying data are provided in Table 7.3.1a. Based on these measurements, the failure probability of the U900-1 component subjected to axial compression was estimated according to Equation (8.1.14). The experimental failure probability and the numerical failure probabilities are compared in graph given in Figure 10.3.9c. The graph shows the failure probability on the ordinate and the displacement of the loading plate on the abscissa. The experimental failure probability is plotted as a row of red triangles. The numerical failure probability obtained from the solid mesh is plotted in blue, the numerical failure

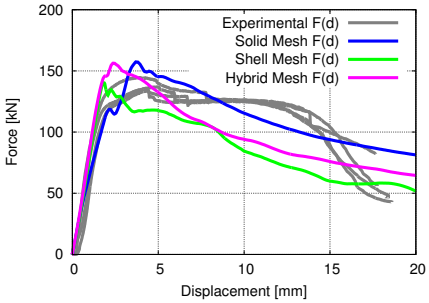

(a) Comparison of experimental force-displacement curves (grey) and numerical force-displacement curves obtained from solid mesh (blue), shell mesh (green) and hybrid mesh (magenta).

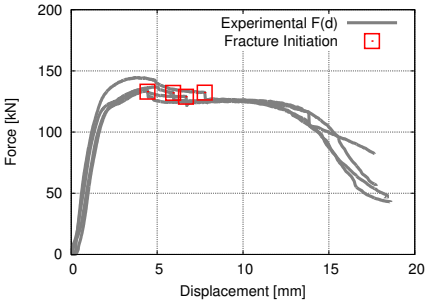

(b) Identification of fracture initiation (red squares) in the experimental force-displacement curves (grey) .

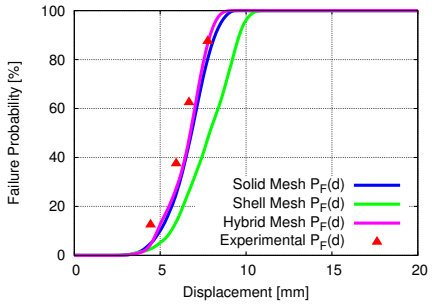

(c) Comparison of experimental failure probability (red triangles) and numerical failure probability obtained from the solid mesh (blue), the shell mesh (green) and the hybrid mesh (magenta).

Figure 10.3.9: Comparison of experimental results and numerical results obtained from solid mesh, shell mesh and hybrid mesh (U900-1 component subjected to axial compression).

Dissipated Energy - U900-1 Subjected to Axial Compression					
Experimental Results			Solid Mesh	Shell Mesh	Hybrid Mesh
Test	d_f^{exp}	E_f^{exp}	E_f^{num}	E_f^{num}	E_f^{num}
AC11	7.77	948.59 (100%)	928.33 (−2%)	827.19 (−13%)	923.68 (−3%)
AC12	5.93	617.69 (100%)	674.60 (+9%)	629.09 (+2%)	717.72 (+16%)
AC13	6.68	748.27 (100%)	782.65 (+5%)	710.70 (−5%)	804.06 (+7%)
AC14	4.44	427.01 (100%)	461.03 (+8%)	453.20 (+6%)	520.91 (+22%)
Average	6.21	685.39 (100%)	711.65 (+4%)	655.05 (−4%)	741.59 (+8%)

Table 10.3.4: Comparison of experimental dissipated energy and numerical dissipated energy obtained from solid mesh, shell mesh and hybrid mesh $\left(E_f = \int_0^{d_f^{exp}} F(d)\,dx\right)$.

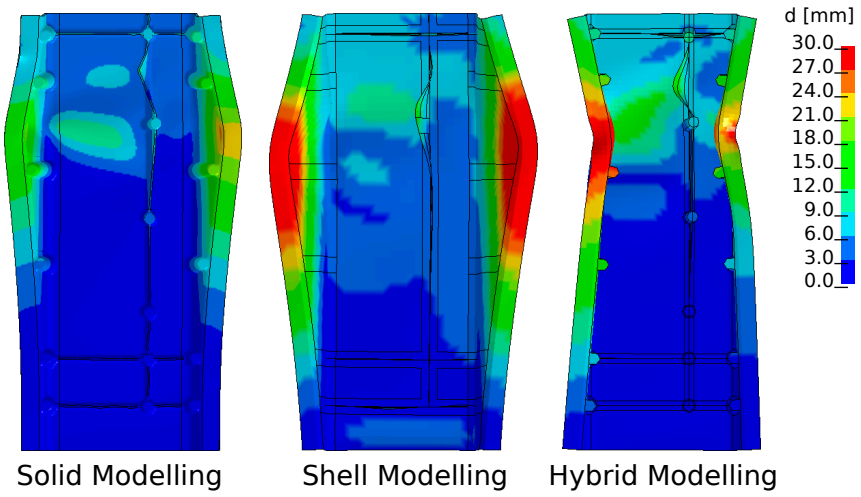

Figure 10.3.10: Numerical prediction of the deformation of the half U900-1 component subjected to axial compression using solid modelling, shell modelling and hybrid modelling at a loading plate displacement of 7.5 mm.

probability obtained from the shell mesh in green and the numerical failure probability obtained from the hybrid mesh in magenta. A very good correlation is achieved between the experimental failure probability and the numerical failure probability obtained from the solid mesh as well as the hybrid mesh. The numerical failure probability obtained from the shell mesh underestimates strongly the experimental failure probability. It can be assumed that the the local stress distribution (and W distribution) is not well captured by the soft shell mesh. However, these results show that the solid mesh and the hybrid mesh as well as the applied probabilistic failure criterion based on the Cockcroft-Latham criterion and the weakest-link approach by Weibull provide a very good prediction of the failure probability of the U900-1 component subjected to axial compression. It is important to mention that the experimental failure probability was estimated based on only four parallel test results. Here, more test results provide a more reliable estimation and, thus, enable a more reliable comparison between experimental and numerical results.

Finally, the computational costs of the applied FE meshes are compared in Table 10.3.5.

Computational Cost - U900-1 Subjected to Axial Compression			
Modelling	Computational Time	Number of CPU's	Mass Scaling
Solid Mesh	13985 sec (+3828%)	64	Yes
Shell Mesh	356 sec (100%)	8	No
Hybrid Mesh	1837 sec (+416%)	8	No

Table 10.3.5: Comparison of the computational cost of the different modelling approaches of the U900-1 component subjected to axial compression.

As expected, the shell mesh is the cheapest one and the solid mesh is the most expensive one. In the hybrid mesh, the discretisation of the ejector domes by solid elements increases the computational cost. Here, the computational cost of the hybrid mesh can easily be reduced using mass scaling and, thus, the computational cost of the shell mesh can be reached.

10.4 Concluding Remarks

The first numerical study was based on the simulation of a uniaxial tensile test and the prediction of its failure probability. It was shown that the failure probability estimated from the experimental results can be reproduced by a single simulation using material routine MR#1 as well as a Monte-Carlo simulation using material routine MR#2. Moreover, it was shown that the predicted failure probability is mesh size independent provided that the applied mesh size predicts the correct deformation behaviour until fracture initiation. Hence, the consistency of material routine MR#1 and material routine MR#2 was demonstrated. This implies that the varying numerical results obtained from the usage of material routine MR#2 can reproduce the true experimentally observed scatter provided that the correct distribution function is estimated. This conclusion is very important since any application of a pseudo-randomly distributed failure parameter produces a scatter, but it is not known if the numerical predicted scatter reproduces the experimentally observed scatter. The benefit of the uncoupled modelling approach implemented in material routine MR#3 and MR#4 was shown by mesh convergence studies. Here, the subject of each mesh convergence study was the numerical prediction of fracture initiation in the uniaxial tensile test. As a result, mesh convergence could not be reached using material routine MR#2, but it was reached using material routines MR#3 and MR#4. Moreover, it was demonstrated that the uncoupled modelling approach implemented in material routine MR#4 combined with a Gaussian random field provides a possibility to consider smooth transitions in the distribution of a critical failure parameter. However, it is important to note that the MS mesh size applied in the uncoupled approach as well as the parameters of the applied Gaussian random field were freely chosen. Here, further experimental-numerical investigations are necessary.

The second numerical study was based on the simulation of a U-shaped component subjected to three-point bending. The consistency of material routine MR#1 and material routine MR#2 was confirmed. The usage of material routine MR#1 and the usage of material routine MR#2 combined with a Monte-Carlo simulation provided the same prediction of the failure probability of the entire FE model. Moreover, the failure probabilities of the three model parts could be identically predicted by both approaches. Besides this, it was shown that a simulation using material routine MR#2 can reproduce in general structural behaviour of the U-shaped component subjected to three-point bending. In addition,

a mesh convergence study was performed based on material routine MR#3 and it was shown that mesh convergence is reached through the uncoupled modelling approach. Finally, the through-process modelling approach presented in the work by Dørum et al. [32] was numerically investigated. It was shown that this approach results in a distribution of material cards according to the distribution of discrete casting qualities. The distribution of discrete casting qualities were found by the result of casting simulation and a mapping rule. The through-process modelling approach could not be validated due to the small experimental database. However, it was demonstrated that the global systematic variation in the material ductility can be captured by the through-process modelling approach and the local pseudo-random variation can be captured by the probabilistic failure model as presented.

The third numerical study was based on the simulation of the U900-1 component tests. The main objective was the numerical prediction of the failure probability of the U900-1 component subjected to three-point bending as well as to axial compression. Hence, only material routine MR#1 was considered and the required material model parameters were found from the material characterisation. Three different types of discretisation were applied. The U900-1 component was discretised using a solid mesh, a shell mesh and a hybrid mesh. An eigenfrequency analysis of the small ejector dome showed that the stiffness of the solid mesh can be estimated by the stiffness of the hybrid mesh but not by the stiffness of the shell mesh. As a result, the comparison of the experimental failure probability and the predicted failure probability obtained from the solid mesh showed a very good correlation in both load cases. The comparison of the experimental failure probability and the predicted failure probability obtained from the hybrid mesh showed a good correlation in both load cases, but the computational costs of the hybrid mesh were much smaller than the computational costs of the hybrid mesh. As expected, the numerical results obtained from the shell meshes were not acceptable. Since the stiffness of the U900-1 cross-section was poorly captured by the shell mesh, the predicted failure probability underestimated strongly the experimental failure probability in both load cases. In summary, it was demonstrated that the experimental failure probability can be predicted by the usage of material routine MR#1 provided that the correct material model parameters are identified and the structural stiffness is sufficiently captured. It can be concluded that the probabilistic approach implemented in material routine MR#1 was validated. This implies that also the probabilistic approach implemented in material routine MR#2 was validated due to the consistency of material routines MR#1 and MR#2. As already mentioned, the validation of material routines MR#3 and MR#4 requires further investigations on the MS mesh size applied in the uncoupled approach and on the parameter identification of a Gaussian random field.

Chapter 11

Conclusions / Outlook

The global systematic variation and the local pseudo-random variation in the material ductility of HPDC alloys were experimentally and numerically analysed in the present work. Both types of variation were confirmed by an extensive experimental analysis of a standard aluminium HPDC alloy. As a result, a probabilistic approach in failure modelling was introduced and implemented in an explicit FE solver. Various numerical studies were performed and the probabilistic approach could be validated. In the following, a conclusion of the present work and outlook for further investigations are given separately for the experimental work and the numerical work.

11.1 Experimental Work

The main objective of the experimental work was the investigation of the global systematic variation and the local pseudo-random variation in the material ductility of an aluminium HPDC alloy. Usually, the material ductility is measured by specimens machined from a plate. Since casting components are characterised by complex geometries and turbulent form filling, this sampling approach would provide artificial results which are not reproducible in a casting component. Therefore, the experimental work was based on the generic HPDC component U900-1 made of the aluminium alloy Castasil-37 in casting condition (F). The material was investigated, first, using component tests and, second, using material tests.

Parallel bending tests were carried out on U900-1 components. The results showed a strong variation in the structural response. It was observed that first fracture initiation occurs in the part close to the vacuum channels and second fracture initiation occurs in the part close to gating channels. Further, it was observed that time and location of fracture initiation in both parts vary pseudo-randomly. Consequently, the force-displacement behaviour exhibited strong scatter. Based on these results, the global systematic variation and the local pseudo-random variation in the material ductility could be suggested. In addition, parallel axial compression tests were performed. Here, the results showed less variation than the bending test results since the structural behaviour was mainly dominated by local buckling and less by material ductility.

Based on the results obtained from the bending tests, an extensive material characterisation was performed using uniaxial tensile tests. The specimens were machined from different extraction positions of the U900-1 component and from duplicated extraction positions of various U900-1 components. Through this sampling approach, it was possible

to analyse the systematic variation as well as the local pseudo-random variation in the material ductility. The mechanical analysis of the tensile test results showed a reproducible strain hardening behaviour in duplicated extraction positions, but the failure strain varied between different extraction positions and within duplicated positions. The critical value of the Cockcroft-Latham failure criterion was chosen to measure the material ductility. Since most specimens failed before diffuse necking, the critical value was directly measured from the tensile test result. As a result, the samples obtained from each extraction position were quantified by the measurements of the critical value. A detailed statistical analysis was performed on these samples. Hypothesis tests were applied to identify extraction positions with comparable material ductility. Based on the results obtained from the hypothesis tests, it was concluded that the U900-1 component can be separated into three characteristic parts: A part close to the gating channels, a part close to the vacuum channels and an intermediate part. This means that it was statistically confirmed that the casting system influences the spatial variation of the material ductility in the U900-1 component. As a result, the material can be characterised as follows "The material found in the part close to the gating channels and the intermediate part can be described as ductile, whereas the material in the part close to the vacuum channels can be described as almost quasi-brittle. However, the material ductility exhibits strong scatter in each part." It was shown that the local pseudo-random variation of the material ductility can be described by a weakest-link Weibull distribution. Furthermore, the volume dependence included in the weakest-link approach was investigated using specimens of different size and machined from extraction positions with comparable material failure behaviour. A clear volume dependence was only found in the results obtained from specimens machined from the part close to the vacuum channels. Finally, the fracture surfaces of selected specimens were examined by a SEM analysis and, as expected, casting defects were found on each fracture surface and identified as the dominating factor for fracture.

For the first time, the global systematic variation and the local pseudo-random variation in the material ductility of an HPDC alloy were experimentally analysed at the same time. Both types of variation were confirmed and it was demonstrated that these need to be considered in failure modelling of HPDC alloys. The experimental approach as presented and the usage of realistic components are recommended for further investigations of casting materials and other materials which are strongly influenced by the manufacturing process. The sample sizes should be generated as large as possible to increase the statistical reliability. The tensile test results were not compared with the result obtained from a casting simulation and, thus, a correlation between measurements of the casting process and the material ductility could not be identified. Therefore, a combined analysis of experimental testing and casting simulation is required to establish a mapping procedure. Further, the influence of the specimen volume on the material ductility was investigated, but it could only be identified in one part. Here, a more detailed analysis with different specimen sizes and larger samples sizes would provide a deeper understanding of the volume dependence.

11.2 Numerical Work

As a consequence of the experimental work, a probabilistic approach in failure modelling was considered to capture the local pseudo-random variation in the material ductility. In the present work, the probabilistic failure model was based on the phenomenological Cockcroft-Latham failure criterion and the weakest-link model by Weibull. The required quantities stress state and equivalent plastic strain were given by an isotropic hypoelastic-

plastic constitutive model. The main objective of the numerical work was the prediction of the failure probability of a FE model. Usually, the failure probability of a FE model is numerically estimated by a Monte-Carlo simulation. Here, various simulations are performed on a FE model using a pseudo-randomly distributed critical value. Since the performance of a Monte-Carlo simulation can be very time consuming, a novel approach was presented to predict the failure probability of a FE model by a single simulation. Both approaches were implemented as user-defined material routines in an explicit FE solver. The first material routine (MR#1) includes a stress-update algorithm and computes directly the failure probability based on multiplication of probabilities. Here, the failure probability gives information about the risk of first fracture initiation in the FE model and, thus, element deletion is not considered. The second material routine (MR#2) is equivalent to material routine MR#1, but element deletion is applied in a stochastic sense. Here, the critical value is given as a pseudo-random variable. As a result, the critical value is pseudo-randomly distributed in a FE model and the failure probability of the FE model can be only computed by a Monte-Carlo simulation. Both material routines are based on the assumption that the elements in the FE mesh are statistical independent.

Material routine MR#1 and material routine MR#2 were analysed and compared by simulation of a uniaxial tensile test. It was shown that the experimentally estimated failure probability and the numerically predicted failure probability using material routine MR#1 are very well correlated. A Monte-Carlo simulation based on material routine MR#2 was performed and the failure probability was estimated from the results. The comparison of the directly computed failure probability and the failure probability estimated from a Monte-Carlo simulation showed that the usage of both material routines lead to the same result. Hence, it was demonstrated that material routine MR#1 and material routine MR#2 are consistent. This consistency was validated by simulation of a component test. It was demonstrated that the usage of material routine MR#1 and material routine MR#2 lead to the same prediction of the failure probability of the component test. Moreover, it was shown that also the failure probability of a particular component part can be predicted by the usage of both material routines. The consistency of material routines MR#1 and MR#2 is very important for probabilistic failure modelling. First, it shows that the failure probability can be predicted by a single simulation using material routine MR#1. Second, the numerical scatter produced by material routine MR#2 can reproduce the experimentally observed scatter. However, it is required that the statistical distribution function is accurately known. This can be checked by comparing the experimentally estimated failure probability and the numerically predicted failure probability as presented.

The pseudo-random distribution produced by material routine MR#2 hinges directly on the FE mesh size. Consequently, mesh convergence studies cannot be performed on FE models using material routine MR#2. Hence, the uncoupled modelling approach was introduced. Here, the considered structure is discretised into a uniform MS mesh and the critical failure value is pseudo-randomly distributed within the MS mesh. This distribution is mapped onto the FE mesh and used in simulations. The uncoupled modelling approach was applied in two variants. Statistical independence of the elements of the MS mesh is assumed in the first variant (MR#3) and statistical dependence of the elements of the MS mesh is assumed in the second variant (MR#4). Both variants were additionally implemented in the explicit FE solver. Based on simulations of the uniaxial tensile test and the component test, it was shown that mesh convergence is reached by the application of material routine MR#3 and material routine MR#4. Here, the statistical dependence required in material routine MR#4 was modelled as Gaussian pseudo-random field.

Finally, simulations were performed on the U900-1 component subjected to three-point bending as well as to axial compression. The simulations were focused on the prediction

of the failure probability and, thus, only material routine MR#1 was considered. The U900-1 component was discretised as solid model, shell model and hybrid model. Each model was partitioned into the three characteristic parts identified from the material characterisation and the material model parameters were found from the corresponding test results. The numerically predicted failure probability using the solid model showed a very good correlation to the experimentally estimated failure probability in both load cases. Due to the low stiffness of the shell model, the experimentally estimated failure probability was strongly underestimated using the shell model in both load cases. The numerically predicted failure probability using the hybrid model showed a good correlation to the experimentally estimated failure probability in both load cases. It was shown that the applied probabilistic failure model provides a reliable prediction of the failure probability of the U900-1 component subjected to three-point bending as well as to axial compression as long as the structural stiffness is correctly captured. Further, it was shown that the hybrid model provides a numerical cheap alternative to the solid model. Hence, it was concluded that material routine MR#1 including the identified parameters are successfully validated. However, the global systematic variation in the material ductility was captured by a part definition which was obtained from experimental results. This approach is useless in the design of HPDC components and, thus, an approach based on material card mapping was presented. Material cards representing different discrete casting qualities were distributed according to a casting simulation. As a result, the global systematic variation in the material ductility was captured by the distribution of different material cards and the local pseudo-random variation in the material ductility was captured by Weibull distribution parameters given in the material card. However, this approach was only numerically investigated without any validation.

Based on the present work, the following recommendations for the numerical design of HPDC components are given: The local pseudo-random variation in the material ductility can be considered using a probabilistic failure criterion. The application of material routine MR#1 enables to compute the failure probability of an HPDC component by a single simulation. This implies that numerical results are given in terms of failure probabilities. Consequently, an acceptable failure probability needs to be defined in the design process. Further, the material card mapping approach as presented is considered as the most reasonable one to capture the global systematic variation in the material ductility. However, further investigations are necessary to identify a validated mapping rule. Moreover, the stiffness of typical casting structures is best captured by a solid model, but a solid model can only be applied for detailed investigations. Here, a hybrid model provides an alternative which can be applied in full scale crash simulations without causing high computational cost.

The knowledge established in the present work can be applied on all materials which exhibit a pseudo-random variation in ductility. A wide study on probabilistic failure modelling was given. Especially, the uncoupled modelling approach showed very interesting results and is recommend for further investigations on the pseudo-random distribution of a critical value. Especially, the critical element length of the MS mesh needs to be analysed since a physical meaning was not identified in the present work. Also, the application of a Gaussian random field needs to be analysed more in detail. Here, the parameter identification and the application in large FE models are of special interest. Furthermore, the presented probabilistic failure model was especially investigated in tensile dominated load cases. An experimental-numerical investigation of other load cases such as shear, compression or plane strain would provide a deeper understanding and more validation.

Bibliography

[1] P. Abrahamsen, *A Review of Gaussian Random Fields and Correlation Functions*, 2nd Ed., Norwegian Computing Center, Oslo, 1997.

[2] Aleris Switzerland GmbH, *Aluminium-Gusslegierungen*, Zürich, 2011.

[3] Altair Engineering Inc: HyperMesh, `http://www.altairhyperworks.com/Product,7,HyperMesh.aspx`, 2014.

[4] Aluminium Rheinfelden GmbH, *Berichte aus dem Gusswerkstofftechnikum: Nicht alternde Druckgusslegierung für den Automobilbau (Castasil-37 - AlSi9Mn)*, Rheinfelden, 2004.

[5] Aluminium Rheinfelden GmbH, *Hüttenaluminium Druckgusslegierungen Handbuch 2007*, 2nd Ed., Rheinfelden, 2007.

[6] Aluminium Rheinfelden GmbH, *Gießerbrief 27: Highlights der EUROGUSS 2008 von Aluminium Rheinfelden*, Rheinfelden, 2008.

[7] ANSYS Inc: ANSYS, `http://www.ansys.com/Products/Simulation+Technology/Structural+Analysis`, 2014.

[8] Y. Bao and T. Wierzbicki, *On fracture locus in the equivalent strain and stress triaxiality space*, International Journal of Mechanical Sciences 46 (2004), 81 – 98.

[9] H.J. Bargel and G. Schulze, *Werkstoffkunde*, 10th Ed., Springer, Berlin, 2009.

[10] K.J. Bathe, *Finite Elemente Methoden*, Springer, Berlin, 2001.

[11] S. Behnia, A. Akhavan, A. Akhshani and A. Samsudin, *A novel dynamic model of pseudo random number generator*, Journal of Computational and Applied Mathematics 235 (2011), 3455 – 3463.

[12] T. Belytschko, R. Gracie and G. Ventura, *A Review of Extended/Generalized Finite Element Methods for Material Modelling*, Modelling and Simulation in Materials Science and Engineering 17 (2009), 1 – 31.

[13] T. Belytschko, W.K. Liu and B. Moran, *Nonlinear Finite Elements for Continua and Structures*, John Wiley & Sons, West Sussex, 2000.

[14] BETA CAE Systems SA: ANSA, `http://www.beta-cae.gr/ansa.htm`, 2014.

[15] BETA CAE Systems SA: META, `http://www.beta-cae.gr/meta.htm`, 2014.

[16] D. Braess, *Finite Elemente*, 3rd Ed., Springer, Berlin, 2003.

[17] J. Campbell, *Complete Casting Handbook - Metal Casting Processes, Techniques and Design*, Butterworth-Heinemann, Oxford, 2011.

[18] G.P. Cherepanov, *The propagation of cracks in a continuous medium*, Journal of Applied Mathematics and Mechanics 31 (1967), 503 – 512.

[19] Chevy Hi-Performance, `http://www.chevyhiperformance.com`, 2014.

[20] M.G. Cockcroft and D.J. Latham, *Ductility and the workability of metals*, Journal of the Institute of Metals 96 (1968), 33 – 39.

[21] R. Corstanje, S. Grunwald and R.M. Lark, *Inferences from fluctuations in the local variogram about the assumption of stationarity in the variance*, Geoderma 143 (2008), 123 – 132.

[22] R.B. D'Agostino and M.A. Stephens, *Goodness-of-Fit Techniques*, Marcel Dekker, New York, 1986.

[23] X. Dai, X. Yang, J. Campbell and J. Wood, *Effects of runner system design on the mechanical strength of Al-7Si-Mg alloy castings*, Materials Science and Engineering 354 (2003), 315 – 325.

[24] Dassault Systèmes SA: Abaqus, `http://www.3ds.com/products-services/simulia/products/abaqus/`, 2014.

[25] Department of Defense, *Composite Materials Handbook Volume I: Polymer Matrix Composites Guidelines for Characterization of Structural Materials*, United States Department of Defense, Pentagon, 2002.

[26] Deutsches Institut für Normung e.V., *Aluminium and Aluminium Alloys; Wrought Products; Temper Designations; German Version EN 515:1993*, Beuth, Berlin, 1993.

[27] S. Dey, *High-strength steel plates subjected to projectile impact*, PhD Thesis, Norwegian University of Science and Technology, Norway, 2004.

[28] D. Dispinar and J. Campbell, *Effect of casting conditions on aluminium metal quality*, Journal of Materials Processing Technology 182 (2007), 405 – 410.

[29] D. Dispinar and J. Campbell, *Porosity, hydrogen and bifilm content in Al alloy castings*, Materials Science and Engineering 528 (2011), 3860 – 3865.

[30] C. Dørum, *Behaviour and modelling of thin-walled cast components*, PhD Thesis, Norwegian University of Science and Technology, Norway, 2005.

[31] C. Dørum, O.S. Hopperstad, T. Berstad and D. Dispinar, *Numerical modelling of magnesium die-castings using stochastic fracture parameters*, Engineering Fracture Mechanics 76 (2009), 2232 – 2248.

[32] C. Dørum, H.I. Laukli and O.S. Hopperstad, *Through-process numerical simulations of the structural behaviour of Al-Si die-castings*, Computational Materials Science 46 (2009), 100 – 111.

[33] C. Dørum, H.I. Laukli, O.S. Hopperstad and M. Langseth, *Structural behaviour of Al-Si die-castings: Experiments and numerical simulations*, European Journal of Mechanics 28 (2009), 1 – 13.

[34] G. Eisa Abadi, P. Davami, S.K. Kim and N. Varahram, *Effects of hydrogen and oxides on tensile properties of Al-Si-Mg cast alloys*, Materials Science and Engineering 552 (2012), 36 – 47.

[35] G. Eisa Abadi, P. Davami, S.K. Kim, N. Varahram, Y.O. Yoon and G.Y. Yeom, *Effect of oxide films, inclusions and fe on reproducibility of tensile properties in cast Al-Si-Mg alloys: Statistical and image analysis*, Materials Science and Engineering 558 (2012), 134 – 143.

[36] G. Eisa Abadi, P. Davami, N. Varahram and S.K. Kim, *On the effect of hydrogen and Fe on reproducibility of tensile properties in cast Al-Si-Mg alloys*, Materials Science and Engineering 565 (2013), 278 – 284.

[37] ESI Group: PAM-CRASH, `https://www.esi-group.com/software-services/virtual-performance/virtual-performance-solution`, 2014.

[38] ESI Group: ProCAST, `https://www.esi-group.com/software-services/virtual-manufacturing/casting-simulation-suite`, 2014.

[39] E. Fagerholt, C. Dørum, T. Børvik, H.I. Laukli and O.S. Hopperstad, *Experimental and numerical investigation of fracture in a cast aluminium alloy*, International Journal of Solids and Structures 47 (2010), 3352 – 3365.

[40] Flow Science Inc: FLOW-3D, `http://www.flow3d.com`, 2014.

[41] Ø. Fyllingen, *Robustness studies of structures subjected to large deformations*, PhD Thesis, Norwegian University of Science and Technology, Norway, 2008.

[42] GNS mbH: Animator4, `http://gns-mbh.com/animator.html`, 2014.

[43] GNU Compiler Collection, `https://gcc.gnu.org/onlinedocs/gfortran/RANDOM_005fNUMBER.html#RANDOM_005fNUMBER`, 2014.

[44] GNU Compiler Collection, `https://gcc.gnu.org/onlinedocs/gfortran/RANDOM_005fSEED.html`, 2014.

[45] L. Greve, *Development of a PAM-CRASH material model for die casting alloys*, 6th International Conference on Magnesium Alloys and their Application | Wolfsburg (2003).

[46] A.A. Griffith, *The phenomena of rupture and flow in solids*, Philosophical Transactions of the Royal Society of London 221 (1921), 163 – 198.

[47] D. Gross and T. Seelig, *Fracture Mechanics - With an Introduction to Micromechanics*, 2nd Ed., Springer, Berlin, 2011.

[48] G. Gruben, O.S. Hopperstad and T. Børvik, *Evaluation of uncoupled ductile fracture criteria for the dual-phase steel Docol 600DL*, International Journal of Mechanical Sciences 62 (2012), 133 – 146.

[49] A.L. Gurson, *Continuum theory of ductile rupture by void nucleation and growth: Part I - Yield criteria and flow rules for porous ductile media*, Journal of Engineering Materials and Technology 99 (1977), 2 – 15.

[50] J.O. Hallquist, *LS-DYNA - Theory Manual*, Livermore Software Technology Corporation, Livermore, 2006.

[51] J.O. Hallquist, *LS-DYNA - Keyword User's Manual, Version 971*, Livermore Software Technology Corporation, Livermore, 2007.

[52] M. Haßler, *Quasi-Static Fluid-Structure Interactions Based on a Geometric Description of Fluids*, Doctoral Thesis, University of Karlsruhe, Germany, 2009.

[53] S. Henn, *Bauteilorientierte Entwicklung von Rissinitiierungsmodellen für Aluminiumgusslegierungen unter monotoner Belastung*, Doctoral Thesis, University of Karlsruhe, Germany, 2005.

[54] A.V. Hershey, *The plasticity of an isotropic aggregate of anisotropic face-centered cubic crystals*, Journal of Applied Mechanics 21 (1954), 241 – 249.

[55] P. Hildebrandt, *Korrelation zwischen Simulationsergebnissen und mechanischen Bauteileigenschaften im Druckguss bei Verwendung einer naturharten Al-Gusslegierung*, Diploma Thesis, University of Kassel, Germany, 2009.

[56] G.A. Holzapfel, *Nonlinear Solid Mechanics - A Continuum Approach for Engineering*, John Wiley & Sons, West Sussex, 2000.

[57] H. Hooputra, H. Gese, H. Dell and H. Werner, *A comprehensive failure model for crashworthiness of aluminium extrusions*, International Journal of Crashworthiness 9 (2004), 449 – 463.

[58] E. Hornbogen and H.P. Warlimont, *Metalle - Struktur und Eigenschaften der Metalle und Legierungen*, 5th Ed., Springer, Berlin, 2006.

[59] W.F. Hosford, *A generalised isotropic yield criterion*, Journal of Apllied Mechanics 39 (1972), 607 – 609.

[60] T.J.R. Hughes, *The Finite Element Method - Linear Static and Dynamic Finite Element Analysis*, Dover Publications, New York, 2000.

[61] IBM Corporation: SPSS, `http://www-01.ibm.com/software/analytics/spss/`, 2014.

[62] Impetus Plastics Group, `http://www.impetus-plastics.de`, 2014.

[63] F. Irgens, *Continuum Mechanics*, Springer, Berlin, 2008.

[64] A.A. Jennings and M. Sumeet, *The microcomputer performance of uniform variate random number generators expressed in FORTRAN*, Enviromental Software 7 (1992), 9 – 27.

[65] G.R. Johnson and W.H. Cook, *Fracture characteristics of three metals subjected to various strains, strain rates, temperatures and pressures*, Engineering Fracture Mechanics 21 (1985), 31 – 48.

[66] C. Kleeberg, *Latest advancements in modelling and simulation for high pressure die castings*, ALUCAST | Chennai (2010).

[67] K. Knothe and H. Wessels, *Finite Elemente - Eine Einführung für Ingenieure*, 3rd Ed., Springer, Berlin, 1999.

[68] V.G. Kouznetsova, *Computational homogenization for the multi-scale analysis of multi-phase materials*, PhD Thesis, Eindhoven University of Technology, Netherlands, 2002.

[69] H. Kuhn and D. Medlin, *ASM Handbook Volume 8 - Mechanical Testing and Evaluation*, 10th Ed., ASM International, Materials Park, 2000.

[70] H.I. Laukli, *High pressure die casting of aluminium and magnesium alloys - grain structure and segregation characteristics*, PhD Thesis, Norwegian University of Science and Technology, Norway, 2004.

[71] S.G. Lee, A.M. Gokhale, G.R. Patel and M. Evans, *Effect of process parameters on porosity distributions in high-pressure die-cast AM50 mg-alloy*, Materials Science and Engineering 427 (2006), 3860 – 3865.

[72] S.G. Lee, G.R. Patel, A.M. Gokhale, A. Sreeranganathan and M.F. Horstemeyer, *Variability in the tensile ductility of high-pressure die-cast AM50 Mg-alloy*, Scripta Materialia 53 (2005), 851 – 856.

[73] E.L. Lehmann and J.P. Romano, *Testing Statistical Hypotheses*, 3rd Ed., Springer, Berlin, 2005.

[74] J. Lemaitre and J.L. Chaboche, *Mechanics of solid materials*, Cambridge University Press, Cambridge, 1994.

[75] J. Lemaitre and R. Desmorat, *Engineering Damage Mechanics - Ductile, Creep, Fatigue and Brittle Failures*, Springer, Berlin, 2005.

[76] C. Leppin, H. Hooputra, H. Werner, S. Werner, S. Weyer and R.V. Büchi, *Crashworthiness simulation of aluminium pressure die castings including fracture prediction*, VIII International Conference on Computational Plasticity | Barcelona (2005).

[77] Livermore Software Technology Corporation: LS-DYNA, `http://www.lstc.com/products/ls-dyna`, 2014.

[78] Livermore Software Technology Corporation: LS-PrePost, `http://www.lstc.com/products/ls-prepost`, 2014.

[79] J. Lubliner, *Plasticity Theory*, Dover Publications, New York, 2008.

[80] H. Mae, X. Teng, Y. Bai and T. Wierzbicki, *Calibration of ductile fracture properties of a cast aluminum alloy*, Materials Science and Engineering 459 (2007), 156 – 166.

[81] MAGMA Gießereitechnologie GmbH: MAGMAsoft, `http://www.magmasoft.com/en/solutions/diecasting.html`, 2014.

[82] S. Matange and D. Heath, *Statistical Graphics Procedures by Example - Effective Graphs Using SAS*, SAS Institute, Cary, 2011.

[83] MathWorks Inc: MATLAB, `http://www.mathworks.com`, 2014.

[84] MathWorks Inc: MATLAB Statistics Toolbox, `http://www.mathworks.com/products/statistics/`, 2014.

[85] Microsoft Corporation: Excel, `http://products.office.com/EN/excel`, 2014.

[86] N. Moës, J. Dolbow and T. Belytschko, *A finite element method for crack growth without remeshing*, International Journal for Numerical Methods in Engineering 75 (1999), 131 – 150.

[87] D. Mohr and R. Treitler, *Onset of fracture in high pressure die casting aluminum alloys*, Engineering Fracture Mechanics 75 (2008), 97 – 116.

[88] D.C. Montgomery, *Design and analysis of experiments*, 7th Ed., John Wiley & Sons, West Sussex, 2010.

[89] Norsk Hydro ASA, *New Alloys for High Pressure Die Casting - AlMgSiMn*, Oslo, 2010.

[90] Norsk Hydro ASA, *New Alloys for High Pressure Die Casting - AlSi4Mg0.2Mn*, Oslo, 2010.

[91] OriginLab Corporation: Origin Lab, `http://www.originlab.com`, 2014.

[92] F. Ostermann, *Anwendungstechnologie Aluminium*, 2nd Ed., Springer, Berlin, 2007.

[93] H. Parisch, *Festkörper-Kontinuumsmechanik - Von den Grundgleichungen zur Lösung mit Finiten Elementen*, Springer, Berlin, 2003.

[94] Penn State Web Applications Engines - PHP Web Service, `http://php.scripts.psu.edu/djh300/cmpsc202-f12/project-midterm/rand-demo.f`, 2014.

[95] G. Pijaudier-Cabot and Z.P. Băzant, *Nonlocal damage theory*, Journal of Engineering Mechanics 113 (1987), 1512 – 1533.

[96] RANDOM.ORG, `http://www.random.org`, 2014.

[97] J.R. Rice, *A path independent integral and the approximate analysis of strain concentration by notches and cracks*, Journal of Applied Mechanics 35 (1968), 379 – 386.

[98] J.L. Romeu, *Anderson-Darling: A Goodness of Fit Test for Small Samples Assumptions*, Selected Topics in Assurance Related Technologies 10 (2003).

[99] J.L. Romeu, *Kolomogorov-Smirnov: A Goodness of Fit Test for Small Samples*, Selected Topics in Assurance Related Technologies 10 (2003).

[100] J.L. Romeu, *The Chi-Square: A Large-Sample Goodness of Fit Test*, Selected Topics in Assurance Related Technologies 10 (2003).

[101] S.M. Ross, *Introduction to Probability Models*, 9th Ed., Elsevier, Amsterdam, 2007.

[102] Schlaich Bergermann und Partner GmbH, `http://www.sbp.de`, 2014.

[103] K. Siebertz, D. van Bebber and T. Hochkirchen, *Statistische Versuchsplanung - Design of Experiments (DoE)*, Springer, Berlin, 2010.

[104] M.A. Sutton, J.J. Orteu and H. Schreier, *Image correlation for shape, motion and deformation measurements - basic concepts,theory and applications*, 1st Ed., Springer, Berlin, 2009.

[105] X. Teng, H. Mae and Y. Bai, *Probability characterization of tensile strength of an aluminum casting*, Materials Science and Engineering 527 (2010), 4169 – 4176.

[106] X. Teng, H. Mae, Y. Bai and T. Wierzbicki, *Pore size and fracture ductility of aluminum low pressure die casting*, Engineering Fracture Mechanics 76 (2009), 983 – 996.

[107] R. Treitler, *Vom Gießprozess zur Festigkeitsberechnung am Beispiel einer Aluminium-Magnesium-Druckgusslegierung*, Doctoral Thesis, University of Karlsruhe, Germany, 2005.

[108] M. Unosson, L. Olovsson and K. Simonsson, *Failure modelling in finite element analyses: Random material imperfections*, Mechanics of Materials 37 (2005), 1175 – 1179.

[109] M. Unosson, L. Olovsson and K. Simonsson, *Weakest link model with imperfection density function: Application to three point bend of a tungsten carbide*, International Journal of Refractory Metals and Hard Materials 25 (2007), 6 – 10.

[110] L. Verlet, *"Experiments" on classical Fluids I. Thermomechanical Properties of Lennard-Jones Molecules*, Physical Review 159 (1967), 98 – 103.

[111] R.E. Walpole, *Probability and Statistics for Engineers and Scientists*, 9th Ed., Pearson, Boston, 2011.

[112] W. Weibull, *A statistical distribution function of wide appilcability*, Journal of Applied Mechanics 18 (1951), 293 – 297.

[113] T. Wierzbicki, Y. Bao, Y.W. Lee and Y. Bai, *Calibration and evaluation of seven fracture models*, International Journal of Mechanical Sciences 47 (2005), 719 – 743.

[114] R. Wilcox, *Introduction to Robust Estimation and Hypothesis Testing*, 3rd Ed., Elsevier, Amsterdam, 2011.

[115] T. Williams and C. Kelley, `http://www.gnuplot.info`, 2014.

[116] Wolfram Research Inc: Mathematica, `http://www.wolfram.com/mathematica/`, 2014.

[117] P. Wriggers, *Nonlinear Finite Element Methods*, Springer, Berlin, 2008.

[118] Z.J. Yang, X.T. Su, J.F. Chen and G.H. Liu, *Monte carlo simulation of complex cohesive fracture in random heterogeneous quasi-brittle materials*, International Journal of Solids and Structures 46 (2009), 3222 – 3234.

[119] Y. Zhang, X. Wang, N. Pan and R. Postle, *Weibull analysis of the tensile behaviour of fibres with geometrical irregularities*, Journal of Materials Science 37 (2002), 1401 – 1406.

Appendix A

Structural Behaviour

A.1 Three-Point Bending Test - Technical Drawings

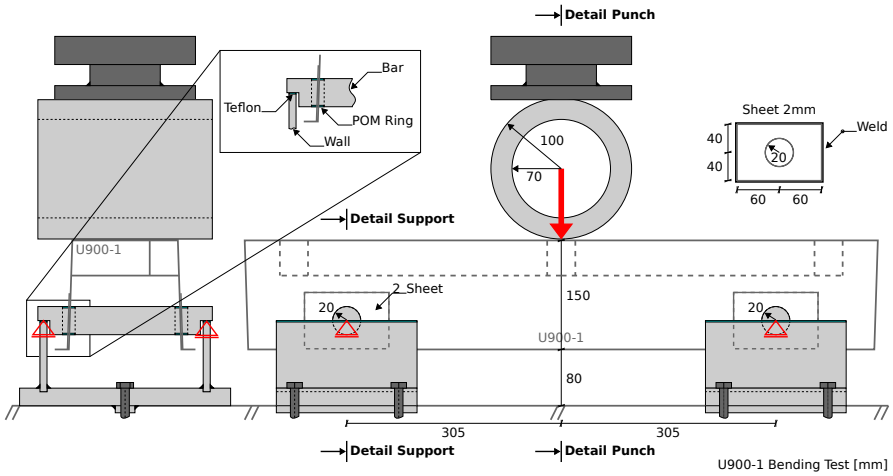

Figure A.1.1: Technical drawing of the three-point bending test set-up for the U900-1 component.

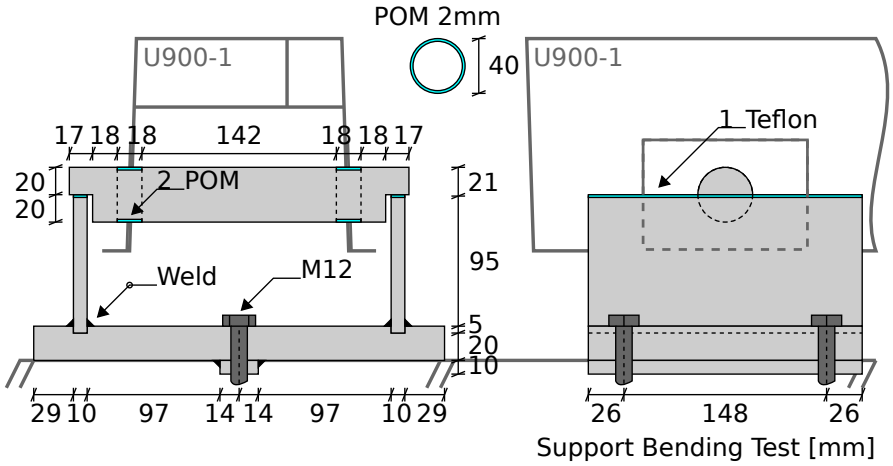

Figure A.1.2: Technical drawing of the three-point bending test set-up for the U900-1 component: Detail support.

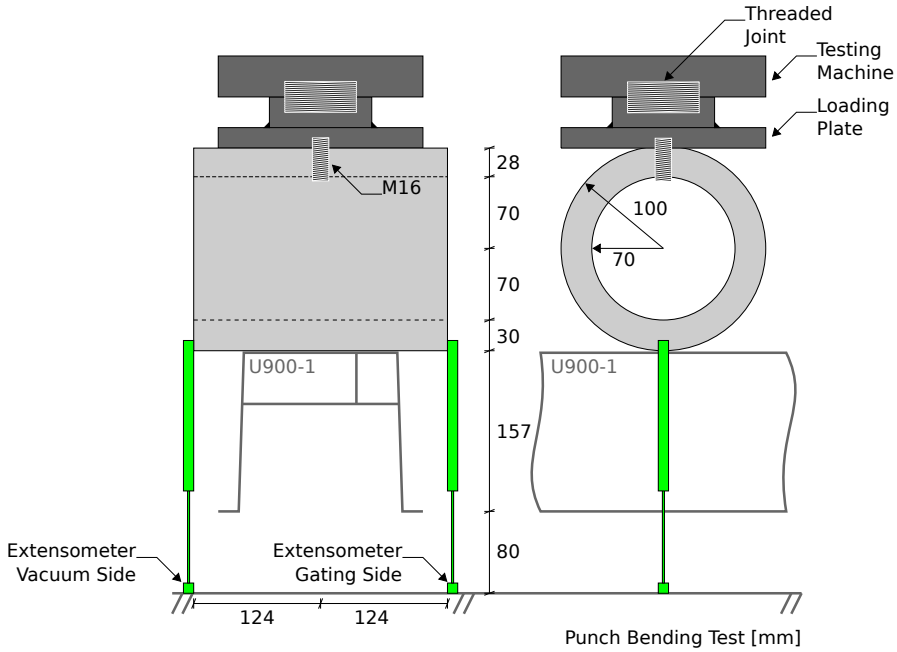

Figure A.1.3: Technical drawing of the three-point bending test set-up for the U900-1 component: Detail Punch.

A.2 Three-Point Bending Test - Experimental Results

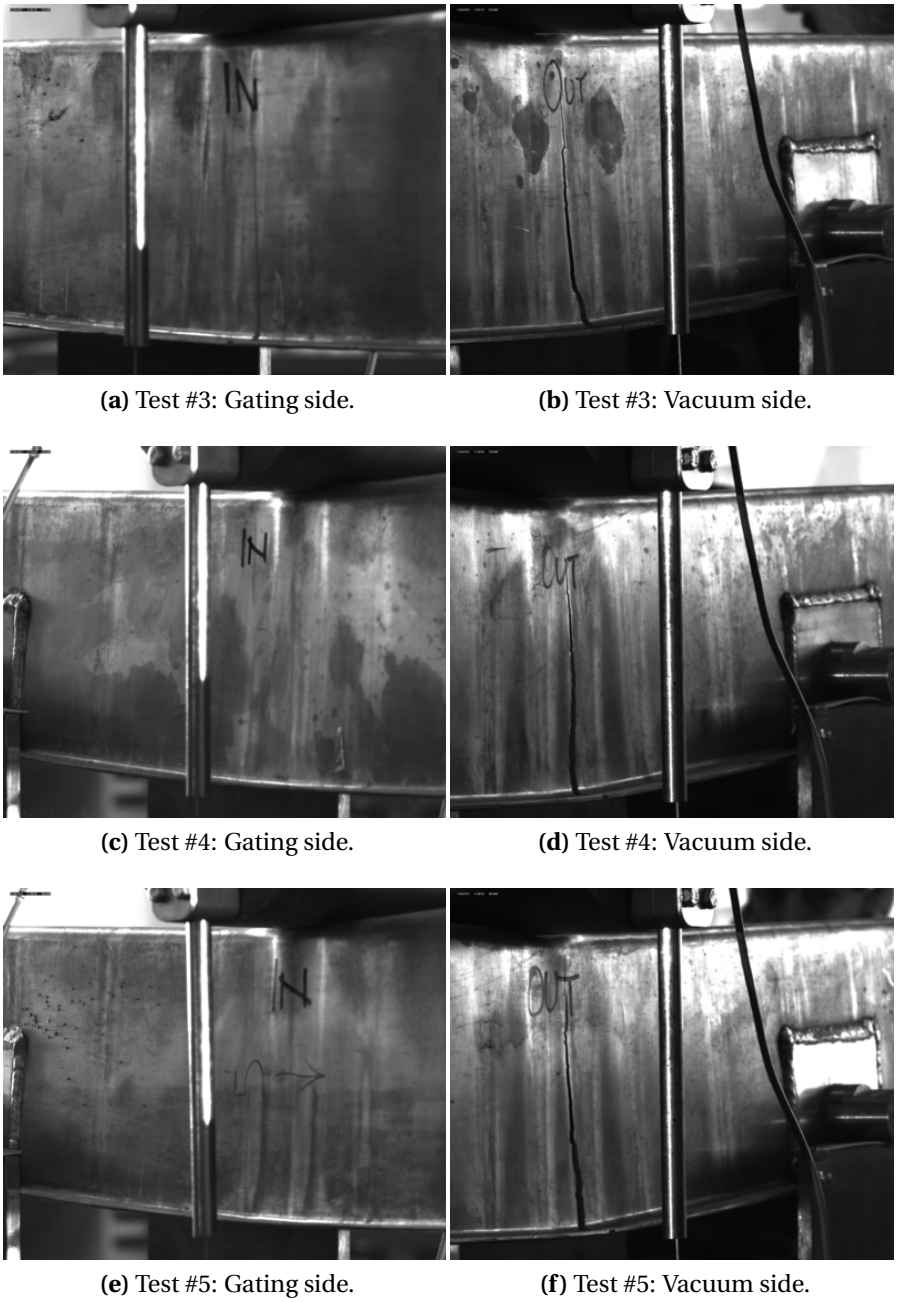

(a) Test #3: Gating side. **(b)** Test #3: Vacuum side.

(c) Test #4: Gating side. **(d)** Test #4: Vacuum side.

(e) Test #5: Gating side. **(f)** Test #5: Vacuum side.

Figure A.2.1: Camera images at first fracture initiation obtained from six parallel three-point bending tests on U900-1 components with focus on gating side and vacuum side: Tests #3 - #5.

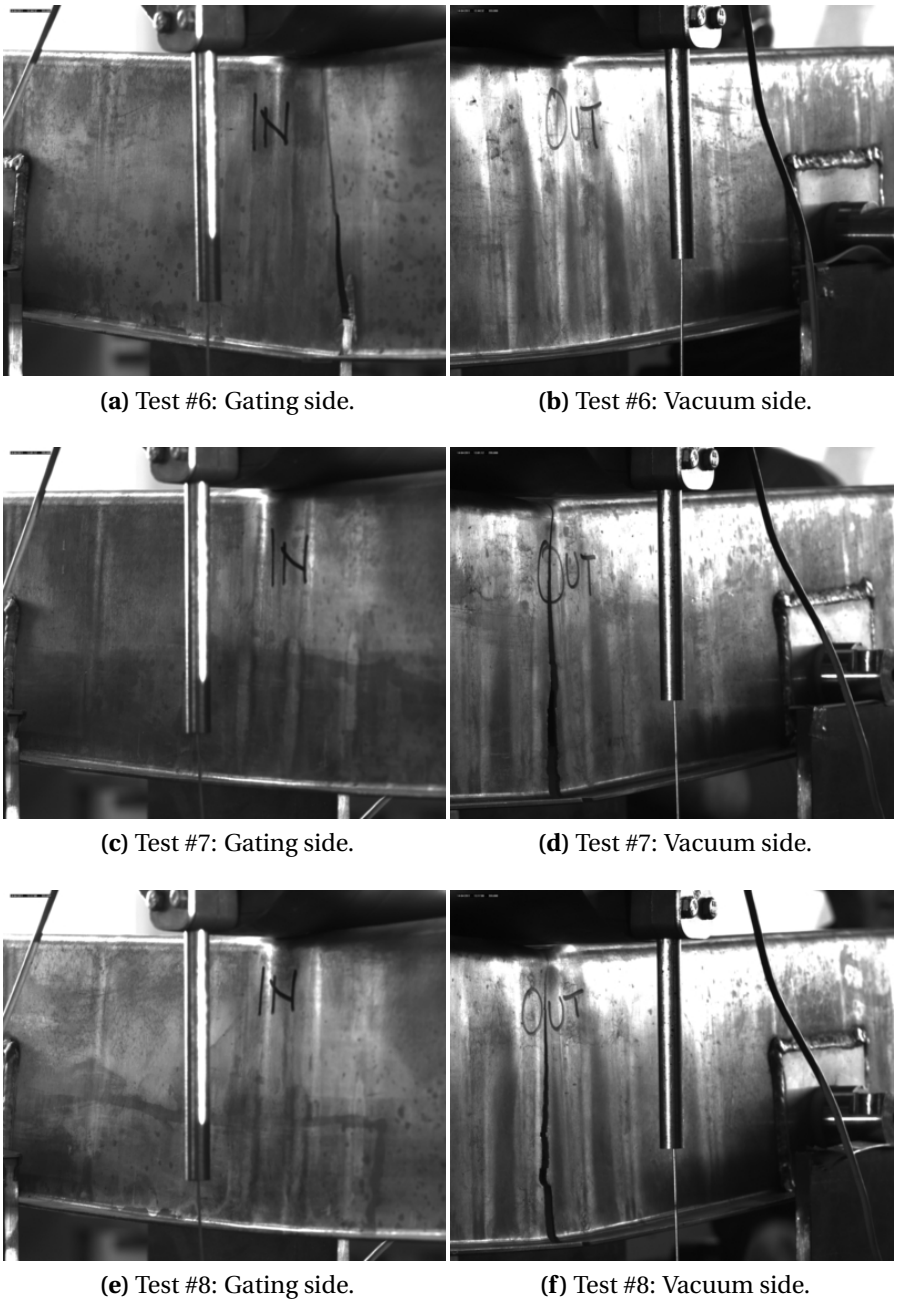

(a) Test #6: Gating side. **(b)** Test #6: Vacuum side.

(c) Test #7: Gating side. **(d)** Test #7: Vacuum side.

(e) Test #8: Gating side. **(f)** Test #8: Vacuum side.

Figure A.2.2: Camera images at first fracture initiation obtained from six parallel three-point bending tests on U900-1 components with focus on gating side and vacuum side: Tests #6 - #8.

(a) Test #3: Gating side.

(b) Test #3: Vacuum side.

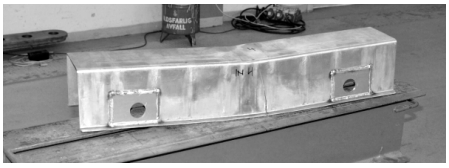

(c) Test #4: Gating side.

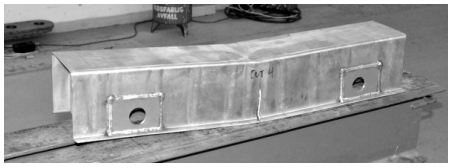

(d) Test #4: Vacuum side.

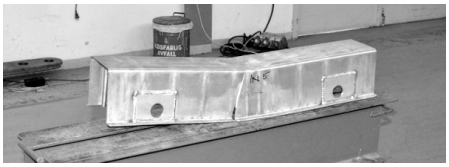

(e) Test #5: Gating side.

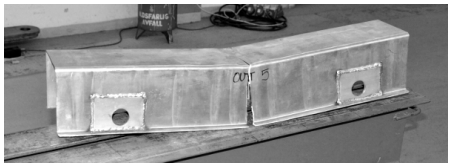

(f) Test #5: Vacuum side.

(g) Test #6: Gating side.

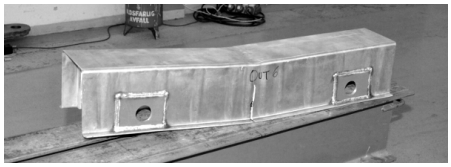

(h) Test #6: Vacuum side.

(i) Test #7: Gating side.

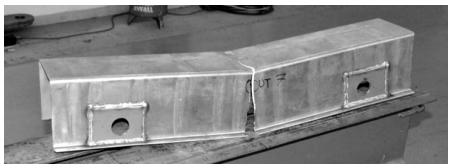

(j) Test #7: Vacuum side.

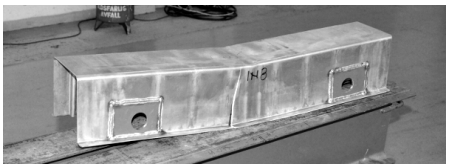

(k) Test #8: Gating side.

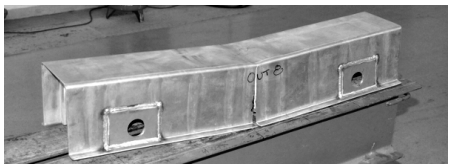

(l) Test #8: Vacuum side.

Figure A.2.3: Images of six deformed and fractured U900-1 components subjected to three-point bending.

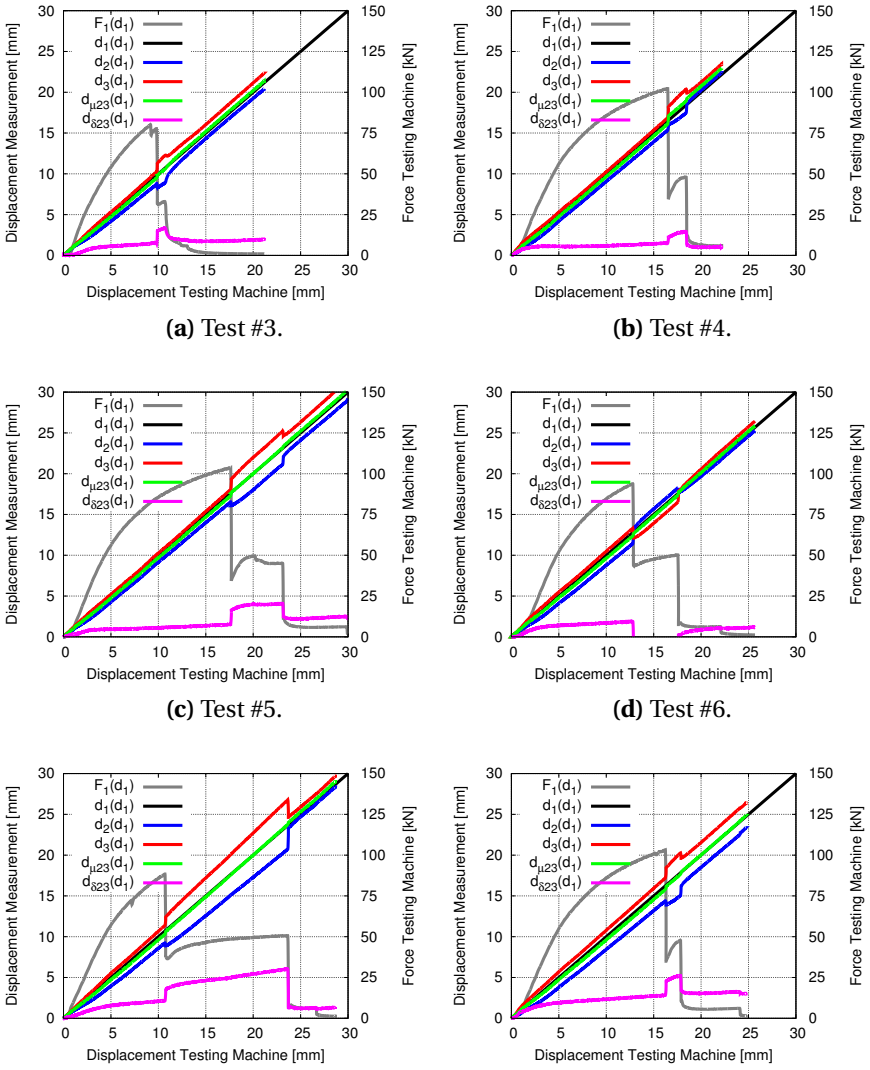

(a) Test #3. **(b)** Test #4.

(c) Test #5. **(d)** Test #6.

(e) Test #7. **(f)** Test #8.

Figure A.2.4: Experimental measurements obtained from six parallel three-point bending tests on U900-1 components: Force $F_1(d_1)$ measured by the testing machine (grey), displacement $d_1(d_1)$ measured by the testing machine (black), displacement $d_2(d_1)$ measured by the extensometer at gating side (blue), displacement $d_3(d_1)$ measured by the extensometer at vacuum side (red), mean $d_{\mu 23}(d_1)$ of both extensometer measurements (green) and gap $d_{\delta 23}(d_1)$ between both extensometer measurements (magenta).

A.3 Axial Compression Test - Technical Drawings

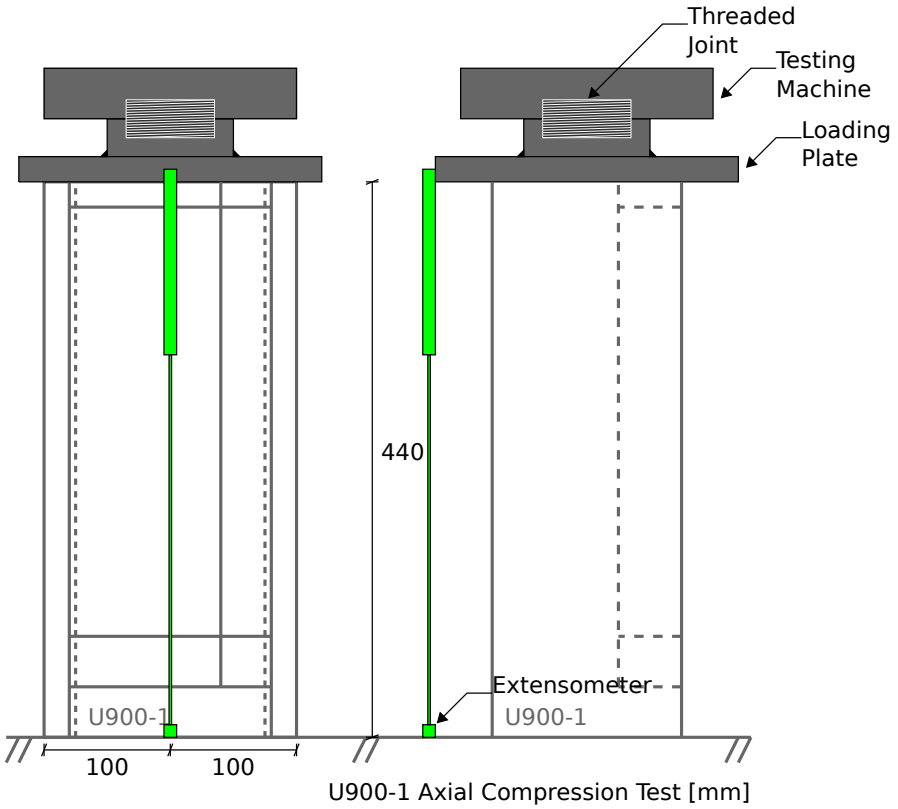

Figure A.3.1: Technical drawing of the axial compression test set-up for the U900-1 component.

A.4 Axial Compression Test - Experimental Results

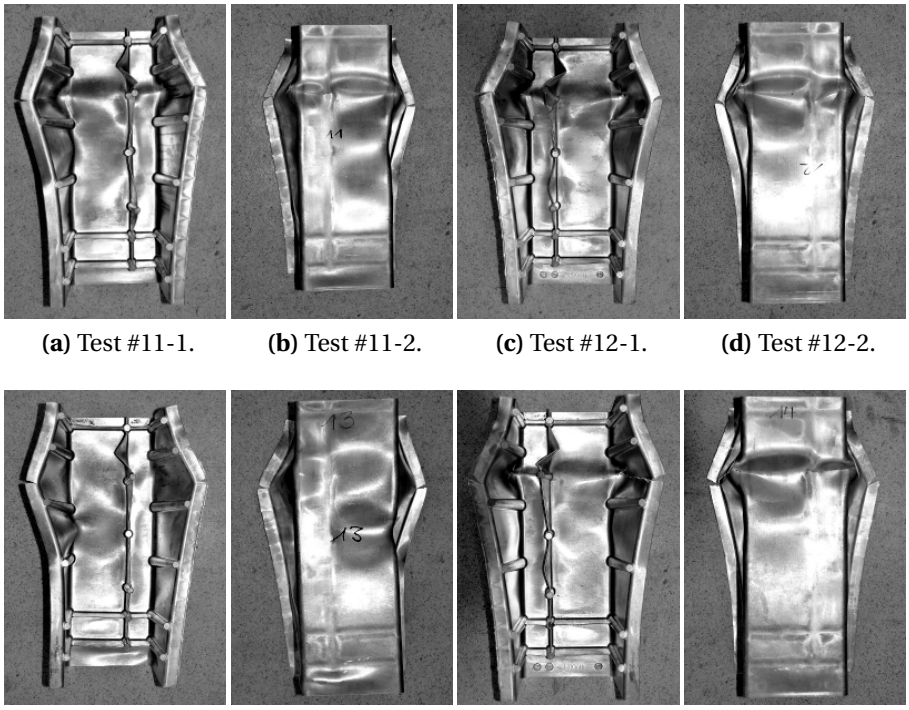

(a) Test #11-1. **(b)** Test #11-2. **(c)** Test #12-1. **(d)** Test #12-2.

(e) Test #13-1. **(f)** Test #13-2. **(g)** Test #14-1. **(h)** Test #14-2.

Figure A.4.1: Images of four deformed and fractured U900-1 components subjected to axial compression.

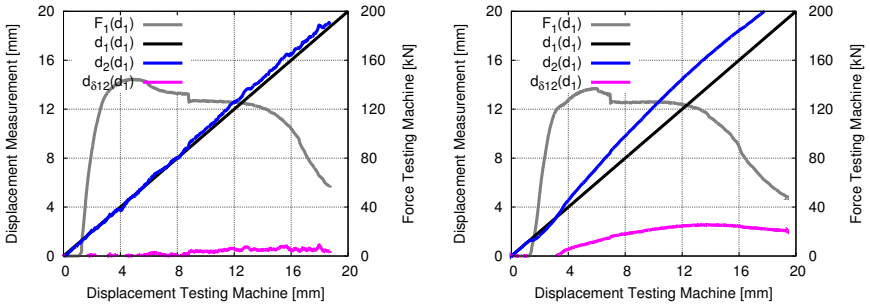

(a) Test #11. **(b)** Test #12.

(c) Test #13. **(d)** Test #14.

Figure A.4.2: Experimental measurements obtained from four parallel axial compression tests on U900-1 components: Force $F_1(d_1)$ measured by the testing machine (grey), displacement $d_1(d_1)$ measured by the testing machine (black), displacement $d_2(d_1)$ measured by the extensometer (blue) and gap $d_{\delta 12}(d_1)$ between both displacement measurements (magenta).

Appendix B

Material Characterisation

B.1 Material Characterisation I - Technical Drawings

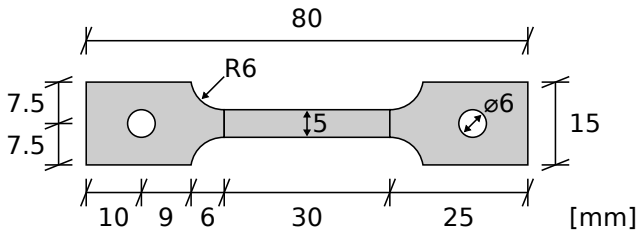

Figure B.1.1: Uniaxial tensile test specimen UT80 ($t = 2.5\,\text{mm}$).

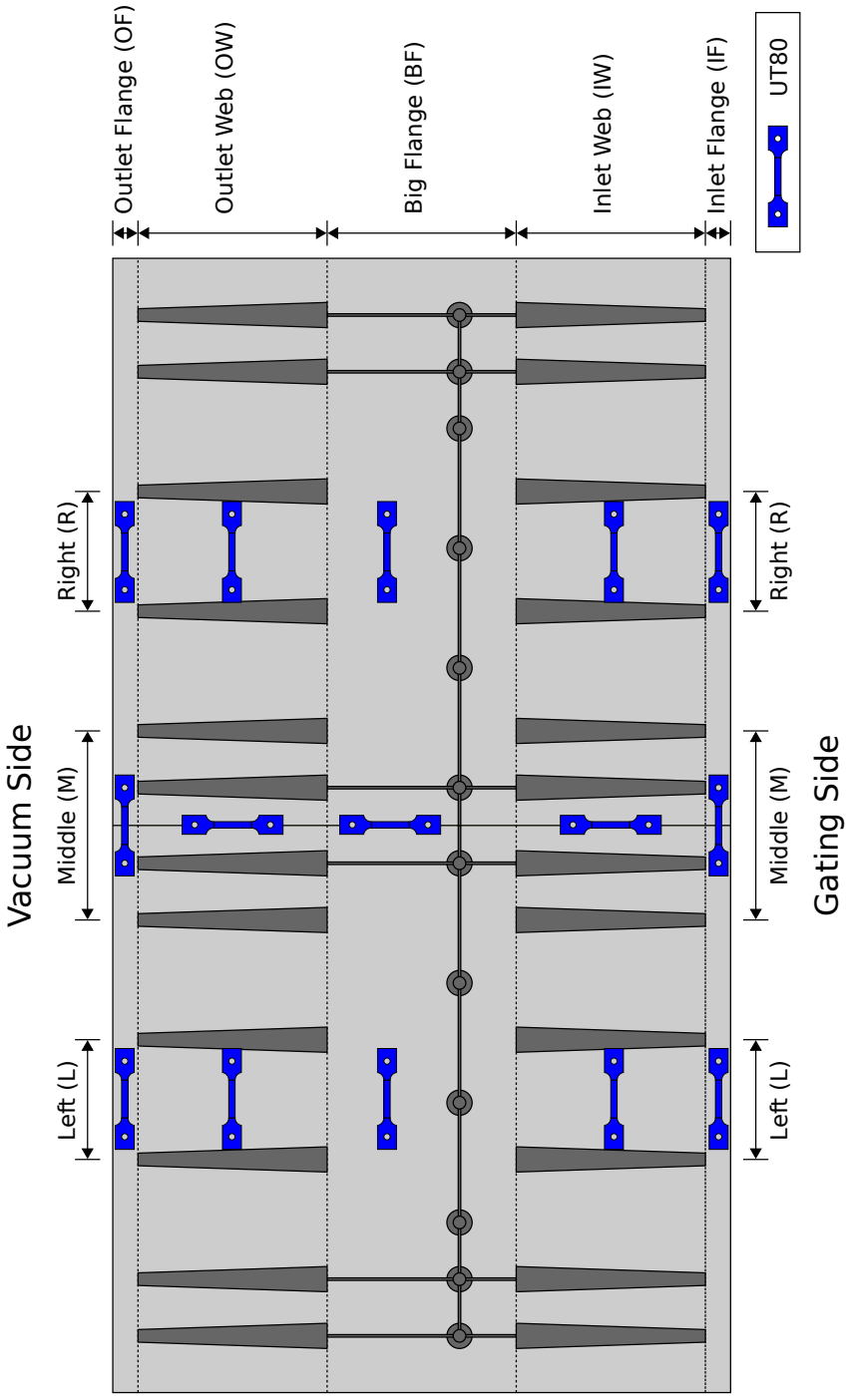

Figure B.1.2: Extraction plan of UT80 specimens machined from U900-1 components.

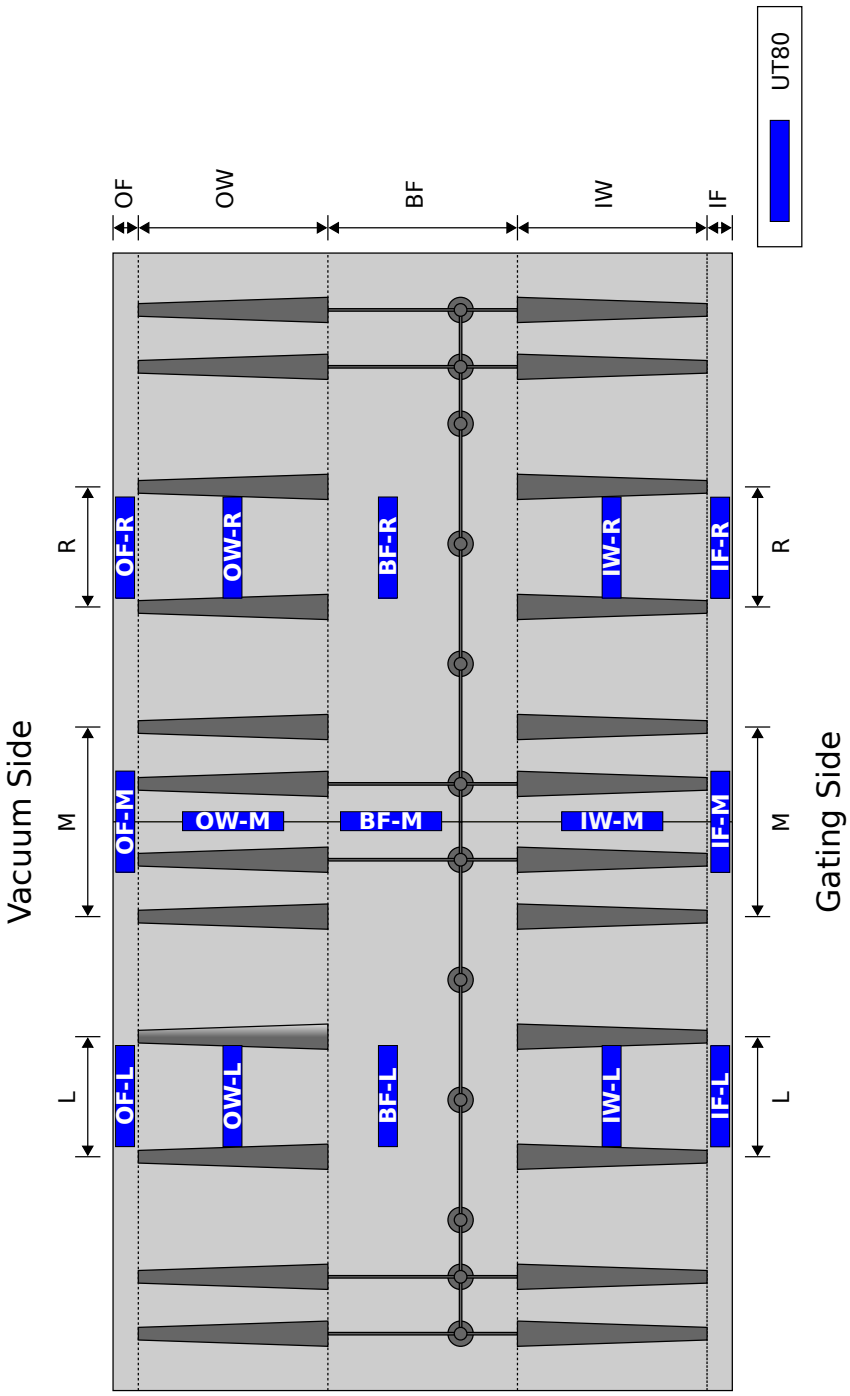

Figure B.1.3: Labelling system of UT80 specimens machined from U900-1 components.

B.2 Material Characterisation I - Experimental Results

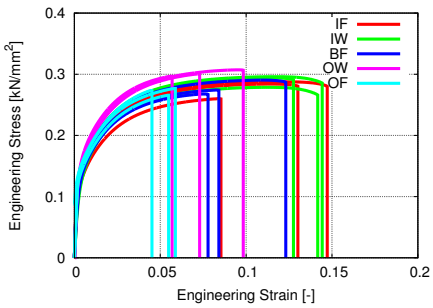

(a) Component #1.

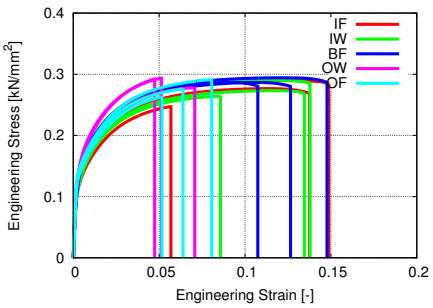

(b) Component #2.

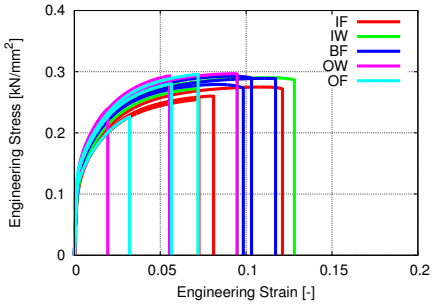

(c) Component #3.

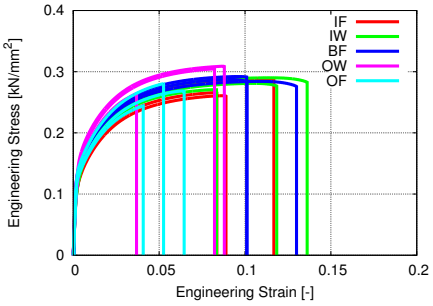

(d) Component #4.

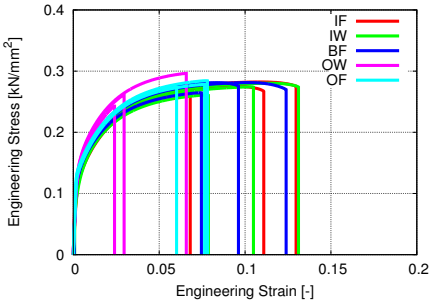

(e) Component #5.

Figure B.2.1: Engineering stress-strain curves obtained from UT80 specimens machined from five U900-1 components presented according to used components.

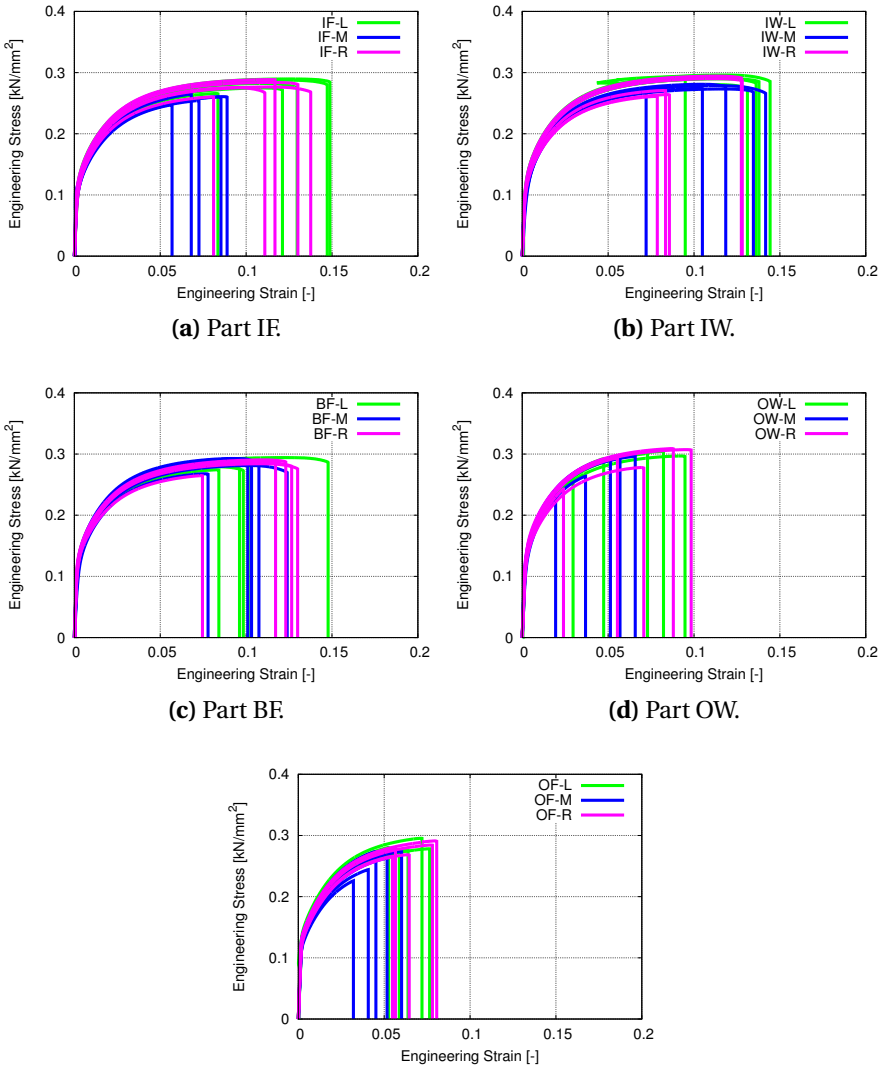

(a) Part IF.

(b) Part IW.

(c) Part BF.

(d) Part OW.

(e) Part OF.

Figure B.2.2: Engineering stress-strain curves obtained from UT80 specimens machined from five U900-1 components presented according to extraction positions.

Uniaxial Tensile Test Specimen UT80 / Part IF and Part IW of the U900-1 Component							
Specimen	$R_{p0.2}$	R_m	R_f	A_g	A_f	W_c	t
1-IF-L	0.138521	0.287654	0.279953	0.114002	0.144113	0.037926	2.55
2-IF-L	0.134325	0.289632	0.284554	0.116080	0.144987	0.038273	2.51
3-IF-L	0.129622	0.274983	0.271637	0.103837	0.117493	0.029000	2.64
4-IF-L	0.131904	0.265797	0.265364	0.077806	0.079341	0.018364	2.75
5-IF-L	0.134216	0.282313	0.275325	0.101315	0.124873	0.031847	2.51
1-IF-M	0.125678	0.260082	0.259655	0.079561	0.081233	0.018348	2.78
2-IF-M	0.122360	0.246985	0.246811	0.052465	0.053380	0.011035	2.70
3-IF-M	0.128519	0.254180	0.254007	0.068892	0.069828	0.015244	2.75
4-IF-M	0.126922	0.260718	0.260047	0.081787	0.085035	0.019359	2.82
5-IF-M	0.125171	0.264599	0.264414	0.064260	0.064809	0.014488	2.58
1-IF-R	0.135687	0.284009	0.280530	0.107990	0.126006	0.032385	2.62
2-IF-R	0.131731	0.276525	0.267786	0.106454	0.133070	0.033458	2.60
3-IF-R	0.128459	0.260090	0.259833	0.074649	0.076706	0.017332	2.78
4-IF-R	0.137837	0.288564	0.288380	0.106249	0.113433	0.029282	2.60
5-IF-R	0.135343	0.275566	0.266837	0.089567	0.108190	0.026735	2.55
1-IW-L	0.145034	0.296004	0.285569	0.108156	0.140355	0.038022	2.51
2-IW-L	0.146144	0.290176	0.285183	0.107225	0.132667	0.035164	2.49
3-IW-L	0.143799	0.293085	0.291353	0.083336	0.090838	0.023527	2.49
4-IW-L	0.141133	0.289997	0.282738	0.105969	0.131642	0.034748	2.53
5-IW-L	0.137776	0.280300	0.273938	0.108806	0.127226	0.032309	2.51
1-IW-M	0.135423	0.278688	0.266159	0.102805	0.135688	0.034542	2.51
2-IW-M	0.119237	0.273235	0.267902	0.109979	0.131337	0.032470	2.50
3-IW-M	0.129162	0.272623	0.272433	0.068044	0.068616	0.016005	2.54
4-IW-M	0.129510	0.280929	0.276565	0.097942	0.114578	0.028956	2.56
5-IW-M	0.116270	0.274337	0.273862	0.099827	0.101770	0.024559	2.52
1-IW-R	0.143079	0.294314	0.291148	0.108627	0.123850	0.033046	2.50
2-IW-R	0.129491	0.264137	0.263526	0.080208	0.081562	0.018786	2.73
3-IW-R	0.138972	0.290178	0.286642	0.108448	0.123912	0.032517	2.51
4-IW-R	0.135919	0.270676	0.270408	0.077137	0.079056	0.018720	2.67
5-IW-R	0.130903	0.261002	0.260555	0.072677	0.075145	0.017040	2.67
Units	[kN/mm²]			[–]		[kN/mm²]	[mm]

Table B.2.1: Measurements of the mechanical quantities obtained from UT80 specimens machined from part IF and part IW of five U900-1 components.

Uniaxial Tensile Test Specimen UT80 / Part BF and Part OW of the U900-1 Component							
Specimen	$R_{p0.2}$	R_m	R_f	A_g	A_f	W_c	t
1-BF-L	0.144923	0.274219	0.273870	0.079048	0.080944	0.019534	2.74
2-BF-L	0.149666	0.294265	0.286289	0.113149	0.143851	0.038881	2.55
3-BF-L	0.146944	0.279276	0.272803	0.079835	0.094896	0.023791	2.59
4-BF-L	0.146447	0.287386	0.283621	0.084902	0.096905	0.024820	2.62
5-BF-L	0.146527	0.281231	0.275739	0.077684	0.092238	0.023152	2.58
1-BF-M	0.139571	0.267726	0.267064	0.069272	0.072272	0.016908	2.88
2-BF-M	0.141219	0.286665	0.280369	0.086350	0.102846	0.026429	2.67
3-BF-M	0.145898	0.292784	0.289464	0.087251	0.099580	0.026110	2.67
4-BF-M	0.144298	0.292088	0.291302	0.089538	0.096936	0.025217	2.73
5-BF-M	0.138909	0.281307	0.269857	0.096983	0.120343	0.030654	2.65
1-BF-R	0.149066	0.290481	0.287051	0.106322	0.119586	0.031486	2.72
2-BF-R	0.142749	0.286652	0.280087	0.101770	0.122920	0.031986	2.70
3-BF-R	0.143003	0.289066	0.288436	0.104562	0.112961	0.029297	2.67
4-BF-R	0.145468	0.284229	0.275780	0.103238	0.127083	0.032920	2.76
5-BF-R	0.140344	0.264683	0.264430	0.069350	0.071018	0.016343	2.83
1-OW-L	0.155885	0.300512	0.300207	0.067498	0.068460	0.017733	2.36
2-OW-L	0.159018	0.292230	0.292230	0.042440	0.042599	0.010392	2.35
3-OW-L	0.152298	0.296806	0.296107	0.087214	0.090711	0.023872	2.40
4-OW-L	0.159391	0.304357	0.304054	0.076177	0.077504	0.020655	2.38
5-OW-L	0.157249	0.260921	0.260921	0.025597	0.025757	0.005565	2.35
1-OW-M	0.157804	0.296940	0.296631	0.052721	0.053090	0.013447	2.33
2-OW-M	0.157437	0.293529	0.293529	0.046931	0.047113	0.011699	2.31
3-OW-M	0.157315	0.239383	0.239383	0.016565	0.016565	0.003296	2.29
4-OW-M	0.147548	0.263725	0.263725	0.032261	0.032261	0.007051	2.36
5-OW-M	0.152770	0.296133	0.296133	0.061604	0.062493	0.015945	2.32
1-OW-R	0.154887	0.307215	0.306601	0.089279	0.093962	0.025629	2.35
2-OW-R	0.146956	0.277991	0.277144	0.064431	0.066519	0.016053	2.53
3-OW-R	0.159154	0.293195	0.293195	0.051549	0.051731	0.012874	2.36
4-OW-R	0.163366	0.308926	0.308524	0.081996	0.083917	0.022892	2.38
5-OW-R	0.147315	0.242685	0.242685	0.020354	0.020514	0.004068	2.34
Units	[kN/mm²]			[−]		[kN/mm²]	[mm]

Table B.2.2: Measurements of the mechanical quantities obtained from UT80 specimens machined from part BF and part OW of five U900-1 components.

Uniaxial Tensile Test Specimen UT80 / Part OF of the U900-1 Component							
Specimen	$R_{p0.2}$	R_m	R_f	A_g	A_f	W_c	t
1-OF-L	0.150762	0.276734	0.276650	0.054745	0.055407	0.013056	2.83
2-OF-L	0.143274	0.275749	0.275579	0.058888	0.059825	0.014053	2.81
3-OF-L	0.153575	0.295365	0.295276	0.067402	0.068680	0.017470	2.71
4-OF-L	0.154675	0.280245	0.280159	0.047637	0.048004	0.011310	2.77
5-OF-L	0.143772	0.278260	0.278176	0.071578	0.072514	0.017449	2.85
1-OF-M	0.150944	0.273496	0.273157	0.040626	0.041360	0.009400	2.83
2-OF-M	0.140093	0.262684	0.262603	0.047538	0.047722	0.010475	2.96
3-OF-M	0.132167	0.225867	0.225867	0.028758	0.028758	0.005353	2.91
4-OF-M	0.138119	0.244191	0.244191	0.036866	0.036866	0.007480	2.98
5-OF-M	0.148161	0.273572	0.273331	0.055979	0.056735	0.013230	2.97
1-OF-R	0.141594	0.265772	0.265772	0.050742	0.050924	0.011390	3.04
2-OF-R	0.149119	0.291172	0.290515	0.075246	0.076554	0.019292	2.91
3-OF-R	0.148993	0.279899	0.279651	0.052646	0.053356	0.012632	2.90
4-OF-R	0.140610	0.268508	0.267965	0.059820	0.061012	0.013980	3.07
5-OF-R	0.147434	0.284337	0.284254	0.072770	0.074435	0.018323	2.89
Units	[kN/mm²]			[−]		[kN/mm²]	[mm]

Table B.2.3: Measurements of the mechanical quantities obtained from UT80 specimens machined from part OF of five U900-1 components.

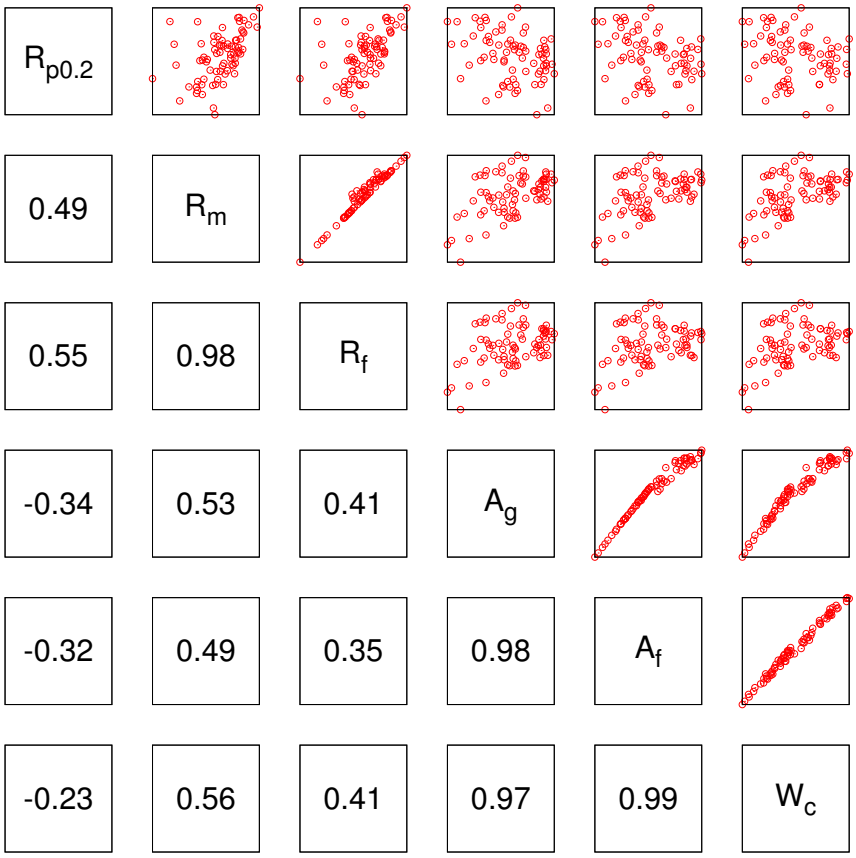

Figure B.2.3: Correlation matrix of the measured mechanical quantities obtained from UT80 specimens machined from five U900-1 components.

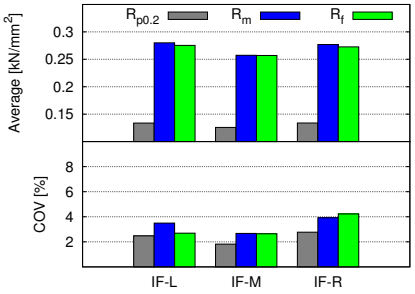

(a) Part IF: $R_{p0.2}$, R_m and R_f.

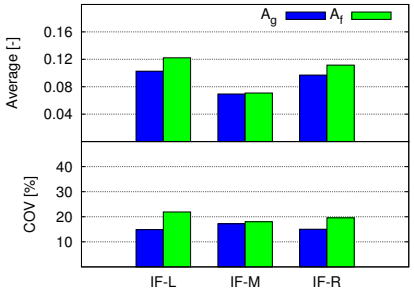

(b) Part IF: A_g and A_f.

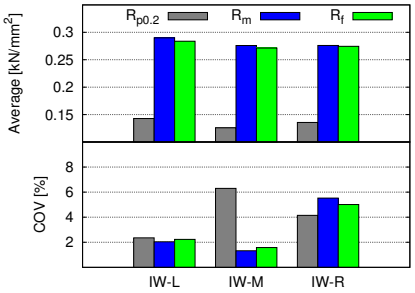

(c) Part IW: $R_{p0.2}$, R_m and R_f.

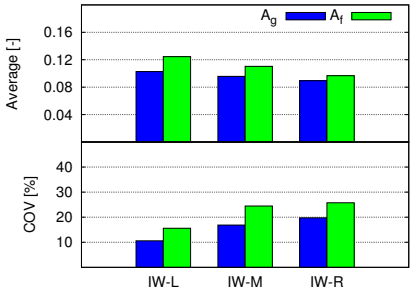

(d) Part IW: A_g and A_f.

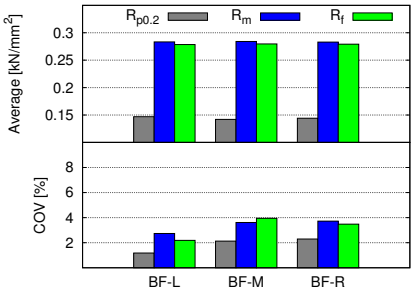

(e) Part BF: $R_{p0.2}$, R_m and R_f.

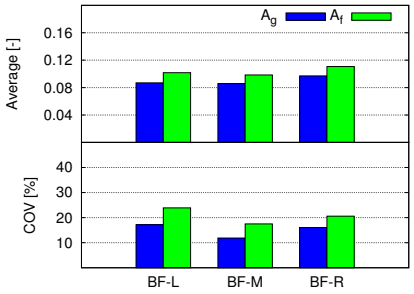

(f) Part BF: A_g and A_f.

Figure B.2.4: Averages and COVs of the measured mechanical quantities obtained from UT80 specimens machined from five U900-1 components (Part IF, Part IW and Part BF).

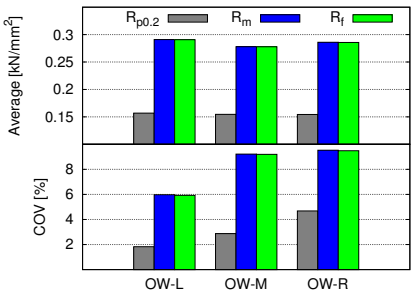

(a) Part OW: $R_{p0.2}$, R_m and R_f.

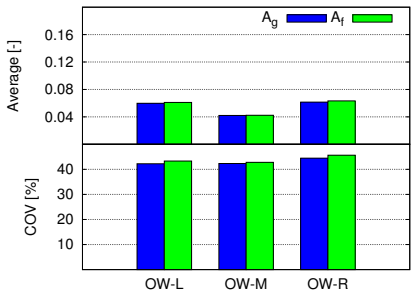

(b) Part OW: A_g and A_f.

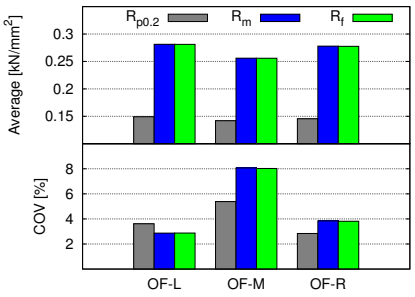

(c) Part OF: $R_{p0.2}$, R_m and R_f.

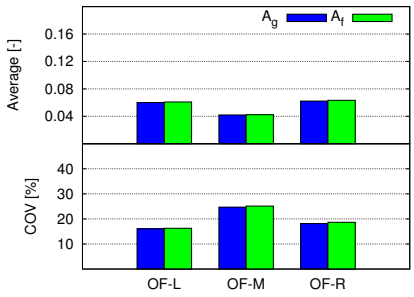

(d) Part OF: A_g and A_f.

Figure B.2.5: Average and COVs of the measured mechanical quantities obtained from UT80 specimens machined from five U900-1 components (Part OW and Part OF).

B.3 Material Characterisation II - Technical Drawings

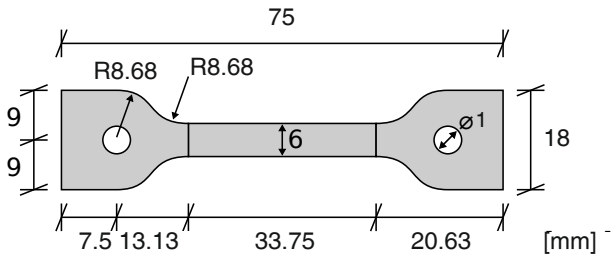

(a) Uniaxial tensile test specimen UT75 ($t = 2.5\,\text{mm}$).

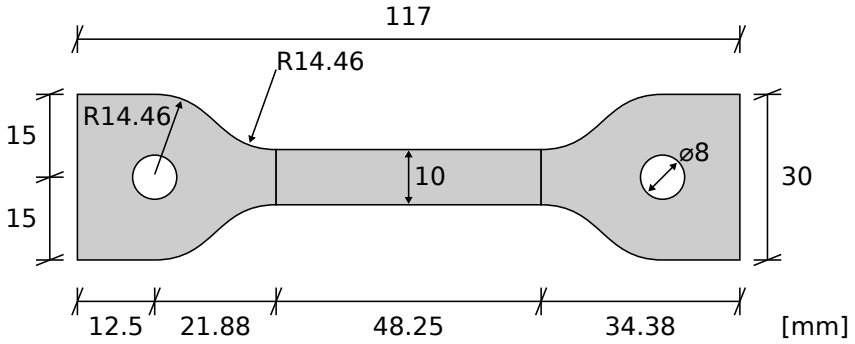

(b) Uniaxial tensile test specimen UT177 ($t = 2.5\,\text{mm}$).

Figure B.3.1: Uniaxial tensile test specimen UT75 and uniaxial tensile test specimen UT117.

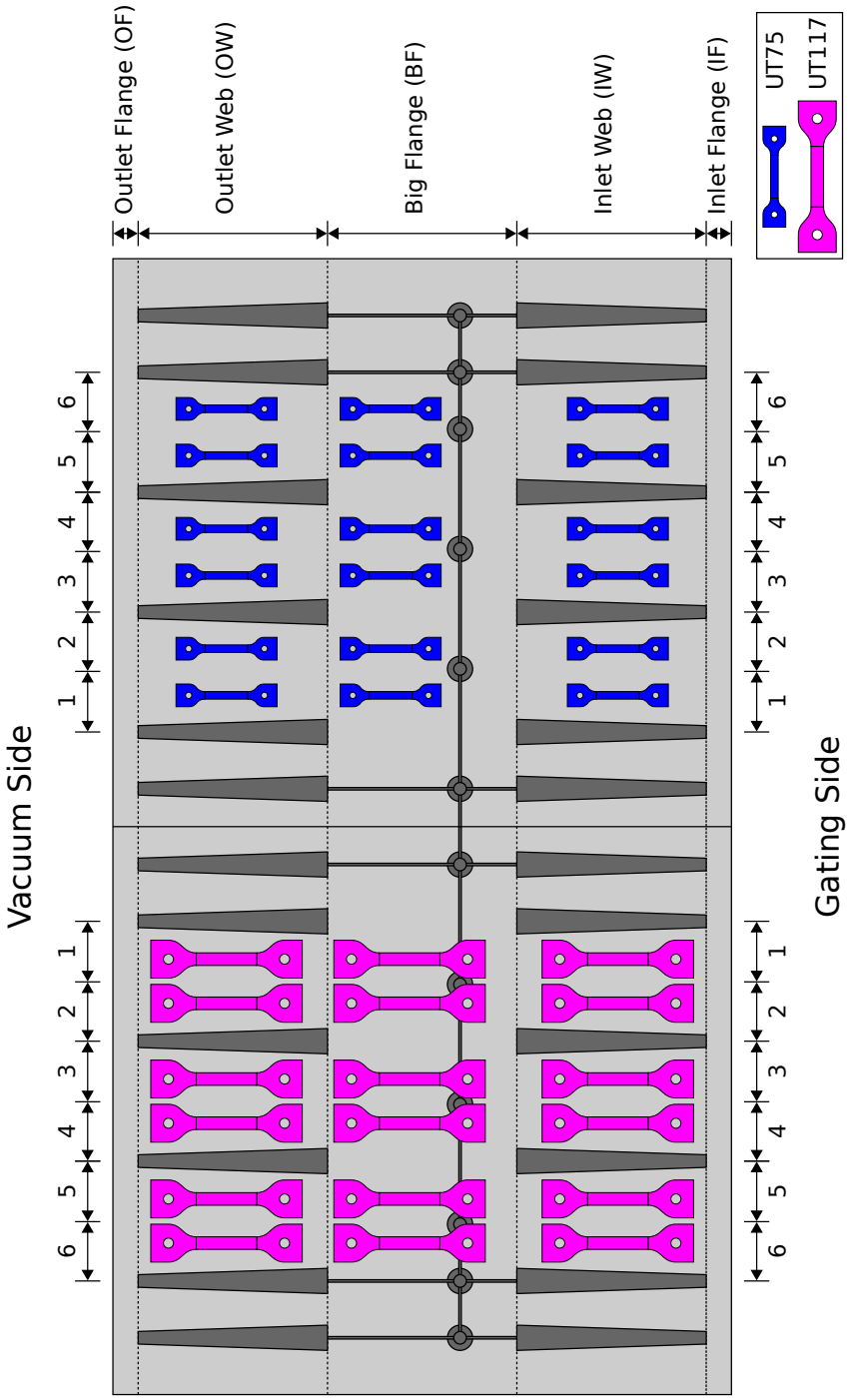

Figure B.3.2: Extraction plan of UT75 specimens and UT117 specimens machined from U900-1 components.

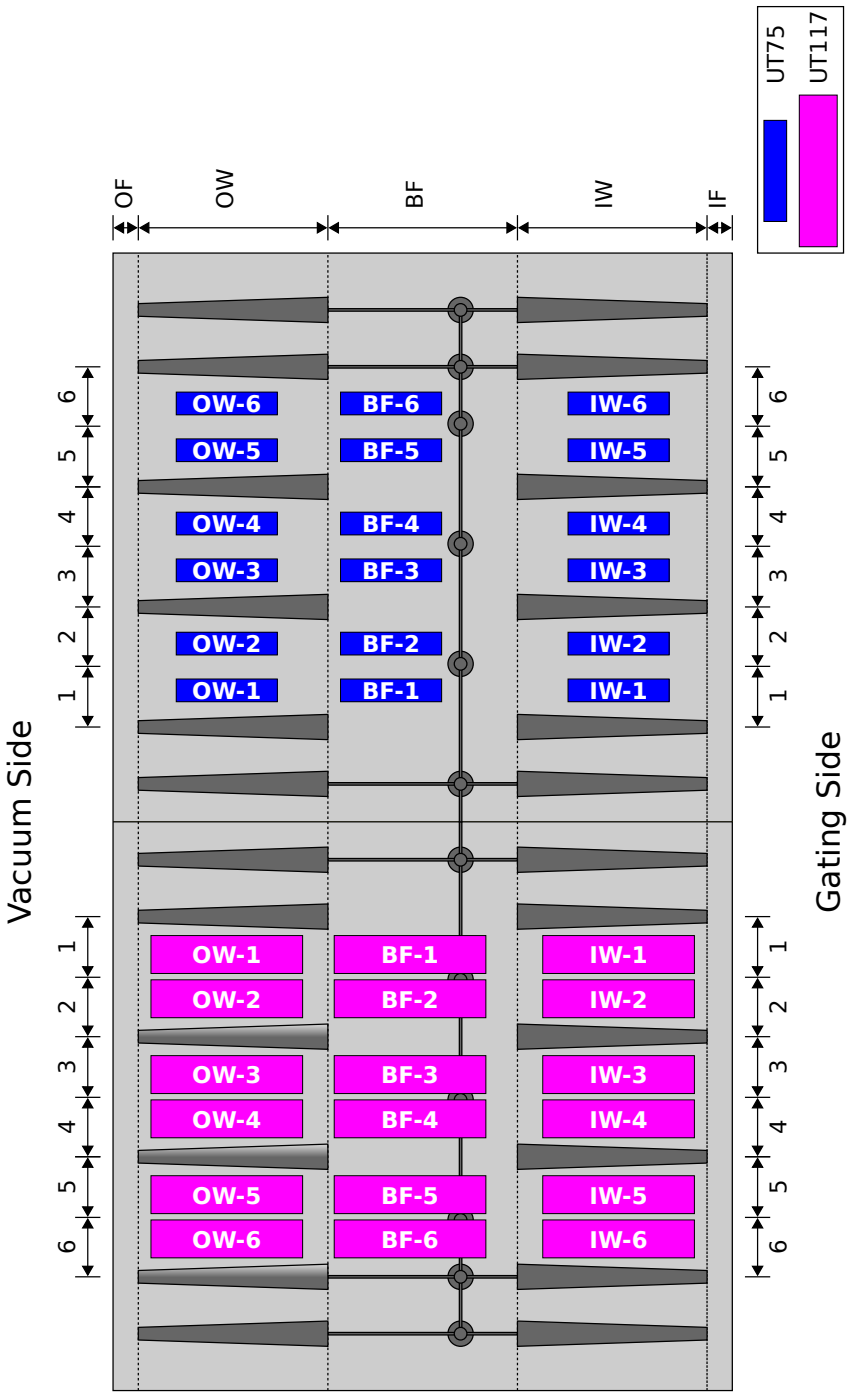

Figure B.3.3: Labelling system of UT75 specimens and UT117 specimens machined from U900-1 components.

B.4 Material Characterisation II - Experimental Results

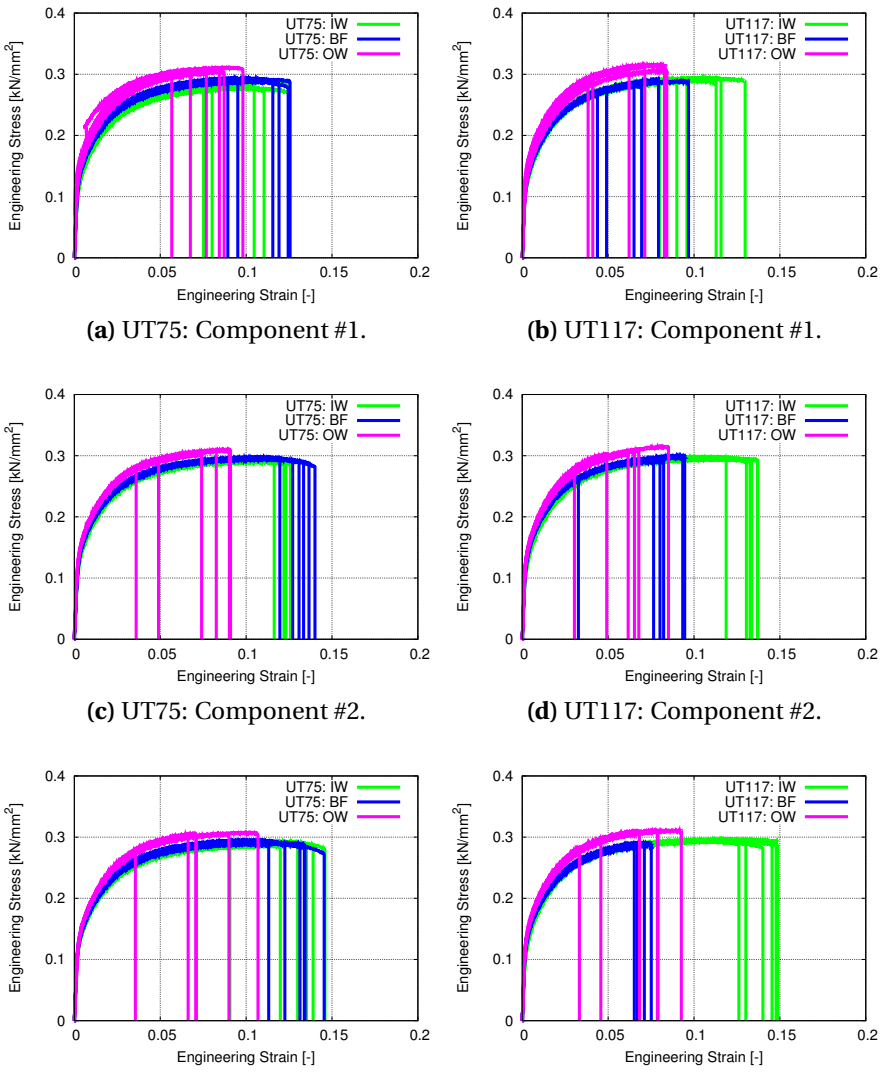

(a) UT75: Component #1.

(b) UT117: Component #1.

(c) UT75: Component #2.

(d) UT117: Component #2.

(e) UT75: Component #3.

(f) UT117: Component #3.

Figure B.4.1: Engineering stress-strain curves obtained from UT75 and UT117 specimens machined from six U900-1 components presented according to used components (component #1 - #3).

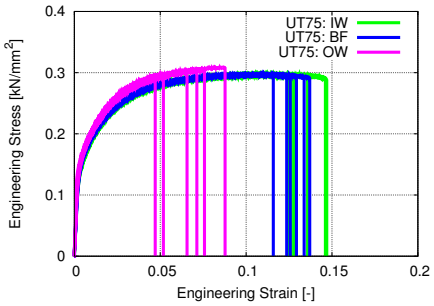

(a) UT75: Component #4.

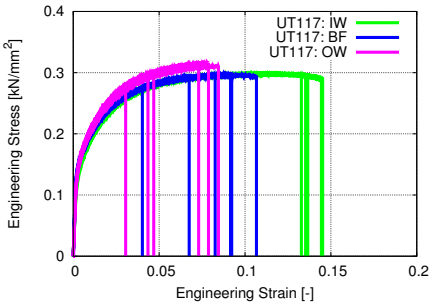

(b) UT117: Component #4.

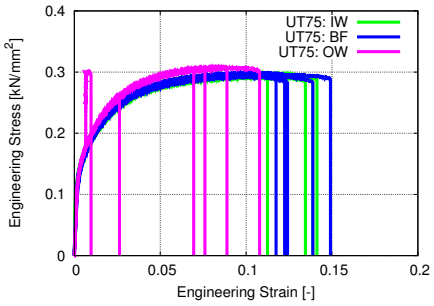

(c) UT75: Component #5.

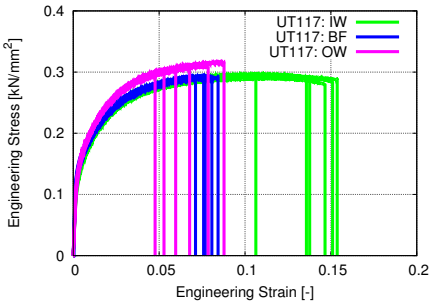

(d) UT117: Component #5.

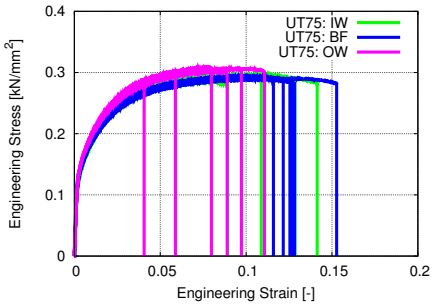

(e) UT75: Component #6.

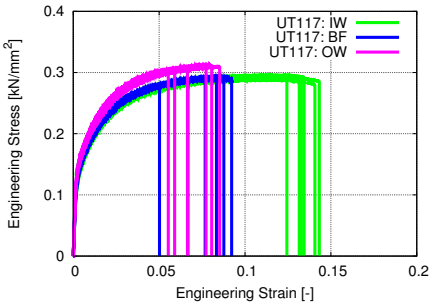

(f) UT117: Component #6.

Figure B.4.2: Engineering stress-strain curves obtained from UT75 and UT117 specimens machined from six U900-1 components presented according to used components (component #4 - #6).

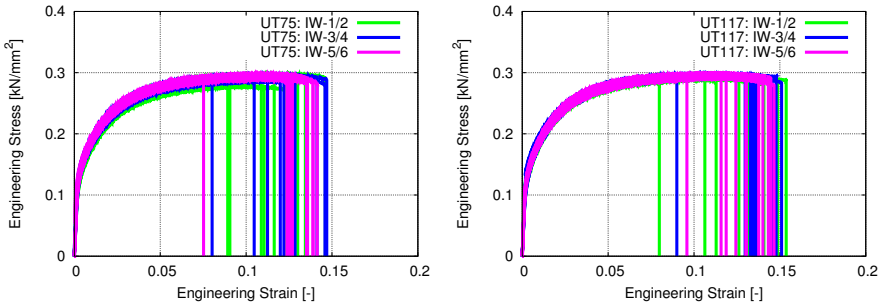

(a) UT75: Part IW.

(b) UT117: Part IW.

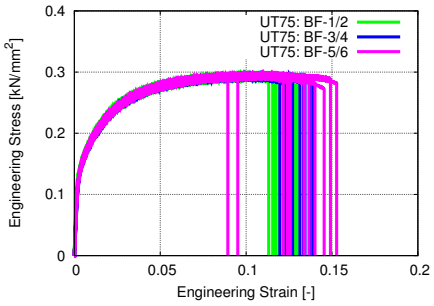

(c) UT75: Part BF.

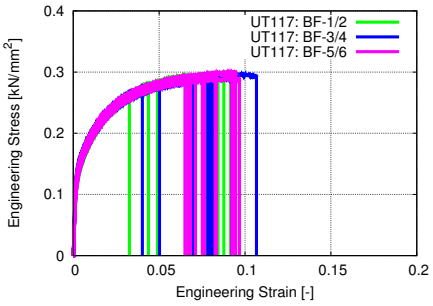

(d) UT117: Part BF.

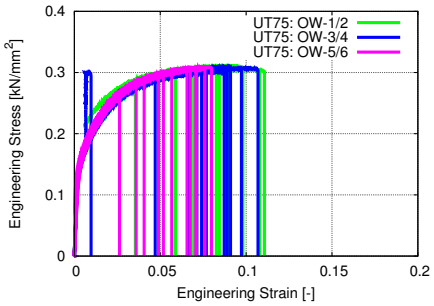

(e) UT75: Part OW.

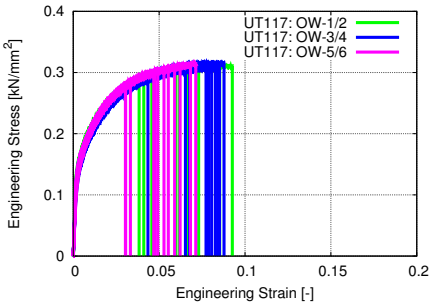

(f) UT117: Part OW.

Figure B.4.3: Engineering stress-strain curves obtained from UT75 and UT117 specimens machined from six U900-1 components presented according to extraction positions.

Uniaxial Tensile Test Specimen UT75 / Part IW of the U900-1 Component							
Specimen	$R_{p0.2}$	R_m	R_f	A_g	A_f	W_c	t
1-IW-1	0.131460	0.277323	0.267583	0.098472	0.120756	0.030276	2.58
2-IW-1	0.145240	0.292991	0.285394	0.099854	0.119003	0.031587	2.55
3-IW-1	0.141435	0.286845	0.285517	0.083061	0.086412	0.021770	2.57
4-IW-1	0.147230	0.294621	0.288532	0.102787	0.123136	0.033005	2.53
5-IW-1	0.144387	0.291159	0.284026	0.102923	0.119880	0.031628	2.53
6-IW-1	0.138871	0.286216	0.277208	0.073654	0.085223	0.021516	2.51
1-IW-2	0.133996	0.280742	0.269097	0.090588	0.105723	0.026566	2.56
2-IW-2	0.144943	0.292662	0.287286	0.094259	0.111952	0.029533	2.55
3-IW-2	0.140436	0.292582	0.285911	0.108530	0.125967	0.033377	2.56
4-IW-2	0.147254	0.297701	0.290649	0.108960	0.141870	0.038792	2.52
5-IW-2	0.145306	0.291954	0.285169	0.107093	0.130252	0.034685	2.50
6-IW-2	0.143541	0.294353	0.285247	0.085433	0.104669	0.027670	2.49
1-IW-3	0.138738	0.288088	0.283009	0.088148	0.100135	0.025771	2.55
2-IW-3	0.146715	0.294995	0.285401	0.101752	0.121369	0.032470	2.53
3-IW-3	0.142997	0.291897	0.279485	0.115134	0.142045	0.037958	2.53
4-IW-3	0.148047	0.295927	0.291888	0.104548	0.119936	0.032148	2.52
5-IW-3	0.149554	0.297124	0.287717	0.113762	0.138219	0.037751	2.49
6-IW-3	0.148083	0.296381	0.286606	0.100482	0.124554	0.033603	2.47
1-IW-4	0.137531	0.287128	0.285904	0.075723	0.076783	0.019118	2.54
2-IW-4	0.144855	0.289980	0.284929	0.102507	0.116668	0.030585	2.54
3-IW-4	0.136779	0.285504	0.283927	0.110330	0.115600	0.029642	2.55
4-IW-4	0.145640	0.295230	0.287753	0.117040	0.142692	0.038657	2.52
5-IW-4	0.158155	0.293421	0.289270	0.089055	0.108359	0.028855	2.50
6-IW-4	0.144640	0.291995	0.287681	0.109540	0.122361	0.032458	2.48
1-IW-5	0.139795	0.289212	0.284397	0.103405	0.120259	0.031517	2.49
2-IW-5	0.143146	0.294454	0.286837	0.103797	0.121257	0.032398	2.49
3-IW-5	0.140023	0.289621	0.281018	0.108863	0.130817	0.034426	2.51
4-IW-5	0.146580	0.294985	0.289767	0.104139	0.122101	0.032672	2.49
5-IW-5	0.148890	0.295249	0.284963	0.109291	0.134961	0.036506	2.48
6-IW-5	0.143012	0.294766	0.287327	0.106556	0.121758	0.032476	2.44
1-IW-6	0.141878	0.286730	0.285827	0.070461	0.070746	0.017532	2.46
2-IW-6	0.149640	0.294892	0.284004	0.096767	0.122406	0.032858	2.46
3-IW-6	0.148885	0.291740	0.284147	0.111995	0.134564	0.035991	2.47
4-IW-6	0.151584	0.298840	0.289477	0.101286	0.130927	0.035793	2.46
5-IW-6	0.167943	0.295704	0.288977	0.096941	0.117973	0.031973	2.45
6-IW-6	0.145623	0.292357	0.281930	0.111630	0.137212	0.036767	2.44
Units	[kN/mm²]			[−]		[kN/mm²]	[mm]

Table B.4.1: Measurements of the mechanical quantities obtained from UT75 specimens machined from part IW of six U900-1 components.

Uniaxial Tensile Test Specimen UT75 / Part BF of the U900-1 Component							
Specimen	$R_{p0.2}$	R_m	R_f	A_g	A_f	W_c	t
1-BF-1	0.142157	0.287643	0.282140	0.103053	0.115966	0.030084	2.78
2-BF-1	0.148859	0.294947	0.287525	0.105637	0.126334	0.033981	2.79
3-BF-1	0.150511	0.288749	0.284319	0.095440	0.109188	0.028536	2.89
4-BF-1	0.158469	0.296492	0.290751	0.108230	0.124469	0.033805	2.80
5-BF-1	0.148720	0.292823	0.288953	0.097863	0.114710	0.030482	2.78
6-BF-1	0.145630	0.289144	0.282096	0.102504	0.124823	0.032891	2.85
1-BF-2	0.148614	0.293171	0.288723	0.097977	0.111400	0.029522	2.75
2-BF-2	0.148706	0.297807	0.290418	0.103737	0.122502	0.033172	2.78
3-BF-2	0.147869	0.295360	0.288132	0.095430	0.118473	0.031742	2.86
4-BF-2	0.152104	0.297650	0.294073	0.101414	0.112053	0.030240	2.79
5-BF-2	0.151135	0.298805	0.295080	0.099632	0.118231	0.032109	2.76
6-BF-2	0.147739	0.294071	0.285056	0.097101	0.113101	0.030064	2.82
1-BF-3	0.145490	0.288350	0.276677	0.097901	0.121114	0.031820	2.76
2-BF-3	0.150573	0.295523	0.287891	0.105337	0.129463	0.034933	2.76
3-BF-3	0.145313	0.291128	0.286499	0.110285	0.130200	0.034524	2.83
4-BF-3	0.155186	0.296483	0.289768	0.109868	0.131937	0.035806	2.76
5-BF-3	0.147644	0.293221	0.282814	0.109972	0.133874	0.035901	2.75
6-BF-3	0.143954	0.291558	0.282898	0.101831	0.121594	0.032173	2.80
1-BF-4	0.139775	0.291548	0.286920	0.107129	0.122001	0.032175	2.72
2-BF-4	0.152777	0.296817	0.291511	0.097783	0.114868	0.030884	2.77
3-BF-4	0.144275	0.289475	0.283023	0.106047	0.126906	0.033418	2.87
4-BF-4	0.155553	0.297267	0.292130	0.102516	0.118154	0.031903	2.77
5-BF-4	0.152319	0.295611	0.292339	0.104946	0.118677	0.031844	2.76
6-BF-4	0.143981	0.291603	0.286894	0.106905	0.123078	0.032551	2.83
1-BF-5	0.142699	0.293795	0.291055	0.086628	0.090668	0.023437	2.66
2-BF-5	0.150551	0.294498	0.285380	0.107263	0.132594	0.035672	2.75
3-BF-5	0.143137	0.291567	0.280572	0.106663	0.129561	0.034366	2.83
4-BF-5	0.154206	0.298731	0.289491	0.105751	0.129798	0.035477	2.74
5-BF-5	0.151085	0.295467	0.288158	0.114872	0.144853	0.039411	2.73
6-BF-5	0.144241	0.290334	0.281566	0.119853	0.148902	0.039775	2.80
1-BF-6	0.147201	0.291447	0.290006	0.083262	0.084372	0.021620	2.66
2-BF-6	0.152674	0.294149	0.281456	0.102176	0.135406	0.036551	2.74
3-BF-6	0.145690	0.290423	0.272091	0.104991	0.141525	0.037686	2.83
4-BF-6	0.154520	0.295126	0.289917	0.101191	0.121094	0.032584	2.76
5-BF-6	0.152105	0.293622	0.282431	0.094525	0.119861	0.032089	2.73
6-BF-6	0.144319	0.292215	0.286035	0.100311	0.117794	0.031123	2.79
Units	[kN/mm²]			[−]		[kN/mm²]	[mm]

Table B.4.2: Measurements of the mechanical quantities obtained from UT75 specimens machined from part BF of six U900-1 components.

Uniaxial Tensile Test Specimen UT75 / Part OW of the U900-1 Component							
Specimen	$R_{p0.2}$	R_m	R_f	A_g	A_f	W_c	t
1-OW-1	0.153710	0.310949	0.307580	0.083765	0.093801	0.025949	2.45
2-OW-1	0.161495	0.308987	0.306520	0.083601	0.085715	0.023416	2.43
3-OW-1	0.152662	0.304565	0.303051	0.082804	0.085264	0.022808	2.42
4-OW-1	0.155590	0.303385	0.301458	0.070021	0.071255	0.018768	2.46
5-OW-1	0.158368	0.306887	0.300662	0.089215	0.102978	0.028410	2.41
6-OW-1	0.152813	0.306153	0.301053	0.092646	0.106851	0.029444	2.42
1-OW-2	0.156321	0.309780	0.307448	0.076998	0.079737	0.022302	2.43
2-OW-2	0.161623	0.308221	0.305858	0.076090	0.078174	0.021180	2.42
3-OW-2	0.152725	0.271949	0.270960	0.031134	0.031572	0.007073	2.45
4-OW-2	0.157666	0.308608	0.307568	0.081434	0.083307	0.022601	2.44
5-OW-2	0.155359	0.304526	0.303541	0.064776	0.065426	0.017101	2.40
6-OW-2	0.155852	0.295481	0.294258	0.053577	0.054810	0.013752	2.42
1-OW-3	0.152135	0.304188	0.303152	0.082123	0.083138	0.022203	2.43
2-OW-3	0.159573	0.310031	0.308550	0.085233	0.086892	0.023817	2.44
3-OW-3	0.152967	0.299750	0.299191	0.061245	0.061698	0.015796	2.45
4-OW-3	0.163517	0.293970	0.293523	0.042770	0.043046	0.010674	2.44
5-OW-3	0.158665	0.308829	0.307605	0.083847	0.084652	0.022994	2.42
6-OW-3	0.156417	0.306641	0.304460	0.090745	0.092811	0.025258	2.41
1-OW-4	0.153435	0.302479	0.301188	0.071330	0.072383	0.019015	2.43
2-OW-4	0.154392	0.301957	0.301350	0.069677	0.070138	0.018348	2.47
3-OW-4	0.155401	0.307277	0.303454	0.095307	0.102486	0.028196	2.47
4-OW-4	0.170403	0.303444	0.301772	0.065748	0.066503	0.017618	2.47
5-OW-4	0.157312	0.303332	0.301432	0.076994	0.079284	0.021151	2.45
6-OW-4	0.152929	0.301502	0.299397	0.082907	0.084909	0.022578	2.45
1-OW-5	0.169377	0.307906	0.307506	0.063373	0.064137	0.017176	2.41
2-OW-5	0.158768	0.294931	0.293981	0.044251	0.044919	0.011133	2.45
3-OW-5	0.153555	0.305600	0.304340	0.064104	0.066118	0.017343	2.43
4-OW-5	0.157600	0.303679	0.302921	0.062277	0.062482	0.016362	2.45
5-OW-5	0.158673	0.306877	0.305473	0.069894	0.071249	0.019002	2.44
6-OW-5	0.156194	0.309114	0.307501	0.073529	0.075209	0.020252	2.42
1-OW-6	0.158568	0.299002	0.297000	0.051927	0.053044	0.013497	2.40
2-OW-6	0.158671	0.280244	0.278186	0.030634	0.031584	0.007335	2.44
3-OW-6	0.159169	0.305873	0.304872	0.063067	0.064899	0.017147	2.44
4-OW-6	0.161619	0.298248	0.296238	0.045553	0.046832	0.011825	2.44
5-OW-6	0.157884	0.261224	0.259699	0.021942	0.022551	0.004838	2.43
6-OW-6	0.157530	0.286272	0.285900	0.036358	0.036451	0.008634	2.40
Units	[kN/mm²]			[−]		[kN/mm²]	[mm]

Table B.4.3: Measurements of the mechanical quantities obtained from UT75 specimens machined from part OW of six U900-1 components.

Uniaxial Tensile Test Specimen UT117 / Part IW of the U900-1 Component							
Specimen	$R_{p0.2}$	R_m	R_f	A_g	A_f	W_c	t
1-IW-1	0.130889	0.286114	0.282871	0.073959	0.075861	0.018744	2.51
2-IW-1	0.148641	0.295514	0.289912	0.105560	0.129391	0.034939	2.50
3-IW-1	0.137613	0.295385	0.286024	0.108954	0.144828	0.039161	2.51
4-IW-1	0.144189	0.297244	0.294666	0.113872	0.128154	0.034669	2.51
5-IW-1	0.135585	0.293455	0.291904	0.099669	0.101491	0.026463	2.49
6-IW-1	0.140351	0.288336	0.278759	0.111396	0.136947	0.036134	2.50
1-IW-2	0.143839	0.290514	0.284621	0.098440	0.109139	0.028577	2.51
2-IW-2	0.149919	0.296339	0.290017	0.105064	0.133111	0.036228	2.50
3-IW-2	0.135418	0.292740	0.287280	0.102503	0.121481	0.032154	2.53
4-IW-2	0.148451	0.296812	0.290385	0.108254	0.141202	0.038595	2.51
5-IW-2	0.149389	0.293066	0.286890	0.114259	0.149340	0.040509	2.50
6-IW-2	0.138772	0.289715	0.284205	0.104965	0.127742	0.033653	2.50
1-IW-3	0.135289	0.289804	0.288553	0.084851	0.086273	0.021809	2.48
2-IW-3	0.147282	0.296411	0.292397	0.108245	0.133125	0.036064	2.49
3-IW-3	0.139778	0.296666	0.292494	0.117070	0.143478	0.039001	2.51
4-IW-3	0.146283	0.298598	0.296347	0.110314	0.131285	0.035880	2.51
5-IW-3	0.147829	0.293432	0.283334	0.111813	0.147372	0.039897	2.51
6-IW-3	0.144350	0.295420	0.290494	0.111286	0.130457	0.035177	2.48
1-IW-4	0.135178	0.292486	0.287084	0.108695	0.125580	0.033340	2.47
2-IW-4	0.136402	0.293735	0.289268	0.107729	0.128527	0.034301	2.49
3-IW-4	0.139663	0.293750	0.286048	0.106310	0.140542	0.037898	2.50
4-IW-4	0.148548	0.297557	0.293170	0.108779	0.132398	0.036064	2.49
5-IW-4	0.146517	0.296575	0.291621	0.105824	0.131285	0.035710	2.47
6-IW-4	0.163086	0.293882	0.287516	0.110364	0.128963	0.034932	2.47
1-IW-5	0.141457	0.294146	0.290880	0.106086	0.112288	0.029774	2.44
2-IW-5	0.142212	0.298062	0.288977	0.096152	0.126418	0.034308	2.47
3-IW-5	0.147847	0.293073	0.281313	0.100729	0.135688	0.036517	2.50
4-IW-5	0.148018	0.296997	0.286442	0.106795	0.140217	0.038304	2.49
5-IW-5	0.147915	0.296040	0.288657	0.109582	0.133926	0.036367	2.48
6-IW-5	0.137652	0.292462	0.284586	0.109134	0.138778	0.037093	2.47
1-IW-6	0.142728	0.288259	0.287112	0.090313	0.092078	0.023421	2.45
2-IW-6	0.150321	0.297738	0.297222	0.110507	0.114826	0.030877	2.43
3-IW-6	0.143555	0.292992	0.289108	0.111728	0.126522	0.033772	2.46
4-IW-6	0.150063	0.299422	0.290954	0.103053	0.140906	0.038891	2.44
5-IW-6	0.139675	0.289561	0.279398	0.107938	0.142363	0.037844	2.48
6-IW-6	0.139553	0.290931	0.288611	0.111031	0.120472	0.031728	2.44
Units	[kN/mm²]			[−]		[kN/mm²]	[mm]

Table B.4.4: Measurements of the mechanical quantities obtained from UT117 specimens machined from part IW of six U900-1 components.

Uniaxial Tensile Test Specimen UT117 / Part BF of the U900-1 Component							
Specimen	$R_{p0.2}$	R_m	R_f	A_g	A_f	W_c	t
1-BF-1	0.143919	0.267194	0.266812	0.039856	0.040120	0.008909	2.80
2-BF-1	0.151111	0.291887	0.287969	0.069457	0.072268	0.018372	2.68
3-BF-1	0.148346	0.288102	0.286828	0.065719	0.066987	0.016682	2.74
4-BF-1	0.153378	0.296839	0.292317	0.084043	0.088111	0.023164	2.70
5-BF-1	0.149146	0.291189	0.289106	0.075695	0.080329	0.020533	2.67
6-BF-1	0.152262	0.291976	0.287285	0.079841	0.084184	0.021791	2.71
1-BF-2	0.138700	0.274868	0.274237	0.044758	0.044883	0.010238	2.78
2-BF-2	0.155515	0.262187	0.261749	0.029019	0.029233	0.006358	2.65
3-BF-2	0.151605	0.287549	0.285217	0.060639	0.062061	0.015326	2.71
4-BF-2	0.160839	0.292672	0.289168	0.062298	0.064115	0.016267	2.66
5-BF-2	0.156489	0.291514	0.288604	0.069738	0.072297	0.018458	2.63
6-BF-2	0.153989	0.290370	0.286101	0.070037	0.073185	0.018577	2.68
1-BF-3	0.143673	0.282132	0.280575	0.064617	0.065942	0.016012	2.77
2-BF-3	0.152931	0.292204	0.290345	0.074184	0.076332	0.019550	2.62
3-BF-3	0.148414	0.284749	0.284173	0.063279	0.063931	0.015626	2.70
4-BF-3	0.158300	0.295412	0.291384	0.091168	0.103482	0.027671	2.64
5-BF-3	0.147127	0.289894	0.285985	0.074126	0.076793	0.019445	2.62
6-BF-3	0.153492	0.290754	0.284416	0.083839	0.089050	0.023008	2.65
1-BF-4	0.141647	0.290319	0.288356	0.074257	0.075197	0.018889	2.75
2-BF-4	0.155191	0.294394	0.291535	0.075627	0.078722	0.020332	2.60
3-BF-4	0.149346	0.286307	0.283949	0.061968	0.063392	0.015601	2.67
4-BF-4	0.159795	0.274429	0.273774	0.037271	0.037405	0.008606	2.62
5-BF-4	0.153254	0.292337	0.288277	0.073331	0.075446	0.019334	2.60
6-BF-4	0.153028	0.278565	0.278146	0.046070	0.046277	0.010895	2.64
1-BF-5	0.143326	0.282161	0.280704	0.060709	0.061323	0.014771	2.74
2-BF-5	0.147322	0.298454	0.296219	0.085690	0.088849	0.023396	2.56
3-BF-5	0.143540	0.288523	0.282674	0.068231	0.071170	0.017764	2.64
4-BF-5	0.155879	0.294512	0.294351	0.077661	0.079446	0.020596	2.59
5-BF-5	0.156775	0.292256	0.290670	0.067134	0.068132	0.017272	2.55
6-BF-5	0.142424	0.291102	0.287923	0.075030	0.078975	0.020027	2.61
1-BF-6	0.144328	0.288408	0.285479	0.088533	0.092987	0.023836	2.78
2-BF-6	0.149639	0.298175	0.296604	0.087257	0.090476	0.023810	2.53
3-BF-6	0.147473	0.288529	0.284745	0.062733	0.064576	0.015997	2.62
4-BF-6	0.159962	0.297029	0.290288	0.082350	0.088592	0.023484	2.57
5-BF-6	0.145201	0.290700	0.289464	0.071122	0.072256	0.018140	2.53
6-BF-6	0.147342	0.287260	0.286483	0.061891	0.062706	0.015418	2.57
Units	[kN/mm²]			[−]		[kN/mm²]	[mm]

Table B.4.5: Measurements of the mechanical quantities obtained from UT117 specimens machined from part BF of six U900-1 components.

Uniaxial Tensile Test Specimen UT117 / Part OW of the U900-1 Component							
Specimen	$R_{p0.2}$	R_m	R_f	A_g	A_f	W_c	t
1-OW-1	0.169990	0.294265	0.293277	0.036900	0.037236	0.009218	2.36
2-OW-1	0.153536	0.302670	0.301247	0.057014	0.057348	0.014726	2.38
3-OW-1	0.155823	0.310531	0.309233	0.085847	0.088307	0.024212	2.37
4-OW-1	0.158455	0.310604	0.309949	0.079392	0.079944	0.021747	2.40
5-OW-1	0.155534	0.310288	0.309502	0.073594	0.074497	0.020099	2.37
6-OW-1	0.155007	0.305765	0.304684	0.061865	0.062585	0.016345	2.34
1-OW-2	0.149791	0.288215	0.287949	0.034011	0.034067	0.007977	2.38
2-OW-2	0.160238	0.308463	0.307904	0.063284	0.063915	0.016964	2.39
3-OW-2	0.156670	0.294202	0.294060	0.041985	0.042036	0.010306	2.38
4-OW-2	0.159193	0.308781	0.307729	0.067039	0.068763	0.018425	2.40
5-OW-2	0.155709	0.303645	0.302256	0.054843	0.055340	0.014297	2.39
6-OW-2	0.151918	0.309549	0.308652	0.079117	0.081270	0.021966	2.37
1-OW-3	0.146638	0.305717	0.304624	0.077335	0.079256	0.021119	2.37
2-OW-3	0.156635	0.314750	0.314176	0.080257	0.080828	0.022262	2.39
3-OW-3	0.156501	0.310670	0.309955	0.072977	0.074738	0.020197	2.39
4-OW-3	0.163345	0.316509	0.315993	0.073409	0.074412	0.020535	2.39
5-OW-3	0.159173	0.315214	0.314005	0.080363	0.083003	0.023033	2.37
6-OW-3	0.159914	0.311697	0.309899	0.073857	0.076469	0.020948	2.35
1-OW-4	0.165724	0.314794	0.312934	0.075776	0.078244	0.021726	2.36
2-OW-4	0.156103	0.306734	0.306340	0.061196	0.061697	0.016195	2.39
3-OW-4	0.153498	0.309992	0.309412	0.073208	0.074456	0.020091	2.39
4-OW-4	0.161458	0.295625	0.295275	0.039589	0.039767	0.009792	2.40
5-OW-4	0.155288	0.305968	0.305021	0.063249	0.063586	0.016692	2.40
6-OW-4	0.164136	0.311957	0.310221	0.072819	0.073363	0.020027	2.36
1-OW-5	0.167653	0.314305	0.312864	0.065745	0.067077	0.018409	2.39
2-OW-5	0.161500	0.278164	0.277959	0.026129	0.026414	0.006020	2.38
3-OW-5	0.156432	0.309899	0.308597	0.062713	0.064087	0.017072	2.37
4-OW-5	0.166108	0.278710	0.278472	0.026835	0.026883	0.006195	2.39
5-OW-5	0.160316	0.297639	0.297125	0.043549	0.043919	0.010930	2.38
6-OW-5	0.164524	0.304554	0.303444	0.050814	0.051547	0.013411	2.36
1-OW-6	0.160596	0.307319	0.306568	0.057095	0.057807	0.015162	2.39
2-OW-6	0.157961	0.302406	0.301745	0.044476	0.044867	0.011367	2.38
3-OW-6	0.163904	0.281766	0.281625	0.029483	0.029562	0.006889	2.37
4-OW-6	0.160286	0.299762	0.298939	0.041924	0.042714	0.010722	2.39
5-OW-6	0.151898	0.303431	0.302840	0.047186	0.047663	0.012072	2.37
6-OW-6	0.166516	0.305750	0.305221	0.053932	0.054560	0.014289	2.35
Units	[kN/mm²]			[−]		[kN/mm²]	[mm]

Table B.4.6: Measurements of the mechanical quantities obtained from UT117 specimens machined from part OW of six U900-1 components.

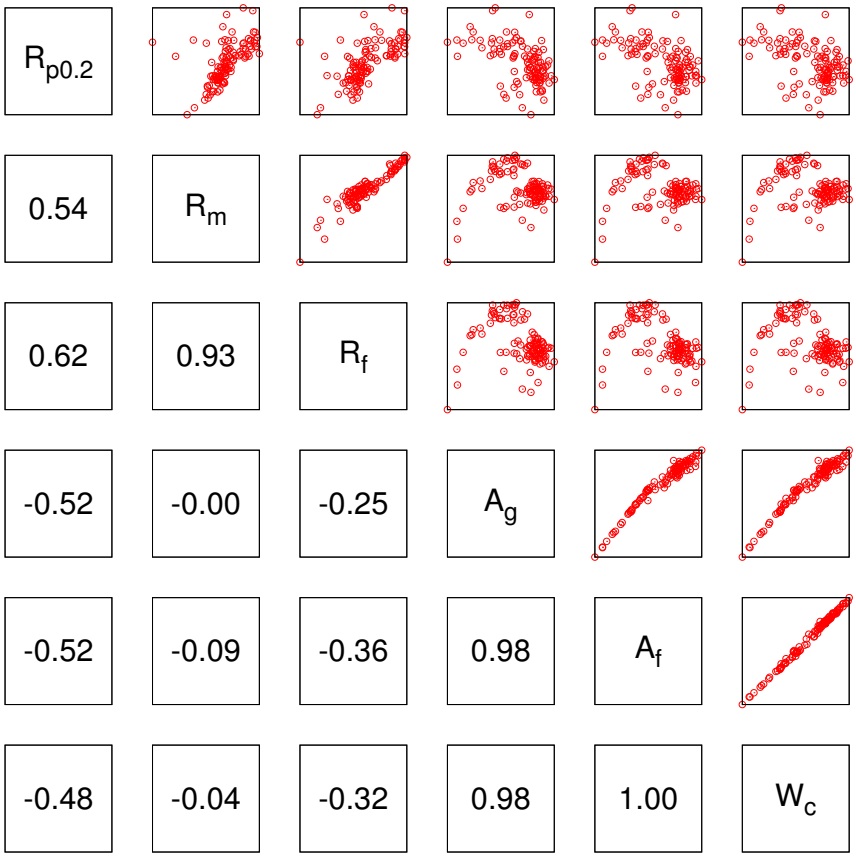

Figure B.4.4: Correlation matrix of the measured mechanical quantities obtained from UT75 specimens machined from six U900-1 components.

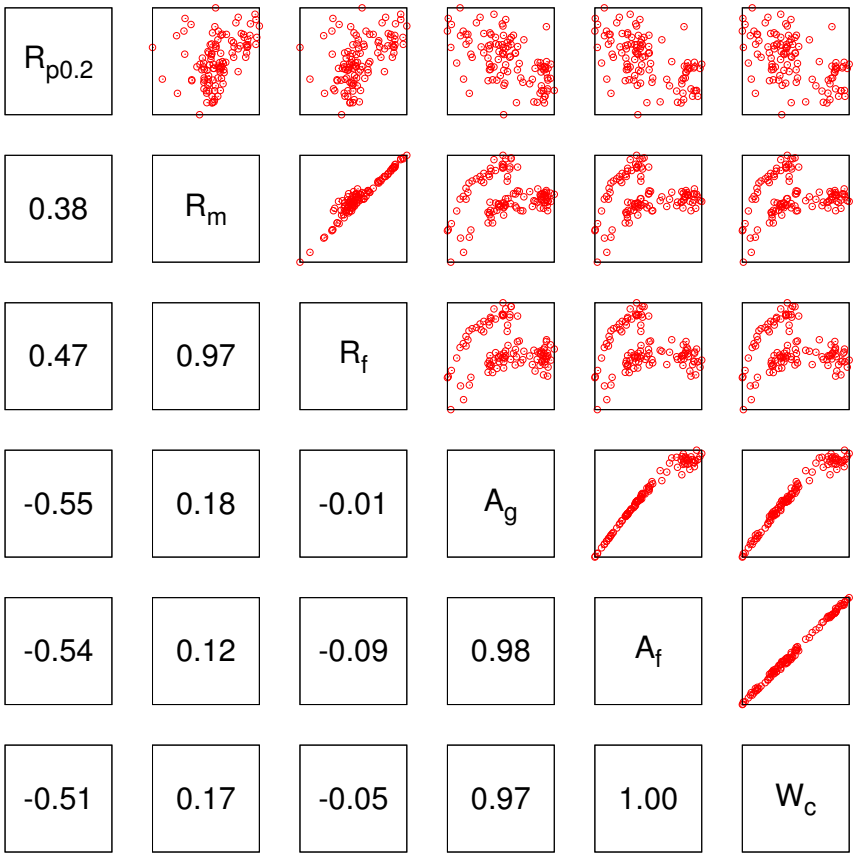

Figure B.4.5: Correlation matrix of the measured mechanical quantities obtained from UT117 specimens machined from six U900-1 components.

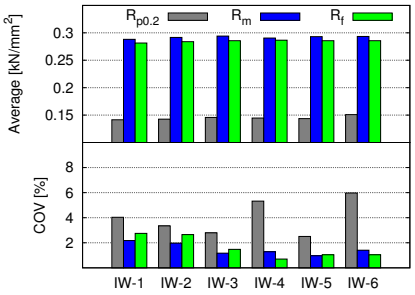

(a) Part IW: $R_{p0.2}$, R_m and R_f.

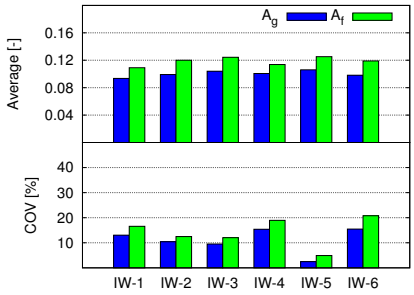

(b) Part IW: A_g and A_f.

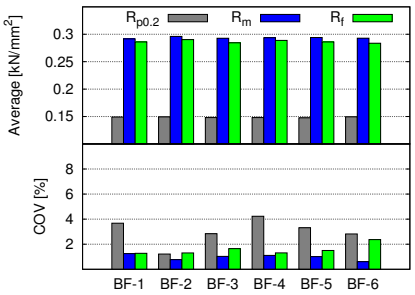

(c) Part BF: $R_{p0.2}$, R_m and R_f.

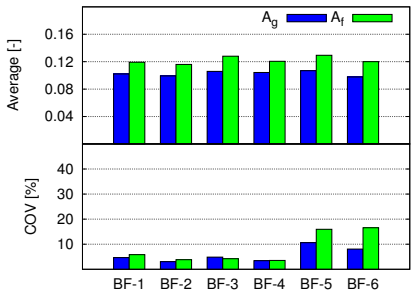

(d) Part BF: A_g and A_f.

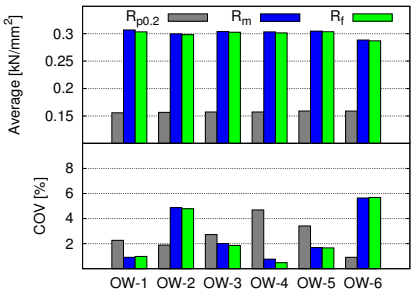

(e) Part OW: $R_{p0.2}$, R_m and R_f.

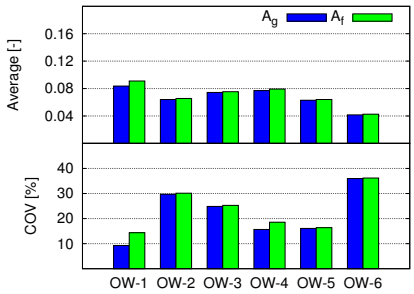

(f) Part OW: A_g and A_f.

Figure B.4.6: Average and COVs of the measured mechanical quantities obtained from UT75 specimens machined from six U900-1 components.

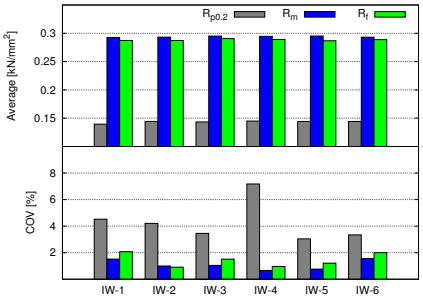

(a) Part IW: $R_{p0.2}$, R_m and R_f.

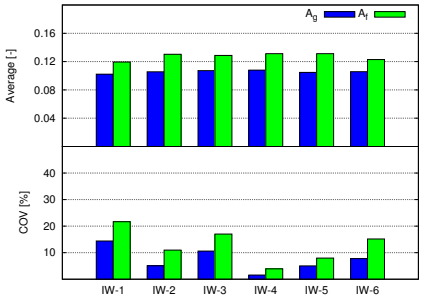

(b) Part IW: A_g and A_f.

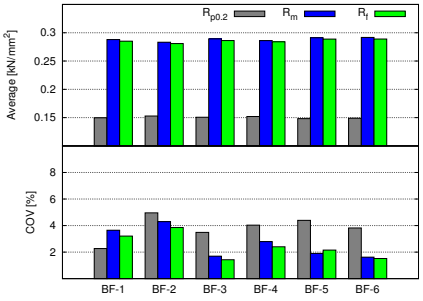

(c) Part BF: $R_{p0.2}$, R_m and R_f.

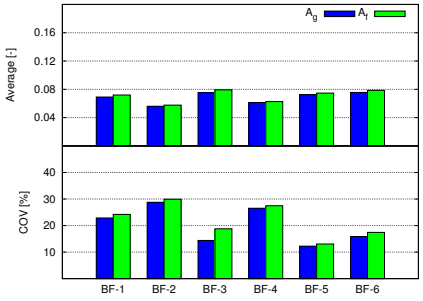

(d) Part BF: A_g and A_f.

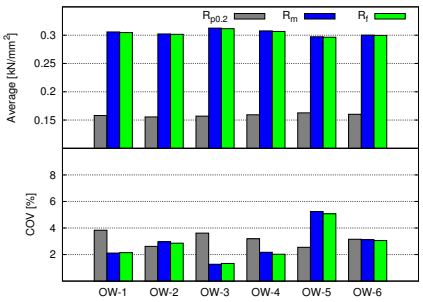

(e) Part OW: $R_{p0.2}$, R_m and R_f.

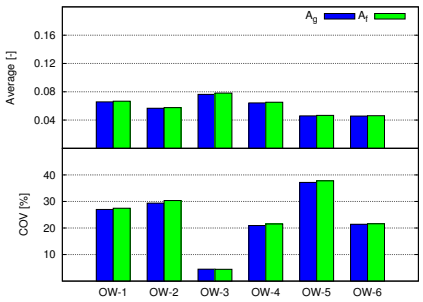

(f) Part OW: A_g and A_f.

Figure B.4.7: Average and COVs of the measured mechanical quantities obtained from UT117 specimens machined from six U900-1 components.

Uniaxial Tensile Test Specimen UT75 / W_c

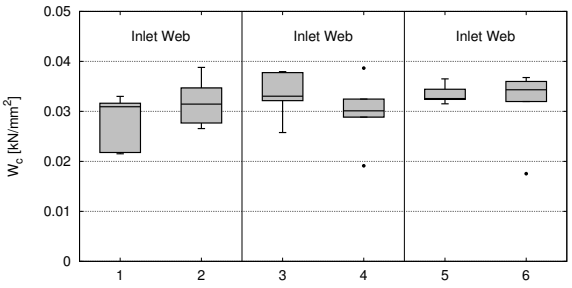

Samples		AD_N-Test A		AD_N-Test B		F-Test		t-Test		KS-Test	
A	B	H_0	p	H_0	p	H_0	p	H_0	p	H_0	p
IW-1	IW-2	0	0.06	0	0.62	0	0.81	0	0.25	0	0.32
IW-3	IW-4	0	0.39	0	0.37	0	0.46	0	0.31	0	0.32
IW-5	IW-6	0	0.21	**1**	0.03	~~**1**~~	~~0.01~~	~~**0**~~	~~0.63~~	0	0.81

(a) UT75: Part IW.

Uniaxial Tensile Test Specimen UT117 / W_c

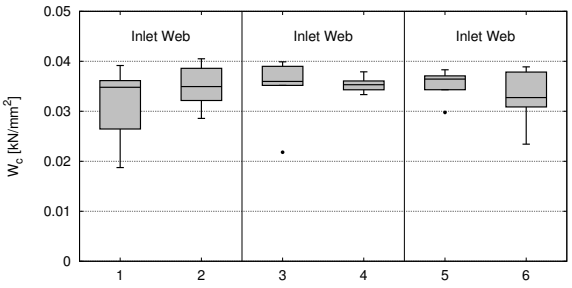

Samples		AD_N-Test A		AD_N-Test B		F-Test		t-Test		KS-Test	
A	B	H_0	p	H_0	p	H_0	p	H_0	p	H_0	p
IW-1	IW-2	0	0.22	0	0.78	0	0.25	0	0.38	0	0.81
IW-3	IW-4	**1**	0.04	0	0.73	~~**1**~~	~~0.01~~	~~**0**~~	~~0.79~~	0	0.81
IW-5	IW-6	0	0.19	0	0.55	0	0.21	0	0.33	0	0.32

(b) UT117: Part IW.

Table B.4.7: Statistical hypothesis testing of samples based on measurements of W_c obtained from UT75 and UT117 specimens machined from part IW of six U900-1 components: Results of AD_N-tests, F-test, t-test and KS-test (significance level $\alpha = 0.05$).

Uniaxial Tensile Test Specimen UT75 / W_c

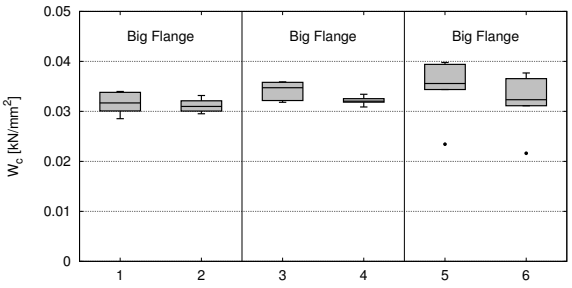

Samples		AD_N-Test A		AD_N-Test B		F-Test		t-Test		KS-Test	
A	B	H_0	p	H_0	p	H_0	p	H_0	p	H_0	p
BF-1	BF-2	0	0.41	0	0.51	0	0.34	0	0.66	0	0.81
BF-3	BF-4	0	0.25	0	0.63	0	0.12	**1**	0.03	0	0.08
BF-5	BF-6	0	0.11	0	0.27	0	0.93	0	0.43	0	0.32

(a) UT75: Part BF.

Uniaxial Tensile Test Specimen UT117 / W_c

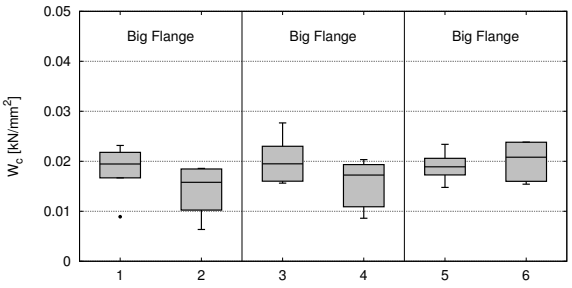

Samples		AD_N-Test A		AD_N-Test B		F-Test		t-Test		KS-Test	
A	B	H_0	p	H_0	p	H_0	p	H_0	p	H_0	p
BF-1	BF-2	0	0.34	0	0.31	0	0.92	0	0.19	0	0.32
BF-3	BF-4	0	0.47	0	0.33	0	0.88	0	0.12	0	0.32
BF-5	BF-6	0	0.73	0	0.12	0	0.53	0	0.59	0	0.32

(b) UT117: Part BF.

Table B.4.8: Statistical hypothesis testing of samples based on measurements of W_c obtained from UT75 and UT117 specimens machined from part BF of six U900-1 components: Results of AD_N-tests, F-test, t-test and KS-test (significance level $\alpha = 0.05$).

Uniaxial Tensile Test Specimen UT75 / W_c

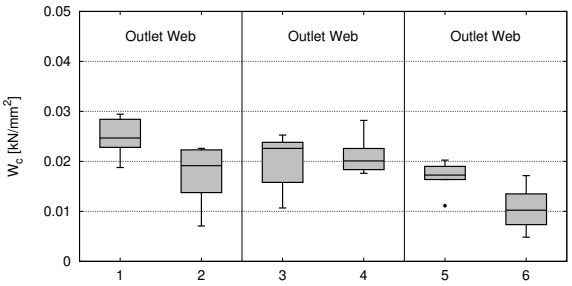

Samples		AD_N-Test A		AD_N-Test B		F-Test		t-Test		KS-Test	
A	B	H_0	p	H_0	p	H_0	p	H_0	p	H_0	p
OW-1	OW-2	0	0.67	0	0.34	0	0.37	**1**	0.03	**1**	0.01
OW-3	OW-4	0	0.19	0	0.31	0	0.44	0	0.72	0	0.81
OW-5	OW-6	0	0.29	0	0.75	0	0.46	**1**	0.02	0	0.08

(a) UT75: Part OW.

Uniaxial Tensile Test Specimen UT117 / W_c

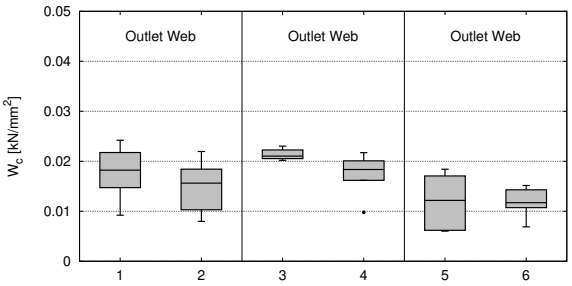

Samples		AD_N-Test A		AD_N-Test B		F-Test		t-Test		KS-Test	
A	B	H_0	p	H_0	p	H_0	p	H_0	p	H_0	p
OW-1	OW-2	0	0.71	0	0.74	0	0.93	0	0.39	0	0.81
OW-3	OW-4	0	0.46	0	0.32	**1**	0.01	~~0~~	~~0.06~~	**1**	0.01
OW-5	OW-6	0	0.51	0	0.59	0	0.22	0	0.92	0	0.81

(b) UT117: Part OW.

Table B.4.9: Statistical hypothesis testing of samples based on measurements of W_c obtained from UT75 and UT117 specimens machined from part OW of six U900-1 components: Results of AD_N-tests, F-test, t-test and KS-test (significance level $\alpha = 0.05$).

B.5 Material Characterisation I + II - Thickness Measurements

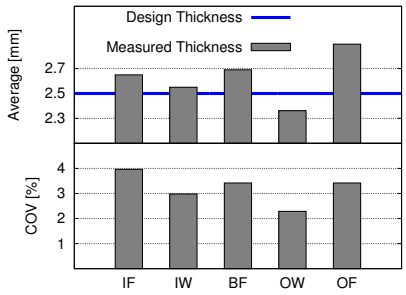

Figure B.5.1: Average and COVs of the measured thickness obtained from UT80 specimens machined from five U900-1 components.

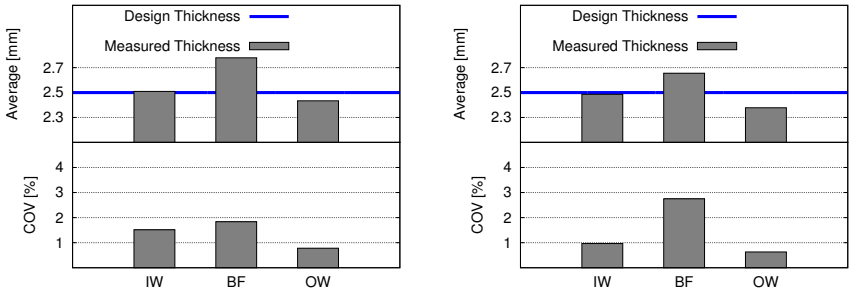

(a) UT75 specimen. **(b)** UT117 specimen.

Figure B.5.2: Average and COVs of the measured thickness obtained from UT75 and UT117 specimens machined from six U900-1 components.

Appendix C

Numerical Material Modelling

C.1 Stress-Update Algorithm and Element Deletion Algorithm

1. Elastic predictor ($t \geq 0$):

$$\boldsymbol{\sigma}_{n+1}^{tr} = \boldsymbol{\sigma}_n + \lambda_{el}\,\mathrm{tr}\left[\triangle\boldsymbol{\varepsilon}_{n+1}\right]\mathbf{I} + 2\mu_{el}\triangle\boldsymbol{\varepsilon}_{n+1}$$

2. Yield condition ($t \geq 0$):

$$f\left(\boldsymbol{\sigma}_{n+1}^{tr}, \bar{\varepsilon}_n\right) \leq 0: \quad \text{go to 5} \quad \text{with } \triangle\bar{\varepsilon}_{n+1} = 0$$
$$f\left(\boldsymbol{\sigma}_{n+1}^{tr}, \bar{\varepsilon}_n\right) > 0: \quad \text{go to 3}$$

3. Plastic corrector and Newton iteration ($t \geq 0$):

$$\bar{\varepsilon}_{n+1}^{(k)} = \bar{\varepsilon}_n + \triangle\bar{\varepsilon}_{n+1}^{(k)}$$
$$\boldsymbol{\sigma}_{n+1} = \boldsymbol{\sigma}_{n+1}^{tr} - \left[\lambda_{el}\,\mathrm{tr}\left[\triangle\bar{\varepsilon}_{n+1}^{(k)}\frac{\partial f\left(\boldsymbol{\sigma}_{n+1}^{tr}, \bar{\varepsilon}_{n+1}^{(k)}\right)}{\partial\boldsymbol{\sigma}_{n+1}^{tr}}\right]\mathbf{I} + 2\mu_{el}\triangle\bar{\varepsilon}_{n+1}^{(k)}\frac{\partial f\left(\boldsymbol{\sigma}_{n+1}^{tr}, \bar{\varepsilon}_{n+1}^{(k)}\right)}{\partial\boldsymbol{\sigma}_{n+1}^{tr}}\right]$$
$$f_{n+1}^{(k)} = \bar{\sigma}\left(\boldsymbol{\sigma}_{n+1}\right) - \sigma_Y\left(\bar{\varepsilon}_{n+1}^{(k)}\right)$$
$$f_{n+1}^{\prime(k)} = \frac{\partial f_{n+1}^{(k)}}{\partial\triangle\bar{\varepsilon}_{n+1}^{(k)}}$$
$$\triangle\bar{\varepsilon}_{n+1}^{(k+1)} = \triangle\bar{\varepsilon}_{n+1}^{(k)} - \frac{f_{n+1}^{(k)}}{f_{n+1}^{\prime(k)}}$$

4. Abort criterion ($t \geq 0$):

$$\left|\frac{f_{n+1}^{(k+1)}}{\sigma_Y\left(\bar{\varepsilon}_{n+1}^{(k+1)}\right)}\right| < tol: \quad \text{go to 5 with} \quad \triangle\bar{\varepsilon}_{n+1} = \triangle\bar{\varepsilon}_{n+1}^{(k+1)}$$
$$\left|\frac{f_{n+1}^{(k+1)}}{\sigma_Y\left(\bar{\varepsilon}_{n+1}^{(k+1)}\right)}\right| \geq tol: \quad \text{go to 3 with} \quad k \leftarrow k+1$$

5. Update equivalent plastic strain and stress tensor ($t \geq 0$):

$$\bar{\varepsilon}_{n+1} = \bar{\varepsilon}_n + \triangle\bar{\varepsilon}_{n+1}$$
$$\boldsymbol{\sigma}_{n+1} = \boldsymbol{\sigma}_{n+1}^{tr} - \left[\lambda_{el}\,\mathrm{tr}\left[\triangle\bar{\varepsilon}_{n+1}\frac{\partial f\left(\boldsymbol{\sigma}_{n+1}^{tr}, \bar{\varepsilon}_{n+1}\right)}{\partial\boldsymbol{\sigma}_{n+1}^{tr}}\right]\mathbf{I} + 2\mu_{el}\triangle\bar{\varepsilon}_{n+1}\frac{\partial f\left(\boldsymbol{\sigma}_{n+1}^{tr}, \bar{\varepsilon}_{n+1}\right)}{\partial\boldsymbol{\sigma}_{n+1}^{tr}}\right]$$

Figure C.1.1: Stress update algorithm.

1. Element deletion flag = false ($t \geq 0$):

   Stress update algorithm (Figure C.1.1)

2. Element deletion flag = true ($t \geq 0$):

$$\boldsymbol{\sigma}_{n+1} = \mathbf{0}$$

3. Cockcroft-Latham integral ($t \geq 0$):

$$W_{n+1} = W_n + \max\left[0, \max\left[\left(\sigma_{I,II,III}\right)_{n+1}\right] \triangle\bar{\varepsilon}_{n+1}\right]$$

4. Cockcroft-Latham failure criterion ($t \geq 0$):

$$\begin{aligned} W_{n+1} < W_c &: \quad \text{Element deletion flag} = \text{false} \\ W_{n+1} \geq W_c &: \quad \text{Element deletion flag} = \text{true} \end{aligned}$$

Figure C.1.2: Element deletion algorithm.

C.2 Material Routine MR#1

1. Stress update algorithm ($t \geq 0$):

   Stress update algorithm, see Figure C.1.1

2. Cockcroft-Latham integral ($t \geq 0$):

$$W_{n+1} = W_n + \max\left[0, \max\left[\left(\sigma_{I,II,III}\right)_{n+1}\right] \triangle\bar{\varepsilon}_{n+1}\right]$$

3. Survival and failure probability (integration point) ($t \geq 0$):

$$\begin{aligned} \left(P_S^{i,j}\right)_{n+1} &= \exp\left(-\frac{\frac{V}{n}}{V_0}\left(\frac{W_{n+1}}{W_{c0}}\right)^m\right) \\ \left(P_F^{i,j}\right)_{n+1} &= 1 - \left(P_S^{i,j}\right)_{n+1} \end{aligned}$$

4. Survival and failure probability (element) ($t \geq 0$):

$$\begin{aligned} \text{if } i = 1: \quad &\rightarrow \quad X^{elem} = \left(P_S^{1,j}\right)_{n+1} \\ \text{if } i > 1: \quad &\rightarrow \quad X^{elem} = X^{elem} \cdot \left(P_S^{i,j}\right)_{n+1} \\ \text{if } i = n: \quad &\rightarrow \quad \left(P_S^{elem,j}\right)_{n+1} = X^{elem} \\ &\qquad\quad \left(P_F^{elem,j}\right)_{n+1} = 1 - X^{elem} \end{aligned}$$

5. Survival and failure probability (FE model) ($t \geq 0$):

$$\begin{aligned} \left(P_S^{model}\right)_{n+1} &= \left(X^{model}\right)_n \\ \left(P_F^{model}\right)_{n+1} &= 1 - \left(P_S^{model}\right)_{n+1} \\ \left(X^{model}\right)_{n+1} &= \left(X^{model}\right)_{n+1} \cdot \left(P_S^{i,j}\right)_{n+1} \end{aligned}$$

6. Survival and failure probability (FE model part j) ($t \geq 0$):

$$\begin{aligned} \left(P_S^j\right)_{n+1} &= \left(\mathbf{X}(j)\right)_n \\ \left(P_F^j\right)_{n+1} &= 1 - \left(P_S^j\right)_{n+1} \\ \left(\mathbf{X}(j)\right)_{n+1} &= \left(\mathbf{X}(j)\right)_{n+1} \cdot \left(P_S^{i,j}\right)_{n+1} \end{aligned}$$

Figure C.2.1: Material routine MR#1.

C.3 Material Routine MR#2

1. Uniform pseudo-random number ($t = 0$):

$$\text{if } i = 1: \quad \rightarrow \quad \text{rand\_number}[u]$$
$$x^{elem} = u$$

2. Critical value of the Cockcroft-Latham failure criterion ($t = 0$):

$$W_c = W_{c0} \sqrt[m]{\left(-\frac{V_0}{V_{ini}}\right) \ln\left(1 - x^{elem}\right)}$$

3. Element deletion flag = false ($t \geq 0$):

Stress update algorithm, see Figure C.1.1

4. Element deletion flag = true ($t \geq 0$):

$$\boldsymbol{\sigma}_{n+1} = \mathbf{0}$$

5. Cockcroft-Latham integral ($t \geq 0$):

$$W_{n+1} = W_n + \max\left[0, \max\left[\left(\sigma_{I,II,III}\right)_{n+1}\right] \triangle\bar{\varepsilon}_{n+1}\right]$$

6. Cockcroft-Latham failure criterion ($t \geq 0$):

$$W_{n+1} < W_c: \quad \text{Element deletion flag} = \text{false}$$
$$W_{n+1} \geq W_c: \quad \text{Element deletion flag} = \text{true}$$

Figure C.3.1: Material routine MR#2.

C.4 Material Routine MR#3

1. Element centre ($t = 0$):

$$\text{if } i = 1: \quad \rightarrow \quad x_m = \frac{1}{n_{nod}} \sum_{k=1}^{n_{nod}} x_k$$
$$y_m = \frac{1}{n_{nod}} \sum_{k=1}^{n_{nod}} y_k$$
$$z_m = \frac{1}{n_{nod}} \sum_{k=1}^{n_{nod}} x_k$$

2. Creation of the MS mesh ($t = 0$):

$$\text{if } i = 1: \quad \rightarrow \quad n_x^{max} = \text{ceiling}\left[\frac{x_{max} - x_{min}}{l_{crit}}\right]$$
$$n_y^{max} = \text{ceiling}\left[\frac{y_{max} - y_{min}}{l_{crit}}\right]$$
$$n_z^{max} = \text{ceiling}\left[\frac{z_{max} - z_{min}}{l_{crit}}\right]$$

3. Mapping of the MS mesh onto the FE mesh ($t = 0$):

$$\text{if } i = 1: \quad \rightarrow \quad n_x = \text{ceiling}\left[\frac{x_m - x_{min}}{l_{crit}}\right]$$
$$n_y = \text{ceiling}\left[\frac{y_m - y_{min}}{l_{crit}}\right]$$
$$n_z = \text{ceiling}\left[\frac{z_m - z_{min}}{l_{crit}}\right]$$
$$n = (n_z - 1)\, n_y^{max} n_z^{max} + \left(n_y - 1\right) n_x^{max} + n_x$$

4. Uniform pseudo-random number ($t = 0$):

$$\text{if } i = 1: \quad \rightarrow \quad \text{init\_random\_seed}\,[clock] \tag{C.4.1}$$
$$\text{rand\_number}\left[\mathbf{u}\begin{pmatrix} 1 \\ \vdots \\ n \end{pmatrix}\right] \tag{C.4.2}$$
$$x^{elem} = \mathbf{u}(n) \tag{C.4.3}$$

Figure C.4.1: Material routine MR#3 (first part).

5. Volume of an element of the MS mesh ($t = 0$):

$$V_{crit} = \begin{cases} l_{cirt} \cdot l_{crit} \cdot t_{ini} & \text{for shell elements with inital thickness } t_{ini} \\ l_{crit} \cdot l_{crit} \cdot l_{crit} & \text{for solid elements} \end{cases} \tag{C.4.4}$$

6. Critical value of the Cockcroft-Latham failure criterion ($t = 0$):

$$W_c = W_{c0} \sqrt[m]{-\frac{V_0}{\min\left[V_{ini}, V_{crit}\right]} \ln\left(1 - x^{elem}\right)} \tag{C.4.5}$$

7. Element deletion flag = false ($t \geq 0$):

   Stress update algorithm, see Figure C.1.1

8. Element deletion flag = true ($t \geq 0$):

$$\boldsymbol{\sigma}_{n+1} = \mathbf{0}$$

9. Cockcroft-Latham integral ($t \geq 0$):

$$W_{n+1} = W_n + \max\left[0, \max\left[\left(\sigma_{I,II,III}\right)_{n+1}\right] \triangle\bar{\varepsilon}_{n+1}\right]$$

10. Cockcroft-Latham failure criterion ($t \geq 0$):

$$\begin{aligned} W_{n+1} < W_c &: \quad \text{Element deletion flag} = \text{false} \\ W_{n+1} \geq W_c &: \quad \text{Element deletion flag} = \text{true} \end{aligned}$$

Figure C.4.2: Material routine MR#3 (second part).

C.5 Material Routine MR#4

1. Read uniform pseudo-random number u_{ini} from user-input (u_{ini} is defined for each integration point of an element in the current FE model).
2. Volume of an element of the MS mesh ($t = 0$):

$$V_{crit} = \begin{cases} l_{cirt} \cdot l_{crit} \cdot t_{ini} & \text{for shell elements with inital thickness } t_{ini} \\ l_{crit} \cdot l_{crit} \cdot l_{crit} & \text{for solid elements} \end{cases}$$

3. Critical value of the Cockcroft-Latham failure criterion ($t = 0$):

$$W_c = W_{c0} \sqrt[m]{-\frac{V_0}{\min[V_{ini}, V_{crit}]} \ln(1 - u_{ini})}$$

4. Element deletion flag = false ($t \geq 0$):

Stress update algorithm, see Figure C.1.1

5. Element deletion flag = true ($t \geq 0$):

$$\boldsymbol{\sigma}_{n+1} = \mathbf{0}$$

6. Cockcroft-Latham integral ($t \geq 0$):

$$W_{n+1} = W_n + \max\left[0, \max\left[\left(\sigma_{I,II,III}\right)_{n+1}\right] \triangle\bar{\varepsilon}_{n+1}\right]$$

7. Cockcroft-Latham failure criterion ($t \geq 0$):

$W_{n+1} < W_c$: Element deletion flag =false
$W_{n+1} \geq W_c$: Element deletion flag = true

Figure C.5.1: Material routine MR#4.

DEPARTMENT OF STRUCTURAL ENGINEERING
NORWEGIAN UNIVERSITY OF SCIENCE AND TECHNOLOGY

N–7491 TRONDHEIM, NORWAY
Telephone: +47 73 59 47 00 Telefax: +47 73 59 47 01

"Reliability Analysis of Structural Systems using Nonlinear Finite Element Methods",
C. A. Holm, 1990:23, ISBN 82-7119-178-0.

"Uniform Stratified Flow Interaction with a Submerged Horizontal Cylinder",
Ø. Arntsen, 1990:32, ISBN 82-7119-188-8.

"Large Displacement Analysis of Flexible and Rigid Systems Considering
Displacement-Dependent Loads and Nonlinear Constraints",
K. M. Mathisen, 1990:33, ISBN 82-7119-189-6.

"Solid Mechanics and Material Models including Large Deformations",
E. Levold, 1990:56, ISBN 82-7119-214-0, ISSN 0802-3271.

"Inelastic Deformation Capacity of Flexurally-Loaded Aluminium Alloy Structures",
T. Welo, 1990:62, ISBN 82-7119-220-5, ISSN 0802-3271.

"Visualization of Results from Mechanical Engineering Analysis",
K. Aamnes, 1990:63, ISBN 82-7119-221-3, ISSN 0802-3271.

"Object-Oriented Product Modeling for Structural Design",
S. I. Dale, 1991:6, ISBN 82-7119-258-2, ISSN 0802-3271.

"Parallel Techniques for Solving Finite Element Problems on Transputer Networks",
T. H. Hansen, 1991:19, ISBN 82-7119-273-6, ISSN 0802-3271.

"Statistical Description and Estimation of Ocean Drift Ice Environments",
R. Korsnes, 1991:24, ISBN 82-7119-278-7, ISSN 0802-3271.

“Properties of concrete related to fatigue damage: with emphasis on high strength concrete”,
G. Petkovic, 1991:35, ISBN 82-7119-290-6, ISSN 0802-3271.

"Turbidity Current Modelling",
B. Brørs, 1991:38, ISBN 82-7119-293-0, ISSN 0802-3271.

"Zero-Slump Concrete: Rheology, Degree of Compaction and Strength. Effects of Fillers as Part Cement-Replacement",
C. Sørensen, 1992:8, ISBN 82-7119-357-0, ISSN 0802-3271.

"Nonlinear Analysis of Reinforced Concrete Structures Exposed to Transient Loading",
K. V. Høiseth, 1992:15, ISBN 82-7119-364-3, ISSN 0802-3271.

"Finite Element Formulations and Solution Algorithms for Buckling and Collapse Analysis of Thin Shells",
R. O. Bjærum, 1992:30, ISBN 82-7119-380-5, ISSN 0802-3271.

"Response Statistics of Nonlinear Dynamic Systems",
J. M. Johnsen, 1992:42, ISBN 82-7119-393-7, ISSN 0802-3271.

"Digital Models in Engineering. A Study on why and how engineers build and operate digital models for decisison support",
J. Høyte, 1992:75, ISBN 82-7119-429-1, ISSN 0802-3271.

"Sparse Solution of Finite Element Equations",
A. C. Damhaug, 1992:76, ISBN 82-7119-430-5, ISSN 0802-3271.

"Some Aspects of Floating Ice Related to Sea Surface Operations in the Barents Sea",
S. Løset, 1992:95, ISBN 82-7119-452-6, ISSN 0802-3271.

"Modelling of Cyclic Plasticity with Application to Steel and Aluminium Structures",
O. S. Hopperstad, 1993:7, ISBN 82-7119-461-5, ISSN 0802-3271.

"The Free Formulation: Linear Theory and Extensions with Applications to Tetrahedral Elements
with Rotational Freedoms",
G. Skeie, 1993:17, ISBN 82-7119-472-0, ISSN 0802-3271.

"Høyfast betongs motstand mot piggdekkslitasje. Analyse av resultater fra prøving i Veisliter'n",
T. Tveter, 1993:62, ISBN 82-7119-522-0, ISSN 0802-3271.

"A Nonlinear Finite Element Based on Free Formulation Theory for Analysis of Sandwich Structures",
O. Aamlid, 1993:72, ISBN 82-7119-534-4, ISSN 0802-3271.

"The Effect of Curing Temperature and Silica Fume on Chloride Migration and Pore Structure of High Strength Concrete",
C. J. Hauck, 1993:90, ISBN 82-7119-553-0, ISSN 0802-3271.

"Failure of Concrete under Compressive Strain Gradients",
G. Markeset, 1993:110, ISBN 82-7119-575-1, ISSN 0802-3271.

"An experimental study of internal tidal amphidromes in Vestfjorden",
J. H. Nilsen, 1994:39, ISBN 82-7119-640-5, ISSN 0802-3271.

"Structural analysis of oil wells with emphasis on conductor design",
H. Larsen, 1994:46, ISBN 82-7119-648-0, ISSN 0802-3271.

"Adaptive methods for non-linear finite element analysis of shell structures",
K. M. Okstad, 1994:66, ISBN 82-7119-670-7, ISSN 0802-3271.

"On constitutive modelling in nonlinear analysis of concrete structures",
O. Fyrileiv, 1994:115, ISBN 82-7119-725-8, ISSN 0802-3271.

"Fluctuating wind load and response of a line-like engineering structure with emphasis on motion-induced wind forces",
J. Bogunovic Jakobsen, 1995:62, ISBN 82-7119-809-2, ISSN 0802-3271.

"An experimental study of beam-columns subjected to combined torsion, bending and axial actions",
A. Aalberg, 1995:66, ISBN 82-7119-813-0, ISSN 0802-3271.

"Scaling and cracking in unsealed freeze/thaw testing of Portland cement and silica fume concretes",
S. Jacobsen, 1995:101, ISBN 82-7119-851-3, ISSN 0802-3271.

"Damping of water waves by submerged vegetation. A case study of laminaria hyperborea",
A. M. Dubi, 1995:108, ISBN 82-7119-859-9, ISSN 0802-3271.

"The dynamics of a slope current in the Barents Sea",
Sheng Li, 1995:109, ISBN 82-7119-860-2, ISSN 0802-3271.

"Modellering av delmaterialenes betydning for betongens konsistens",
Ernst Mørtsell, 1996:12, ISBN 82-7119-894-7, ISSN 0802-3271.

"Bending of thin-walled aluminium extrusions",
Birgit Søvik Opheim, 1996:60, ISBN 82-7119-947-1, ISSN 0802-3271.

"Material modelling of aluminium for crashworthiness analysis",
Torodd Berstad, 1996:89, ISBN 82-7119-980-3, ISSN 0802-3271.

"Estimation of structural parameters from response measurements on submerged floating tunnels",
Rolf Magne Larssen, 1996:119, ISBN 82-471-0014-2, ISSN 0802-3271.

“Numerical modelling of plain and reinforced concrete by damage mechanics”,
Mario A. Polanco-Loria, 1997:20, ISBN 82-471-0049-5, ISSN 0802-3271.

“Nonlinear random vibrations - numerical analysis by path integration methods”,
Vibeke Moe, 1997:26, ISBN 82-471-0056-8, ISSN 0802-3271.

“Numerical prediction of vortex-induced vibration by the finite element method”,
Joar Martin Dalheim, 1997:63, ISBN 82-471-0096-7, ISSN 0802-3271.

“Time domain calculations of buffeting response for wind sensitive structures”,
Ketil Aas-Jakobsen, 1997:148, ISBN 82-471-0189-0, ISSN 0802-3271.

"A numerical study of flow about fixed and flexibly mounted circular cylinders",
Trond Stokka Meling, 1998:48, ISBN 82-471-0244-7, ISSN 0802-3271.

“Estimation of chloride penetration into concrete bridges in coastal areas”,
Per Egil Steen, 1998:89, ISBN 82-471-0290-0, ISSN 0802-3271.

“Stress-resultant material models for reinforced concrete plates and shells”,
Jan Arve Øverli, 1998:95, ISBN 82-471-0297-8, ISSN 0802-3271.

“Chloride binding in concrete. Effect of surrounding environment and concrete composition”,
Claus Kenneth Larsen, 1998:101, ISBN 82-471-0337-0, ISSN 0802-3271.

“Rotational capacity of aluminium alloy beams”,
Lars A. Moen, 1999:1, ISBN 82-471-0365-6, ISSN 0802-3271.

“Stretch Bending of Aluminium Extrusions”,
Arild H. Clausen, 1999:29, ISBN 82-471-0396-6, ISSN 0802-3271.

“Aluminium and Steel Beams under Concentrated Loading”,
Tore Tryland, 1999:30, ISBN 82-471-0397-4, ISSN 0802-3271.

"Engineering Models of Elastoplasticity and Fracture for Aluminium Alloys",
Odd-Geir Lademo, 1999:39, ISBN 82-471-0406-7, ISSN 0802-3271.

"Kapasitet og duktilitet av dybelforbindelser i trekonstruksjoner",
Jan Siem, 1999:46, ISBN 82-471-0414-8, ISSN 0802-3271.

“Etablering av distribuert ingeniørarbeid; Teknologiske og organisatoriske erfaringer fra en norsk ingeniørbedrift”,
Lars Line, 1999:52, ISBN 82-471-0420-2, ISSN 0802-3271.

“Estimation of Earthquake-Induced Response”,
Símon Ólafsson, 1999:73, ISBN 82-471-0443-1, ISSN 0802-3271.

“Coastal Concrete Bridges: Moisture State, Chloride Permeability and Aging Effects”
Ragnhild Holen Relling, 1999:74, ISBN 82-471-0445-8, ISSN 0802-3271.

”Capacity Assessment of Titanium Pipes Subjected to Bending and External Pressure”,
Arve Bjørset, 1999:100, ISBN 82-471-0473-3, ISSN 0802-3271.

“Validation of Numerical Collapse Behaviour of Thin-Walled Corrugated Panels”,
Håvar Ilstad, 1999:101, ISBN 82-471-0474-1, ISSN 0802-3271.

“Strength and Ductility of Welded Structures in Aluminium Alloys”,
Miroslaw Matusiak, 1999:113, ISBN 82-471-0487-3, ISSN 0802-3271.

“Thermal Dilation and Autogenous Deformation as Driving Forces to Self-Induced Stresses in High Performance Concrete”,
Øyvind Bjøntegaard, 1999:121, ISBN 82-7984-002-8, ISSN 0802-3271.

“Some Aspects of Ski Base Sliding Friction and Ski Base Structure”,
Dag Anders Moldestad, 1999:137, ISBN 82-7984-019-2, ISSN 0802-3271.

"Electrode reactions and corrosion resistance for steel in mortar and concrete",
Roy Antonsen, 2000:10, ISBN 82-7984-030-3, ISSN 0802-3271.

"Hydro-Physical Conditions in Kelp Forests and the Effect on Wave Damping and Dune Erosion. A case study on Laminaria Hyperborea",
Stig Magnar Løvås, 2000:28, ISBN 82-7984-050-8, ISSN 0802-3271.

"Random Vibration and the Path Integral Method",
Christian Skaug, 2000:39, ISBN 82-7984-061-3, ISSN 0802-3271.

"Buckling and geometrical nonlinear beam-type analyses of timber structures",
Trond Even Eggen, 2000:56, ISBN 82-7984-081-8, ISSN 0802-3271.

”Structural Crashworthiness of Aluminium Foam-Based Components”,
Arve Grønsund Hanssen, 2000:76, ISBN 82-7984-102-4, ISSN 0809-103X.

“Measurements and simulations of the consolidation in first-year sea ice ridges, and some aspects of mechanical behaviour”,
Knut V. Høyland, 2000:94, ISBN 82-7984-121-0, ISSN 0809-103X.

”Kinematics in Regular and Irregular Waves based on a Lagrangian Formulation”,
Svein Helge Gjøsund, 2000-86, ISBN 82-7984-112-1, ISSN 0809-103X.

”Self-Induced Cracking Problems in Hardening Concrete Structures”,
Daniela Bosnjak, 2000-121, ISBN 82-7984-151-2, ISSN 0809-103X.

"Ballistic Penetration and Perforation of Steel Plates",
Tore Børvik, 2000:124, ISBN 82-7984-154-7, ISSN 0809-103X.

"Freeze-Thaw resistance of Concrete. Effect of: Curing Conditions, Moisture Exchange and Materials",
Terje Finnerup Rønning, 2001:14, ISBN 82-7984-165-2, ISSN 0809-103X

"Structural behaviour of post tensioned concrete structures. Flat slab. Slabs on ground",
Steinar Trygstad, 2001:52, ISBN 82-471-5314-9, ISSN 0809-103X.

"Slipforming of Vertical Concrete Structures. Friction between concrete and slipform panel",
Kjell Tore Fosså, 2001:61, ISBN 82-471-5325-4, ISSN 0809-103X.

"Some numerical methods for the simulation of laminar and turbulent incompressible flows",
Jens Holmen, 2002:6, ISBN 82-471-5396-3, ISSN 0809-103X.

“Improved Fatigue Performance of Threaded Drillstring Connections by Cold Rolling”,
Steinar Kristoffersen, 2002:11, ISBN: 82-421-5402-1, ISSN 0809-103X.

"Deformations in Concrete Cantilever Bridges: Observations and Theoretical Modelling",
Peter F. Takâcs, 2002:23, ISBN 82-471-5415-3, ISSN 0809-103X.

"Stiffened aluminium plates subjected to impact loading",
Hilde Giæver Hildrum, 2002:69, ISBN 82-471-5467-6, ISSN 0809-103X.

"Full- and model scale study of wind effects on a medium-rise building in a built up area",
Jónas Thór Snæbjørnsson, 2002:95, ISBN82-471-5495-1, ISSN 0809-103X.

“Evaluation of Concepts for Loading of Hydrocarbons in Ice-infested water”,
Arnor Jensen, 2002:114, ISBN 82-417-5506-0, ISSN 0809-103X.

”Numerical and Physical Modelling of Oil Spreading in Broken Ice”,
Janne K. Økland Gjøsteen, 2002:130, ISBN 82-471-5523-0, ISSN 0809-103X.

”Diagnosis and protection of corroding steel in concrete”,
Franz Pruckner, 20002:140, ISBN 82-471-5555-4, ISSN 0809-103X.

“Tensile and Compressive Creep of Young Concrete: Testing and Modelling”,
Dawood Atrushi, 2003:17, ISBN 82-471-5565-6, ISSN 0809-103X.

“Rheology of Particle Suspensions. Fresh Concrete, Mortar and Cement Paste with Various Types of Lignosulfonates”,
Jon Elvar Wallevik, 2003:18, ISBN 82-471-5566-4, ISSN 0809-103X.

“Oblique Loading of Aluminium Crash Components”,
Aase Reyes, 2003:15, ISBN 82-471-5562-1, ISSN 0809-103X.

“Utilization of Ethiopian Natural Pozzolans”,
Surafel Ketema Desta, 2003:26, ISSN 82-471-5574-5, ISSN:0809-103X.

"Behaviour and strength prediction of reinforced concrete structures with discontinuity regions", Helge Brå, 2004:11, ISBN 82-471-6222-9, ISSN 1503-8181.

"High-strength steel plates subjected to projectile impact. An experimental and numerical study", Sumita Dey, 2004:38, ISBN 82-471-6282-2 (printed version), ISBN 82-471-6281-4 (electronic version), ISSN 1503-8181.

"Alkali-reactive and inert fillers in concrete. Rheology of fresh mixtures and expansive reactions."
Bård M. Pedersen, 2004:92, ISBN 82-471-6401-9 (printed version), ISBN 82-471-6400-0 (electronic version), ISSN 1503-8181.

"On the Shear Capacity of Steel Girders with Large Web Openings".
Nils Christian Hagen, 2005:9 ISBN 82-471-6878-2 (printed version), ISBN 82-471-6877-4 (electronic version), ISSN 1503-8181.

"Behaviour of aluminium extrusions subjected to axial loading".
Østen Jensen, 2005:7, ISBN 82-471-6873-1 (printed version), ISBN 82-471-6872-3 (electronic version), ISSN 1503-8181.

"Thermal Aspects of corrosion of Steel in Concrete".
Jan-Magnus Østvik, 2005:5, ISBN 82-471-6869-3 (printed version), ISBN 82-471-6868 (electronic version), ISSN 1503-8181.

"Mechanical and adaptive behaviour of bone in relation to hip replacement." A study of bone remodelling and bone grafting.
Sébastien Muller, 2005:34, ISBN 82-471-6933-9 (printed version), ISBN 82-471-6932-0 (electronic version), ISSN 1503-8181.

"Analysis of geometrical nonlinearities with applications to timber structures".
Lars Wollebæk, 2005:74, ISBN 82-471-7050-5 (printed version), ISBN 82-471-7019-1 (electronic version), ISSN 1503-8181.

"Pedestrian induced lateral vibrations of slender footbridges",
Anders Rönnquist, 2005:102, ISBN 82-471-7082-5 (printed version), ISBN 82-471-7081-7 (electronic version), ISSN 1503-8181.

"Initial Strength Development of Fly Ash and Limestone Blended Cements at Various Temperatures Predicted by Ultrasonic Pulse Velocity",
Tom Ivar Fredvik, 2005:112, ISBN 82-471-7105-8 (printed version), ISBN 82-471-7103-1 (electronic version), ISSN 1503-8181.

"Behaviour and modelling of thin-walled cast components",
Cato Dørum, 2005:128, ISBN 82-471-7140-6 (printed version), ISBN 82-471-7139-2 (electronic version), ISSN 1503-8181.

“Behaviour and modelling of selfpiercing riveted connections”,
Raffaele Porcaro, 2005:165, ISBN 82-471-7219-4 (printed version), ISBN 82-471-7218-6 (electronic version), ISSN 1503-8181.

”Behaviour and Modelling og Aluminium Plates subjected to Compressive Load”,
Lars Rønning, 2005:154, ISBN 82-471-7169-1 (printed version), ISBN 82-471-7195-3 (electronic version), ISSN 1503-8181.

”Bumper beam-longitudinal system subjected to offset impact loading”,
Satyanarayana Kokkula, 2005:193, ISBN 82-471-7280-1 (printed version), ISBN 82-471-7279-8 (electronic version), ISSN 1503-8181.

“Control of Chloride Penetration into Concrete Structures at Early Age”,
Guofei Liu, 2006:46, ISBN 82-471-7838-9 (printed version), ISBN 82-471-7837-0 (electronic version), ISSN 1503-8181.

“Modelling of Welded Thin-Walled Aluminium Structures”,
Ting Wang, 2006:78, ISBN 82-471-7907-5 (printed version), ISBN 82-471-7906-7 (electronic version), ISSN 1503-8181.

”Time-variant reliability of dynamic systems by importance sampling and probabilistic analysis of ice loads”,
Anna Ivanova Olsen, 2006:139, ISBN 82-471-8041-3 (printed version), ISBN 82-471-8040-5 (electronic version), ISSN 1503-8181.

“Fatigue life prediction of an aluminium alloy automotive component using finite element analysis of surface topography”.
Sigmund Kyrre Ås, 2006:25, ISBN 82-471-7791-9 (printed version), ISBN 82-471-7791-9 (electronic version), ISSN 1503-8181.

”Constitutive models of elastoplasticity and fracture for aluminium alloys under strain path change”,
Dasharatha Achani, 2006:76, ISBN 82-471-7903-2 (printed version), ISBN 82-471-7902-4 (electronic version), ISSN 1503-8181.

“Simulations of 2D dynamic brittle fracture by the Element-free Galerkin method and linear fracture mechanics”,
Tommy Karlsson, 2006:125, ISBN 82-471-8011-1 (printed version), ISBN 82-471-8010-3 (electronic version), ISSN 1503-8181.

“Penetration and Perforation of Granite Targets by Hard Projectiles”,
Chong Chiang Seah, 2006:188, ISBN 82-471-8150-9 (printed version), ISBN 82-471-8149-5 (electronic version), ISSN 1503-8181.

"Deformations, strain capacity and cracking of concrete in plastic and early hardening phases",
Tor Arne Hammer, 2007:234, ISBN 978-82-471-5191-4 (printed version), ISBN 978-82-471-5207-2 (electronic version), ISSN 1503-8181.

"Crashworthiness of dual-phase high-strength steel: Material and Component behaviour", Venkatapathi Tarigopula, 2007:230, ISBN 82-471-5076-4 (printed version), ISBN 82-471-5093-1 (electronic version), ISSN 1503-8181.

"Fibre reinforcement in load carrying concrete structures",
Åse Lyslo Døssland, 2008:50, ISBN 978-82-471-6910-0 (printed version), ISBN 978-82-471-6924-7 (electronic version), ISSN 1503-8181.

"Low-velocity penetration of aluminium plates",
Frode Grytten, 2008:46, ISBN 978-82-471-6826-4 (printed version), ISBN 978-82-471-6843-1 (electronic version), ISSN 1503-8181.

"Robustness studies of structures subjected to large deformations",
Ørjan Fyllingen, 2008:24, ISBN 978-82-471-6339-9 (printed version), ISBN 978-82-471-6342-9 (electronic version), ISSN 1503-8181.

"Constitutive modelling of morsellised bone",
Knut Birger Lunde, 2008:92, ISBN 978-82-471-7829-4 (printed version), ISBN 978-82-471-7832-4 (electronic version), ISSN 1503-8181.

"Experimental Investigations of Wind Loading on a Suspension Bridge Girder",
Bjørn Isaksen, 2008:131, ISBN 978-82-471-8656-5 (printed version), ISBN 978-82-471-8673-2 (electronic version), ISSN 1503-8181.

"Cracking Risk of Concrete Structures in The Hardening Phase",
Guomin Ji, 2008:198, ISBN 978-82-471-1079-9 (printed version), ISBN 978-82-471-1080-5 (electronic version), ISSN 1503-8181.

"Modelling and numerical analysis of the porcine and human mitral apparatus",
Victorien Emile Prot, 2008:249, ISBN 978-82-471-1192-5 (printed version), ISBN 978-82-471-1193-2 (electronic version), ISSN 1503-8181.

"Strength analysis of net structures",
Heidi Moe, 2009:48, ISBN 978-82-471-1468-1 (printed version), ISBN 978-82-471-1469-8 (electronic version), ISSN1503-8181.

"Numerical analysis of ductile fracture in surface cracked shells",
Espen Berg, 2009:80, ISBN 978-82-471-1537-4 (printed version), ISBN 978-82-471-1538-1 (electronic version), ISSN 1503-8181.

"Subject specific finite element analysis of bone – for evaluation of the healing of a leg lengthening and evaluation of femoral stem design",
Sune Hansborg Pettersen, 2009:99, ISBN 978-82-471-1579-4 (printed version), ISBN 978-82-471-1580-0 (electronic version), ISSN 1503-8181.

"Evaluation of fracture parameters for notched multi-layered structures",
Lingyun Shang, 2009:137, ISBN 978-82-471-1662-3 (printed version), ISBN 978-82-471-1663-0 (electronic version), ISSN 1503-8181.

"Modelling of Dynamic Material Behaviour and Fracture of Aluminium Alloys for Structural Applications"
Yan Chen, 2009:69, ISBN 978-82-471-1515-2 (printed version), ISBN 978-82 471-1516-9 (electronic version), ISSN 1503-8181.

"Nanomechanics of polymer and composite particles"
Jianying He 2009:213, ISBN 978-82-471-1828-3 (printed version), ISBN 978-82-471-1829-0 (electronic version), ISSN 1503-8181.

"Mechanical properties of clear wood from Norway spruce"
Kristian Berbom Dahl 2009:250, ISBN 978-82-471-1911-2 (printed version) ISBN 978-82-471-1912-9 (electronic version), ISSN 1503-8181.

"Modeling of the degradation of TiB_2 mechanical properties by residual stresses and liquid Al penetration along grain boundaries"
Micol Pezzotta 2009:254, ISBN 978-82-471-1923-5 (printed version) ISBN 978-82-471-1924-2 (electronic version) ISSN 1503-8181.

"Effect of welding residual stress on fracture"
Xiabo Ren 2010:77, ISBN 978-82-471-2115-3 (printed version) ISBN 978-82-471-2116-0 (electronic version), ISSN 1503-8181.

"Pan-based carbon fiber as anode material in cathodic protection system for concrete structures"
Mahdi Chini 2010:122, ISBN 978-82-471-2210-5 (printed version) ISBN 978-82-471-2213-6 (electronic version), ISSN 1503-8181.

"Structural Behaviour of deteriorated and retrofitted concrete structures"
Irina Vasililjeva Sæther 2010:171, ISBN 978-82-471-2315-7 (printed version) ISBN 978-82-471-2316-4 (electronic version) ISSN 1503-8181.

"Prediction of local snow loads on roofs"
Vivian Meløysund 2010:247, ISBN 978-82-471-2490-1 (printed version) ISBN 978-82-471-2491-8 (electronic version) ISSN 1503-8181.

"Behaviour and modelling of polymers for crash applications"
Virgile Delhaye 2010:251, ISBN 978-82-471-2501-4 (printed version) ISBN 978-82-471-2502-1 (electronic version) ISSN 1503-8181.

"Blended cement with reducted CO_2 emission – Utilizing the Fly Ash-Limestone Synergy",
Klaartje De Weerdt 2011:32, ISBN 978-82-471-2584-7 (printed version) ISBN 978-82-471-2584-4 (electronic version) ISSN 1503-8181.

"Chloride induced reinforcement corrosion in concrete" Concept of critical chloride content – methods and mechanisms.
Ueli Angst 2011:113, ISBN 978-82-471-2769-9 (printed version) ISBN 978-82-471-2763-6 (electronic version) ISSN 1503-8181.

"A thermo-electric-Mechanical study of the carbon anode and contact interface for Energy savings in the production of aluminium".
Dag Herman Andersen 2011:157, ISBN 978-82-471-2859-6 (printed version) ISBN 978-82-471-2860-2 (electronic version) ISSN 1503-8181.

"Structural Capacity of Anchorage Ties in Masonry Veneer Walls Subjected to Earthquake". The implications of Eurocode 8 and Eurocode 6 on a typical Norwegain veneer wall.
Ahmed Mohamed Yousry Hamed 2011:181, ISBN 978-82-471-2911-1 (printed version) ISBN 978-82-471-2912-8 (electronic ver.) ISSN 1503-8181.

"Work-hardening behaviour in age-hardenable Al-Zn-Mg(-Cu) alloys".
Ida Westermann , 2011:247, ISBN 978-82-471-3056-8 (printed ver.) ISBN 978-82-471-3057-5 (electronic ver.) ISSN 1503-8181.

"Behaviour and modelling of selfpiercing riveted connections using aluminium rivets".
Nguyen-Hieu Hoang, 2011:266, ISBN 978-82-471-3097-1 (printed ver.) ISBN 978-82-471-3099-5 (electronic ver.) ISSN 1503-8181.

"Fibre reinforced concrete".
Sindre Sandbakk, 2011:297, ISBN 978-82-471-3167-1 (printed ver.) ISBN 978-82-471-3168-8 (electronic ver) ISSN 1503:8181.

"Dynamic behaviour of cablesupported bridges subjected to strong natural wind".
Ole Andre Øiseth, 2011:315, ISBN 978-82-471-3209-8 (printed ver.) ISBN 978-82-471-3210-4 (electronic ver.) ISSN 1503-8181.

"Constitutive modeling of solargrade silicon materials"
Julien Cochard, 2011:307, ISBN 978-82-471-3189-3 (printed ver). ISBN 978-82-471-3190-9 (electronic ver.) ISSN 1503-8181.

"Constitutive behavior and fracture of shape memory alloys"
Jim Stian Olsen, 2012:57, ISBN 978-82-471-3382-8 (printed ver.) ISBN 978-82-471-3383-5 (electronic ver.) ISSN 1503-8181.

“Field measurements in mechanical testing using close-range photogrammetry and digital image analysis”
Egil Fagerholt, 2012:95, ISBN 978-82-471-3466-5 (printed ver.) ISBN 978-82-471-3467-2 (electronic ver.) ISSN 1503-8181.

“Towards a better under standing of the ultimate behaviour of lightweight aggregate concrete in compression and bending”,
Håvard Nedrelid, 2012:123, ISBN 978-82-471-3527-3 (printed ver.) ISBN 978-82-471-3528-0 (electronic ver.) ISSN 1503-8181.

“Numerical simulations of blood flow in the left side of the heart”
Sigrid Kaarstad Dahl, 2012:135, ISBN 978-82-471-3553-2 (printed ver.) ISBN 978-82-471-3555-6 (electronic ver.) ISSN 1503-8181.

“Moisture induced stresses in glulam”
Vanessa Angst-Nicollier, 2012:139, ISBN 978-82-471-3562-4 (printed ver.) ISBN 978-82-471-3563-1 (electronic ver.) ISSN 1503-8181.

“Biomechanical aspects of distraction osteogensis”
Valentina La Russa, 2012:250, ISBN 978-82-471-3807-6 (printed ver.) ISBN 978-82-471-3808-3 (electronic ver.) ISSN 1503-8181.

“Ductile fracture in dual-phase steel. Theoretical, experimental and numerical study”
Gaute Gruben, 2012:257, ISBN 978-82-471-3822-9 (printed ver.) ISBN 978-82-471-3823-6 (electronic ver.) ISSN 1503-8181.

“Damping in Timber Structures”
Nathalie Labonnote, 2012:263, ISBN 978-82-471-3836-6 (printed ver.) ISBN 978-82-471-3837-3 (electronic ver.) ISSN 1503-8181.

“Biomechanical modeling of fetal veins: The umbilical vein and ductus venosus bifurcation”
Paul Roger Leinan, 2012:299, ISBN 978-82-471-3915-8 (printed ver.) ISBN 978-82-471-3916-5 (electronic ver.) ISSN 1503-8181.

“Large-Deformation behaviour of thermoplastics at various stress states”
Anne Serine Ognedal, 2012:298, ISBN 978-82-471-3913-4 (printed ver.) ISBN 978-82-471-3914-1 (electronic ver.) ISSN 1503-8181.

“Hardening accelerator for fly ash blended cement”
Kien Dinh Hoang, 2012:366, ISBN 978-82-471-4063-5 (printed ver.) ISBN 978-82-471-4064-2 (electronic ver.) ISSN 1503-8181.

“From molecular structure to mechanical properties”
Jianyang Wu, 2013:186, ISBN 978-82-471-4485-5 (printed ver.) ISBN 978-82-471-4486-2 (electronic ver.) ISSN 1503-8181.

"Experimental and numerical study of hybrid concrete structures"
Linn Grepstad Nes, 2013:259, ISBN 978-82-471-4644-6 (printed ver.) ISBN 978-82-471-4645-3 (electronic ver.) ISSN 1503-8181.

"Mechanics of ultra-thin multi crystalline silicon wafers"
Saber Saffar, 2013:199, ISBN 978-82-471-4511-1 (printed ver.) ISBN 978-82-471-4513-5 (electronic ver). ISSN 1503-8181.

"Through process modelling of welded aluminium structures"
Anizahyati Alisibramulisi, 2013:325, ISBN 978-82-471-4788-7 (printed ver.) ISBN 978-82-471-4789-4 (electronic ver.) ISSN 1503-8181.

"Combined blast and fragment loading on steel plates"
Knut Gaarder Rakvåg, 2013:361, ISBN978-82-471-4872-3 (printed ver.) ISBN 978-82-4873-0 (electronic ver.). ISSN 1503-8181.

"Characterization and modelling of the anisotropic behaviour of high-strength aluminium alloy"
Marion Fourmeau, 2014:37, ISBN 978-82-326-0008-3 (printed ver.) ISBN 978-82-326-0009-0 (electronic ver.) ISSN 1503-8181.

"Behaviour of threated steel fasteners at elevated deformation rates"
Henning Fransplass, 2014:65, ISBN 978-82-326-0054-0 (printed ver.) ISBN 978-82-326-0055-7 (electronic ver.) ISSN 1503-8181.

"Sedimentation and Bleeding"
Ya Peng, 2014:89, ISBN 978-82-326-0102-8 (printed ver.) ISBN 978-82-326-0103-5 (electric ver.) ISSN 1503-8181.

"Impact against X65 offshore pipelines"
Martin Kristoffersen, 2014:362, ISBN 978-82-326-0636-8 (printed ver.) ISBN 978-82-326-0637-5 (electronic ver.) ISSN 1503-8181.

"Formability of aluminium alloy subjected to prestrain by rolling"
Dmitry Vysochinskiy, 2014:363,, ISBN 978-82-326-0638-2 (printed ver.) ISBN 978-82-326-0639-9 (electronic ver.) ISSN 1503-8181.

"Experimental and numerical study of Yielding, Work-Hardening and anisotropy in textured AA6xxx alloys using crystal plasticity models"
Mikhail Khadyko, 2015:28, ISBN 978-82-326-0724-2 (printed ver.) ISBN 978-82-326-0725-9 (electronic ver.) ISSN 1503-8181.

"Behaviour and Modelling of AA6xxx Aluminium Alloys Under a Wide Range of Temperatures and Strain Rates"
Vincent Vilamosa, 2015:63, ISBN 978-82-326-0786-0 (printed ver.) ISBN 978-82-326-0787-7 (electronic ver.) ISSN 1503-8181.